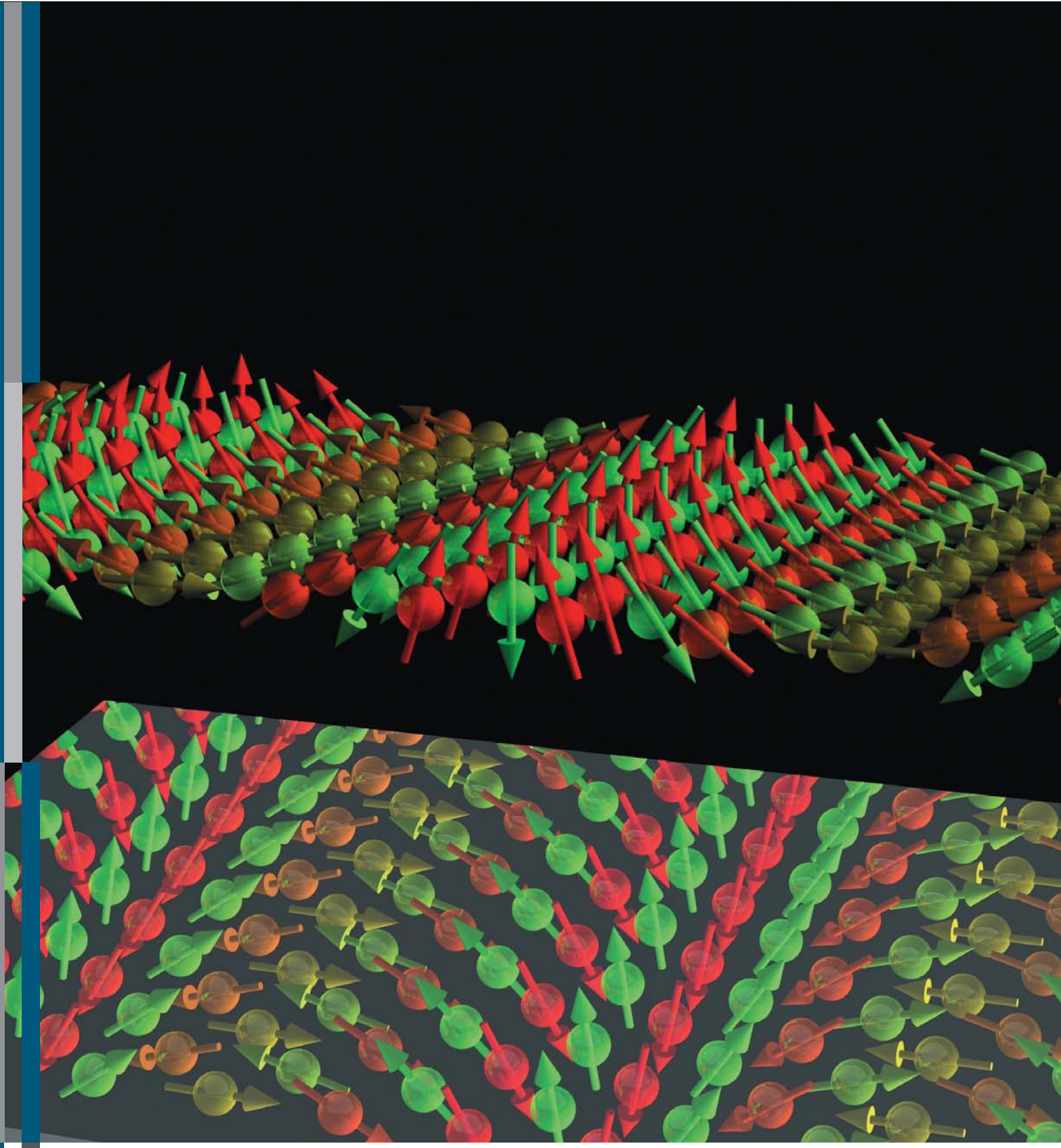

Scientific Report 2007

Institut für Festkörperforschung
Institute of Solid State Research

JÜLICH
FORSCHUNGSZENTRUM

Mitglied der Helmholtz-Gemeinschaft

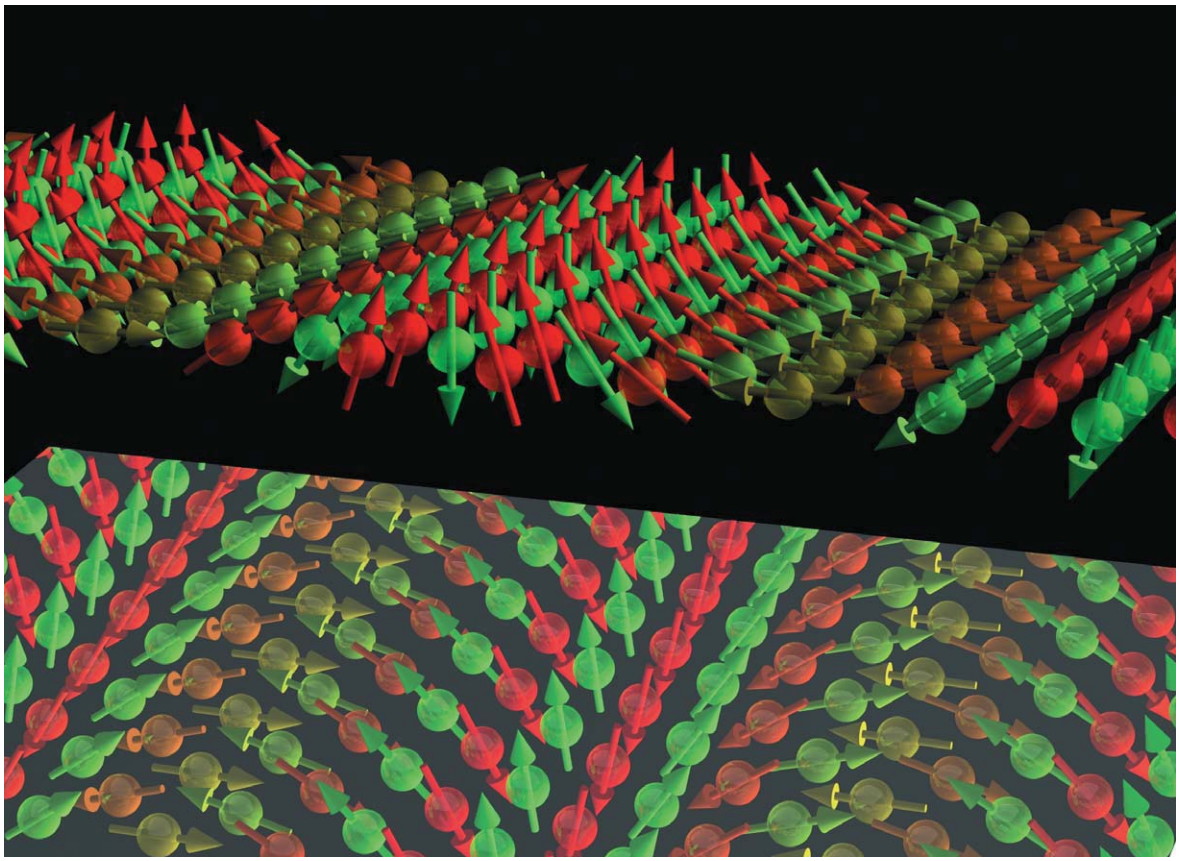

Homochiral magnetic order in a one-atomic layer thick film of Mn atoms on a W(110) surface. The local magnetic moments at Mn atoms shown as red and green arrows are aligned antiferromagnetically between nearest-neighbor atoms. Superimposed is a spiral pattern of unirotational direction.

The top picture shows a left-rotating cycloidal spiral, which was found in nature. The bottom picture shows the mirror image, a right rotating spiral, which does not exist. The work results from a collaboration between the IFF and the Institute of Applied Physics at the University of Hamburg. The results have been published in Nature 447, p190 (2007).

Scientific Report 2007

Institut für Festkörperforschung
Institute of Solid State Research

Contents

HGF Research Programme
Information Technology with Nanoelectronic Systems page 134

Research Reports

Directors of the Institute of Solid State Research (IFF) from left:

Prof. Dr. Jan K. G. Dhont (IFF-7: Soft Condensed Matter)
Prof. Dr. Knut Urban (IFF-8: Microstructure Research
Prof. Dr. Heiner Müller-Krumbhaar (IFF-3: Theory of Structure Formation)
Prof. Dr. Dieter Richter (IFF-5: Neutron Scattering)
Prof. Dr. Thomas Brückel (IFF-4: Scattering Methods)
Prof. Dr. Stefan Blügel (IFF-1: Quantum Theory of Materials)
Prof. Dr. Rainer Waser (IFF-6: Electronic Materials)
Prof. Dr. Claus M. Schneider (IFF-9: Electronic Properties)
Prof. Dr. Gerhard Gompper (IFF-2: Theoretical Soft-Matter and Biophysics)

Foreword

Slowly approaching its 40th anniversary, with the year 2007 the IFF experienced one of the most important and spectacular periods of its history. The events which happened in the course of this year will have far-reaching consequences for the IFF, the Forschungszentrum Jülich, and the entire region.

The annual report 2007 is intended to inform the international scientific community, including our scientific advisory board and the gremia of the Helmholtz-Gesellschaft (HGF) about the IFF activities in science and science policy during the past year. We have attempted to present a typical cross section through the research done at the IFF, including scientific highlights as well as results of long-term developments, e.g. the construction of new instruments at large scale facilities. These contributions also reflect the participation of the IFF in the Helmholtz-Research Programmes "Condensed Matter Physics", "Information Technology with Nanoelectronic Systems", and "Photons, Neutrons, and Ions".

The most prominent event in 2007 which generated an enormous public response was doubtlessly the news that the Nobel Prize in Physics went to Prof. Peter Grünberg and Prof. Albert Fert (Paris) for the discovery of the Giant Magnetoresistance (GMR). Being announced on October 9 and presented by the Swedish king on December 10, the Nobel Prize was the crowning of Peter Grünberg's scientific career and at the same time a glaring acknowledgement of the importance of fundamental research for future technologies. Peter Grünberg also received the first Helmholtz Professorship which enables him to pursue his research interests in the fields of magnetism and spinelectronics in the upcoming years.

Another event with far-reaching consequences for the IFF was the foundation of the Jülich-Aachen Research Alliance (JARA), which is going to put the collaboration between the RWTH Aachen and Jülich on an entirely new level. JARA provides the framework to expand and strengthen research and education in a joint effort of both partners. This effort was already yielding fruit in October 2007 when RWTH Aachen was promoted to the rank of an elite university. JARA-FIT being the section concerned with the Fundamentals of Future Information Technology will coordinate the research activities in this area between the IFF institutes and partner institutes at the RWTH. It will also provide the platform for strategic decisions.

The Jülich Centre for Neutron Science (JCNS) continues to implement state-of-the-art instrumentation at the FRM II in Munich, at the spallation neutron source SNS in Oak Ridge (USA), and at the Institute Laue Langevin ILL in Grenoble, France. Several instruments were successfully relocated to the FRM II and went into operation. The Ernst Ruska Center (ER-C) takes another step forward in the field of high-resolution electron microscopy and started with construction of a new building, which is specifically designed to house the new generation of aberration-corrected microscopes. The Nano-Spintronics Cluster Tool went into operation and will enable new experiments in nano-magnetism. The IFF was also particularly successful in establishing new Young Investigator Groups for Dr. Raphaël P. Hermann (Lattice Dynamics in Emerging Functional Materials), Dr. Marjana Lezaic (Computational Nanoferronics Laboratory), and Dr. Maarten Wegewijs (Single-Molecule Quantum Transport).

The quality of the research at the IFF is widely accepted and honoured by the scientific community. This is not only reflected by the numerous awards, for example, the Ikeda Award to Prof. Waser, but also a successful mid-term review of our research programmes in October 2007. Being awarded the prestigious Helmholtz-v. Humboldt Research Prize, Prof. Dr. Tomoya Ono from Osaka University (Japan) has chosen the IFF as his host institute for the development of first-principles electronic structure calculation codes and will use the new supercomputing facilities of the Research Centre.

The 2007 Nobel Prize in Physics has once more highlighted the importance of scientific curiosity and open-mindedness. These are the main driving forces of our research in the IFF. Our task – particularly with respect to the societal challenges, which lie ahead of us – is to leave the beaten tracks and break new scientific ground, bringing forward new ideas, which may form the basis for new technologies.

I hope you will enjoy reading the report and learning about our activities.

Prof. Claus M. Schneider
Managing Director of IFF in 2008
Director of IFF-9 "Electronic Properties"
April 2008

Snapshots 2007

Congratulations to Peter Grünberg!

10 December 2007: An important moment for Prof. Peter A. Grünberg (left): The King of Sweden Carl Gustav presenting the IFF researcher with the Nobel Prize for Physics 2007. The celebrations in Stockholm provide the perfect conclusion to a memorable year for the solid-state physicist who received numerous high-ranking prizes in 2007 for his discovery of giant magnetoresistance (GMR).

Photo: The Nobel Foundation 2007, Hans Mehlin

11 January:
Japan Prize Goes to Peter Grünberg

Prof. Peter Grünberg was announced as the winner of the Japan Prize 2007. He shared the prize in the category "Innovative Devices Inspired by Basic Research" with Prof. Albert Fert from the Université Paris-Sud. The internationally prestigious prize was presented in April by Emperor Akihito. The two solid-state physicists received the award in honour of their work on giant magnetoresistance (GMR).

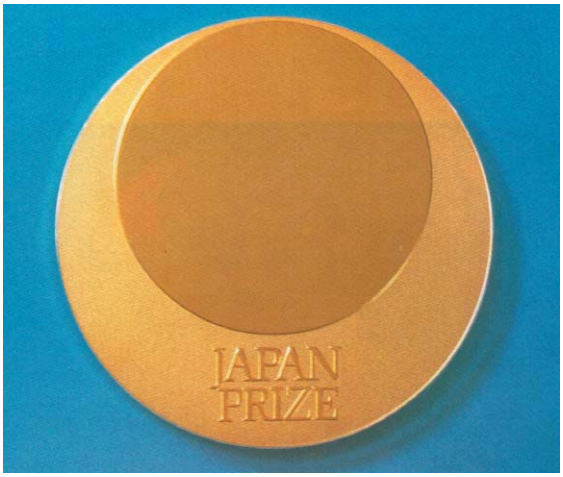

The Japan Prize medal

Photo: The Science and Technology Foundation of Japan

16 January:
Peter Grünberg Wins Israeli "Wolf Prize"

Israel's world-famous "Wolf Prize" was awarded to Prof. Peter Grünberg. He shared the prize in the field of physics with Prof. Albert Fert from the Université Paris-Sud. The prize was presented in the Knesset by the Israeli President in May. The two solid-state physicists received the prize for their discovery of giant magnetoresistance.

Prof. Peter Grünberg receives his certificate from Dalia Itzik, Acting President of the State of Israel.

Photo: Sasson Tiram

28 March:
Jülich Scientist Wins DPG's Highest Award

The coveted Stern-Gerlach Medal of the German Physics Society (DPG) was awarded to Prof. Peter Grünberg at the DPG Annual Meeting in Regensburg. The solid-state physicist received the medal for his discovery of giant magnetoresistance. In their statement, the jury said that Grünberg's work "initiated a new field of research known as spintronics and led to revolutionary progress in the field of magnetic storage devices".

3 April:
Alexander von Humboldt Research Fellow to Work at IFF

Dr. Tomoya Ono from Osaka University, Japan, began his Alexander von Humboldt research fellowship at IFF-1. During his twelve-month stay, he will focus on the development of first-principle calculation codes for electronic structures. Ono develops and uses such calculations mainly to explore the interactions

of surfaces and atoms or molecules, as well as the quantum transport of nanoscale structures. The determination of the electronic properties of atomic-scale structures is attracting more and more interest, as the miniaturisation of electronic devices progresses. Ono's decision to come to Jülich was based on his conviction that his simulations of electron transport and IFF's simulations of spin transport will complement each other well. This is his fourth time at IFF so far.

First-principle calculations need immense computer power. Ono's real-space code is suitable for massively parallel computers such as the IBM Blue Gene/L "JUBL". Ono will work with the Jülich supercomputer.

May:
JCNS Moves into New Building at FRM II

Jülich scientists moved into their outstation at the FRM II research reactor in Munich. A total of 30 staff members from the Jülich Centre for Neutron Science (JCNS) are now working and conducting research on a permanent basis in Garching near Munich. They are setting up and looking after the seven measuring instruments that were previously located in Jülich and are worth around € 45 million. The Free State of Bavaria constructed an experimental hall in order to house the instruments right beside the research reactor. Germany's most powerful neutron source and the most sensitive measuring instruments have thus been combined.

Excellent Training for Ph.D. Students in the First Jülich-Helmholtz Research School

An official ceremony marked the foundation of the "International Helmholtz Research School on Biophysics and Soft Matter" (IHRS-BioSoft). The Research School run jointly by Research Centre Jülich, Heinrich Heine University of Düsseldorf and the University of Cologne offers highly qualified graduates from all over the world structured doctoral training in the fields at the boundary between physics and biology. It teaches Ph.D. students how to investigate complex biological systems, beginning with the interaction of macromolecules extending up to the function of the cell as a whole. In this manner, IHRS enhances the traditional courses in biology, physics and chemistry with its interdisciplinary curriculum.

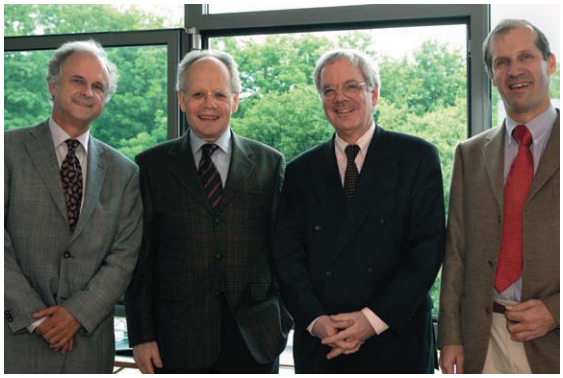

The two spokesmen of IHRS-BioSoft, Prof. U. Benjamin Kaupp (left, INB-1) and Prof. Gerhard Gompper (right, IFF-2), Prof. Alfons Labisch (second from the left, Rector of the Heinrich Heine University Düsseldorf) and Prof. Achim Bachem (second from the right, Chairman of the Board of Directors of Forschungszentrum Jülich).

19 June:
Andreas Pinkwart and Thomas Rachel Learn More about Nanoelectronics at Jülich

Prof. Andreas Pinkwart (middle right) and Thomas Rachel (middle left) follow the change in electrical resistance on the monitor, which shows the sensor's position in an external magnetic field.

Photo: Kampert

At the largest European conference on nanotechnology, the EuroNanoForum 2007 in Düsseldorf, NRW Innovation Minister Andreas Pinkwart and Thomas Rachel, Parliamentary State Secretary of the Federal Ministry of Education and Research, learned more about the work of Forschungszentrum Jülich in the field of nanoelectronics. A demonstration model from IFF showcased Jülich's research and revealed how GMR sensors work. Pinkwart and Rachel were impressed by the success story of this Jülich discovery, which has made its way from basic research to industrial application within an exceptionally short period.

29 June:
JDZB Science Award Goes to Hiroshi Noguchi

Dr. Hiroshi Noguchi was awarded the Science Award 2006 of the Japanese-German Center Berlin (JDZB). The theoretical physicist received the award for his achievements and publications in the field of biophysics and soft matter. Noguchi focuses on computer simulations of membrane properties such as the coating layers of red blood cells and their flow behaviour. The prize aims to promote young scientists in Germany and Japan and is awarded annually to a Japanese scientist in Germany and a German scientist in Japan for outstanding scientific achievements.

Dr. Hiroshi Noguchi, IFF (left);
Prof. Günter Stock, President of the Berlin-Brandenburg Academy of Sciences (right)

Photo: Japanese-German Center Berlin

1 – 4 October:
Hard Facts on Soft Matter
More than 600 researchers from science and industry attended the first "International Soft Matter Conference" in Aachen. The conference focused on biological and biomimetic systems in particular. Forschungszentrum Jülich has held "Soft Matter Days" since 2001.

Researchers from science and industry attended presentations and lectures at the first international conference organised by IFF on soft matter.

30 October:
Foundation of the German Research School for Simulation Sciences
The Research School for Simulation Sciences GmbH (GRS) was founded by Forschungszentrum Jülich and RWTH Aachen University. The GRS will be jointly financed – initially for a period of five years – by BMBF, MIWFT-NRW, the Helmholtz Association, RWTH Aachen University and the Research Centre. Prof. Heiner Müller-Krumbhaar from IFF and Manfred Nettekoven, Chancellor of RWTH Aachen University, were jointly appointed as managing directors.

19 November:
Helmholtz Professorship for Peter Grünberg
Forschungszentrum Jülich awarded Prof. Peter Grünberg the first Helmholtz Professorship, thus making sure that his expertise remains in Jülich. The Nobel Laureate in Physics intends to use the resources provided by this position to continue research on spintronics together with his team at IFF.

From left to right: Prof. Peter Grünberg, Dr. Annette Schavan, Federal Research Minister, Prof. Achim Bachem, Chairman of the Board of Directors of Forschungszentrum Jülich und Thomas Rachel, State Secretary of the Federal Ministry of Education and Research.

23 November:
RWTH Honorary Doctorate for Peter Grünberg
Together with Albert Fert and IBM expert Dr. Stuart Parkin, Prof. Peter Grünberg was awarded an honorary doctorate by RWTH Aachen University.

Awards, Honours, Scholarships

Awards, Honours, Scholarships

- Dr. Sergiy Balanetskyy was awarded the "Prize for Young Scientists" by the National Academy of Sciences of Ukraine.
- Sabrina Disch was awarded a scholarship by the German National Academic Foundation ("Studienstiftung des deutschen Volkes").
- Dr. Jens Elgeti was awarded the Günter-Leibfried-Preis 2007.
- Prof. Peter Grünberg was awarded:
  - the Stern-Gerlach Medal by the German Physics Society (DPG),
  - the "Wolf Prize" by the Israeli President, which he shared with the French physicist Prof. Albert Fert,
  - the "Japan Prize" by the Japanese Emperor, which he shared with Albert Fert,
  - the Nobel Prize in Physics, which he shared with Albert Fert,
  - the first Helmholtz Professorship, and
  - an Honorary Doctorate by RWTH Aachen Universtiy.
- Dr. Björn Lüssem was awarded the "Promotionspreis" by VDE North Rhine-Westphalia.
- Dr. Hiroshi Noguchi was awarded the Science Award of the Japanese-German Center Berlin (JDZB).
- Prof. Takao Ohta was awarded the Humboldt Research Award.
- Dr. Tomoya Ono from Osaka University, Japan, started his twelve-month Alexander von Humboldt research fellowship at IFF.
- Dr. Keisuke Shibuya received an award from the Marubun Research Promotion Foundation.
- Prof. Rainer Waser was awarded the Ikeda Award by the Ikeda Memorial Foundation (Japan).
- Dr. Martin Weides was awarded the "Klaus Liebrecht Preis" by the University of Cologne.

Appointments

- Prof. Thomas Brückel was appointed Vice Chairman Instrument Advisory Committee at Laboratoire Leon Brillouin LLB, France.
- Prof. Heiner Müller-Krumbhaar was appointed member of the Strategy Commission for Supercomputing at the French research ministry.
- Dr. Eva Pavarini was appointed professor of theoretical physics at RWTH Aachen University. She is also head of the "Strongly Correlated Electron Systems" group in IFF-3: "Theory of Structure Formation" and follows Prof. Peter H. Dederichs in this position.
- Prof. Dr. Dieter Richter was appointed member of the NanoGUNE Advisory Board (Nanoscience initiative of the Basque country).

New Helmholtz Young Investigator Groups

- Dr. Raphaël P. Hermann: "Lattice Dynamics in Emerging Functional Materials."
- Dr. Marjana Lezaic: "Computational Nanoferronics Laboratory".
- Dr. Maarten Wegewijs: "Single-Molecule Quantum Transport".

Institute of Solid State Research (IFF)

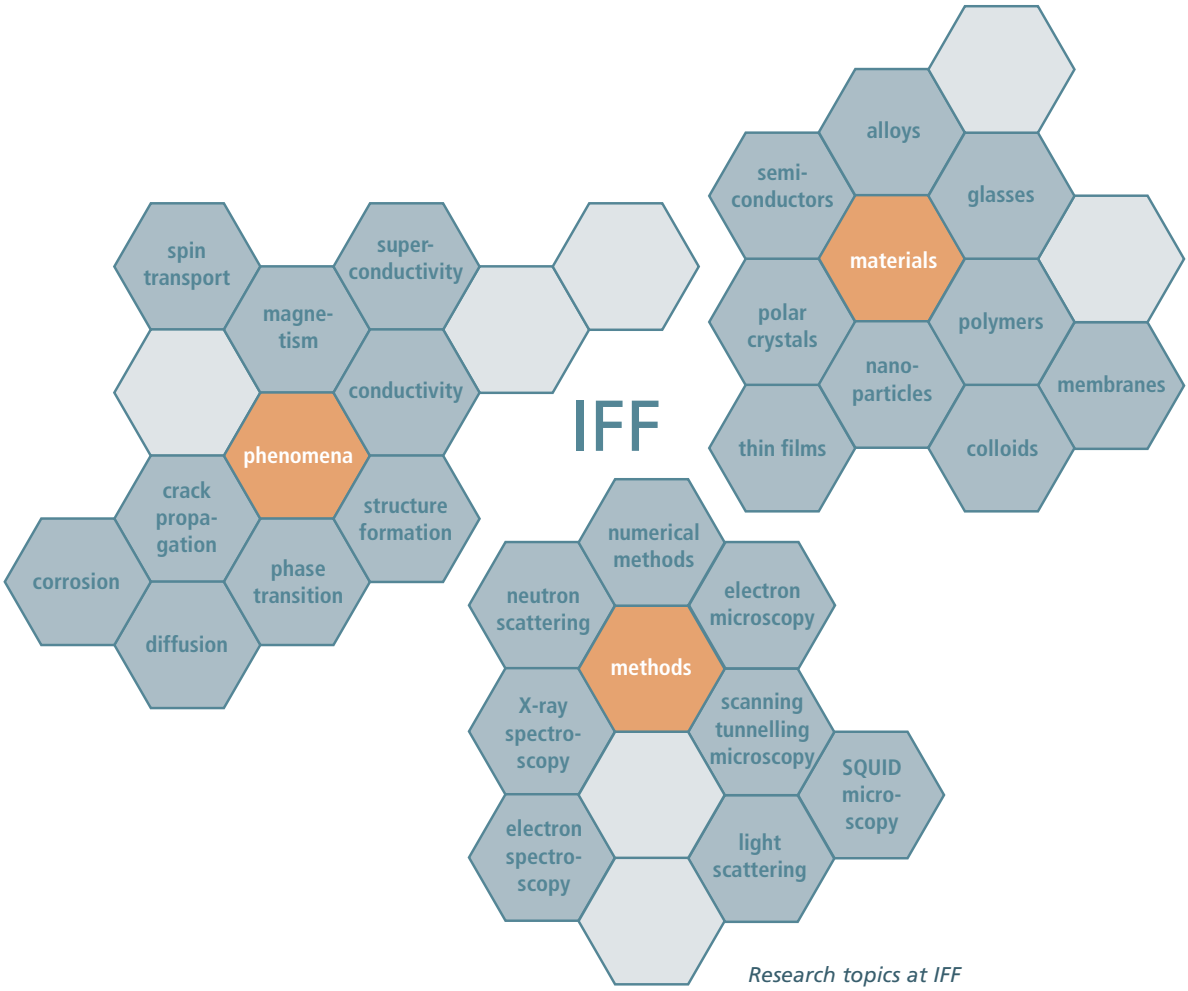

Research topics at IFF

Founded in 1969, the scientific reputation of the Institute of Solid State Research (Institut für Festkörperforschung – IFF) still owes much to the conception of its founders that new discoveries are made at the boundaries of disciplines. This is as true today as it was almost forty years ago. In this spirit, the IFF has pioneered new research fields such as spintronics and set trends towards multi- and cross-disciplinary activities in both fundamental research as well as technological innovations.

Today, the IFF is engaged in investigating a multitude of condensed matter phenomena with special emphasis on three prime objectives:

- studies of fundamental physical mechanisms and phenomena of condensed matter,
- the development and improvement of experimental and theoretical analysis methods, as well as
- the elucidation and utilization of new material properties in complex systems.

The corresponding research programmes follow the main theme to exploit the full scale of analytical and numerical methods to elucidate interrelations between structural, electronic, and magnetic properties of the solid state together with describing underlying physical mechanisms.

Research efforts are directed at obtaining a microscopic and atomistic understanding of phenomena based on fundamental interaction mechanisms. Research at the IFF rests firmly on quantum mechanics and statistical physics. On a microscopic scale, they describe the interaction of electrons and atomic building blocks and determine how these entities respond to external influences. Particular strengths encompass the theory of electronic structures, clusters and polymer physics, micromechanics of lattice imperfections, the dynamics of structure formation and phase transitions, materials and phenomena of magneto- and nanoelectronics, spintronics, spin dynamics, strongly correlated electron systems, as well as the instrumentation of electron, neutron, and synchrotron sources and their application to the study of condensed matter.

The experimental portfolio together with an acknowledged expertise enables the IFF to tackle complex problems in close cooperation with scientists and industry worldwide. Special state-of-the-art laboratories exist for thin film deposition and growth of bulk crystals as well as for the preparation of soft matter materials. In addition to standard methods for materials characterization, highly specialized techniques ranging from superconducting microscopy and spinpolarized microscopies to femtosecond laser spectroscopy are available at the IFF and are being constantly improved in performance.

Ernst Ruska-Centre
for
Microscopy and Spectroscopy
with
Electrons
ER-C

With the Ernst Ruska-Centre for Microscopy and Spectroscopy with Electrons (ER-C) the IFF operates a national user facility housing several of the world's most advanced electron microscopes and tools for nanocharacterization. In-house research programmes cover topical issues in condensed matter physics and – as a matter of course – future developments of subångström and sub-electronvolt microscopy.

JCNS
Jülich Centre for Neutron Science

The Jülich Centre for Neutron Science (JCNS) operates advanced neutron scattering instruments at the worldwide most modern and highest flux neutron sources. As a complement to local research opportunities, instruments are designed and operated at external national and international neutron sources, such as the FRM II in Munich or the neutron spallation source in Oak Ridge, USA.

JCCSS

Within the framework of the Jülich Competence Centre for Synchrotron Science (JCCSS) a broad variety of spectroscopy, microscopy, and scattering experiments at various synchrotron radiation facilities are designed and realized. The centre also provides expertise for the development of new beamlines and experimental concepts and, thus, acts as a valuable partner for synchrotron radiation laboratories throughout the world.

cni

The international networking of the IFF is a main pillar of its success; the institute initiated two EU Networks of Excellence (NoE) , “Soft Matter Composites” and “Complex Metallic Alloys”, and co-founded the Centre of Nanoelectronic Systems for Information Technology (CNI). CNI is a center of excellence for nanoelectronics at the Research Center Juelich and provides an excellent basis for future developments of nanoelectronics and information technology. To identify technology drivers the research areas cover quantum-electronics, magneto-electronics, ferro-electric and molecular nanostructures as well as Terahertz-electronics and bioelectronic signal processing.

The IFF is partner of more than one hundred universities and research institutions from all around the world.

Last but not least, the IFF has a long tradition in the teaching and training of students, not only through the approximately 30 IFF staff scientists steadily giving lectures at universities, but in particular through the annual IFF Spring Schools, Neutron Laboratory Courses, and the Nanoelectronic Days.

Actually representing a department, the IFF currently comprises six experimental and three theoretical divisions as well as joint service facilities, which, however, cannot be regarded separately. The divisions present themselves on the following pages.

Being an institute of the Forschungszentrum Jülich – itself belonging to the Hermann von Helmholtz Association of German Research Centres (HGF) – the IFF provides key contributions to the strategic mission of the Helmholtz Association within three research programmes:

- Condensed Matter Physics (pages 30 – 133),
- Large-Scale Facilities for Research with Photons, Neutrons, and Ions (pages 134 – 197),
- Information Technology with Nanoelectronic Systems (pages 198 – 219).

As a matter of fact, much of the success of the IFF rests upon the inventiveness and initiative of its more than 300 staff members. The IFF supports independent research by encouraging the responsibility of individual scientists – a philosophy that contributes greatly to the stimulating atmosphere in the department. In order to sustain this level on the long run, special encouragement is given to young scientists.

The casual observer may be struck by the wide range of topics and extensive networking at the IFF, whose strength is to link complex issues together with its scientific and industrial partners. In the sixties, Germany seemed to be about to miss the boat in solid-state research. The success of the IFF demonstrates, how a leading global position may be achieved by a sound and clear-sighted research strategy, which is able to identify and address new developments and challenges at an early stage.

Department IFF

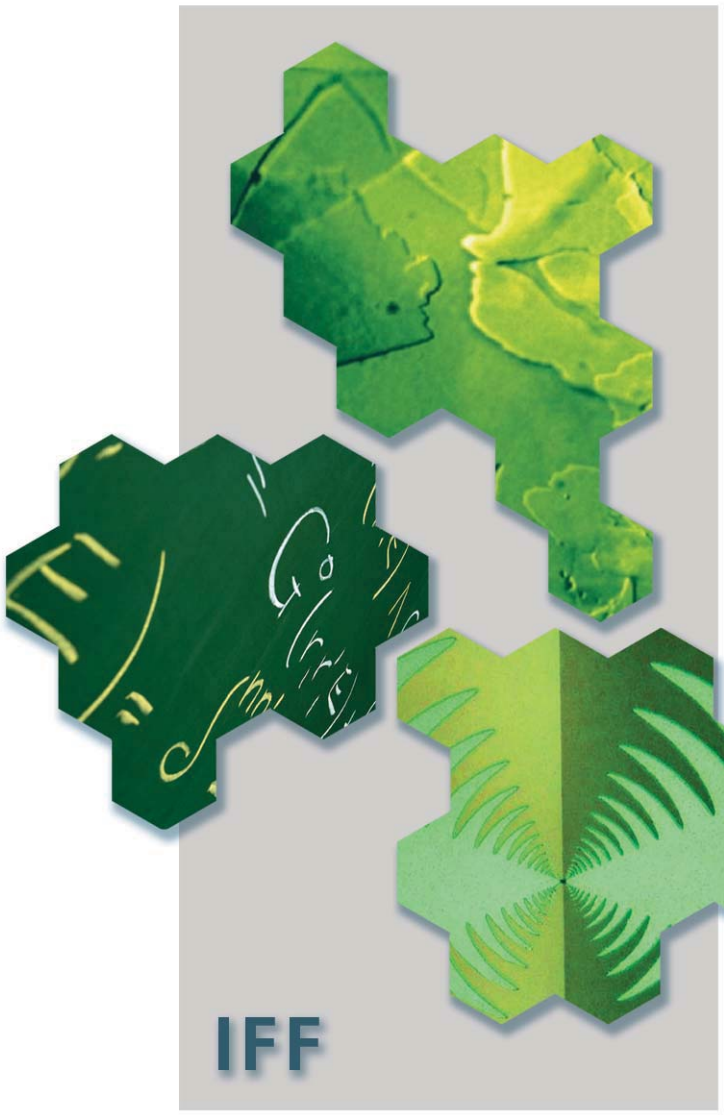

comprising the Institutes

IFF-1:	Quantum Theory of Materials	Prof. Dr. Stefan Blügel
IFF-2:	Theoretical Soft-Matter and Biophysics	Prof. Dr. Gerhard Gompper
IFF-3:	Theory of Structure Formation	Prof. Dr. Heiner Müller-Krumbhaar
IFF-4:	Scattering Methods	Prof. Dr. Thomas Brückel
IFF-5:	Neutron Scattering	Prof. Dr. Dieter Richter
IFF-6:	Electronic Materials	Prof. Dr. Rainer Waser
IFF-7:	Soft Condensed Matter	Prof. Dr. Jan K. G. Dhont
IFF-8:	Microstructure Research	Prof. Dr. Knut Urban
IFF-9:	Electronic Properties	Prof. Dr. Claus M. Schneider

IFF-1: Quantum Theory of Materials

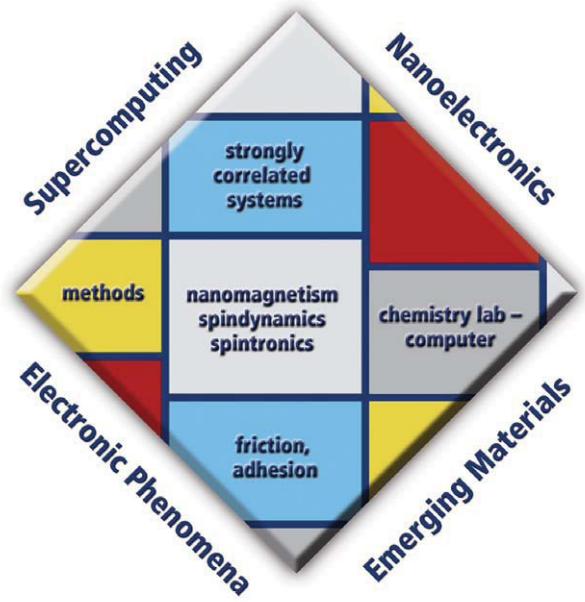

A major focus at "Quantum-Theory of Materials" is the analysis and computation of structural, electronic, magnetic, transport and chemical properties and processes in molecules and solids, in terms of both basic research and practical applications. The goal is to achieve a microscopic understanding of such complex phenomena.

Our research covers key areas of condensed matter theory, computational materials science, nanoelectronics and supercomputing. We explore the electronic and structural properties of systems from large organic (including biological) molecules, low-dimensional magnets, and magnetic multilayers, to complex solids. We consider transport properties across interfaces and molecules as relevant for spintronics and molecular electronics. We investigate the electronic excitations, and dynamical properties of atomic and molecular clusters, solids, and solid surfaces, as well as the quasiparticle behaviour of semiconductors, oxides and transition metals that results from electronic correlations. We analyze the physics of strongly correlated materials such as transition-metal oxides and molecular crystals paying particular attention to complex ordering phenomena. Other areas include nanoscale tribology, including friction, plastic deformation, adhesion, and brittle fracture, as well as nonlinear processes in the atmosphere and agrosphere.

A major asset of our institute is the competence in developing conceptual and computational methods based on density functional theory, molecular dynamics simulations, and Quantum Monte Carlo methods.

IFF-2: Theoretical Soft-Matter and Biophysics

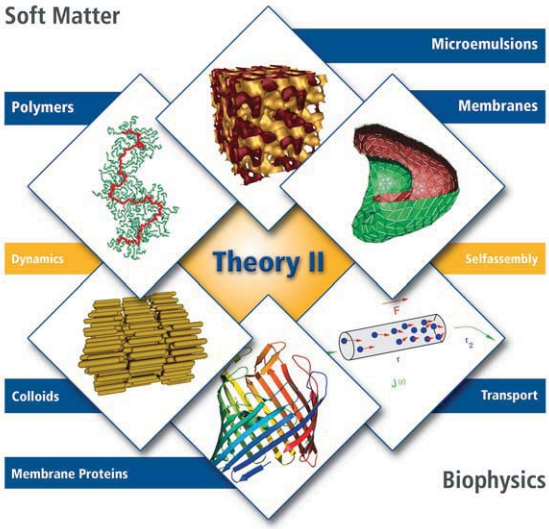

The main research topic of the Institute "Theoretical Soft Matter and Biophysics" is the theory of macromolecular systems. Soft matter physics and biophysics are interdisciplinary research areas encompassing statistical physics, materials science, chemistry, and biology. Our systems of interest include polymer solutions and melts, colloidal suspensions, membranes, vesicles and cells, but also composite systems ranging from colloids in polymer solutions to mixtures of surfactants and amphiphilic block copolymers. A major focus is the hydrodynamic behaviour of complex fluids and biological systems, both in equilibrium and under flow conditions.

At IFF-2, a large variety of methods are applied. In fact, a combination of analytical and numerical methods is often required to successfully characterize the properties of these complex systems. In particular, simulation methods (Monte Carlo, molecular dynamics), mesoscale hydrodynamic simulation techniques, field theory, perturbation theory, and exact solutions are employed. Since the building blocks of soft matter systems often contain a large number of molecules, "simplified" mesoscale modelling is typically required, which is then linked to the molecular architecture.

A characteristic feature of soft-matter research is the fruitful interaction between theory and experiment. IFF-2 closely cooperates with the Institute for Neutron Scattering (Prof. Richter) and the Institute for Soft Condensed Matter (Prof. Dhont) to successfully tackle many of the essential aspects of the systems investigated.

IFF-3: Theory of Structure Formation

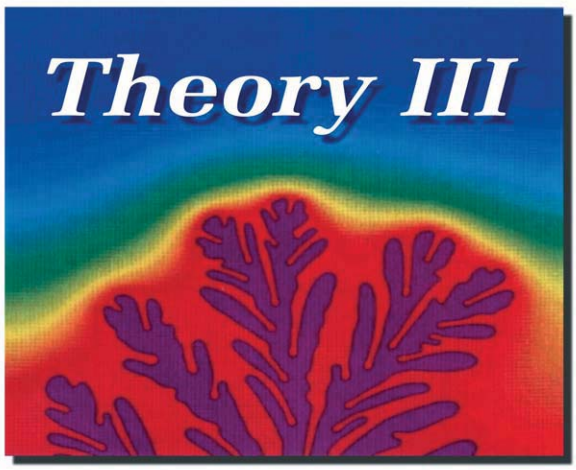

The research of the Institute "Theory of Structure Formation" is concerned with the mechanisms of the formation of structures and their consequences in condensed matter. The investigations start from electronic properties which define the shortest length and time scales, but they also encompass the macroscopic consequences. The analytical and numerical studies are in many ways closely connected to experimental research performed in other groups of the IFF, but also to activities in other Jülich institutes. The institute contributes mainly to the research programmes "Condensed Matter Physics" and "Information Technology with Nanoelectronic Systems" of the Research Centre.

Central points of interest for the research at IFF-3 are in the field of electronic structure of solids, in particular effects of strong electronic correlations. A specific interest concerns materials relevant for Information technology. A second mainstream is formed by cooperative phenomena in condensed matter. Questions here aim at the dynamics of structure and pattern formation and the statistical mechanics of order and disorder processes. Specific activities concern the effect of long-range interactions like elastic effects in solids, friction and fracture phenomena, or hydrodynamic interactions in solid-liquid systems.

The research of IFF-3 employs all analytical and numerical techniques applicable to many-body problems of equilibrium and non-equilibrium phenomena in condensed matter. In addition, the development of new methodological concepts and numerical procedures is part of our research interest. The development of parallel programme codes adapted to massively parallel computers has received special attention in recent years.

IFF-4: Scattering Methods

At the Institute for Scattering Methods, we focus on the investigation of structural and magnetic order, fluctuations and excitations in complex or nanostructured magnetic systems and highly correlated electron systems. Our research is directed at obtaining a microscopic atomic understanding based on fundamental interaction mechanisms. The aim is to relate this microscopic information to macroscopic physical properties. To achieve this ambitious goal, we employ the most advanced synchrotron X-ray and neutron scattering methods and place great emphasis on the complementary use of these two probes. Some of our efforts are devoted to dedicated sample preparation and characterization from thin films and multilayers via nano-patterned structures to single crystals for a wide range of materials from metals to oxides.

A significant part of our activity is devoted to the development of novel scattering techniques and the construction and continuous improvement of instruments at large facilities in the framework of the Jülich Centre for Neutron Science JCNS and the Jülich Competence Centre for Synchrotron Science JCCSS.

IFF-5: Neutron Scattering

The Institute for Neutron Scattering is concerned with neutron research placing major emphasis on soft condensed matter, i.e. materials that react strongly to weak forces. Neutron scattering is a valuable tool for these systems because it reveals structure and dynamics of Soft Matter on the relevant length- and timescales.

A major part of the Soft Matter studies is done on polymers. Apart from their structure, we are interested in the dynamics of polymers in melts and solutions (e.g. gels, rubbery networks, aggregates). These polymers often have a complex architecture (copolymers, star-polymers etc.) to tailor them for industrial applications. Another field of interest are complex liquids such as microemulsions or colloid systems. Finally, biological materials (e.g. proteins) are studied concerning their structure and dynamics.

The institute has modern chemical laboratories for the synthesis, characterisation, and modification of Soft Matter. In order to complement neutron scattering experiments several ancillary techniques are used in the institute: rheology, light scattering, calorimetry, x-ray scattering, impedance spectroscopy, and computer simulation.

The Institute for Neutron Scattering is partner in the Jülich Centre for Neutron Science JCNS. In this position it operates several neutron scattering instruments at the research reactor FRM II in Munich, at the Institut Laue-Langevin in Grenoble, and at the Spallation Neutron Source in Oak Ridge, USA. These instruments are available to guest researchers on request. Another focus of research is the development of neutron instrumentation for research reactors and future spallation sources worldwide.

IFF-6: Electronic Materials

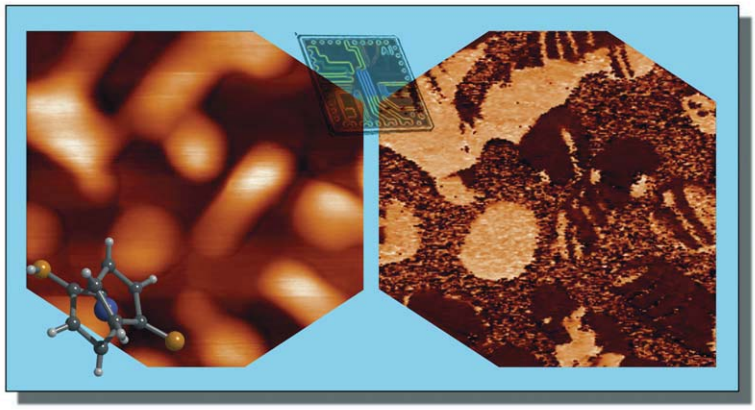

The Institute of Electronic Materials focuses on the physics and chemistry of electronic oxides and organic molecules, which are promising for potential memory, logic, and sensor functions. Our research aims at the fundamental understanding of nanoelectronic functions based on ferroelectricity, piezoelectricity, space charge effects, and electrochemical redox processes and at the elucidation of their potential for future device application.

In particular, true non-volatility and extended scaling represent the two major issues of Random Access Memories (RAM) dealt with in our institute. In the area of charge-based RAM, our research focuses on the scalability of ferroelectric RAM with respect to the vertical and lateral scaling limits. In addition, the impact of interfaces in epitaxial ferroelectric and superparaelectric thin films on the polar properties is investigated. In the area of resistance-based RAMs, we aim at the classification, the elucidation, and the subsequent exploitation of redox-based hysteretic switching phenomena. Other resistance switching phenomena such as the phase-change mechanism and potential tunneling-based effects are studied for comparison. Our research in technology aims at the deposition of ultrathin oxide films on 3D-structured surfaces by e. g. atomic layer deposition (ALD) and template growth techniques of nanostructures.

For execution these studies, our institute provides a broad spectrum of facilities reaching from dedicated material synthesis, atomically controlled film deposition methods, molecular self-assembly routes, and integration technologies, to the characterisation of processes, structures, and electronic properties with atomic resolution.

IFF-7: Soft Condensed Matter

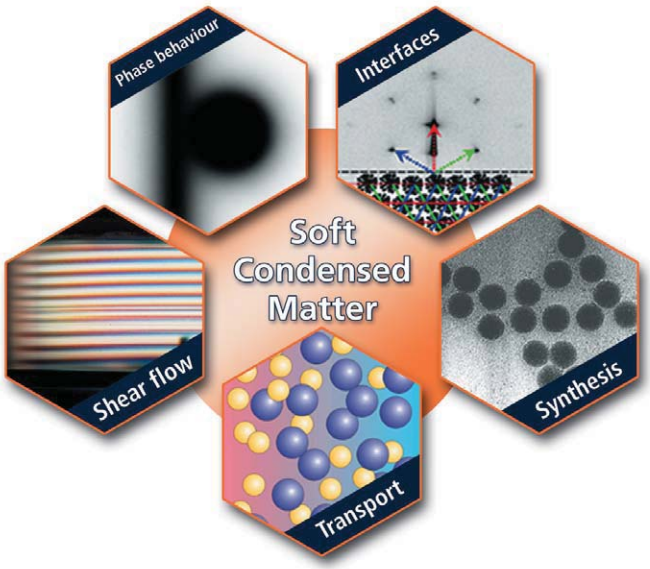

The Soft Condensed Matter group investigates the chemistry and physics of colloidal systems. Colloidal systems can be regarded as solutions of very large molecules which exhibit phase transitions and show non-equilibrium phenomena that are also found for simple molecular systems. Due to the slow dynamics of colloids and the tuneable interactions between the colloidal particles, however, there are many transitions and non-equilibrium phenomena that do not occur in simple molecular systems, like gellation and shear-band formation. The aim is to understand structure, dynamics and non-equilibrium phenomena on a microscopic basis with an open eye for possible technological applications.

The main topics that are studied include,

- the phase behaviour, pattern formation, phase separation kinetics and dynamics of suspensions of spherical and rod-like colloids under shear flow,
- mass transport induced by temperature gradients,
- dynamics and micro-structural properties of colloidal systems near walls and interfaces,
- the effects of pressure on interactions, the location of phase transition lines and gellation transitions and the dynamics of colloids and polymers,
- response of colloids to external electric fields,
- the equilibrium phase behaviour of mixtures of colloids and polymer-like systems,
- dynamics of various types of colloidal systems in equilibrium, and
- the synthesis of new colloidal model particles, with specific surface properties, interaction potentials and particle geometries.

IFF-8: Microstructure Research

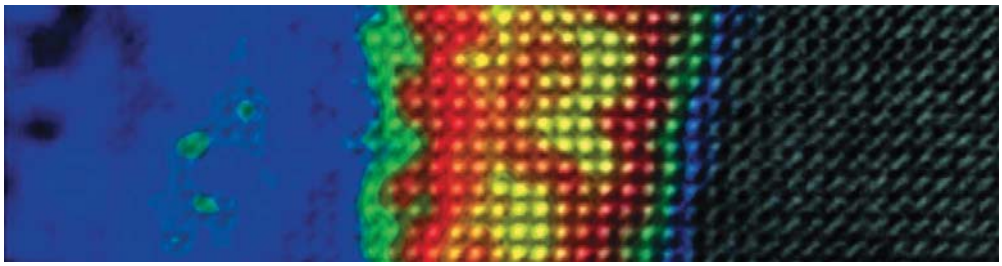

The Institute "Microstructure Research" focuses on the atomic and microstructural understanding of crystalline material properties with a special emphasis on electroceramics, metal alloys, nanostructured semiconductors and oxide superconductors. In some of these fields, the competence covers the whole range from basic research to the development and preparation of prefabricated technical devices. In other fields, access to novel material classes and intricate problems is provided by qualified collaborations. Current research programmes, performed either exclusively at the institute or in the framework of international cooperations, range from pure material preparation carried out hand in hand with all-embracing electron microscopic analyses to the design of electronic circuits and the development of advanced structural analysis techniques.

Over and above these general physics and technology-related projects, as a globally established organization, the institute continuously focuses and complements special competence in the field of advanced transmission electron microscopy techniques accompanied by the development of novel investigation methods. For these purposes, the institute operates and maintains the Ernst Ruska-Centre for Microscopy and Spectroscopy with Electrons (ER-C), which, as a supraregional user facility, benefits from the unique scientific expertise in the field of transmission electron microscopy, which is being continuously extended at the institute.

IFF-9: Electronic Properties

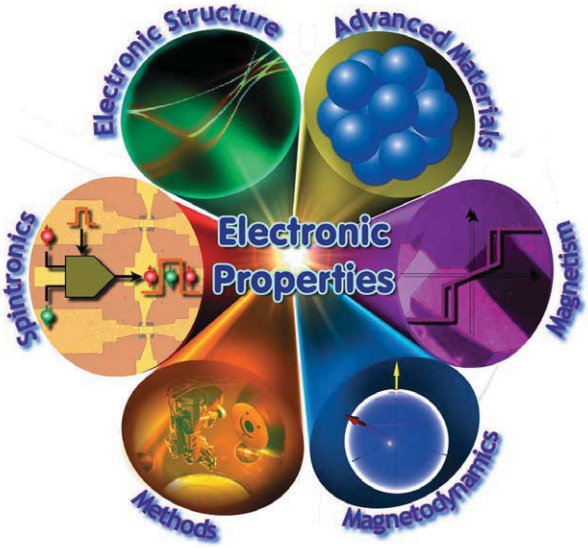

At the Institute "Electronic Properties" we explore the multifaceted interrelations between the electronic structure and the physical properties of matter. Our current research focus lies on magnetism, magnetic phenomena, and their exploitation in nanoscience and information technology. Systems of interest range from ultrathin films and thin film layer stacks through quantum wires and dots to clusters and molecules.

Magnetism displays a complicated interplay of competing interactions taking place on different length, energy, and time scales. We are particularly interested in the influence of the reduced dimensionality and the formation of quantum effects in nanoscale magnetic structures. The crosslinks between electronic structure and magnetism are addressed by a variety of spin-resolving spectroscopic techniques, such as spin-polarized photoemission and x-ray magnetooptics. These studies are carried out at dedicated beamlines at the synchrotron radiation facilities BESSY and DELTA.

The second line of research addresses the response of magnetic systems on short (magnetodynamics) and ultrashort timescales (spin dynamics). The magnetodynamics is experimentally accessed by pump-probe schemes and interpreted via micromagnetic simulations. Laser-based techniques provide high time-resolution, whereas time-resolved photoemission microscopy combines high lateral resolution with large magnetic sensitivity and element selectivity. In the realm of spin dynamics, we study energy and angular momentum transfer processes between the electron, spin, and lattice subsystems. Such experiments are performed by femtosecond pump-probe methods.

The third topic in the IFF-9 is Spintronics, i.e. the physics of spin-dependent transport processes. Resting on a long-standing experience with magnetoresistive phenomena, the current studies focus on the fundamental physics of spin transfer phenomena. This includes the development of new magnetic material systems and nanoscale devices. Particular emphasis lies on the exploration of smart magnetic switching alternatives involving spin-polarized electrical currents and photons.

Supercomputers make virtual experiments in an otherwise unattainable precision possible and also facilitate the examination of theoretical models that cannot otherwise be tested. Supercomputers have long been the third pillar of research – alongside theory and experiment. Researchers at IFF use some of the worlds fastest Supercomputers at the Jülich Supercomputing Centre for their research and, at the same time, drive technological developments.

Condensed Matter Physics

Research in Condensed Matter is concerned with the complex interplay of the myriads of atoms in a solid or a liquid. Research in this field can thus be understood as the exploration of the „third infinity", being on equal footing with the exploration of the very small scales of elementary particle physics and the very large scales of astrophysics. The conceptual framework of quantum physics and statistical physics forms the basis for our understanding of Condensed Matter. The cooperation of the electrons and atoms within a many-body system is responsible for the different properties of the substances and determines why they are solid, fluid or gaseous, soft or hard, transparent or opaque, magnetic, metallic or even superconducting. Extreme length and time scales give rise to the characteristic complexity of Condensed Matter, ranging from subatomic sizes up to macroscopic measures, from electronic reaction times in the femtosecond range up to geological periods.

Our activities focus, in particular, on multi-scale phenomena in solid state and liquid phases and are organized in three topics:

- Electronic and Magnetic Phenomena,
- From Matter to Materials, and
- Soft Matter and Biophysics.

The studies in the first topic encompass electronic and magnetic quantum states and their properties. This includes problems in highly-correlated materials, superconductivity, magnetism in low dimensions and on short time scales. The second topic deals with phase transitions and transport processes, glass-like states, and complex metallic alloys, and finally structure formation and self-organization. In the third topic, structure formation and self-organization, mesoscopic dynamics and driven systems, as well as biology-inspired physics are addressed. The spectrum of the materials investigated covers a wide range from metals, semiconductors and ceramics, through macromolecular systems up to biological systems and cells. For this purpose, a broad portfolio of theoretical and experimental techniques is utilized, which are constantly improved and progressed. The experimental emphasis lies on neutron scattering, synchrotron-radiation methods and ultrahigh resolution electron microscopy, whereas the theoretical treatments range from quantum theory to statistical physics and involve both analytical and numerical procedures.

Commensurate and Incommensurate Charge Order in Fe_2OBO_3

R. P. Hermann[1,2], W. Schweika[1], M. Angst[3]

[1] IFF-4: Scattering Methods
[2] Department of Physics, Université de Liège, Belgium
[3] Materials Science and Technology Division, Oak Ridge National Laboratory, USA

Charge ordering is the localization in an ordered pattern of charge carriers on ions with different valences. This type of ordering phenomenon is of timely interest because it is related to colossal magnetoresistance, high-T_c superconductivity, and ferroelectricity. Charge order is further analogous to the idealized concept of Wigner crystallization, outlined in one of the earliest papers in correlated electron physics[1]. In real materials, however, perfect charge order with integer valence states is only approximated, because the bonding is not 100% ionic. The adequacy of ionic charge order for transition metal oxides is not clear, in particular for the classical example, Fe_3O_4, magnetite, in which the valence difference is less than one half electron. For such non-integer valence separation, a charge density wave scenario is usually invoked. We have shown that Fe_2OBO_3 exhibits charge order with integer valence states[2]. Surprisingly, in an intermediate phase, geometrical frustration leads to the coexistence of incommensurate charge order and integer valence order[3].

Charge ordering is the ability of electrons to localize periodically on the underlying ion lattice as a function of an external effect, such as temperature, pressure or an applied field. Materials that possibly can exhibit charge ordering usually exhibit an electron balance that is such that one cation must accommodate two different valence state. For example, in Fe_2OBO_3, two Fe cations must share a formal charge of 5+. This requires either a sharing of one electron and a formal $Fe^{2.5+}$ state or a charge separated state with both Fe^{2+} and Fe^{3+}. Based on Mössbauer spectral measurements on polycrystalline Fe_2OBO_3, Attfield has proposed[4] that such a valence separation occurs upon cooling through an accompanying structural transition at 317 K. However, the degree of charge separation was not quantified and no superstructure reflections indicating actual charge ordering had been detected. Resistivity and thermal analysis measurements of the first single crystals of pure Fe_2OBO_3 that were grown indicate two sharp transitions at 340 and 280 K, upon cooling[3], instead of the broad transition observed by Attfield[4]. In order to elucidate the nature of the three phases delineated by these transitions, single crystal structure refinement, synchrotron radiation scattering and Mössbauer spectral measurements were performed.

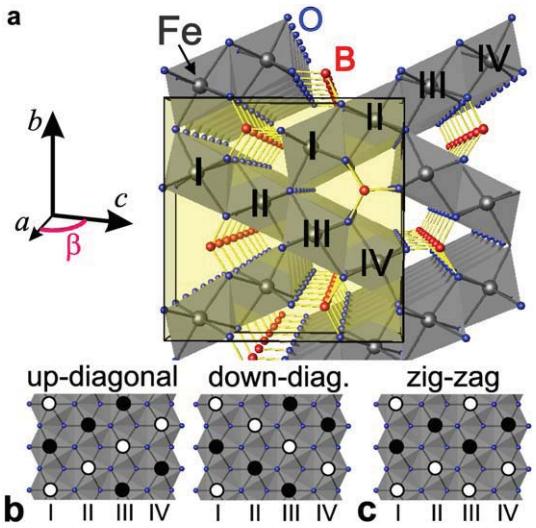

FIG. 1: (a) Fe_2OBO_3 crystal structure at 355 K. The structure consists of edge sharing ribbons of four octahedrally oxygen coordinated Fe, with the ribbon length in a. Fe occupies two distinct sites on the ribbon outside, Fe_1 on I and IV, and inside, Fe_2 on II and III. (b) Charge order configuration inside one ribbon. Black and white dots denote Fe^{2+} and Fe^{3+}, respectively. The doubly degenerate diagonal order has the lowest energy, other configurations, such as zig-zag (c), have only slightly larger energy (see text).

The crystal structure of Fe_2OBO_3, *Fig. 1a*, is of the Warwickite type. The unit cell is orthorhombic above 350 K, has a small monoclinic distortion below 340 K, and distorts more below 280 K. The single crystal refinement reveals that the oxygen positions shift significantly between 350 K and 100 K. A detailed bond-valence-sum analysis of the Fe-O bond length reveals that the amplitude of the valence separation is 1 electron[2]. The same conclusion is reached by the analysis of the isomer shift obtained by Mössbauer spectral measurements, see *Fig. 2*. Both the single crystal diffraction and the synchrotron radiation scattering measurements reveal superstructure reflections at $(h$+0.5,k,$l)$, see *Fig. 3a*, below 280 K. The charge order pattern in the ground state is diagonal, see *Fig. 1b*. This pattern minimizes the electrostatic energy. Indeed, the near neighbor chains, I and II, for example, are shifted by a/2 and thus do

have no net electrostatic interaction. In contrast, the next near neighbor chains, I and III, for example, can be either anti-phase, *Fig. 1b*, or in phase, *Fig. 1c*, the latter configuration having larger energy.

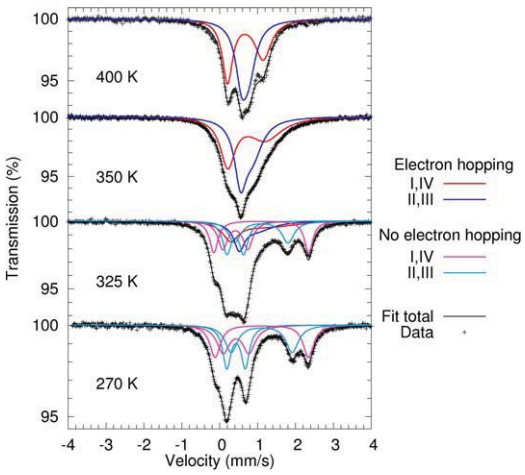

FIG. 2: Mössbauer spectra of Fe_2OBO_3. Below 270 K, Fe^{2+}, with the large splitting, and Fe^{3+} doublets, with the small splitting, are observed on the I,IV and on the II,III site. Above 350 K, slow valence relaxation that averages the hyperfine parameters, occurs and at 325 K a mixture of relaxing and non-relaxing components is observed.

Surprisingly, between 280 and 345 K, we have observed that the charge order superstructure peaks split, corresponding to an incommensurate propagation vector (1/2,0,τ), see *Fig. 3b*. In order to determine whether the order is truly incommensurate or obeys a devil's staircase scenario, we have completed the data with high energy scattering, that reveals a continuous change of τ, see *Fig. 3c*. The existence of these three phases, commensurately ordered, incommensurately ordered and disordered is consistent with the Mössbauer spectral measurements that reveal a static spectra in the commensurate phase, relaxation spectra in the charge disordered phase, and a phase mixing in the intermediate region. Both the incommensurate structure and the phase mixing can be understood by the existence of coherently arranged charge order domains with diagonal order, separated by phase boundaries in which electron hopping is possible. Within these phase boundaries, the charge order must be of non-diagonal type, $e.g.$ zig-zag. An examination of the four charge order configurations shown in *Fig. 1b* and *1c* reveals that the double degeneracy of near neighboring chain configuration arises from a first level of geometrical frustration related to the a/2 shift of near-neighboring chains and more generally of the shift of a/2 all (I,III) chains with respect to the (II,IV) chains. The net interaction between these groups of chains is zero and thus discussion can be restricted to one of these sublattices, for example (I,III).

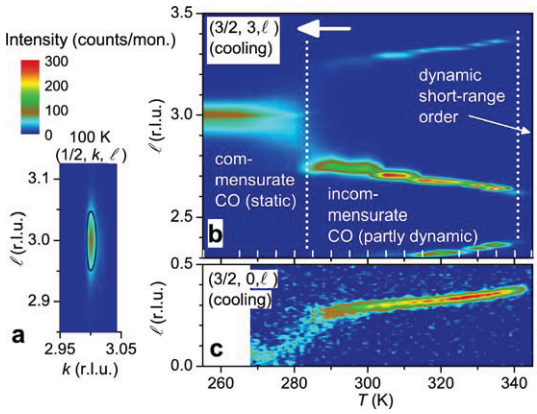

FIG. 3: Superstructure reflections obtained by synchrotron radiation scattering at MuCAT, APS. a) (1/2,k,l) superstructure reflection at 100 K. b) Temperature dependence of the scattering at (3/2,3,l) with 7.1 keV radiation at 6-ID-B and (c) of the integrated intensity at (3/2,0,l) obtained with 96 keV radiation at the 6-ID-D JCCSS sidestation.

Minimization of electrostatic energy requires that chains I and III be anti-phase. This is possible inside one ribbon, however inside the full crystal a second level of frustration arises, see triangle (I,I,III) in *Fig. 1a*. This second level of geometrical frustration reduces the energy difference between the zigzag and diagonal configuration, *Fig. 1b* and *1c*, and the close proximity in energy, confirmed by electronic structure calculations, permits the appearance of coherently arranged phase boundaries that are mobile owing to the electron hopping[3]. It should be noted that the Mössbauer spectrum at 325 K indicates that within the domains delineated by the phase boundaries integer valence charge order is likely retained.

In conclusion we have observed in Fe_2OBO_3 the first example of integer valence charge ordering and to date the best realization of Wigner crystallization in transition metal oxides. We also found that geometrical frustration leads an incommensurate structure in a temperature range intermediate between the charge disordered and charge ordered state. Quite surprisingly this incommensurate structure is not related to a charge density wave but to the coherent arrangement of phase boundaries. This observation is reminiscent of nanoscale stripes in manganites and cuprates, but in Fe_2OBO_3 they exhibit long range order.

[1] E. Wigner, Phys. Rev. 46, 1002 (1934).

[2] M. Angst, P. Khalifah, R. P. Hermann, H. J. Xiang, M.-H. Whangbo, V. Varadarajan, J. W. Brill, B. C. Sales, and D. Mandrus, Phys. Rev. Lett. 99, 086403 (2007).

[3] M. Angst, R. P. Hermann, W. Schweika, J.-W. Kim, P. Khalifah, H. J. Xiang, M.-H. Whangbo, D.-H. Kim, B. C. Sales, D. Mandrus, Phys. Rev. Lett. 99, 256402 (2007).

[4] J. P. Attfield, A. M. T. Bell, L. M. Rodriguez-Martinez, J. M. Greneche, R. J. Cernik, J. F. Clarke, and D. A. Perkins, Nature 396, 655 (1998).

Orbital Fluctuations in the Different Phases of $LaVO_3$ and YVO_3

E. Pavarini[1,2] , M. De Raychaudhury[3], O.K. Andersen[4]

[1] IFF-1: Quantum Theory of Materials
[2] IFF-3: Theory of Structure Formation
[3] S.N. Bose National Centre for Basic Sciences, Kolkata 700098, India
[4] Max-Planck-Institut für Festkörperforschung, Heisenbergstrasse 1, D-70569 Stuttgart, Germany

We investigate the importance of quantum orbital fluctuations in the orthorhombic and monoclinic phases of the Mott insulators $LaVO_3$ and YVO_3. We show that in $LaVO_3$ quantum fluctuations remain surprising strong in the orthorhombic phase, but they are completely suppressed in the monoclinic 140 K phase. In YVO_3 the suppression happens already at 300 K. We show that Jahn-Teller and $GdFeO_3$-type distortions are both crucial in determining the type of orbital and magnetic order in the low temperature phases.

The Mott insulating t_{2g}^2 perovskites $LaVO_3$ and YVO_3 exhibit an unusual series of structural and magnetic phase transitions (Fig. 1) with temperature-induced magnetization reversal phenomena [1] and other exotic properties [2]. While it is now recognized that the V-t_{2g} orbital degrees of freedom and the strong Coulomb repulsion are the key ingredients, it is still controversial whether classical (orbital order) [1, 3] or quantum (orbital fluctuations) [2, 4] effects are responsible for the rich physics of these vanadates.

At 300 K, $LaVO_3$ and YVO_3 are orthorhombic paramagnetic Mott insulators. Their structure (Fig. 2) can be derived from the cubic perovskite AVO_3, with A=La,Y, by tilting the VO_6 octahedra in alternating directions around the $\mathbf{b}$-axis and rotating them around the $\mathbf{c}$-axis. This $GdFeO_3$-type distortion is driven by AO covalency which pulls a given O atom closer to one of its four nearest A-neighbors [5]. Since the Y $4d$ level is closer to the O $2p$ level than the La $5d$ level, the AO covalency increases when going from $LaVO_3$ to YVO_3; hence, the $GdFeO_3$-type distortion increases. These 300 K, structures are similar to those of the t_{2g}^1 La and Y titanates [5].

The t_{2g}^2 vanadates, however, have a much richer phase diagram than the t_{2g}^1 titanates. At, respectively, 140 K and 200 K, $LaVO_3$ and YVO_3 transform to a monoclinic structure in which $\mathbf{c}$ is turned slightly around $\mathbf{a}$ whereby the two subcells along $\mathbf{c}$, related by a horizontal mirror plane in the orthorhombic structure, become independent (Fig. 2). Most important: a sizable (3-4%) Jahn-Teller (JT) elongation of a VO bond, that along $\mathbf{y}$ in cells 1 and 4, and along $\mathbf{x}$ in cells 3 and 2, deforms the VO_6 octahedra. At about 140 K in $LaVO_3$ and 116 K in YVO_3, antiferro*magnetic* (AFM) C-type order develops (ferromagnetic stacking of AFM ab-layers). At 77 K, YVO_3

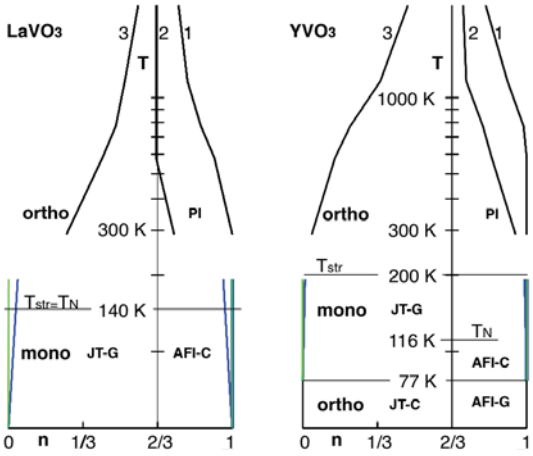

FIG. 1: Temperature-dependent structural and magnetic phases of $LaVO_3$ and YVO_3. The lines show LDA+DMFT (quantum Monte Carlo) results for the occupations, n, of the three t_{2g} crystal-field orbitals, 1, 2, and 3. Black lines: orthorhombic phases. Green and blue lines: monoclinic, sites 1 and 3 (see Fig. 2). For each structure we calculated the occupations down the temperature at which the orbital polarizations are essentially complete ($T \sim 200$ K) and then extrapolated in a standard way to $T = 0$ K.

recovers the orthorhombic structure and the magnetic order changes from C- to G-type (3D-AFM), while the long VO bond becomes that along $\mathbf{x}$ in cells 1 and 3, and along $\mathbf{y}$ in 2 and 4.

It has been suggested [1] that these phase transitions are driven by the changes in a static orbital order (OO) following the observed pattern of JT-distortions. According to this JT-OO model, which assumes that the crystal-field (CF) is due to the oxygen octahedra, the t_{2g} orbital which is *most* antibonding with the O $2p$ orbitals, i.e. $|sz\rangle$ where s is the direction of the *short* in-plane VO bond, is *empty*; the other two t_{2g} orbitals, due to Hund's rule coupling, are *singly* occupied. This OO is C-type in the orthorhombic structure and G-type in the monoclinic structure. Later, this JT-OO model was challenged by a theory which assumes that the two highest orbitals, $|xz\rangle$ and $|yz\rangle$, are basically degenerate so that orbital *fluctuations* play a key role [2, 4]. Recently, ab initio LDA+U [3] calculations gave support to the JT-OO model.

In order to clarify this issue, we perform [6] electronic structure calculations based on the LDA+DMFT

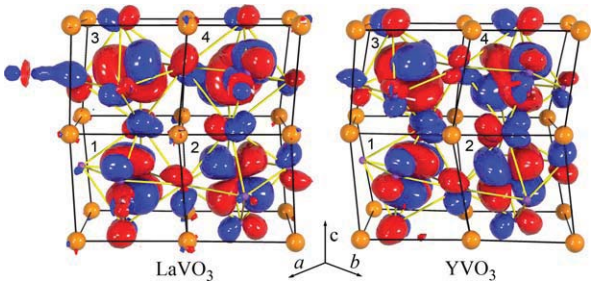

FIG. 2: Primitive cell containing four ABO_3 units. A-ions are orange, B-ions are at the centers of yellow O-octahedra. In terms of the primitive translation vectors, $\mathbf{a}$, $\mathbf{b}$, and $\mathbf{c}$ the global $\mathbf{x}$, $\mathbf{y}$, and $\mathbf{z}$ axes, directed approximately along the BO bonds, are: $\mathbf{x} = \mathbf{a}/(2+2\alpha) + \mathbf{b}/(2+2\beta)$ $\mathbf{y} = -\mathbf{a}/(2+2\alpha) + \mathbf{b}/(2+2\beta)$ and $\mathbf{z} = (\mathbf{c} - \mathbf{c}\cdot\mathbf{b})/(2+2\gamma)$. Here, α, β, and γ are small and $|\mathbf{x}| = |\mathbf{y}| = |\mathbf{z}|$ =3.92Å (3.82Å) for $LaVO_3$ (YVO_3). The B-containing bc-plane glide-mirrors (with translation $(\mathbf{b}-\mathbf{a})/2$) unit 1 in 2 and 3 in 4, and exchanges the local, B-centered x and y coordinates. In the orthorhombic Pbnm structure (but not in the monoclinic $P2_1/a$ structure), the A-containing ab-plane mirrors unit 1 in 3 and 2 in 4. The empty crystal-field orbitals $|3\rangle_i$ of the monoclinic phase were put on sites $i = 1, 2, 3, 4$. Red (blue) indicate positive (negative) lobes.

method [7], fully accounting for the orbital degrees of freedom [5]. First, using the downfolding technique based on the N^{th}-order muffin-tin-orbital method, we construct *ab-initio* a basis of localized t_{2g} Wannier functions and the corresponding LDA Hamiltonian, H^{LDA}. The many-body Hamiltonian is then a material-specific t_{2g} Hubbard model, $\hat{H}^{\mathrm{LDA}} + \hat{U}$; we solve it in dynamical mean-field theory (DMFT) [8], using Hirsch-Fye quantum Monte Carlo as impurity solver and working with the full self-energy matrix. This scheme was introduced Refs. [5].

Remarkably, we found that in the orthorhombic $300\,\mathrm{K}$ phase the CF orbitals are basically identical to those of the t_{2g}^1 titanates, but the CF splittings are half the values in the titanates. This happens because the CF orbitals are essentially determined by the $GdFeO_3$-type distortion via the A-ligand field, specifically the AB and AOB covalency. Since V is on the right of Ti in the periodic table, the V $3d$ level is closer to the O $2p$ and further from the A d level that the Ti $3d$; thus in the vanadates the sensitivity of the B t_{2g} Wannier functions to $GdFeO_3$-type distortions decreases, while the sensitivity to JT increases. Hence, the CF splitting are smaller in the vandates while the CF orbitals are identical to those of the titanates. Concerning the spectral function, we found a Mott gap ~ 1 eV for $LaVO_3$, and ~ 1.2 eV for YVO_3, and Hubbard bands centered around -1.5 eV and 2.5 eV for $LaVO_3$ and around -1.5 eV and 3 eV for YVO_3. These results are in good accord with photoemission [9].

What about orbital fluctuations? As Fig. 1 shows for $LaVO_3$ orbital fluctuations remain surprisingly sizable down to room temperature. Due to the stronger cation covalency in YVO_3, the Coulomb repulsion causes substantial orbital polarization already at $800\,\mathrm{K}$. Thus, YVO_3 is orbitally ordered well above the magnetic phase transition. In the paramagnetic phase, since, at site 1, $|xz\rangle$ is basically empty, the OO happens to agree with the prediction of the JT-OO model, even though the CF is caused mainly by the $GdFeO_3$-type distortion.

In the low temperature JT-distorted phases orbital fluctuations turned out to be completely suppressed for both systems. This is because the temperature decreases, favoring OO, and, for $LaVO_3$, the CF splittings substantially increases mainly due to the larger JT distortions. Remarkably, for $LaVO_3$ we find that the occupied CF orbitals depend crucially not only on the Jahn-Teller but also on the $GdFeO_3$-type distortions and that the OO is not of G-type, but is intermediate between C- and G-type. For YVO_3, on all sites in the monoclinic structure the empty orbital is almost the same as in the orthorhombic $300\,\mathrm{K}$ phase so OO does not follow the JT distortions but is almost C-type. In the orthorhombic $77\,\mathrm{K}$ phase, the empty orbital at site 1 only roughly equals $|xz\rangle$.

In conclusion, we find [6] that the orthorhombic $LaVO_3$ is one of the few Mott insulators which exhibits large quantum effects at room temperature. In the low temperature phases, orbital fluctuations are negligible for both vanadates. This supports the view that the magnetic structures of the vanadates can be explained by orbital-order. Recent LDA+U [3] calculations agree with this, but previous literature ascribed OO mainly to JT-distortions. In contrast, we proved that both the JT *and* the $GdFeO_3$-type distortions are crucial for the CF orbitals and their hopping integrals, and thus for the type of orbital and magnetic order. The effects of the GdFeO-type distortions are weaker and those of JT stronger than in t_{2g}^1 titanates; their interplay is responsible for the rich phase diagram of the vanadates.

[1] Y. Ren *et al.*, Nature (London) **396**, 441 (1998).

[2] C. Ulrich *et al.*, Phys. Rev. Lett. **91**, 257202 (2003).

[3] Z. Fang and N. Nagaosa, Phys. Rev. Lett. **93**, 176404 (2004).

[4] G. Khaliullin, P. Horsch and A. M. Oles, Phys. Rev. Lett. **86**, 3879 (2001).

[5] E. Pavarini *et al.*, Phys. Rev. Lett. **92**, 176403 (2004); E. Pavarini *et al.*, New J. Phys. **7** 188 (2005).

[6] M. De Raychaudhury, E. Pavarini, O.K. Andersen, Phys. Rev. Lett. **99**, 126402 (2007).

[7] V. Anisimov *et al.*, J. Phys: Condens. Matter **9**, 7359 (1997); A. I. Lichtenstein and M. I. Katsnelson, Phys. Rev. B **57**, 6884 (1998).

[8] A. Georges *et al.*, Rev. Mod. Phys. **68**, 13 (1996).

[9] H. F. Pen *et al.*, Phys. Rev. B **59**, 7422 (1999); K. Maiti and D. D. Sarma, *ibid.* **61**, 2525 (2000).

Quantum Phase Transition in the Two-Band Hubbard Model

T. A. Costi[1], A. Liebsch[2]

[1] IFF-3: Theory of Structure Formation
[2] IFF-1: Quantum Theory of Materials

The interaction between itinerant and Mott localized electronic states in strongly correlated materials is studied within dynamical mean field theory in combination with the numerical renormalization group method. A novel nonmagnetic zero temperature quantum phase transition is found in the bad-metallic orbital-selective Mott phase of the two-band Hubbard model, for values of the Hund's exchange which are relevant to typical transition metal oxides.

The nature of the metal insulator transition in multicomponent systems, with competing energy scales associated with differing bandwidths and Coulomb and exchange interactions, is currently of great interest [1]. For instance, in transition metal oxides such as $Ca_{2-x}Sr_xRuO_4$ or manganites (e.g. $La_{1-x}Sr_xMnO_3$), the Coulomb interaction between weakly and strongly correlated subbands can give rise to complex phase changes as a function of temperature, pressure, or impurity concentration. An interesting aspect of such systems is the coexistence of itinerant wide band electrons with partially or completely localized narrow band electrons. This gives rise to bad-metallic behavior as observed, for example, in the resistivity of the paramagnetic phases of VO_2 [2] and $Ca_{2-x}Sr_xRuO_4$ at $x = 0.2$ [3]. Even in standard Mott insulators such as V_2O_3 and $LaTiO_3$, the presence of inequivalent orbitals leads to strong orbital polarization where in the vicinity of the transition nearly localized electrons coexist with weakly itinerant bands [4, 5, 6].

A simple model which captures some of the essential physics occurring in the systems mentioned above is the two-band Hubbard model consisting of narrow and wide subbands, coupled via local Coulomb energy U and Hund's exchange J [7, 8]. As a result of the various energy scales contained in this model, its phase diagram turns out to be remarkably rich, with differing bandwidths and a finite Hund's exchange stabilizing an orbital-selective Mott phase, in which the wide band itinerant electrons coexist with localized spins arising from Mott localization of the narrow band electrons.

In the present work [9] we identify the character of the wide band transition from the orbital-selective Mott phase to the insulating phase. We use DMFT [10] in combination with the numerical renormalization group (NRG) method [11, 12].

We consider an effective low-energy model specific for the orbital-selective Mott phase [13], in which the electrons in the narrow band of the original two-band Hubbard model have undergone Mott localization so their low-energy degrees of freedom are represented by localized spins. These couple to the itinerant wide band electrons via a Hund's exchange. The resulting model is the ferromagnetic Kondo lattice model with interactions in the band,

$$H_{\rm fkl} = -\sum_{ij\sigma} t_{ij} c^\dagger_{i\sigma} c_{j\sigma} + U \sum_i n_{i\uparrow} n_{i\downarrow} - \sum_i \left[2J\, S^z_i s^z_i + 2J'(S^+_i s^-_i + S^-_i s^+_i)\right] \quad (1)$$

where s^z_i and $s^\pm_i$ are the z-component and raising/lowering operators, respectively, for electrons in the wide band at site i and S^z_i and $S^\pm_i$ are the corresponding operators for the localized spin at site i. The anisotropy of the Hund's exchange is measured by $J'/J \leq 1$. The DMFT-NRG calculations have been carried out for fixed values of J/U and increasing values of U/D, as we consider the situation where correlations are tuned by reducing the bandwidth D whereas the ratio J/U is material dependent, being, for example, larger than unity for manganites and smaller than unity for most transition metal oxides.

The behavior of the effective conduction electron magnetic moment, $\langle s^2_z \rangle$, as a function of increasing/decreasing U through the metal-insulator transition is shown in Fig. 1 for several fixed values of J/U. One sees that for $J/U > j_c \approx 0.1$ hysteresis is absent indicating a continuous transition, while for smaller J/U first-order behavior is found. The inset to Fig. 1 shows the $T = 0$ phase diagram for the wide band metal-insulator transition. The critical Coulomb interaction for the Mott transition is seen to decrease monotonically with increasing J/U.

Let us now look closer at the continuous quantum phase transition for $J/U > j_c$. Fig. 2(a) shows the evolution of the spectral density as a function of U for fixed $J/U = 1/4$, a value typical for transition metal oxides. At small U, the density of states at the Fermi level, $E_F = 0$, satisfies the pinning condition, $A(0) = 2/\pi$, approximately. Near $U \approx 1$ the spectrum begins to exhibit a pseudogap which gets progressively deeper with increasing U. The characteristic scale for this pseudogap is J. At $U_c = 1.183$ this pseudogap becomes a soft gap before a full insulating gap opens at $U > U_c$. In the bad-metallic

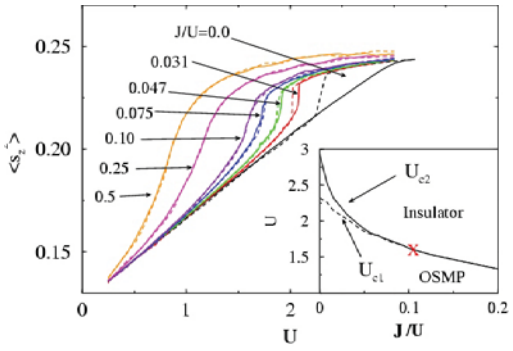

FIG. 1: Effective magnetic moment $\langle s_z^2 \rangle$ per site of the conduction electrons for several values of J/U, $J' = 0$ as a function of U. Solid (dashed) lines: increasing (decreasing) values of U. For $0 < J/U < 0.1$ the Mott transition is of first order with hysteresis in a region $U_{c1} < U < U_{c2}$. For $J/U > 0.1$ the transition becomes a continuous quantum phase transition. Inset: $T = 0$ phase diagram and dependence of $U_{c1,2}$ on J/U. OSMP denotes the orbital-selective Mott phase. X denotes the critical point $J/U = j_c \approx 0.1$, $U = u_c \approx 1.6$ where the Mott transition changes from first to second order.

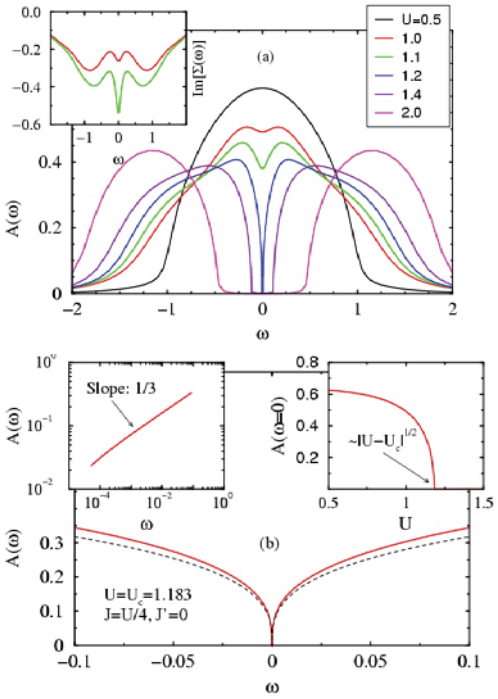

FIG. 2: Upper panel: Spectral density of wide band for several values of U, for $J = U/4$, $J' = 0$. The Mott transition occurs at $U_c = 1.183$ and is continuous. Inset: imaginary part of the self-energy for $U < U_c$, indicating a bad metal. Lower panel: Low-frequency region of spectral density $A(\omega)$ for $J = U/4$, $J' = 0$ at $U_c = 1.183$ (red solid line; logarithmic plot left inset); the analogous spectrum for the exactly solvable model at $J_c = 2$, $U = 0$, is shown by the dashed line. Right inset: $A(0)$ as a function of U.

region below the Mott transition, the electronic lifetime $\tau(\omega = 0) \sim -1/\mathrm{Im}[\Sigma(\omega = 0)]$ is finite (see inset to Fig. 2(a)) and vanishes at $U = U_c$. Because of the presence of the pseudogap the spectra exhibit a characteristic four-peaked structure, with low-energy features limiting the gap and high-energy peaks associated with Hubbard bands.

We have analysed the low-frequency behavior of the spectral density at the quantum phase transition in the region $J/U > j_c$ and find $A(\omega) \sim |\omega|^{\delta}$ with $\delta = 1/3$, as shown in Fig. 2(b). Moreover, $A(0) \sim |U - U_c|^{1/2}$ for $U \to U_c^-$. Remarkably, this behavior coincides with the one obtained for the continuous Mott transition in the exactly solvable model $J/U \to \infty$ with $U \to 0$ on increasing J. Solving the DMFT equations for this model we find a band-splitting transition at $J_c = 2$ with $A(\omega) \sim |\omega|^{1/3}$ and $A(0) \sim |J - J_c|^{1/2}$ for $J \to J_c^-$. This suggests that the low-frequency excitations in the whole region $J/U > j_c$ are governed by the Ising Hund's exchange and that the paramagnetic metal insulator transition belongs to the same universality class as the band-splitting transition in the model with $U = 0$ on increasing J.

In summary, we have studied the metal insulator transition in the two-band Hubbard model with bands of different widths and for Ising Hund's exchange, arguing that the results for the metal insulator transition in the wide band apply for all anisotropies $J' < J$ [9]. The results reveal a continuous quantum phase transition for $J/U > 0.1$, i.e., in the region relevant for many transition metal oxide materials. Close inspection of the critical properties of this transition show that they coincide with the ones of the band-splitting transition in the model with $U = 0$ and variable J.

[1] M. Imada, A. Fujimori and Y. Tokura, Rev. Mod. Phys. **70**, 1039(1998).

[2] P. B. Allen et al., Phys. Rev. B **48**,4359 (1993).

[3] S. Nakatsuji and Y. Maeno, Phys. Rev. B **62**, 6458 (2000).

[4] G. Keller et al., Phys. Rev. B **70**, 205116 (2004).

[5] A. I. Poteryaev et al., Phys. Rev. B **76**, 085127 (2007).

[6] E. Pavarini et al., Phys. Rev. Lett. **92**, 176403 (2004).

[7] V. I. Anisimov et al., Eur. Phys. J. B **25**, 191 (2002).

[8] A. Liebsch, Phys. Rev. Lett. **91**, 226401 (2003).

[9] T. A. Costi and A. Liebsch, Phys. Rev. Lett. **99**, 236404 (2007).

[10] A. Georges, G. Kotliar, W. Krauth and M. J. Rozenberg, Rev. Mod. Phys. **68**, 13 (1996).

[11] K. G. Wilson, Rev. Mod. Phys. **47**, 773 (1975).

[12] T. A. Costi, A. C. Hewson and V. Zlatić, J. Phys.: Condens. Matter **6**, 2519 (1994).

[13] S. Biermann, L. de' Medici and A. Georges, Phys. Rev. Lett. **95**, 206401 (2005).

Effect of Orbital Degrees of Freedom on the Doping-Driven Mott Transition in $La_{1-x}Sr_xTiO_3$

A. Liebsch

IFF-1: Quantum Theory of Materials

The insulator to metal transition in $LaTiO_3$ induced by La substitution via Sr is studied within multi-band exact diagonalization dynamical mean field theory at finite temperatures. It is shown that weak hole doping triggers a large interorbital charge transfer, with simultaneous electron and hole doping of t_{2g} subbands. The transition is first-order and exhibits phase separation between insulator and metal. In the metallic phase, subband compressibilities become very large and have opposite signs. Electron doping gives rise to an interorbital charge flow in the same direction as hole doping. These results can be understood in terms of a strong orbital depolarization.

The remarkable sensitivity of the electronic and magnetic properties of transition metal oxides to small changes of parameters such as temperature, pressure, or impurity concentration has attracted wide attention during recent years. A phenomenon of particular interest is the filling-controlled metal insulator transition in the vicinity of integer occupancies of partially filled valence bands. For instance, $LaTiO_3$ is known to be a Mott insulator which becomes metallic if La is replaced by a few percent of Sr ions. Similarly, Ca_2RuO_4 is a Mott insulator which becomes metallic if Ca is substituted by small amounts of Sr.

The doping driven Mott transition has been investigated so far only within single-band models [1] or multi-band models based on identical subbands [2]. On the other hand, it has recently been demonstrated that orbital degrees of freedom play a crucial role in the Mott transition of materials consisting of non-equivalent partially occupied subbands. Examples are $LaTiO_3$, V_2O_3 and Ca_2RuO_4 [3, 4, 5]. In view of the nearly complete orbital polarization of the Mott phase in these materials it is evidently necessary to go beyond single-band models or multi-band models for identical subbands to describe the effect of doping.

In the present work [6] we investigate the destruction of the Mott phase of $LaTiO_3$ due to replacement of small amounts of La by Sr. Whereas in models based on equivalent subbands doping naturally modifies all subbands in the same way, the interplay between orbital and charge degrees of freedom yields a very different picture: The addition of only a few percent of holes to the t_{2g} bands triggers a substantially larger interorbital charge rearrangement, with a strong flow of electrons from the nearly half-filled subband towards the nearly empty ones. In other words, weak "external" hole doping of the t_{2g} bands causes a much larger "internal" simultaneous electron and hole doping of different subbands. Thus, the density-driven insulator to metal transition in $La_{1-x}Sr_xTiO_3$ is accompanied by a significant reduction of orbital polarization. Similar depolarization effects can be expected to occur in other multi-band transition metal oxides.

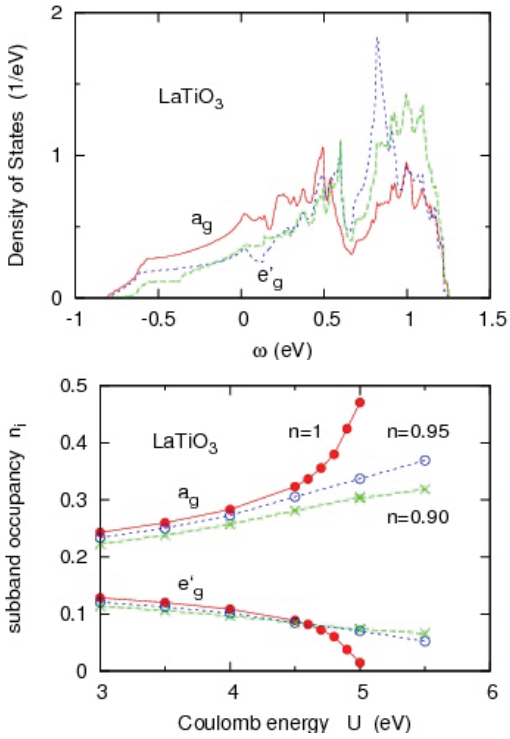

FIG. 1: (Color online) Upper panel: density of states components of $LaTiO_3$ [3]. Lower panel: a_g, e'_g subband occupancies (per spin band) of $La_{1-x}Sr_xTiO_3$ as functions of Coulomb energy, calculated within ED/DMFT [6]

To account for local Coulomb interactions among the Ti $3d$ electrons we use finite temperature dynamical mean field theory (DMFT) combined with multi-band exact diagonalization (ED) [7, 5, 8]. The orthorhombic lattice of $LaTiO_3$ gives rise to a crystal field splitting between the a_g and e'_g density of states

components, as shown in the upper panel of Fig. 1. Coulomb correlations enhance the orbital polarization resulting from this crystal field, as indicated in the lower panel. Interestingly, integer and non-integer occupancies reveal qualitatively different behavior. For $n = 1$, Coulomb interactions gradually suppress orbital fluctuations up to $U \approx 4.5$ eV. In the subsequent narrow range up to $U \approx 5$ eV, the a_g band is rapidly becoming nearly half-filled and the two e'_g bands nearly empty, in agreement with Ref. [3].

For hole doping with $n = 0.95$ and 0.90, on the other hand, the situation is rather different: Orbital polarization increases smoothly with increasing Coulomb energy, without any sign of the critical behavior that is characteristic of the pure La compound. Evidently, the rapid suppression of orbital fluctuations near $U = 5$ eV is a phenomenon intimately associated with the first-order phase transition for integer occupancy of the t_{2g} bands. Decreasing n to 0.95, at fixed $U = 5$ eV, yields a similar orbital polarization as reducing U to about 4.6 eV, at fixed $n = 1$.

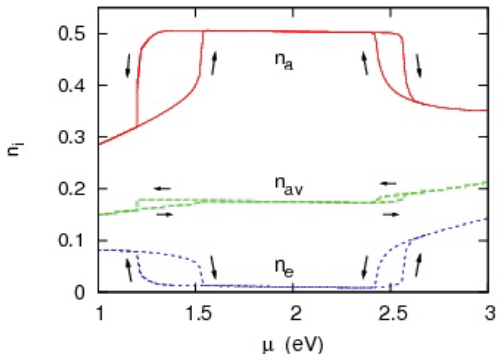

FIG. 2: (Color online) DMFT a_g and e'_g subband occupancies (per spin band) of $LaTiO_3$ as functions of chemical potential. Also shown is the average occupancy $n_{av} = (n_{a_g} + 2n_{e'_g})/3$. The arrows mark the hystereses for increasing/decreasing μ. [6]

The striking feature of these results is that the charge rearrangement among t_{2g} orbitals is much larger than the number of holes induced via La $\rightarrow$ Sr substitution. For instance, for $x = 0.05$ ($n = 0.95$) the total a_g occupancy (both spins) changes from near unity at $U = 5$ eV to 0.64, whereas the total e'_g occupancy (four spin bands) changes from near zero to 0.31. Thus, the internal charge transfer from a_g to e'_g bands is six times larger than the external charge transfer due to doping with Sr. Clearly, the destruction of the Mott phase of $LaTiO_3$ via hole doping does not proceed via approximately equal participation of all subbands. Instead, weak external hole doping generates a much larger simultaneous electron and hole doping in different subbands.

The physical reason for this effect is the fact that the subband charge compressibilities become extremely large upon crossing the first-order phase boundary between insulator and metal. This is illustrated in Fig. 2 which shows the charge transfer among a_g, e'_g bands as a function of chemical potential for $U = 5$ eV and $J = 0.65$ eV. The temperature is $T \approx 20$ meV. Hole doping occurs for $\mu < 1.5$ eV, electron doping for $\mu > 2.5$ eV. Because of the insulating gap, the charge compressibility $\kappa = \partial n/\partial\mu$ vanishes in the intermediate range. The hysteresis loops demonstrate that the hole and electron driven Mott transitions at finite T are first order. Phase separation, where an insulating solution with $n = 2n_{a_g} + 4n_{e'_g} = 1$ coexists with a metallic solution for $n \neq 1$, is seen to occur at both transitions. Moreover, the compressibility gets very large as the upper and lower critical values of μ at both hysteresis loops are approached. Note that the hysteresis behavior of the a_g, e'_g subbands is much more pronounced than that of the average t_{2g} charge. Accordingly, the subband compressibilities $\kappa_i = \partial n_i/\partial\mu$ have opposite signs and their absolute values are much larger than the average t_{2g} compressibility. Thus, small variations of the chemical potential yield large variations in n_{a_g} and $n_{e'_g}$. The destruction of the $n = 1$ insulator is therefore accompanied by a sudden, large charge redistribution between a_g and e'_g orbitals, with partial filling of the nearly empty e'_g states at the expense of the nearly half-filled a_g states. These results indicate that the combined effect of charge and orbital degrees of freedom leads to a non-trivial generalization of the one-band picture close to half-filling and of the multiband picture based on equivalent orbitals.

In summary, we have studied the interplay of charge and orbital degrees of freedom in the density-driven Mott transition in $La_{1-x}Sr_xTiO_3$. The key result is that the transition from insulator to metal induced by weak doping is accompanied by a striking interorbital charge rearrangement. Injection of only a few percent of holes into the Ti t_{2g} bands via doping with Sr causes a much larger simultaneous electron and hole doping of different subbands. Doping of the Mott phase therefore induces a pronounced orbital depolarization, i.e., a strong reduction of the nearly complete orbital polarization that occurs at integer occupancy. Since other multi-band Mott insulators such as V_2O_3 and Ca_2RuO_4 also exhibit orbital polarization, it is likely that doping these systems with electron or hole donors will lead to a similar enhancement of orbital fluctuations as discussed here for $La_{1-x}Sr_xTiO_3$.

[1] M. Eckstein *et al.*, Phys. Rev. B **75**, 125103 (2007).

[2] V.S. Oudovenko *et al.*, Phys. Rev. B **70**, 125112 (2004).

[3] E. Pavarini *et al.*, Phys. Rev. Lett. **92**, 176403 (2004); New J. Phys. **7**, 188 (2005).

[4] G. Keller *et al.*, Phys. Rev. B **70**, 205116 (2004). A.I. Poteryaev *et al.*, Phys. Rev. B **76**, 085127 (2007).

[5] A. Liebsch and H. Ishida, Phys. Rev. Lett. **98**, 216404 (2007).

[6] A. Liebsch submitted to Phys. Rev. Lett.

[7] C.A. Perroni, H. Ishida, and A. Liebsch, Phys. Rev. B **75**, 045125 (2007). See also: A. Liebsch, Phys. Rev. Lett. **95**, 116402 (2005); A. Liebsch and T.A. Costi, Eur. Phys. J. **51**, 523 (2006).

[8] A. Liebsch and H. Ishida, cond-mat/0705.3627; H. Ishida and A. Liebsch, cond-mat/0711.0516.

First-Principles Simulation Code Based on Real-Space Method

T. Ono, P. Baumeister, S. Blügel
IFF-1: Quantum Theory of Materials

We develop a first-principles simulation code based on the real-space finite-difference method. Since the real-space method does not use fast Fourier transforms, parallel algorithms are easily achieved, enabling high-speed calculation using a massively parallel computer like JUGENE of Jülich supercomputer center. We can also implement highly accurate calculation by combining the projector augmented-wave method. In order to demonstrate the potential power of our code, we present several applications for electronic structure calculations of nanostructures.

In this project, we develop a first-principles electronic-structure and electron-transport calculation code based on the real-space finite-difference method [1, 2, 3]. The real-space methods have desirable properties compared with the usual plane-wave and/or the linear combination of atomic orbitals approaches: (i) Since all of the calculations are carried out in real space, it is easy to incorporate localized Wannier-type orbitals, which are localized in a finite region required for the realization of $O(N)$ calculations, into the algorithm. (ii) A technique utilizing a real-space double-grid [3] is available within the real-space finite-difference formalism, where many grid points are put in the vicinity of nuclei, so that the integrals involving rapidly varying pseudopotentials inside the core regions of atoms can be calculated with a high degree of accuracy. (iii) In order to improve the calculation accuracy, the grid spacing should be narrowed, the procedure of which is simple and definite. Even more important is that (iv) boundary conditions are not constrained to be periodic, e.g., combinations of periodic and nonperiodic boundary conditions for surfaces and wires, uneven boundary condition for triclinic system, and twist boundary conditions for helical nanotubes are applicable.

Figure 1 depicts the scaling behavior of the computation time of the our real-space code for the models consisting of 96 atoms and 1000 atoms on JUBL of Jülich supercomputer center. In both the cases, our real-space code exhibits good parallelization behavior on massively parallel computers. We then explore the atomic configuration of the peapod where a C_{180} is encapsulated by a (20,0) carbon nanotube. The computational model which consists of 500 carbon atoms per supercell is illustrated in Fig. 2. By executing the first-principles structural optimization,

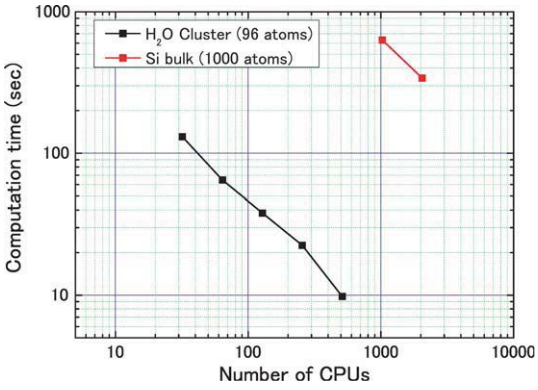

FIG. 1: Scaling behavior of computation time per one iteration as a function of the number of CPU. The benchmark test was carried out on JUBL of Jülich supercomputer center.

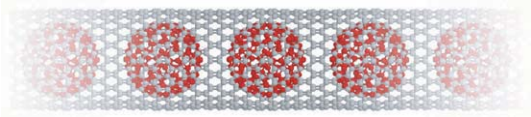

FIG. 2: Computational model of peapod. The grey (red) spheres are carbon atoms of (20,0) nanotube (C_{180}).

we found that the diameter of the carbon nanotube increases by 4% and the diameter of the C_{180} increases (decreases) by 1% (6%) in the longitudinal (lateral) direction.

In order to enhance the computation accuracy of the first-principles calculation, we started to include the projector augmented-wave (PAW) pseudopotential [4] instead of the conventional norm-conserving one. Since the PAW method enables us to treat the behavior of electrons vicinity of nuclei, we can calculate the electronic properties of nanostructures, in particular the systems including transition metals, more accurately with large grid spacings. In the real-space finite-difference formalism, wave functions, electronic charge density, and potentials are all

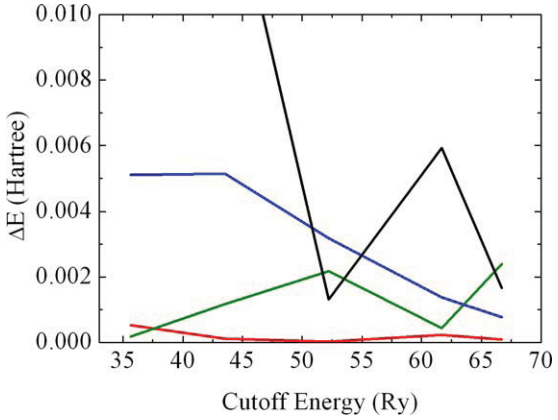

FIG. 3: Total energy dependency on relative position of carbon atom with respect to grid points as a function of the cutoff energy. The red, green, blue, and black lines correspond to the results with the double-grid and Fourier filtering, with only the double-grid, with only the Fourier filtering, and without any prescriptions, respectively.

represented on the discrete grid. In general, the discretizations of them are not invariant under uniform translations of the system respect to the position of the grid, which leads a serious problem in practical simulations: the total energy varies unphysically depending on the relative positions of grid points and the nucleus. This problem is more serious in the simulations using the PAW method because we implement simulations with larger grid spacings than those used in the conventional norm-conserving pseudopotential method. Here, we introduce the prescription combining the timesaving double-grid technique [3] with the Fourier filtering of the pseudopotential [5]. To demonstrate the efficiency of our prescription, we show in Fig. 3 the difference in total energy of carbon atom when the atom is located on the grid plane and between the grid plane as a function of the cutoff energy. One can clearly see that the spurious total-energy variation is suppressed when both the timesaving double-grid and Fourier filtering techniques are adopted.

We then compute several bulk properties of transition metals using PAW pseudopotentials. Table 1 collects lattice constants, bulk moduli, and magnetic moments of fcc Cu, fcc Ru, and bcc Fe. Although there are some disagreements with experimental data due to the usage of the local density approximation, our results are in good agreement with the results obtained by other theoretical calculations.

Finally, we examine the total energy difference between fcc Cu and hcp Cu. Because the energy difference between these systems is very small, this calculation is a good benchmark test to check the potential of our code. Table 2 lists the lattice constants of hcp Cu, and the energy difference between fcc Cu and hcp Cu. These results also agree with those obtained by other theoretical calculations.

In conclusion, we have developed the first-principles

	Cu	Ru	Fe
Lattice constant (bohr)			
Experiment	6.84	—	5.42
This work	6.76	7.13	5.20
Other method	6.73	7.20	5.22
Bulk modulus (Mbar)			
Experiment	1.37	—	1.68
This work	1.65	3.32	2.39
Other method	1.62	3.33	2.45
Magnetic moment (μ_B)			
Experiment	—	—	2.22
This work	—	—	2.05
Other method	—	—	2.04

TAB. 1: Calculated lattice constants, bulk moduli, and magnetic moments of fcc Cu, fcc Ru, and bcc Fe.

	a (bohr)	c/a	ΔE (meV)
This work	4.77	1.63	5.1
Other method	4.74	1.62	4.0

TAB. 2: Calculated lattice constants a and c of hcp Cu, and energy difference ΔE between fcc Cu and hcp Cu.

calculation code based on the real-space finite-difference method and presented several examples to demonstrate the efficiency and applicability of our code. The combination of the timesaving double-grid technique and the Fourier filtering of the pseudopotential can suppress the spurious difference of the total energy for the displacement of the atom relative to the grid points. From what has been demonstrated above, our code enables us to implement accurate first-principles calculations and are efficiently applicable to various systems. When coupled with electron-transport calculations [1], our code would be useful in studying electron-transport behavior of nanostructures.

[1] K. Hirose, T. Ono, Y. Fujimoto, and S. Tsukamoto, *First-Principles Calculations in Real-Space Formalism, Electronic Configurations and Transport Properties of Nanostructures* (Imperial College Press, London, 2005).

[2] J.R. Chelikowsky, N. Troullier, and Y. Saad, Phys. Rev. Lett. **72**, 1240 (1994).

[3] T. Ono and K. Hirose, Phys. Rev. Lett. **82**, 5016 (1999); Phys. Rev. B **72**, 085105 (2005); Phys. Rev. B **72**, 085115 (2005); K. Hirose and T. Ono, Phys. Rev. B **64**, 085105 (2001).

[4] P.E. Blöchl, Phys. Rev. B **50**, 17953 (1994).

[5] R.D. King-Smith, M.C. Payne, and J.S. Lin, Phys. Rev. B **44**, 13063 (1991).

Image Potential and Field States at Transition Metal Surfaces

A. Hanuschkin, D. Wortmann, S. Blügel
IFF-1: Quantum Theory of Materials

By combining the first-principles concept based on the density functional theory with a model vacuum potential we calculate image potential states in the presence of an electric field applied on a magnetic Fe(110) surface. Our investigations are based on the Green function embedding technique which allows to treat a truly semi-infinite surface and whence yields a continuum of bulk states. This turns out to be of crucial importance in order to investigate the qualitative difference between localized image or field states located in a band gap of the substrate and states in resonance with bulk states present at the same energies. This difference leads to remarkable changes in the binding energy versus field dispersion of the states. Furthermore, we show that in case of the Fe(110) surface the calculated magnetic exchange splitting increases with the electric field and is also modified by the transition from field states to surface resonance states.

For the understanding of the electronic properties of surfaces in particular and surface science in general image potential states proved to play a prominent role. These states occur as a Rydberg-like series of surface states close to the vacuum level confined by the surface on the one side and the slowly $1/z$ like decaying image potential on the other side. Hence, image states are located relatively far away from the surface, have a long lifetime and thus can be ideally observed experimentally by modern methods like two-photon photoemission, inverse photoemission and scanning tunneling microscopy (STM). These states and the corresponding experimental results are also easily described by rather simple theoretical models making them ideal spectator states to probe the surface and the electronic structure. The binding energies can be expressed by a series of image potential (or Rydberg) states labeled by an index n and measured from the vacuum level E_{vac},

$$E_n = E_{\mathrm{vac}} - \frac{0.85\ \mathrm{eV}}{(n+a)^2},\ n = 1, 2, 3, ..., \quad (1)$$

where the quantum defect a has to be introduced due to the finite tail of the wavefunction overlapping with the crystal.

Recently increasing efforts are made to extract details of the electronic structure of the surface from such measurements. For example, the investigation of the exchange splitting of the image states became feasible. Using the spectroscopy mode of a spin-polarized STM the magnetic splitting of the image states can be investigated locally and hence the underlying magnetic structure can be resolved [2]. In these experiments a rather large bias voltage is applied between the STM tip and the sample surface such that electrons can tunnel into the image states. Strictly speaking, the states observed are no longer simple image states as the applied bias leads to a substantial electric field applied to the surface. Hence, the electrons are no longer confined by a $1/z$ like potential but experience the additional linear potential of the field. We will use the term “field states” for these generalized image states.

Within the conventional approximations used for the exchange correlation potential to the density functional theory (DFT), the calculation of image potential states is not possible. In particular, the only input into the popular local density approximation is the exponentially decaying local charge density in the vacuum and hence this approximation yields a potential decaying exponentially towards the vacuum level. In order to fix this deficiency we replaced the DFT vacuum potential by a model potential with the correct $1/z$ asymptotic tail. Following similar work by other groups and adding a constant electric field ξ we assumed the following form of the potential in the vacuum

$$V_{\mathrm{im}}(z) = V_{\mathrm{vac}} - \frac{e^2}{4\pi\epsilon_0} \cdot \frac{1}{4|z - z_{\mathrm{i}}|} + z\xi. \quad (2)$$

Where z is the coordinate normal to the surface, V_{vac} denotes the vacuum level of the potential and z_{i}, the so-called image plane position, is a parameter.

Our actual DFT calculations [1] are performed using the embedded Green-function method [5] which has been implemented within the context of the full-potential linearized augmented plane-wave (FLAPW) method [3] as part of the FLEUR project [4]. In this method, the surface is modeled by few atomic layers (the embedded region) which is embedded as a sandwich between semi-infinite bulk and vacuum.

In *Fig. 1* the spin resolved local density of states (LDOS) is shown for $\vec{k}_{\parallel} = \overline{\Gamma}$. The first four image potential states are clearly visible. In principle,

these states lead to a delta peak in the density of states, which is, however, artificially broadened by adding a small imaginary part of 2.7 meV to the energy. The dashed vertical lines indicate experimentally measured energies. An exchange splitting of the states can be observed. This splitting is most pronounced for the $n = 1$ state and decays rapidly for the higher Rydberg states. For the first Rydberg state ($n = 1$) we obtain a spin splitting of 133 meV. The calculated splitting is nearly unaffected by variations of the image plane position and applied mixing region. Furthermore, using different approximations for the exchange correlation potential the magnitude of the splitting does not change significantly.

By applying a positive electric field to the surface the image potential states turn into field states. The electric field applied pushes the electron back into the substrate and thus it is expected to have a particularly strong effect on the higher image states which have a considerable weight in the vacuum. Even for small fields the energy for the Rydberg states $n \to \infty$ is no longer the vacuum energy. *Fig. 2* shows the evolution of the image potential states with applied electric field, the peak positions of *Fig. 1* can be found to be the data points at zero field strength. The lower panel of *Fig. 2* additionally shows the exchange splitting, i.e. the difference of the majority and minority curves of the upper panel. This plot shows rather drastic changes of the exchange splitting with respect to the applied field. For zero field the spitting is very small for all states except the $n = 1$ state. 3 This can be understood from the fact that the higher Rydberg states have their main weight in the vacuum where the potential is spin degenerate and only the lowest states have a significant overlap with the bulk potential. However, this picture changes for larger field strength. The states are pushed towards the surface and the exchange splitting strongly increases. Two further interesting features are marked in *Fig. 2*. At mark (A) the magnetic exchange splitting of the $n = 2$ state becomes larger than the splitting of the $n = 1$ state. Such an interesting crossover seems to be also present in experiment [2]. Furthermore,

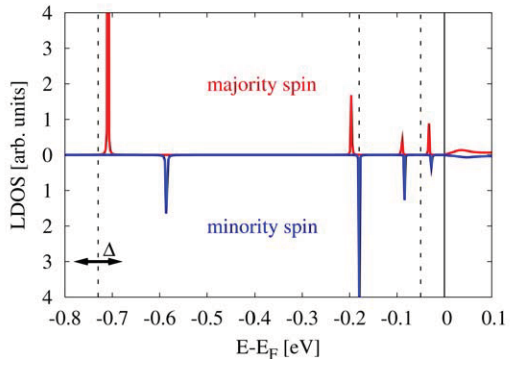

FIG. 1: Spin resolved LDOS of Fe(110) at $\vec{k}_{\|} = \overline{\Gamma}$. Dashed lines indicate experimental values of the spin averaged image state energies. All energies are given relative to the vacuum energy marked by the black line.

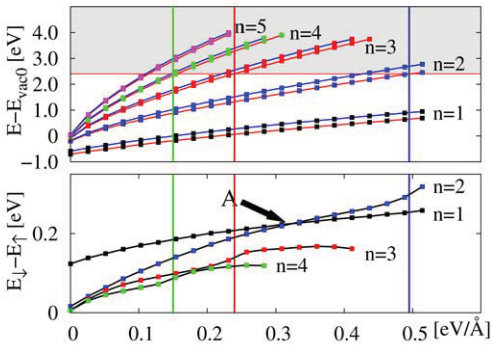

FIG. 2: In the upper panel the field states of Fe(110) at $\vec{k}_{\|} = \overline{\Gamma}$ are shown. The difference between the majority and the minority state is plotted in the lower panel.

the curves for the $n > 1$ states exhibit a change in slope. The positions of the change are marked (vertical lines) for the $n = 2, 3, 4$ states and projected into the plot of the Fe(110) field states. They all appear at the same energy (horizontal line) of ∼2.4 eV. At this energy, the majority band gap of the Fe(110) substrate ends. Hence, it can be concluded that the change in slope is a consequence of the field state approaching the continuum of Fe majority states and turning into a resonance. Before that they are deflected giving rise to bigger spin splitting.

We investigated image states and field states using the truly semi-infinite surface provided by the Green function embedding method. Our DFT calculations confirm the general trend found in simple one-dimensional models but additionally indicate that these states also show features of the electronic structure of the surface and the substrate. In particular the exchange splitting of the image and field states reflect the spin polarization of the surface potential. The transition from image and field states from being localized between the vacuum potential and a gap in the bandstructure of the substrate into a resonance state hybridizing with substrate states at energies not in a projected band gap can also lead to experimentally accessible changes in the energy versus field dispersion. These effects might be the origin of the experimentally observed field dependence of the exchange splitting in STS.

[1] Hanuschkin, Wortmann and Blügel, Phys. Rev. B **76**, 165417 (2007)

[2] Kubetzka, Bode, and Wiesendanger, Appl. Phys. Lett. **91**, 012508 (2007)

[3] Wortmann, Ishida, and Blügel, Phys. Rev. B **65**,165103 (2002) and Phys. Rev. B **66**, 075113 (2002).

[4] see: http://www.flapw.de

[5] Inglesfield, J. Phys. C **14**, 3795(1981)

The Fe/MgO Interface: The Important Role of Oxygen

F. Matthes, M. Müller, C. M. Schneider
IFF-9: Electronic Properties

Utilizing spin and angle-resolved valence band photoemission spectroscopy, we systematically studied the effect of an oxygen excess or deficiency on the electronic band structure at the interface of Fe/MgO(001). Our data revealed a multifaceted modification of the spin polarization at the Fermi level that we can ascribe to the different nature of the oxygen bonding. The most prominent observation, a strong enhancement of the spin polarization in the case of an oxygen depletion at the interface, may be exploited to further improve the functionality of single crystalline magnetic tunnelling junctions (MTJs).

Due to their manifold application potential, e.g. in magnetic data storage technology (read heads of hard discs, non-volatile magneto-resistive random access memory), the further development of MTJ's functionalities is in the focus of current spintronic research. Today, MTJs based on single crystalline Fe(100)/MgO or Co(100)/MgO systems provide the highest achievable tunnelling magneto-resistance (TMR) ratios. The progress compared to amorphous MTJs is related to an utilization of the MgO tunnelling barrier as a spin filter. This new functionality is associated with different conductivities of the electron wave functions in the gap of the tunnel barrier that depend on their spatial symmetry character. It is thus obvious that the interfacial band structures in MTJs will have a strong influence on their spin dependent transport properties. For the theoretical calculation of high TMR ratios in single crystalline Fe/MgO/Fe MTJs an atomically sharp and perfectly ordered interface is often assumed. In contrast, a realistic interface may suffer upon morphological and chemical deviations from ideality. One resulting consequence is an ongoing discussion about the formation of FeO and its influence upon the maximum obtainable TMR value. For an asymmetric system, Fe/FeO/MgO/Fe, the charge redistribution due to the iron oxide formation was predicted to drastically reduce the TMR ratio[1], while Tusche et al. [2] predicted high TMR values for a symmetric Fe/MgO/Fe MTJ with one monolayer of FeO at both interfaces. Our spin polarized photoemission study aims to clarify the influence of a chemical modified interface upon the electronic band structure and its consequences for the spin polarization at the Fe/MgO interface.

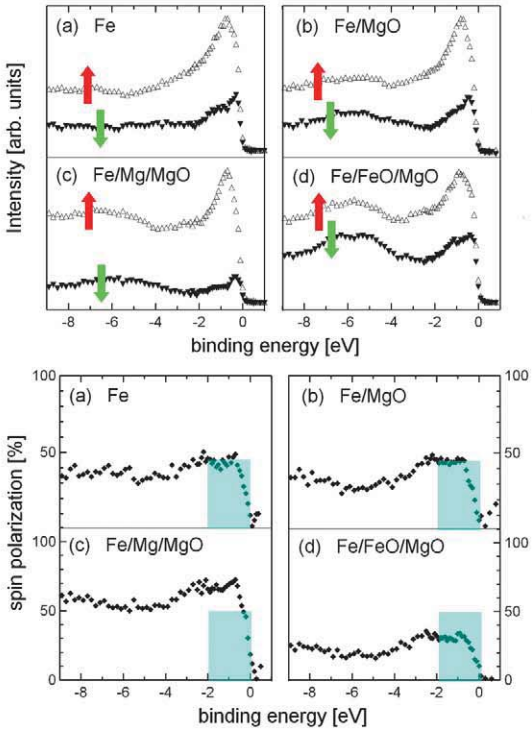

FIG. 1: Spin-resolved photoemission spectra(top) and spin polarization(bottom) for (a) pure Fe surface, (b) stoichiometric, (c) underoxidized and (d) overoxidized Fe/MgO(001) interface. The spectra were collected in normal emission. Non-relativistic dipole selection rules allow transitions from initial states with Δ_1 and Δ_5 spatial symmetry. Filled/open triangles display spin down/up photoelectrons. The underlying light blue rectangles represent the spin polarization of the pure Fe surface.

For this purpose, three different sample classes were prepared representing a stoichiometric (Fe/MgO), underoxidized (Fe/Mg/MgO) and overoxidized (Fe/FeO/MgO) MgO film at the interface. Special emphasis was laid on the chemical characterization of the MgO/Fe interface. Besides Auger electron spectroscopy, the degree of Mg and Fe oxidation was supervised by probing the chemically induced shifts of the Mg 2p and Fe 3p core levels, thereby using a photon energy of 88.3 eV to ensure high surface sensitivity. A more detailed description of the preparation procedure and experimental geometry is given in [3]. The spin and angle-resolved pho-

toemission spectra were recorded at the beamline U250-PGM operated by the research centre Jülich at the storage ring DELTA (Dortmund) using a cylindrical mirror-type analyzer with integrated spin polarized low-energy electron diffraction detector (SPLEED).

Fe-system: The photoemission spectra always reveal two peaks, one is located at (-0.4 ± 0.2)eV below the Fermi energy and the other at (-0.9 ± 0.2)eV binding energy. They originate from bulk Fe initial states with Δ_5 and Δ_1 spatial symmetry. For uncovered Fe films, a positive spin polarization of about 40% to 50% in an energy interval from -0.2 eV to E_F was obtained (Fig. 1a).

Fe/MgO system: Besides the peak formation in the range of -3.5 to -8.5 eV, originating from oxygen 2p levels, the spectra and the spin polarization (Fig.1b) do not display noteworthy differences when we study stoichiometric MgO films in contact to the Fe electrode. This observation reflects the strong ionicity of the MgO bonds which allows no reaction with the adjacent metal.

Fe/FeO/MgO system: The spectral intensities originating from the Fe Δ_5 and Δ_1 states approach each other, leading to a reduced spin polarization of about 30% (Fig.1d). Moreover, the spin resolved measurements displayed a spin-splitting in the oxygen-related features that we associate with FeO formation (Fig.2). We thus conclude that the partial oxidation of the Fe surface layer is accompanied by a reduction of the spin polarization at the interface. Our conclusion is consistent with theoretical calculations that predict a strong decrease of Δ_1 majority density of states at the interface. The reduction is caused by an increased in-plane bonding between the surface Fe and oxygen atoms positioned in the bcc hollow-sites.

Fe/Mg/MgO system: Our spectra display a gain in intensity for the direct transitions emerging from initial states with Δ_1 symmetry and spin up character when compared to those with Δ_5 symmetry and opposite spin. The resulting effect is a strong enhancement of the spin polarization close to the Fermi level, exceeding a value of 70% (Fig.1c). These systems possess an excess of metallic magnesium atom with two uncombined valence electrons.

For MgO, having only a low content of unbounded Mg atoms, it is known that strongly localized defect states will develop in the bandgap, so called oxygen vacancies or F-color centers. In our samples, the oxygen vacancy concentration is high: (Mg^{2+}/MgO $\sim$ 0.5). As a consequence, these oxygen vacancy states may interact with each, e.g. form defect bands. Furthermore, the symmetry of the localized defect states has been calculated to exhibit a Δ_1 spatial symmetry character [4]. Recent performed scanning tunneling spectroscopy and microscopy (STS/STM) experiments on ultrathin MgO(001) layers deposited on Ag(001) gave evidence for a ground-state of the oxygen point defects beeing located around -0.1 eV below the Fermi level [5]. Based on these findings we may consider, that an extended oxygen vacancy concentration may form an Δ_1-like electronic state with a band-like character in the energy region close to E_F. Using this assumption, the presence of extended oxygen vacancies at under-oxidized Fe/MgO interfaces may involve a hybridization between Δ_1-like oxygen defect states with the Fe 3d $\Delta_1^{\uparrow}$ valence bands. Our observed increased spin polarization close to E_F would then be consistent within this qualitative model.

Recent electronic transport calculations, performed by Velev et al. [6], predicted that oxygen point defects located in the middle of a thin MgO film will lead to a strong reduction of the TMR values, because they will establish a spin-independent conduction channel between the two electrodes. Expanding these findings, we conclude that not only the existence/density of uncombined Mg but also its position in the barrier will have a decisive influence upon the performance of MTJs. According to the model proposed above, we suppose that the enhancement in the functionality of MTJs should be most effective, if the oxygen vacancies are located only at the Fe/MgO interface.

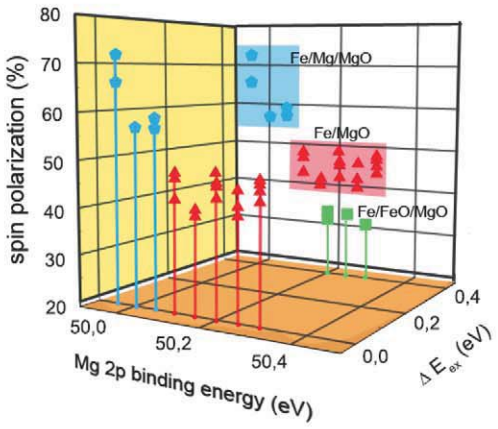

FIG. 2: Spin polarization (SP) at the Fermi level E_F for the systems Fe/Mg/MgO (blue pentagrams) and Fe/MgO (red triangles) as a function of the binding energy of the Mg **2p** peak maximum. The Fe/FeO/MgO samples (green rectangles) are characterized by an additional exchange splitting ΔE_{ex} in the O **2p** levels.

[1] X.-G. Zhang, W.H. Butler and A. Bandyopadhyay, Phys. Rev. B 68, 092402 (2003).

[2] C. Tusche, H. L. Meyerheim, N. Jedrecy, G. Renaud, A. Ernst, J. Henk, P. Bruno, and J. Kirschner, Phys. Rev. Lett. 95, 17610 (2005).

[3] M. Müller, F. Matthes and C. M. Schneider, Europhys. Lett. 80, 17007 (2007).

[4] A. Gibson, R. Haydock and J.P. LaFemina, Phys. Rev. B 50, 2582 (1994).

[5] M. Sterrer, M. Heyde,M. Novicki, N. Nilius, T. Risse, H.P. Rust, G. Pacchioni and H.J. Freund, J. Phys. Chem. B 110, 47 (2006).

[6] J. Velev, K.D. Belashchenko, S.S. Jaswal and E.Y. Tsymbal, Appl. Phys. Lett. 90, 072502 (2007).

Electronic Properties of Individual Point Defects at Semiconductor Surfaces

A. Schindlmayr[1], Ph. Ebert[2]

[1] IFF-1: Quantum Theory of Materials
[2] IFF-8: Microstructure Research

Intrinsic defects play a decisive role for the electric characteristics of semiconductor surfaces, but so far it has proved very difficult to identify the electronic properties of individual point defects reliably by either experimental or theoretical methods. On the one hand, standard spectroscopic techniques like photoemission (PES) cannot be applied straightforwardly due to the low defect concentration. On the other hand, all theoretical calculations until now suffered from fundamental limitations of density-functional theory, which lead to systematic errors not only for the band gap itself but also for the positions of localized gap states. In order to overcome these problems, we recently developed a range of novel quantitative techniques: For the experimental measurements we combine PES with scanning tunneling microscopy (STM) [1], while our computational approach employs many-body perturbation theory with proper quasiparticle corrections for band gaps and defect states [2, 3].

The (110) surfaces of III–V semiconductors have several features that make them especially interesting for defect studies: STM can probe both filled and empty states by reversing the bias, thus revealing a wealth of information about local atomic geometries and charges, and as there are no surface states in the band gap, electrically active defects may pin the Fermi level. This pinning always occurs at the positions of the charge-transition levels, which mark the values of the Fermi energy where the charge state of the defect changes. A precise determination of the charge-transition levels is hence of considerable interest for many technological applications.

As an example we now consider the P vacancy at InP(110), whose geometry is illustrated in Fig. 1. The In–In bonds across the vacancy give rise to a nondegenerate defect state $1a''$ inside the band gap that can accommodate zero, one or two electrons, corresponding to the positive, neutral or negative charge state, respectively. To emphasize that the sign of the charge accumulation also modifies the local atomic relaxation, we write the formation energy for the positive charge state, relative to the neutral one, as $E^{\mathrm{form}}(+/0) = E^{\mathrm{vac}}(+,Q_+) - E^{\mathrm{vac}}(0,Q_0) + E_{\mathrm{F}}$, where $E^{\mathrm{vac}}(q,Q)$ denotes the total energy of a InP(110) surface featuring a single P vacancy with the actual electron population $q \in \{+,0,-\}$ and a relaxed atomic geometry corresponding to the charge state $Q \in \{Q_+,Q_0,Q_-\}$. The final term accounts for the transfer of one electron between the defect state and the electron reservoir, i.e., the Fermi energy E_{F}. The relevant charge-transition level

$$\epsilon^{+/0} = E^{\mathrm{vac}}(0,Q_0) - E^{\mathrm{vac}}(+,Q_+)\,. \qquad (1)$$

is defined as the value of the Fermi energy where the energetically most favorable charge state changes.

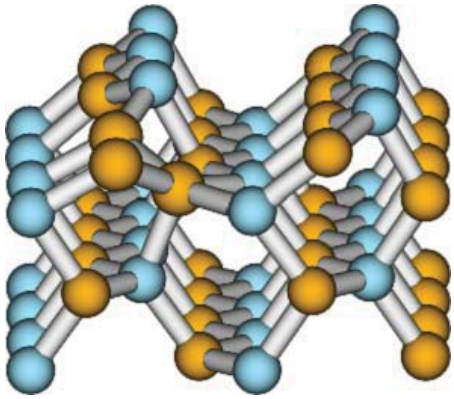

FIG. 1: Geometry of the P vacancy at InP(110). In and P atoms are colored orange and blue, respectively. The three In atoms surrounding the vacancy in the top row form bonds among each other, giving rise to a localized defect state.

All theoretical studies so far used density-functional theory within the local-density approximation (LDA) to evaluate the right-hand side of eq. (1) directly [1, 4]. This approach predicts defect geometries with high accuracy, but the calculated charge-transition levels suffer from systematic errors, which arise because $E^{\mathrm{vac}}(0,Q_0)$ and $E^{\mathrm{vac}}(+,Q_+)$ refer to systems with different electron numbers, and the LDA ignores the discontinuous behavior of the exact exchange-correlation potential that is crucial in such cases. As a consequence, the charge-transition levels, like the band gaps, are underestimated. For a better quantitative scheme we rewrite eq. (1) by adding and subtracting the total energy $E^{\mathrm{vac}}(0,Q_+)$ of a constrained nonequilibrium system with $q = 0$ but the geometry of the positive vacancy. In this way the charge-transition level naturally decomposes into two distinct contributions. The first term $E^{\mathrm{vac}}(0,Q_0) - E^{\mathrm{vac}}(0,Q_+)$ equals

the energy difference between the relaxed neutral vacancy and the constrained nonequilibrium geometry and is always negative. As the electron number remains constant, the LDA is applicable and yields a value of $-0.54\,\mathrm{eV}$. The second term $E^{\mathrm{vac}}(0,Q_+) - E^{\mathrm{vac}}(+,Q_+)$ accounts for the transfer of one electron from the reservoir to the defect state and equals the electron affinity of the positive vacancy. Within a *many-body* treatment the latter is identical to the position of the unoccupied defect state $\epsilon_{1a''}$ in the band gap. For this step we employ many-body perturbation theory and the GW approximation for the electronic self-energy Σ, which does not suffer from any discontinuity problem and yields accurate band structures for III–V semiconductors and their surfaces. In practice we evaluate the defect level as the sum

$$\epsilon_{1a''} = \epsilon_{1a''}^{\mathrm{LDA}} + \langle\varphi_{1a''}^{\mathrm{LDA}}|\Sigma(\epsilon_{1a''}) - V_{\mathrm{xc}}^{\mathrm{LDA}}|\varphi_{1a''}^{\mathrm{LDA}}\rangle \quad (2)$$

of the LDA eigenvalue $\epsilon_{1a''}^{\mathrm{LDA}}$ and a state-dependent self-energy correction. A detailed discussion of our computational method can be found in Ref. [3]. With $\epsilon_{1a''} = 1.36\,\mathrm{eV}$ we eventually obtain a total theoretical value of $0.82\,\mathrm{eV}$ for the charge-transition level.

The experimental measurement of the charge-transition level is based on a simple concept: Singly positively charged P vacancies are produced in high concentrations by annealing initially defect-free p-doped InP(110) cleavage surfaces. Simultaneously, the position of the Fermi level, which is originally close to the top of the valence band, shifts towards midgap as shown in Fig. 2. The filled diamonds (left axis) show the band bending at the surface, as determined through PES, whereas the open circles show the vacancy concentration (from STM, right axis) as a function of the annealing time. The band bending reaches a saturation value of $0.65\,\mathrm{eV}$ at a vacancy concentration of $5 \times 10^{12}\,\mathrm{cm}^{-2}$. Fig. 2 also demonstrates that the Fermi-level shift is directly correlated to the increase of the vacancy concentration. By combining the vacancy concentration with the band bending it induces, it is possible to determine the energy of the charge-transition level in the band gap E_{sd}, because the charge per surface area in the surface layer Q_{ss} is exactly compensated by the charge density per surface area in the depletion layer Q_{sc}. The charge per surface area induced by a concentration n_{sd} of singly positive P surface vacancies is $Q_{\mathrm{ss}} = en_{\mathrm{sd}}/[\exp((E_{\mathrm{F}} - E_{\mathrm{sd}})/kT) + 1]$. The difference in energy of the charge-transition level and the Fermi level $E_{\mathrm{sd}} - E_{\mathrm{F}}$ is given by $(E_{\mathrm{sd}} - E_{\mathrm{sv}}) - (E_{\mathrm{v}} - E_{\mathrm{sv}}) - (E_{\mathrm{F}} - E_{\mathrm{v}})$ (definitions see inset in Fig. 2; E_{v} and E_{sv} are the positions of the valence band in the bulk and at the surface, respectively), where $E_{\mathrm{v}} - E_{\mathrm{sv}}$ is the band bending eV_{s} measured by PES at the surface. The charge density Q_{sc} in the depletion layer compensating Q_{ss} is

$$Q_{sc} = \sqrt{2\epsilon_0\epsilon_{\mathrm{r}}n_{\mathrm{dop}}kT\left[\exp\left(\frac{-eV_{\mathrm{s}}}{kT}\right) + \frac{eV_{\mathrm{s}}}{kT} - 1\right]}\,. \quad (3)$$

The energy difference between the Fermi level and the valence-band maximum in the bulk has been determined for a nondegenerate InP crystal from the carrier concentration according to

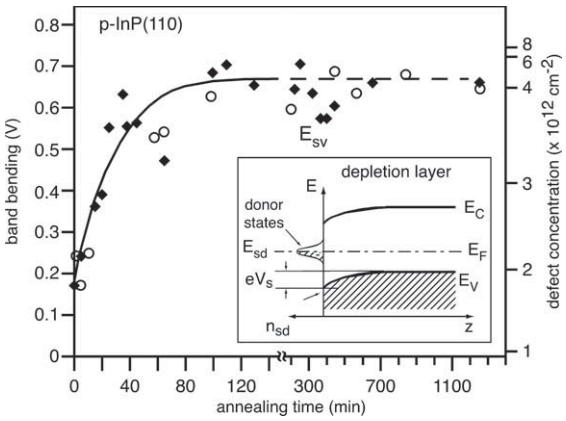

FIG. 2: The band bending (filled diamonds, left axis) and the vacancy concentration (empty circles, right axis) on the InP(110) surface as a function of the annealing time at 160°C. The solid line is the vacancy concentration calculated from the formuls for Q_{ss} and Q_{sd} and a fit through the measured band-bending values. The dashed line shows the saturation value. The inset shows the schematic drawing of the depletion region in case of a fully pinned surface.

$$E_{\mathrm{F}} - E_{\mathrm{v}} = -kT\ln\left[4n_{\mathrm{dop}}\left(\frac{2m_{\mathrm{p}}kT}{\pi\hbar^2}\right)^{-3/2}\right] \quad (4)$$

with m_{p} being the mass of the holes. These equations permit a determination of the difference in energy of the charge-transition level E_{sd} and the surface valence-band maximum E_{sv} using the vacancy-concentration dependence of the band bending. We obtain an energy for the charge-transition level of the P vacancy of $0.75 \pm 0.1\,\mathrm{eV}$ at room temperature. Note that the knowledge of the defect concentrations is crucial to determine the charge-transition level from a measurement of the band bending.

In summary, we introduced novel theoretical as well as experimental techniques designed for a quantitative identification of thermodynamic charge-transition levels of point defects at semiconductor surfaces. As a demonstration we studied the P vacancy at InP(110), for which we obtained an experimental value $\epsilon^{+/0} = 0.75 \pm 0.1\,\mathrm{eV}$. While our own LDA calculation yields $0.47\,\mathrm{eV}$, in agreement with earlier published results $0.52\,\mathrm{eV}$ [1] and $0.388\,\mathrm{eV}$ [4] at the same level of approximation, and underestimates the experimental value significantly, the GW approximation ensures a more accurate treatment of electronic many-body effects. In this way we obtain an improved theoretical value of $0.82\,\mathrm{eV}$ that lies perfectly within the experimental error bar.

[1] Ph. Ebert, K. Urban, L. Aballe, C. H. Chen, K. Horn, G. Schwarz, J. Neugebauer and M. Scheffler, Phys. Rev. Lett. **84**, 5816 (2000).

[2] M. Hedström, A. Schindlmayr, G. Schwarz and M. Scheffler, Phys. Rev. Lett. **97**, 226401 (2006).

[3] A. Schindlmayr and M. Scheffler, in *Theory of Defects in Semiconductors*, edited by D. A. Drabold and S. K. Estreicher (Springer, Berlin, Heidelberg, 2007), p. 165.

[4] M. C. Qian, M. Göthelid, B. Johansson and S. Mirbt, Phys. Rev. B. **66**, 155326 (2002).

Trends of Exchange Interactions in Dilute Magnetic Semiconductors

B. Belhadji[1], L. Bergqvist[1], R. Zeller[1], P. H. Dederichs[1], K. Sato[2], H. Katayama-Yoshida[2]

[1] IFF-3: Theory of Structure Formation

[2] Institute for Scientific and Industrial Research, Osaka University, Japan

We discuss the importance of different exchange mechanisms like double exchange, p-d exchange and superexchange in dilute magnetic semiconductors (DMS). Based on *ab-initio* calculations in conjunction with the coherent potential approximation (CPA) for the electronic structure of the DMS, we show that the different mechanisms exhibit different dependences on the concentration of the magnetic impurities and on the position of the Fermi level in the band gap. Common to all interactions is that they are determined by the hybridization of the impurity orbitals with the orbitals of neighbouring impurities and by the resulting energy gain due to the formation of spin dependent bonding and anti-bonding hybrids.

Ever since the discovery of ferromagnetism by Ohno et al. of $Ga_{1-x}Mn_xAs$ [1], dilute magnetic semiconductors (DMS) like (Ga,Mn)As, (Ga,Mn)N or (Zn,Cr)Te are regarded as promising materials for spintronics. They show a particularly rich magnetic behaviour, being governed by different kinds of exchange interactions like Zener's double exchange, Zener's p-d exchange and superexchange. The magnetic properties can be successfully calculated by *ab initio* methods and many calculations for such systems have been performed, see e.g. [2, 3]. However, the physical understanding of the involved exchange mechanisms is a very delicate and difficult problem, since no simple and elementary magnetic interaction exists, and a multitude of mechanisms can lead to ferromagnetism or anti-ferromagnetism and some of them might even act simultaneously. Our discussion is concentrated on the spin-polarized density of states (DOS) and the interaction effects introduced in the DOS by the hybridization of the wavefunctions with those of neighbouring atoms. We describe below qualitatively the Zener's double exchange and the Zener's kinetic p-d exchange mechanisms which stabilize ferromagnetism in DMS. In addition we discuss the superexchange mechanism which normally leads to a disordered magnetic phase [4].

Double exchange: A schematic DOS of a transtion metal impurity in a wide band gap semicondutor, such as Mn or Cr in GaN is shown in Fig.1a. We consider the ferromagnetic phase. The Fermi level is assumed to fall within the partially occupied majority band of the t_{2g} anti-bonding states. Increasing the magnetic impurity concentration leads to an increase of the bandwidth and thus a gain in energy, since the occupied states just below E_F are transfered to lower energies. This gain in energy is proportional to the hopping matrix element t between two neighbouring impurities and scales in the dilute limit as the square root of the concentration $\sqrt{c}$. Thus due to the increase of the band width with increasing concentration ferromagnetism is stabilized. This is a very strong mechanism.

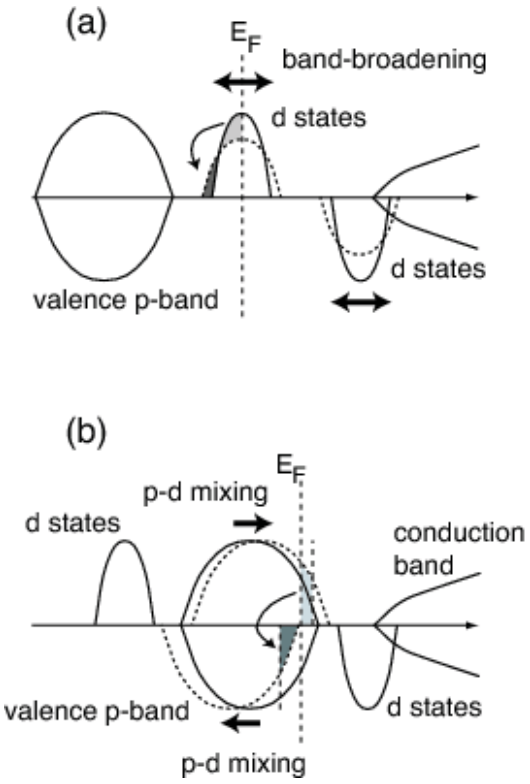

FIG. 1: a) Schematic figure of the spin-polarized DOS of a transition metal impurity in a wide gap semiconductor. b) Schematic figure of the spin-polarized DOS in the case of p-d exchange, when the majority d level lies below the valence p band and the minority level above.

Kinetic p-d exchange: Fig.1b sketches the physical situation of the Zener's p-d exchange. In narrow gap

semiconductors like GaSb or InSb the Mn d majority level lies below or at the lower edge of the Sb p band, while the minority d level lies well above E_F. This means that Mn has a magnetic moment of 5 μ_B, well localized at the Mn site. Then, in the neutral state, due to charge neutrality one electron per Mn atom is missing in the valence band as indicated by the position of E_F in figure 1(b). Since the impurity d wavefunctions hybridize with the p wavefunctions of the neighbouring p elements, the majority p band is shifted to higher energies, while the minority p band is shifted to lower energies due to hybridization with the higher liying minority d state (Fig.1b). If the hybridization is sufficiently strong, the minority p band becomes completely occupied, while one electron per Mn atom is missing in the majority p band, leading to a half-metallic density of states. As a result the Sb atoms carry small magnetic moments of 1 μ_B/Mn in total, being aligned anti-parallel to the local moment of Mn, such that the total magnetic moment per Mn atom is 4 μ_B.

Characteristic for both interactions is that they favour ferromagnetism and that the Fermi level lies within the band. If, in the case of p-d exchange, the Fermi level lies above the valence band or, in the case of double exchange, above or below the impurity d band, the hybridization effects are the same, but no energy can be gained to favour ferromagnetism.

Superexchange interaction: Superexchange mechanism does not require finite density of states at the Fermi level. The reason for this is related to the hybridization of states energetically localized well below and well above E_F. Fig.2 shows the density of states for two impurity systems with moments $\mathbf{S}_1$ and $\mathbf{S}_2$, being anti-parallel aligned and having equal concentrations $c/2$. Since the electronic states with the same spin direction hybridize with each other, the lower occupied energy peaks are shifted to lower energies, the higher empty ones to higher energies. Due to the down-shift of the lower occupied level binding energy is gained, which stabilizes the antiferromagnetic coupling. The energy gain is inversely proportional to the energy difference of hybridizing states and proportional to the hopping t matrix element.

The superexchange interaction is independent of the position of the Fermi level, as long as it lies between the two impurity bands. If it enters these bands, e.g. the lower one, it decreases, roughly by a factor of two, if the Fermi level lies in the middle of the band and it vanishes if E_F lies below this band. Thus, if the Fermi level lies in the band, there is a competition between double exchange and superexchange, which is usually won by double exchange, resulting in ferromagnetism, except when E_F approaches the upper band edge, where superexchange takes over. Thus when the Fermi level lies between the t_{2g} majority and minority states of neighbouring sites, as it is the case for (Ga,Fe)N or (Zn,Mn)Se, superexchange favors antiferromagnetic alignment leading to a disordered local moment state. However, when the Fermi level lies between the t_{2g} and e_g majority states, as it is the case for (Ga,V)As the analogous hybridization induced superexchange mechanism favors ferromagnetism [4].

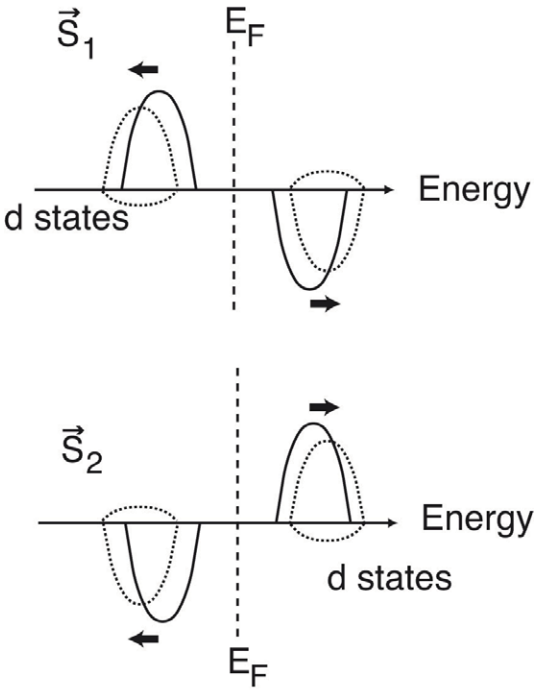

FIG. 2: Schematic figure of the DOS of two anti-parallel aligned impurities 1 and 2 with equal concentrations $c/2$.

In summary, we have presented the trends of the magnetic exchange interactions in diluted magnetic semiconductors (DMS). Several different exchange mechanisms have been identified and analyzed from an electronic structure point of view by simple hybridization models which leads to better understanding of the magnetic properties of DMS.

[1] Matsukura F, Ohno H and Dietl T 2002 *Handbook of Magnetic Meterials* vol 14 (Amsterdam: Elsevier) p1

[2] Sato K, Dederichs P H and Katayama-Yoshida H 2003 *Phys. Rev.* B **68** 81203(R)

[3] Kudrnovsky J, Turek I, Drchal V, Maca F, Weinberger P and Bruno P 2004 *Phys. Rev.* B **69** 115208

[4] Belhadji B, Bergqvist L, Zeller R, Dederichs P H, Sato K and Katayama-Yoshida H. 2007 J. Phys.: Condens. Matter **19** 436227

Dumbbell Rattling in Thermoelectric Zinc-Antimony

W. Schweika[1], R. Hermann[1], M. Prager[2], J. Perßon[1]

[1] IFF-4: Scattering Methods
[2] IFF-5: Neutron Scattering

A significant reduction in energy consumption through the recovery of waste heat could be achieved by efficient materials for thermoelectric power generation. Efficient thermoelectric materials require "electron crystal, phonon glass" behavior, combining both good electric and poor thermal conductivity [1]. Dynamic disorder of "rattling" heavy atoms has been shown to impede the thermal transport in filled cage structures such as skutterudites and clathrates [2, 3]. We report [4] inelastic neutron scattering and heat capacity measurements that identify a new type of dynamical disorder in Zn_4Sb_3, namely localized dumbbell vibrations. The anharmonicity of this soft vibration is in quantitative agreement with the low thermal conductivity. Soft localized phonon modes appear to be a universal feature of good thermoelectric materials not restricted to cage-like structures.

Among thermoelectric materials, zinc antimony exhibits an outstanding figure of merit particularly due to its low thermal conductivity. While the structure and precise stoichiometry of the Zn_4Sb_3 compound has been under debate for decades, it has been speculated that the low thermal conductivity originates from structural disorder due to Zn-interstitials ($\approx$ 17%) and Zn-vacancies ($\approx$ 10%) [5]. However, efficient phonon scattering can be expected from the interaction of the heat carrying acoustic phonons with phonons that are sufficiently low in energy to cross the acoustic branches and are highly thermally populated, directing research towards soft local modes. In view of masses and bonding distances in Zn_4Sb_3, rather than the Zn-interstitials a more likely candidate for such a soft mode is the rattling of the heavy Sb_2 dumbbells, see Fig. 1, particularly so because the dimerization of antimony along the c-axis into tightly bonded dumbbells opens rattling space. Herein, we report inelastic neutron scattering and heat capacity measurements that identify in Zn_4Sb_3 a new type of dynamical disorder: soft localized dumbbell vibrations of Sb-dimers with an energy of 5.3 meV (62 K). This dynamic disorder evolves from regular atoms rather than from structural disorder and is believed to be the origin of low thermal conductivity found in this material.

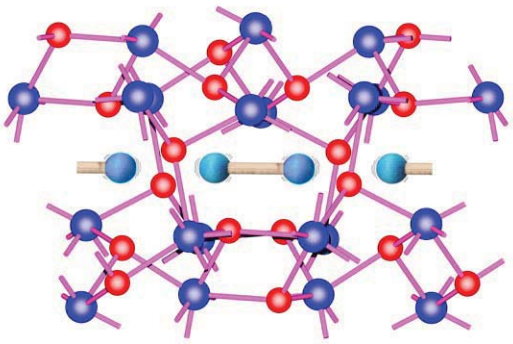

FIG. 1: Vibrating Sb-dumbbells in Zn_4Sb_3 are depicted in their neighborhood of Zn-atoms (red) and Sb-atoms (blue).

Our heat capacity measurements of Zn_4Sb_3 reveal the signature of a prominent soft local mode in the low temperature regime, see Fig. 2. Within a simple model, one Einstein mode in addition to the Debye contribution is required to account for the heat capacity. This modeling yields that 15% of the atomic degrees of freedom exhibit an Einstein oscillator behavior with energy E=5.3(1) meV, and a Debye temperature of 240(2) K for the remaining average phonon contribution.

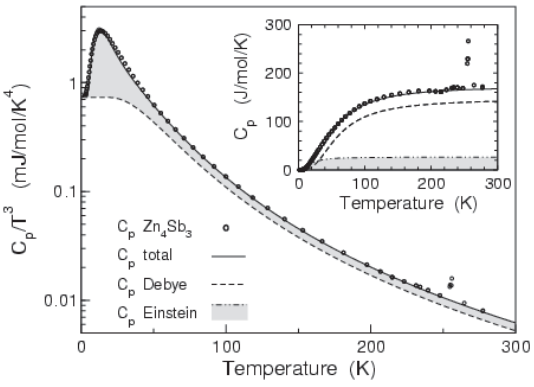

FIG. 2: The heat capacity of Zn_4Sb_3 consisting of a Debye contribution (240 K) and a 5.3 meV Einstein mode.

The inelastic neutron scattering experiments have been carried out on the thermal time-of-flight spectrometer SV29 at the Jülich research reactor using a polycrystalline sample. Inelastic neutron powder

scattering may provide an estimate for the phonon density of states and reveal specific correlations in the dynamics. The main feature of the dynamic response in Zn_4Sb_3 observed by neutron scattering is a non-dispersive inelastic signal near 5 meV that is symmetric in energy to both sides of the elastic line, see Fig. 3. The lack of dispersion attests of the localized character of the mode that must be strongly anharmonic because of its unusually large intrinsic width. Most importantly, the inelastic coherent scattering intensity does not increase monotonically with scattering angle as would be expected for phonon scattering of individual atoms, but instead the intensity modulation is characteristic of the pair correlation of a dimer. The best modeling was obtained by assuming longitudinal dumbbell vibrations, *i. e.* a preferred direction along the dumbbell axis, resulting in a characteristic Q-dependence of the inelastic scattering $S(Q,E) \propto \frac{2}{3}x^2(1+3\sin(x)/x+6\cos(x)/x^2-6\sin(x)/x^3)$, where $x = Qd$, Q is the modulus of the scattering vector, and d is the Sb-distance in the dumbbell.

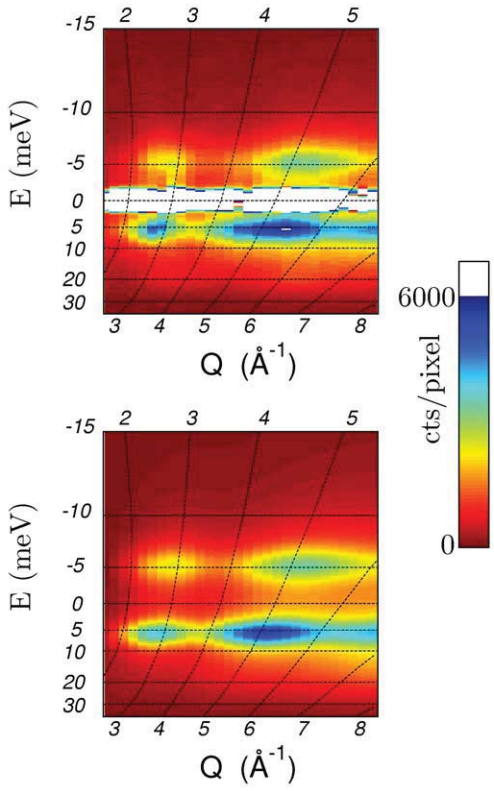

FIG. 3: Neutron inelastic scattering by polycrystalline Zn_4Sb_3 at 300 K obtained in time-of-flight measurements (top) compared to model refinements (bottom) for weakly coupled Sb-dumbbell vibrations along the dumbbell axis. The dynamic response is dominated by the soft dumbbell modes with a Lorentzian broadening due to short phonon life times, further remaining contributions are essentially due to multi-phonons described by a single, broad Gaussian.

The energy dependence of the dynamic response is described by a single Lorentzian for the damped harmonic oscillations of the dumbbells and one common broad (Gaussian) component for a multi-phonon background (proportional to Q^2), yielding a quantitative description of the observed inelastic neutron scattering. The refinement yields an Einstein mode energy of 5.3 meV consistent with heat capacity measurements, a dumbbell distance of d = 2.75 Å, slightly smaller than expected from diffration, specific atomic displacement parameters of the dumbbell that fill the rattling space to next neighbors in c-direction, a weak 6 % (anti-phase) correlation of neighboring dumbbells, and finally, a Lorentzian width corresponding to a very short phonon life-time $\tau = \hbar/\Gamma \approx 3.9 \times 10^{-13}$ s at 300 K. Assuming that these phonon interactions are the dominant scattering term for heat transport at this temperature and using measured data of the sound velocity, a simple kinetic gas theory model yields a thermal conductivity that is in favourable agreement with macroscopic data from steady state experiments. Measurements and analysis at two temperatures 200 K and 300 K gave consistent results, which is noteworthy also in view of the previously proposed role of Zn-interstitials, because an ordering of these defects near 260 K (see Fig. 2) apparently has no significant influence on the dynamics.

In conclusion, inelastic neutron scattering reveals local soft and strongly anharmonic modes of Sb-dimers that dominate and drive the dynamic response. The dynamic disorder by soft dumbbell modes of antimony is quantitatively consistent with the low thermal conductivity in zinc-antimony. The present result underscores that dynamic "rattling" disorder is crucial for thermoelectric properties and is a feature not restricted to single atoms in cage structures. Here, the size of the objects scattering the phonons is intermediate between single rattling atoms and nanosized objects in superlattice structures whose phonon scattering mechanisms are yet to be explored. Vibrating Sb-dumbbells are a striking illustration of "*schwingende Elementargebilde*", the general term originally used in Einstein's centennial work on heat capacity in solids. The search for structures with such more complex swinging elementary units and exploiting their anisotropic properties may pave new ways for thermoelectric material research.

[1] V. Keppens, D. Mandrus, B. C. Sales, B. C. Chakoumakos, P. Dai, R. Coldea, M. B. Maple, D. A. Gajewski, E. J. Freeman, and S. Bennington, *Nature* **395**, 876-878 (1998).

[2] R. Hermann, R. Jin, W. Schweika, F. Grandjean, D. Mandrus, B.C. Sales, & G.J. Long, *Phys. Rev. Lett.* **90**, 135505 (2003).

[3] R. P. Hermann, W. Schweika, O. Leupold, R. Rüffer, G. S. Nolas, F. Grandjean, and G. J. Long, *Phys. Rev. B* **72**, 174301 (2005).

[4] W. Schweika, R. P. Hermann, M. Prager, J. Perßon, V. Keppens, *Phys. Rev. Lett.* **99**, 125501 (2007).

[5] G. J. Snyder, M. Christensen, E. Nishibori, & T. Caillat, *Nature Materials* **3**, 458-463 (2004).

Flipping Magnetic Vortex Cores on the Picosecond Time Scale

R. Hertel, S. Gliga, C. M. Schneider
IFF-9: Electronic Properties

The study of dynamic magnetization processes and the search for increasingly faster switching times is one of the strongest driving forces in magnetism research. A fundamental understanding of these processes is paramount and can naturally lead to technological applications. An ultrafast magnetic reversal process induced by an external field is the precessional switching. In this case, the magnetization rotates homogeneously within about 300 ps. The high speed of this process is achieved by exploiting the dipolar field of the ferromagnet. This was until recently believed to represent the fundamental speed limit of field-induced magnetic switching. A novel type of magnetization reversal consists in the switching of the core of a magnetic vortex. Using advanced micromagnetic simulations we have resolved the microscopic details of this process which unfolds on a length scale of only a few nanometers, and we discovered an ultrafast route to switching of a magnetic vortex core within a few tens of picoseconds. This constitutes the fastest field-induced magnetic switching mechanism ever reported and opens new possibilities for future data storage applications with ultimate speeds.

Ferromagnetic materials in confined geometries typically form domain structures that close the magnetic flux. In the center of such flux-closure structures there is a region of only a few nanometers in size known as a magnetic vortex, where the magnetization circulates around a core. In the vortex core, the magnetization points out of the vortex plane, thereby preventing a singularity of the exchange energy density. The strength of the exchange interaction (which is of the order of 10 Tesla) confers the vortex core a very high structural stability. The very small size of the vortex core, in combination with the fact that it can have two stable orientations: “up” or “down” with respect to the sample plane naturally makes it a good candidate for data storage, given a mechanism allowing to easily switch it. The experimental demonstration that vortex cores can be switched by low in-plane magnetic fields has been provided only very recently [1]. In the experiment of Ref. [1], short oscillating magnetic field pulses of low amplitude were used, tuned to the gyrotropic resonance frequency of the system [2]. This frequency depends on the particle size and shape and is typically in the order of a few 100 MHz. By exploiting this resonance, it was demonstrated that the vortex core reversal can be triggered with sinusoidal field pulses a few ns in duration.

We have studied the dynamics of vortex core reversal with micromagnetic simulations using a fully three-dimensional finite-element algorithm based on the Landau-Lifshitz-Gilbert equation [3]. Our simulations show that the time scale required for a vortex core reversal is not limited by the relatively slow gyrotropic resonance frequency: A vortex core reversal process can also be triggered by a non-resonant, unipolar, and very short field pulse (below 100 ps) of moderate strength (∼80 mT) applied parallel to the film plane of, *e.g.*, a sub-micron sized $Ni_{81}Fe_{19}$ (Permalloy, Py) disk (Fig.1). We found that the core reversal occurs through a sequence consisting of a vortex-antivortex pair creation, followed by an annihilation process, resulting in a final magnetic structure of a single vortex with opposite polarization. The time required for the core reversal is of the order of 40 ps. These results are reported in detail in Ref. [4].

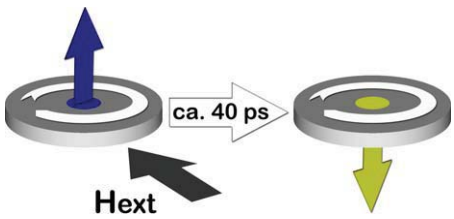

FIG. 1: Schematics of a field-pulse driven vortex core switching. The vortex core magnetization can be switched by a short magnetic field pulse applied in the film plane. This switching process requires only about 40 ps.

A typical example of the vortex-antivortex pair creation mediated core switch process is shown in Fig. 2 for a disk-shaped Py sample (radius of 100 nm and thickness of 20 nm). An 80 mT Gaussian-shaped field pulse of a duration of 60 ps is applied in the plane of the Py disk, which is initially in a symmetric vortex state. To clearly identify the microscopic processes leading to the core reversal, we have highlighted the $m_x = 0$ and $m_y = 0$ isosurfaces [3], the

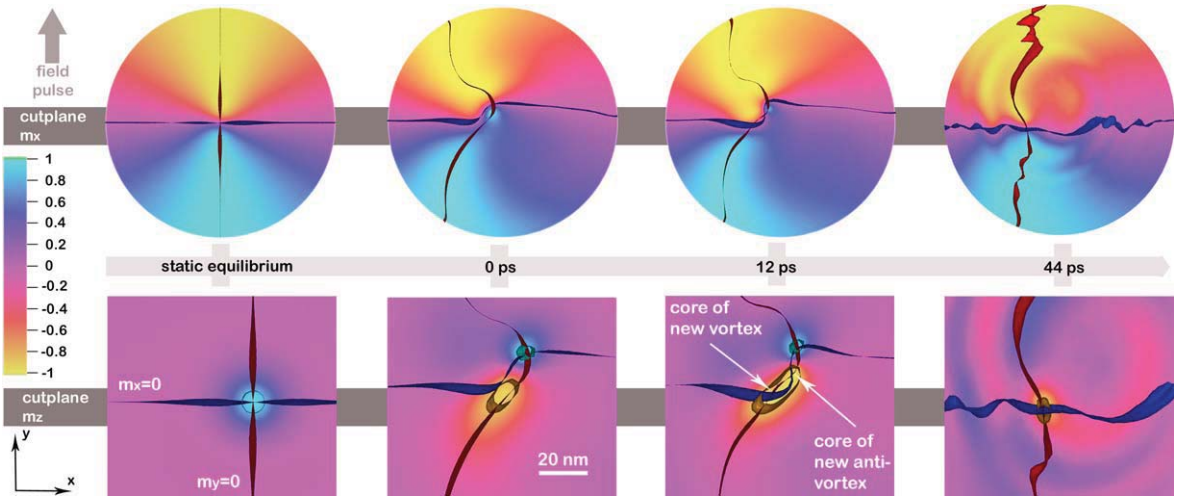

FIG. 2: Pair-creation mediated vortex core reversal in a Py disk of 100 nm radius and 20 nm thickness. A Gaussian field pulse is applied in the disk plane, parallel to the y axis. The top row shows the x component of the magnetization m_x in the initial state, followed by the state of the sample at the pulse maximum ("0 ps") and then at two different times after the pulse maximum has been reached. The blue and red ribbons represent the $m_x = 0$ and $m_y = 0$ isosurfaces, respectively. The bottom row shows a magnification of the region where these ribbons intersect, marking the cores of the original vortex, then at 12 ps after the pulse maximum, of the newly created vortex-antivortex pair, and finally of the remaining vortex core. This core has opposite polarization with respect to the initial vortex core, indicated by the yellow color on the underlying cut plane representing the z component of the magnetization m_z . The green and orange cylindrical ribbons are the isosurfaces where $m_z = 0.8$ and $m_z = -0.8$, respectively.

intersection of which determines the exact position of the vortex core. Before an external field is applied, these $m_x = M_x/M_s = 0$ and $m_y = M_y/M_s = 0$ isosurfaces appear as straight ribbons (oriented parallel to the x and y axis, respectively) crossing each other perpendicularly at the center of the vortex core. As the field pulse perturbs the system, the vortex shifts away from its original position and the formerly circular arrangement of the magnetization around the core is stretched, resulting in bent isosurfaces. As the isosurfaces approach each other, the distance over which the magnetization rotates by 90° in the plane shrinks to a few nanometers. The magnetization thus rotates out of the sample plane in order to locally reduce the exchange energy. This rotation occurs in the direction opposite direction to the original vortex orientation owing to the strong dipolar field of the vortex core. A few picoseconds after the peak value of the pulse is reached, the isosurfaces are bent strongly enough to form two additional intersections. These intersections mark the creation of a vortex-antivortex pair. Once a pair is created, the antivortex quickly moves towards the original vortex and, through a rapid process, they annihilate each other. We have reported the micromagnetic details of the annihilation process in Ref. [3], showing that it is connected with a sudden generation of spin waves. After the sequence of pair creation and annihilation processes, the magnetic structure is again in a vortex state, but with opposite polarization with respect to the original vortex.

Additionnally, we conducted a systematic study on the influence of the applied pulse's duration and strength on the core switch. We found that it occurred in our disk-shaped sample for well-defined combinations of the applied pulse's duration and strength. In particular, we observed that by increasing the applied field strength to 120 mT, it was possible to trigger a core switch with field pulses only 5 ps long.

In conclusion, we presented a novel ultrafast process in nanomagnetism for switching the core of magnetic vortices. Although this reversal mode involves a series of complex processes on the nanometer scale – the creation of a vortex-antivortex pair, a subsequent annihilation process – the chain of events only requires a very short field pulse of suitable shape to be initiated. A further advantage of the vortex core reversal mechanism lies in the simplicity of the required sample and magnetic structure: all that is needed is a magnetic vortex, which is a structure that forms naturally in sub-micron sized magnetic disks. The high speed of this switching mechanism is due to the fact that it is driven by the exchange field and represents a promising advance in the search for the ultimate speed limit of magnetic switching.

[1] B. Van Waeyenberge, A. Puzic, H. Stoll, K. W. Chou, K. W., T .Tyliszczak, R. Hertel, *et al.*, Nature 444, 461 (2006)

[2] S. B. Choe, Y. Acremann, A. Scholl, A. Bauer, A. Doran, J. Stohr, H.A. Padmore, Science 304, 420 (2004)

[3] R. Hertel and C. M. Schneider, Phys. Rev. Lett. 97, 177202 (2007)

[4] R. Hertel, S. Gliga, M. Fähnle, and C. M. Schneider, Phys. Rev. Lett. 98, 117201 (2007)

Three-Dimensional Magnetic Normal Modes in Mesoscopic Permalloy Prisms

M. Yan, R. Hertel, C. M. Schneider
IFF-9: Electronic Properties

Static flux-closure structures in three-dimensional mesoscopic ferromagnets are known to differ quite significantly from their two-dimensional counterparts. How these differences reflect in the dynamic properties of the magnetization is, to date, an open question. Magnetic excitations in laterally confined thin-film structures have been a topic of broad interest over the past years. In particular, the special dynamic properties of magnetic vortex structures have been studied intensively by numerous groups. Using micromagnetic simulations, we have extended this field by investigating the magnetic normal modes of *three-dimensional* mesoscopic samples, thereby probing the influence of a three-dimensional spatial confinement on magnetic excitations. Fourier analysis methods were applied to extract well-defined oscillation modes. We find that the vortex dynamics in three-dimensional samples displays an interesting variety of features that were not reported previously. The simulations provide specific predictions concerning the occurence of new excitation modes and their variation with particle size. It should be possible to identify these modes experimentally.

Magnetic flux-closure structures of three-dimensional mesoscopic particles display distinct differences compared with those known from thin-film elements. In practical terms, a "thick" magnetic particle can be defined as one with significant variations of the magnetic structure along the film thickness. In contrast to this, the magnetic structure of a thin-film element only varies along the plane of the element. It has been predicted by simulations [1] and confirmed experimentally [2] that the magnetic domain structure in thick particles dislplays a pronounced asymmetry which is absent in thin-film elements of similar size. Contrary to the numerous realizations of flux-closure-patterns observed in sub-micron-sized thin-film elements [3], thicker samples of comparable size are almost exclusively magetized in one state, known as the generalized Landau pattern [2]. This flux-closure pattern can be coarsely characterized by a subdivision of the sample into four domains, as displayed on the top frame of Fig. 1.Alternatively, this domain structure can be regaded as a variant of the vortex state, with characteristic three-dimensional properties: The magnetization circulates around a "core", either in clockwise or anti-clockwise direction. On the surfaces, the vortex is located at one of the two junctions at which two 90° domain walls meet the central 180° domain wall. The surface vortices are located at opposite sides on the the top and bottom surface. This is shown in the bottom panel of Fig. 1, where the core of the vortex is dispayed using an isosurface representation. The details of this complex structure, which contains characteristic asymmetric domain walls, has been thoroughly described in Refs. [1, 2].

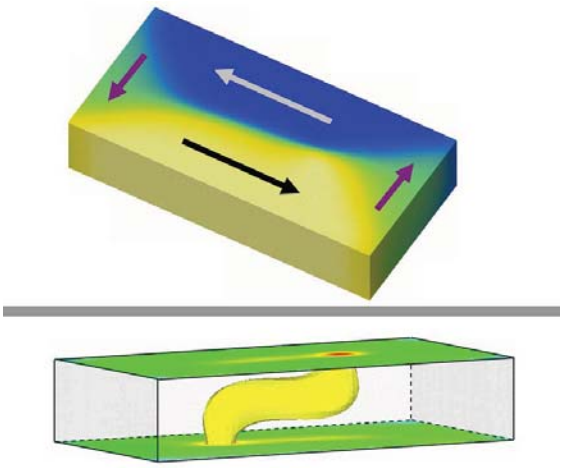

FIG. 1: Top: Simulatied static magnetization structure in a $400 \times 200 \times 80$ nm^3 Permalloy prism. The structure is divided into four domains. On the surface, the magnetization circulates around a point (vortex). Bottom: The vortex contains a core that is stretched along the sample. The yellow surface displays the core region, where the perpendicular magnetization component exceeds a value of 70%.

The dynamic properties of this structure, however, had not been investigated before. Our goal was therefore to investigate how the characteristics of the static three-dimensional magnetic structure modify the dynamic modes compared to the well-known case of thin-film elements. Using micromagnetic finite-element simulations and Fourier filtering techniques, we could identify a large number of characteristic normals modes of the magnetization oscillations occuring in this complex magnetic structure [4]. The structure was tipped away from equilibrium by

applying a short and weak magnetic field pulse to the sample and recording the subsequent oscillations of the magnetization. We studied Permalloy prisms of different size in the sub-micron range. The thickness was varied between 60 and 80 nm. All prisms had the same aspect ratio.

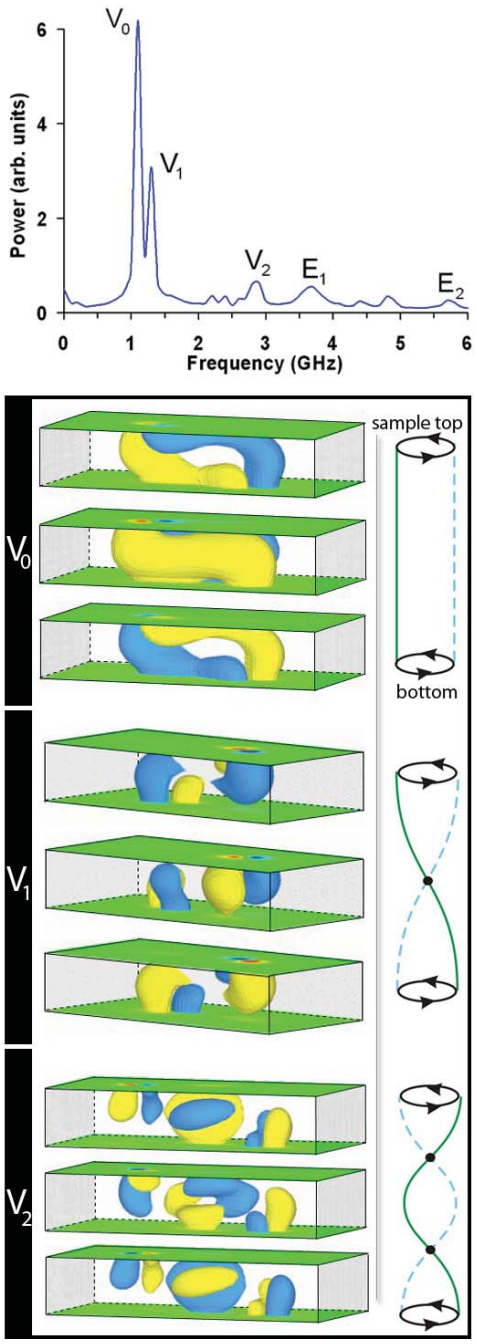

FIG. 2: Top: Typical Fourier spectrum of the oscillations occuring in a thick, mesoscopic Permalloy element following the excitation by a weak, short field pulse (simulated). Bottom: Three modes of the vortex oscillation. The V_0 mode is the three-dimensional variant of the gyrotropic vortex mode. The other modes represent higher-order variants of it. The figures display snapshots of the magnetic fluctuations δm at three different instants of a half-period of the oscillation. The yellow surfaces denote areas of positive variations, while the blue areas show the regions with negative variation.

A typical Fourier spectrum of the oscillations obtained from the simulations is shown on the top of Fig. 2. We identified various modes connected with the oscillations of the vortex (V), the edges (E) and the corners. A detailed analysis of these modes and their size dependence is given in Ref. [4]. Some of these modes are variants of the previously known modes in thin-film elements, while others are identified as genuinely three-dimensional modes connected with the special properties of the generlaized Landau structure. In particular, we found a previously unreported splitting of the rotational vortex mode frequency. In thin-fim elements, the gyrotropic excitation is a well-known magnetic mode with one specific frequency, which describes the in-plane rotation of the vortex core around its equilibrium position. In contrast this, we find that various gyrotropic modes (denoted as V_0, V_1 and V_2 in Fig. 2) can appear in the case of *thick* elements. On the sample surface, these modes appear as gyrations of the core. However, internally, the profile of the oscillations is very different. A simple "string" model as sketched on the right side of Fig. 2 explains the qualitative difference between these modes. Due to the additional degree of freedom along the film thickness, the vortex core as shown in Fig. 1 can not only exhibit a lateral displacement, but also an oscillation with varying profile along the thickness. Therefore, higher-order oscillations of the vortex core can occur, which contain one or more "nodes" inside the sample, where the magnetization does not fluctuate. Our simulations predict that these new modes should appear as clear peaks (V_1, V_2) in the Fourier spectrum of the oscillations, which should be observable in an experiment. Moreover, we make specific preditions concerning the variation of the frequencies of these new modes with increasing particle size [4].

In conclusion, our micromagnetic simulations with Fourier filtering analysis clearly predict the occurrence of new magnetic normal modes in mesoscopic ferromagnets of elevated thickness. The transition from two-dimensional to three-dimensional sample is therefore connected with a significant qualitative modification of the magnetic modes known from thin-film elements. Experimental evidence for these findings is expected to be feasible.

[1] R. Hertel and H. Kronmüller, Phys. Rev. B 60, 7366 (1999)

[2] R. Hertel, O. Fruchart, S. Cherifi, P.-O. Jubert, S. Heun, A. Locatelli and J. Kirschner, Phys. Rev. B 72, 214409 (2005)

[3] S. Cherifi, R. Hertel, J. Kirschner, H. Wang, R. Belkhou, A. Locatelli, S. Heun. A. Pavlovska and E. Bauer, J. Appl. Phys. 98, 0430901 (2005)

[4] M. Yan, R. Hertel and C. M. Schneider, Phys. Rev. B 76, 094407 (2007)

Breakdown of the Macrospin Picture in Magnetodynamics from Spin Valves

F. Wegelin[1], D. Valdaitsev[1], A. Krasyuk[1], S. A. Nepijko[1], G. Schönhense[1], H. J. Elmers[1], I. Krug[2], and C. M. Schneider[2]

[1] Inst. f. Physik, Universität Mainz
[2] IFF-9: Electronic Properties

Magnetic coupling effects play a fundamental role in the dynamic behavior of magnetic layer structures. Using time-resolved photoemission microscopy we measured the time-dependent spatial magnetization distribution in micron-sized spin valve structures in response to ultrashort magnetic field pulses. Quantitatively analyzing the magnetization dynamics we find that although the averaged magnetization vector reacts to the excitation according to a single-spin model with critical damping, local modes are excited depending on the shape of the spin valve structure.

A spin valve (SV) represents a basic magnetic device structure being widely employed in sensors and hard disk read heads. Its functionality depends on the interplay of magnetic coupling phenomena. The simplest SV comprises two ferromagnetic (FM) layers separated by a non-magnetic (NM) spacer, which mediates an *indirect exchange coupling* [1]. More sophisticated structures fix the magnetization in one of the FM layers (hard layer) by a strong coupling (*exchange biasing*) to an antiferromagnet. In addition, further coupling mechanisms such as Néel and edge coupling may be at work. Thus, spin valves are extremely interesting structures from a fundamental point of view, providing unique access to the interplay of different types of magnetic coupling.

Often the dynamic behavior of the magnetization $\vec{M}(t)$ is treated within the "macrospin" (MS) picture, assuming a uniform precessional motion of $\vec{M}$. Quantitatively, the magnetodynamic response may be described by the Landau-Lifshitz-Gilbert (LLG) equation, $d\vec{M}/dt = -\gamma(\vec{M} \times \vec{H}_{\text{eff}}) + (\alpha/M_s)(\vec{M} \times d\vec{M}/dt)$, with the gyromagnetic ratio γ, the Gilbert damping parameter α, and the saturation magnetization M_s. The effective field $\vec{H}_{\text{eff}}$ contains all coupling contributions and exerts a torque on $\vec{M}$, which initiates its precessional motion. For microscopic elements with small magnetic anisotropy and well-defined shape, however, the high-frequency behavior has been shown to be governed by confined spin wave eigenmodes [2].

In order to shed light on the dynamic response of coupled layer systems we explored the magnetodynamics in a dedicated spin valve [3]. The sample studied comprises an advanced layer structure designed to optimize the GMR effect [4, 5] (courtesy of NAOMI/Sensitec, Mainz). The SV layer stack was grown on Cu films (100 nm) on Si(111) substrates. Subsequent lithography steps defined the final structure of a coplanar Cu waveguide (20 μm central lead width) with microscopic SV elements of several shapes on top. In the SV a magnetically soft CoFe/NiFe free layer is separated from the CoFe hard layer by an ultrathin Cu interlayer providing an antiferromagnetic coupling field of 0.6 mT, as derived from the easy axis loop in conventional magnetometry ($H||y$). Corresponding hard axis ($H||x$) loops reveal a nearly reversible magnetization rotation, their initial slope indicating a total anisotropy field of 1.5 mT. The difference might be ascribed to a magnetic field-grown related uniaxial anisotropy.

For a quantitative analysis of the magnetization dynamics in these micro-elements we mapped the temporal evolution of the magnetization pattern using a pump-probe imaging approach based on photoemission electron microscopy [6]. The sample was illuminated with circularly polarized X-ray pulses (Δt = 3 ps, repetition rate 500 MHz) from BESSY II. The magnetic contrast was derived from magnetic X-ray circular dichroism (MXCD) at the Ni L_3 absorption edge. In this way, the response of the element was probed via the SV's top electrode. The magnetic field pulses (pump) were synchronized to the light pulses by means of a variable electronic delay t, yielding a stroboscopic picture of the magnetization pattern [6].

In the ground state the exchange bias forces the microscopic SV elements into an almost uniform magnetization state resulting in a weak contrast in Fig. 1 at $t = 0$ ps). Only close to the edges the soft layer magnetization turns parallel to the boundaries, thus comprising a positive (negative) value of $M_x(t)$ and reducing stray field energy. The magnetic field pulse rotates the magnetization $\vec{M}(\vec{r}, t)$ into the direction of the external field $\vec{H}_p(t)$ (bright contrast at $t = 600$ ps). After the pulse has passed, $\vec{M}(\vec{r}, t)$ rotates through the equilibrium position into the opposite direction (dark contrast at $t = 600$ ps) and finally back to its initial direction. In order to test the homogeneity of this precessional motion across the structure, we analyzed line profiles (not shown) taken along the diagonal of the structures (marked by the white lines in Fig. 1). These profiles revealed that $\vec{M}(\vec{r}, t)$ is *not*

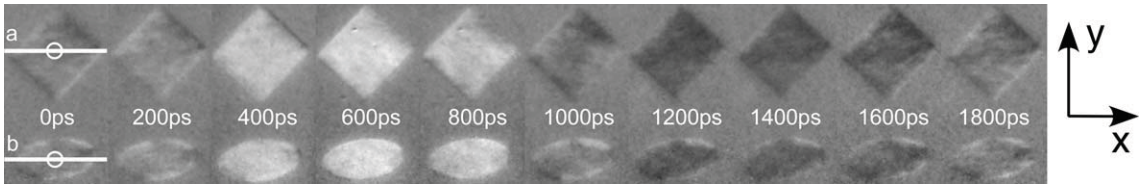

FIG. 1: Sequence of selected domain image snapshots of a quadratic ($5\times5\ \mu m^2$) and elliptical ($6\times3\ \mu m^2$) SV element acquired at the indicated time delay after the field pulse. The external field (peak value $\mu_0 H = 1$ mT; time dependence see Fig. 2(a)) acts along the x axis, the magnetic easy axis points along y. The gray level encodes the $M_x(t)$ magnetization component.

phase-coherent in the case of the square, but rather develops a mode structure as a function of time. In contrast, similar profiles taken across the ellipse indicated an almost coherent rotation of $\vec{M}(\vec{r},t)$ consistent with a macrospin picture. In order to analyze the deviations from the macrospin picture in more detail we compare in Fig. 2(b) the time dependence of $M_x^m(t)$ averaged over the total field of view with the local value $M_x^s(t)$ ($M_x^e(t)$) measured in the central circular area of the square (ellipse) (indicated in Fig. 1). At first glance the time dependences $M_x^i(t)$ are close to each other and resemble that of a critically damped oscillation.

The local variations of $M_x(t)$ are emphasized in the difference image shown as an inset in Fig. 2(b) and by the differences $\Delta M_x(t) = M_x^i(t) - M_x^m(t)$ revealing the true discrepancies between averaged and local magnetization dynamics [Fig. 2(c)]. Residual small edge domains that do not participate in the magnetization rotation cause the positive (negative) constant offset of $\Delta M_x^i(t)$ for the ellipse (square). For the ellipse $\Delta M_x^e(t)$ reveals a broad maximum coinciding with the strong counter-clockwise rotation of $\vec{M}(\vec{r},t)$. This behavior indicates a slower rebound of $\Delta M_x^e(t)$ that can be explained by the attenuation of the bias field by the in-plane demagnetization field of the ellipse, which reveals a hard axis parallel to the bias field. Contrarily, $\Delta M_x^s(t)$ shows an oscillation with a frequency of 1.7 GHz. The difference image shown in the inset of Fig. 2(b) relates this frequency to a spin wave mode identified by the two circularly shaped black areas. The wavelength of this mode along the diagonal amounts to 3.5 μm, i.e. half the value of the diagonal.

The fundamental eigenmode frequency of the square estimated from a similar measurement using smaller and shorter field pulses takes a value of $f = 0.8$ GHz in the field-free time range. Neglecting lateral demagnetizing fields and assuming a macrospin model the ferromagnetic resonance frequency for exchange biased films is given by $2\pi f = \gamma\sqrt{M_s H_A}$ with $H_A = H_{\mathrm{bias}} + H_s$ including the exchange bias field H_{bias} and an induced in-plane uniaxial anisotropy H_s. Under these conditions, the observed eigenmode frequency corresponds to $H_A = 0.6$ mT, in agreement with the quasistatic value of H_{bias} derived from the easy axis magnetization curve.

This example clearly shows the limitations of the macrospin picture in magnetically complex layered systems. For a better understanding of the magnetodynamic behavior and its shape dependence more detailed micromagnetic descriptions are needed.

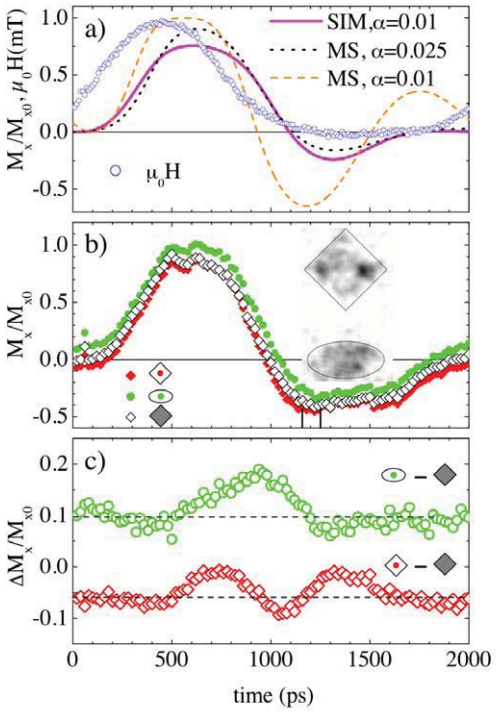

FIG. 2: (a) Experimentally determined field pulse $H_x(t)$ [$\circ$]. Magnetization component $M_x(t)$ predicted by the macrospin (MS) model at low (dashed line) and high (dotted line) damping coefficients. $M_x(t)$ calculated by a micromagnetic simulation (SIM) for the square pattern is shown by the full line. (b) $M_x(t)$ averaged over the entire field of view [$M_x^m(t)$, $\diamond$] and in the central area of the square platelet [$M_x^s(t)$, $\blacklozenge$] and the elliptical particle [$M_x^e(t)$, $\bullet$]. Inset: difference between images acquired at $t = 1160$ ps and 1260 ps. (c) Magnetization variation $\Delta M_x = M_x^i - M_x^m$ for the central areas of the square [$\diamond$] and ellipse [$\circ$].

[1] P. Grünberg *et al.*, Phys. Rev. Lett. **57**, 2442 (1986).

[2] S. O. Demokritov *et al.*, Phys. Rep. **348**, 441 (2001).

[3] F. Wegelin *et al.*, Phys. Rev. B **76**, 134410 (2007).

[4] M. N. Baibich *et al.*, Phys. Rev. Lett. **61**, 2472 (1988).

[5] G. Binasch *et al.*, Phys. Rev. B **39**, 4828 (1989).

[6] G. Schönhense *et al.*, Adv. Imaging Electr. Phys. **142**, 159 (2006).

Brillouin Light Scattering from Multilayers with Noncollinear Spin Configurations

M. Buchmeier , H. Dassow , D. E. Bürgler , C. M. Schneider

IFF-9: Electronic Properties
CNI: Center of Nanoelectronic Systems for Information Technology

Brillouin light scattering (BLS) is a well-established technique for the study of layered magnetic systems. Information about the magnetic state and properties of the sample is contained in the frequency position, width, and intensity of the BLS peaks. We have extended our previous ultrathin film approach for the calculation of spin wave frequencies to the calculation of BLS peak intensities. The derived formalism, which allows an easy calculation of BLS intensities even for noncollinear spin configurations, is applied to a Fe/Cr/Fe/Ag/Fe multilayer system. Good agreement with the experimental spectra is found for a wide variety of spin configurations.

In a Brillouin light scattering (BLS) experiment spin waves in a magnetic system are probed via inelastic scattering of photons. The spin wave mode or magnon appears as a peak in the recorded spectrum, which is shifted by the magnon frequency relative to the central elastic peak. The shift reflects either an energy loss or energy gain corresponding to the creation (Stokes condition) or annihilation (anti-Stokes condition) of a magnon, respectively.

Most experiments focus on an analysis of the spin wave frequencies, which contain information about many magnetic properties, e.g. saturation magnetization, anisotropies, and interlayer coupling. With a suitable experimental geometry and procedure, these properties can be determined solely on the basis of the magnon frequencies. The peak width Δ contains information about the spin wave lifetime. However, in many cases Δ is much smaller than the apparatus broadening of about 1 GHz and cannot be resolved. On the other hand, the *scattering intensities*, which are the topic of this work, carry information mainly about the precessional amplitudes of the spin waves, the mode types, the alignment of the magnetic moments, and can even be used to investigate the magneto-optic coupling. Very few publications have yet addressed the issue of the scattering intensities. The detailed information hidden in the peak intensities is of high relevance for many technological applications, such as data storage and communication technology, because the operation frequencies of contemporary magnetic devices approach the GHz regime, where the magnetization dynamics is closely related to the spin wave modes.

Previously [1], we have shown that spin wave frequencies can be conveniently calculated within the ultrathin film approach, treating the intralayer exchange as an effective bilinear interlayer coupling between thin virtual sheets of the ferromagnetic layers. Recently, we have consequently extended this approach to the calculation of the BLS peak intensities [2]. Given the very close relation of the BLS cross-section to the magneto-optic Kerr effect, the depth-resolved longitudinal and polar MOKE coefficients calculated numerically via the usual magneto-optic formalism can be employed in combination with the spin wave precessional amplitudes to calculate full BLS spectra for a given magnetic system. This approach allows an easy calculation of BLS intensities even for noncollinear spin configurations including the exchange modes [2].

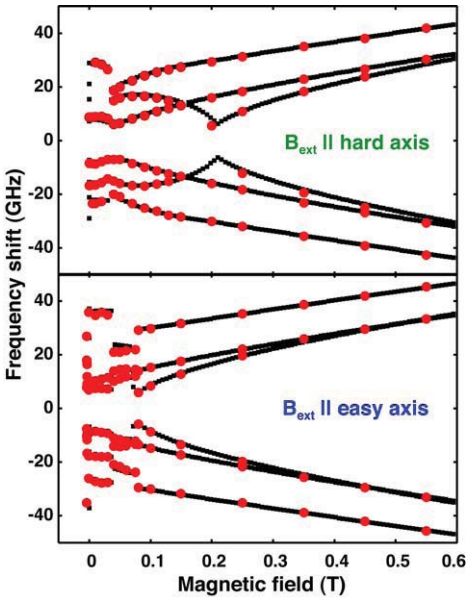

FIG. 1: Field dependence of measured BLS data (red) and least square fit (black) of a Fe(14 nm)/Cr(0.9 nm)/Fe(10 nm)/Au(6 nm)/Fe(2 nm) sample.

Here, we apply the derived formalism to an epitaxial Fe(14 nm)/Cr(0.9 nm)/Fe(10 nm)/Ag(6 nm)/Fe(2 nm) spin valve structure with three ferromagnetic Fe layers. This kind of structures are interesting model systems, which we are also employing to investi-

gate current-induced magnetization switching [3]. Samples have been prepared by molecular beam epitaxy on top of a GaAs/Ag(001) buffer system. The samples have been capped with a 50 nm-thick antireflection ZnS layer. The preparation is described in detail elsewhere [3]. The Cr thickness has been chosen in order to obtain a strong antiferromagnetic coupling in the bottom Fe/Cr/Fe trilayer. The top thin Fe layer is decoupled and can be switched more easily by an external field. As the samples are fully epitaxial and therefore mainly in a magnetic single domain state the remagnetization behavior can be modeled easily. However, as a consequence of the various competing interactions – Zeeman energy, magnetocrystalline anisotropy of all Fe layers, interlayer exchange coupling – a rich variety of different magnetization configurations is possible. The BLS spectra have been recorded using a Sandercock type (2×3) pass tandem Fabry-Pérot interferometer in the 180° backscattering geometry. The external field was applied in the film plane and perpendicular to the magnon wave vector.

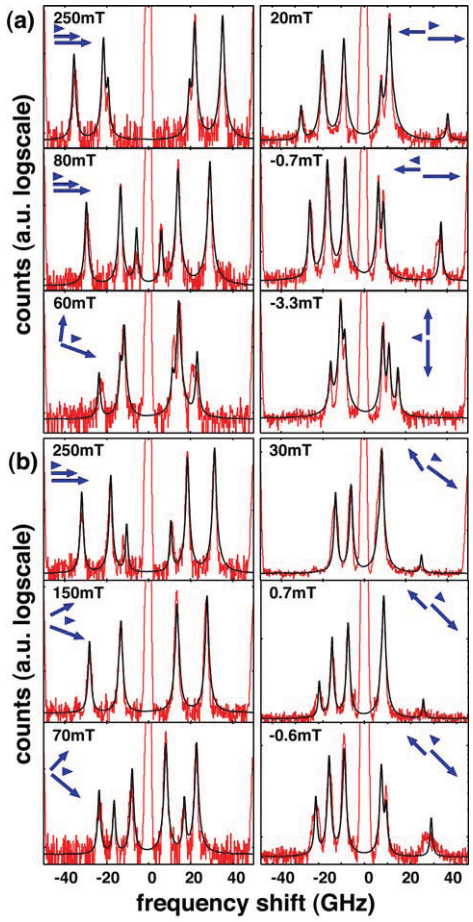

FIG. 2: Experimental (red) and calculated (black) BLS spectra at different fields applied along the easy (a) and hard (b) axis of the magnetocrystalline anisotropy. The computed directions of the magnetic moments of the three Fe layers are indicated with arrows.

Figure 1 shows the experimental spin wave frequencies (red) as a function of the external field applied parallel to the easy [001] (bottom graph) and hard [011] direction (top graph) of the cubic magnetocrystalline anisotropy. Corresponding spectra are shown in Fig. 2. Only the three dipolar modes, which are lowest in frequency, are shown. The graphs can be divided into three distinct field regions bounded by switching events: For low field values ($B_{ext} < 35$ mT) there is a distinct asymmetry between the Stokes and the anti-Stokes side. This unique feature proves an antiparallel alignment of the magnetic moments of the two bottommost Fe layers collinear with the external field applied in easy axis direction [4]. At higher fields ($B_{ext} > 35$ mT) the antiferromagnetically coupled bottom Fe/Cr/Fe double layer switches into a canted configuration with a relative angle between the layers magnetizations of about 90°. The sample saturates at an external field of about 80 and 180 mT in the easy and hard axis configuration, respectively. The hard and easy axis data have been fitted simultaneously in order to extract the magnetic parameters of the Fe layers and the interlayer coupling. For a proper description of the modes all three ferromagnetic layers are divided into 1 nm-thick sheets. This is sufficient to take care of the partial nonuniformity of the modes in the vertical direction. The calculated field dependences using these parameters are plotted as solid lines in Fig. 1. As can be seen, the results of the calculation are in excellent overall agreement with the experimental data.

Experimental spectra for the easy and hard axis configuration are shown as red curves in Fig. 2. Calculated spectra are plotted as black lines. For the intensity calculations we have only used the magnetic parameters extracted from the fit in Fig. 1, and literature values for the indices of refraction of the layers. As the experimental linewidths of all peaks have approximately the same value of about 1 GHz, which is the resolution of the spectrometer, we have assumed a Lorentzian lineshape with this linewidth for the calculation of the spectra. The background level and the absolute intensity have been adjusted manually in order to match the experimental spectra. The surprisingly good overall agreement of both the frequencies as well as the entire spectra proves that the theory well describes the spin wave properties.

In conclusion, our calculation scheme given in Ref. [2] is well suited to gain technologically relevant, quantitative information about spin wave modes, the alignment of the magnetic moments, and the magneto-optic coupling in complex magnetic multilayers.

[1] M. Buchmeier, B. K. Kuanr, R. R. Gareev, D.E. Bürgler, and P. Grünberg. Phys. Rev. B **67**, 184404 (2003).

[2] M. Buchmeier, H. Dassow, D. E. Bürgler, and C. M. Schneider. Phys. Rev. B **75**, 184436 (2007).

[3] H. Dassow, R. Lehndorff, D. E. Bürgler, M. Buchmeier, P. A. Grünberg, C. M. Schneider, and A. van der Hart. Appl. Phys. Lett. **89**, 222511 (2006).

[4] P. Grünberg, R. Schreiber, Y. Pang, M. B. Brodsky, and H. Sowers. Phys. Rev. Lett. **57**, 2442 (1986).

Novel Type of Metadislocation in the Complex Metallic Alloy Al-Pd-Fe

M. Heggen, M. Feuerbacher, S. Balanetskyy, K. Urban

IFF-8: Microstructure Research

We report on the observation of new variants of metadislocations in the orthorhombic complex metallic alloy phase Al-Pd-Fe. At Fe contents above about 3 at.% we find a novel type of metadislocation in the ξ-structure, which has a complementary counterpart hosted in all ε-type phases possessing phason lines as structural elements.

Among the group of complex metallic alloys (CMAs), materials which feature a few hundreds of even thousands of atoms per unit cell, the so-called ε-type phases are one of the most fascinating. Several structurally related orthorhombic phases have been identified and are denoted ε_l (l = 6, 16, 22, 28, 34) according to the index of the strong (0 0 l) reflection. They are ternary extensions of the binary Al_3Pd phase in the Al-Pd-(Mn, Fe) alloy systems [e.g. 1]. ε-type phases are also found in the alloy systems Al-Pd-(Rh, Re, Ru, Co, Ir) and Al-Rh-(Ru, Cu, Ni) [2].

In the CMA phase ε_6-Al-Pd-Mn, which features about 350 atoms per unit cell, Metadislocations (MDs) were firstly observed [3]. The concept of metadislocations addresses an inherent problem in the plasticity of large-unit-cell crystals: if the lattice parameters of a structure are large, conventional dislocation mechanisms tend to fail. Perfect dislocations are unfavourable as they involve very high elastic line energies (the elastic line energy of a dislocation increases with b_2, where b is the length of the dislocations Burgers vector) and partial dislocations are connected to high stacking fault energies. The concept of MDs provides a solution to this problem. A MD consists of a core dislocation with a short Burgers vector, typically of the order of 1 or 2 Å. Its elastic line energy is therefore comparable to that of simple metals as Al or Cu. The core dislocation, which is a partial in the large-unit-cell structure, is associated with a local phase transformation to a related structure. The latter has lattice parameters related to those of the host structure in such a way that the partial dislocation is accommodated into the lattice.

MDs were up to now found only in the orthorhombic phase ε_6-Al-Pd-Mn and the related phase ?28-Al-Pd-Mn [3, 4]. They are associated to a distinct number of so-called phason planes, the number of which follow a series of double Fibonacci numbers, i.e. 2,4,6,10,16... [4].

Here, we report on the observation of a novel type of MD in the Al-Pd-Fe alloy system. The defects observed possess the essential structural features of a MD, i.e. they consist of small partials in a large-unit-cell crystal, accommodated into the lattice by a local phase transformation. On the other hand, they display characteristic features distinguishing them from the formerly observed MDs, which allows us to classify them as a novel type of MDs.
The investigations described were performed on samples with a composition of $Al_{72.0}Pd_{22.8}Fe_{5.2}$. The samples were annealed at 750°C for 981 h in a closed quartz ampoule with Ar atmosphere and subsequently quenched in water. Transmission electron microscopy (TEM) investigations were performed using a JEOL 4000FX electron microscope.

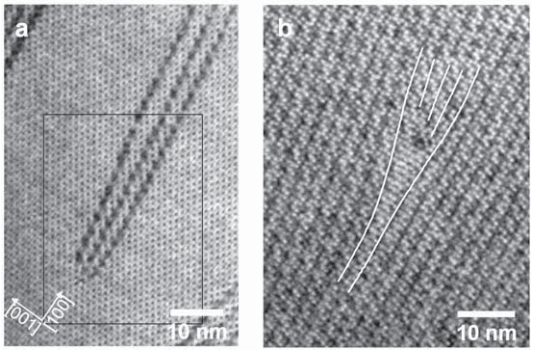

FIG. 1: TEM micrographs of metadislocations with three associated phason half-planes in the ξ-structure (a) and in the monoclinic variant (-1,1) of the ε_{22}-structure (b).

Fig. 1a is a transmission electron micrograph of a dislocation in this phase. The dislocation core is located in the lower left part of the image. It is associated with three phason planes extending to the upper right (dark contrast). The surrounding host structure is formed by a parallel arrangement of flattened hexagons and can be identified as ξ-phase. Fig. 1b is a micrograph of a dislocation in a sample region with a high density of phason planes. The host structure can be identified as the monoclinic (1,-1) variant of the ε_{22} structure with additional local modulations [5]. The dislocation core terminates three phason planes extending to the upper right part of the image. Below the core, a small region showing parallel flattened hexagons, i.e. of ξ-structure, is observed.

The phason planes surrounding the dislocation core are marked by white lines as a guide to the eye.

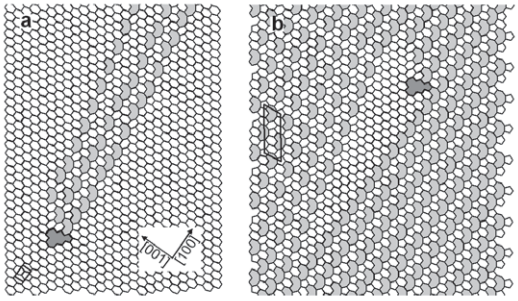

FIG. 2: Tiling representations of metadislocations with three associated phason half-planes in different host structures (see text).

Fig. 2 shows structural models of these dislocations using a tiling approach [cf 3, 5]. The host structure in Fig. 2 a is given by parallel hexagons, representing the ξ-phase. The corresponding unit-cell projection is depicted by a thick rectangle in the lower left corner. The dislocation core is represented by the dark-grey tile and the three associated phason half-planes by the light-grey tiles. A closed circuit in terms of edges of the hexagon tiles around the dislocation core reveals a closure failure, which corresponds to the dislocations Burgers vector. We obtain $1/2\tau^4$ [1 0 1] in terms of the ξ-lattice, corresponding to a Burgers vector length of 1.79 Å. Fig. 2b can be understood as an ideal hexagon-tiling representation of the MD in Fig. 1b. The experimental image shows, however, that structural relaxation of the phason planes takes place which are not accounted for in the structural model. The host structure is still mainly given by the monoclinic (1,-1)-phase, but now on the left hand side of the schematic, an area containing the monoclinic (3,-1) phase [5] is drawn.

Comparing the tiles representing the dislocation cores in the ξ- and the ε_6-structure (Fig. 2 and Ref. [3]) it is obvious that the same polygon is used. The differences in Burgers-vector length for ε-Al-Pd-Fe and ε_6-Al-Pd-Mn (the latter amounts to 1.83 Å[3]]) is only due to the slightly different lattice parameters of these phases. Accordingly, it is expected that the dislocation core structures in these phases are very similar. However, detailed information cannot be resolved from the present TEM images. For this dedicated work using high-resolution electron microscopy is currently performed.

Fig. 3 shows a TEM micrograph of MDs with five and eight associated phason half-planes in the monoclinic variant (-1,1) of the ε_{22}-structure. A structural model for these MDs can be set up in the same way like for the MDs shown in Fig. 1. It is shown that the cores of those MDs and their Burgers-vectors correspond to those of MDs associated to 10 and 16 phason planes in the ε_6- and ε_{28}-structure [cf. 4, 6]. It can be generalized that the number of phason planes of MDs in ξ- and ε_6-structures [4] and in the material investigated in the present study correspond to Fibonacci and a double Fibonacci sequence.

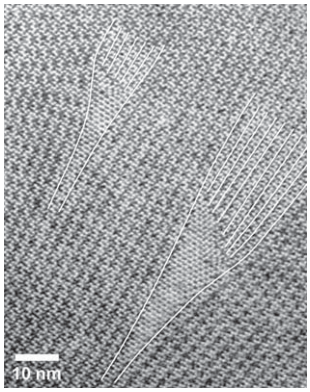

FIG. 3: TEM micrograph of metadislocations with five and eight associated phason half-planes in the monoclinic variant (-1,1) of the ε_{22}-structure.

The present study shows that the concept of MDs can be applied to various ε-type complex metallic alloys. The construction principle can be generalized: on the one hand, the MD in the ε_6-structure can have associated phason half-planes forming a slab of any variant of ε-phase that possesses phason lines as structural elements. On the other hand, the complementary MDs can be embedded in host structures of any type of ε-phase possessing phason lines as structural elements. The decisive difference between the two types of MD, the previously known and the novel one, is the local structure in which the dislocation core is embedded: that of the previously observed MDs is embedded into the ε_6-structure, while that of the novel type is embedded into the ξ-structure. The different host structures directly result in different numbers of associated phason half-planes required for accommodation of the metadislocation core, i.e. a Fibonacci and a double Fibonacci sequence for MDs in ξ- and ε_6-structures, respectively.

Acknowledgements: This work was supported by the Deutsche Forschungsgemeinschaft, (PAK 36) and the 6$^{\text{th}}$ Framework EU Network of Excellence "Complex Metallic Alloys" (Contract No. NMP3-CT-2005-500140).

[1] S. Balanetsky, B. Grushko, T.Y. Velikanova, and K. Urban, J. *All. Comp.* **376**, 158 (2004).

[2] S. Balanetskyy, B. Grushko, and T.Y. Velikanova, *Z. Kristallogr.* **219**, 548 (2004).

[3] Klein, M. Feuerbacher, P. Schall, and K. Urban, *Phys Rev.* Lett. **82**, 3468 (1999).

[4] H. Klein, M. Feuerbacher, *Phil. Mag.* **83**, 4103 (2003).

[5] M. Heggen, M. Engel, S. Balanetskyy, H.R. Trebin, and M. Feuerbacher, *Phil. Mag.* , in press (2008).

[6] M. Feuerbacher, S. Balanetskyy, and M. Heggen, *Acta Mat.*, in press (2008).

Physical Properties of the Complex Metallic Alloy β-Al_3Mg_2

M. Feuerbacher, M. Heggen, K. Urban

IFF-8: Microstructure Research

We have characterized the physical properties of the complex metallic alloy phase β-Al_3Mg_2 by several means. We have measured transport and magnetic properties, the thermal conductivity, and the thermopower. We observe that, despite the complexity of the structure, the material behaves in many respects like a structurally simple material. A surprising finding is the presence of bulk superconductivity in the absence of inversion symmetry of the crystal structure.

The class of Complex metallic alloys (CMAs) latterly attracts increasing interest [1]. While the structural properties of many CMAs are well characterized, the physical properties of most members of this new class of materials are essentially unexplored.

β-Al_3Mg_2 has space group Fd3m and a large lattice parameter of 2.82 nm. The unit cell contains 1168 atoms. The local order is mostly coordinated in icosahedral symmetry. The structure inherently possesses a high degree of disorder [2]. Our measurements were performed on polycrystalline single-phase samples and on single crystals grown by means of the Czochralski- and the Flux-growth technique [3].

The electrical resistivity ρ was determined in the temperature interval between 4 and 300 K [4] using the standard four-terminal technique. Fig. 1 shows the resistivity for single crystalline (triangles) and polycrystalline (circles) β-Al-Mg scaled by the respective values at 300 K. The absolute values found and the positive temperature coefficient indicate that lattice vibrations play an important role. The temperature behaviour dependence, showing T^2 dependence in the low-temperature and linear T dependence in the high-temperature regime closely resembles that of nonmagnetic amorphous alloys with Pauli paramagnetism of conduction electrons [5]. This finding is contrasting to ordinary metals, where a T^5 Bloch-Grüneisen behaviour is commonly found at low temperatures.

The magnetization and the magnetic susceptibility were measured with a Quantum Design 5 T SQUID magnetometer [4]. The susceptibility was investigated in the temperature interval between 2 and 300 K in a magnetic field $H = 1$ kOe. The $M(H)$ dependence is linear in the whole investigated field range up to 50 kOe. The temperature dependence of the susceptibility exhibits a Curie upturn below 10 K. The susceptility values are of the same order (but of opposite sign) as the Larmor diamagnetic susceptibility, indicating that the samples are dominated by the Pauli paramagnetic susceptibility of conduction electrons. The thermal conductivity was measured [4] between 8 and 300 K using an absolute steady-state heat-flow method.

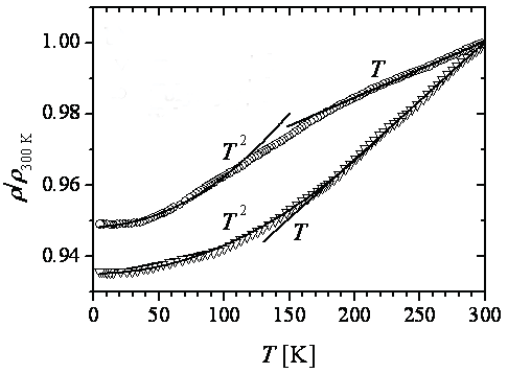

FIG. 1: Temperature dependence of the resistivity for single crystalline (triangles) and polycrystalline (circles) β-Al_3Mg_2 scaled by the respective values at 300 K.

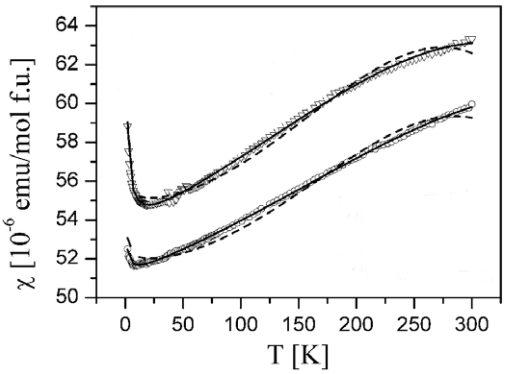

FIG. 2: Temperature dependence of the susceptibilty for single crystalline (triangles) and polycrystalline (circles) β-Al_3Mg_2.

The thermal conductivity at 300 K amounts to 34 W/mK, which is considerably smaller than the corresponding value for pure fcc Al (240 W/mK) and the temperature dependence is positive. The data can be excellently fitted assuming a superposition of an electronic and a Debye contribution, and hopping of localized vibrations with a single activation energy. While hopping becomes the dominant lattice heat-carrying channel at temperatures above 60 K, the Debye term dominates at low temperatures and exhibits a maximum at about 50 K. At the lowest measured temperature (8 K), the scattering of phonons on stacking-fault-like defects limits the heat transport, whereas at higher temperatures, *umklapp* processes become excited. The room-temperature values of the electronic and lattice thermal conductivities are approximately equal, a feature that is intermediate to simple metals and Al-based Quasicrystals.

Thermoelectric power measurements [4] were performed between 4 and 300 K by applying a differential method with two identical thermocouples attached to the sample. The thermoelectric power (Seebeck coefficient) at room temperature amounts to -2.8 mV/K. This rather small value shows that β-Al_3Mg_2 does not appear to be a promising thermoelectric material. The thermopower shows a strong (negative) increase between 4 and 15 K, followed by a weaker, almost linear increase to higher temperatures.

Low-temperature characterizations [6] were performed down to 100 mK. Field and temperature dependent resistivity was measured in a 3He cryostat (400 mK up to 100 K) in fields up to 12 T and in a standard He cryostat from 4.2 K to room temperature.

The low-temperature electrical resistivity is shown in Fig. 3(a). In agreement with the high-temperature measurements the resistivity at low temperatures follows roughly a T^2 power law. Measurements performed below 4 K (inset, Fig. 3a) demonstrate that β-Al_3Mg_2 undergoes a sharp superconducting transition around 0.9 K. The application of a magnetic field lowers the transition temperature which finally becomes suppressed at the upper critical field of about 0.14 T. These data allow to establish the temperature dependence of $\mu_0 H_{c2}$, displayed in Fig. 3b.

Though β-Al_3Mg_2 possesses highly complex structural features, no spectacular differences with respect to simple metals and alloys were found. The dominant local icosahedral atomic coordination in the giant unit cell together with the inherent disorder of the CMA structure make β-Al_3Mg_2 to resemble amorphous metals on the local scale, which is nicely demonstrated in the temperature-dependent electrical resistivity. This also shows that the electronic transport properties of β-Al_3Mg_2 are predominantly determined by the small-scale atomic clustering, whereas the large-scale periodicity of the CMA lattice is of more or less marginal importance.

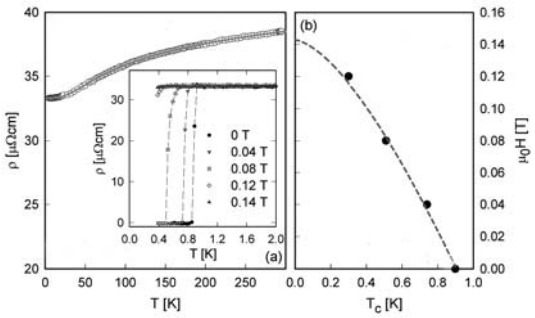

FIG. 3: Low-temperature resistivity of SS-Al3Mg2 (a) and upper critical field (b).

Superconductivity in β-Al_3Mg_2 occurs in a crystal environment without inversion symmetry. Presently, only a small number of superconductors without inversion symmetry has been found. Broken inversion symmetry has a distinct influence on the superconducting phase, which usually relies on the formation of pairs of electrons in degenerate states with opposite momentum. The availability of such states is normally guaranteed by time reversal and inversion symmetries. The absence of inversion symmetry would favour a strong antisymmetric spin orbit coupling, and as a consequence, a mixture of spin singlet and spin triplet pairs in the superconducting condensate can be expected. The small values of the upper critical field, however, seem to exclude a substantial portion of spin-triplet pairs in the condensate. Moreover, the lightweight elements Al and Mg may be responsible for only a minimal spin-orbit coupling and hence the spin-singlet condensate dominates. Additionally, the very complex crystal structure is supposed to smooth the effect of the missing inversion symmetry.

Further studies on β-Al_3Mg_2 were carried out, characterizing plasticity, dislocations and other structural defects [7], the crystal structure and phase transitions [8], and the specific heat [6].

Acknowledgments: Work supported through the European Network of Excellence "Complex Metallic Alloy" by the EU under contract NMP3-CT-2005-500140 and in intense collaboration with J. Dolinsek (U. Ljubljana) and E. Bauer (TU Vienna).

[1] K. Urban and M. Feuerbacher, J. Non Cryst. Sol. 334 - 335, 143 (2004)

[2] S. Samson, Acta Cryst. 19, 401 (1965)

[3] M. Lipinska et al., Intermetallics, in press (2007)

[4] J. Dolinsek et al., Intermetallics 15, 1367 (2007)

[5] U. Mizutani, Introduction to the Electron Theory of Metals (Cambridge University Press, 2001), p. 479.

[6] E. Bauer et al., Phys. Rev. B 76, 014528 (2007)

[7] S. Roitsch et al., Intermetallics 15, 833, 2007

[8] M. Feuerbacher et al., Z. Kristallogr. 222, 259 (2007)

Instability of a Homogeneous State of a Dilute Bose Gas Upon Cooling

R. B. Saptsov

IFF-3: Theory of Structure Formation

The behavior of a dilute Bose gas with a finite particle lifetime has been studied in the framework of hydrodynamic equations under the conditions of a continuous mass and energy inflow in the presence of external cooling. A spatially homogeneous state of such a gas is shown to be unstable with respect to the formation of an inhomogeneous density structure. A possible connection of the present results with experiments [3, 4] is discussed.

Previously, we showed that the superfluid phase nucleation already starts at a temperature above T_c in a dilute Bose gas upon cooling due to thermal fluctuations of density and temperature in Bose gas [1]. Physically, it is associated with the high compressibility of the Bose gas near and below the critical temperature.

However, the situation considered in [1] is clearly nonstationary, as it was implied that the nonequilibrium state of the Bose gas is produced instantly (e.g., excitons generated in the lattice by a laser pulse) and then the bosons interact only with each other and with the lattice. The lifetime of quasiparticles was assumed to be much longer than both the time of internal thermalization of the gas and the characteristic time of gas – lattice equilibration. At the same time, in experiments reported in [3, 4], the lifetime of quasiparticles (two-dimensional excitons) is not very long. The study of an exciton gas was performed under continuous pumping, i.e., permanent laser generation of excitons. As a result, a stationary but nonequilibrium state of the Bose gas was formed. In this work [2], I consider the influence of the previously described instability [1] on the steady state in such experiments. In particular, I show that the homogeneous steady state of a weakly interacting Bose gas near its critical temperature is unstable, provided that the lifetime of quasiparticles exceeds the characteristic time of cooling due to the emission of lattice phonons. The instability of the homogeneous state of an exciton gas was also already reported in experimental works where the formation of ordered structures was observed [3, 4]. At present, there is no consensus about the causes for the appearance of such structures. Instead, different theoretical approaches are used to explain the phenomenon. The instability described in this work possibly plays a role in the formation of the observed structures.

I describe behavior of the Bose gas placed in a overcooled (with respect to gas) solid matrix within the framework of the following hydrodynamic equations first disregarding the superfluid phenomena assuming that the homogeneous steady state of the system (it will be found below) corresponds to a temperature either slightly above or well below the critical temperature, so that the role of superfluidity is negligible

$$\frac{\partial \rho}{\partial t} = -\mathrm{div}(\rho \mathbf{v}) + G - \frac{\rho}{\tau}$$

where G is the pumping rate and τ is the average lifetime of excitons;

$$T\rho\frac{\partial s}{\partial t} = \kappa\nabla^2 T + Jc_v\rho - c_v T\frac{\rho^2}{\tau_0\rho_0}$$

$$-\left(G - \frac{\rho}{\tau}\right)\left(\frac{v^2}{2} + w\right)$$

where J is the external heat income per unit mass of the exciton gas, $\tau_0 = n_0 v_T \sigma_{ph}$ is the average time of the phonon emission into the solid lattice at a homogeneous density of $n_0 = \rho_0/m = G\tau/m$ [1] and $w = \epsilon + p/\rho$ is the enthalpy per unit mass;

$$\frac{\partial \mathbf{v}}{\partial t} = -(\mathbf{v}, \nabla)\mathbf{v} - \frac{\nabla p}{\rho} + \nu\nabla^2\mathbf{v}$$

where ν is the kinematic viscosity;

$$p = m^{3/2}T^{5/2} + m\rho^2 a_0$$

Here, m is the mass of an exciton and s stays for the specific entropy of the gas. The pressure given phenomenologically takes into account the finite compressibility of a three-dimensional Bose gas associated with its weak nonideality [2]. Set of this equations has homogeneous stationary solution

$$\rho = \rho_0 = G\tau; \quad T = J\tau_0 \equiv T_0; \quad v = 0$$

We can choose ρ and T as independent thermodynamical variables, so system can be described in terms of variables ρ, T and v. Seeking solution of the equations linearized near this stationary solution in the form $\rho^{'}(t) = \exp(\lambda t + i\mathbf{kr})\rho^{'}(k)$, $T^{'}(t) = \exp(\lambda t + i\mathbf{kr})T^{'}(k)$, $\mathrm{div}\mathbf{v}(t) = \exp(\lambda t + i\mathbf{kr})\mathrm{div}\mathbf{v}(k)$ It the work is shown, that there is unstable solution (exists range of k with $\lambda(k) > 0$ (in the case considered λ is purely real)) for k:

$$k_0 \leq \sqrt{-\frac{1}{\chi\tau_0}\left[1 - \frac{1 - \tau_0/\tau}{\eta^{1/3} + \nu/\tau v_T^2}\right]}$$

where $\chi = \kappa/\rho_0 c_v$ - is thermal diffusivity, $\eta = na_0^3 \ll 1$ is (small for dilute gas) gas parameter, $v_T = \sqrt{T_0/m}$ - is average bose-partile velocity.

Thus, the existence of the instability requires the condition $\tau > \tau_0$.

In the limit $\tau \gg \tau_0$ it is shown that unstable branch behaves like

$$\lambda_1 \approx \frac{1}{\tau_0} - k^2 \chi \eta^{1/3}$$

in a wide range of $1/\tau_0 v_T \ll k \ll v_T/\chi$ and like

$$\lambda_1 = v_T |k|$$

for $k < 1/v_T \tau_0$. Existence of such a mode leads to nonhomogeneous density stuctures formation.

Stable modes behave like

$$\lambda_2 = -v_T |k|$$

$$\lambda_3 = -1/\tau_0$$

in the range $k < 1/v_T \tau_0$ and like usual weakly decaying (due to viscousity, thermodifussion and phonon cooling) sound

$$\lambda_{2,3} \approx \pm i k v_T - \frac{(\chi + \nu)}{2} k^2 - \frac{1}{2\tau_0}$$

in the range of $1/\tau_0 v_T \ll k \ll v_T/\chi$. This is schematically presented in Fig. 1.

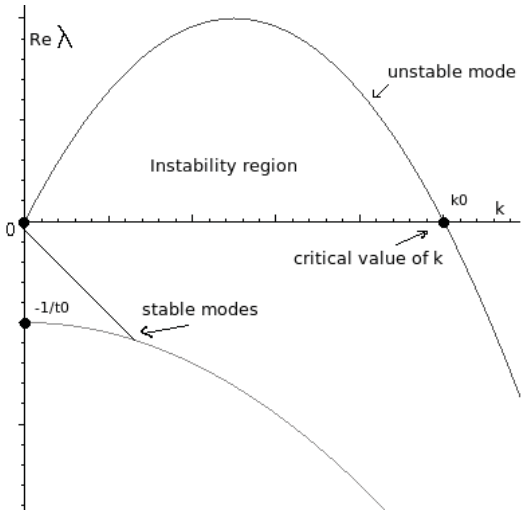

FIG. 1: Real part of λ for the limit $\tau \to \infty$. Unstable mode is purely real ($\lambda > 0$ corresponds to instability). Instability take place for $k < k_0$. Two stable modes have also imaginary parts and correspond to usual weakly decaying sound at lage k.

At J values such that T_0 is below T_c the role of superfluid phenomena increases gradually. For T_0 slightly below T_c superfluidity can be taken into account. As result we get same conditions for instability occurence, but now it arises as instability in a second sound solution.

$$\lambda \approx -\frac{1}{\tau_0}\left[\eta^{1/3}\tau_0 \chi k^2 - 1\right] \pm i \sqrt{c_{2s}^2 - \frac{1}{\tau_0^2}\left[\eta^{1/3}\tau_0 \chi k^2 - 1\right]^2}$$

Here as $c_{2s} = v_T \sqrt{\eta^{1/3} \rho_s S/\rho_n C_v}$ is the second sound velocity denoted. Where $C_v = c_v m$ is the dimensionless specific heat and $S = sm$ is dimensionless entropy (both are of order unity).

Experiments [3, 4] where carried out in the twodimensional case. Nonuniform structures were observed in a gas of indirect excitons with laser pumping near the Berezinskii – Kosterlitz – Thouless (BKT) transition. The main difference in the two-dimensional system near the BKT transition is the replacement of expression for pressure by the expression

$$p = \frac{n^2}{m \ln(1/na_0{}^2)} + mT^2$$

Here, dimensionless coefficients of order unity are omitted as in the three-dimensional case. Another important difference is the expression for the transition temperature

$$T_c = \frac{n}{m \ln\ln(1/na_0{}^2)}$$

As result instability conditions have form:

$$k < k_0 = \sqrt{-\frac{1}{\chi\tau_0}\left[1 - \frac{1 - \tau_0/\tau}{\alpha^2 \exp(-\alpha) + \alpha\nu/\tau v_T^2}\right]}$$

where $\alpha = \ln\ln(1/na_0{}^2) \gg 1$.

In conclusion it was shown that there is instability of a homogenious steady state in a dilute Bose gas near T_c (limits up and below are considered) upon external cooling due to large compressibility of such a gas near and below critical temperature and due to nonlinear mechanism of cooling. This effect probably can play some role in explanation of nonhomogeneous structure formation observed in the experiments [3, 4].

[1] E. Brener, S.V. Iordansky, R.B. Saptsov, Phys. Rev. E **73**, 016127 (2006).

[2] R. Saptsov. JETP Lett. **8**6, 687 (2007).

[3] A. Gorbunov, V. Timofeev, JETP Lett. **83**, 146 (2006).

[4] A.V. Gorbunov and V.B. Timofeev, JETP Lett. **84**, 329 (2006).

Quasi-Localized Vibrations, Boson Peak and Tunneling in Glasses

H. R. Schober[1], D. A. Parshin[2], V. L. Gurevich[3]

[1] IFF-3: Theory of Structure Formation
[2] Saint Petersburg State University, 195251 Saint Petersburg, Russia
[3] A. F. Ioffe Institute, 194021 Saint Petersburg, Russia

In the analysis of the low frequency vibrations in glasses one regularly observes in computer simulations quasi-localized vibrations (QLV) which can be understood as soft localized vibrations hybridized with the sound waves. We show that such modes explain both the Boson peak (BP) and the two-level-systems (TLS), the two most prominent glassy effects at low energies or temperatures. The weak interaction between the soft local vibrations causes a vibrational instability. Stability is restored by anharmonicity resulting in a universal shape of the BP and TLS's.

At low temperatures or low energies amorphous materials and glasses exhibit two typical glassy features: the two-level systems (TLS), causing e.g. a linear temperature dependence of the specific heat for $T \lesssim 1$ K, and the Boson peak, seen as a maximum in the inelastic scattering intensity around 1 THz. These two effect are usually described by separate models without any interrelation.

The TLS are an intrinsically quantum mechanical effect, observed when a group of atoms can tunnel between two adjacent minima of the potential energy, double well system. The ground state energy is then split by

$$E = \sqrt{\Delta_0^2 + \Delta^2} \qquad (1)$$

where Δ_0 is the tunnel-splitting in a symmetric double-well system and Δ is the asymmetry between the two minima. The tunnel splitting can be written approximately as

$$\Delta_0 = \hbar\omega e^{-\lambda}. \qquad (2)$$

where $\hbar\omega$ is the zero-point energy for the motion in either of the two minima.

The Boson peak (BP) is due to an excess of harmonic vibrations over the Debye density of states of the sound waves. It corresponds to a maximum in $g(\omega)/\omega^2$ but mostly only to a shoulder in the density of vibrational states, $g(\omega)$, itself. Since there is a continuum of frequencies the harmonic eigenmodes are extended. The BP-states, being harmonic, can be obtained from a dynamic matrix which will reflect disorder. The weakness of such an ansatz is that one has to use some extra conditions to obtain the needed soft vibrations while avoiding negative eigenvalues.

Our approach [1] is different; we start from the quasi-localized vibrations which have been ubiquitously observed in computer simulations[2]. Instead of using the exact harmonic eigenstates we use the sound waves and cores of these vibrations as basis as was implied in our earlier work on the soft potential model[3]. Here we exploit fully the interaction between the soft mode cores which will downshift the low frequency spectrum and even cause a vibrational instability. Invoking anharmonicity to lift the instability we find both a universal (harmonic) BP-excess-spectrum and TLS's.

Let us assume we have randomly distributed soft oscillators with a broad distribution of frequencies. Including the interaction between these oscillators their total potential energy is

$$U = \sum_i \frac{k_i}{2} x_i^2 - \frac{1}{2} \sum_{i,j \neq i} I_{ij} x_i x_j + \frac{1}{4} \sum_i A_i x_i^4. \qquad (3)$$

Here x_i are the generalized coordinates describing the vibrations, $k_i > 0$ are the quasielastic constants of noninteracting oscillators and I_{ij} determines the weak bilinear interaction between the oscillators. To stabilize the system we have added in this equation the anharmonic terms, $A_i x_i^4$ (with $A_i > 0$). Taking the elastic dipole interaction between the oscillators, the interaction strength is given by

$$I_{ij} = g_{ij} J / r_{ij}^3 \qquad (4)$$

where $g_{ij} \simeq \pm 1$ accounts for the relative orientation of the HO's, r_{ij} is the distance between HO's and J the dipole strength which can be determined from the coupling of the oscillators to the sound waves in the glass. We assume that all oscillators are stable without interaction and have a broad distribution of quasielastic constants. To be specific we will use $\Phi_0(k) = 3/2\sqrt{(k)}$ for $0 \leq k \leq 1$ corresponding to a density of states of the noninteracting oscillators $g_0(\omega) = 3\omega^2$, $\omega \leq 1$. The exact harmonic vibrations can then be obtained by matrix diagonalization neglecting the anharmonic term. The result is a downshift of the low frequency part of the spectrum as shown in Fig. 1.

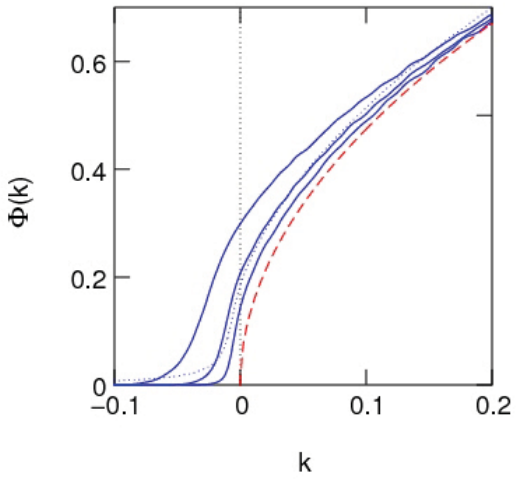

FIG. 1: Low frequency part of the distribution Function of the renormalized quasielastic constants, $\Phi(k)$, calculated as ensemble average by exact diagonalization of systems of $N = 2197$ oscillators for coupling strengths $J = 0.07, 0.10, 0.15$ (solid curve) and without interaction (dashed curve). The dotted line is an analytic approximation for $J = 0.01$

This result is similar to the one obtained for random matrices without restrictions to ensure stability ($k \geq 0$). Instead of introducing some not well understood restriction on the matrix elements we show that this harmonic vibrational instability creates a universal shape of the BP and additionally a realistic density of TLS's.

Stability is restored by anharmonicity. The downshift of $\Phi(k)$ for small k is caused by the action of higher frequency oscillators on soft ones. One can show that there is a critical frequency $\omega_c = \sqrt{mk_c} \propto J$ below which the spectrum is strongly affected by the interaction. One can eliminate the high frequency motion by an adiabatic approximation and obtains for the low frequency oscillator an effective quartic potential

$$U_{\rm eff}(x_1) = \frac{1}{2}(k_1 - \kappa)x_1^2 + \frac{1}{4}A_1 x_1^4 \qquad (5)$$

where κ is the effect of the interaction and $k_1 - \kappa$ is the renormalized quasielastic constant whose spectrum is shown in Fig. 1. For negative values of $k_1 - \kappa$ stability is restored by moving the oscillator to either minimum where one regains a positive constant $2(\kappa - k_1)$. Apart from the factor 2 the negative part of $\Phi(k)$ is thus reflected onto the positive part. It is remarkable that this effect is due to the anharmonicity but the actual value of it does not enter the result.

This harmonic approximation plus stabilization so far gives a finite value of $\Phi(k = 0)$ which corresponds to a vibrational spectrum $g(\omega) \propto \omega$ for $\omega \lesssim \omega_c$. Such a spectrum is highly unstable against perturbations. In our system such a perturbation is inherent. Changing the origin of the oscillators to either minimum in Eq. (5) implies a static displacement which via the bilinear coupling, Eq. (3) translates into a force on the other oscillators which, together with the anharmonicity, shifts the lowest part of the density of states upwards, creating the seagull singularity, $g(\omega) \propto \omega^4$ for $\omega << \omega_c$, of the soft potential model[3]. The excess vibrational spectrum has a universal shape function

$$g_{\rm tot}(\omega) \propto \omega^4 \int_0^{\sqrt{3/2}} \frac{dt}{1 + (\omega/\omega^\star)^6 \, t^2(3 - 2t^2)^2} \qquad (6)$$

Where $\omega^\star$ is approximately the BP frequency. Fig. 2 shows the excess density of vibrational states in the usual reduced representation.

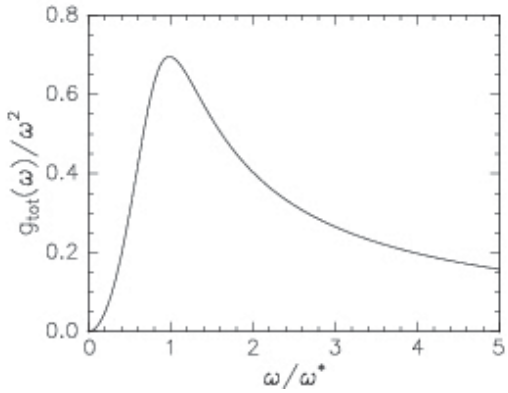

FIG. 2: The Boson peak: the reduced density of states $g_{\rm tot}(\omega)/\omega^2$ of the excess modes given by Eq. (6).

This BP-shape is in good agreement with experiment [4]. The theory can also be used to explain the pressure dependence of the BP.

Eq. (5) represents a two well potential which will give rise to TLS's. Apart from logarithmic corrections, already found in the soft potential model [3] the distribution of the standard tunneling model is recovered. Our theory, however, allows us to estimate the magnitude of the constants of this model. We can explain for instance the low number of observable TLS's and the low value of the so called tunneling strength C. These values are small because only a small fraction of double-well systems allow tunneling in observable times due to the exponential dependence of the tunneling element, Eq. (2).

[1] D. A. Parshin, H. R. Schober and V. L. Gurevich, Phys. Rev. B **76**, 064206 (2007).

[2] H. R. Schober and B. B. Laird Phys. Rev. B **44**, 6746 (1991).

[3] U. Buchenau, Yu. M. Galperin, V. L. Gurevich and H. R. Schober, Phys. Rev. B **43**, 5039 (1991).

[4] V. L. Gurevich, D. A. Parshin and H. R. Schober, Phys. Rev. B **67**, 094203 (2003).

Crack Propagation as a Free Boundary Problem

D. Pilipenko, R. Spatschek, E. A. Brener, H. Müller-Krumbhaar

IFF-3: Theory of Structure Formation

A sharp interface model of crack propagation as a phase transition process is discussed. We develop a multipole expansion technique to solve this free boundary problem numerically. We obtain steady state solutions with a self-consistently selected propagation velocity and shape of the crack, provided that elastodynamic effects are taken into account.

One of the most challenging riddles in physics and technology is the phenomenon of fracture, as it gives rise to material failure on all scales. Most fundamentally, the initiation of crack growth is due to a competition of the release of elastic energy and an increase of surface energy, which has been pointed out by Griffith [1] and has been used to describe many features of cracks.The interpretation of brittle fracture as the successive breaking of atomic bonds is in agreement with models of sharp crack tips, but still the theoretical predictions depend significantly on empirical interaction potentials. On the other hand, if dissipative plastic effects or large scale deformations are important, the crack tips are extended and have a finite tip radius r_0. Here, a detailed description of fracture necessitates equations of motion for each interface point of the extended crack instead of just the mentioned integral energy balance. A full modeling of fracture should then not only predict the growth velocity but also determine the entire shape of the crack self-consistently.

Continuum Model of Fracture. Imagine that the crack is filled with a soft condensed phase instead of vacuum, and the growth is then interpreted as a first order phase transformation of the hard solid matrix to this soft phase [2, 3]. The inner phase becomes stress free if its elastic constants vanish. Then, the boundary conditions on the crack contour are $\sigma_{nn} = \sigma_{n\tau} = 0$, where indices n and τ denote the normal and tangential directions with respect to the interface. In the bulk, the elastic displacements u_i have to fulfill Newton's equation of motion,

$$\frac{\partial \sigma_{ij}}{\partial x_j} = \rho \ddot{u}_i, \tag{1}$$

where ρ is the mass density. The difference in the chemical potentials between the two phases at the interface is given by [4]

$$\Delta\mu = \Omega(\frac{1}{2}\sigma_{ij}\epsilon_{ij} - \gamma\kappa), \tag{2}$$

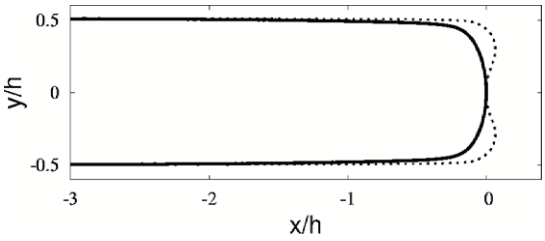

FIG. 1: Solid curve: Shape of the crack obtained for $\Delta = 1.3$; Dashed curve: Crack shape in the unstable regime for $\Delta = 2.3$. h is the tail opening.

with γ being the interfacial energy per unit area; ϵ_{ij} is a strain field; the interface curvature κ is positive if the crack shape is convex; the atomic volume Ω appears since the chemical potential is defined as free energy per particle. For elastically induced phase transitions to a "dense gas" phase with the same density as the solid, the motion of the interface is locally expressed by the normal velocity

$$v_n = \frac{D}{\Omega\gamma}\Delta\mu \tag{3}$$

with a kinetic coefficient D with dimension [D]=m^{2}s^{-1}. *The Multipole Expansion Method.* We discuss the steady state propagation of a semi-infinite crack in an isotropic medium. We assume a two-dimensional plane strain situation and mode I loading, which means that the applied tensile forces act perpendicularly to the crack. We start with the description in the laboratory frame of reference and assume that the crack is moving with a given constant velocity v. We can write the formal stress field expansion as

$$\sigma_{ij} = \frac{K_{dyn}}{(2\pi r)^{1/2}}\left(f_{ij}^{(0)} + \sum_{n=1}^{N=\infty}\frac{A_n f_{ij,d}^{(n)} + B_n f_{ij,s}^{(n)}}{r^n}\right),$$

where $f_{ij,d}^{(n)}(\theta_d, v)$ and $f_{ij,s}^{(n)}(\theta_s, v)$ are the known universal angular distributions for the dilatational and shear contributions which also depend on the propagation velocity. The unknown coefficients of expansion A_n, B_n can be found by solving the linear problem of fulfilling the boundary conditions $\sigma_{nn} = \sigma_{n\tau} = 0$ on the crack contour. The tangential stress $\sigma_{\tau\tau}$ is determined only through the solution of the elastic problem, and enters into the equations of motion (2)

and (3), leading to a complicated coupled and nonlocal problem. The strategy of solution of the problem is as follows: first, for a given guessed initial crack shape and velocity, we determine the unknown coefficients A_n and B_n from the boundary conditions. Second, we calculate the chemical potential and the normal velocity at each point of the interface. Afterwards, the new shape is obtained by advancing the crack according to the local interface velocities. This procedure is repeated until the shape of the crack in the co-moving frame of reference remains unchanged. It provides a natural way to solve the problem, as it follows the physical configurations to reach the steady state. Then the following relation between the local normal velocity and the steady state tip velocity v holds:

$$v_n = v \cos \eta, \tag{4}$$

with η being the angle between the normal to the crack contour and the x axis. Alternatively to this "quasi-dynamical approach", we also directly solve the nonlinear equation (4) as a functional of the crack shape and the tip velocity v.

Results and Discussion. We discuss crack growth in a strip geometry, with the width of the strip being very large in comparison to the crack tip scale. We introduce the dimensionless driving force $\Delta = K_{stat}^2(1-\nu^2)/2E\gamma$,where E is Young's modulus and ν the Poisson ratio. The static stress intensity factor K_{stat} is assumed to be given and finite. The multipole expansion technique confirms that the simple phase transformation model, based on Eqs. (1)-(3), provides a selection of the steady state shape and the velocity of the crack [5]. A typical crack shape is shown in Fig. 1.

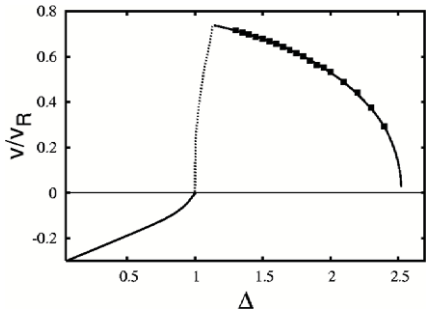

FIG. 2: Steady state velocity as a function of the dimensionless driving force Δ. The solid line corresponds to the steady state code, the squares to the quasi-dynamical code. Below the point $\Delta_c \approx 1.14$ the dissipation-free solution is selected by a microscopic length scale. Also for $\Delta < 1$ the tip scale is not selected, and the presented solution is obtained for the specific parameter $v_R h/D = 10$.

The dimensionless crack velocity v/v_R (v_R is the Rayleigh speed) as function of the driving force Δ is shown in Figs. 2. All results are obtained both by the "steady state approach" and the "quasi-dynamical code", and they are in excellent agreement with each other. In principle, one would expect steady state solutions for crack growth to exist for all driving forces beyond the Griffith point, $\Delta > 1$. However, in the framework of the model, they exist only in the interval $\Delta = 1.14 - 2.5$. At the limiting value, $\Delta \approx 2.5$, the propagation velocity tends to zero and the length scale h diverges. Nevertheless, at this point the product vh/D remains finite, as it is required for finite driving forces. This termination of the steady state solution is surprising, as one would expect the tip blunting to continue to arbitrarily large values of Δ. At the lower limit, $\Delta \approx 1.14$, the steady state crack velocity is finite, but the tail opening tends to zero in the framework of the model. At this point, the dissipation becomes zero, and all energy is converted to surface energy apart from kinetic contributions which are transported through the soft phase and out of the system. Below this point, i.e. for $1 < \Delta < 1.14$, dissipative solutions do not exist. Naturally, the tip scale should then be determined by an intrinsic microscopic length scale which is not contained in the present model. If it was introduced here explicitly, the behavior of the crack speed would behave as depicted by the dotted curve in Fig. 2; then it would become zero at the Griffith point $\Delta = 1$. Precisely this behavior near the Griffith threshold was observed in phase field simulations [3], where this cutoff naturally appears as the phase field interface width. We suppose that the solutions become unstable against a secondary Asaro-Tiller-Grinfeld instability beyond the point $\Delta \approx 1.8$, in agreement with previous conjectures [2] and phase field simulations [3]. Nevertheless, unstable steady state solutions persist up to $\Delta \approx 2.5$. Finally, we discuss the healing of cracks below the Griffith point, $\Delta < 1$; the velocity v of the crack becomes negative in this regime. In contrast to the case of growth, one expects these steady state solutions to exist for arbitrarily prescribed openings h and only the velocity v to be selected. This prediction is numerically confirmed by our simulations, see Fig. 2. We note that without elastic stresses, i.e. for $\Delta = 0$, the problem has a simple analytical solution: $x(y)/h = (1/\pi)\ln\cos(\pi y/h)$ with velocity $v = \pi D/h$.

In summary, we have presented a continuum theory of fracture based only on the linear theory of elasticity and a phase transformation process at the crack surface; we employ a sharp interface method to find steady state solutions of crack growth and are able to predict the growth velocity and the self-consistently selected shape of the crack.

[1] A. A. Griffith, Phil. Trans. R. Soc. A **221**, 163 (1921).

[2] E. A. Brener and R. Spatschek, Phys. Rev. E **67**, 016112 (2003)

[3] R. Spatschek, M. Hartmann, E. Brener, H. Müller-Krumbhaar, and K. Kassner, Phys. Rev. Lett. **96**, 015502 (2006).

[4] P. Nozières, J. Phys. I (France) **3**, 681 (1993).

[5] D. Pilipenko, R. Spatschek, E.A. Brener, H. Müller-Krumbhaar Phys. Rev. Lett. **98**, 015503 (2007)

Influence of Strain on the Kinetics of Phase Transitions in Solids

E. Brener[1], R. Spatschek[1], V. Marchenko[2]

[1] IFF-3: Theory of Structure Formation

[2] P.L. Kapitza Institute for Physical Problems, RAS 119334, Kosygina 2, Moscow, Russia

We consider a sharp interface kinetic model of phase transitions accompanied by elastic strain, together with its phase-field realization. Quantitative results for the steady-state growth of a new phase in a strip geometry are obtained and different pattern formation processes in this system are investigated.

Many magnetic, superconducting and structural phase transitions in solids are accompanied by small lattice distortions which lead to the presence of elastic deformations [1]. For each phase transition a characteristic deformation can be assigned, i.e., the deformation acquired by the new phase relative to the initial phase in the absence of external forces. In some cases, these effects are of minor influence and can be ignored, but nevertheless for many applications the elastic strain causes qualitatively new and observable effects [2]. In particular, the systematic theoretical study of the growth *kinetics* of such phase transitions accompanied by a lattice strain is still in its beginning. The aim of the current paper is therefore to develop a "'minimum" kinetic model, from which even quantitative results concerning the influence of strain effects can be obtained [3]. It differs from earlier descriptions in the sense that explicit equations of motion for sharp interfaces are set up and finally solved numerically, leading to peculiar interfacial pattern formation processes.

Dilatational mismatch model. The free energy density of an initial phase is

$$F_1 = F_1^0 + \frac{1}{2}\lambda u_{ii}^2 + \mu u_{ik}^2, \qquad (1)$$

where F_1^0 is the free energy density without elastic effects, u_{ik} are the components of the strain tensor, λ and μ are the elastic moduli of isotropic linear elasticity. The free energy density of a new phase is

$$F_2 = F_2^0 + \frac{1}{2}\lambda \left(u_{ii} - u_{ii}^0\right)^2 + \mu \left(u_{ik} - u_{ik}^0\right)^2, \qquad (2)$$

with u_{ik}^0 being a characteristic lattice strain assigned to the phase transition.

Let us consider the simplest case, $u_{ik}^0 = \varepsilon\delta_{ik}$, at first, where the bond lengths of the new phase are uniformly longer or shorter in all directions in comparison to the original phase. The coherency condition at the interface reads $\mathbf{u}^{(1)} = \mathbf{u}^{(2)}$, where $\mathbf{u}$ is the displacement vector. The superscripts (1) and (2) refer to the initial and the newly created phase respectively. Mechanical equilibrium at the interface demands the equality of normal and shear stresses, $\sigma_{nn}^{(1)} = \sigma_{nn}^{(2)}$ and $\sigma_{n\tau}^{(1)} = \sigma_{n\tau}^{(2)}$. The condition of phase equilibrium requires the continuity of a new potential $\tilde{F} = F - \sigma_{nn}u_{nn} - 2\sigma_{n\tau}u_{n\tau}$ across the flat interface, which takes into account the coherency constraint [4]. In the general case of curved interfaces also the surface energy γ has to be incorporated, and the phase equilibrium condition for each interface point reads in the case of isotropic surface energy $\tilde{F}_1 - \tilde{F}_2 - \gamma\mathcal{K} = 0$, where $\mathcal{K}$ is the local curvature of the interface.

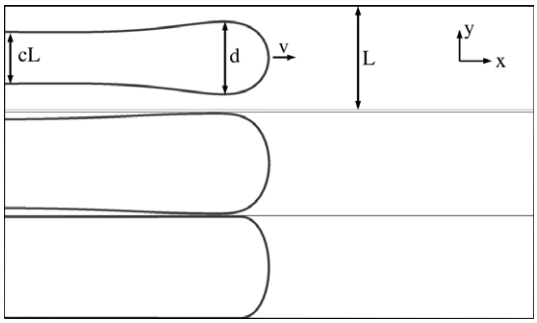

FIG. 1: Shapes of propagating fingers calculated for three values of the driving force, see Eq. (3). Top: $\Delta = 0.5 < \Delta_t$. Center: $\Delta = 0.85 > \Delta_t$. Bottom: $\Delta = 1.05$. The Poisson ratio is $\nu = 1/3$ and $L/L^* = 10$.

We discuss a simple strip configuration which allows the steady-state growth of an elastic "finger" consisting of the new phase (see Fig. 1), as a possible setup for experimental investigations. The unstrained elastic strip of width L is attached to fixed grips at the upper and lower boundary ($\mathbf{u} = 0$ there) and initially composed of the reference phase. We discuss a two-dimensional elastic problem using plane strain conditions ($u_z = 0$). Also, we assume the complete wetting of the walls by the initial phase. Far ahead of the propagating finger the initial phase remains unstrained. In contrast, far behind the tip a phase coexistence is possible within a certain parameter interval near the transition temperature, which is due to elastic effects. We find the volume fraction of the new phase,

$$c = \Delta = \frac{1-2\nu}{1+\nu}\left[\frac{1-\nu}{E\varepsilon^2}(F_1^0 - F_2^0) - 1\right], \qquad (3)$$

which defines a dimensionless driving force Δ for this process. Then the parameter range for coexistence is $0 < \Delta < 1$. The total free energy gain per unit area in the xz plane of this two-phase configuration compared to the unstrained initial phase is

$$\Delta\mathcal{F} = 2\gamma\left(\frac{\Delta^2}{\Delta_L^2} - 1\right), \qquad (4)$$

where

$$\Delta_L^2 = \frac{L^*}{L}, \qquad L^* = \frac{4(1-2\nu)(1-\nu)\gamma}{(1+\nu)E\varepsilon^2}. \qquad (5)$$

The finger grows if $\Delta\mathcal{F} > 0$, or, equivalently, if $\Delta > \Delta_L$. This condition corresponds to the Griffith point in fracture mechanics. We note that the value of the driving force for the transition can be controlled not only by temperature, but also by external strain.

Following our general aim to develop a minimum kinetic model, we assume that the growth is controlled only by interface kinetics. Then, the local equation of motion of the interface reads $v_n = \kappa(\tilde{F}_1 - \tilde{F}_2 - \gamma\mathcal{K})$, where v_n is the normal velocity and κ a kinetic coefficient. The characteristic velocity scale of this process is $v_0 = 2\kappa\gamma/L^*$.

Phase Field Modeling. In order to obtain quantitative results for this problem we use a phase field code as numerical tool, together with elastodynamics to describe phase transformations accompanied by stress, which we developed recently [5]. Let ϕ denote the phase field with values $\phi = 1$ for the initial phase and $\phi = 0$ for the new phase. The free energy density contribution is $F = F_1 h(\phi) + F_2[1 - h(\phi)]$, where the switching function $h(\phi) = \phi^2(3 - 2\phi)$ interpolates between the phases. The gradient energy is $F_s(\phi) = 3\gamma\xi(\nabla\phi)^2/2$ with the interface width ξ. Finally, $F_{dw} = 6\gamma\phi^2(1-\phi)^2/\xi$ is the double well potential. Thus the total free energy functional is $\tilde{\mathcal{F}} = \int dV\,(F + F_s + F_{dw})$. The elastodynamic equations are derived from the free energy by variation with respect to the displacements u_i, $\rho\ddot{u}_i = -\delta\tilde{\mathcal{F}}/\delta u_i$, where ρ is the mass density. The dissipative phase field dynamics follows from $\partial\phi/\partial t = -\kappa\delta\tilde{\mathcal{F}}/\delta\phi 3\xi$. These equations lead in the limit $\xi \to 0$ to the sharp interface description above.

Characteristic shapes of the stationary fingers are presented in Fig. 1. The finger selects a symmetrical shape even if the initial configuration was vertically off-centered, i.e. the symmetrical configuration is stable. The dependence of the dimensionless steady-state growth velocity v/v_0 on the dimensionless driving force Δ is presented in Fig. 2.

Transitions with Shear Strain. A simple type of transition involving shear strain can occur in hexagonal crystals. For the transitions lowering the symmetry from C_6 to C_2, the shear strain in a basic plane appears; this is the case for example in hexagonal-orthorhombic transitions in ferroelastics. Let the principal axis C_6 be oriented in z direction. By proper choice of the crystal orientation around the main axis in the initial phase, we obtain the new phase in three possible states due to the original hexagonal symmetry. Then the nonvanishing components of the strain tensor u_{ik}^0 are $u_{xx}^0 = -u_{yy}^0 = \varepsilon\cos 2\theta$ and $u_{xy}^0 = \varepsilon\sin 2\theta$, where the angle θ is $\theta = 0, \pm 2\pi/3$.

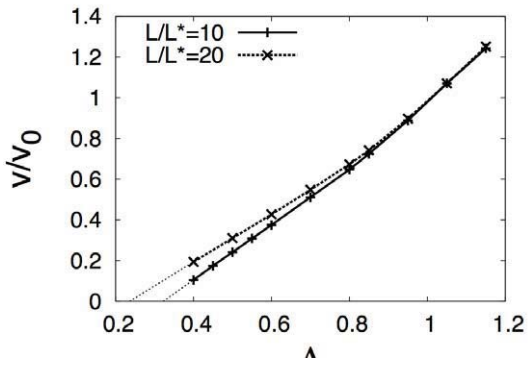

FIG. 2: The dimensionless growth velocity v/v_0 as a function of the dimensionless driving force Δ.

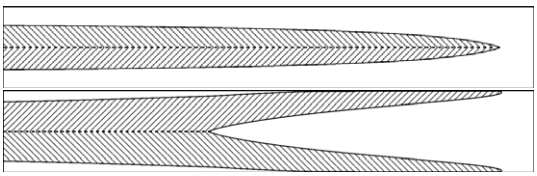

FIG. 3: Growth of bicrystal patterns for $L/L^* = 5$. The shading illustrates the orientation of the shear strain u_{xy}. The growth velocities are $v/v_0 = 1.14$ (top) and $v/v_0 = 0.48$ (bottom).

A straightforward analysis of the stress state far behind the tip shows that among the possible configurations of new phases the energetically most favorable scenario are bicrystals, $\theta = \pm 2\pi/3$, as presented in Fig. 3. Although both patterns in Fig. 3 are energetically equivalent far away from the tip, symmetry is broken by the choice of the propagation direction. For growth to the right, the orientation $\theta = 2\pi/3$ in the upper and $\theta = -2\pi/3$ in the lower half, leading to propagation with a single tip (upper panel of Fig. 3), is superior to the opposite case with repelling fingers (lower panel), as the growth velocity is higher.

[1] A.G. Khachaturyan, *Theory of Structural Transformation in Solids* (Wiley, New York, 1983).

[2] E.A. Brener and V.I. Marchenko, Sov. JETP Lett. **56**, 368 (1992).

[3] E. Brener, V. Marchenko, and R. Spatschek, Phys. Rev. E **75**, 041604 (2007).

[4] R. Spatschek and M. Fleck, Phil. Mag. Lett. **87**, 909 (2007).

[5] R. Spatschek, M. Hartmann, E. Brener, H. Müller-Krumbhaar, and K. Kassner, Phys. Rev. Lett. **96**, 015502 (2006).

Tomographic Reconstruction and Reduction of Measuring Points in Fuel Cells

H. Lustfeld[1], M. Reißel[2], U. Schmidt[2,3], B. Steffen[4]

[1] IFF-1: Quantum Theory of Materials
[2] FH Aachen, Abt. Jülich
[3] Rechen- und Kommunikationszentrum der RWTH Aachen
[4] Jülich Supercomputing Centre

In this paper the tomographic problem arising in the diagnostics of a fuel cell is discussed: How well can the electric current density $\mathbf{j}(\mathbf{r})$ be reconstructed by measuring its external magnetic field. We show: A procedure can be applied determining the optimum measuring positions, essentially decreasing the number of measuring points - without a loss of fine resolution. This procedure can easily be generalized. Here we present explicit results by applying our formulas to a realistic case of an experimental Direct Methanol Fuel Cell (DMFC).

Fuel cells[1] avoid the by Carnot's law limited efficiency of machines first converting chemical energy into heat and then heat into electric energy. For this reason the theoretical efficiency factor η of fuel cells, e.g. that of the DMFC, is distinctively larger than that of thermal engines and close to 1. However, in real life its mean value for DMFC's in operation is still only about $\eta = 0.35$.

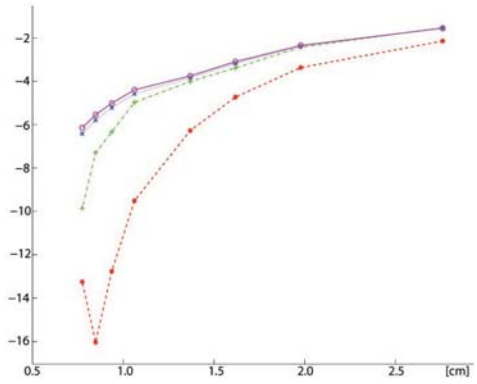

FIG. 1: Resolution of $\mathbf{j}(\mathbf{r})$ in the MEA versus logarithm of the required relative precision when measuring the magnetic field. Distance between the fuel cell and the planes in which the magnetic field is measured is 1 cm. (Red) dashed line: spacing $d_P \approx 5$ cm. (Green) dashed dotted line: $d_P \approx 2.5$ cm. (Blue) dotted line: $d_P \approx 1.2$ cm. (Magenta) full line: $d_P \approx 0.6$ cm. Note that a spacing of 5 cm is much too large leading to meaningless results.

Hence a lot of further development and ideas are required and one prerequisite for that is a good diagnostics, i.e. reasonable insight into the distribution of electric currents in the fuel cell. Now typical for every fuel cell are the high electric currents in the range of 10 A to 100 A suggesting measurements of the exterior magnetic fields for reconstructing the internal current distribution of the fuel cell[2].

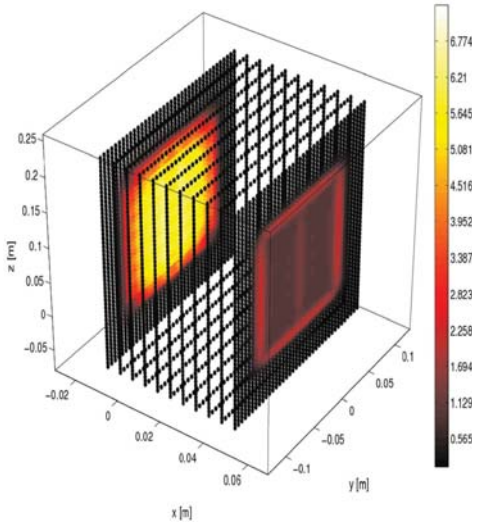

FIG. 2: All 5536 measuring points located in the 6 planes surrounding the fuel cell are marked. Distance between fuel cell and planes is 1 cm. Spacing d_p of the measuring points is about 0.6 cm. At each measuring point the value of the ζ function is indicated by the color and thickness of the corresponding marker. The two planes close to the frontend and backend of the fuel cell have the highest ζ values. Note that the scales in depth, width and height are not identical.

This is a tomographic problem. To get reasonable resolution for the currents in the fuel cell, in particular in the layer of the **M**embrane **E**lectrode **A**ssembly (MEA) the magnetic field is measured in 6 planes surrounding the fuel cell.

There are two rules of the thumb:

i) The smaller the distance between fuel cell and measuring plane the better the resolution.

ii) The smaller the spacing d_p of the measuring points in a given plane the better the resolution.

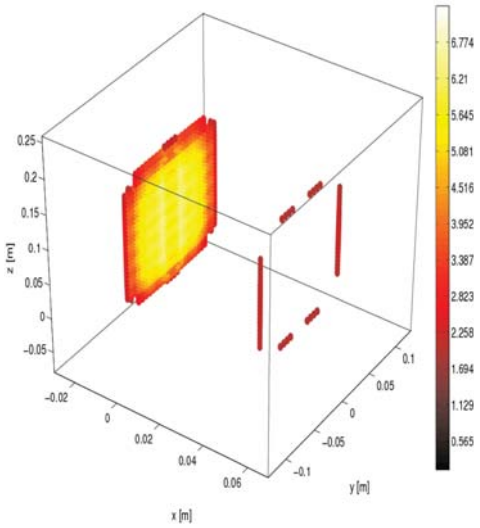

FIG. 3: The remaining 868 measuring points after all measuring points with $\zeta(\mathbf{r}_j) < 2$ have been dropped. Nomenclature and other parameters as in Fig. 2.

If a regular network of measuring points is chosen in every plane the spacing d_p of the measuring points has to be about 0.5 cm, cf Fig. 1. Unfortunately the required number of measuring points is not small in this case, (about 5500), cf Fig.2.

We have shown[3] that rule ii) is much less strict than at first expected because the number of measuring points on a given plane can be reduced drastically in a systematic manner (typically by 80% or even more), cf Fig.3, and *without* loosing resolution, cf Fig.4.

This is very important because the timescale of the measuring apparatus depending on the number of measuring points is thus essentially reduced as well, enabling the reconstruction of faster dynamical perturbations.

At first sight it might seem paradoxical that a reduction of measuring points can even enhance the relative precision, as is shown in fig.4. The reason is that each measuring point supplies additional information but noise as well. We have found a function $\zeta(\mathbf{r}_i)$ computing for each point $\mathbf{r}_i$ the tradeoff between its relevance of information and its sensitivity with respect to noise. The higher the ζ value the more relevant a measuring point becomes.

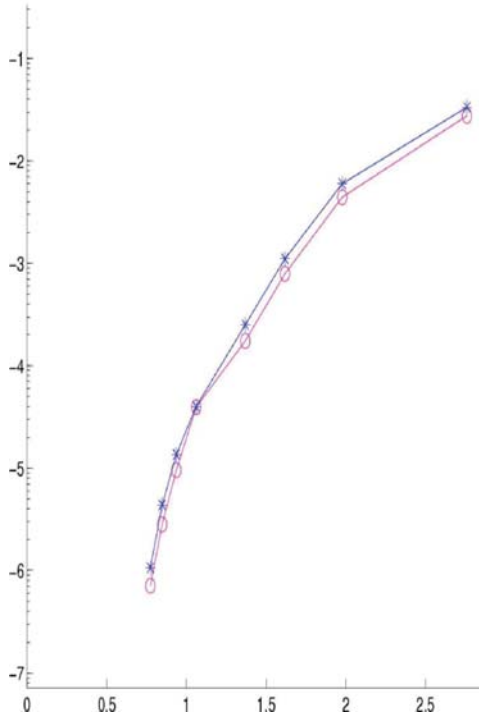

FIG. 4: Resolution [in cm] of $\mathbf{j}(\mathbf{r})$ in the MEA versus logarithm of the required relative precision when measuring the magnetic field. Lower (magenta) line: all 5536 measuring points are taken into account with a spacing of 0.6 cm between measuring points. Upper (blue) line: Out of the 5536 measuring points only the 868 points with $\zeta(\mathbf{r}_j) \geq 2$ are taken into account. Note that reducing the number of measuring points leads to a better resolution.

[1] K. Kordesch and G. Simader, *Fuel cells and their applications*, VCH Verlagsgesellschaft, Weinheim (1996).

[2] R. Kress, L. Kühn and R. Potthast, Inverse Problems, 18, 1127 (2002).

[3] H. Lustfeld, M. Reiß, U. Schmidt and B. Steffen, Fuel Cell Science and Technology, in press.

[4] H. Lustfeld, M. Reißel, U. Schmidt and B. Steffen, patent pending, patentNo: DE 10 2007 044 257 (2007).

Optical Stability of Ultra-High Resolution Transmission Electron Microscopes

A. Thust, J. Barthel, L. Houben, M. Lentzen, K. Tillmann, K. Urban

IFF-8: Microstructure Research
ER-C: Ernst Ruska-Centre for Microscopy and Spectroscopy with Electrons

The presently available first generation of sub-angstrom transmission electron microscopes yields high-resolution images with unprecedented quality. At the same time such microscopes impose new efforts in controlling their imaging properties. The smaller the resolved object details are, the stronger becomes the influence of unwanted lens imperfections. Both, measurement and control of such imperfections, which are called lens aberrations, represent substantial challenges on the way to quantitative sub-angstrom work. We performed time-stability measurements of lens aberrations with unprecedented accuracy. These measurements support new design concepts for an upcoming generation of high-resolution microscopes.

In order to make quantitatively use of the information transferred by a high-resolution transmission electron microscope, it is mandatory to know the imaging properties of its objective lens. These imaging properties are characterized completely by the so-called aberration function $\chi(\vec{g})$. The aberration function represents a phase shift imposed by the objective lens on a diffracted beam with wavevector $\vec{g}$. The aberration function is composed of single basic aberrations, which differ from each other in strength (power-law dependency on the transferred spatial frequency $|\vec{g}|$) and in rotational symmetry. Denoting the wavevector $\vec{g}$ in polar coordinates by (g, φ), and the electron wavelength by λ, one obtains for the aberration function the expression

$$\chi(g,\varphi) = 2\pi \sum_{\substack{m\geq 1 \\ 0\leq n\leq m \\ m+n=2N}} \frac{a_{mn}}{m}\,\lambda^{m-1} g^m \cos\left[n(\varphi-\varphi_{mn})\right] ,$$

where a_{mn} denotes the wave aberration coefficients and φ_{mn} the corresponding azimuth angles. The subscript m relates to the power of the spatial frequency g, and the subscript n to the angular symmetry of the respective basic aberration. Whereas in the past it was sufficient to deal with only a few aberrations like defocus a_{20}, twofold astigmatism a_{22}, axial coma a_{31}, threefold astigmatism a_{33}, and spherical aberration a_{40}, sub-angstrom imaging requires now the knowledge and control of all wave aberrations up to the sixth order of the wavevector $\vec{g}$. The decomposition of a typical aberration function into basic aberrations a_{mn} is illustrated in Fig. 1.

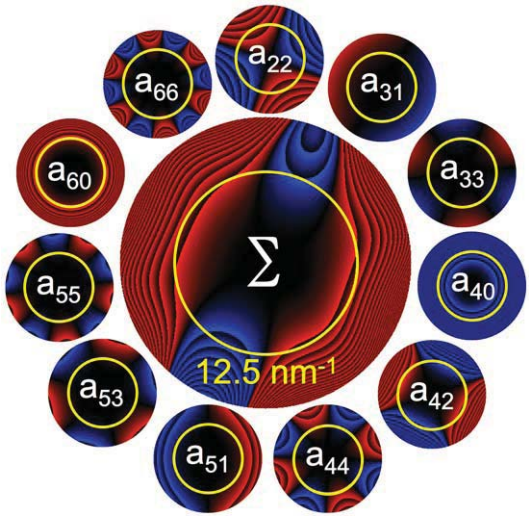

FIG. 1: Typical aberration function (center) and its decomposition into basic aberrations (surrounding). Positive values of the aberration function are depicted in red and negative values in blue. Sawtooth jumps occur in intervals of $\pi/4$. The yellow circle in the diffraction plane marks a value of g = 12.5 nm^{-1} corresponding to a resolution of 0.08 nm. Aberration-free imaging is achieved when the modulus of the total aberration function in the center does not exceed $\pi/4$ within the circle defining the resolution limit.

It is widely accepted that the aberration function $\chi(\vec{g})$ is fairly constant in time and that an optical adjustment of the microscope by the operator must be repeated only a few times during a microscope session. With our newly devised ATLAS aberration measurement software [1], which yields an improvement in measurement precision by an order of magnitude compared to the manufacturer supplied solution, we managed to investigate in detail the time stability of all aforementioned basic aberrations. These measurements were performed for the first time with a precision guaranteeing aberration-clean quantitative sub-angstrom imaging. The ATLAS software offers especially for the defocus a_{20} and the twofold astigmatism a_{22} an automated monitoring mode. Typical

snapshots of the focal variation with time are shown in Fig. 2 for two different microscopes.

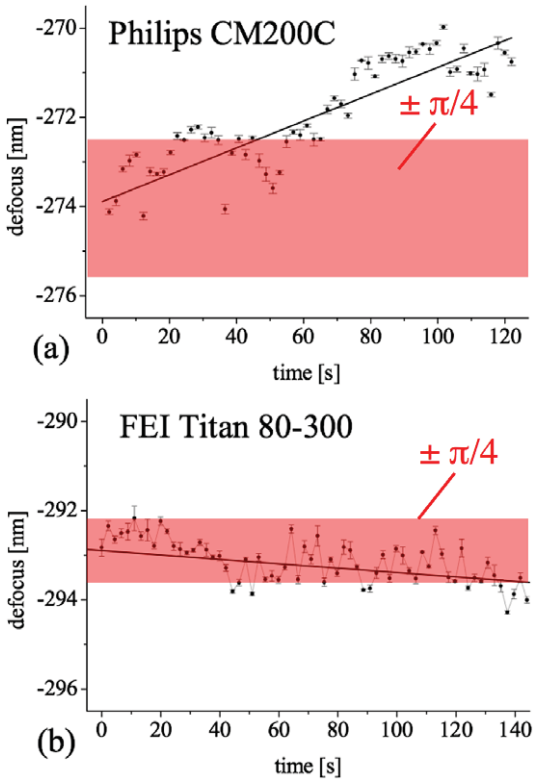

FIG. 2: Time variation of the objective lens defocus a_{20} during a period of approximately 2 minutes for (a) a 200 kV Philips CM200 microscope with a resolution of 0.12 nm and for (b) a 300 kV FEI Titan microscope with a resolution of 0.08 nm. Apart from a thermally induced long-term drift, also short-term fluctuations are observed, which are caused by instabilities of the accelerating voltage and of the objective lens current. In both cases the defocus-related part of the aberration function exceeds the $\pi/4$ tolerance range for aberration-free imaging after 1–2 minutes.

It is clearly insufficient to consider each single basic aberration separately for the assessment of aberration-free imaging, as is shown for the defocus in Fig. 2, but to observe the combined effect of all contributing aberrations. Hereby accumulation as well as compensation effects with respect to the resulting phase shift can occur in different regions of the Fourier-space plane. Fortunately our experiments reveal a rough trend according to which higher-order aberrations beginning with the fourth order (i.e. $m = 4$) tend to be stable for hours at least. Strong variations of the imaging properties are frequently due to second order aberrations ($m = 2$). The time evolution of an aberration function composed of defocus a_{20} and twofold astigmatism a_{22}, which was monitored over an interval of 96 seconds, is displayed in Fig. 3.

We could identify a number of different reasons leading to unwanted deviations of the imaging conditions from an initially aberration-free microscope setting. Apart from electric and magnetic field inhomogeneities near the object, which play a role when moving the sample over a sub-micron distance to the place of interest, the long-term time variations shown here result mainly from a thermally induced mechanical movement of the electron-optical set up. We could successfully relate such time variations of the transfer properties to temperature variations of the cooling water and to room temperature changes on the order of 0.1 – 0.5 Kelvin. The room temperature changes are correlated with the presence of an operator near the microscope.

Regarding the microscope hardware, the results of our investigation are shared with a major microscope manufacturer in the framework of a cooperation agreement. Our investigation supports the concept of a new generation of ultra-high resolution microscopes, which are thermally insulated from the surrounding and which are remotely controlled. Moreover, the ultra-precise measurement of residual lens aberrations enables their successful a-posteriori elimination by means of software phase-retrieval procedures, improving significantly the output of materials science investigations [2].

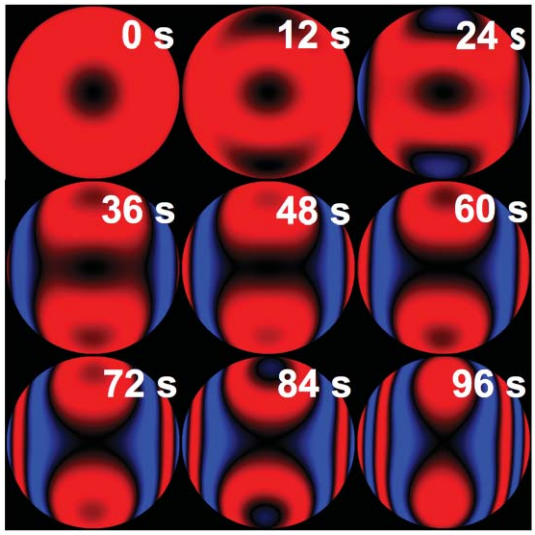

FIG. 3: Degradation of an initially ideal contrast transfer within a time interval of 96 seconds observed at a 200 kV Philips CM200 electron microscope. The sine of the aberration function including defocus a_{20} and twofold astigmatism a_{22} is displayed in Fourier space up to a resolution of 0.08 nm. Red areas indicate positive values of $\sin\chi$ and blue areas negative values. The initial condition corresponds to ideal phase contrast, where the aberration function is close to a value of $\pi/2$, i.e. $\sin\chi \approx 1$.

[1] J. Barthel, PhD Thesis, RWTH Aachen (2007).

[2] K. Tillmann, J. Barthel, L. Houben, M. Lentzen, A. Thust and K. Urban, Springer Proceedings in Physics, edited by A.G. Cullis and P.A. Midgley, in press (2008).

Advances in Applied Aberration Corrected HRTEM of Solids

K. Tillmann, J. Barthel, L. Houben, M. Lentzen, A. Thust, and K. Urban

IFF-8: Microstructure Research
ER-C: Ernst Ruska-Centre for Microscopy and Spectroscopy with Electrons

Recent progress in applied spherical aberration corrected high-resolution transmission electron microscopy (HRTEM) performed in troika with the ultra-precise measurement of residual wave aberrations and the numerical retrieval of the exit plane wavefunction (EPWF) from through focus series of micrographs is illustrated by highlighting their combined use for the atomic-scale measurement of lattice displacements coming along with extrinsic stacking faults in GaAs.

With considerable improvements in instrumental resolution well beyond the Ångstöm barrier, also accompanied by a simultaneous minimisation of image delocalisation, aberration-corrected HRTEM is presently enjoying increased popularity in the atomic-scale imaging of lattice imperfections and heterointerfaces in crystalline solids.

The sole availability of ultimate resolution, however, only represents a *sine qua non* for the imaging of object details of the very same length scale. Additionally, an unaltered transfer of information through the microscope's lens system constitutes a mandatory requirement in the direct interpretability of recorded micrographs. Recent experience with the Ernst Ruska-Centre's (ER-C) state-of-the-art instruments, however, shows that the time-dependent variation of environmental-induced parasitic higher-order wave aberrations a_{ij} together with a system-inherent residual image delocalisation still present at instruments equipped with spherical aberration-corrector unit, may dramatically deteriorate information transfer and virtually represents the key limitation during experimental analyses at present.

Thence, to bring out most of recorded micrographs, a three-step course of action, as illustrated by the process chart displayed in Fig. 1, was recently excogitated and implemented at the ER-C to fully make use of the improved resolution offered by neoteric instrumentation [1, 2]. Residual wave aberrations a_{ij} are measured at utmost precision making use of the ATLAS (Advanced Treatment of Lens Aberrations and Stability) package [3] and entirely eliminated *a posteriori* by applying phase retrieval methods making use of recorded through-focus series.

By this means true structure information can now be retrieved in the vicinity of lattice imperfections and across heterointerfaces in crystalline solids meeting uncertainties in the measurement of individual atom column positions with 2σ confidence intervals as far as to about 5 picometres.

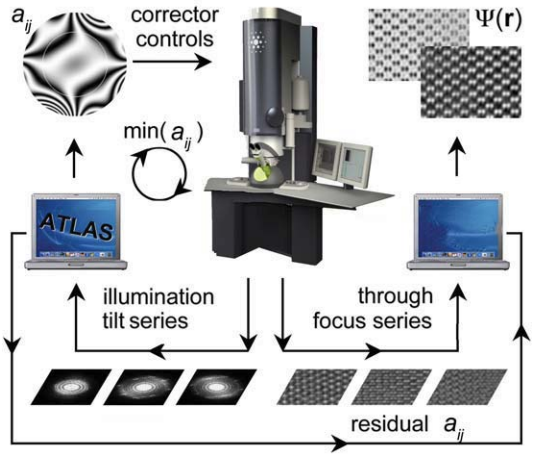

FIG. 1: Process diagram illustrating the course of successive procedures to (i) minimise residual wave aberrations a_{ij} during setup of a spherical aberration corrected microscope (left) followed by (ii) the numerical retrieval amplitude and phase $\Phi(\mathbf{r})$ of the exit-plane wavefunction $\Psi(\mathbf{r})$ from a through-focus series of micrographs (right) also involving (iii) an *a posteriori* correction of residual aberrations a_{ij} measured from illumination tilt series of images taken from amorphous specimen areas using the ATLAS package [2, 3].

As a materials science application of example, we report on locally inhomogeneous distortions of atomic dumbbells across extrinsic stacking faults in a GaAs capping layer grown by molecular epitaxy on top of a plastically relaxed $In_{0.3}Ga_{0.7}As$ layer. Measurements on actual dumbbell lengths, amounting to 141 pm in case of unstrained material when viewed along the crystallographic [110] direction, have been performed on the phase image $\Phi(\mathbf{r})$ displayed in Fig. 2 (a); the associated exit-plane wavefunction $\Psi(\mathbf{r})$ was retrieved from a through focus series of 30 micrographs with residual wave aberrations a_{ij} measured by the ATLAS package [2, 3] and subsequently corrected up to the third order. The centre of the phase image is

5.2 nm left of a 90° partial dislocation core terminating the faulted double ribbon [4].

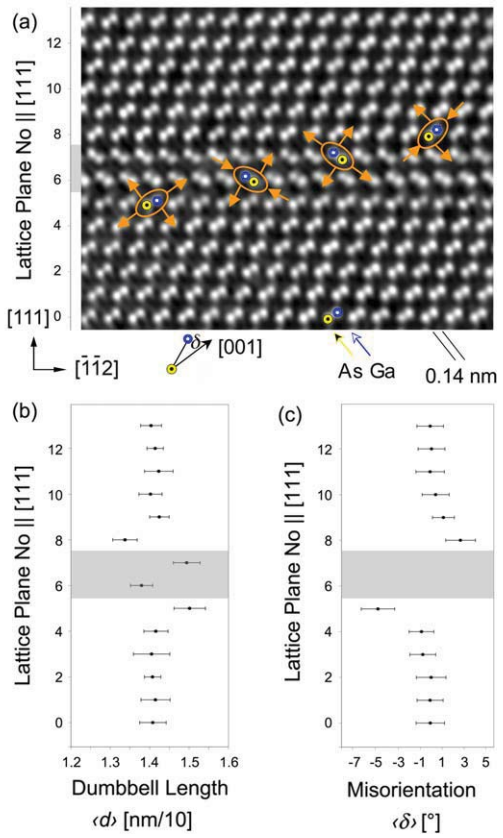

FIG. 2: Inhomogeneous distortion of atomic dumbbells across an extrinsic stacking fault in GaAs (110). (a) Retrieved phase image $\Phi(r)$ with atomic column positions superimposed and dumbbell distortions indicated exemplarily (orange arrows) in dependence on specific positions along the [111] direction. (b) Average projected bond length $\langle d \rangle$ and (c) misorientation angle $\langle \delta \rangle$ of the dumbbells along the [111] direction. The lattice planes belonging to the double faulted ribbon are indicated in lighter grey colour.

Actual lengths and orientations of individual dumbbells have been measured and normalised to mean values associated with the lower (planes no. 0 - 3) and upper (planes no. 1 - 13) areas of the $\Phi(\mathbf{r})$ image. For statistical error reduction purposes 15 data points have been averaged along the $[1\bar{1}2]$ direction and median values are plotted in Figs. 2 (b) and (c) in dependence on specific (111) lattice planes.

As can be seen from both plots, the dumbbells on either side of the double ribbon rearrange roughly antisymmetric with regard to the faulted (111) planes. The dumbbells of the bottommost plane of the upper domain (plane no. 8) are compressed to a length of $\langle d \rangle$ = 133 $\pm$ 4 pm and turn towards the double ribbon with a misorientation angle $\langle \delta \rangle \approx 2.6° \pm 1.3°$ compared to the reference planes. In contrast, the uppermost dumbbells of the lower crystal area (plane no. 5) are stretched to a length of $\langle d \rangle$ = 150 pm $\pm$ 4 pm and bend away from the double ribbon at a misorientation angle of $\langle \delta \rangle \approx 4.9° \pm 1.5°$.

In order to gauge whether the observed antisymmetric distortions represent a genuine structural property or not, potential implications of scattering and imaging artefacts need to be ruled out. Since a hypothetical global misalignment of the sample cannot give rise to any local torsion and dilatation of projected atomic dumbbells we may disenfranchise from this explanation. An argument of the same kind holds true of the potential impact of not fully compensated residual wave aberrations a_{ij} as they would take effect on the entire image and, hence, would distort all atomic dumbbells of the same orientation equally. Beyond electron-optical reasoning, a supposed strictly antisymmetric lattice distortion caused by a dedicated combination of higher-order wave aberrations a_{ij} with the faulted ribbon incidentally acting as the symmetry plane, may be ruled out from a probability point of view because of an almost immense number of possible combinations which will not give raise to the observed distortion behaviour.

Hence, measurements firmly suggest a true materials science background, as opposed to an electron-optical artifact, and one may speculate about indium diffusion from the underlying $In_{0.3}Ga_{0.7}As$ layer to the GaAs layer along the faulted ribbon. As long as an inhomogeneous incorporation of indium atoms is not considered, this approach, however, cannot explain the observed antisymmetry. Admittedly, these distortions become perspicuous when considering the elastic distortions associated with 90° partial dislocations in the framework of continuum theory of elasticity [5] which basically follow the measured characteristics of the dumbbell's measured expansion and torsion but, alas, yield only alterations of dumbbells lengths smaller than $\pm$ 3 pm and misorientation angles smaller than $\pm$ 0.4° for the image area under investigation. Thence, a more likely explanation would be that the terminating partial dislocation biases the rearrangement of atomic columns in the vicinity of the faulted ribbons and that next but one neighbour interactions between different atomic species will indeed play an important role during this process.

[1] K. Tillmann, J. Barthel, L. Houben, M. Lentzen, A. Thust, and K. Urban, Springer Proceedings in Physics, edited by A. G. Cullis and P. A. Midgley, *in press* (2008).

[2] A. Thust, J. Barthel, L. Houben, M. Lentzen, K. Tillmann, and K. Urban, *separate contribution to this report* (2008).

[3] J. Barthel, PhD Thesis, Research Centre Jülich in cooperation with RWTH Aachen University (2007).

[4] K. Tillmann, L. Houben, and A. Thust, Phil. Mag. 86, 4589 (2006).

[5] J.P. Hirth and J. Lothe, Theory of Dislocations, New York, McGraw-Hill (1968).

Atomic Structure of β-phase Tantalum Nanocrystallites

K. Tillmann[1,2], A. Thust[1,2], A. Gerber[3,4], M. Weides[3,4], and K. Urban[1,2]

[1] IFF-8: Microstructure Research
[2] ER-C: Ernst Ruska-Centre for Microscopy and Spectroscopy with Electrons
[3] IFF-6: Electronic Materials
[4] CNI: Center of Nanoelectronic Systems for Information Technology

The atomic structure of β-phase tantalum nanocrystallites has been measured by spherical aberration-corrected high-resolution transmission electron microscopy (HRTEM) performed in tandem with the numerical retrieval of the exit-plane wavefunction (EPWF) as obtained from a through-focus series of experimental micrographs. For the first time ever, the existence of grain boundaries of 30° tilt type in β-phase tantalum was substantiated whose formation could be well explained by atomic agglomeration processes taking place during sputter deposition.

Room-temperature magnetron sputter deposition of tantalum thin films on a multitude of solids usually results in the formation of polycrystalline coatings with nanometre-sized crystallites. These crystallites initially nucleate in the metastable tetragonal β-phase, whose unit cell is displayed in Fig. 1 in two projections, and the material usually undergoes a phase transformation towards the cubic α-phase at film thicknesses of about 10 nm to 20 nm.

The current technological interest in tantalum thin films is, however, primarily due to the ability of tantalum interlayers to promote the adhesion of copper to dielectrics and because of good barrier properties against the diffusion of copper to silicon. Because of the polycrystalline structure of tantalum thin films, grain boundary diffusion becomes admittedly relevant at elevated temperatures [1] and molecular-dynamics simulations indicate a pronounced anisotropic migration behaviour of vacancies mediating diffusion processes in β-phase tantalum [2]. Understanding the fundamental growth phenomena by measuring the local structure of the crystallites is, hence, directly related to assessing the technological relevance and durability of corresponding layer systems for thin film applications.

This, up to now, missing information is primarily due to β-phase tantalum column spacings which may be as small as of 127 pm when viewed along the crystallographic [001] direction and which so far could not be resolved with commercially available medium-voltage electron microscopes limited by a point-to-point resolution of about 170 pm at directly interpretable image contrast features. Recently commissioned ER-C state-of-the-art instruments equipped with double hexapole corrector units, however, allow extension of the point resolution of the instruments well below the 1 Ångström (100 pm) barrier. Moreover, numerical retrieval techniques enable the accurate extraction of amplitude $A(\mathbf{r})$ and phase $\Phi(\mathbf{r})$ of the exit-plane wavefunction from a through-focus series of high-resolution images. By this means, all spatial information up to the information limit of the instrument can now be retrieved, also allowing for a subsequent elimination of residual lens aberrations [3].

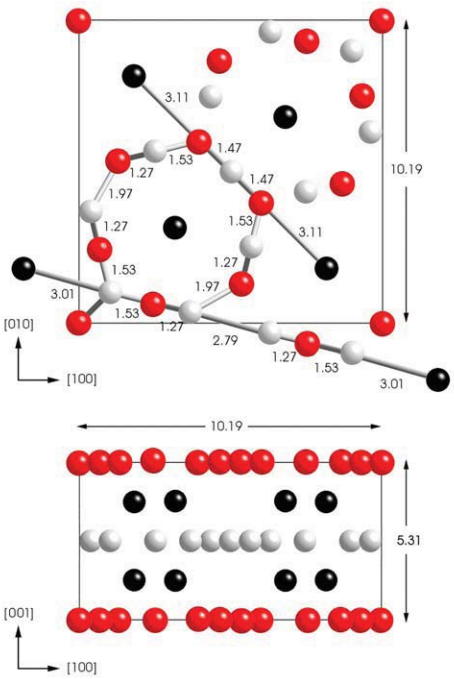

FIG. 1: Tetragonal β-tantalum unit cell ($P4_2/mnm$) viewed along the crystallographic [001] and [010] directions, respectively. Pseudo-hexagonal planes are formed by the red and lighter grey atoms located at positions z = 0 and z = c/2 along the [001] axis, respectively, while black atoms lie in the intermediate planes at z = c/4 and z = 3c/2. When viewed along the [001] direction, the black atom positions represent doubly-occupied columns whereas the red and lighter grey labelled columns are singly-occupied. Atoms belonging to the pseudo-hexagonal planes appear as septagons enclosing doubly-occupied tantalum columns. The spacings indicated between adjacent atom columns represent projected distances given in Ångström (100 pm) units.

Due to the atomic-resolution capabilities coming along with the aforementioned improvements, in-depth defect structure analyses together with the discussion of the underlying mechanisms of crystallite growth henceforth represent a viable task to undertake.

To illustrate operating efficiency, the numerically retrieved amplitude image $A(\mathbf{r})$ of an extended β-phase tantalum nanocrystallite is displayed in Fig. 2. Singly-occupied tantalum columns are superimposed onto the image together with individual [001] unit-cell edgings. The associated network reveals the crystallite to be composed of four grains, which are highlighted by different colours and are rotated against each other by variable multiples of approximately 30° thus proving the existence of asymmetric 30° tilt grain boundaries of the type:

$$(001)_\kappa \,||\, (001)_\phi \quad \text{and} \quad [010]_\kappa \,||\, [\bar{1}\sqrt{3}0]_\phi$$

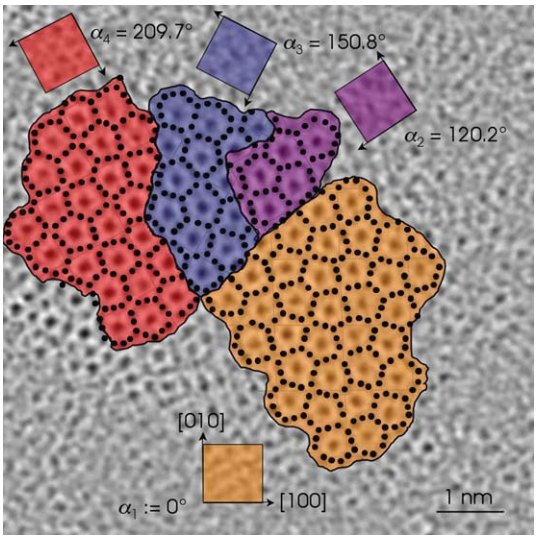

FIG. 2: Amplitude image $A(\mathbf{r})$ of an extended β-tantalum crystallite viewed along the [001] zone axis evaluated from a through-focus series of 15 micrographs. Positions of the singly-occupied tantalum columns are superimposed (•) and the borders of the unit cells indicated by faint grey squares. The crystallite as a whole is found to be composed of four grains rotated against each other by multiples of 30° and highlighted by different colours.

with κ and ϕ denoting neighbouring grains. In spite of the uniform 30° tilt properties, a common likewise uniform habitat plane cannot be assigned to all three boundaries. However, most boundary segments run along directions that satisfy the principle that the atomic columns in the adjoining grains have closely similar patterns and spacings at the common boundary. Main boundary segment directions cover the crystallographic ⟨100⟩ and ⟨110⟩ directions as can be seen from the interface structure between the orange and the violet grains, which shows local mirror symmetry with respect to the habit plane.

Larger amorphous areas between adjacent grains are not observed. The same finding is true for the boundary between the orange and blue grains as well as for most areas in the vicinity of the boundary between the red and blue grains.

The nearly precisely 30° rotational relationship between adjacent grains and the absence of amorphous zones in-between allows some insights with respect to the nucleation process of the crystallite. As it is quite unlikely that all four grains will have already started growing with the observed rotational orientation on an amorphous carbon substrate and since a spontaneous rotational re-alignment of monolithic grains by means of an integrative ad hoc rotation immediately before they coalescence would require a dedicated activation energy, both of these potential mechanisms may be ruled as being fairly improbable.

Instead, a more reasonable explanation would be that the 30° tilt boundaries are directly grown-in at the free surfaces of a single laterally expanding grain, which involves the adsorption of tantalum atoms at misaligned unit-cell positions. In this respect, it is of no importance whether the trapped atoms impinge directly from the vapour or if they are detached from any cluster and migrate via surface diffusion to an adjacent grain. Due to a certain amount of energy transfer from impinging atoms these processes may even take place during room temperature sputtering of metal systems. The direct grain-boundary formation during adsorption is also corroborated by the observed mirror-symmetric habit planes and the absence of twist components between all four grains and, especially, by the absence of thin amorphous interspacings between adjacent grains.

[1] D. Gupta, Mater. Chem. Phys. 41, 199 (1995).

[2] P. Klaver and B. Thijssee, Thin Solid Films 413, 110 (2002).

[3] K. Tillmann, A. Thust, and K. Urban, Microsc. Microanal. 10, 185 (2005).

[4] K. Tillmann, L. Houben, A. Thust, and K. Urban, J. Mater. Sci. 41, 4420 (2006).

Contrast Transfer and Resolution Limits for Sub-Angstrom High-Resolution TEM

M. Lentzen, K. Urban

IFF-8: Microstructure Research
ER-C: Ernst Ruska-Centre for Microscopy and Spectroscopy with Electrons

The optimum imaging of an object structure at the sub-angstrom length scale requires precise adjustment of the lens aberrations of a high-resolution instrument up to the fifth order. A least-squares optimisation of defocus aberration C_1 and third-order spherical aberration C_3 yields a set of aberration coefficients for strong phase contrast up to the information limit. For instruments with sub-angstrom information limit the ultimate structure resolution, the power to resolve adjacent atom columns in a crystalline object, depends on both the instrumental pointspread and an object pointspread due to finite width of the atomic column potentials. A simulation study on a simple double-column model yields a range for structure resolutions, dependent on the atomic scattering power, from 0.070 nm down to 0.059 nm, for a hypothetical 300-kV instrument with an information limit of 0.050 nm.

In the past years the information limit of high-resolution transmission electron microscopes has improved notably through the combined use of new instrumentation, such as field-emission sources, more stable lens and high-voltage power supplies, spherical-aberration correctors, and, recently, gun monochromators. The interpretability of high-resolution images has improved particularly due to the strong reduction of contrast delocalisation in the image plane by spherical-aberrration correction. At the same time exit-wave reconstruction, either by focus-variation or electron holography, in tandem with numerical aberration-correction has further improved the interpretable resolution of structure images.

Today high-resolution electron microscopy is about to penetrate the sub-angstrom scale considerably, and it is therefore important to explore how far that improvement will further the interpretable resolution. The high-energy scattering of electrons by the projected potential of a thin specimen generates a local phase modulation of the exit wave function, and the subsequent imaging by electron optic lenses forms the image intensity, which is recorded by a camera. It is therefore instructive to assess and compare the interpretable resolution at three levels: the projected potential map, the phase map of the exit wave function, and the recorded image intensity.

For many materials science investigations a direct view of the projected atomic structure and its assessment by an observer is the starting point for modelling the object of interest. We have adopted in this work the common Rayleigh criterion in order to evaluate the interpretability of a structure image. If the contrast peaks of two adjacent atomic columns are considered, the criterion states that the pair of columns appears resolved if the distance between the two peaks is larger than $\sim$1.15 times the full width at half maximum (FWHM) of the peaks. The pair of columns appears just resolved if the contrast between the columns drops to $\sim$0.81 times the peak contrast.

For this simulation study on interpretable resolution we have chosen hypothetical model structures of isolated C, Si, and Ge columns each comprising 5 atoms with an inter-atom spacing of 0.4 nm along the columns. Using the EMS software package [1] the respective projected potential maps, phase maps of the exit wave function, and image intensities were calculated for a hypothetical 300-kV microscope with an information limit of 0.05 nm. The microscope was set to the bright-atom contrast condition [2, 3], at an overfocus of 2.2 nm and a negative third-order spherical aberration of -1.85 μm, where the Scherzer passband extends to the information limit. In order to compare the effect of different scattering powers of C, Si, and Ge, the simulation conditions for electron scattering were otherwise equal; in particular a Debye-Waller factor of 0.006 nm^2 was chosen throughout. The contrast width of the C, Si, and Ge columns was measured by drawing line-scans across the peaks in the potential maps, the phase maps of the exit wave function, and the image intensity maps. The results are compiled in Table 1. Then the minimum distance at which two adjacent columns should appear resolved to an observer were calculated via the Rayleigh criterion. The resolved distances are compiled in Table 2.

From the simulated contrast widths the following tendencies can be concluded: 1. In the potential map the weakly scattering C column appears wider than the Si and Ge columns. 2. In the phase map of the exit wave function the apparent column width increases with decreasing scattering power. 3. In the intensity map the strongly scattering Ge column appears narrower than the C and Si columns, and together with the peaks sidelobes appear. 4. The contrast width is larger in the phase map than in the potential map. 5. The contrast width is narrower in the intensity map than in the phase map. Observations 2 and 4 are in accordance with the quantum-mechanical properties of the first bound state of a potential, in the framework of the channelling the-

Atom	Potential (nm)	Exit wave (nm)	Image intensity (nm)
C	0.047	0.070	0.059
Si	0.039	0.063	0.059
Ge	0.039	0.047	0.044

TAB. 1: Simulated contrast widths (FWHM) of atom columns.

Atom	Potential (nm)	Exit wave (nm)	Image intensity (nm)	Image intensity/sidelobes (nm)
C	0.054	0.081	0.068	0.078
Si	0.045	0.072	0.068	0.078
Ge	0.045	0.054	0.051	0.061

TAB. 2: Interpretable resolution of atom column distances.

ory of electron scattering. Observation 5 is at first sight suprising, because one might expect that the additional point-spread of the microscope should increase the contrast width compared to the exit wave. The image intensity, however, is the square of the exit wave convoluted with the point-spread function. Taking the square 'sharpens' the peaks, and this effect over-compensates the blur induced by the small point-spread of a corrected instrument.

From the resolved distances, which were calculated from the contrast widths via the Rayleigh criterion, additional tendencies can be concluded: 1. The hypothetical microscope has an information limit of 0.05 nm, yet only a Ge–Ge column distance of 0.05 nm can be resolved; Si–Si and C–C column distances smaller than 0.07 nm are not resolved. 2. The resolved distance, and hence the interpretable resolution, is dependent on the scattering power of the column pair. 3. The interpretable resolution in the potential map poses a limit of 0.045 nm for any direct structural view.

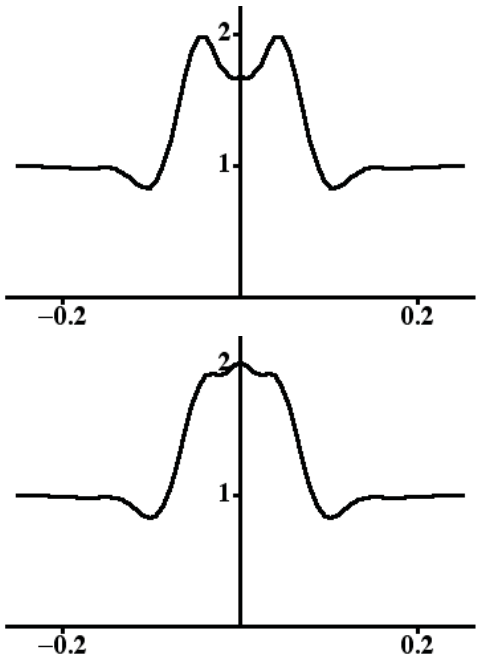

FIG. 1: Image intensity across a pair of Si columns. Column distance: (upper) 0.08 nm, (lower) 0.07 nm. Abscissae denote the spatial coordinate in nm.

Values for the resolved distance in the image intensity map, calculated as before, may be falsified by the above-mentioned appearance of sidelobes. In order to evaluate their effect, maps for two Si column pairs were simulated, with intercolumn distances of 0.07 nm and 0.08 nm, and all other parameters as above. Both column pairs are well-resolved in the potential map; in the phase map of the exit wave function the 0.08-nm pair is well-resolved, the 0.07-nm pair just resolved; in the image intensity map the 0.08-nm pair is just resolved, see Figure 1 (upper), the 0.07-nm pair is not resolved, see Figure 1 (lower). Hence, the sidelobes induce in the image intensity map an additional loss of interpretable resolution of about 0.01 nm. The respective corrected values are shown in Table 2, last column: the interpretable resolution of the intensity map ranges from 0.06 nm to 0.08 nm, dependent on the scattering power and despite an instrumental information limit of 0.05 nm.

Improved estimates for the interpretable resolution including the effect of fifth-order spherical aberration C_5 and object thickness were derived recently [4].

[1] P. Stadelmann, Ultramicroscopy 21, 131 (1987).

[2] C.L. Jia, M. Lentzen, and K. Urban, Microsc. Microanal. 10, 174 (2004).

[3] M. Lentzen, Ultramicroscopy 99, 211 (2004).

[4] M. Lentzen, Microsc. Microanal. 14, (2008), DOI: 10.1017/S1431927608080045.

Quantitative Aberration-Corrected HRTEM of Grain Boundaries in YBCO

L. Houben, A. Thust, K. Urban

IFF-8: Microstructure Research
ERC: Ernst Ruska-Centre for Microscopy and Spectroscopy with Electrons

Structural and electronic reconstructions at interfaces in oxide materials determine their physical properties. They can give rise to fundamentally unique and technologically relevant behaviour on a nanocale. Analysis and engineering of such interfaces demand for appropriate techniques in nanoscale characterisation besides theoretical understanding. The latest advances in aberration-corrected high-resolution transmission electron microscopy towards quantitative research allow for an accurate determination of the atomic structure of such interfaces. The analysis of the structural reconstruction of atomic bonds of a 90° [100] grain boundary in $YBa_2Cu_3O_{7-\delta}$ demonstrates the new capabilities for the localisation of bond environment changes and their quantification with pm-accuracy and of local disorder and stoichiometry changes on the atomic scale.

The performance of intermediate voltage electron microscopes has undergone major improvements in the past decade through novel electron optical components of particular sophistication, e. g. spherical aberration corrector elements [1]. The use of such hardware components means a tremendous facilitation of solid-state analysis on the atomic scale. For high-resolution TEM, the combination of spherical-aberration correction in the microscope with the numerical exit-plane wave function reconstruction from focal series in particular improves control of residual lens aberrations. It also increases the signal-to-noise ratio, turning the electron microscope into a quantitative measurement tool of high precision on the atomic scale.

In this particular example of a 90° [100] tilt-grain boundary in $YBa_2Cu_3O_{7-\delta}$ (YBCO) a three-step course of action illustrated in the report by K. Tillmann [2] was used to fully make use of the improved capabilities of modern field-emission instruments equipped with a spherical aberration corrector unit. The approach especially guarantees to overcome uncertainties in image contrast interpretation due to image delocalisation and residual lens aberrations.

The three step action constitutes successive procedures to minimise residual wave aberrations C_{ij}, which put limits to the quantitative accuracy of structure determination in TEM. The first step targets at the precise alignment and suppression of the C_{ij} during set-up of a spherical aberration corrected microscope using the ATLAS package [3]. With this set-up, focal series are acquired followed by the numerical retrieval of the exit-plane wavefunction $\Psi(r)$ from a through-focus series of micrographs [4]. In a third step a numerical phase-plate is applied to $\Psi(r)$ for the a posterior correction of residual aberrations. The phase plate is calculated from measured residual aberrations and tuned for temporal drift of aberrations prone to instrument instabilities, e.g. two-fold astigmatism C_{22}. The minimisation of residual aberrations consequently provides experimental data that can be used for quantification by refinement through matching calculated data derived from a structure model.

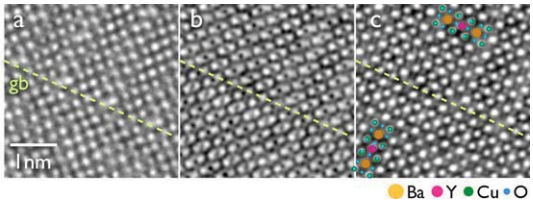

FIG. 1: (a) Optimum focus micrograph and (b) phase image retrieved from a focal series of 20 micrographs of a 90° [100] tilt grain boundary in YBCO. viewed along the [100] zone axis. (c) Numerically corrected phase image.Two-fold astigmatism and axial coma were removed. Structure projections of the YBCO unit cell are indicated.

In this example, aberration-corrected images of thin YBCO films were recorded at an accelerating voltage of 200 kV in a Philips CM200 FEG microscope equipped with a double-hexapole corrector. The corrector elements were adjusted to provide a negative value of the spherical aberration constant C_{40}. The choice of C_{40}=$-\frac{64}{27}\lambda^{-3}g_{\mathrm{max}}^{-4}$=$-40\mu$m enables the extension of the point resolution up to the instrument's information limit g_{max}=7.7 nm^{-1} at λ=0.002508 nm [5]. Imaging at negative C_{40} provides directly interpretable bright atom contrast for the ease of structure interpretation.

Through-focus series for focal-series reconstruction were recorded on a charge-coupled device (CCD) camera.The focal range included the special defocus setting Z_{opt}=11.6 nm for optimised phase contrast, where the residual image delocalisation is as low as R=$\frac{16}{27}g_{\mathrm{max}}^{-1}$= 0.08 nm [5]. The exit-plane wave function was retrieved for the frequency band between 1 nm^{-1} and 8 nm^{-1}.

Fig. 1 displays images of the grain boundary viewed along the [100] direction close to optimum defocus Z_{opt} and the corresponding phase of the wave function $\Psi(r)$ retrieved from 20 images in a focal series from the same place. The symmetry relation between

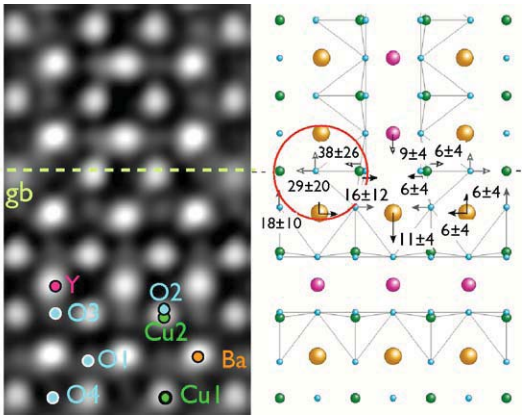

FIG. 2: Left: Magnified image of the repeat cell in the periodic grain boundary structure. Right: Atom column displacements with respect to the position in the bulk structure depicted in the model structure. Arrows indicate the direction of displacement and numbers are given in picometres together with the 2 σ confidence intervals for the statistical measurement error. Significant displacements are present in the grain boundary plane and the two neighbouring planes. Evident is the shift of the O1 atom towards the Cu1 atom in the grain boundary plane (red circle).

the two domains was exploited for the numerical fine-tuning of the parasitic axial coma C_{31} in addition to the twofold astigmatism C_{22}. The notable number of $\pi/2$ phase wraps brought about by the two-fold astigmatism lead to considerable distortion in the direct image in the experiment. Though related to an atom column, a single bright image dot therefore hardly concides with the true postion of an atomic column therefore. Likewise the intensity is barely a direct measure for the projected potential of a column. The numerical a posterior correction of aberrations on the holographic wavefunction data after restoration however restores the structure, as can be seen in Fig. 1c.

Atomic column positions, the scattering intensity and their statistical uncertainties were calculated by maximum likelihood parameter estimation from the amplitude and phase data of the wavefunction $\Psi(r)$. In parallel, a similar evaluation was done on simulated data derived from a structure model. The model parameters were refined iteratively in the course of matching the simulated wavefunction data to the experimental $\Psi(r)$. Picometre accurate quantitative data for single atom column displacements could be derived in this way. The accordingly measured column displacements with respect to the periodic structure are displayed in detail in Fig. 2. The plot shows the displacements for a single repeat cell of the periodic grain boundary structure. 2σ confidence intervals of 4 pm were achieved for columns in the cation sublattice. The weaker scattering signal on the oxygen positions results in the larger 2σ confidence intervals of more than 10 pm. Systematic errors were avoided by the refinement by comparison with simulated exit plane wavefunction data.

Displacements are restricted to the grain boundary plane and directly neighbouring planes. Elsewhere, the bondlengths are in excellent agreement with neutron scattering data for orthorhombic YBCO. In particular, changes in the bondlengths between the Cu1 atom in the basal plane, the O1 atom in the BaO plane and the Cu2 atom in the superconducting CuO2 plane are important since the shift of the oxygen atom O1 towards the Cu1 atom signifies a local doping effect and goes along with largely increased static or dynamic disorder on the Cu1 site in the boundary. The increase of the static disorder on the Cu1 site in the boundary is revealed by the refinement of the match between calculated and experimental wavefunction data dislayed in more detail in Fig. 3.

In a similar fashion the integrated signal of oxygen atomic columns gave data for the local oxygen stoichiometry. In a distance of more than two atomic monolayers from the boundary δ is less than 0.35, and the orthorhombic structure of the superconductive phase of YBCO is measured independently from the phase maxima spacings.

It is concluded that the order parameter of the YBCO is reduced on a very local scale only, i.e. in the grain boundary as well as in the neighbouring planes. The structural changes tracked here involve bond-length distortions leading to local doping and increased static disorder leading to local vibrational properties.

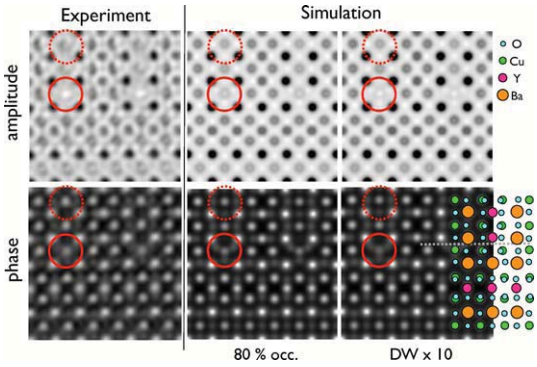

FIG. 3: The Cu1 site in the plane of the 90° [100] tilt grain boundary in YBCO (solid circle) exhibits a phase and amplitude signal different from an equivalent bulk-like position (dotted circle). In the simulation, this observation is reproduced by an increased (static) disorder parameter on this Cu site.

[1] M. Haider, H. Rose, S. Uhlemann, E. Schwan, B. Kabius, K. Urban, Nature 392 (1998) 768.

[2] K. Tillmann, J. Barthel, L. Houben, C.L.. Jia, M. Lentzen, A. Thust, K. Urban, Microscopy of Semiconducting Materials, Cambridge, April 2-5 2007.

[3] ATLAS is a software package for the ultra-precise measurement of lens imperfections in the imaging process of electron microscopes, developed by J. Barthel and A.Thust, IFF-8.

[4] A. Thust, M. Overwijk, W. Coene, M. Lentzen, Ultramicroscopy 64 (1996) 249.

[5] M. Lentzen, Microscopy and Microanalysis, 12 (2006) 191.

Dislocations in $SrTiO_3$ Single Crystals as Potential Easy Diffusion Pathways for SrO-Complexes and Oxygen

K. Szot[1], P. Meuffels[1], W. Speier[2]

[1] IFF-6: Electronic Materials
[2] Wissenschaftlich Technische Planung

$SrTiO_3$ is a model band-insulating perovskite and its electrical properties are traditionally considered as bulk phenomena which can be described on the basis of point defect models. A new picture, however, is emerging which takes into account the role of extended defects like dislocations. There are strong indications that dislocations can modify the electrical and mass transport properties of $SrTiO_3$ crystals. To figure out whether dislocations can be related to changes in electrical conductivity and to segregation phenomena, $SrTiO_3$ single crystals were plastically deformed by bending experiments in order to artificially enhance the dislocation density within the slip-band regions. After thermal reduction of the deformed crystals, numerous locations with an appreciably higher electrical conductivity — compared to the un-deformed parts of the crystal — were found along the slip-bands. After thermal oxidation, droplet-like features which can be attributed to SrO emerged on the crystal surface clustering along the slip-bands. The experiments provide evidence that dislocations in $SrTiO_3$ channel the mass and charge transport while acting as easy diffusion pathways for both SrO-complexes and oxygen atoms.

The perovskite oxide $SrTiO_3$ serves as a marvelous model material for electronic oxides in general and for perovskites in particular. $SrTiO_3$ is a band-insulator and its electrical transport properties are traditionally considered as bulk phenomena which can be described on the basis of point defect models [1]. In real crystals, however, various forms of so-called extended defects such as dislocations exist. Fig. 1 shows, for example, a structure model of an edge dislocation in $SrTiO_3$ viewed along the dislocation core [2]. There are strong indications that dislocations can modify the electrical and mass transport properties of $SrTiO_3$ crystals [3–6]. Thus, a new picture is emerging which takes into account the role of extended defects like dislocations.

The possible influence of dislocations on transport properties puts the focus on the distribution of dislocations in $SrTiO_3$ crystals in relation to changes in electrical conductivity and to segregation phenomena. Recent work has shown that $SrTiO_3$ crystals can be plastically deformed even at low or moderate

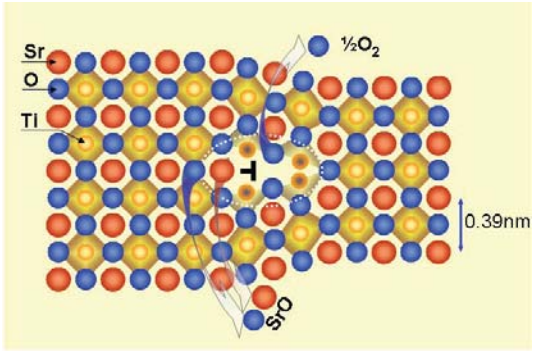

FIG. 1: Schematic structure model of an edge dislocation in $SRTiO_3$ viewed along the dislocation core.

temperatures [8]. There is thus an opportunity to artificially introduce dislocations into the $SrTiO_3$ lattice and/or to change their spatial distribution within the slip-band regions of the crystals.

Verneuil-grown, nominally un-doped $SrTiO_3$ single crystals with (100)-orientation and dimensions of 10 x 3 x 1 mm^3 were used for our experiments. The crystals were plastically deformed by bending experiments at room temperature (see fig. 2a)) yielding around 4 % plastic strain. Afterwards, the crystals were either thermally reduced or oxidized at temperatures 700 – 900 °C in order to figure out whether the enhanced dislocation density within the slip-band areas could be related to specific surface features. Surface topography was inspected by means of atomic force microscopy (AFM) at room temperature. Maps of the local electrical conductivity of the surface of $SrTiO_3$ crystals were recorded by using an atomic force microscopy with an electrically conducting cantilever (LC-AFM).

Fig. 2 b) shows the surface topography of a $SrTiO_3$ (100) crystal after plastic deformation. It is clearly seen that the deformation is not homogeneous but concentrated in slip-bands which appear as steps on the surface of the deformed crystal. Fig. 2 c) depicts the local electrical conductivity on the surface of a plastically deformed crystal directly after the bending experiment, i. e. before any thermal treatment. The scanned surface area was selected in such a way that data from the region around one slip-band were recorded.

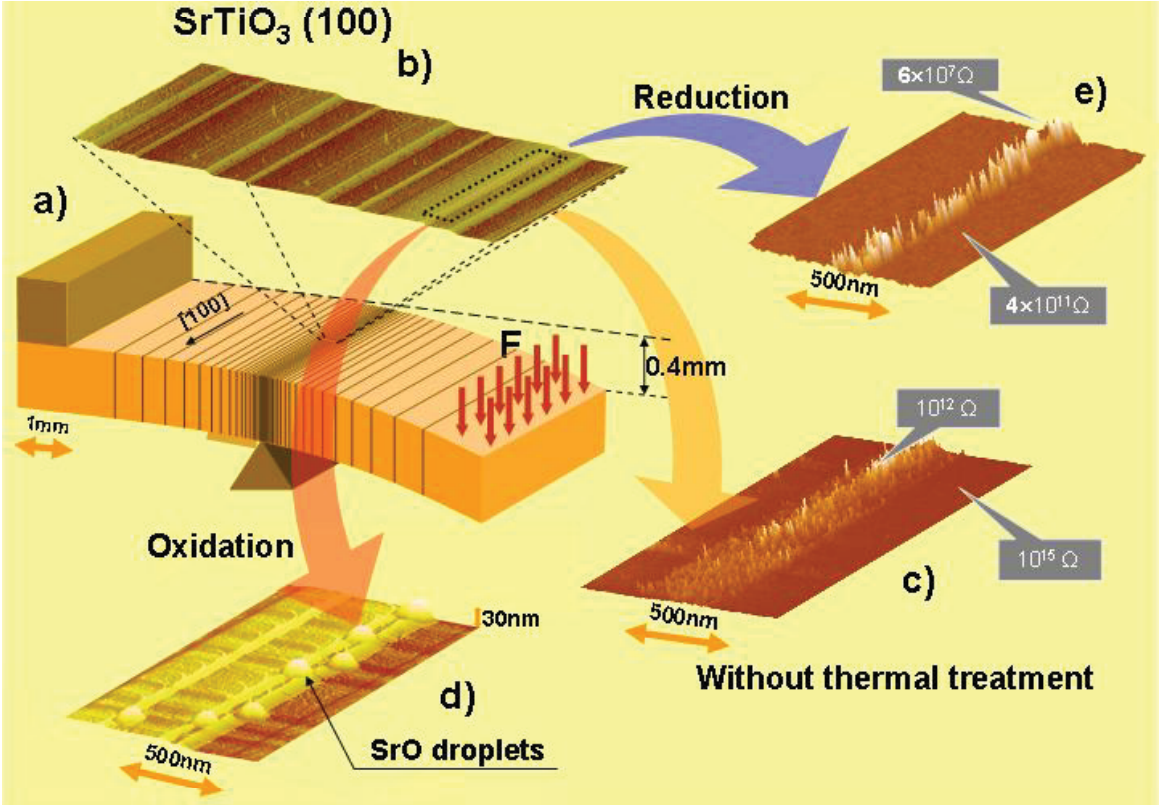

FIG. 2: Surface topographies (AFM) and mappings of the local electrical conductivity (LC-AFM) on the surface of plastically deformed $SrTiO_3$ (100) crystal after different thermal treatments (for details see text).

As is evident from fig. 2 c), within the slip-band area there exist numerous locations which possess an enhanced electrical conductivity compared to the surrounding matrix indicating filamentary electrical conduction. On the other hand, the un- or less-deformed parts of the crystal seem to be free from exit points of electrically conducting filaments. This picture becomes even clearer in case the deformed crystals are subjected to a thermal reduction treatment (see fig. 1 e)). Under reducing conditions, $SrTiO_3$ releases oxygen which results in a higher electrical conductivity because of the so-called "self-doping" effect. As can be seen from fig. 1 e), reduction leads to a more pronounced formation of bundles of conducting filaments along the slip-bands indicating a preferential loss of oxygen within these regions of the crystal.

A quite different — but somehow correlated —- picture is found when deformed crystals are treated under oxidizing conditions. Fig. 2 d) shows the surface topography of a deformed crystal after thermal oxidation. It is clearly seen that droplets have emerged on the surface which cluster along the slip-bands. It is known from previous work [8] that prolonged heating under oxidizing conditions leads to the occurrence of randomly distributed SrO droplets on the surface of $SrTiO_3$ crystals. The observed droplet-like features along the slip-bands can thus be attributed to the segregation of SrO.

As intense plastic deformation of the crystal occurs within the slip-band ranges, it is reasonable to assume that new dislocations are introduced into these regions and/or that existing dislocations are rearranged and bundled owing to dislocation motion as a consequence of mechanical stress. The observed effects — enhanced local electrical conductivity, preferential loss of oxygen under reducing and preferential segregation of SrO under oxidizing conditions within the slip-band regions — seem thus to be correlated to the enhanced dislocation density. These experiments provide phenomenological evidence that dislocations in $SrTiO_3$ channel the mass and charge transport in $SrTiO_3$ (see the symbolic arrows in fig. 1) and act — compared to the surrounding matrix — as potential short-circuit pathways for both SrO-complexes and oxygen atoms. One thus arrives at the conclusion that the influence of dislocations has to be taken into account when one aims at a profound understanding of the electrical and mass transport properties of $SrTiO_3$ crystals.

[1] R. A. De Souza, J. Fleig, R. Merkle, J. Maier: Z. Metallkd. **94** (2003) 218.

[2] C. L. Jia, A. Thust, K. Urban: Phys. Rev. Lett. **95** (2005) 225506.

[3] A. E. Paladino: J. Am. Ceram. Soc. **48** (1965) 476.

[4] K. Szot , W. Speier, R. Carius, U. Zastrow, W. Beyer: Phys. Rev. Lett. **88** (2002) 075508.

[5] K. Szot, W. Speier, G. Bihlmayer , R. Waser: Nature Materials **5** (2006) 312.

[6] I. Sakaguchi, M. Komastu, A. Watanabe, H. Haneda: J. Mater. Res. **15** (2000) 2598.

[7] S. Taeri, D. Brunner, W. Sigle, M. Rühle: Z. Metallkd. **95** (2004) 433.

[8] K. Szot, W. Speier: Phys. Rev. B. **60** (1999) 5909.

Ab Initio Modeling of Atomic Force Microscopy: Benzene on Cu(110)

N. Atodiresei[1], V. Caciuc[2], H. Hölscher[2], S. Blügel[1]

[1] IFF-1: Quantum Theory of Materials
[2] Physikalisches Institut, Westfälische Wilhelms Universität Münster

We performed *ab initio* calculations to simulate the interaction of clean silicon tips with a benzene molecule adsorbed on a Cu(110) surface. The apex structure of the AFM tip was modeled by Si_4H_3 and Si_4H_9 clusters. The forces acting on the Si_4H_3 nano-tip are always repulsive and lead to a displacement of the benzene molecule on the Cu(110) surface. On the contrary, the forces acting on the Si_4H_9 nano-tip can be attractive or repulsive depending on the approached molecular site. In this case the benzene molecule can bind to the tip and is retracted from the surface.

The prospect of using organic molecules as building blocks to construct electronic devices has received considerable attention. A first crucial step in the development of such nanodevices is to understand their structure at atomic scale. Well-established instruments to imaging surfaces with atomic resolution are the *scanning tunneling microscope* (STM) and the *non-contact atomic force microscope* (NC-AFM). The imaging mechanisms of these two scanning probe methods are based on different physical processes. The STM probes the electronic structure of the molecule-substrate interface near its Fermi level by monitoring the tunneling current flowing between a tip and the sample surface. On the other hand, the NC-AFM relies on the short-range interactions between an atomically sharp tip and the system under consideration.

The NC-AFM experiments performed on molecules adsorbed on surfaces revealed no atomic-scale contrast,at most a sub-molecular resolution. However, in many cases, the topography of the substrate on which molecules are adsorbed is atomically resolved during the same experiment. In the context of the development of nanoscale devices, this intriguing limit of the NC-AFM technique deserves a special attention. This issue has not been addressed by *ab-initio* simulations up to now, therefore the purpose of this study is to investigate the NC-AFM imaging mechanism of organic molecules by means of first-principles calculations.

As a model system for such NC-AFM simulations, we focused our attention on a single benzene (C_6H_6) molecule adsorbed on Cu(110) surface. In this study we calculated the short-range forces acting on a clean silicon tip placed above three different molecular sites of the benzene molecule. The clean silicon tip was modeled by two different types of silicon nano-clusters (Si_4H_3 and Si_4H_9) in order to highlight the role of the apex structure of the AFM tip on the NC-AFM imaging process of the benzene molecule. Finally, the behaviour at atomic scale of the tip-molecule-substrate system bears strong similarities with that showed by experimental STM studies done on this system.

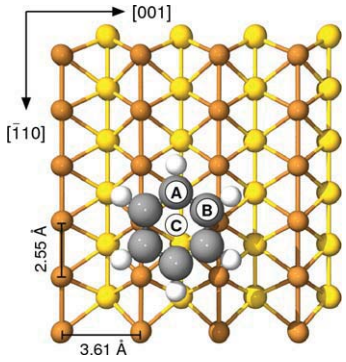

FIG. 1: Top view of the benzene molecule adsorbed on the Cu(110) surface. The NC-AFM simulations were performed by approaching clean silicon tips at three different sites above the benzene molecule marked by **A**, **B** and **C**.

We first calculated the energetically favored positions of a single benzene molecule on the Cu(110) surface. We found that the benzene is chemisorbed between two rows of atoms along $[1\bar{1}0]$-direction of the Cu(110) surface. The lowest adsorption energy (-0.401 eV) is obtained for the so-called 'long-bridge' position where the benzene ring is on top of two Cu-atoms (see Fig. 1). In the following, this configuration is our starting point in calculating the force acting on a clean silicon tip placed on top of benzene molecule.

To investigate the imaging of benzene on Cu(110) surface by NC-AFM, the two nano-tips were placed on top of three different molecular sites labeled as A-,B-, and C-site (see Fig.1). Since the interaction pattern for *each* nano-tip is quite similar for A- and B-sites, in the following we will focus mainly on the force curves calculated for B- and C-site. Depending on the apex structure of the AFM tip and on the specific molecular site, the forces acting on the tip can be

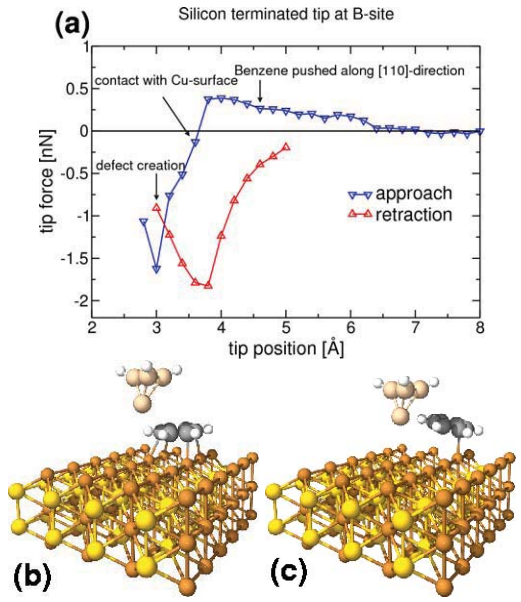

FIG. 2: **(a)** Short-range forces acting on the Si_4H_3 tip during approach and retraction at the B-site. Configurations marked by arrows in graph are also shown: **(b)** On the approach path the benzene molecule is displaced on the surface along the $[\bar{1}10]$-direction. **(c)** As the benzene is moved away, the silicon tip comes in direct contact with the Cu(110) surface.

attractive or repulsive (see Figs.2, 3). A detailed analysis of the dynamics of our system at atomic scale clearly showed that when the tip-sample force is repulsive, the benzene molecule is pushed into or along the surface. A similar behavior was observed in the case of STM experiments.

We analyzed the role of the electronic structure of the tip-sample system to understand why the interaction between the AFM tip and the adsorbed benzene molecule is repulsive or attractive depending on the specific apex structure of the tip. The overlap between the HOMO (p_y) of the Si_4H_3 nano-tip and LUMO (π) of the benzene results in a repulsive interaction for any A-, B- or C-site, because no bonding combination can be formed. Besides this general feature, the approach of the Si_4H_3 cluster above A- and B-site increases the repulsion between the tip and molecule and the benzene slides along the $[1\bar{1}0]$-direction. On the contrary, the overlap between the HOMO (p_z) of the Si_4H_9 tip and LUMO (π) of the benzene results in an attractive interaction for the A- and B-site. The repulsive interaction between the Si_4H_3 nano-tip and Si_4H_9 one deserves a special attention. In this case, the molecule is squeezed between tip and surface up to a point where the π system and the planarity of the benzene are destroyed. Because of the bond formed between the tip and the benzene molecule, the carbon atom which binds the Si atom of the tip changes its hybridization from sp^2 to sp^3.

In the present *ab initio* study we analyzed the NC-AFM imaging mechanism of organic molecules adsorbed on metallic surfaces. In particular we focused on the role of the apex structure of clean silicon tips in NC-AFM imaging of a benzene molecule adsorbed on a Cu(110) surface. A stable NC-AFM imaging process is possible if the AFM tip is sufficiently far away from the sample surface. However, at large tip-sample distances the magnitude of the forces acting on the nano-tips is roughly the same regardless on the molecular site. This finding provide a clear explanation why NC-AFM imaging of the benzene molecule adsorbed on Cu(110) surface is likely to yield only a molecular resolution instead of an atomic one.

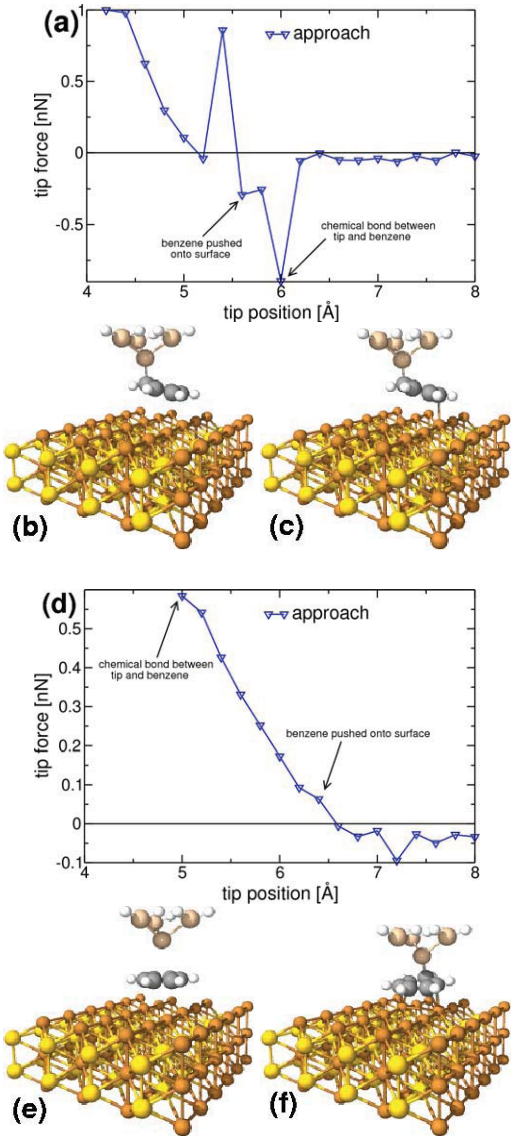

FIG. 3: **(a)** Short-range forces acting on the Si_4H_9 tip during the approach path at the B-site. **(b)** A chemical bond between the tip and benzene molecule is formed. **(c)** The silicon tip pushes the benzene into the surface. **(d)** Short-range forces acting on the Si_4H_9 tip during the approach path at the C-site. **(e)** Due to a repulsive interaction between the tip and molecule, the benzene is pushed into the surface. **(f)** By decreasing the tip-molecule distance, a chemical bond between the tip and benzene is formed.

[1] N. Atodiresei, V. Caciuc, H. Hölscher, S. Blügel, accepted in Phys. Rev. B (2008).

Charge Transfer in a Molecular Alloy Measured by CH_3 Rotational Tunneling

M. Prager[1,2], A. Pietraszko[3], L. Sobczyk[3], A. Pawlukojc[3], E. Grech[3], T. Seydel[4], A. Wischnewski[1], M. Zamponi[1]

[1] IFF-5: Neutron Scattering
[2] JCNS: Jülich Centre for Neutron Science
[3] Institutes of Wroclaw, Warsaw and Szczecin Universities, Poland
[4] Institut Laue Langevin, Grenoble, France

Charge redistribution in molecules by polarization or charge transfer is a fundamental effect in hydrogen bonded molecular compounds. In the tetramethylpyrazine:chloranilic acid complex this effect is studied by rotational tunneling neutron spectroscopy. The four tunnel bands of the four crystallographically inequivalent methyl groups are observed at He temperature by high resolution neutron spectroscopy. With increasing pressure most splittings shift proportional to $r^{-6.9}$ due do increasing steric hindrance. For one band the effect of reduced intermolecuar distances is almost exactly compensated by a charge transfer of δe/e=0.3MPA^{-1}. A phase transition occurs between 0.34MPa and the highest pressure 0.47MPa.

In the framework of a broad program on molecular alloys with hydrogen bonds and charge transfer properties [1] we have investigated the complexes of the acceptor molecule tetramethylpyrazine (TMP) with electron donor partners. The ability to form complexes being both a π- and n-electron donor makes TMP mixable with a large number of counter molecules. In this report the counterpart in the complex is chloranilic acid (CLA) which shows both proton-donor and π-electron-acceptor properties. The mixed material forms a 1:1 hydrogen bonded complex. These complexes are interesting from the point of view of materials science. CLA can be viewed as a component of supramolecular synthons in crystal engineering and, belonging to benzoquinones, is interesting also from the point of view of electron transfer processes including biological systems [2]. Moreover the fundamental question on the interaction in hydrogen bonded systems can be exemplaryly studied at TMP-CLA dimers. Its most precise fingerprint is found in the tunnel splittings of the CH_3 groups [3].

The crystal structure of the complex was determined at sample temperatures T=100K and T=14K. The lattice consists of infinite chains along the a-axis with strong hydrogen bonds (fig. 1), while the TMP and CLA rings are stacked along the b-axis (monoclinic, space group $P2_1/c$, Z=2). The irreducible unit at T=14K is one formula unit with four inequivalent methyl groups in TMP (fig. 1).

The standard description of rotational tunneling is the single particle model (SPM) where the environment of the molecule is represented by a rotational potential $V(\varphi)$ of the threefold symmetry of the rotor. To first approximation

$$V(\varphi) = \frac{V_3}{2}(1 - cos(3\varphi)). \qquad (1)$$

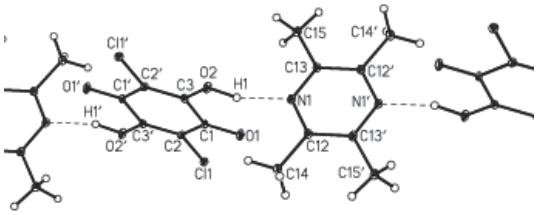

FIG. 1: Hydrogen bond network in the crystal structure of the TMP(1:1)CLA complex at T=14K. All methyl groups are crystallogrphically different.

At low temperatures this potential determines the excitations of the hindered quantum rotor by the eigenvalues E_i of the stationary single particle Schrödinger equation

$$\{-B\frac{\partial^2}{\partial\varphi^2} + V(\varphi)\}\Psi_i = E_i\Psi_i \qquad (2)$$

Here $B = \frac{\hbar^2}{2\Theta} = 0.655meV$ is the rotational constant of the methyl group with the moment of inertia Θ. The tunnel splitting is the difference between the two lowest levels $\hbar\omega_t = E_1 - E_0$.

It has been shown [4] that the rotational potentials in molecular crystals can be well modelled by electrostatic multipole interaction with characteristic exponent n

$$V_{ii} \sim \frac{ee}{r^n}. \qquad (3)$$

The application of pressure δp reduces the intermolecular distances r. Since we do not know the crystal structure as a function of pressure we assume an affine change with pressure characterized by an isothermal volume compressibility κ

$$\frac{\delta r}{r} = -\frac{1}{3}\kappa\delta p \qquad (4)$$

With decreasing r the intermolecular interaction energy increases. Under the asumption that the rotational potential changes with pressure according to the r-dependence of the intermolecular interaction V_{ii} we obtain

$$V(\varphi, r) = V(\varphi, r_0) \times n\frac{\delta r}{r_0} \qquad (5)$$

This leads to positive Grüneisen parameters of lattice modes but to negative ones for tunneling modes: the overlap of molecular wavefunctions diminishes with increasing rotational potential/pressure. This reduction is exponential and characterizes the sensitivity of rotational tunneling spectroscopy. The outlined behavior is expected for materials where all intermolecular distances change affinely with pressure and when the *interaction parameters are independent of pressure*. The figure 2 shows tunneling spectra of TMP:CLA measured with the offset configuration of the IN10 spectrometer of the ILL, Grenoble. Two of the four tunneling modes fall into the accessible energy regime. The tunneling energies are presented as a function of pressure in fig. 3. Two different behaviors are observed: one splitting is exponentially reduced as expected from the outlined theory while the other one is almost unaffected of pressure.

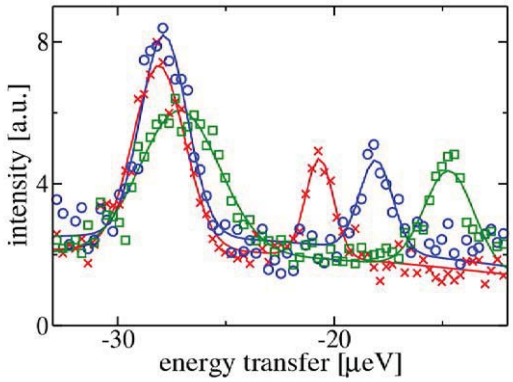

FIG. 2: Selected tunneling spectra of the TMP(1:1)CLA complex measured at pressures between p= 0.001kbar (xxx), 0.835kbar ($\circ\circ\circ$) and 2.286kbar($\square\square\square$). Sample temperature T=4.5K. Spectrometer: IN10 of ILL. Wavelength λ=6.27Å. Average momentum transfer Q=1.6Å^{-1}.

The exponential shift of the low energy tunneling peak from $\hbar\omega_t = 20.6\mu eV$ at 1bar to $\hbar\omega_t = 12.2\mu eV$ at 3.4kbar the potential requires an increase of the rotational potential from V_3=24.6meV to V_3=28.7meV

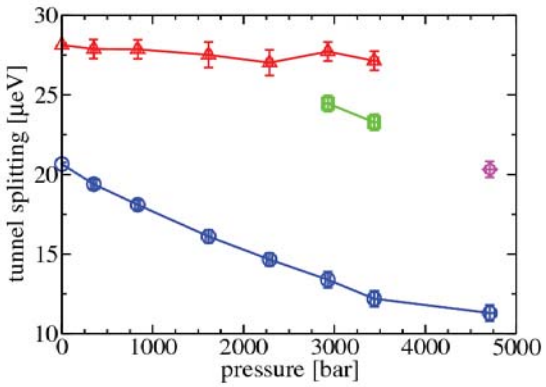

FIG. 3: Evolution of the high energy tunneling splittings with pressure.

or normalized to pressure $\frac{dV_3}{dp}$=1.2$[\frac{meV}{kbar}]$. This value depends somewhat on the shape of the rotational potential. If we introduce these numbers into eqns 1 and 4 we get $\kappa\times$n=0.146. Using $\kappa = 0.021kbar^{-1}$ of solid methane for the unknown compressibility of our material we obtain n=6.9. This value is expected for electrostatic octopole-octopole interaction and fits reasonably into the general experience.

If the pressure independent tunneling band experiences the same geometric change of its environment there must be second contribution to the intermolecular interaction which weakens with pressure. An obvious effect in hydrogen bonded charge transfer systems is charge exchange δe between the two constituents due to properties of the hydrogen bond changing with bond length. Under this condition the change of the potential strength is given by the total differential of eq. 3

$$\delta V = -2\frac{\delta e}{e} - n\frac{\delta r}{r}$$

According to experiment this expression nust be zero. The right hand term is known from the above evaluation and we obtain $\frac{\delta e}{e} \sim 0.03kbar^{-1}$.

Further experiments to support the outlined interpretation are planned.

[1] A. Pawlukojc, L. Sobczyk, Trends Appl. Spectr. 5, 117 (2004)

[2] *Functions of Quinones in Energy Converting Systems,* B.L. Trimpower, editor, Academic Press, New York, 1982

[3] M. Prager, A. Pietraszko, L. Sobczyk, A. Pawlukojc, E. Grech, T. Seydel, A. Wischnewski, M. Zamponi, J. Chem. Phys. 125, 194525 (2006)

[4] A. Hüller, J.W. Kane. J. Chem. Phys. 61, 3599 (1974)

Velocity Selection Problem in the Presence of the Triple Junction

E. A. Brener, C. Hüter, D. Pilipenko, D. E. Temkin

IFF-3: Theory of Structure Formation

Melting of a bicrystal along the grain boundary is discussed. A triple junction plays a crucial role in the velocity selection problem in this case. In some range of the parameters an entirely analytical solution of this problem is given. This allows to present a transparent picture of the structure of the selection theory. We also discuss the selection problem in the case of the growth of a "eutectoid dendrite" where a triple junction is present because three phases are involved in the eutectoid reaction.

During the last decades, our understanding of pattern formation in various nonlinear dissipative systems has made remarkable progress. Building on this foundation, it has now become possible to develop a description of a large class of patterns that are found in diffusional growth. In this classical problem of dendritic growth, velocity selection is controlled by tiny singular effects of the anisotropy of the surface energy (see, for example, [1]). However, this tiny effect can be neglected in the presence of a triple junction, which dominates the pattern selection, like in the melting along defects such as grain boundaries. The idea to discuss the melting process along the grain boundary in a crystal (see Fig. 1) was expressed in [2]. We also discuss the importance of a triple junction for the selection problem of the growth of a "eutectoid dendrite" (see Fig. 2).

Melting along a grain boundary: We consider the two dimensional melting problem of a pure bicrystal with a straight grain boundary as shown in Fig. 1. The contact angle ϕ is given by Young's law: $2\gamma\cos\phi = \gamma_b$, where γ is the surface energy on the liquid-solid interface and γ_b is the surface energy of the grain boundary. We introduce the dimensionless temperature field $u = c_p(T_\infty - T)/L$, where L is the latent heat, c_p is heat capacity, and T_∞ is the temperature in the crystal far away from the interface. The temperature field u obeys the following heat diffusion equation and boundary conditions:

$$D\nabla^2 u = \partial u/\partial t, \quad (1)$$

$$v_n = D\vec{n}(\vec{\nabla}u_L|_{int} - \vec{\nabla}u_S|_{int}), \quad (2)$$

$$\Delta - d_0\kappa = u|_{int}, \quad (3)$$

where L and S refer to the liquid and solid, respectively, $d_0 = \gamma T_M c_p/L^2$ is the capillarity length, T_M is the melting temperature, and κ is the curvature of the liquid-solid interface, which is assumed to be positive for convex interfaces (as in Fig. 1).

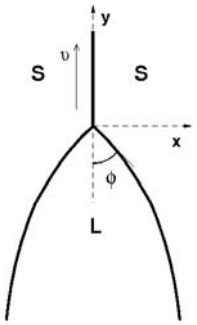

FIG. 1: Propagation of the melt zone along the grain boundary ($x = 0$). The melting front propagates with velocity v along the y-direction. S corresponds to two solid grains and L corresponds to the liquid phase. The triple junction is at the origin of the coordinate system.

We introduce the dimensionless overheating $\Delta = c_p(T_\infty - T_M)/L$, and the Peclet number $p = vR/2D$ with D being the thermal diffusion constant (assumed to be the same in both phases), R is the radius of curvature of the asymptotically fitted Ivantsov parabola and v is the velocity of the steady-state motion. The physics underlying Eqs. (1-3) is quite simple. Requirement of the heat conservation at the interface gives us Eq. (2) ($\mathbf{n}$ is the normal to the front pointing into the solid phase; v_n is the normal velocity of the front). The local thermodynamical equilibrium in the interfacial region implies Eq. (3), the Gibbs-Tomson relation. Standard Green's Function techniques allow the closed representation of Eqs. (1-3) in steady state in a comoving frame of reference:

$$\Delta(p) - \frac{d_0}{R}\kappa = \frac{p}{\pi}\int_{-\infty}^{\infty} dx' e^{-p(y-y')} K_0(p\eta(x,x')), \quad (4)$$

where $\eta = [(x-x')^2 + (y-y')^2]^{\frac{1}{2}}$, and K_0 is the modified Bessel function of third kind in zeroth order; all lengths are measured in units of R. The relation between the overheating Δ and the Peclet number p is given by the Ivantsov relation [3]: $\Delta = \sqrt{p\pi}\exp(p)\,\mathrm{erfc}(\sqrt{p})$. For small opening angles ϕ and small overheatings, proceeding as explained in [4] reduces the original *nonlinear* Eq. (4) to the fol-

lowing *linear* equation:

$$1+\mu_d\frac{d^2x}{dy^2}=\frac{2}{\pi}\sqrt{\frac{p}{\pi\phi^2}}\int_0^\infty dy'\frac{dx(y')}{dy'} \times e^{-\frac{p}{\phi^2}(y'-y)}K_0(\frac{p}{\phi^2}|y'-y|), \quad (5)$$

where $\mu_d = d_0\phi^3/R\Delta$. Here, the eigenvalue μ_d is a function only of one parameter, p/ϕ^2, and we solve Eq. (5) numerically using standard linear algebra routines. Small values of $p/\phi^2 \ll 1$ lead to the following scaling relations for the selected tip radius and velocity [4]:

$$\frac{R}{d_0}\approx 0.81\phi^4\Delta^{-2}, \quad \frac{vd_0}{D}\approx 0.79\phi^{-4}\Delta^4, \quad (6)$$

which show good agreement with the results obtained in [5]. For large values of $p/\phi^2 \gg 1$, the steps illustrated in [4] yield

$$1+\mu_d\frac{d^2x}{dy^2}=\frac{\sqrt{2}}{\pi}\int_0^y\frac{dx(y')}{dy'}dy'\frac{1}{\sqrt{y-y'}}, \quad (7)$$

and the existence of physically relevant solutions only for $\mu_d = \pi/2$.

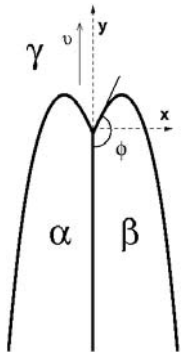

FIG. 2: Schematic picture of the interface structure in the eutectoid reaction. The structure propagates with a constant velocity v in the y direction. The triple junction is located at the origin of the coordinate system.

To our best knowledge this is the first example where the problem of velocity selection in dendritic growth is solved entirely analytically. As described in [4], the derivative of the interface profile can be derived, and the same analytical treatment is possible also in the case where interface kinetics effects are included.

Eutectoid "dendrite": We consider here a rather simple model of the eutectoid system, described by the phase diagram in Fig. 3, in order to obtain the equation in the spirit of Eq. (4). We restrict the consideration to the case of an isolated eutectoid dendrite (Fig. 2). The symmetry assumptions leading to closed representation of the eutectoid system on the $\gamma-\beta$ interface as

$$\Delta-\frac{d_0}{R}\kappa=-\frac{p}{\pi}\int_{-\infty}^0 dx'e^{-p(y-y')}K_0(p\eta(x,x')) +\frac{p}{\pi}\int_0^\infty dx'e^{-p(y-y')}K_0(p\eta(x,x')) \quad (8)$$

are described in [4]. Here d_0 is the capillary length [4], κ is the curvature of the interface which is positive in Fig. 2, and $\Delta=(C_E-C^e_{\gamma\beta})/(C_\beta-C_E)$ is the supersaturation. This equation differs from Eq. (4) only by the sign in front of the first integral, which represents the source at the $\alpha-\gamma$ interface, while the second integral corresponds to the sink at the $\beta-\gamma$ boundary. In other words, this simple modification of the classical equation of dendritic growth already contains the key ingredient of the eutectoid reaction. As explained in [4], for small supersaturation Δ Eq. (8) reads:

$$2-\sigma\kappa=\frac{1}{2\pi}\int_0^\infty dx'\ln\left(\frac{(x+x')^2+(y-y')^2}{(x-x')^2+(y-y')^2}\right), \quad (9)$$

where $\sigma = d_0/Rp$. We solve this nonlinear equation numerically in the spirit of Ref [5], see [4] for results. Since the eigenvalue σ^* is found, the velocity of the process can be written as $v = 2\sigma^* Dp^2/d_0$. Consequently, for $\Delta = 2p$ (see [4]), the velocity of eutectoid growth is proportional to Δ^2, while for the classical dendritic growth it scales as Δ^4.

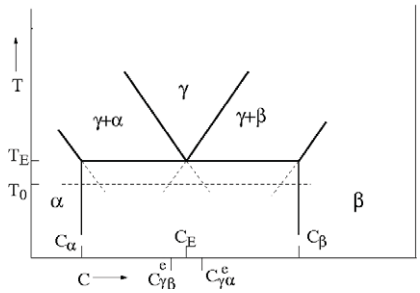

FIG. 3: The schematic phase diagram of the eutectoid reaction. T_0 is the temperature of the system, T_E is the eutectoid temperature. The regions γ, α and β correspond to the one phase equilibrium state. $\gamma+\alpha$ and $\gamma+\beta$ are regions of two-phase equilibrium. C_α, C_β and C_E are the equilibrium concentrations at the eutectoid temperature. For this diagram the eutectoid composition $C_E=(C_\alpha+C_\beta)/2$; the lines of the $\gamma-\alpha$ phase equilibrium are parallel, the same for lines of $\gamma-\beta$ equilibrium; the equilibrium concentrations at the $\alpha-\beta$ interface, C_α and C_β do not depend on the temperature.i

In conclusion, the selection mechanism due to the presence of the triple junction is very different from the anisotropy effects which are responsible for the selection of the classical theory of dendritic growth. In the regime of small opening angles the problem of velocity selection in melting along the grain boundary has been solved entirely analytically. This exact analytical treatment represents in a very transparent way the structure of the selection theory.

[1] Brener E. A., and Mel'nikov VI. Adv. Phys 1991;40:53

[2] D. E. Temkin, Abstracts of ICASP, June 7-10 2005, Stockholm, Sweden.

[3] G. P. Ivantsov, Dokl. Akad. Nauk USSR **58**, (1947)

[4] E.A. Brener, C. Hüter, D. Pilipenko, D. E. Temkin, Phys. Rev. Lett. **99**, 105701 (2007)

[5] D. I. Meiron, Phys. Rev. A **33**, 2704 (1986)

Contact Mechanics: Relation Between Interfacial Separation and Load

B. N. J. Persson

IFF-1: Quantum Theory of Materials

I study the contact between a rigid solid with a randomly rough surface and an elastic block with a flat surface. I derive a relation between the (average) interfacial separation $\bar{u}$ and the applied normal squeezing pressure p. I show that for non-adhesive interaction and small applied pressure, $p \sim \exp(-\bar{u}/u_0)$, in good agreement with recent experimental observation.

When two elastic solids with rough surfaces are squeezed together, the solids will in general not make contact everywhere in the apparent contact area, but only at a distribution of asperity contact spots[1]. The separation $u(\mathbf{x})$ between the surfaces will vary in a nearly random way with the lateral coordinates $\mathbf{x} = (x, y)$ in the apparent contact area. When the applied squeezing pressure increases, the average surface separation $\bar{u} = \langle u(\mathbf{x}) \rangle$ will decrease, but in most situations it is not possible to squeeze the solids into perfect contact corresponding to $\bar{u} = 0$. The space between two solids has a tremendous influence on many important processes, e.g., heat transfer, contact resistivity, lubrication, sealing, optical interference, ... In this paper I will present a very simple theory for the (average) separation $\bar{u}$ as a function of the squeezing pressure p (Ref. [2]). I will show that for randomly rough surfaces at low squeezing pressures $p \sim \exp(-\bar{u}/u_0)$ where the reference length u_0 depends on the nature of the surface roughness but is independent of p, in good agreement with experiments[3].

We consider the frictionless contact between elastic solids with randomly rough surfaces. If $z = h_1(\mathbf{x})$ and $h_2(\mathbf{x})$ describe the surface profiles, E_1 and E_2 are the Young's elastic moduli of the two solids and ν_1 and ν_2 the corresponding Poisson ratios, then the elastic contact problem is equivalent to the contact between a rigid solid (substrate) with the roughness profile $h(\mathbf{x}) = h_1(\mathbf{x}) + h_2(\mathbf{x})$, in contact with an elastic solid (block) with a flat surface and with an Young's modulus E and Poisson ratio ν choosen so that

$$\frac{1-\nu^2}{E} = \frac{1-\nu_1^2}{E_1} + \frac{1-\nu_2^2}{E_2}.$$

Introduce a coordinate system xyz with the xy-plane in the average surface plane of the rough substrate, and the z-axis pointing away from the substrate, see Fig. 1. The separation between the average surface plane of the block and the average surface plane of the substrate is denoted by $\bar{u}$ with $\bar{u} \geq 0$. When the applied squeezing force p increases, the separation between the surfaces at the interface will decrease, and we can consider $p = p(\bar{u})$ as a function of $\bar{u}$. The elastic energy $U_{\rm el}(\bar{u})$ stored in the substrate asperity–elastic block contact regions must equal to the work done by the external pressure p in displacing the lower surface of the block towards the substrate, i.e.,

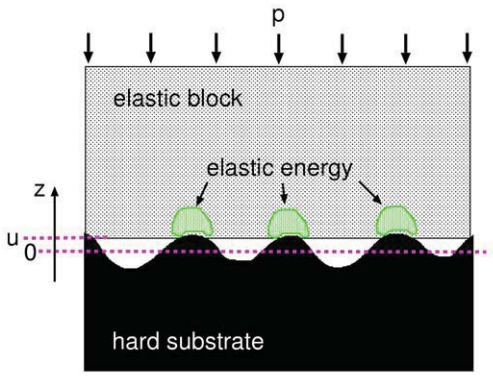

FIG. 1: An elastic block squeezed against a rigid rough substrate. The separation between the average plane of the substrate and the average plane of the lower surface of the block is denoted by $\bar{u}$. Elastic energy is stored in the block in the vicinity of the asperity contact regions.

$$\int_{\bar{u}}^{\infty} du' A_0 p(u') = U_{\rm el}(\bar{u}) \qquad (1)$$

or

$$p(\bar{u}) = -\frac{1}{A_0}\frac{dU_{\rm el}}{d\bar{u}}, \qquad (2)$$

where A_0 is the nominal contact area. Equation (2) is exact. Theory shows that for low squeezing pressure, the area of real contact A varies linearly with the squeezing force pA_0, and that the interfacial stress distribution, and the size-distribution of contact spots, are independent of the squeezing pressure. That is, with increasing p existing contact areas grow and new contact areas form in such a way that in the thermodynamic limit (infinite-sized system) the quantities referred to above remain unchanged. It follows immediately that for small load *the elastic energy stored in the asperity contact region will increase linearly with the load*, i.e., $U_{\rm el}(\bar{u}) = u_0 A_0 p(\bar{u})$, where u_0 is a char-

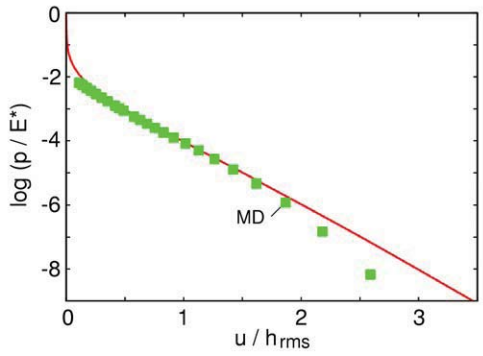

FIG. 2: The relation between the (natural) logarithm of the squeezing pressure p (normalized by E^*) and the interfacial separation $\bar{u}$ (normalized by the root-mean-square roughness amplitude $h_{\rm rms}$) for an elastic solid squeezed against a rigid surface.

acteristic length which depends on the surface roughness (see below) but is independent of the squeezing pressure p. Thus, for small pressures (2) takes the form

$$p(\bar{u}) = -u_0 \frac{dp}{d\bar{u}}$$

or

$$p(\bar{u}) \sim e^{-\bar{u}/u_0} \qquad (3)$$

in good agreement with experimental data for the contact between elastic solids when the adhesional interaction between the solids can be neglected. We note that the result (3) differs drastically from the prediction of the Bush et al theory, and the theory of Greenwood and Williamson (GW), which for low squeezing pressures (for randomly rough surfaces with Gaussian height distribution) predict $p(\bar{u}) \sim \bar{u}^{-a}\exp(-b\bar{u}^2)$, where $a = 1$ in the Bush et al theory and $a = 5/2$ in the GW theory. Thus *these theories do not correctly describe the interfacial spacing between contacting solids*.

To test the theory presented above we have performed Molecular Dynamics simulations[4] for the contact between a randomly rough, self affine fractal[5] surface and an elastic block with a flat surface[6]. The solid squares in Fig. 2 shows the MD result for the dependence of the (natural) logarithm of the normalized average pressure p/E on the normalized separation $\bar{u}/h_{rms}$ between the average plane of the substrate and the average plane of the lower surface of the block. In the figure $\bar{u} = 0$ corresponds to the separation 0.44 nm between the plane through the center of the atoms of the top layer of substrate atoms and bottom layer of block atoms. Since the atoms interact with a long-range repulsive $\sim r^{-12}$ pair potential, it is possible to squeeze the surfaces closer to each other than what corresponds to $\bar{u} = 0$. This explains why simulation data points occur also for $\bar{u} < 0$. The theory described above assumes a contact interaction potential so that $\bar{u} \geq 0$, and can therefore not be compared with the MD simulations for very small (and negative) $\bar{u}$.

In Fig. 2 we compare the MD resultswith the theoretical prediction calculated from[2] using the same surface roughness power spectra (and other parameters) as in the MD-calculation. The theory is in good agreement with the numerical data for $0.2 < \bar{u}/h_{rms} < 2$. For $\bar{u}/h_{rms} < 0.2$ the two curves differ because of the reason discussed above, i.e., the "soft" potential used in the MD simulation allow the block and substrate atoms to approach each other beyond $\bar{u} = 0$, while in the analytical theory a contact potential is assumed where the repulsive potential is infinite for $\bar{u} < 0$ and zero for $\bar{u} > 0$. The difference between the theory and the MD results for $\bar{u}/h_{rms} > 2$ is due to a finite size effect. That is, since the MD calculations uses a very small system, the highest asperities are only $\sim 3h_{rms}$ above the average plane, and for large $\bar{u}$ very few contact spots will occur, and in particular for $\bar{u} > 3h_{rms}$ no contact occurs and p must vanish. In the analytical theory the system is assumed infinite large so that even for a Gaussian distribution of asperity height there will always be (infinitely) many infinitely high asperities and contact will occur at arbitrary large separation $\bar{u}$, and the asymptotic relation $\bar{u} \sim \log p$ will hold for arbitrary large $\bar{u}$ (or small squeezing pressures p).

The theory presented above can be easily generalized in various ways. Thus, it is possible to include the adhesional interaction. In this case the work done by the external pressure p will be the sum of the stored (asperity induced) elastic energy plus the (negative) adhesional energy, i.e., the right hand side of (1) will now be $U_{\rm el} + U_{\rm ad}$. The theory can also be applied to study how the spacing $u(\zeta)$ depends on the magnification. Here $u(\zeta)$ is the (average) spacing between the solids in the apparent contact areas observed at the magnification ζ. The quantity $u(\zeta)$ is of crucial importance for lubricated seals. The results of these generalizations of the theory will be presented elsewhere.

Finally we note that the observation of an effective exponential repulsion has important implications for tribology, colloid science, powder technology, and materials science. For example, the density or volume of granular materials has long been known to have a logarithmic dependence on the externally applied isotropic pressure or stress, as found, for example, in the compression stage during processing of ceramic materials. Recent work on the confinement of nanoparticles have also indicated an exponential force upon compression, suggesting that this relationship could be prevalent among quite different types of heterogeneous surfaces.

[1] B.N.J. Persson, Surf. Science Reports **61**, 201 (2006).

[2] B.N.J. Persson, Phys. Rev. Lett. **99**, 125502 (2007).

[3] M. Benz, K.J. Rosenberg, E.J. Kramer and J.N. Israelachvili, J. Phys. Chem. B**110**, 11884 (2006).

[4] C. Yang, U. Tartaglino and B.N.J. Persson, Eur. Phys. J E**19**, 47 (2006).

[5] See, e.g., B.N.J. Persson, O. Albohr, U. Tartaglino, A.I. Volokitin and E. Tosatti, J. Phys. Condens. Matter **17**, R1 (2005).

[6] C. Yang and B.N.J. Persson, Phys. Rev. Lett. (in press)

Dynamics of Argon in Reduced Dimensionality

K. Schmalzl[1], D. Wallacher[2], M. M. Koza[3], D. Strauch[4]

[1] JCNS: Jülich Centre for Neutron Science
[2] HMI, 14109 Berlin, Germany
[3] ILL, 38042 Grenoble, France
[4] Universität Regensburg, 93040 Regensburg, Germany

It is well established that geometrical confinement like surfaces, interfaces or a free-standing film (in two dimensions) or quantum wires, thin tubes, etc. (in one dimension) modifies the properties of a material [1]. The study of the influence of reduced dimensionality or surface effects on the dynamics of these systems can give valuable information on general trends for measurable parameters like, e.g., specific heat.
We have investigated the dynamics of ^{36}Argon adsorbed in nanoporous gelsil glass by inelastic neutron scattering. By fractional filling the 'dimensionality' of the system is tuned from a two-dimensional towards the bulk state. The experimental results are compared with ab initio calculations. A shift of various phonon modes to lower energies with decreasing dimensionality is observed in the results of both methods.

To study the general trends in the dynamics in systems with low dimensions we condensated Argon in a glass matrix with a pore diameter of 75 Å and created in this way 1,2,3,... etc. layers of Argon on the pore wall. The isotope ^{36}Ar has a very strong scattering power for neutrons. Besides as a noble gas Argon shows with its van der Waals bonding a very different bonding energy to the substrate (covalent bonding). In this way the Argon eigenmodes are well separated from the dynamics of the silica matrix.

The neutron scattering experiment was performed on the time-of-flight spectrometer IN4 at the ILL, Grenoble, France. By the use of a gas handling system and the control of the vapor pressure a controlled deposition of Ar on the silica surface has been made possible. The knowledge of the absorption isotherm [2] allowed to prepare a monolayer, two or three layers, up to the capillary condensate in the pore center.
At very low filling fractions the atoms form an amorphous adsorbate film smoothing out the rough pore walls due to an attractive adsorbate-substrate potential [2]. Now additionally adsorbed atoms can form more easily an ordered structure and establish a quasi-fcc pattern at full fillings. Thus, the first few layers are expected to behave like a two-dimensional film and the completely filled pore is similar to the bulk state.

The experiment was accompanied by ab initio calculations performed with the ABINIT code [3] employing a plane-wave basis set and pseudopotentials. For demonstrating the effects of reduced dimensionality we will focus here primarily on the case of a three layer system and the bulk adsorbate.
The adsorbed Argon layers in the experiment were simulated with hexagonal two-dimensional plane sheets of Argon atoms. As the used code involves periodic boundary conditions we introduced a superstructure with empty layers between different piles of Ar sheets.

Fig. 1 shows a schematic view of the successive creation of layers in the experiment and the calculated system of a pile of three hexagonal layers of Argon atoms. It is well known that van der Waals bonding is difficult to describe within conventional ab initio techniques, but the bulk dynamical properties are well reproduced with an overestimation of calculated frequencies by a factor of about 1.3 [4].

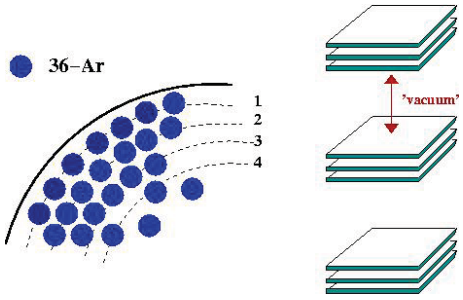

FIG. 1: Left: Schematic view of the deposition of Ar on the silica surface and the successive creation of the layered system. Right: Calculated system of a pile of three hexagonal layers with periodicity in the plane of the layer and ABC-stacking with 'vacuum' perpendicular to the pile.

From the relaxed positions and lattice constants we calculated the corresponding phonon dispersion curves. Fig. 2 shows the phonon dispersion along main symmetry directions in the plane of the layers for the hexagonal three layer system and fcc bulk Argon in hexagonal description. Both dispersion curves show similar features. However, a striking difference can be found in the slope of the transverse acoustic branches (marked with a red dashed line in Fig. 2) indicating the sound velocity. The bulk Argon system shows an increase in the slope compared to the

three layer system. In a heat pulse experiment the pulse would propagate slower in the three layer system. On the other hand the specific heat c_v at low temperatures is higher compared to the bulk. In a simple kinetic gas theory model the thermal conductivity κ is directly related to the sound velocity v_s via

$$\kappa = c_v v_s l/3,$$

where l is the mean free path of the phonons. The thermal conductivity of three layer and bulk system will be the result of the competing quantities.

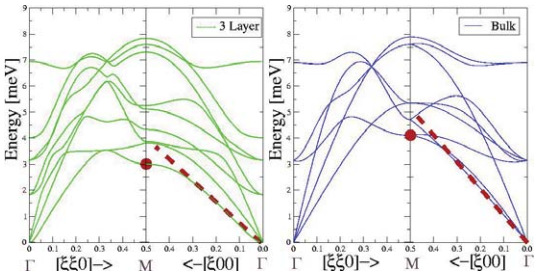

FIG. 2: Left: Phonon dispersion of the hexagonal three layer system. Right: Phonon dispersion of fcc bulk Argon in hexagonal description. Marked in red are the lowest zone boundary mode as well as the slope of the lowest acoustic branch.

Besides the different slopes of the acoustic branch also the lowest frequency at the zone boundary is shifted to higher energies from the three layer to the bulk system. The upper panel of Fig. 3 shows the experimental density of states (DOS). The lower panel shows the theoretical DOS for bulk and the three-layer system of Ar. The energy axis of the calculated curves has been scaled by a factor of 0.75 to match the experimental one-phonon cut-off. The frequencies of Ar monolayer weakly adsorbed on graphite (where the Ar–Ar interaction dominates) or calculated and measured for a monolayer are at about 3.5 and 6 meV, respectively, at the Brillouin-zone boundary [5]. That is similar to where the main dynamical features in our experimental and calculated data can be found indicating a similarly weak glass–adsorbent interaction. The overall two-peak structure is found in all four spectra. Clearly visible is also the expected shift to lower frequencies for the three layer system compared to bulk what has been indicated with the shift of the lowest frequency at the zone boundary, see Fig. 2. This effect can especially be seen in the experimental results as well as in the theoretical data. In addition to this general frequency shift to lower energies due to weak (or missing) bonds there is another effect: Whereas the phonon DOS $G(\omega)$ in a 3D system behaves like $G(\omega) \propto \omega^2$, the DOS of a 2D layer is $G(\omega) \propto \omega^1$ for small ω. This is a fingerprint of the reduced dimensionality, leading to an additional enhancement of 2D over 3D modes at small ω. However, differences between experiment and calculation are apparent. Even though we have smoothed the theoretical results with the experimental resolution function, the experimental data are much more washed out; this indicates an appreciable effect of defect broadening. Besides idealized assumptions about the realistic systems differences could arise due to experimental conditions like energy resolution and, above 8 meV, multi-phonon effects.

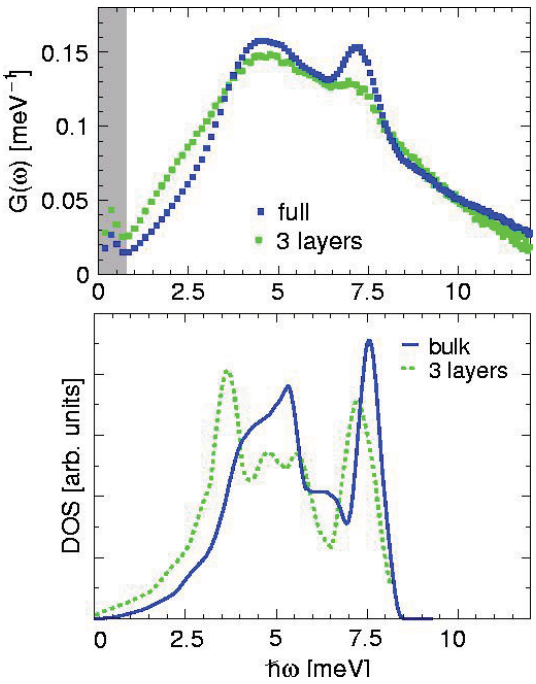

FIG. 3: Upper panel: Experimental DOS for full filling and three layers. The shaded area shows the energy resolution. Lower panel: Theoretical DOS for bulk and three layers of Ar, convoluted with a resolution of 0.5 meV (FWHM).

Beyond the low-energy regime we can equally reproduce in the calculated spectra the general trends of the experimental intensity distribution. Except for the width, the peak at about 7.5 meV is very similar in theory and experiment. Thus, the general reproducibility of the features of the experimental data points out that their origin is to be found in the reduced dimensionality of the layered argon system. The trend of lower sound velocities with lower dimension has its reason in the reduction of the orthogonal restoring forces.

[1] See the collection of articles in Eur. J. Phys. J E 12, 1-204 (2003).

[2] P. Huber and K. Knorr, Phys. Rev. B 60, 12657 (1999).

[3] X. Gonze, Comp. Mat. Science 25, 478 (2002).

[4] K. Schmalzl and D. Wallacher and M. M Koza and M. Rheinstädter and D. Strauch and K. Knorr, Eur. Phys J. ST 141, 117 (2007).

[5] H. Taub and L. Passell and J. K. Kjems and K. Carneiro and J. P. Mc Tague and J. G. Dash, Phys. Rev. Lett 34, 654 (1975).

Hydrodynamic Screening of Star Polymers in Shear Flow

M. Ripoll, R. G. Winkler, G. Gompper
IFF-2: Theoretical Soft-Matter and Biophysics

Star polymers, which consist in f identical polymers connected by one of their ends to a common center, exhibit with increasing f a crossover in their flow properties from those of linear polymers to a novel behavior, which resembles the tank-treading motion of elastic capsules. The mutual effects of the conformations of a star polymer in simple shear flow and the deformation of the solvent flow field are investigated by a hybrid mesoscale simulation technique. Moreover, we have characterized the flow field near the star polymer as a function of its functionality f. A strong screening of the imposed flow is found inside the star polymer, which increases with increasing f. The polymer orientation changes quantitatively when hydrodynamic interactions are switched off, while the rotation frequency changes qualitatively.

Polymers and polymer assemblies exhibit a unique behavior in flow which is related to their conformational degrees of freedom. Their flexibility leads to a simultaneous deformation of the coil and the fluid flow field, which strongly affect each other. To elucidate the dynamical and conformational properties of such systems is of fundamental importance with a broad spectrum of consequences in technical applications – an example is drag reduction by polymer additives. Star polymers, where f linear polymers are anchored to a common center [1], are an example of a polymer architecture whose properties can be tuned by varying the functionality f as well as the arm length. Technologically, these polymers are interesting for a variety of applications, such as drug delivery systems or as motor oil viscosity modifiers.

We have analized how the average shape of linear and star polymers results distorted and oriented, together with an induced rotation movement, under the effect of the applied shear flow [2]. We have also understood the influence of the polymer on the fluid flow. The intimate coupling of the star-polymer dynamics and the fluid flow leads to a strong modification of the flow behavior at and next to the ultra-soft colloid. We analyze the velocity field of the solvent quantitatively as a function of the star polymer's functionality. In addition, we characterize the importance of hydrodynamic interactions on the scaling properties of star polymers [3].

Hydrodynamic interactions (HI) play a fundamental role in the dynamic behavior of complex fluids. Since the large length- and time scale gap between the solvent molecules and the embedded polymers makes atomistic simulation studies prohibitively time consuming. In this work, we have used a hybrid approach in which the polymer conformations are sampled by standard molecular dynamics simulations (MD), whereas the solvent is described by multiparticle collision dynamics (MPC) [4]. Furthermore, we have introduced a variant of the MPC method, named random MPC solvent, in which all HI interactions are switched off, while most of the original solvent properties of MPC remain essentially unchanged. This method is very well suited to quantify the effect of HI in soft-matter systems.

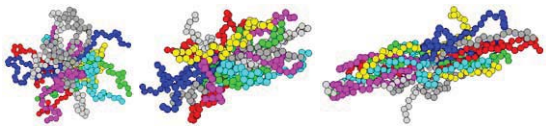

FIG. 1: Snapshots of star polymers with $f = 25$ arms, $L_f = 20$ monomers per arm under shear flows with $Wi = 0.0, 6.4, 32$ (from left to right). Configurations displayed in the flow-gradient plane.

Structural and dynamical properties of a dilute solution of star polymers are investigated as a function of the arm number f, and the arm length L_f. A linear fluid velocity profile $(v_x, v_y, v_z) = (\dot{\gamma} r_y, 0, 0)$ is obtained in the absence of a polymer, where $\dot{\gamma}$ is the shear rate. To facilitate a comparison with experimantal data and between stars of various sizes, we use the Weissenberg number $Wi = \dot{\gamma}\tau$ to characterize the shear rate, where τ is the longest star relaxation time. In Fig. 1 typical snapshots of a star polymer with $f = 25$ arms are displayed for increasing value of the applied shear. It can be easily observed that the system becomes elongated in the flow direction and shrinks in the gradient direction. This induced anisotropy and the aligment with the flow direction increase with the strength of the applied flow.

Fluid stream lines in the flow-gradient plane of the star's center-of-mass reference frame are presented in Fig. 2 together with a typical star configuration. In the region where the fluid coexists with the star polymer, the externally imposed flow field is strongly screened and the fluid velocity is no longer aligned

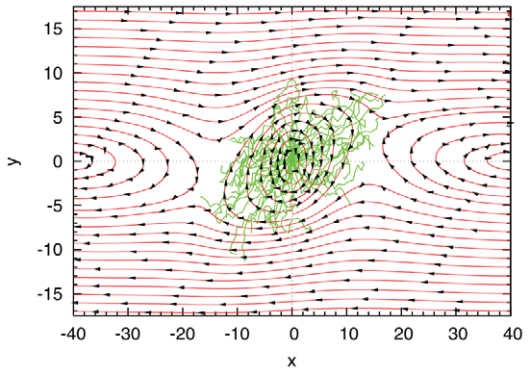

FIG. 2: Fluid stream lines in the flow-gradient plane of the star polymer's center-of-mass reference frame. Flow lines are shown for star polymers with $f = 50$ arms, $L_f = 20$ monomers per arm, and an applied shear field with $Wi = \dot{\gamma}\tau = 22$.

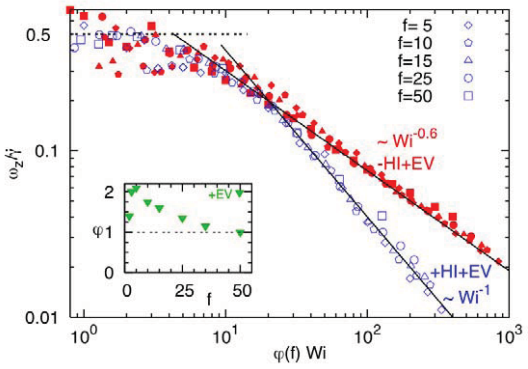

FIG. 3: Scaled rotation frequency $\omega_z/\dot{\gamma}$, as a function of a rescaled Weissenberg number, for stars with $L_f = 20$ monomers per arm. Open symbols correspond to simulations with HI, full symbols without HI. The asymptotic behaviors of $\omega_z/\dot{\gamma}$ for small and large Wi are indicated by dashed and solid lines, respectively. The inset shows the factor $\varphi(f)$; it is the same with and without HI.

with the shear flow direction, but rotates around the polymer's center of mass. Outside the region covered by the star polymer, the fluid adapts to the central rotation by generating a counter-rotating vortex and correspondingly two hyperpolic *stagnation points* of vanishing fluid velocity.

The fluid flow in the vicinity of the star polymer is distinctively different from that of a sphere but resembles the flow around an ellipsoid. In contrast to the latter, the fluid penetrates into the area covered by the star polymer. While the fluid in the core of the star rotates together with the polymer, the fluid in the corona follows the external flow to a certain extent.

We have performed simulations for star polymers of functionalities ranging from $f = 2$ to $f = 50$ for various applied shear fields with hydrodynamic and non-hydrodynamic solvents. With the random MPC solvent, we also compare results of simulations with and without excluded-volume (EV) interactions.

The resistance of a macromolecule to be oriented in the presence of a flow can be characterized by the orientational resistance parameter $m_G(f, Wi)$. This quantity is related to the angle χ_G between the eigenvector of the average gyration tensor, $G_{\alpha\beta}$, with the largest eigenvalue with the flow direction, via $\tan(2\chi_G) = 2G_{xy}/(G_{xx} - G_{yy}) \equiv m_G/Wi$. From the obtained results we conclude that $m_G(f, Wi)$ displays a power-law growth as a function of the shear rate in the form $m_G(f, Wi) = f^{\alpha} Wi^{\mu}$. Remarkably, the exponent $\mu = 0.65$ is super-universal, while the exponents α depend strongly on the type of interaction. In the presence of HI, the star polymer drags the fluid along with it (cf. Fig. 2) and strongly perturbs the linear flow profile, which is not the case in the absence of HI. Therefore, $m_G \sim f^{\alpha}$, with $\alpha = 0.30$, in the presence of HI is larger compared to the case without HI, where $\alpha = 0.18$.

It is well known by now that linear polymers show a tumbling behavior in flow, with alternating collapsed and stretched configurations. However, for $f > 5$, a qualitatively different behavior is observed, where the overall shape and orientation depend very little on time, while the arms rotate around the center of the star. Interestingly, this motion resembles the continuous tank-treading rotation observed for fluid droplets and capsules. The behavior of a single, selected arm is qualitatively not much different from a linear polymer, as it also rotates by collapsing and stretching during the *tank-treading-like* motion.

In the cases with and without HI, the rotational dynamics is not only quantitatively different but also qualitatively. Figure 3 shows that all data for the rotation frequency ω_z and the various functionalities collapse on two master curves, when the Weissenberg number is rescaled by a factor $\varphi(f)$, which turns out to be the same with and without HI. For small Wi, all frequencies approach $\omega_z = 0.5\dot{\gamma}$, as expected. For large Wi, the master curves follow a power law decay, $\omega_z/\dot{\gamma} \sim Wi^{-\theta}$, with $\theta = 1$ in the presence of HI, and $\theta = 0.6$ without HI. This implies that without HI the rotation frequency keeps growing with the applied shear rate as $\omega_z \sim \dot{\gamma}^{0.4}$, while with HI it approaches a constant for large shear rates. In both cases, the effect of the deformation and alignment under shear flow leads to a sub-linear growth with Wi. In the presence of HI, the co-rotating fluid core, dragged along by the star polymer, screens the driving force even more and a limiting velocity appears, similar to the motion of a capsule.

[1] C. N. Likos, Phys. Rev. **348**, 267 (2001).

[2] M. Ripoll , R. G. Winkler , and G. Gompper , Phys. Rev. Lett. **96**, 188302 (2006).

[3] M. Ripoll , R. G. Winkler , and G. Gompper , Europ. Phys. J. E **23 (4)**,349-354 (2007).

[4] A. Malevanets and R. Kapral, J. Chem. Phys. **110**, 8605 (1999).

Diffusion and Rheology of Charged Colloids and Bio-Macromolecules

M. G. McPhie[1], A. J. Banchio[2], G. Nägele[1]

[1] IFF-7: Soft Condensed Matter
[2] Universidad Nacional de Córdoba, Argentina

We have studied dynamic processes in suspensions of charge-stabilized colloidal particles and biological macromolecules. Transport properties such as the long-time diffusion coefficient and short-time viscosity, have been calculated using a many-component mode-coupling theory extended to ionic mixtures with hydrodynamic interactions, and by means of a recently developed accelerated Stokesian Dynamics simulation tool. We have quantified the electrokinetic influence of salt ions on the colloidal long-time diffusion in non-dilute dispersions. While this influence is small for large particles, it is significant for small particles such as polymers, proteins and other bio-molecules. An explanation is given for the unexpected non-monotonic concentration dependence of long-time self-diffusion observed in solutions of DNA fragments. We show that this non-monotonicity is of purely hydrodynamic origin. Moreover, we have made the first comprehensive simulation study of short-time dynamic properties in dense charge-stabilized suspensions, including the high-frequency viscosity.

With the increasing importance of biophysics there is a greater overlap between the subjects of the physics of biological molecules and colloid physics, which deals with mesoscale particles dispersed in a low-molecular solvent like water. Charge-stabilized colloidal dispersions occur ubiquitously in chemical, environmental and food industry. Many of the theoretical and computer simulation techniques developed in colloid physics are directly applicable to biological systems such as proteins and DNA. A particular feature of DNA that is of interest to colloid scientists is its very high surface charge density. It has been shown that the structure of DNA fragments, and of small colloidal particles in general, is strongly affected by this charge density. Consequently, other effects associated with the strong surface charge, such as counterion condensation, charge inversion and like-charge attraction in the presence of multivalent salt ions have been investigated in the past. In contrast, comparatively little work has been done on the dynamics of highly charged colloids and bio-molecules. To understand the transport behavior of these particles on the basis of their interactions is essential to numerous problems of practical relevance in material processing, dynamic phase transitions and biology.

The diffusion and rheology of dispersions of charged particles are determined by a complicated interplay of electro-steric and hydrodynamic interaction (HI) forces. The latter type of forces is transmitted by the intervening solvent, and is in general of many-body nature, making its theoretical description very demanding. We have explored the long-time self-diffusion coefficient, $D_{\rm L}$, in dispersions of charged colloids and bio-molecular particles using a recently developed theoretical method based on a many-body diffusion equation and a mode-coupling scheme. This theory is a marked improvement on previous methods since it is of many-component nature and includes the far-field HI between all ionic species, which allows us to study electrokinetic effects for non-zero colloid concentrations [1, 2].

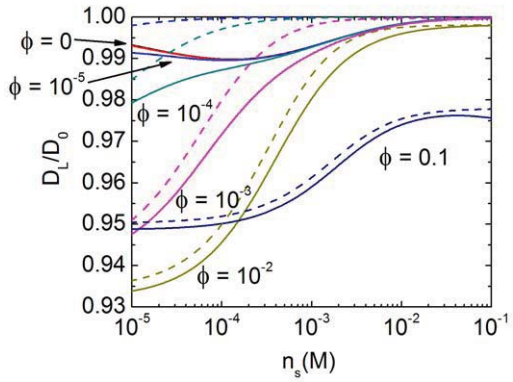

FIG. 1: $D_{\rm L}/D_0$ calculated for the protein Apoferritin versus salt concentration, n_s, for volume fractions, ϕ, as indicated. The solid (dashed) lines are $D_{\rm L}$ resulting from the colloidal and electrolyte (colloidal only) friction. From [1].

The diffusion coefficient, $D_{\rm L}$, is obtained from calculating the friction exerted on a colloid particle. The friction consists of two contributions: a colloid contribution arising from static and hydrodynamic interactions with other colloid particles, and an electrolyte friction reflecting the non-instantaneous relaxation of the electrolyte ion cloud surrounding each colloidal macroion.

Fig. 1 shows the calculated long-time self-diffusion coefficient of the globular protein Apoferritin as function of salt concentration and protein volume fraction.

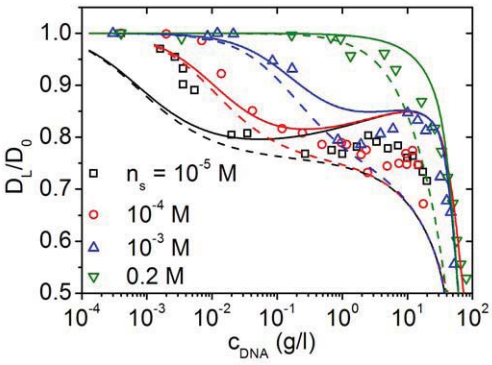

FIG. 2: $D_{\rm L}/D_0$ of 20-mer DNA solutions versus DNA concentration and added salt contents as indicated. Solid (dashed) lines are the theoretical results with (without) far-field HI, accounting for the renormalization of the DNA charge [2]. The symbols are experimental data from [3].

There is a general trend in which $D_{\rm L}$ increases from low salt to high salt concentrations, an effect arising from the static screening of the electrostatic interactions which lowers the colloid friction contribution. The additional electrolyte friction contributes most strongly for zero volume fraction, $\phi = 0$, and for an electrolyte concentration where the width of the double layer is comparable to the protein size, corresponding to the minimum in $D_{\rm L}$. A salient trend we observe is that the electrolyte friction decreases with increasing colloid concentration and decreasing microion-macroion size disparity, reflecting a homogenization of the background electrolyte density and smoothing out of chemical potential gradients.

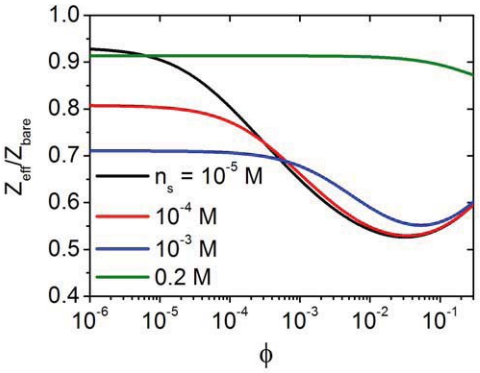

FIG. 3: Renormalized DNA charge versus volume fraction ϕ, obtained using the renormalized spherical jellium model.

Another effect seen in Fig. 1 is that, at low salt concentrations, there is a non-monotonic dependence of $D_{\rm L}$ on the colloid concentration. This unexpected effect is also seen experimentally in the $D_{\rm L}$ of short DNA fragment solutions (aspect ratio ~ 3), which have been studied by Wilk *et al.* [3]. We have shown that this striking non-monotonic behavior of $D_{\rm L}$ in low-salt suspensions is of hydrodynamic origin, and comes from the suppressed near-field part of the HI caused by the long-range electrostatic repulsion between the colloids (see Fig. 2). It is known that at low salt concentrations, the effective charge, as calculated, e.g., from the renormalized jellium model describing the quasi-condensation of counter-ions, also displays a non-monotonic dependence on ϕ (see Fig. 3). This static feature, however, is not the cause of the non-monotonicity in $D_{\rm L}$, as one clearly notices in Fig. 2 which shows our theoretical results for $D_{\rm L}$ with and without HI included. The non-monotonic concentration behavior of the effective DNA charge, $Z_{\rm eff}$, divided by the bare charge, $Z_{\rm bare}$, is depicted in Fig. 3.

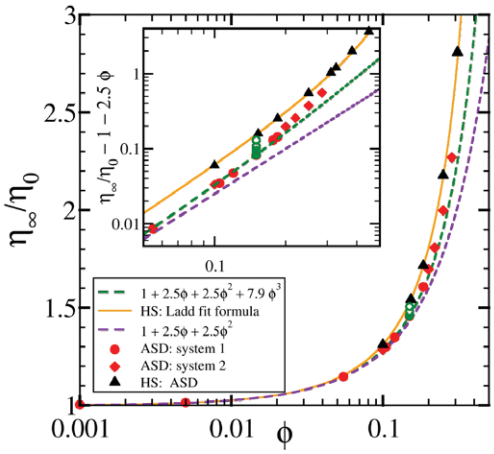

FIG. 4: Simulation results for the high-frequency limiting shear viscosity, η_∞, of charge-stabilized aqueous suspensions of colloidal spheres. For details see [4].

The dynamics in dense charge-stabilized suspensions is significantly influenced by the near-field HI part which is non-pairwise additive. Using a recently developed accelerated Stokesian Dynamics simulation method, we have calculated a large variety of properties characterizing the short-time dynamics in these systems [5]. Results have been obtained, e.g., for the high-frequency-limiting shear viscosity, η_∞, non-dimensionalized by the solvent viscosity η_0, as a function of density and salt concentration (see Fig. 4). The trends observed Fig. 4, in particular the weak ionic strength dependence of the short-time viscosity, are in full agreement with the experimental findings.

[1] M.G. McPhie and G. Nägele, J. Chem. Phys. **127**, 034906 (2007).

[2] M.G. McPhie, A.J. Banchio and G. Nägele, submitted.

[3] A. Wilk, J. Gapinski, A. Patkowski and R. Pecora, J. Chem. Phys. **121**, 10794 (2004).

[4] A.J. Banchio and G. Nägele, submitted.

[5] J. Gapinski, A. Patkowski, A.J. Banchio, P. Holmqvist, G. Meier, M.P. Lettinga and G. Nägele, J. Chem. Phys. **126**, 1 (2007).

Thermal-Diffusive Behavior of a Dilute Solution of Charged Colloids

H. Ning, J. K. G. Dhont, S. Wiegand
IFF-7: Soft Condensed Matter

We studied the thermal diffusion behavior of a dilute solution of charged silica colloidal particles by a holographic grating technique. The Soret coefficient of the charged colloids is measured as a function of the Debye screening length and the surface-charge density of the colloids. The latter is varied by means of variation of the pH. The experimental Soret coefficients are compared with several theoretical predictions. The surface-charge density is independently obtained from electrophoresis measurements, the size of the colloidal particles is obtained from electron microscopy and the Debye length is calculated from ion concentrations. The only adjustable parameter in the comparison with theory is therefore the intercept at zero Debye length, which measures the contribution to the Soret coefficient of the solvation layer and possibly the colloid-core material.

Thermal diffusion, or thermophoresis, of colloids in a liquid medium describes the movement of colloids due to the inhomogeneity of the temperature distribution. In the stationary state, the colloidal mass fluxes induced by the temperature gradient and the concentration gradient cancel. The ratio of the concentration gradient ∇c and temperature gradient ∇T that comply with such a stationary state is characterized by the Soret coefficient S_{T}, which is defined as, $S_{\mathrm{T}} = D_{\mathrm{T}}/D$, where D_{T} is the thermal diffusion coefficient and D is the mass-diffusion coefficient. Here, the thermal diffusion coefficient is defined such that the contribution of the thermal gradient to the equation of motion for the colloid concentration c is taken equal to $c\, D_{\mathrm{T}} \nabla^2 T$. The sign of Soret coefficient determines the temperature-gradient induced migration direction of the colloidal particles. For positive values of the Soret coefficient colloids move to the cold side while for negative Soret coefficients colloids will enrich at the warm side. Thermal diffusion for macromolecules is of interest because of its potential to be applied for polymer characterization, crude oil exploration and the investigation of this effect might contribute to the understanding of some fundamental aspects related to life science [1]. A deeper understanding of the effect of temperature gradients is also important, if one wants to understand how sperm cells navigate towards the egg [2]. The first observation of this effect [3] dates back one and a half century. Up to this date, however, there exists no satisfactory theory that explains thermal-diffusive behavior of simple liquids, while for colloids a few theories have been proposed recently. The development of new experimental techniques [4] during the last decade made it possible to measure the Soret coefficients of macromolecular systems.

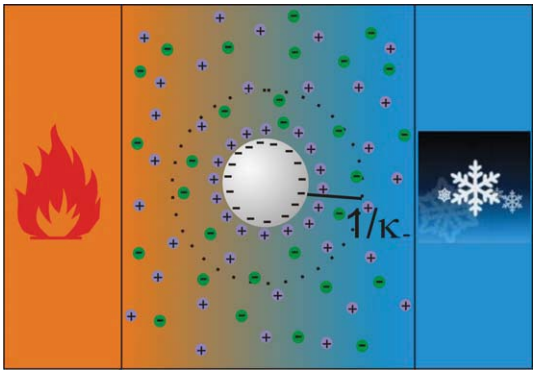

FIG. 1: Schematic illustration of a charged colloidal particle in a temperature gradient, which induces a deformation of the ionic double layer.

The thermophoresis of charge stabilized colloids was extensively investigated for several systems, such as silica particles, DNA, proteins and ionic surfactant with different experimental methods. It is found that the thermal-diffusive behavior of charged colloids depends on several parameters such as salinity, temperature, mutant variants of the protein that is studied, the particular type of electrolyte that is used, surface charge density, the colloidal concentration and the size of the colloids. In some cases a modification of those parameters changes the behavior from thermophobic to thermophilic. A distinction should be made between thermophoresis in very dilute systems and concentrated systems. In highly diluted dispersions the interaction between colloid particles and surrounding solvent, and also the formation of the double layer, dominate the physical properties of the colloids, while in concentrated dispersions the behavior is complicated by colloid-colloid inter-particle electrostatic repulsion. The Soret coefficient at high

dilution, where colloid-colloid interactions are negligible, is referred to as the single-particle Soret coefficient [4, 5].

Recently, several different theoretical approaches for single-particle Soret coefficient of charged colloids have been developed [6]. In order to test the validity of the available theories, we measured the thermal-diffusive behavior of charged silica colloids (Ludox TMA) at high dilutions using a holographic grating technique. At high salt content, the charged colloids as well as the salt contribute to the holographic-grating signal, which indicates a thermophoretic motion of both salt ions and colloids. The separation in time scales for salt diffusion and colloid diffusion, however, allows us to measure the pure colloid Soret coefficient. Furthermore, the Debye length, the surface charge density and the radius of the colloids are measured independently. This allows for an unambiguous test of the available theories for the double-layer contribution to the single-particle Soret coefficient.

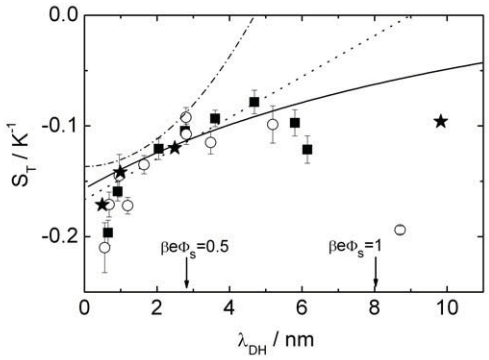

FIG. 2: Soret coefficients of Ludox particles, ϕ=0.1% (◯), ϕ=0.5% (■) and ϕ=1.12% (★)[7], as functions of the Debye length, λ_{DH}

The obtained Soret coefficients of the Ludox particles are plotted in Fig.2. The plot shows that in the probed Debye-length range, the Soret coefficients of the Ludox particles are negative, which corresponds to movement of the Ludox particles to the warm side. Negative Soret coefficients were also observed by Rusconi *et al.* [7] (the star in Fig.2) for higher concentrated Ludox particles dispersions (ϕ=1.12 wt%). The data from Rusconi *et al.* are also included in the plot in Fig.2. We found that for small Debye lengths, the experimental results from the present TDFRS-study are consistent with the results from Rusconi, who employed a thermal lens setup. At larger Debye lengths, the data from Rusconi *et al.* deviates from our results. This is due to colloid-colloid interactions, which indeed become more pronounced for larger Debye lengths. The negative sign of S_{T} is due to contributions from the hydration layer (and possibly the core of the colloidal material) [8]. From Fig.2 it can be seen that the Soret coefficient increases with increasing Debye length and reaches a shallow maximum at $\lambda_{\mathrm{DH}} \approx 5$ nm. In the range $\lambda_{\mathrm{DH}} < 5$ nm, the Soret coefficients for the Ludox particles are identical within the error bars for both concentrations ϕ =0.1% and 0.5% , which implies that we are indeed in the diluted regime where colloid-colloid interactions can be neglected.

The lines in Fig.2 correspond to the different theoretical models discussed in Ref.[6]. In fitting the data for the Ludox particles, the only fitting parameter is the intercept $A(T)$ at zero Debye length, which is due to the solvation-layer and core-material contributions to the Soret coefficient. For Ludox particles, in the Debye-length range between 1 nm$< \lambda_{\mathrm{DH}} <$5 nm, we find that the approach by Dhont [9] agrees with the experimental results for S_{T}. The experimental data deviate systematically at smaller Debye lengths (λ_{DH} <1 nm) and above $\lambda_{\mathrm{DH}} > 5$ nm. The deviations at smaller Debye lengths ($\lambda_{\mathrm{DH}} \leq 1$ nm) is probably due to the high salinity, which leads to a violation of the Debye-Hückel approximation where the finite extent of ions is neglected. For large Debye lengths ($\lambda_{\mathrm{DH}} > 6$ nm) the surface potential is high ($e\Phi_s/k_BT > 0.9$), so that linearization of the Poisson-Boltzmann equation is probably no longer allowed. Also the predictions by Würger and the capacitor model by Braun (the dotted line) agrees reasonably well in the intermediate Debye-length range. The theoretical prediction by Ruckenstein (the dash-dotted line) deviates significantly from the experimental data in the entire λ_{DH}-range. Note that in Ruckenstein's prediction $S_{\mathrm{T}} \propto R/\kappa^2$, while the the other theories predict that $S_{\mathrm{T}} \propto R^2/\kappa$ (for thin double layers). Also the dependence of the dielectric constant on temperature (signified by the terms $\propto d\ln\epsilon/d\ln T$) is absent in Ruckenstein's expression. The intercept $A(T)$ is around -0.16 K^{-1} for the Ludox particles.

[1] D. Braun and A. Libchaber. *Phys. Rev. Lett.*, 89, 2002.

[2] A. Bahat, I. Tur-Kaspa, A. Gakamsky, L. C. Giojalas, H. Breitbart, and M. Eisenbach. *Nat. Med.*, 9:149–150, 2003.

[3] C. Ludwig. Diffusion zwischen ungleich erwärmten orten gleich zusammengesetzter lösungen. *Sitz. ber. Akad. Wiss. Wien Math.-naturw. Kl*, 20:539, 1856.

[4] S. Wiegand. *J.Phys.:Condens. Matter*, 16:R357–R379, 2004.

[5] J.K.G Dhont. *J. Chem. Phys.*, 120(3):1642–1653, 2004.

[6] H. Ning, J. K. G. Dhont, and S. Wiegand. *Langmuir*, 2008. to be published.

[7] R. Rusconi, L. Isa, and R. Piazza. *Journal of the Optical Society of America B-Optical Physics*, 21(3):605–616, 2004.

[8] S. Duhr and D. Braun. *Proc. Nat. Acad. Sci. U.S.A.* , 103:19678–19682, 2006.

[9] J. K. G. Dhont, S. Wiegand, S. Duhr, and D. Braun. *Langmuir*, 23:1674–1683, 2007.

SANS Study of Polymer-Linked Droplets

S. Maccarrone, H. Frielinghaus, J. Allgaier, D. Richter
IFF-5: Neutron Scattering

We report the experimental results obtained from SANS on microemulsion droplets connected by a telechelic polymer. Thanks to its ability to anchor droplets through its short stickers, the addition of this polymer leads to the formation of transient aggregates. Measurements were performed on samples at low surfactant content in such a way that the droplets appear isolated with a separation distance longer than the end-to-end distance of the polymer. The locally spherical structure of the micelles is maintained unchanged in size upon polymer addition while the large rise of the scattered intensity at low Q is due to the induced effective attractive interaction between droplets. The fitting model we propose allows a quantitative description of the bridging effect.

Microemulsions are thermodynamically stable and homogeneous mixtures of two non-miscible components, namely oil and water, which are mediated by the surfactant. The control of the emulsification behavior and/or the structural properties is fundamental as these systems find nowadays a wide range of applications. For example, they are used in food industry and cosmetics to produce detergents, paints, soaps, etc. At the molecular scale, oil and water form domains and the surfactant, consisting of amphiphilic molecules with a hydrophilic and hydrophobic part, is arranged at the water-oil interface.

Moreover, the use of polymer additives can modify the phase behavior and the structural properties of such systems. Historically, rheological studies were reported initially [1]. It was found that the addition of a class of telechelic polymer, namely hydrophobically end-capped Poly(ethylene oxide), affects the intermicellar interaction in oil-in-water droplet microemulsions, leading to an increasing ordering of the micelles [2]. Recently, oil-in-water droplets microemulsion linked by triblock telechelic polymers was proposed as model in order to study the viscoelastic properties of transient network-forming systems [3, 4]. Such a telechelic polymer consists in a water soluble middle chain (PEO) with two short "stickers" hydrophobic chains (alkyl chains) by which is able to create loops anchoring at two points of the same droplet or eventually to bridge two points on different droplets. The advantage in using this system is based on the possibility to control independently important parameters like the concentration of the droplets and the connectivity of the network through the number of polymers per droplet that define the structural properties.

Experimental Section: We intended to measure three samples of decane droplets in D_2O with $C_{10}E_4$ as surfactant and two of those were prepared with different polymer mass fraction $\phi_\delta = m_P/(m_P + m_S + m_O + m_W)$. The idea was to have isolated droplets with separation distance four times larger than the end-to-end distance of the polymer. So we fixed the surfactant/water volume fraction $\omega = V_S/(V_S + V_W)$ at 0.012 and the oil mass fraction, defined as $w_B = m_O/(m_P+m_S+m_O+m_W)$, was chosen to be 0.036. The large asymmetry introduced in the oil/water volume fraction is the condition to obtain oil-in-water droplets.

Small Angle Neutron Scattering: SANS experiments were performed on D11 machine at ILL in Grenoble, France. We measured the samples at three detector distances (2, 5 and 20 m) and at different temperatures. The collimation was set at 5.5m for the first short detector distances and 20.5m for the 20m; the wavelength λ was chosen equal to 6Å. The scattering curves were put on an absolute scale by using water as standard with intensities in absolute units (cm^{-1}) with an accuracy of 10%. We made experiments under bulk contrast substituting H_2O with D_2O so that the contribution of the scattering comes from the whole hydrogenated droplet made by the oil core and the surfactant shell.

Theoretical Model: We modelled the sample without polymer considering the droplets like colloidal particles. In this way the scattered intensity as function of the scattering vector has the following form:

$$I(Q) = \Phi V (\Delta\rho)^2 P(Q) S(Q) \qquad (1)$$

where Φ is the volume fraction of the droplets, V is the volume and $\Delta\rho$ is the contrast. $P(Q)$ is the form factor that for $Q \to 0$ is 1 and $S(Q)$ is the structure factor which expresses the interaction between the particles. The low surfactant content yields the formation of droplets with large separation distance and this allows us to simplify the expression for the intensity considering $S \approx 1$. A simple form factor for spherical objects was used. Polydispersity was modelled by a Schulz-Zimm distribution.

Structure factor: When the telechelic polymer is added, an effective attractive interaction is introduced bringing together the droplets. To calculate the structure factor $S(Q)$, one needs to solve the Ornstein-Zernike equation for the direct correlation function $C(R)$ using a known interaction potential [5]. An expression for the potential $U(R)$ can be built considering the droplets as hard spheres and the polymer chains introduce a parabola-shape attractive interaction:

$$U(R) = \begin{cases} +\infty & R \leq \sigma \\ \frac{\hat{A}}{R_e^2}(\sigma - R)(R - \sigma - 2R_e) & \sigma < R \leq \sigma + 2R_e \\ 0 & R > \sigma + 2R_e \end{cases} \quad (2)$$

R_e is the position where the minimum occurs and σ is the radius of the colloids. When the potential is constituted by a hard core plus an attractive tail, the direct correlation function can be obtained under the mean spherical approximation

$$C(R) = \begin{cases} C_{HS}(R) & R \leq \sigma \\ C_{att}(R) & R > \sigma \end{cases} \quad (3)$$

with $C_{HS}(R)$ is a known direct correlation function for the simple hard sphere system. Our parabola model is a phenomenological model which reflects three properties. At smaller distances $R > \sigma$ the potential is usually slightly repulsive. There is a broad minimum (here at $R = R_e + \sigma$), and the attractive interaction has a finite range (here at $R = 2R_e + \sigma$). Potentials calculated from first principles give a deeper physical insight – especially when varying more parameters – but the fit-quality was worse [6].

Results and Discussion: In Figure 1 the scattering intensity profiles for all the three samples at fixed temperature of 6.54°C are shown. At first look, the unchanged position of the minimum at high Q is the sign that the average size of the droplets is not influenced by the polymer while the upturn of the intensity at low Q indicates the presence of big objects, likely linked droplet aggregates that become larger with increasing polymer concentration: the bridging induces an effective attractive interaction and the bump at moderate Q, more visible for the sample with the highest polymer content, shows that there is a preferred distance between droplets in the transient clusters.

A quantitative analysis of the scattering data based on equation 1, permit to extract the mean radius of the spherical droplets σ equal to 43Å and the volume fraction of the droplets around 0.013 in the case of DROP1 (bottom curve in figure 1). Due to the low surfactant content the droplets in the pure microemulsion should be well separated making reasonable the assumption $S \approx 1$. Indeed, the estimated average distance is quite large, about 295Å, considering a droplet arrangement on a cubic network with volume fraction and radius values as from the fitting.

For the other two samples, the fitting of the SANS spectra (middle and top curves in figure 1) gave us the same values for the mean radius and volume fraction of the droplets that we did not expect to vary. Moreover, the fitting parameters that determines the position and the amplitude of the attractive well potential are consistent between the two sample with different polymer concentration. In particular, the sample DROP3 with the double amount of the polymer has an amplitude two times bigger than the sample with half of the polymer DROP2. The depth of the minimum $\hat{A}$ is equal to $-1.45k_BT$ in the case of DROP2 and two times bigger ($-2.81k_BT$) for DROP3. These values are reasonable in agreement with the work of Bathia [7].

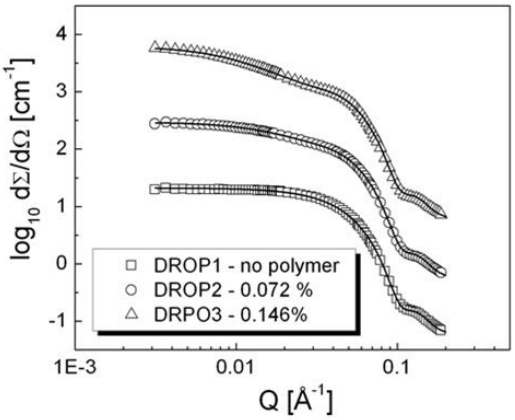

FIG. 1: Scattering-intensity profiles for the three samples with different polymer concentrations ϕ_δ and relative fitting curves. The spectra DROP2 and DROP3 were multiplied by factors of 10 and 100, respectively, for a better view. Errors are approximately the same as or less than the size of the symbols.

Summary and Conclusion: SANS experiments were carried out on polymer-modified droplet microemulsions. The telechelic polymer bridges the droplets, starting an aggregative process with the formation of clusters. This effective attraction was modelled with a simple potential made up by the sum of a hard sphere contribution and an attractive parabola tail. Its equilibrium state occurs at a separation distance between droplets of 78Å and continues until is switched off at 156Å while the polymer end-to-end distance is 61Å. Thus, the attractive interaction of the polymer is still active in a rather extended state.

[1] M. Odenwald, H.F. Eicke, W. Meier, *Macromolecules* **28**, 5069, 1995

[2] H. Bagger-Jörgensen, L.Coppola, K. Thuresson, U. Olsson, K. Mortensen, *Langmuir* **13**, 4204, 1997

[3] M. Filali, M.J. Ouazzani, E. Michel, R. Aznar, G. Porte, J. Appell, *J. Phys. Chem. B* **105**, 10528, 2001

[4] F. Molino, J. Appell, M. Filali, E. Michel, G. Porte, S. Mora, E. Sunyer, *J. Phys.: Condens. Matter* **12**, A491, 2000

[5] J.P. Hansen, I.R. McDonald, *Theory of simple liquids* Academic Press, London, 1991

[6] G. Porte, C. Ligoure, J. Appell, R. Aznar, *J. Stat. Mechanics* P05005, 2006

[7] S.R. Bathia, W.B. Russel, *Macromolecules* **33**, 5713, 2000

Enhanced Slowing Down of the Colloidal Near Wall Dynamics in a Suspension of Rods

P. Holmqvist, D. Kleshchanok, P. R. Lang
IFF-7: Soft Condensed Matter

In this report, we will show the influence of rodlike particles, fd-virus, on the diffusion of spherical polystyrene colloids close to a wall. The sphere diffusivity normal to the wall, $< D_\perp >$, is strongly affected by the presence of the rods, while the effect on the parallel diffusivity, $< D_\parallel >$, is less pronounced except in the immediate vicinity of the wall [1].

The slowing down and the anisotropy of Brownian motion close to a wall due to hydrodynamic drag forces has been theoretically predicted [2] and recently experimentally verified [3]. So far, only the case of particles interacting by excluded volume with a wall has been considered. The effect of depletion on the dynamics close to a wall has received very little or no attention, neither theoretical nor experimental.

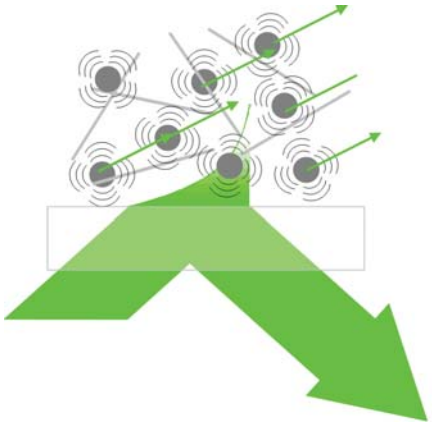

FIG. 1: Schematic picture of the sphere/rod system under evanescent illumination close to the surface

We chose to apply fd–virus as a depletant, which are rodlike mono-disperse particles and nonadsorbing neither on glass nor on polystyrene latex particles. They have a contour length of 880 nm which is comparable to the maximum penetration depth applicable in an EWDLS experiment. In other words, the depletion potential mediated by fd–virus is expected to be effective throughout the entire scattering volume. Further, we performed EWDLS measurements with our tipple axis setup, with which we can determine the parallel and normal component of the diffusivity independently [3]. The depletion potential mediated by rodlike particles has been calculated by Mao et al. to third order in rod number density [5]. In the first order approximation, there is a simple closed analytical form, which can be introduced in the expressions for the initial relaxation rate Γ of the time auto correlation function of the scattered intensity. Our experimental TIRM data for the depletion potential mediated by fd-virus is in quantitative agreement with these predictions. Therefore, we used the first order approximation to estimate the lowest rod concentration at which the depletion potential would cause a notable effect on the near wall dynamics of spherical colloids with a radius of $R = 85$ nm. We note that the Derjaguin approximation is not valid at this radius/rod length ratio, but it will give a lower boundary for the required rod number density, because the strength of the depletion potential decreases with decreasing R/L at constant density. From this, we chose as a starting point a rod concentration of twice the overlap concentration which would give a contact potential of approximately $0.5k_BT$. Further, at this rod concentration, the solvent viscosity will be changed only by a few percent and the fd–virus contribution to the scattering is essentially negligible, which keeps the data treatment on a tractable level. To our surprise, we found a much larger effect on the near wall particle dynamics than expected from these considerations.

Aqueous buffer solutions (20 mM TRIS) of PS latex spheres with a radius of $R = 85$ nm were investigated with two different fd–virus concentrations, that is, 0.05 and 0.17 g/L, above and below the overlap concentration, $c^* = 0.075$ g/L. In bulk solutions with the same fd–virus content, the diffusion of the colloids is reduced by less than 20% [6]. The PS latex spheres are charge stabilized by sulfonate surface groups, and they were diluted from their stock solutions to a volume fraction of 2×10^{-4}. At these conditions, the particles may be regarded as hard spheres, since the Debye screening length is in the range of 3 nm, while the mean interparticle distance is of the order of several thousand nanometers. A schematic picture of the system close to the surface under evanescent illumination can be seen in figure 1. To illustrate the effect of the fd-viruses on the colloidal diffusion close to the wall correlation functions $g_1(t)$ are presented in figure 2 at a constant penetration depth of $2/\kappa = 270$ nm and a total scattering

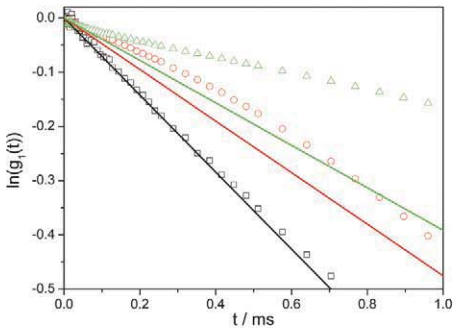

FIG. 2: Initial decay $\ln(g_1(t))$ for 2×10^{-4} volume fraction PS latex spheres ($R = 85nm$) in $c_{fd} = 0.17$ g/L at $Q_{tot} = 0.0157$ nm^{-1} and $2/\kappa = 270$ nm for bulk (open squares) and for two different combinations of $Q_{\|}$ and $Q_{\perp}$ as follows: $Q_{\|} = 0.0136$ nm^{-1} and $Q_{\perp} = 0.00785$ nm^{-1} (open circles), and $Q_{\|} = 0.00785$ nm^{-1} and $Q_{\perp} = 0.0136$ nm^{-1} (open triangles). The lines are the expected $\ln(g_1(t))$ for the same system without fd–viruses for bulk (black), for $Q_{\|} = 0.0136$ nm^{-1} and $Q_{\perp} = 0.00785$ nm^{-1} (red), and for $Q_{\|} = 0.00785$ nm^{-1} and $Q_{\perp} = 0.0136$ nm^{-1} (green).

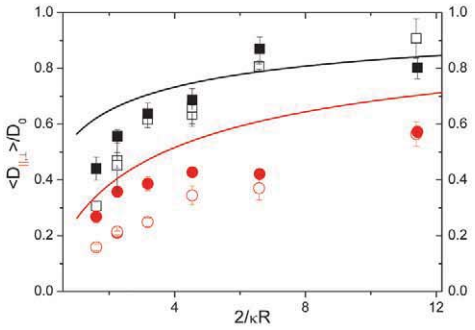

FIG. 3: $< D_{\|} >$ (squares) and $< D_{\perp} >$ (circles) normalized to the bulk diffusion, D_0, are plotted against the reduced penetration depth, $2/\kappa R$, for $c_{fd} = 0.05$ g/L (solid symbols) and $c_{fd} = 0.17$ g/L (open symbols). The lines are the expected curves for the colloid solution without depletant.

vector, $Q_{tot} = 0.0157$ nm^{-1}, for two different combinations of $Q_{\|}$ and $Q_{\perp}$ together with the bulk $g_1(t)$ for a fd–virus concentration of 0.17 g/L. The EWDLS $g_1(t))$ show a much smaller slope than that of the bulk curve. Further, the slope of the $g_1(t)$ at $Q_{\perp} > Q_{\|}$ is significantly smaller than that at $Q_{\perp} < Q_{\|}$, which indicates a strong anisotropy of the near wall diffusion. If these data are compared to the expected $g_1(t)$ for the same system without depletant [3] (lines in figure 2), it is clear that the sphere near wall dynamics is affected much more than the bulk dynamics by the presence of the rods. In bulk, the $g_1(t)$ values with and without the fd–virus are almost identical (the 20% reduction is hardly measurable), while a large difference is obvious for the EWDLS correlation functions. Not only do the near wall dynamics slow down significantly, but the anisotropy increases. This slowing down of the diffusion close to the surface cannot be explained solely by the small reduction of the bulk diffusion. To investigate this in detail, systematic measurements of the diffusivity parallel and normal to the surface at different penetration depths were performed. Using the same procedure described in our recent papers [3] the mean diffusivities for the parallel, $< D_{\|} >$, and the normal diffusion, $< D_{\perp} >$, is determined for the two different fd–virus concentrations. To get a more complete picture of the effect of fd–virus on the colloidal dynamics close to the wall, the procedure described above was performed for a series of six penetration depths. In figure 3, the extracted mean diffusivities normalized to the bulk diffusion constant, D_0, are plotted against the reduced penetration depth, $2/\kappa R$ (where R is the colloidal radius). The anisotropy of the diffusion can nicely be seen as the separation between $< D_{\|} >$ (black squares) and $< D_{\perp} >$ (red circles) for both concentrations, 0.05 g/L (solid symbols) and 0.17 g/L (open symbols). For comparison, we show the expected curves for the colloid solution without fd–virus as solid lines. It is notable that the anisotropy is always larger for the high fd–virus concentration, while for the low fd-virus concentration the anisotropy is close to what can be expected for a system without depletant. If one compares the data with the expected mean diffusivities without depletant (solid lines), no effect on $< D_{\|} >$ can be seen at large penetration depths for both fd–virus concentrations. However, at penetration depths below about 450 nm, that is, $2/\kappa R \lesssim 5$, a pronounced effect can be seen for both fd–virus concentrations. $< D_{\|} >$ is decreasing much more with decreasing penetration depth than was observed for the system where no depletant was present. This effect is more pronounced in the solution with the high fd–virus concentration. If one looks at the normal diffusivity, $< D_{\perp} >$, a significant reduction can be seen as compared to the nondepletant system also at large penetration depths (distances) for both fd–virus concentrations. As for $< D_{\|} >$, $< D_{\perp} >$ decreases with decreasing penetration depth, and for the high fd–virus concentration system $< D_{\|,\perp} >$ drop more strongly at low penetration depths.

[1] Holmqvist P.; Kleshchanok, D.; Lang, P. R. *Langmuir* **23**, 12010 (2007).

[2] Brenner, H. *Chem. Eng. Sci.* **16**, 242 (1961).

[3] Holmqvist, P.; Dhont, J. K. G.; Lang, P. R. *Phys. Rev. E* **74**, 021402 (2006).

[4] Kihm, K. D.; Banerjee, A.; Choi, C. K.; Tagaki, T. *Exp. Fluids* **37**, 811 (2004).

[5] Mao, Y.; Cates, M. E.; Lekkerkerker, H. N. W. *J. Chem. Phys.* **106**, 3721 (1997).

[6] Kang, K.; Gapinski, J.; Lettinga, M. P.; Buitenhuis, J.; Meier, G.; Ratajczyk, M.; Dhont, J. K. G.; Patkowski, A. *J. Chem. Phys.* **122**, 044905 (2005).

Effect of Polydispersity on Depletion Interaction

D. Kleshchanok, P. R. Lang
IFF-7: Soft Condensed Matter

The polydispersity of depletants has a significant influence on the depth and the range of depletion potentials. Both for polymeric and for rod–shaped colloidal depletants we find that the absolute value of the contact potential and the range of the potential become larger if the relative width of the depletants' size distribution is larger than about 50%

Depletion interactions occur when two or more kinds of colloidal particles of different size or colloidal particles and polymers are mixed in a suspending medium. If two particles of one species approach each to such a degree that the other species is excluded from the gap between them, the resulting osmotic pressure imbalance causes an attractive force between the two particles. Asakura and Oosawa [1] were the first to calculate the depletion force between two plates immersed in a dilute solution of ideal polymer chains. Later the same authors calculated the attractive force between two parallel plates in a solution of infinitely thin rigid rods [2]. Auvray derived a closed analytical expression for the potential between two spheres in a dilute suspension of rods with $L/R \ll 1$ [3]. Later Mao et al published [4] a series expansion in density up to third order for the depletion potential mediated by rods of finite aspect ratios in the Derjaguin limit. Surprisingly, the effect of a finite size distribution of the depletant on the interaction has attracted limited attention. Most of the theoretical and computer modelling work on the effect of polydispersity was done on polydisperse spheres [5, 6, 7, 8, 9, 10] as depletant. Tuinier and Petukhov calculated the depletion force between two plates in a solution of polydisperse ideal chain macromolecules [11]. For the case of rod–like depletants no systematic study on polydispersity effects has been published so far although Yaman et al. published a numerical method [12, 13] to calculate the depletion interaction between two spheres of radius R mediated by an ideal gas of infinitely thin rods of length L for arbitrary L/R.

To our knowledge there are only a few contributions, in which the effect of polydispersity has been studied systematically in experiments. Piech et al. found semi quantitative agreement between theoretical predictions and their atomic force microcopy measurements of the depletion potential between a spherical silica particle and a silica flat mediated by an ensemble of polydisperse nanospheres [14]. The depletion interaction between a wall and a sphere due to boehemite rods was investigated by Helden et al. [15, 16]. However, in this case the influence of polydispersity was not considered explicitly.

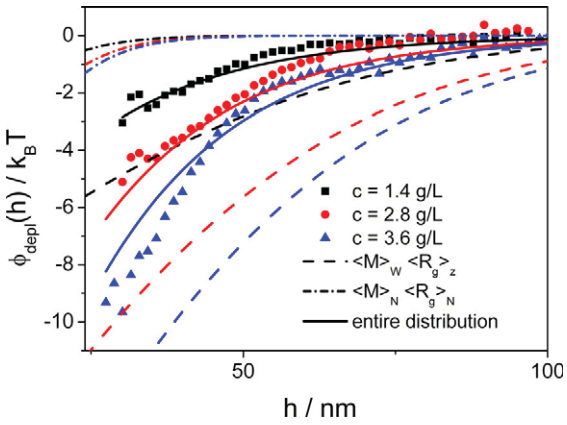

FIG. 1: Depletion interaction between a polystyrene latex sphere with $R = 2850$ nm and a glass wall in a solution of polydisperse dextran. Symbols are experimental data obtained by total internal reflection microscopy at different polymer concentrations as indicated in the legend. The dashed lines were calculated by introducing $< M >_W = 2.7 \times 10^6$ g/mol and $< R_g >_z = 44$ nm into standard expressions for depletion interaction. The dash–dotted lines were calculated with the same equations using number averaged quantities.

In this report we will describe our total internal reflection (TIRM) [17] results concerning the effect of polydispersity on the depletion interaction mediated by polymers [18]. Further we report on numerical calculations of the depletion interaction mediated by polydisperse rods [19].

In Fig. 1 we present the depletion interaction between a polystyrene sphere with a radius of $R = 2850$ nm and a glass wall in a solution of polydisperse dextran at different polymer concentrations. The mass averaged molar mass and the z–averaged radius of gyration of the polymer were determined by light scattering as $< M >_W = 2.7 \times 10^6$ g/mol and $< R_g >_z = 44$ nm respectively. Introducing these values into the standard expression for the depletion interaction yields the curves which are shown as dashed lines in Fig. 1. The dash–dotted lines in the graph were were calculated using the number aver-

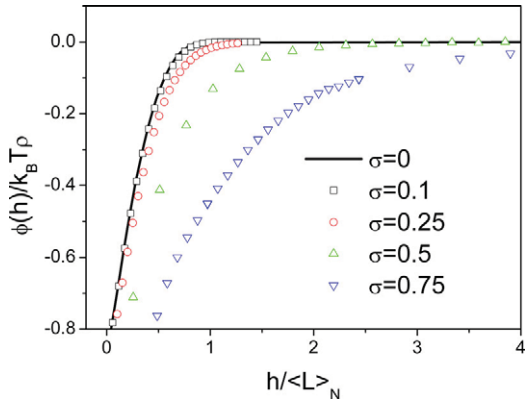

FIG. 2: Depletion interaction between a sphere and a wall mediated by an ensemble of rods with a logarithmic normal length distribution. The curves were calculated with constant $< L >_N /R = 1$ for different relative widths of the distribution as indicated in the legend.

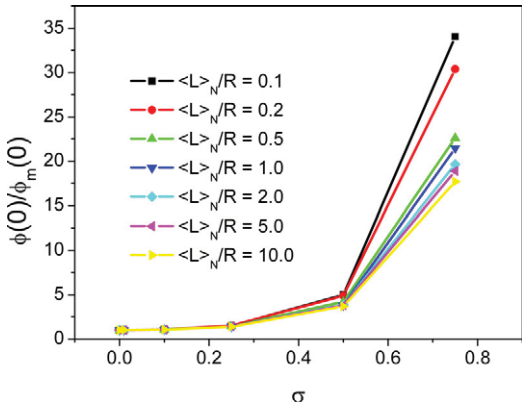

FIG. 3: Contact values of the depletion potential between a sphere and a wall mediated by an ensemble of rods with a logarithmic normal length distribution normalized to the contact values due to monodisperse rods. The data were calculated for different $< L >_N /R$ as indicated in the legend.

aged quantities for the molar mass $< M >_N$ and the radius of gyration $< R_g >_N$, which could be obtained from the known molar mass distribution of the polymer. It is thus obvious from Fig. 1 that is not possible to predict the depletion interaction due to polydisperse polymers correctly if averaged quantities for polymer mass and size are used. This is in line with the theoretical prediction by Tuinier et al. [11] who found that for a molar mass distribution with a relative width larger than $\sigma \approx 0.7$ the entire molar mass distribution has to be included in the calculation of the depletion interaction. The full lines in Fig. 1, which are in reasonable agreement with the experimental data, were calculated following the theory by Tuinier et al. It is important to note that polydisperse polymers cause a deeper and a longer ranging depletion potential than the monodispers analog at the same mass concentration of the polymer.

Since rod–like particles are much more effective depletants than polymers, it is also interesting to investigate the effect of length polydispersity on the depletion potential mediated by rods. This was done by numerical calculations of the potentials between a sphere and a wall due to infinitely thin rods with a logarithmic normal (LN) length distribution. The distribution is characterized by the number averaged length $< L >_N$ and the relative width σ. In Fig. 2 we show the dependence of the depletion potential on σ for $< L >_N /R = 1$.

No deviation from the potential mediated by monodisperse rods can be observed if $\sigma \lesssim 0.1$. Even for a relative standard deviation of 25% the difference is smaller than would be discernible with state of the art experimental techniques like TIRM [17]. At larger standard deviations, both the absolute contact value and the range of the potential increase with σ. The general trend visible from these data is also observed for an other value length to radius ratio . The effect on the contact potential is however more pronounced for small $< L >_N /R$ as is shown in Fig. 3.

To conclude, we have shown, both for polymers and rods, that polydispersity has a significant effect on depletion potentials if the relative width of of the distribution is larger than about 50%. In this case it is not possible to approximate the depletion potentials by introducing averaged properties of the depletant into standard equations. Further, it is noteworthy for technical applications that polydisperse depletants are more efficient than their monodisperse analogs at the same mass concentration.

[1] S. Asakura and F. Oosawa *J. Chem. Phys.* **22**, 1255 (1954).

[2] S. Asakura and F. Oosawa *J. Polym. Sci.* **33**, 183 (1958).

[3] L. Auvray, *J. Phys. (Paris)* **42**, 79 (1981).

[4] Y. Mao, M. E. Cates, and H. N. W. Lekkerkerker, *J. Chem. Phys.* **106**, 3721 (1997).

[5] Y. Mao, *J. Phys. II* **5**, 1761 (1995).

[6] Y. Walz, *J. Colloid Interface Sci.* **178**, 505 (1996).

[7] P. B. Warren, *Langmuir* **13**, 4388 (1997).

[8] R. P. Sear and D. Frenkel, *Phys. Rev. E* **55**, 1677 (1997).

[9] M. Piech and J. Y. Walz, *J. Colloid Interface Sci.* **225**, 134 (2000).

[10] D. Goulding and J. P. Hansen, *Mol. Physs* **99**, 865 (2001).

[11] R. Tuinier and A. V. Pethukhov, *Macromol. Theory Sim.* **11**, 975 (2002).

[12] K. Yaman, M. Jeng, P. Pincus, C. Jeppesen, and C. M. Marques, *Physica* **A 247**, 159 (1997).

[13] K. Yaman, C. Jeppesen, and C. M. Marques, *Europhys. Lett.* **42**, 221 (1998).

[14] M. Piech and J. Y. Walz, *J. Colloid Interface Sci.* **253**, 117 (2002).

[15] L. Helden, R. Roth, G. H. Koenderink, P. Leiderer, and C. Bechinger, *Phys. Rev. Lett.* **90**, 048301 (2003).

[16] L. Helden, G. H. Koenderink, P. Leiderer, and C. Bechinger, *Langmuir* **20**, 5662 (2004).

[17] D. C. Prieve, *Adv. Colloid Interface Sci.* **82**, 93 (1999).

[18] D. Kleshchanok, R. Tuinier, and P. R. Lang, *Langmuir* **22**, 9121 (2006).

[19] P. R. Lang, *J. Chem. Phys.* **127**, 124906 (2007).

Biological Nanomachines

A. Baumgärtner, J.-F. Gwan, S. Grudinin, M. Haan
IFF-2: Theoretical Soft-Matter and Biophysics

Biomolecular machines are large protein complexes whose activities are essential for providing "life" to a biological cell. Among the various known biomolecular devices, ion channels, which reside in cell membranes, are one of the simplest bionanomachines. We have investigated using computer simulations the molecular mechanism of selectivity and transport of ions through a specific potassium ion channel.

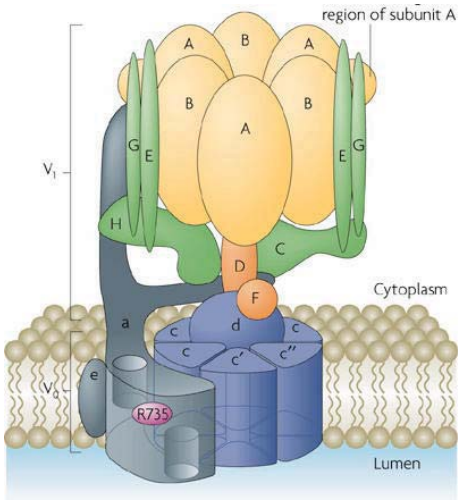

FIG. 1: Cartoon representation of the V-ATPase, a biological nanomachine which acts as a ATP-driven proton pump.

Nanotechnology is perfectly realized in biological systems. Cells are essentially biological assemblers that build thousands of custom-designed molecules and construct new assemblers. This view was pioneered by Richard Feynman's [1] evocative idea of a self-replicating assembler building nanoscale devices atom by atom. Living cells are made up of these complexes, which carry out many of the functions essential for their existence, differentiation, and reproduction. In many cases the malfunction of these proteins can be a source of disease. Many of these complexes can be described as "molecular machines" or "molecular motors" or "molecular devices", depending on their sizes, complexity and tasks [2]. The essential question in understanding biomolecular machines is concerned with the explanation of the macroscopic phenomenology in terms of the atomic structures and forces involved. Although a complete description is not yet available even for the best-characterized system, considerable progress has been made recently, not only from an experimental point of view, but also with respect to computational and theoretical achievements. One of the most fascinating biomolecular machines is the class of vacuolar H^+-ATPases (or V-ATPases), which are a family of ATP-dependent proton pumps responsible for acidification of intracellular compartments and proton transport across the cell plasma membrane. V-ATPases are multisubunit complexes (Fig.1) composed of a peripheral domain V_1 (yellow and orange) responsible for ATP hydrolysis and an integral domain V_0 (blue and grey) responsible for proton translocation. The V-ATPases are thought to operate by a rotary mechanism in which ATP hydrolysis in V_1 drives rotation of a ring of proteolipid subunits in V_0. The V_1 and V_0 domains are connected by both a central stalk which is thought to play a crucial role in the assumed rotary mechanism of ATP-driven proton transport. The molecular details at atomic resolution are only partly resolved. The theoretical understanding are currently beginning to emerge. This molecular machine is under investigation using elaborate modelling and computer simulations.

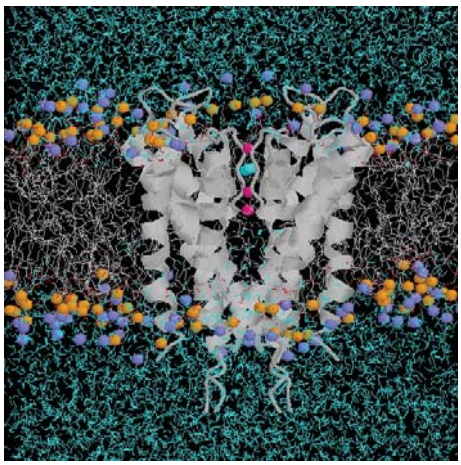

FIG. 2: Structure of the KcsA potassium channel embedded in a water solvated lipid bilayer membrane. Only two monomers of the tetrameric protein are shown.

A much simpler and much more well characterized bionanomachine is the KcsA potassium channel [3], which acts as a valve in the plasma membrane of prokaryotic cells. The cutaway view of the atomic structure of the protein complex (in ribbon representation) is shown in Fig.2. The figure shows only two monomers of the tetrameric protein complex embedded in a water solvated lipid bilayer membrane. Each monomer consists of three helices, one extracellular loop, and as the central part of the channel the selectivity filter containing three potassium ions (depicted by balls) and one water molecule between. The structural details of the filter are decisive for ion selectivity and transport. The selectivity filter facilitates the diffusion of potassium ions at rates approaching 10^8 ions per second under physiological electrochemical gradients. The ability of potassium channels to conduct several K^+ ions simultaneously in a single file through the narrow pore at levels near the limit of diffusion is usually described in terms of concerted mechanisms. It has been suggested that to reach a high conduction rate in a long-pore channel, ions must move through the channel pore in a multi-ion fashion : the permeating ions line up in the narrow channel pore and move in a single file through the channel. This is known as "the multi-ion permeation process", and is believed to be a common feature of the ion transportation process in all potassium channels. The multi-ion theory has been acepted over decades, but the molecular mechanism of it remained elusive.

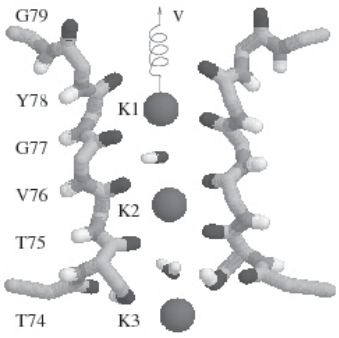

FIG. 3: Molecular view of the selectivity filter of the KcsA potassium channel including ions and water molecules.

Employing MD simulations on the basis of the X-ray structure of the KcsA channel, our studies [4, 5] have provided useful insights into the structure-conductivity relationship. By pulling out the outermost ion from the exit of the pore (Fig.3), we observed subsequent collective cooperative movements of ions, water and carbonyl groups lining the backbone of the pore. A detailed analysis of these movements lead to the development of a simple two-dimensional model of ion-water transport. Based on our molecular dynamics simulations [4, 5] we found three distinct features of the molecular mechanism.

(1) *The movements of neighboring ions and water molecules are strongly correlated.* They mostly moved in pairs or triples ("permons"). One important fact for the understanding of the efficiency of the correlated movements is that the periodicity of the potential in the selectivity filter, $\approx$ 3 Å, practically matches with the distance of the lowest Coulomb energy $U_{KW}(\Delta z)$ between one ion and one water molecule. The classical potential energy $U_{KW}(\Delta z)$ between a single ion and a single water molecule at distance Δz, consisting of Coulomb and van der Waals interactions, exhibits energy minima at characteristic distances of $\Delta z \approx 3$ Å ("bound states"). The depth of the potential depends on the orientation of the water molecule with respect to the ion.

(2) *Permons are polarized*. The absolute minimum of $U_{KW}(\Delta z) \approx 30\ k_BT$ is at distance Δz = -2.65 Å and when the oxygen of the water dipol is oriented towards the ion ("polarized bound state"). When the outermost ion exits the channel to the periplasmic side, the next neigboring ion hops to this vacancy, the ion's neighboring water molecule prefers to maintain its bound state and follows almost simultaneously the preceding ion towards the vacancy. This is the movement of a permon.

(3) *The movements of permons are rectified.* Another interesting observation from our MD simulations is that very rarely a water molecule has been observed to hop back to the vacancy and join the other ion to form a bound state. The absence of such an event is explained by the energy barrier imposed by the periodic pore potential on the water molecule. This implies that a water molecule acts as a "pawl" in a ratchet mechanism. One implication is that the transport of ion-water pairs through an ion channel is much more efficient than the transport of ions only.

In summary, the high permeation rate at which ion and water molecules pass through the KcsA ion channel is based on the cooperative hopping of pairs of ions and water molecules mediated by the flexible charged carbonyl groups lining the backbone of the channel. These observations provide the basis of an atomistic concept of the molecular mechanism of the multi-ion transport mechanism.

[1] R. P. Feynman, in *Miniaturisation*, page 282-296, ed. by H. D. Gilber, Reinhold, New York, 1961.

[2] A. Baumgaertner, in *Handbook of Theoretical and Computational Nanotechnology*, ed. by M. Rieth and W. Schommers, Am. Sci. Publ., 2006.

[3] D.A.Doyle, J. Morais-Cabral, R. A. Pfuetzner, A. Kuo, J. M. Gulbis, S .L Cohen, B. T. Chait and R. MacKinnon, Science 280, 69 (1998).

[4] J. F. Gwan and A. Baumgaertner, J. Chem. Phys. 127, 045103 (2007).

[5] J. F. Gwan and A. Baumgaertner, J. Compt. Theor. Nanoscience 4, 50 (2007).

Structure of Interacting Aggregates of Silica Nanoparticles in a Polymer Matrix as Determined from SANS

W. Pyckhout-Hintzen[1], J. Overdisse[2]

[1] IFF-5: Neutron Scattering
[2] Universite de Montpellier, Laboratoire des Colloids, Verres et Nanomateriaux, F-34095 Monpellier

Understanding the reinforcement of elastomers by colloidal nanoparticles is a prerequisite if macroscopic mechanical properties are to be tuned. We show that the three-dimensional structure of big aggregates of nanometric silica particles embedded in a soft polymeric matrix can be conveniently determined by Small Angle Neutron Scattering (SANS). A strong reinforcement seems to be related to strong interaction between aggregates, judged from the structure factor peak. The total scattering cross section is described by decomposing in a classical colloidal structure factor for aggregate interaction and an aggregate form factor. Reverse Monte Carlo techniques provided new insights in the shape of aggregates and their complex interaction in elastomers. The results compare well to fractal models for aggregate scattering limited to the dilute case.

There is an intimate relationship between microscopic structure and mechanical properties of composite materials [1]. Knowledge of both is therefore a must if one wishes to model this link and to push forward to novel materials. However, the characterization of three-dimensional structure of composites is difficult and is often derived only from two-dimensional images using Electron Microscopy techniques or Atomic Force Microscopy. Scattering by xrays or neutrons, however, is the ideal tool to access the bulk structure in a non-destructive way [2, 3]. Complementary, neutrons allow even to extract the conformation of polymeric chains inside a crosslinked composite rubber [4]. The studied nanocomposite sytems was obtained by blending aqueous colloidal suspensions of Silica (Akzo) and Nanolatex polymer beads (Rhodia). Latter core-shell type latex consists of randomly copolymerized Poly(methyl methacrylate) (PMMA) and Poly(butylacrylate) (PBuA). Films with 3 to 15% of silica were obtained after appropriate pH adjustment and subsequent slow evaporation.. SANS experiments were performed at D11 (ILL, Grenoble), yielding a scattering vector range from $0.001 < q < 0.2A^{-1}$. The pure Nanolatex showed no q-dependence as expected for a statistical copolymer.

For monodisperse, interacting silica nanospheres of volume V_{si}, the scattered intensity due to an arbitrary spatial organization can be decomposed in the product of contrast $(\Delta\rho)^2$, volume fraction of spheres Φ, the structure factor of interaction S(q) and the normalized spherical form factor, P(q) [2]. If the particles cluster into aggregates, this structure factor can be factorized into an intra-aggregate structure factor $S_{\rm intra}(q)$ and an *inter*-aggregate structure factor of the center-of-mass correlations of aggregates, $S_{\rm inter}(q)$ as

$$I(q) = \Delta\rho^2 \Phi V_{\rm si} S_{\rm inter}(q) S_{\rm intra}(q) P(q)$$

The product $S_{\rm intra}(q)$ P(q) can now be interpreted as the average form factor of aggregates $P_{\rm agg}$ [5, 6]]. Assuming monodispersity throughout will not hamper the analysis as the width of the distribution is still narrow and as it cannot be expected that this simple model will ever describe the intensity in all its facets. The focus of this work is therefore merely on the in teraction between aggregated particles and its consequences for the reinforcement process as well as the novel approach from real-space models. We will be assume that aggregates interact through an unknown potential. Technically, neither *intra-* nor *inter*-aggregate structure factor, respectively denoted $S_{\rm intra}(q)$ and $S_{\rm inter}(q)$ are known a priori, however.

We have proposed therefore a method allowing the separation of the scattered intensity in terms of $P_{\rm agg}(q)$ and $S_{\rm inter}(q)$ assuming narrowly dispersed aggregates. For the inter-aggregate structure factor we have adopted a classical model structure factor (RMSA) for simple liquids and applied routinely to repulsively interacting colloids and parametrized for our purposes [7]. The aggregate form factor, on the other hand, was analyzed first with fractal models [6] after which its modeling in direct space by Reverse Monte Carlo was implemented [7]. Latter both approaches are dealing with the aggregate structure itself i.e. basing on internal correlations of its constituents and no model for interaction whatsoever is included.

These interacting aggregates give rise to a pronounced interaction peak, pointing at the presence of a typical distance inside the nanocomposite, obtained as $2\pi/q_{\rm p}$ with $q_{\rm p}$ the peak position. Such a peak is lacking in typical filler systems due to e.g. polydispersity effects. From geometrical estimates the aggregation number of beads in the aggregate is obtained as $N_{agg} = (2\pi/q_{\rm p})^3 \Phi/V_{\rm si}$. The electrostatic

charge Q and Debye length λ_D in the used potential have now lost their initial meaning but remain valid control parameters for comparison. They basically do not depend on Φ

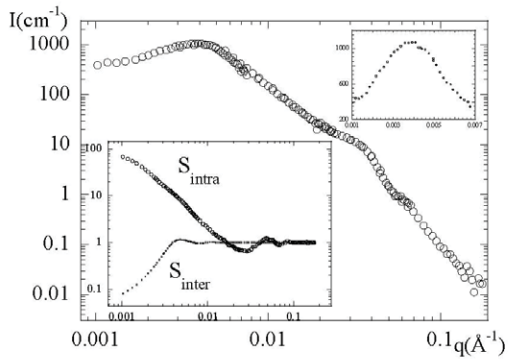

FIG. 1: SANS intensity for a silica-latex nanocomposite with Φ=5% of silica. The inset show structure factor peak and corresponding intra- and inter-contributions, basing on the primary particle structure.

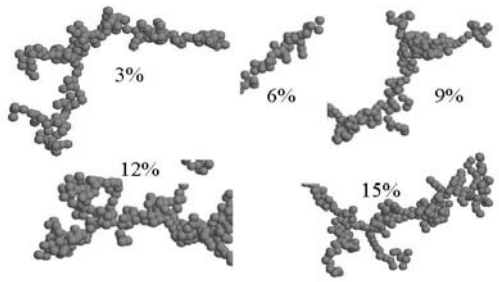

FIG. 2: Representative aggregate structures as obtained from fitting experimental SANS curves using the reverse Monte Carlo method and visualizing the growth and mass fractal dimensional as a function of silica content.

Using the classical unified approach for hierarchical scattering, basing on Guinier functions, power-law scattering at high q and cross-over functions between levels of hierarchy, the primary particle size, their aggregation number and most interestingly the mass fractal dimension result. This dimension D is around 2.0, far from a compact branched structure which has 3.0 as the mass scales with r^D . This is indicative for open, tentatively linear aggregates. A reverse Monte Carlo simulation starting from random, non-overlapping aggregates with N_{agg} beads and optimized by allowing only edge-particles to be re-located to other end positions and comparing the calculated form factor with the experimental data, leads likewise to rather elongated structures, compatible with the low mass fractal dimension. The method provided thus interesting new insights in the aggregate structure through the visualization of the aggregate as a function of Φ and of its increasing mass fractal D. It is found that aggregates overlap considerably at concentrations above 6% and therefore in our model they *mutually* interpenetrate.

The molecular picture of reinforcement which we observed is based therefore on percolation arguments of silica structures in the nanolatex matrix. This mechanical percolation had been suggested already in silica-rubber networks in which the strain dependence of aggregates and polymeric network response was studied. Here, a critical strain seemed to exist at which the compressive dimension of the aggregates commences to deviate from its isotropic state and to join up the uniaxial strain direction to follow affine displacement of beads. The architecture of the aggregates is tenuous and highly interpenetrating due to long aggregate 'ams'. Below 6% the reinforcement from comparing Young moduli relative to parent Nanolatex is moderate with $E/E_0 \sim 4$ whereas a steep increase to about 40 is obtained for Φ=15%. According to the SANS analysis this is accompanied by an increased aggregate size, a higher compactness and therefore stronger percolation links.

[1] A.I. Medalia, *Rub. Chem. Tech.*, 1974, **47**, 411

[2] Neutrons, X-ray and Light: Scattering Methods Applied to Soft Condensed Matter; P. Lindner, Th. Zemb; North Holland, 2002.

[3] J. Berriot, H. Montes, F. Martin, M. Mauger, W. Pyckhout-Hintzen, G. Meier, H. Frielinghaus *Polymer*, 2003, **44** (17), 4909

[4] A. Botti, W. Pyckhout-Hintzen, D. Richter, V. Urban, E. Straube, *J. Chem. Phys.*, 2006, **124** (17), 174908

[5] J. Teixeira, *J. Appl. Cryst.*, 1988, **21**, 781

[6] G. Beaucage, textitJ. Appl. Cryst., 1995, **28** , 717

[7] J. Oberdisse, P.Hine, W. Pyckhout-Hintzen, *Soft Matter*, 2007, **3**, 476

Tracer-Sphere Diffusion in Rod-Networks

K. Kang[1], A. Patkowski [2], J. K. G. Dhont[1]

[1] IFF-7: Soft Condensed Matter
[2] A. Mickiewics University, Poznan, Poland

Mass transport of colloidal-like particles through networks is relevant for a number of separation-, purification- and characterization techniques of macromolecular mixtures and might play a role in diffusive transport (of proteins) through crowded environments in cells. To gain in understanding on the physics that underlies the transport characteristics through such confining media, translational diffusion of tracer spheres in isotropic and nematic networks formed by long and thin colloidal rods is investigated as a function of ionic strength and rod concentration. In particular, the hydrodynamic screening length of isotropic and nematic rod-networks is determined from a newly developed theory and experimental tracer-diffusion data obtained with Fluorescence Correlation Spectroscopy (FCS).

The majority of reported tracer-diffusion experiments of spherical particles in rod networks focus on proteins in suspensions of F-actin, which are relevant for mass transport in cells. Recently, experiments on tracer diffusion of spheres in host suspensions of slender particles, other than F-actin, have been reported : nucleosome core particles in dispersions of DNA [1], colloidal spheres in solutions of "living polymers" [2] and colloidal spheres in dispersions of xanthan [3]. The host networks in these references exhibit a quite complicated dynamics by themselves. As far as we know, there are no experimental data available on tracer diffusion of colloidal spheres in the much more simple quasi-static networks consisting of relatively stiff, very long and thin rods, aside from three earlier papers of the present authors [4]-[6]. Besides experimental work, an attempt has been made in these papers to develop a microscopic theory for tracer diffusion of spheres through networks of stiff, long and thin rods, where both (screened) hydrodynamic interactions and direct interactions between the tracer sphere and the rod network are explicitly accounted for.

We use fd virus as a rod-like colloidal host particle, which is indeed a very long and thin, rather stiff rod (length $880\ nm$, thickness $7\ nm$ and persistence length $2500\ nm$), and does not exhibit polymerization/de-polymerization nor possible bundle formation (like F-actin, wormlike micelles and

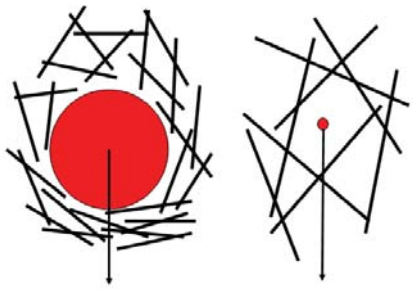

FIG. 1: The two extreme cases where (a) the tracer sphere is large compared to the mesh size of the network, and (b) where the sphere is small compared to the mesh size.

EHUT). Moreover, due to the very small van der Waals attractions between the fd-virus particles, the rod networks are stable over a wide range of salt concentrations, which offers the possibility to study diffusion in these networks as a function of the range of electrostatic interactions.

There are fundamentally different mechanisms leading to slowing down of diffusion of a tracer sphere due to the presence of a rod network, depending on whether the tracer sphere is large or small in comparison to the mesh size of the network. For *large tracer spheres*, translational motion of the tracer sphere is only possible when the network structure is severely distorted (see Fig.1a). In this case, direct interactions between the sphere and the rods is much more pronounced than hydrodynamic interactions. Tracer diffusion can then be described with the neglect of hydrodynamic interactions [4]. For *small tracer spheres*, where the sphere can move through the voids of the network without distorting the structure of the network (see Fig.1b), hydrodynamic interactions are important. Due to entanglement of the rods in the network, hydrodynamic interactions between the tracer sphere and the rods are screened. This screening is quantified by the so-called hydrodynamic screening length κ^{-1}, which measures the penetration depth of shear waves into the network. For the rod networks considered here, there is no theory available yet for the hydrodynamic screening length. Despite

the fact that the network structure remains essentially unchanged during the diffusive motion of such a small sphere, there is nevertheless a distortion of the pair-correlation function between the sphere and the rods. This distortion is due to the fact that, when the sphere moves past a rod, the probability to find the sphere on the side-of-approach of the rod is larger than that on the "shadow side" of the rod. The rod-sphere pair-correlation function is therefore distorted, giving rise to a force on the sphere that affects its diffusive motion. We referred to the distortion of the pair-correlation function in ref.[5] as "the shadowing effect". The shadowing contribution is not only determined by hard-core interactions, but also by charge-charge interactions in case the rods and the sphere carry surface charges. The importance of the shadowing effect relative to hydrodynamic interactions can thus be varied systematically by changing the electrostatic screening length through variation of the ionic strength of the rod suspensions [6].

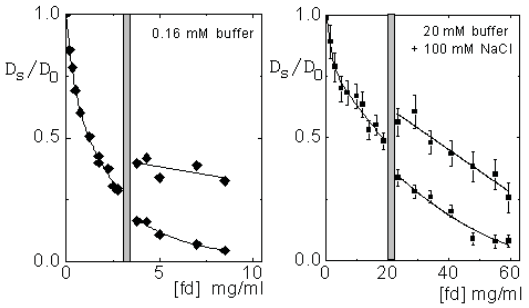

FIG. 2: Long-time self diffusion coefficients of apoferritin in fd-virus particle suspensions for two ionic strengths. (a) TRIS-buffer concentration of $0.16\ mM$ (from ref.[6]) and (b) $20\ mM$ plus $100\ mM$ added $NaCl$ (from ref.[5]). The vertical grey bars indicate the two-phase, isotropic-nematic coexistence region.

Tracer diffusion constants of apoferritin in fd-virus suspensions were measured with Fluorescence Correlation Spectroscopy (FCS). Since fd-virus particles fluoresce to some extent, the resulting contribution to the correlation function must be subtracted [5]. The creation of mono-domain nematics through alignment in a magnetic field and the measurement of orientational order parameters of the nematic samples is discussed in that reference.

In Fig.2 the measured diffusion coefficients are plotted as a function of fd-concentration for two analytical TRIS/HCl-buffer concentrations that are used ($0.16\ mM$, and $20.0\ mM$ plus $100\ mM\ NaCl$). As can be seen, there is a strong effect of the ionic strength on the diffusive behaviour of apoferritin.

The way to extract hydrodynamic screening lengths from the diffusion data, based on the newly developed theory, is extensively discussed in ref.[6].

The hydrodynamic screening length as a function of the fd-concentration for isotropic networks is shown

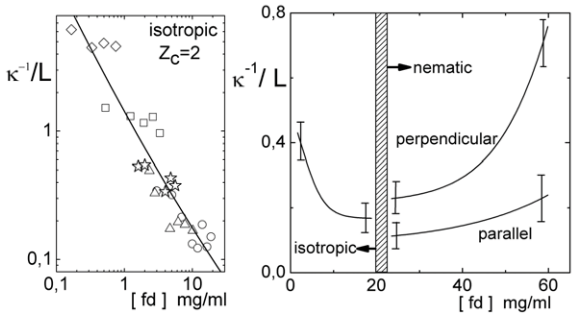

FIG. 3: (a) The hydrodynamic screening length κ^{-1} in units of the rod length L for the isotropic state versus the fd-concentration. The symbols refer to the different buffer concentrations : $c_T = 0.16\ mM$ ◇, $0.80\ mM$ ☆, $4.00\ mM$ △, $20.0\ mM$ ◯, $20\ mM + 100\ mM\ NaCl$ □. (b) The screening length for the highest buffer concentration and $100\ mM$ added salt in the isotropic and the nematic phase versus the fd-concentration.

in Fig.3a. The screening length κ^{-1} for various ionic strengths scale onto a single master curve, and decreases with increasing fd-concentration, as expected. The hydrodynamic screening lengths for the nematic phase are given in Fig.3b. Here, the distinction between directions perpendicular and parallel to the nematic director should be made. Surprisingly, the hydrodynamic screening length increases with increasing fd-concentration in the nematic state. This is probably due to the increasing degree of alignment of the rods with increasing concentration. It thus seems that the hydrodynamic properties of nematic networks is highly sensitive on the orientational degree of order. This is confirmed from measurements of κ^{-1} at a fixed fd-concentration but different orientational order parameter through the variation of ionic strength [6].

[1] S. Mangenot, S. Keller, J. Rädler, Biophys. J. **85**, 1817 (2003).

[2] J. van der Gucht, N.A.M. Besseling, W. Knoben, L. Bouteiller, M.A. Cohen Stuart, Phys. Rev. E **67**, 051106 (2003).

[3] G.H. Koenderink, S. Sacanna, D.G.A. Aarts, A.P. Philipse, Phys. Rev. E **69** (2004) 021804.

[4] K. Kang, J. Gapinski, M.P. Lettinga, J. Buitenhuis, G. Meier, M. Ratajczyk, J.K.G. Dhont, A. Patkowski, J. Chem. Phys. **122**, 044905 (2005).

[5] K. Kang, A. Wilk, J. Buitenhuis, A. Patkowski, J.K.G. Dhont, J. Chem. Phys. **124**, 044907 (2006).

[6] K. Kang, A. Wilk, A. Patkowski, J.K.G. Dhont, J. Chem. Phys. **126**, 214501 (2007).

Red Blood Cells: Fluctuations of Coupled Fluid and Solid Membranes

Th. Auth[1,2], S. A. Safran[2], N. S. Gov[3]

[1] IFF-2: Theoretical Soft-Matter and Biophysics
[2] Weizmann Institute of Science, Department of Materials and Interfaces, Rehovot 76100, Israel
[3] Weizmann Institute of Science, Department of Chemical Physics, Rehovot 76100, Israel

The cell membrane of red blood cells consists of the lipid bilayer with a sparsely attached, two-dimensional cytoskeleton of flexible polymers. The intriguing properties of the red blood cell — its shape, fluctuations, long lifetime in the vascular system, and flexibility when it squeezes through narrow capillaries — are determined only by the cell membrane. Fluctuation experiments follow the motion of the lipid bilayer, but are not capable of simultaneously monitoring the cytoskeleton. The aim of our model is to improve the theoretical understanding of the composite membrane and to relate this understanding to the experimental measurements.

Depending on the available energy that is present in the cell in form of ATP molecules, red blood cells change their shape. The normal shape of the red blood cell is biconcave, discocytic. Cells with less ATP have a spiculated, echinocytic shape and cells with more ATP have a cup-like, stomatocytic shape. Also the fluctuation properties of the membrane differ for different states of the cell. We propose a model of a fluid membrane (the lipid bilayer) interacting with a solid membrane (the cytoskeleton) that improves the theoretical understanding of the composite cell membrane [2], see Fig. 1. The theoretical description of planar, isolated fluid and solid membranes is well known and confirmed by experiment and simulation. However, single surface models with homogeneous elastic properties are not capable of describing the entire range of the experimental fluctuation spectrum of the red blood cell [1]. The fluctuations of a fluid membrane adjacent to a solid membrane has, to our knowledge, not yet been studied theoretically.

Experiments have determined that the thickness of the cytoskeleton is $\approx 60\,\mathrm{nm}$. Our coupled membrane model accounts for the finite average spacing, d, between the fluid and the solid membrane that are described by the height fields above a reference plane, $\boldsymbol{\rho} = (x, y)$, $h_1(\boldsymbol{\rho})$ and $h_2(\boldsymbol{\rho})$. The elastic properties of the isolated membranes are given by their bending moduli, κ_1 and κ_2. Both membranes interact by a contact interaction with interaction constant, v_0. The coupling by the homogeneous pressure, p_e, instead of the discrete anchor complexes in the real cell, is a simplification that allows us to study the system using a continuum theory.

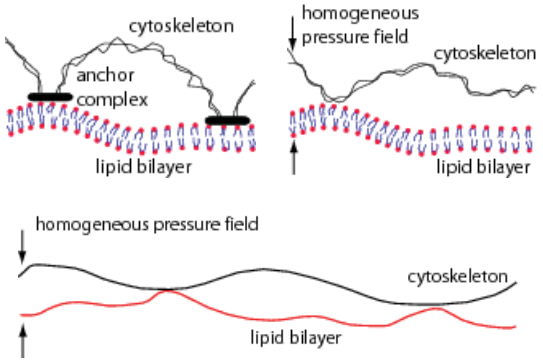

FIG. 1: Different levels of abstraction for the red blood cell membrane: (a) The cytoskeleton of flexible polymers is attached with protein complexes to the lipid bilayer. (b) A homogeneous pressure maintains the average thickness of the cytoskeleton. (c) Bilayer and cytoskeleton are modeled by surfaces with a bending and a shear modulus respectively. They interact via excluded volume and are maintained at fixed distance by a homogeneous pressure.

The Hamiltonian of the system is

$$\mathcal{H} = \int d\boldsymbol{\rho} \Big\{ 2\kappa_1 H_1^2(\boldsymbol{\rho}) + 2\kappa_2 H_2^2(\boldsymbol{\rho}) + v_0\,\delta\left(\Delta h(\boldsymbol{\rho}) - d\right) + p_e\left(\Delta h(\boldsymbol{\rho})\right) \Big\}, \quad (1)$$

with the mean curvatures, $H_i(\boldsymbol{\rho}) = (1/2)\nabla^2 h_i(\boldsymbol{\rho})$, and $\Delta h(\boldsymbol{\rho}) = h_2(\boldsymbol{\rho}) - h_1(\boldsymbol{\rho})$. For the wavevector-dependent effective bending rigidity of the cytoskeleton, $\kappa_2(q)$, the theory of polymerized membranes is used.

The Hamiltonian in Eq. (1) is evaluated in Fourier space by minimization of the free energy using a model Hamiltonian. For weak coupling, both membranes are fluctuating independently from each other. For strong coupling, both membranes fluctuate as if they were a single surface with the sum of both bending moduli, $\kappa_1 + \kappa_2(q)$. In general, whether one is in the weak and strong coupling regime depends on the wavevector, q. For small fluctuation amplitudes, $h(q)$, at large wavevectors, the coupling between both membranes is weak. For large fluctuation amplitudes at small wavevectors, both membranes are strongly coupled. For the red blood cell, we find that the bilayer and cytoskeleton are strongly coupled for fluctuations with wavelengths, $\lambda > 300 - 400\,\mathrm{nm}$.

In particular, our model suggests that for fluctuations with wavelengths that are accessible with present experimental techniques [4, 5], $\lambda > 500\,\mathrm{nm}$, the use of a single-surface model for the composite red blood cell membrane is justified and the more complex and discrete structure of the cell membrane is not important. We expect the sparse coupling between bilayer and cytoskeleton (and the holes in the cytoskeleton mesh), which are not included in our model, to be important for wavelengths of the order of and smaller than the twice the anchor distance, $a \approx 60 - 100\,\mathrm{nm}$. In Ref. [3], we calculate the average membrane deformation due to the pressure that is exerted by the network of flexible spectrin polymers, which is on the lengthscale of the mesh size of the cytoskeleton.

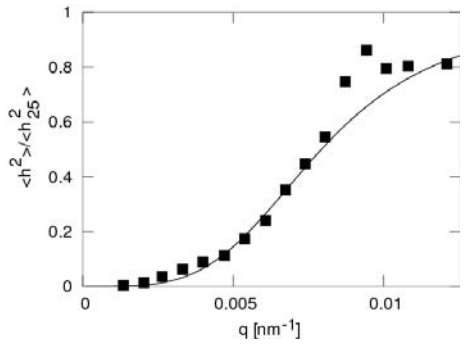

FIG. 2: Experimental fluctuation data [5] for an echinocyte (normalized by the fluctuation amplitudes of a membrane with $\kappa = 25\,k_BT$) and fit with the coupled membrane model.

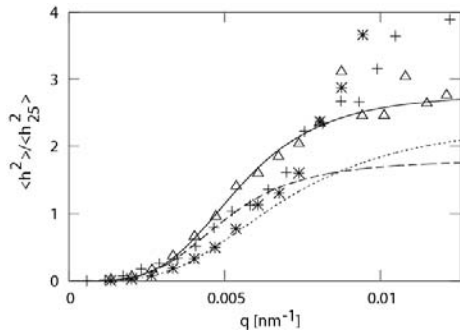

FIG. 3: Normalized experimental fluctuation data [4, 5] and fits with the coupled membrane model for two discocytes (crosses, stars, dashed and dotted lines) and a stomatocyte (triangles and solid line).

The comparison of the coupled membrane model with experimental fluctuation data for an echinocytic cell in Fig. 2 shows that the spectrum is well reproduced for all wavevectors. In Fig. 3, the fluctuation data of the stomatocyte is well fit for the entire range of wavevectors and the data for discocytes if well fit at small q. The failure of the model at large q for discocytes is no surprise, because we found that in this regime bilayer and cytoskeleton fluctuate in a strongly coupled manner. The fluctuations can be described by a single surface with an effective bending rigidity, $\kappa + \alpha(\kappa, \mu)q^{-2} + \beta(\mu)q^{-4}$. The two fit parameters are the bending rigidity of the lipid bilayer, κ, and the shear modulus of the cytoskeleton, μ. The coupled membrane model is thus equivalent to the previous phenomenological, one-surface model in Ref. [1], which also does not describe the entire fluctuation spectrum with a single set of elastic constants. This suggests that both models are still incomplete.

A naive fit of the data that does not account for the membrane activity due to ATP yields: $\kappa = 25\,k_BT$ and $\mu = 6 \times 10^{-3}\,k_BT\mathrm{nm}^{-2}$ for an echinocyte, $\kappa = 14\,k_BT$ and $\mu = 7 \times 10^{-3}\,k_BT\mathrm{nm}^{-2}$ for a discocyte, and $\kappa = 9\,k_BT$ and $\mu = 3 \times 10^{-3}\,k_BT\mathrm{nm}^{-2}$ for a stomatocyte. The values of the elastic constants are of the order of values that have been found in other experiments. An exact comparison with literature values is not possible, because the elastic constants probably to differ for individual cells, they depend on the experimental conditions (e. g. the buffer solution in which the cells are suspended, the time that these cells have spent in the buffer, etc.) However, a clear trend for the bending rigidities is observed. The echinocyte has the largest and the stomatocyte the smallest bending rigidity. This finding might be interpreted by different membrane elastic properties, i. e. by a more floppy lipid bilayer of the stomatocyte. This finding can also be interpreted as indicative of active, ATP-driven fluctuations that provide an additional source for membrane fluctuations above and beyond those that are thermally driven. Using a phenomenological model of an effective, higher temperature, T_{eff}, to account for the active fluctuations and the same bending rigidity, $\kappa = 25\,k_BT$, for all cells, $T_{\mathrm{eff}} \approx 2 - 3\,T$ is found for discocytes and stomatocytes compared with the echinocyte.

We have studied the fluctuations of the red blood cell membrane using a model for coupled fluctuations of a fluid and a solid membrane with a fixed average spacing. The theory of the polymerized membranes allows us to extract membrane elastic coefficients from the experimental spectra. We identified a trend in the fluctuation behavior that is consistent with the shape changes of the red blood cell. Further research includes the complete description of the discocyte fluctuations as well as the identification of the mechanism for our suggestion of possibly ATP-driven fluctuations.

[1] N. Gov, A. G. Zilman, and S. Safran, Phys. Rev. Lett. **90**, 228101 (2003).

[2] T. Auth, S. A. Safran, and N. S. Gov, Phys. Rev. E **76**, 051910 (2007).

[3] T. Auth, S. A. Safran, and N. S. Gov, New J. Phys. **9**, 430 (2007).

[4] G. Popescu *et al.*, Phys. Rev. Lett. **97**, 218101 (2006).

[5] A. Zilker, H. Engelhardt, and E. Sackmann, J. Phys. (France) **48**, 2139 (1987).

Dynamics of Glass-Forming Materials in Nanoscopic Confinement

R. Zorn[1], M. Mayorova[1], D. Richter[1], A. Schönhals[2], B. Frick[3]

[1] IFF-5: Neutron Scattering
[2] Federal Institute for Materials Research and Testing, D-12205 Berlin, Germany
[3] Institut Laue-Langevin, F-38042 Grenoble, France

The aim of the work reported here is to study the influence of spatial restriction on the microscopic dynamics related to the glass transition. Results can be helpful for the detection of a currently speculated cooperativity length of the glass transition. The confining matrices used in this study were 'hard' (silica glass, silicon) or 'soft' (microemulsion droplets). Except for the soft confinement the naïvely expected acceleration effect could not be found at the high temperatures where inelastic neutron scattering (INS) experiments are usually done. A clear effect of confinement could be observed for the glass-typical low energy vibrations (boson peak). This effect seems to be completely different for soft and hard confinement. Surprisingly, experiments on oriented nanopores did not show any signs of an anisotropy of the dynamics.

The influence of spatial confinement on the dynamics of liquids is of wide interest, both for application and for fundamental understanding. In the quest for a possible cooperativity length which might underly the physics of glass formation it seems attractive to study glass-forming systems in confinement. Specifically, one would expect an *acceleration* of dynamics in confinement due to the truncation of the cooperativity length. This subject of interest has motivated many experiments on low molecular and polymeric glass-forming systems spatially confined e.g. within pores or films [1].

Inelastic neutron scattering (INS) plays an important rôle in the observation of the dynamics in confined liquids. Firstly, the dynamics is detected on a true microscopic length scale (Å to nm). This means that the molecular mechanism of a motion can be directly observed and not via a macroscopic quantity. Also important thermodynamic quantities as the vibrational density of states (VDOS) can be measured directly by INS.

Secondly, a technical advantage of neutron scattering (NS) is that it is isotope sensitive. In organic materials one can utilise the high incoherent NS cross section of hydrogen nuclei. Replacing hydrogen by deuterium in the confining matrix reduces unwanted scattering.

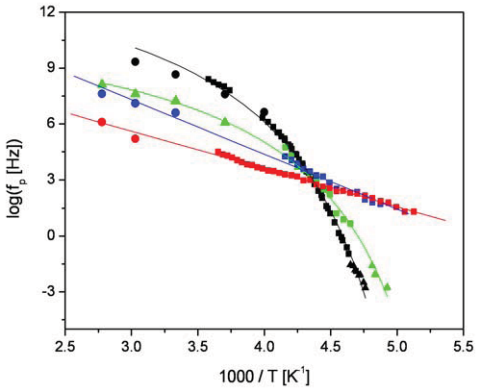

FIG. 1: Map of the reciprocal characteristic time of the α relaxation in confined and bulk PMPS. The circles are from inelastic neutron scattering, the squares from dielectric spectroscopy, and the triangles from thermal spectroscopy. Confinement sizes: 2.5 nm (red), 5.0 nm (blue), 7.5 nm (green), and bulk (black). From [4].

We have performed experiments using nanoporous solids which constitute a rigid ('hard') confinement as well as flexible interfaces ('soft confinement') [2, 3].

Fig. 1 shows typical results for a glass-forming polymer, polymethylphenylsiloxane (PMPS), confined in nanoporous silica glass (Gelsil). INS spectra were measured and fitted by a stretched exponential. An effective characteristic time was extracted in order to allow the comparison with other spectroscopic methods [4]. Fig. 1 shows a relaxation map of the INS data together with data from dielectric and thermal spectroscopy. It can be seen that all three methods fit well together. For confinement of 5 nm and smaller the usual Vogel-Fulcher temperature dependence (curved in this plot) turns into an Arrhenius (straight lines). This is what is expected from theories involving a 'cooperativity length' and what is often found in the experiment. Here, this leads to a crossover of time scales at 230 K/1 kHz. This explains the apparent contradiction that methods as INS which work at high temperatures and short time scales report a slowing-down while methods for longer relaxation times report an acceleration of the dynamics on the same system.

It can be argued that the slowing down in the high temperature range is caused by the rigid walls of the

confinement used here. Therefore, it was suggested to use a 'soft' confinement constituted by microemulsion droplets [5].

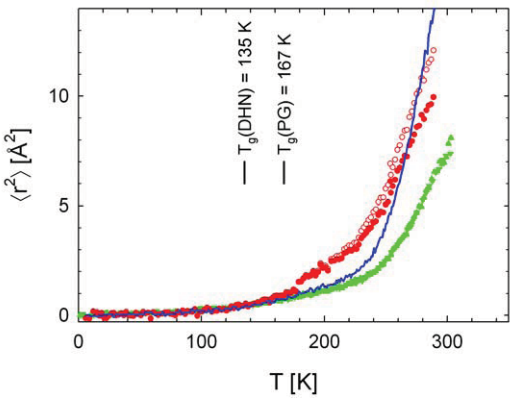

FIG. 2: Mean-square displacements of propyleneglycol in bulk (blue line), soft confinement (red circles), and hard confinement (green triangles). For the soft confinement two variants of the data evaluation are included: without correction of droplet diffusion (empty) and with the maximal allowed correction (filled). Note that there are two runs included for the hard confinement: The upwards pointing triangles correspond to the scattering vector perpendicular to the pores, the downwards pointing to the parallel orientation.

Fig. 2 shows the molecular mean-square displacement of propyleneglycol confined in a microemulsion with 1.7 nm droplet size. It has to be taken into account that for such small objects the droplet diffusion may influence the result. This leads to the indicated uncertainty. Nevertheless, it can be seen without doubt that the dynamics clearly leads to a larger MSD over a large temperature range. Only for temperatures > 270 K this difference seems to revert. This stands in contrast to the data from hard confinement (nanoporous silicon, 4.7 nm diameter) displayed in the same plot.

As an aside we note that the nanopores in silicon were *oriented* so that the anisotropy of the dynamics could be studied. As can be seen from Fig. 2 no orientational difference could be detected.

Apart from the effects on the α relaxation the other ubiquitous finding from INS is a confinement effect on the low frequency vibrational modes in glasses. In the frequency range $\nu = 0.3 \ldots 2$ THz glasses show an excess of the vibrational density of states (VDOS) $g(\omega)$ with respect to what is expected from the Debye model of sound waves, namely $g(\omega) \propto \omega^2$. Because $S(Q,\omega) \propto g(\omega)/\omega^2$ in the one-phonon approximation, this excess is visible as a peak in INS spectra, the so-called boson peak (BP).

Fig. 3 compares the VDOS for PG in bulk, soft and hard confinement. In hard confinement there is a more pronounced cut-off of the BP towards low frequencies. This is the usual finding reported in the literature. In contrast, *soft* confinement has a completely opposite effect. This is insofar surprising as at the temperature of 100 K both components of the microemulsion are vitrified, thus 'hard' in the colloquial sense.

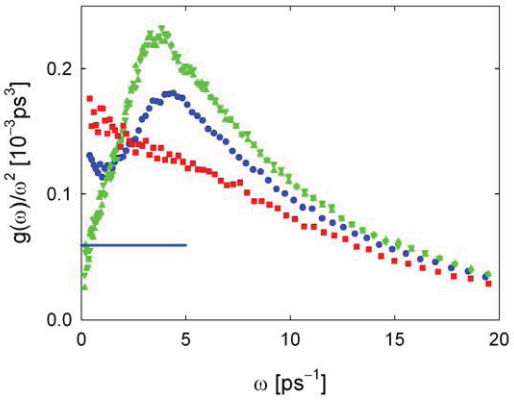

FIG. 3: Vibrational density of states at 100 K of bulk propyleneglycol (blue circles), PG in soft confinement (red squares), and in nanoporous silicon (green triangles). The upwards pointing triangles correspond to the scattering vector perpendicular to the pores, the downwards pointing to the parallel orientation. The blue line indicates the level expected from sound waves in the Debye model.

Comparing the results it becomes clear that the crucial question of confined glassy dynamics—faster or slower?—cannot be answered in a universal way. The answer depends on the system studied, the temperature, and the spectroscopic method used. In general, at low temperatures dynamics is accelerated while it is decelerated at high temperatures. This may be the result of a genuine confinement effect modified by a surface-induced slowing-down. In this respect, the crucial experiment is done here using 'soft' confinement in microemulsion droplets. As expected, the surface effect is less important there shifting the faster-slower cross-over to much higher temperature. We also observe an opposite influence of the soft confinement on the low frequency vibrational spectrum (boson peak) compared to the hard. This may be due to more similar elastic constants of confined and confining media in these systems. Finally, experiments with oriented pores show no anisotropy of the dynamics, neither for the α relaxation nor the vibrations.

[1] References in *J. Phys. IV France* **10** (2000) edited by B. Frick, R. Zorn, and H. Büttner; *Eur. Phys. J. E* **12** (2003) edited by B. Frick, M. Koza, and R. Zorn; *Eur. Phys. J. ST* **141** (2007) edited by B. Frick, M. Koza, and R. Zorn.

[2] R. Zorn, M. Mayorova, B. Frick, and D. Richter, *Soft Matter*, DOI:10.1039/B713465G (2008).

[3] R. Zorn, M. Mayorova, D. Richter, A. Schönhals, L. Hartmann, F. Kremer, and B. Frick, submitted to *AIP Conf. Proc.* (2008).

[4] A. Schönhals, H. Goering, Ch. Schick, B. Frick, M. Mayorova, and R. Zorn, *Eur. Phys. J. ST* **141**, 255 (2007).

[5] Li-Min Wang, Fang He, and R. Richert, *Phys. Rev. Lett.* **92**, 95701 (2004).

On the Interpretation of Dielectric Data in Molecular Glass Formers

U. Buchenau, M. Ohl, A. Wischnewski

IFF-5: Neutron Scattering

Glass formers are liquids which on cooling form amorphous solids, i.e. glasses, rather than ordered crystals. This class of condensed matter encompasses many different species, like polymers and metals. In molecular glass formers, the molecular orientation freezes at the glass transition. In the liquid, one finds the broad α-peak in dielectric measurements, related to the flow process, shifting rapidly to longer relaxation times with lower temperature. Although known for decades and observed in a huge number of glass formers, the nature of the underlying process of this α-peak is still not fully understood.

Literature dielectric data of glycerol, propylene carbonate, ortho-terphenyl (OTP) and salol show that the measured dielectric relaxation is a decade faster than the Debye expectation, but still a decade slower than the breakdown of the shear modulus. From a comparison of time scales, the dielectric relaxation seems to be due to a process which relaxes not only the molecular orientation, but the entropy, the short-range order and the density as well. The physical nature of this process is object of this article.

Broadband dielectric spectroscopy has developed into the most important tool for the study of glass formers [1]. It is able to cover the whole relevant frequency range, from μHz to THz. Therefore it would be very desirable to understand the dielectric susceptibility in terms of physical processes. In particular, one would like to link the α-peak of the dielectric data to the disappearance of the shear modulus at long times, the essence of the flow process.

Such a link is in principle provided by the DiMarzio-Bishop [2] extension of Debye's treatment. The extension considers the molecule as a small sphere with a hydrodynamic radius r_H immersed in a viscoelastic liquid. The liquid has a frequency-dependent complex shear modulus, with the viscosity η as low frequency limit and the infinite frequency shear modulus G as high frequency limit. Their ratio $\tau_{\rm Maxwell} = \eta/G$ is the famous Maxwell time, at which the elastic solid begins to flow.

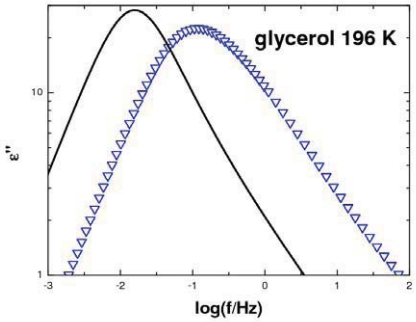

FIG. 1: DiMarzio-Bishop [2] extension of Debye's concept (continuous line) compared to dielectric loss data ϵ'' (symbols, references given in [3]) of glycerol at 196 K.

If one has both the viscosity and the hydrodynamic radius (it can be taken from diffusion data), one can calculate the dielectric relaxation time from the Debye relation:

$$\tau_{\rm Debye} = \frac{4\pi\eta r_H^3}{k_{\rm B}T}$$

with $k_{\rm B}$, Boltzmann constant and T, temperature. However, measurements in many molecular liquids revealed decades ago that the Debye relation tends to give about ten times longer dielectric relaxation times than experiment. The experimental value, though still a factor of 2 to 15 longer than the Maxwell time, is much too small to obey the Debye relation.

Fig. 1 shows dielectric data of the most heavily studied substance of all, glycerol. The data are compared to the DiMarzio-Bishop extension of the Debye concept as described above. The molecular radius r_H can be determined from NMR field gradient diffusion data (r_H = 0.16 nm) via Stokes-Einstein equation, the viscosity from a shear modulus measurement (both references in [3]). The complex shear modulus measurement was done at 196 K. Having r_H and the shear modulus the DiMarzio-Bishop formalism allows to calculate ϵ'' at the same temperature. This is the continuous line in fig. 1. The calculation underestimates the peak frequency in the dielectric loss function by an order of magnitude. Obviously, there is a

much faster molecular reorientation process than the one envisaged by Debye.

In order to learn more about this process, we have studied the relation between the dielectric relaxation constant and the ones found by other techniques.

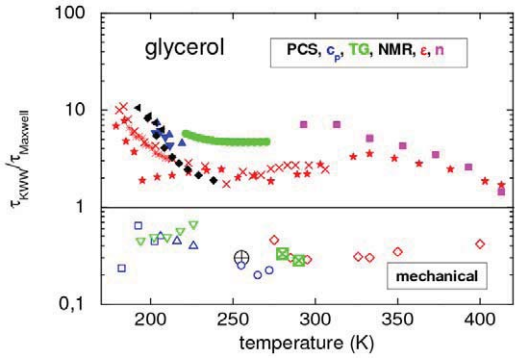

FIG. 2: Kohlrausch-Williams-Watts (KWW) relaxation times in glycerol, normalized to the Maxwell time as described in the text. Open symbols in the lower part show mechnanical data: blue squares shear; blue up triangles shear; green down triangles compression; blue circles longitudinal acoustic; circle with plus shear and compression; green squares with cross transient grating; red diamonds longitudinal Brillouin; full symbols in the upper part: red stars, crosses and asterisks dielectric; blue up triangles and down triangles heat capacity; black left triangles NMR; black diamonds photon correlation spectroscopy; green circles transient grating; magenta squares neutron spin-echo. Note that the transient grating experiment supplies a structural relaxation time as well as the damping of longitudinal ultrasonic waves. References given in [3].

Fig. 2 shows this comparison for glycerol [3]. In order to get rid of the extremely strong temperature dependence of the relaxation times (in particular close to the glass temperature of about 187 K), we plot the ratio of the measured relaxation time τ_{KWW} to the Maxwell time. τ_{KWW} was taken from a fit of the data with the Kohlrausch relaxation function:

$$\phi(t) = \exp -(\frac{t}{\tau_{\mathrm{KWW}}})^{\beta}$$

Here, β is the stretching exponent, typically values between 0.4 and 0.6 are found. Note that this time changes from hours at the lowest temperature to a picosecond at the highest, where the relaxation time begins to approach the vibrational time scale. For a shear modulus following this Kohlrausch function one expects:

$$\frac{\tau_{\mathrm{KWW}}}{\tau_{\mathrm{Maxwell}}} = \frac{\beta}{\Gamma(\beta)}$$

For glycerol with $\beta = 0.45$ this ratio is 0.4, i.e. the mechanical data as shown in fig. 2 all lie precisely where one expects them following the preceding equation, namely a factor of 2.5 lower than the Maxwell time. The dielectric data lie about a decade higher, together with NMR, heat capacity, neutron spin echo and several other techniques.

It is surprising to see only little variation in these ratios, though one goes from a long-lived solid to a liquid with a water-like viscosity. Our finding in Fig. 2 extends earlier results [4] to the domain above the melting temperature, where liquid theories apply. The result was corroborated for three other well-studied molecular substances, ortho-terphenyl, propylene carbonate and salol [5].

The central question is: What is the physical nature of this process? Though we are as unable as anybody else to give a satisfactory answer, Fig. 2 gives several helpful hints. It seems to be essentially the same process at all temperatures, uninfluenced by the dramatic change in time scale. It happens after the breakdown of the shear modulus. The good agreement between dielectric and neutron spin echo data at the first sharp diffraction peak indicates that the decay mechanism of the molecular orientation might be identical with the one of the short range packing order of the molecules (this important result holds for both glycerol and OTP). This supports our conclusion that the underlying physical process is different from the Debye mechanism. The Debye mechanism does not imply a decay of the molecular packing and does in fact predict much too long relaxation times. Something else seems to happen before the Debye mechanism sets in.

[1] U. Schneider, P. Lunkenheimer, R. Brand and A. Loidl, J. Non-Cryst. Solids **235-237**, 173 (1998)

[2] E. A. DiMarzio and M. Bishop, J. Chem. Phys. **60**, 3802 (1974)

[3] U. Buchenau, M. Ohl and A. Wischnewski, J. Chem. Phys. **124**, 094505 (2006)

[4] K. Schröter and E. Donth, J. Non-Cryst. Solids **307-310**, 270 (2002)

[5] U. Buchenau, R. Zorn, M. Ohl and A. Wischnewski, Phil. Mag. **87**, 389 (2007)

Synthesis of Hydrophobic Polyalkylene Oxides and Amphiphilic Polyalkylene Oxide

J. Allgaier
IFF-5: Neutron Scattering

The anionic ring-opening polymerization of alkylene oxides, except ethylene oxide, is accompanied by strong side reactions, leading to large amounts of by-products. In this work we investigated the anionic polymerization of hydrophobic alkylene oxides at different temperatures, solvents and initiating systems [1]. For polymers synthesized above room temperature significant amounts of by-products were found. With the help of crown ethers temperature could be reduced to -23 °C. This measure allowed eliminating by-products almost completely in the synthesis of poly(1,2-butylene oxide), poly(1,2-hexylene oxide), and poly(1,2-octylene oxide). Furthermore the method was employed to synthesize amphiphilic block copolymers of the hydrophobic polyalkylene oxides with polyethylene oxide as the hydrophilic moiety. The new synthetic method is generally of interest due to the rheological and dielectric properties of the polymers and the possibility to tune amphiphilicity of the amphiphilic block copolymers.

In contrast to the limited availability of the higher members, the polyalkylene oxide family offers interesting possibilities with respect to their rheological properties due to the systematic variability of the polymer chain diameters. Because of the dipole moment along the chain PAO represents an alternative to the widely used polyisoprene for dielectric measurements. In addition, by combining PEO with the other PAO, the amphiphilicity of the resulting block copolymers can be varied systematically. In contrast to most other block copolymers the hydrophobic moieties in the PAO block copolymers are soluble in a large variety of oils, making them ideal candidates as additives in microemulsion systems. The lowest members of the polyalkylene oxide (PAO) family, polyethylene oxide (PEO) and polypropylene oxide (PPO), are known for a long time. The most widely employed technique for the polymerization of alkylene oxides is anionic ring-opening polymerization using sodium or potassium alcoholates as initiators. This technique allows to polymerize ethylene oxide (EO) basically free of side reactions. For the polymerization of propylene oxide (PO) strong side reactions are present. The reason for the side reactions is the relatively high acidity of the methyl protons of PO leading to different types of termination and chain transfer reactions. As a result high and low molecular weight by-products are formed [2],[3]. In the older literature, there are reports dealing with the synthesis of the higher and more hydrophobic PAO than PPO. Poly(1,2-butylene oxide) (PBO), poly(1,2-hexylene oxide) (PHO), poly(1,2-octylene oxide) (POO) and even higher PAO were obtained by polymerizing the corresponding monomers with zinc organic catalysts [4],[5],[6]. This technique, however, yields polymers with broad MWD and does not allow producing block copolymers. Scheme 1 illustrates the chemical structures of some polyalkylene oxides and the corresponding monomers.

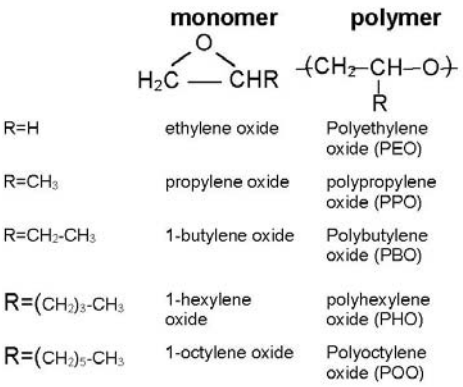

FIG. 1: Structures of different alkylene oxide monomers and polymers.

In a first series of experiments butene oxide was polymerized at different temperatures and using different solvents and initiators. The target molecular weight, defined by the amounts of monomer and initiator introduced into the reactor, was 15,000. The SEC trace of sample PBO-1 is given in Figure 1. In this experiment potassium tert.-butanolate (KOt-Bu) was used as initiator at 80 °C and toluene was chosen as an inert solvent. Beside the main peak the signal contains a low molecular weight tailing and a high molecular weight shoulder at higher and lower elution volumes. In agreement with this result the molecular weight distribution is elevated and the measured molecular weight is about 25% smaller than the calculated molecular weight, obtained from the amounts of initiator and polymerized monomer. In further exper-

iments other alkali metal initioators and more polar aprotic solvents were tested in order to reduce the polymerization temperature without reducing reactivity and extending the polymerization time too much. This measure was successful insofar the by-product content could be reduced. However, at 40 °C still significant amounts of by-product were present and at lower temperatures polymerization was extremely slow.

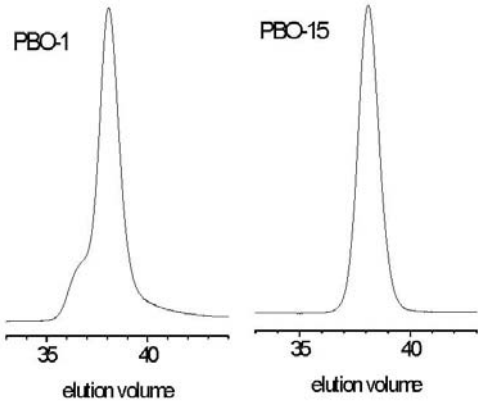

FIG. 2: SEC refractive index signals of PBO samples, polymerized without crown ether at 80 °C in toluene (PBO-1) and with crown ether at -20 °C in toluene (PBO-15).

Therefore a different strategy was chosen based on crown ethers. These additives are strong complexing agents for alkali metal ions. Especially in less polar solvents they increase the degree of ion-pair separation. In case of alkylene oxide polymerization this leads to increasing reactivities and polymerization rates. In our case it was possible to reduce the polymerization temperature considerably below room temperature. Because of the reduced level of by-products already achieved without crown ethers, the target molecular weight was increased from 15,000 to 50,000. This measure generally increases the relative fraction of by-products and helps to get a clearer picture about improvements of the product quality. Again different alkali metal initiators in combination with different crown ethers were tested. It turned out that KOt-Bu together with the crown ether 18C6 was the best combination. Using this system the polymerization temperature could be reduced below -20 °C and within experimental error no by-product could be detected (see Figure 1, sample PBO-15). The more hydrophobic monomers hexene oxide and octene oxide could be polymerized under similar conditions as butene oxide. However it was necessary to purify those monomers by careful fractional distillation due to the lower purity of the commercial raw material compared to butene oxide. With this additional measure molecular weight of 50,000 to 100,000 could be obtained without significant by-product content and low molecular weight distributions.

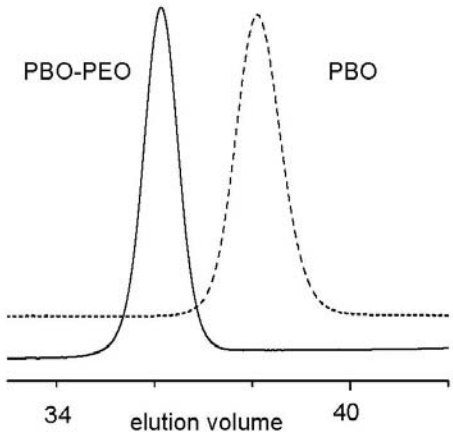

FIG. 3: SEC refractive index signals of a PBO-PEO block copolymer and the corresponding PBO homopolymer with block molecular weights of approximately 10,000.

A-B block copolymers containing PBO, PHO, and POO as hydrophobic blocks and PEO as hydrophilic block were produced using the polymerization techniques described before. This technique allows to synthesize the block copolymers by successively polymerizing the hydrophobic alkylene oxide and EO in a one-pot-reaction. Within experimental error the calculated compositions and the measured ones were similar. The small values of M_w/M_n indicateed narrowly distributed polymers. As an example the SEC trace of a PBO-PEO block copolymer having block molecular weights of 10,000 is given in Figure 2. It shows a symmetrical signal. At higher elution times there is no hint for homopolymer. Even block copolymers having block molecular weights of 50,000 were basically free of homopolymer. This again underlines that the new low-temperature method using crown ethers yields model polymers of high structural quality.

[1] Allgaier, J.; Willbold, S.; Chang, T. *Macromolecules*, **2007**, 40, 518.

[2] Bailey, F. E., Koleske, J. V. In *Alkylene oxides and their polymers, Surfactant Science Series*; Schick, M. J., Frederick, M. F., Eds.; Marcel Dekker: New York, 1991; Vol. 35, Chapter 4.

[3] Whitmarsh R. H. In *Nonionic Surfactants - Polyoxyalkylene Block Copolymers, Surfactant Science Series*; Nace, V. M., Ed.; Marcel Dekker: New York, 1996; Vol. 60, Chapter 1.

[4] Lal, J. *J. Polym. Sci. A-1* **1966**, 4.

[5] Lal, J. *J. Polym. Sci. B* **1967**, 5, 793.

[6] Booth, C.; Orme, R. *Polymer* **1970**, 11, 626.

Nucleation and Growth of $CaCO_3$ Mediated by the Egg-White Protein Ovalbumin

V. Pipich[1], M. Balz[2], S. E. Wolf[2], W. Tremel[2], D. Schwahn[1]

[1] IFF-5: Neutron Scattering
[2] Institut for Inorganic Chemistry, Johannes Gutenberg-University, Mainz

Formation of $CaCO_3$ in the presence of the egg-white protein ovalbumin was studied in aqueous solution by time-resolved small-angle neutron scattering. A particular goal was to achieve a better insight into the early stages of mineralization. Starting from the amorphous phase and the subsequent crystalline polymorphs vaterite and aragonite several stages of mineralization were observed. The formation and dissolution of amorphous $CaCO_3$ is accompanied by Ca^{2+} mediated unfolding and crosslinking of about 50 protein monomers showing the characteristic scattering of linear chains. The protein complexes act as nucleation centers because of their enrichment by Ca^{2+} ions.

Living organisms are capable of developing inorganic minerals with complex architectures to fulfill important biological functions, such as skeletal support or protection of soft tissues [1-3]. The mineral phase of such materials is intimately associated with organic macromolecules, such as proteins and polysaccharides. However, the role of these proteins in mineralization is not well understood. Small-angle neutron scattering (SANS) is a new technique in biomineralization which allows identification and structural analysis of biomineral composites by the method of contrast variation [2-4]. With the particular intention of a better insight into the early stages of mineralization, we performed studies of *in-situ* calcium carbonate formation mediated by the egg-white protein ovalbumin. Details of this work can be found in [4].

A characteristic result after 13 h mineralization by using gas diffusion technique is shown in Figure 1. The scattering pattern is characterized by two power laws representing μm large mineral particles and nm-sized proteins at small and large scattering vector Q, respectively. The Q^{-4} power law is a measure of the total mineral surface (Porod's law: $P_4 \cdot Q^{-4}$) whereas the Q^{-1} power law is caused from the linear chains of ovalbumin [5]. So, the large difference in size of the mineral and protein allows a separate analysis of both constituents. Another important property of SANS is the large variation range of scattering contrast $\Delta\rho^2$ of aqueous solutions by the exchange of H_2O and D_2O. The symbol $\Delta\rho = (\rho - \rho_S)$ describes the difference of the coherent scattering length density ρ of the mineral or protein and of the solvent ρ_S [5]. The corresponding values are summarized in the Table together with Φ representing the D_2O contents when the protein and the mineral polymorphs are matched in water, e.g. $\Delta\rho = 0$.

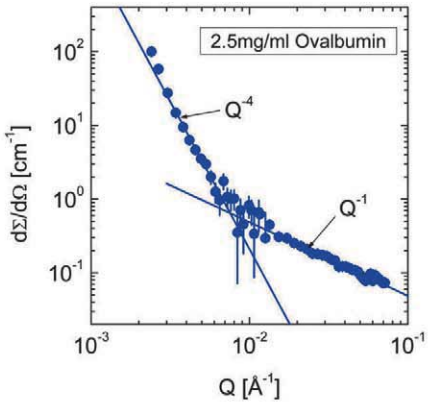

FIG. 1: Scattering pattern after 13 h mineralization in the presence of ovalbumin. The scattering from the mineral and protein are distinguished by the two power laws.

We performed several mineralization experiments in aqueous solution of different D_2O content, in order to identify the mineral polymorphs. Figure 2 shows the time evolution of the amplitude P_4 for four relevant contrast conditions. In all cases a peak becomes visible about 2.5 hours after initiation the mineralization. This scattering was identified from ACC particles as the intercept of $\sqrt{P_4} = 0$ occurred at $\Phi = 0.55 \pm 0.05$ (Table, [4]). So, the mineralization started with the formation of an amorphous polymorph, which after reaching a maximum volume fraction transformed to a crystalline polymorph. The pronounced minimum for the $\Phi = 0.74$ D_2O solvent after 4 h, and the smallest scattering of the $\Phi = 0.82$ sample after 5 h provide the interpretation that $CaCO_3$ follows a polymorph sequence amorphous → vaterite → aragonite (Table).

The scattering patterns in Figure 3 represent the contribution from the protein during mineralization (large Q range in Figure 1). For the first 1.5 h the scattering of the protein is best described by Guinier's law indicating the compact structure of the native state [5]. The slight increase of scattering after 90 minutes

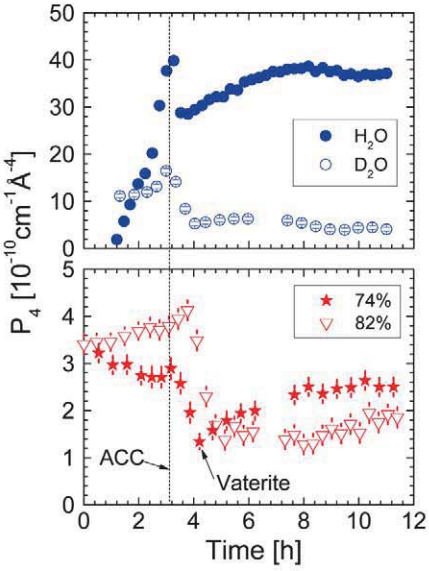

FIG. 2: Porod amplitude versus time of mineralization in the presence of 7.5mg/ml ovalbumin measured for different scattering contrasts. A peak from the amorphous polymorph (ACC) became always visible at ≈ 3h. After 4h the minimum of the 0.74 D_2O solution identifies the vaterite polymorph whereas aragonite appears as the stable phase within 12 h.

	$\rho[10^{10}\mathrm{cm}^{-2}]$	Φ
Calcite	4.69	0.76
Aragonite	5.10	0.81
Vaterite	4.49	0.74
Amorphous	3.29	0.55
Ovalbumin	1.64 + 1.61 Φ	0.41
Water	-0.561 + 6.95 Φ	—

TAB. 1: Relevant SANS parameters of the calcium carbonate polymorphs, ovalbumin, and water.

is the result of a 14.6% increase in the protein scattering length density which can be interpreted as a "loading" of the protein with about 280 Ca^{2+} ions [4]. After 90 minutes a gradual transition to a Q^{-1} power law is observed which was complete after nearly 3 h (see also Figure 1); the structural change of the protein was a continuous process during this time interval. The strong increase in intensity at low *Q* indicated that the process was accompanied by a crosslinking ("salting out") of the protein molecules. In this time interval the formation of the amorphous polymorph proceeded and approached its maximum (Figure 2). After the protein was "salted out", the amorphous phase started to dissolve as seen from the reduction of the amplitude P_4 in Figure 2. In a separate experiment of ovalbumin in 0.1 M $CaCl_2$ aqueous solution we determined a crosslinking of about 50 proteins (inset in Figure 3). This scattering was interpreted in terms of a Gaussian linear chain with relatively large statistical segments.

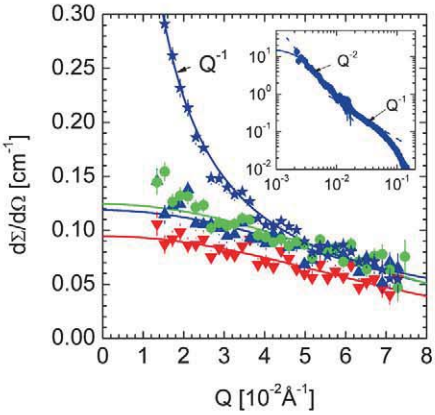

FIG. 3: Time evolution of the scattering from protein during the mineralization observed at large Q (▼ before start, after start of mineralization at ▲ 15 min • 90 min, and ★ nearly 13h). A gradual structural transition due to aggregation of the protein molecules is observed. The inset shows ovalbumin in 0.1 M $CaCl_2$ aqueous D_2O solution. An enlarged scattering is caused by crosslinking of about 52 proteins to an object with the conformation of a Gaussian linear chain as seen by the Q^{-2} and Q^{-1} power laws (Rg≅600Å, statistical segment length of nearly 20Å).

In summary, we give a first clue concerning the role of protein mediated $CaCO_3$ mineralization. Ovalbumin first acts as a "cation sponge" which locally increases the Ca^{2+} concentration. These Ca-rich pockets of ovalbumin aggregates seem to build nucleation centers for the incipient calcium carbonate formation. Calcium carbonate nanocrystals are stabilized by surface bound ovalbumin which is eventually occluded between the individual $CaCO_3$ crystallites, thereby forming a mesocrystal, i.e. an inorganic-organic hybrid material [4,6]. The observed formation from less dense to more dense polymorphs follows the Ostwald-Volmer rule [1].

[1] S. Mann, Biomineralization, Oxford University Press, Oxford 2001.

[2] A. Heiss, W. Jahnen-Dechent, H. Endo, D. Schwahn, Biointerphases **2** (2007) 16-20.

[3] A. Heiß, D. Schwahn, in Handbook of Biomineralization: The Biology of Biominerals Structure Formation (Bäuerlein, E.; Behrens, P.; Epple, M. Eds.), Wiley-VCH, Weinhein, **1** (2007) 415-433.

[4] V. Pipich, M. Balz, S. E. Wolf, W. Tremel, and D. Schwahn, J. Am. Chem. Soc. (2008) in press.

[5] R.J. Roe, Methods of X-Ray and Neutron Scattering in Polymer Science, University Press, Oxford 2000.

[6] D. Schwahn, Y. Ma, H. Cölfen, J. Phys. Chem., **C111** (2007) 3224-3227.

Relevance of Angular Momentum Conservation in Fluid Simulations

I. O. Götze , H. Noguchi , G. Gompper
IFF-2: Theoretical Soft-Matter and Biophysics

The angular momentum is conserved in fluids – with a few exceptions such as ferrofluids in external fields. However, it can be violated locally in fluid simulations to reduce computational costs. The effects of this violation are investigated using multi-particle collision dynamics, a well-established, highly efficient hydrodynamics simulation technique, where an angular-momentum conserving variant is available. We show that there are situations of practical relevance, such as multi-phase flows in Couette geometry, where angular momentum conservation is essential to avoid non-physical results.

In simulations of the hydrodynamic behavior of complex fluids, one is faced with the challenge of bridging the gap between the mesoscopic length and time scales of the solute and the atomic scales of the solvent. As these typically differ by orders of magnitude, a full treatment on a microscopic level is prohibited by the enormous number of involved particles and the large necessary time range. Moreover, often only the dynamics of the colloidal particles are of particular interest, while the microscopic details of the solvent that mediates the hydrodynamic interactions are rather unimportant. Thus, a coarse-grained mesoscopic fluid model is required that is sufficiently simple to be tractable but still captures the correct hydrodynamic behavior. By representing a large number of physical solvent molecules by one model fluid particle at a time, the number of degrees of freedoms can be reduced considerably. Various mesoscopic approaches have been proposed in the last decades, which can be categorized in lattice methods or particle-based methods. We focus on particle-based simulations, where particle positions and velocities are continuous variables that are updated at discrete times. Here, coupling to solute particles as well as moving boundaries can be treated more easily than in lattice methods and thermal fluctuations are naturally contained. Moreover, lattice methods generally suffer from the lack of Galilean invariance.

The method used here, multi-particle collision dynamics (MPC) [1], needs less computational time compared to other particle based methods such as DPD, thus allowing simulations of larger systems. Here, the fluid is represented by point particles that undergo subsequent streaming and collision steps. In the streaming step, the particles move ballistically. Subsequently, they are sorted into collision cells and the collision step then mimics the simultaneous interaction of all particles within each cell by assigning them new velocities. MPC has been applied to various systems such as colloids, polymers, membranes, ternary amphiphilic fluids, and chemical reaction systems. Hybrid simulations combining an MPC fluid with molecular dynamics of solute particles are easily possible. The algorithm is constructed in such way that mass, energy and translational momentum are locally conserved, which is essential for correct hydrodynamic behavior. However, the *angular* momentum is not conserved in the most widespread version of MPC, which is often called stochastic-rotation dynamics. In order to clarify the effects of angular-momentum conservation [2], we mainly use the Andersen-thermostat version of MPC, where angular momentum conserving (MPC-AT$+a$) and non-conserving (MPC-AT$-a$) algorithms are available [3].

In conventional viscous fluids that do conserve angular momentum, the viscous stress tensor has to be symmetric, *i. e.* $\sigma_{\alpha\beta} = \sigma_{\beta\alpha}$. This symmetry is required by the fact that there is no stress expected in a uniformly rotating fluid (rigid body rotation), or alternatively, by the conservation of angular momentum. On the other hand, for a fluid without conservation of angular momentum, the above argument is no longer valid and we have to consider in general an asymmetric tensor. Then, the viscous stress is given by

$$\begin{aligned}\sigma_{\alpha\beta} &= \lambda(\nabla\cdot\mathbf{v})\delta_{\alpha\beta} \\ &+ \bar{\eta}\left(\frac{\partial v_\alpha}{\partial x_\beta}+\frac{\partial v_\beta}{\partial x_\alpha}\right)+\check{\eta}\left(\frac{\partial v_\alpha}{\partial x_\beta}-\frac{\partial v_\beta}{\partial x_\alpha}\right),\end{aligned} \quad (1)$$

where $\alpha,\beta \in \{x,y,z\}$. Here, λ is the second viscosity coefficient, and $\bar{\eta}$ and $\check{\eta}$ are the symmetric and asymmetric components of the viscosity, respectively. The last term in Eq. (1) is linear in the vorticity $\nabla\times\mathbf{v}$, and does not conserve angular momentum. Thus, the last term vanishes (*i. e.* $\check{\eta}=0$) in angular-momentum-conserving systems. The equation of velocity evolution is given by

$$\rho\frac{D\mathbf{v}}{Dt} = -\nabla P+(\lambda+\bar{\eta}-\check{\eta})\nabla(\nabla\cdot\mathbf{v})+(\bar{\eta}+\check{\eta})\nabla^2\mathbf{v}, \quad (2)$$

where D/Dt is Lagrange's derivative and P is the pressure. When a fluid is incompressible, this is the normal Navier-Stokes equation with viscosity $\eta = \bar{\eta}+\check{\eta}$. Since the equations of continuity and velocity evolution are of the same form, the negligence

of angular-momentum conservation does not modify the velocity field of fluids when the boundary conditions are given by velocities. However, it generates an additional torque, so that the velocity field can be changed when the boundary condition is given by forces. In cylindrical coordinates (r, θ, z), the azimuthal stress is given by

$$\sigma_{r\theta} = (\bar{\eta} + \check{\eta}) \frac{r\partial(v_\theta/r)}{\partial r} + 2\check{\eta}\frac{v_\theta}{r}. \qquad (3)$$

The first term is the stress of the angular-momentum-conserving fluid, which depends on the derivative of the angular velocity $\Omega = v_\theta/r$. The second term is the additional stress from the negligence of angular-momentum conservation and is proportional to Ω.

We consider a fluid confined between two coaxial cylinders (Couette flow) rotating with the same angular frequency Ω. Here, no torque is expected to be acting on the cylinders in angular-momentum conserving fluids, as this corresponds to the rotation of a rigid body. However, in simulations without angular-momentum conservation, we *do* observe torques on the confining cylinders, induced by the stress term of the asymmetric viscosity $\check{\eta}$ in Eq. (3). The torque is the tangential stress $2\check{\eta}\Omega_0$ multiplied by the circumference length $2\pi R$ and the radius R. The finite size of the collision cells leads to a correction term, so that the torques on the confining cylinders are found to be

$$T_{\mathrm{in,out}}(R) = \pm 4\pi\check{\eta}\Omega R^2 \left(1 \mp \frac{3a}{4R}\right). \qquad (4)$$

In order to verify that the velocity field is not affected by the lack of angular-momentum conservation if the boundary condition is given by the velocity, we study fluids confined between eccentric cylinders with fixed axes, where the inner one is rotating at constant angular velocity. As expected, the corresponding stream lines, which are shown in Fig. 1, are practically identical for both methods. The occurrence of a back-flow in the large-gap region as well as the resulting total forces on the inner cylinder are in good agreement with theoretical predictions.

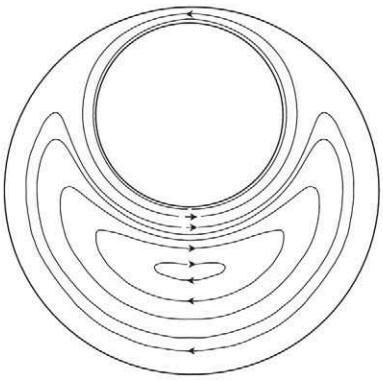

FIG. 1: Stream lines for fluid confined between eccentric cylinders (inner one rotating with constant angular velocity).

A boundary of a fluid does not only exist on solid objects but also between two fluids or on membranes. In order to investigate the fluid-fluid boundary

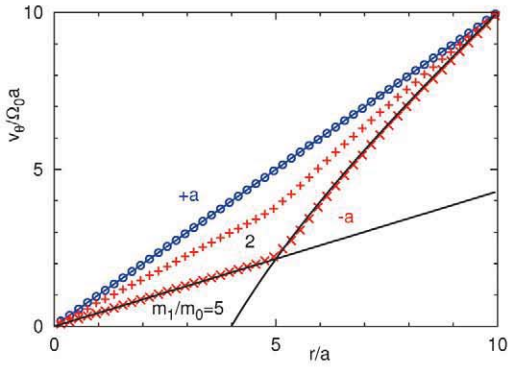

FIG. 2: Azimuthal velocity v_θ of binary fluids in a rotating cylinder. The fluids with different viscosities are located at $r < 5a$ and $5a < r < 10a$, respectively. Symbols represent the simulation results of MPC-AT$-a$ for two different viscosity ratios $(+, \times)$, and MPC-AT$+a$ $(\circ)$. Solid lines represent the analytical results for MPC-AT$-a$.

in MPC-AT$-a$ fluids, we consider binary fluids with a fixed geometry of the boundary surface, which is impenetrable to the fluid particles. The inner cylinder of radius R_1 of circular Couette flow is replaced by a more viscous fluid, and the outer cylinder with radius R_2 rotates with constant velocity Ω_0. This is a simplified description of oil and water phase-separated due to surface tension, or two liquids separated by a membrane. It is assumed that the cylinder rotates very slowly, and that the flow stress does not change the shape of the interface. We choose the fluid inside $(r < R_1 = 5a)$ to have a higher viscosity than the fluid outside. The MPC collision performed in cells crossing the boundary propagates the momentum from one fluid to the other. In MPC-AT$+a$, both fluids rotate with Ω_0 independent of their viscosities. However, in MPC-AT$-a$, the inner fluid rotates more slowly (see Fig. 2). This is caused by the asymmetric stress term $2\check{\eta}\Omega$. If both fluids rotate at the same angular velocity, the inner and outer stresses do not coincide. The theoretical velocity profile is obtained from the stress balance at $r = R_1$ and is in very good agreement with the numerical results (Fig. 2).

Our main conclusion is that simulations which do not conserve angular momentum can lead to quantitatively and even qualitatively incorrect results, when the boundary conditions on walls are given by forces, fluids with different viscosities are in contact, or finite-sized objects rotate in fluids.

[1] A. Malevanets and R. Kapral, J. Chem. Phys. **110**, 8605 (1999).

[2] I. O. Götze, H. Noguchi, and G. Gompper, Phys. Rev. E **76**, 046705 (2007).

[3] H. Noguchi, N. Kikuchi, and G. Gompper, Europhys. Lett. **78**, 10005 (2007).

Diffusion and Segmental Dynamics of Double-Stranded DNA

R. G. Winkler[1], E. P. Petrov[2], T. Ohrt [2], P. Schwille[2]

[1] IFF-2: Theoretical Soft-Matter and Biophysics
[2] Institute of Biophysics/BIOTEC, Dresden University of Technology, Dresden

The diffusion and segmental dynamics of double-stranded λ-phage DNA molecules are quantitatively studied over the transition range from stiff to semiflexible chains. Spectroscopy of fluorescence fluctuations of single-end fluorescently labeled monodisperse DNA fragments unambiguously shows that double-stranded DNA in the length range of $10^2 - 2 \times 10^4$ base pairs behaves as a semiflexible polymer with segmental dynamics controlled by hydrodynamic interactions.

The dynamic behavior of individual macromolecules in solution is governed by chain connectivity and hydrodynamic interactions [1]. Understanding of polymer dynamics and quantitative verification of polymer theories require detailed information on segmental motion of individual polymer molecules. However, the classical experimental techniques, such as dynamic light scattering (DLS) or transient electric birefringence (TEB), predominantly deliver information on large-scale shape fluctuations of macromolecules. Fluorescence correlation spectroscopy (FCS) [2] is a single-molecule technique that can provide more detailed information on the macromolecular dynamics than the classical ensemble-based methods. By fluorescent labelling of individual segments [3] or continuous labelling of the whole molecule [4], the diffusional motion of segments as well as that of the overall molecule can be studied at nanomolar concentration under (quasi)equilibrium conditions in solution and cellular systems.

Precise experiments in polymer physics are impossible without well-defined monodisperse polymer samples covering a wide range of molecular weights. The recent progress in molecular biotechnology resulted in a variety of techniques to produce monodisperse DNA fragments, which stimulated the use of DNA as a model compound in studies of polymer dynamics in solution. We employed the technique of polymerase chain reaction (PCR) to produce monodisperse samples of DNA fragments with predefined sequence, structure, and length, fluorescently labeled at the same single end [3]. Double-stranded (ds) DNA is a biopolymer characterized by a large persistence length $l_p \sim 50$ nm [3]. As a result, dsDNA fragments exhibit rodlike, semiflexible, or even flexible polymer behavior, depending on their length. Thus, simple generic models of polymer dynamics [1] are not expected to provide a quantitative description of dsDNA behavior, and more advanced models, accounting for the persistence of the polymer chain, e.g., the semiflexible polymer model of Ref. [4], are required.

Recent FCS studies raised the question whether dsDNA dynamics in dilute solution is controlled by hydrodynamic interactions [4] or not [5]. Moreover, no experimental studies were reported previously, where diffusion and intramolecular dynamics of dsDNA had simultaneously been investigated over the transition range from stiff to semiflexible chains. Our FCS measurements of lengths L from 10^2 to 2×10^4 base pairs (bp) ($L/l_p \sim 0.7 - 140$) by following the Brownian motion of the labeled ends of single DNA molecules filled this gap and showed that the experimental data can quantitatively be described by the theory for semiflexible polymer dynamics [3], which clearly demonstrates that in this length range dsDNA behaves as a semiflexible polymer with strong hydrodynamic interactions.

In FCS [2], fluctuations of the confocally detected fluorescence signal $F(t) = \langle F\rangle + \delta F(t)$ are studied via the correlation function $G(\tau) = \langle \delta F(t)\, \delta F(t+\tau)\rangle / \langle F\rangle^2$. In the absence of additional photophysical processes and chemical reactions, the fluorescence signal fluctuates as a result of the Brownian motion of fluorescently labeled particles through the detection volume whose shape can be approximated by a 3D Gaussian $\exp\left(-2r^2/r_0^2 - 2z^2/z_0^2\right)$, where r_0 and z_0 are the lateral and axial extensions of the detection volume, respectively. With the mean square displacement (MSD) $\left\langle \Delta \mathbf{r}^2(t)\right\rangle$ of a particle, the FCS correlation function assumes the form

$$G(t) = \frac{1}{\langle N\rangle} \frac{1}{\left(1 + \frac{2}{3}\frac{\left\langle \Delta \mathbf{r}^2(t)\right\rangle}{r_0^2}\right)\sqrt{1 + \frac{2}{3}\frac{\left\langle \Delta \mathbf{r}^2(t)\right\rangle}{z_0^2}}}, \quad (1)$$

where $\langle N\rangle$ is the effective number of molecules in the detection volume.

Utilizing the Gaussian semiflexible polymer model, analytical calculations yield the MSD

$$\left\langle \Delta \mathbf{r}^2(t)\right\rangle = 6Dt + \frac{2k_BT}{\pi\eta}\sum_{n=1}^{\infty}\tau_n\psi_n^2(L/2)\left(1 - e^{-t/\tilde{\tau}_n}\right) \quad (2)$$

for the chain end [4], where T is the temperature, k_B the Boltzmann factor, and η the viscosity. $\psi_n(L/2)$

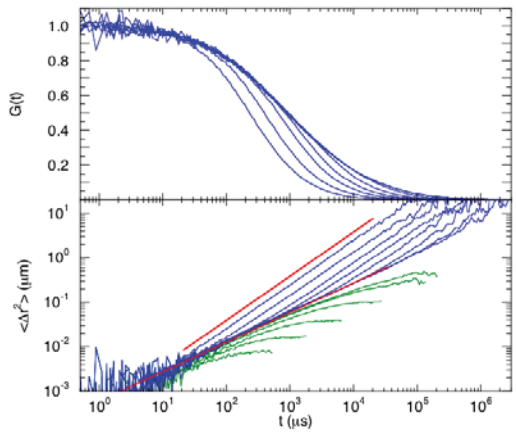

FIG. 1: Normalized FCS correlation functions (top) and determined mean square displacements (bottom) for λ-DNA fragments of lengths 0.1, 0.2, 0.5, 1, 2, 5, 10, and 20 kbp (from left to right). The intramolecular contribution to the MSD is shown by the green lines (bottom). The red lines indicate the power laws $\langle \Delta \mathbf{r}^2 \rangle \sim t$ and $t^{2/3}$, respectively.

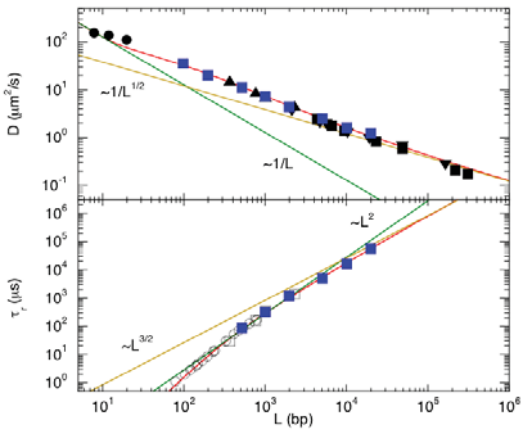

FIG. 2: Diffusion coefficients (top) and longest relaxation times (bottom) of dsDNA. The blue symbols indicate our FCS data. The other data (black symbols) are taken from various sources [3]. The red lines are predictions of the semiflexible polymer model [3, 4] with the parameters $l_p = 50$ nm, $\Lambda_D = 0.9$, and $\Lambda = 0.6$.

is the value of the n-th eigenfunction of a chain of length L at its end, $\tilde{\tau}_n$ is the n-th relaxation time in the presence of hydrodynamic interactions and is related with the free-draining relaxation time τ_n via $\tilde{\tau}_n = \tau_n/(1 + 3\pi\eta\Lambda H_{nn})$. D is the translational diffusion coefficient of the macromolecule, and H_{nn} is the matrix element of the Rotne-Prager tensor within the preaveraging approximation [4]. Here, Λ and Λ_D are fit parameters, which are introduced in our quantitative analysis of the experimental data [3].

For long and flexible molecules, $L/l_p \gg 1$, the theoretical expression yields the short-time behavior $\langle \Delta \mathbf{r}^2(t) \rangle \sim t^\beta$, with the exponents $\beta = 1/2$ (free draining) and $2/3$ (nondraining), in agreement with predictions of the Rouse and Zimm model, respectively [1]. For semiflexible polymers, the short-time behavior is given by $\beta = 3/4$ [4]. However, these power laws are only valid for times much shorter than the longest relaxation time of the polymer, whereas at comparable and longer times the intramolecular contribution to the MSD saturates due to the finite size of the polymer coil, as shown in Fig. 1. Thus, direct application of the power laws to the analysis of the MSD time dependencies, as has been proposed recently in Ref. [5], can be misleading. Indeed, even for the longest sample the apparent power law in $\langle \Delta \mathbf{r}^2(t) \rangle$ observed in the range of $10^0 - 10^5$ μs is to a large extent due to the crossover from intramolecular motion to overall polymer diffusion; only for times shorter than $\sim 10^3$ μs a power law-type behavior can observe in the intramolecular contribution. We would like to point out that such an analysis of the short-time dynamics, still possible in our study for the two longest DNA fragments, clearly rules out the Rouse-type behavior reported for dsDNA in Ref. [5] and leads to a definitive conclusion on the importance of intramolecular hydrodynamic interactions in dsDNA polymer dynamics.

Figure 2 displays diffusion coefficients and longest relaxation times – the upper part is not readily accessible by DLS or TEB – which we obtained by fitting of the normalized FCS curves [3]. The experimental correlation functions are very well reproduced for the parameters $l_p = 51 \pm 1$ nm, $\Lambda = 0.6$, and $\Lambda_D = 0.9$. Within the range of lengths studied, the diffusion coefficients and relaxation times exhibit approximately the power law behavior $D \sim L^{-2/3}$ (note that there is no excluded volume interaction for short DNAs) and $\tau_r \sim L^{1.7}$, and thus do not follow the predictions of the Rouse ($D \sim 1/L$, $\tau_r \sim L^2$) nor the Zimm ($D \sim 1/L^{1/2}$, $\tau_r \sim L^{3/2}$) model. At the same time, our data are in very good agreement with results obtained by other experimental techniques not related to FCS [3] and closely follow the predictions of the semiflexible polymer theory [4].

Therefore, our results clearly demonstrate that in the range of the lengths studied, dsDNA behaves as a semiflexible polymer with strong hydrodynamic interactions . The Zimm regime with $\langle \Delta \mathbf{r}^2 \rangle \sim t^{2/3}$, $D \sim L^{-1/2}$, and $\tau_r \sim L^{3/2}$ (or corresponding expressions modified to account for excluded-volume interactions) [1] can be achieved only for long dsDNA molecules with lengths exceeding 10^5 bp, or $\sim 10^3$ l_p (Fig. 2).

[1] M. Doi, S. F. Edwards, *The Theory of Polymer Dynamics* (Clarendon Pres, Oxford, 1986)

[2] E. P. Petrov, P. Schwille, *State of the Art and Novel Trends in Fuorescence Correlation Spectroscopy* (Springer, Berlin, 2007)

[3] E. P. Petrov, T. Ohrt, R. G. Winkler, P. Schwille, Phys. Rev. Lett. **97**, 258101 (2006)

[4] R. G. Winkler, S. Keller, J. O. Rädler, Phys. Rev. E **73**, 041919 (2006)

[5] R. Shusterman, S. Alon, T. Gavrinyov, O. Krichevsky, Phys. Rev. Lett. **92**, 048303 (2004)

Swinging and Tumbling of Fluid Vesicles in Shear Flow

H. Noguchi, G. Gompper
IFF-2: Theoretical Soft-Matter and Biophysics

The dynamics of fluid vesicles in simple shear flow is studied using mesoscale simulations of dynamically-triangulated surfaces, as well as a theoretical approach based on two variables, a shape parameter and the inclination angle, which has no adjustable parameters. We show that between the well-known tank-treading and tumbling states, a new "swinging" state can appear. We predict the dynamic phase diagram as a function of the shear rate, the viscosities of the membrane and the internal fluid, and the reduced vesicle volume. Our results agree well with recent experiments.

The dynamical behavior of vesicles under shear flow is an important subject not only of fundamental research but also in medical applications. For example, in microcirculation, the deformation of red blood cells reduces the flow resistance of microvessels. In diseases such as diabetes mellitus and sickle cell anemia, red blood cells have reduced deformability and often block microvascular flow. In simple shear flows, with flow velocity $\mathbf{v} = \dot{\gamma} y \mathbf{e}_x$, Lipid vesicles and red blood cells exhibit a tank-treading rotation with a stationary shape and a finite inclination angle $\theta > 0$ with respect to the flow (x) direction at low internal $\eta_{\rm in}$ and membrane viscosities $\eta_{\rm mb}$. They transit to an unsteady tumbling motion with increasing $\eta_{\rm in}$ or $\eta_{\rm mb}$. Recently, Kantsler and Steinberg [1] reported the first observation of a new type of vesicle dynamics in shear flow, which is characterized by oscillations of the inclination angle θ and the deformation, where $-\theta_0 \lesssim \theta(t) \lesssim \theta_0$ with $\theta_0/\pi < 1$ and time average $\langle\theta\rangle \simeq 0$. The vesicles were found to transit from tumbling to this oscillatory motion with increasing shear rate $\dot{\gamma}$.

We have studied the oscillatory dynamics of fluid vesicles, which we will refer to as the "swinging mode", by mesoscale hydrodynamics simulations and a simplified non-linear theoretical model [2]. The main questions we want to address are: How does the bending energy affect the dynamics? Can transitions between modes be induced by varying the shear rate? What happens beyond the quasi-spherical limit, which is the typical experimental situation? What is the effect of the membrane viscosity? Is the swinging mode stable when thermal membrane undulations are taken into account? We will show that the experiments of Ref. [1] can be understood very well on the basis of our theory. Furthermore, we will present a complete phase diagram of vesicle motion as a function of shear rate and viscosity.

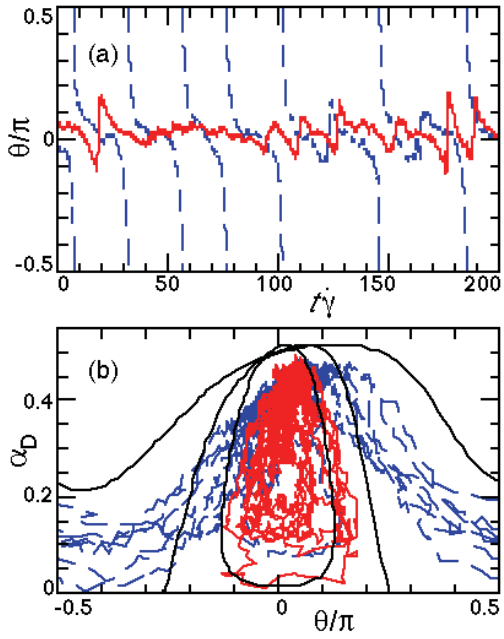

FIG. 1: Temporal evolution of $\alpha_{\rm D}$ and θ, for $V^* = 0.78$ and $\eta^*_{\rm mb} = 2.9$. The solid (red) and dashed (blue) lines represent simulation data for $\dot{\gamma}^* = 3.68$ and 0.92 ($\kappa/k_{\rm B}T = 10$ and 40 with $\dot{\gamma}\eta_0 R_{\rm S}^3/k_{\rm B}T = 36.8$), respectively. The solid lines in (b) are obtained from Eqs. (1), (2) without thermal noise for $\dot{\gamma}^* = 1.8$, 3 and 10 (from top to bottom).

The vesicle dynamics is described by several dimensionless quantities. For a vesicle of volume V and surface area S, the reduced volume V^* and the excess area $\Delta_{\rm S}$ are defined by $V^* = (R_{\rm V}/R_{\rm S})^3 = (1 + \Delta_{\rm S}/4\pi)^{-3/2}$ and $\Delta_{\rm S} = S/R_{\rm V}^2 - 4\pi$, where $R_{\rm V} = (3V/4\pi)^{1/3}$ and $R_{\rm S} = (S/4\pi)^{1/2}$. The relative viscosity of the inside fluid and membrane are $\eta^*_{\rm in} = \eta_{\rm in}/\eta_0$ and $\eta^*_{\rm mb} = \eta_{\rm mb}/\eta_0 R_{\rm S}$, where η_0 is the viscosity of the outside fluid. The shape relaxation time of vesicles with bending rigidity κ is given by $\tau = \eta_0 R_{\rm S}^3/\kappa$ (for $\eta^*_{\rm in} = 1$). This time is used to define a reduced shear rate $\dot{\gamma}^* = \dot{\gamma}\tau$.

The hydrodynamics of fluid vesicle can be studied very well by hybrid simulations of a dynamically-triangulated membrane model and a particle-based mesoscale solvent, multi-particle collision dynamics. We applied this method to the lipid vesicles in shear flow. Previously, we found shape transitions such as the prolate-to-discocyte [3, 4].

We have simulated a prolate vesicle with a viscous membrane at $V^* = 0.78$ and $\eta^*_{\rm in} = 1$. Figure 1 shows the time evolution of the vesicle shape and θ. The shape parameter is $\alpha_{\rm D} = (L_1 - L_2)/(L_1 + L_2)$, where L_1 and L_2 are the maximum lengths in the direction of the eigenvectors of the gyration tensor in the vorticity (x, y) plane. The vesicle is found to exhibit a tumbling motion for $\dot\gamma^* = 0.92$, but a swinging motion for $\dot\gamma^* = 3.68$. The both motions coexist around the critical shear rate $\dot\gamma^*$ because of the thermal fluctuations. The shear rate $\dot\gamma^*$ at the tumbling-to-swinging transition increases with increasing $\eta^*_{\rm mb}$. These results are consistent with the experiments of Ref. [1].

In order to obtain a better understanding of the vesicle dynamics, we now derive an approximate theoretical model. We derived the equation for the shape parameter $\alpha_{\rm D}$ based on the Stokes approximation and perturbation theory for quasi-spherical vesicles.

$$\frac{d\alpha_{\rm D}}{dt} = \left\{1 - \left(\frac{\alpha_{\rm D}}{\alpha_{\rm D}^{\rm max}}\right)^2\right\} \left\{-\frac{A_0}{\tau\kappa V^*}\frac{\partial F}{\partial \alpha_{\rm D}} + \dot\gamma A_1 \sin(2\theta)\right\}, \quad (1)$$

where $A_0 = 45/8\pi(32 + 23\eta^*_{\rm in})$ and $A_1 = 30/(32 + 23\eta^*_{\rm in})$. Since an accurate evaluation of F is very important, we calculate it numerically for ellipsoidal vesicles with $(x_1/a_1)^2 + (x_2/a_2)^2 + (x_3/a_3)^2 = 1$. The prolate ($a_1 > a_2 = a_3$) and oblate ($a_1 = a_2 > a_3$) shapes are energy minima and maxima, respectively. Eq. (1) has the same form as our previous simplified model [3, 4], but now has *no adjustable parameters*.

We employ the equation of K-S theory for the inclination angle θ,

$$\frac{d\theta}{dt} = \frac{\dot\gamma}{2}\{-1 + B\cos(2\theta)\}, \quad (2)$$
$$B = f_0\left\{f_1 + \frac{f_1^{-1}}{1 + f_2(\eta^*_{\rm in} - 1) + f_2 f_3 \eta^*_{\rm mb}}\right\},$$

where the factors f_0, f_1, f_2, and f_3 are the functions of the ellipsoidal shape $(a_2/a_1, a_3/a_1)$, and are given in Ref. [4]. The K-S theory in general shows very good agreement with simulation results [4]. When thermal fluctuations are taken into account, Gaussian white noises are added to Eqs. (1) and (2), which obey the fluctuation-dissipation theorem.

Eqs. (1) and (2) reproduce the simulation results semi-quantitatively (see Fig. 1). At small $\dot\gamma^*$, in the tumbling phase, θ rotates with $\alpha_{\rm D}$-oscillation of small amplitude. This $\alpha_{\rm D}$ amplitude becomes larger at larger $\dot\gamma^*$. Then, when $\alpha_{\rm D}(t)$ reaches zero, θ jumps to $\pi/4$, see Fig. 1. Finally, at even larger $\dot\gamma^*$, $\alpha_{\rm D}$ and θ exhibit oscillations without jumps.

The physical mechanism of swinging can be understood on the basis of Eqs. (1), (2) as follows. At finite κ, the shear force elongates the vesicle ($\alpha_{\rm D}$ increases) for $0 < \theta < \pi/2$, but compresses it ($\alpha_{\rm D}$ decreases) for $-\pi/2 < \theta < 0$, since the $\sin(2\theta)$-term in Eq. (1) changes sign. Thus, the swinging motion is caused by a shape deformation, where B in Eq. (2) crosses the tank-treading-to-tumbling threshold periodically. First, a prolate vesicle starts tumbling because $B < 1$, $\alpha_{\rm D}$ decreases when $\theta < 0$, which implies that B increases; then θ starts to increase again because $B > 1$ at small $\alpha_{\rm D}$; finally $\alpha_{\rm D}$ increases when $\theta > 0$.

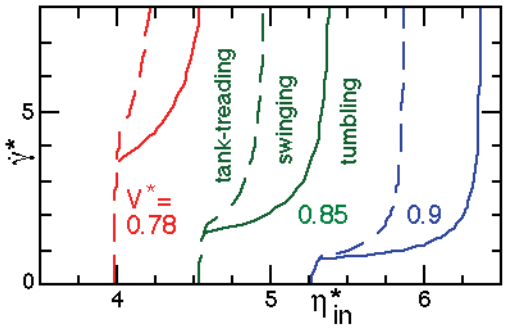

FIG. 2: Dynamical phase diagrams as a function of $\eta^*_{\rm in}$ for $\eta^*_{\rm mb} = 0$, for various reduced volumes V^*, obtained from Eqs. (1), (2) without thermal noise. The tank-treading phase is located on the left-hand-side of the dashed lines. The solid lines represent the tumbling-to-swinging transitions.

Fig. 2 shows the phase diagrams for the dimensionless shear rate and internal viscosity. With increasing V^* the smallest shear rate $\dot\gamma^*_{\rm os}$, at which swinging can be observed, decreases, since the dependence of the energy F on $\alpha_{\rm D}$ becomes more shallow. Also, the swinging region shifts to higher viscosity, $\eta_{\rm in}$, with increasing V^*. For fixed V^*, $\dot\gamma^*_{\rm os}$ is a strongly increasing function of $\eta^*_{\rm in}$. In the experiments of Ref. [1], the swinging (tumbling) motion was observed for $\dot\gamma^* \simeq 17$ (4.5), $\eta^*_{\rm in} = 6$ (8.4), and $V^* \simeq 0.9$, and a very small membrane viscosity $\eta^*_{\rm mb} \sim 0.1$. The swinging motion is observed in the close vicinity to the tank-treading-to-tumbling transition [1]. Thus, the experimental data agree with our predicted phase diagram, Fig. 2, very well. Furthermore, the oscillation amplitudes also show good agreement for both swinging and tumbling [2].

[1] V. Kantsler and V. Steinberg, Phys. Rev. Lett. 96, 036001 (2006).

[2] H. Noguchi and G. Gompper, Phys. Rev. Lett. 98, 128103 (2007).

[3] H. Noguchi and G. Gompper, Phys. Rev. Lett. 93, 258102 (2004).

[4] H. Noguchi and G. Gompper, Phys. Rev. E 72, 011901 (2005).

Do Intra-Molecular Relaxations Influence the Damping of Longitudinal Phonons?

H. Kriegs[1], G. Meier[1], J. Gapinski[2], A. Patkowski[2]

[1] IFF-7: Soft Condensed Matter
[2] Institute of Physics, A. Mickiewicz University, Umultowska 85, 61-614, Poznan, Poland

The effect of intra-molecular relaxations on the damping of longitudinal phonons was studied in poly(methylphenylsiloxane) (PMPS) and poly(ethylmethylsiloxane) (PEMS) polymers by means of Brillouin spectroscopy. It is shown that studies of the polarized Brillouin spectra as functions of temperature and pressure allow for the separation of the contributions of the internal and structural relaxations to the damping of longitudinal phonons according to theoretical predictions.

In liquids, propagating density fluctuations exist in the form of longitudinal and, if viscosity is high enough, transverse phonons. The velocity and damping of these phonons at high frequencies of the order of a few GHz can be studied by means of the polarized (VV - longitudinal phonons) and depolarized (VH - transverse phonons) Brillouin spectroscopy. The polarized spectrum consists of the central Rayleigh line and two Brillouin lines which are symmetrically shifted by $\pm\omega_B$ and have the half-width at half heights (HWHH) Γ_B. The Brillouin shift ω_B is the measure of the sound velocity v: $\omega_B = qv$, where $q = (4\pi n \sin\theta/2)/\lambda$ is the length of the scattering vector, n is the refractive index of the scattering medium, λ - the scattering angle and λ - the wavelength of the incident light in vacuum. The phonons are damped due to the relaxation processes present in the liquid and the measure of this damping is the Brillouin line width Γ_B. In the case of a single relaxation process of a relaxation time τ_s the classical acoustic relaxation theory predicts the maximum of damping when $\omega_B\tau_s = 1$. In the case of supercooled liquids the situation is much more complicated due to the presence of several relaxation processes. Additional complications might result from the fact that intramolecular relaxation processes in the liquid might also contribute to the damping of phonons.

Theories describing the propagation and damping of longitudinal and transverse phonons in terms of the structural relaxation, i.e. translational motion of the molecules and translational-rotational coupling, have been developed, improved and tested experimentally [1]. Usually they did not take into account the coupling of intra-molecular relaxations to the structural relaxation.

For liquids which consist of molecules having internal relaxation, a theoretical model was developed in the limit of weak coupling of intra-molecular relaxations to the translational degrees of freedom [2].

In order to estimate the contribution of internal relaxations to the broadening of the Brillouin lines, it is necessary to separate this contribution from that of structural relaxation. This can be achieved by studying the pressure dependence of Γ_B [3], since the pressure dependence of the structural relaxation times $d\log\tau_s/dP \sim 5 \times 10^{-3}\mathrm{bar}^{-1}$ [4] is much stronger than that of the internal relaxation time $d\log\tau_{int}/dP \sim 2 - 5 \times 10^{-4}\mathrm{bar}^{-1}$ [5,6,7]. The efficiency of the phonon damping depends mainly on the separation in frequency between the relaxation frequency $1/\tau$ and the phonon frequency ω_B. Thus the contribution of the structural relaxation to the Γ_B should change from zero at the glass transition temperature T_g to a maximum, when $\omega_B\tau_s = 1$, while the internal relaxations should contribute almost equally at all temperatures, since their relaxation frequency is changing very little with temperature and pressure.

In some cases an assignment to structural (inter-) and intra-molecular relaxations can be performed on a molecular level, as it has been done in the case of two chemically very similar polymeric supercooled liquids: PMPS and PEMS [4]. The only difference in their chemical structure is the presence of a phenyl ring in PMPS which replaces the ethyl group in PEMS. In PMPS in addition to the structural relaxation an intramolecular process is present which is assigned to the phenyl flip. In PEMS this internal process is not present. This well identified difference in the internal dynamics makes this pair of polymeric liquids a perfect choice to study the effects of internal relaxations on damping of phonons.

Polarized (VV) Brillouin spectra were measured at ambient pressure for PMPS and PEMS in the backscattering geometry in a broad temperature range from T_g to about $T_g + 200$ K. We determined the position ω_B and HWHH Γ_B of the Brillouin peaks. These Γ_B values are plotted for PMPS and PEMS versus $T - T_g$ in Fig. 1.

The temperature dependence of ω_B is similar for both polymers. However, there are two important differences in the temperature dependence of Γ_B: (i) the maximum of the dependence $\Gamma_B(T-T_g)$ for PMPS is much broader than that for PEMS, and (ii) the residual width at the glass transition temperature $\Gamma_B(T_g)$

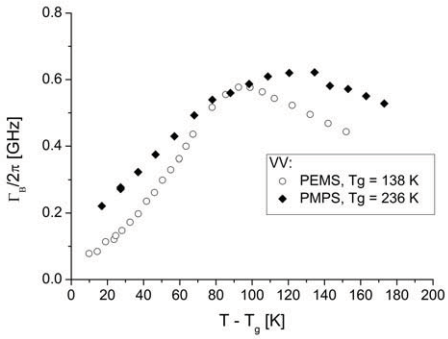

FIG. 1: Temperature dependence of the half width at half heights Γ_B of the polarized Brillouin peak measured for PMPS and PEMS at ambient pressure.

is also larger for PMPS than for PEMS. The pressure dependence of the polarized Brillouin spectra in the temperature range close to T_g could be measured only for PMPS, because the temperatures close to $T_g = 138$ K of PEMS could not be reached in our high pressure light scattering setup. The pressure dependence of the half width Γ_B of the longitudinal phonon peaks at temperatures of -21, 0 and $20°$C is shown in Fig. 2. As already observed for low molecular weight liquids [3], the Brillouin width Γ_B is decreasing with increasing pressure, reaching a high pressure plateau value. In order to obtain this value Γ_0, the data was analyzed using the formula:

$$\Gamma_B(P) = \Gamma_0(T) + A(T)\exp\left(\frac{-D_P P}{P_0 - P}\right) \quad (1)$$

where $\Gamma_0(T)$ is the residual width at T_g, due to internal relaxations, $A(T)$ is the amplitude, D_P is a fit parameter identical for all temperatures and P_0 is the parameter characterizing the pressure dependence of the structural (α-) relaxation obtained from our earlier high pressure photon correlation spectroscopy study [4]. The temperature dependence of Γ_0 and A is shown in Fig.3. We conclude from our recent work [8]:

In the temperature dependent studies on both polymers at ambient pressure, PMPS - a polymer with stronger internal relaxations (phenyl and methyl group rotations) exhibited much larger residual broadening at T_g than PEMS - a polymer with weaker internal processes (ethyl and methyl group rotations). This residual broadening is due to the contribution of the intra-molecular processes, since at T_g, as we have shown, the amplitude of the structural relaxation contribution is negligible.

It is also shown that the pressure dependent measurements allow for the separation of the contributions due to intra-molecular and structural relaxations to the polarized Brillouin line widths and the damping of the longitudinal phonons.

From the pressure dependent polarized Brillouin line width of PMPS the temperature dependent contributions of internal and structural relaxations to the Γ_B and the damping of longitudinal phonons were estimated. The internal contribution is changing from 0.12 to 0.18 GHz and the structural one from 0 to 0.25 GHz in the temperature range from T_g to $T_g + 60$ K.

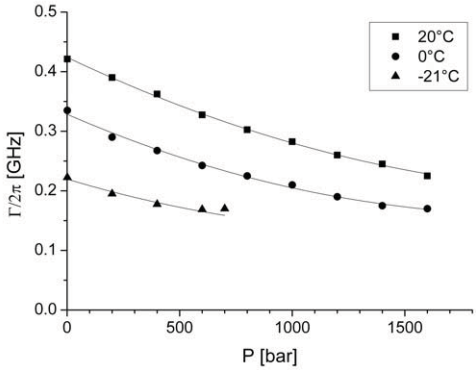

FIG. 2: Pressure dependence of the half width of the polarized Brillouin peak measured for PMPS at indicated temperatures.

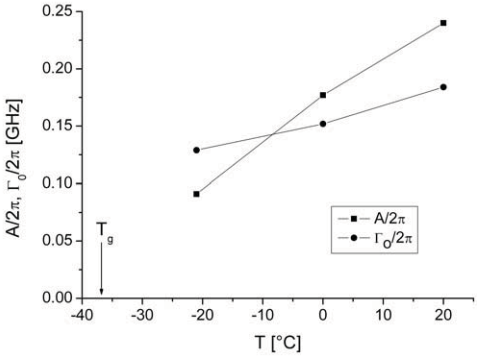

FIG. 3: Temperature dependence of Γ_0 and A obtained for PMPS from the polarized Brillouin spectra.

[1] A. Aouadi et al., *J. Chem. Phys.* 112, 9860 (2000); C. Dreyfus et al., *Europhys. Lett.*, 42, 55 (1998)

[2] R. Zwanzig, *J. Chem. Phys.*, 43, 714 (1965)

[3] A. Patkowski et al., *Europhys. Lett.*, 73, 607 (2006); A.Patkowski et al.,*J. Chem. Phys.* 126, 014508 (2007)

[4] H. Kriegs et al., *J. Chem. Phys.* 124, 104901 (2006)

[5] S. Saito et al., *J. Polym. Sci. Part A2*, 6, 1297 (1968)

[6] G. Williams, *Trans. Faraday Soc.*, 62, 2091 (1966)

[7] G. Fytas et al., *Coll. Polym. Sci*, 260, 949 (1982)

[8] H. Kriegs et al., *J. Chem. Phys.* 128, 014507 (2008)

Boundary-Induced Phase Transition in Single-File Diffusion

A. Brzank, S. Chatterjee, G. M. Schütz
IFF-2: Theoretical Soft-Matter and Biophysics

Single-file diffusion is a stochastic many-body process where particles cannot pass each other during diffusion due to geometric constraints (e.g. in a narrow channel) or complex transport mechanisms (e.g. in molecular motors). In recent work this generic quasi one-dimensional phenomenon has been suggested to explain an experimentally observed trapping effect of a binary mixture of hydrocarbon molecules adsorbed in certain zeolites. Also unexpected boundary layers and a non-equilibrium pumping effect known from symporter ion channels have been reported in simulation studies of single-file diffusion. We show that these observations (and more!) can be fully explained in terms of the two-component symmetric exclusion process with open boundaries. Indeed, exact analytical treatment of this model for single-file diffusion reveals the existence of a novel discontinuous phase transition in the far-from equilibrium regime of this one-dimensional system with short range interaction.

We consider single-file diffusion in an open system with two species A, B of particles. At the boundaries we assume different reservoir densities which drive the system into a non-equilibrium steady state. As a model we use an one-dimensional two-component simple symmetric exclusion process with two different hopping rates D_A, D_B and open boundaries. Following [1] we consider a one-dimensional lattice with L lattice sites (Fig. 1). Each site i can be empty or occupied by a particle of type A or B. Due to hard-core interaction any site carries at most one particle. Particles can hop to nearest neighbour sites (provided the target site is empty) with hopping rates $D_{A/B}$. In the case of open boundary conditions, particles are injected and removed according to the boundary rates $\alpha_{A/B}, \gamma_{A/B}, \beta_{A/B}$ and $\delta_{A/B}$ as illustrated in Fig. 1. Jump events occur after an exponentially random time which in dynamic Monte Carlo simulations (DMCS) is modelled by random sequential update [1].

We consider

$$\alpha_{A/B} = D_{A/B}\rho^-_{A/B}, \quad \gamma_{A/B} = D_{A/B}(1 - \rho^-_A - \rho^-_B) \tag{1}$$

$$\delta_{A/B} = D_{A/B}\rho^+_{A/B}, \quad \beta_{A/B} = D_{A/B}(1 - \rho^+_A - \rho^+_B). \tag{2}$$

FIG. 1: Two-component symmetric exclusion model with open boundaries. Each species of particles has its own hopping rates D_A, D_B. At the boundaries particles are extracted and injected with rates as indicated.

If the equilibrium condition $\rho^-_{A,B} = \rho^+_{A,B}$ of equal reservoir densities or chemical potentials $\mu^-_{A,B} = \mu^+_{A,B}$ holds then the process has an unique uncorrelated stationary equilibrium distribution with constant local particle densities equal to the reservoir densities. In a non-equilibrium setting the left reservoir densities ρ^-_A, ρ^-_B are not equal to those on the right boundary (ρ^+_A, ρ^+_B). In this boundary-driven case the system evolves towards a complicated stationary state with non-vanishing particle currents.

Since we are not interested in the microscopic details of the distribution of particles in the model we investigate the coarse-grained behaviour that emerges under diffusive scaling of small lattice constant and macroscopic time scales. In order address experimentally relevant problems we need to investigate both relaxation dynamics and stationary behaviour.

For investigating the dynamics in this hydrodynamic limit we extend the rigorous approach of Quastel [2] and make an ansatz for the dynamics of a single particle (of species A or B) localized at position x. This test particle acts as a tracer particle in the background of other particles, with a diffusive motion partially determined by its self-diffusion coefficient. Additionally, the test particle is subject to a background drift b caused by the collective evolution of the entire system towards stationarity. This yields a system of coupled non-linear diffusion equations for the coarse-grained particle densities

$$\partial_t \rho_A(x,t) = \partial_x^2 D_s \rho_A(x,t) - \partial_x b(x,t)\rho_A(x,t) \tag{3}$$

$$\partial_t \rho_B(x,t) = \partial_x^2 D_s \rho_B(x,t) - \partial_x b(x,t)\rho_B(x,t). \tag{4}$$

The drift term b can then be determined by using

$$\partial_t \left(\frac{\rho_A(x,t)}{D_A} + \frac{\rho_B(x,t)}{D_B} \right) = \partial_x^2 (\rho_A(x,t) + \rho_B(x,t)). \tag{5}$$

Here we used diffusive rescaling of the time-

coordinate. One finds

$$b = \frac{1}{\sigma}\partial_x(D_s\sigma - \rho). \tag{6}$$

In an infinite system the self-diffusion coefficient vanishes, as is indicated by the well-known subdiffusive nature of single-file diffusion. However, as argued in [1] we expect that in a finite system with open boundaries correction terms of leading order $1/L$ appear. This is confirmed by the exact result

$$D_s = \frac{1}{L}\frac{1-\rho}{\sigma} \tag{7}$$

proved in [3] for a finite periodic system with L sites. With these quantities we have obtained an exact coarse-grained description of the time evolution of the microscopic particle model in terms of a system of nonlinear partial differential equations. The microscopic open boundary conditions correspond to constant boundary densities in the macroscopic description.

The relaxation of the initial density profile is analyzed by numerical integration and good agreement is found with Monte-Carlo simulation of the process [3]. Single-file diffusion is expected for zeolites whose crystalline structure leads to long diffusion channels. Assuming Arrhenius behaviour single-particle diffusion rates we can describe the trapping of light particles by heavy particles as observed experimentally in a binary loading of the zeolite EUO [4]. In fact, according to numerical simulation of our model a small shift in the two empirical desorption peaks for toluene and propane resp. indicates a violation of the strict single-file assumption.

The stationary density profiles have an interesting structure. Under generic nonequilibrium conditions with non-zero exterior boundary gradients a boundary layer develops at one boundary. Inside this layer the current flows against the local density gradient. Generically the width of the boundary layer and the bulk density profiles do not depend on the two hopping rates. For vanishing exterior gradient of the total, colourblind density, however, the individual density profiles depend strongly on the ratio D_A/D_B. Dynamic Monte Carlo simulation confirm our theoretical predictions, see Fig. 2.

For the current we find for positive exterior grandient to leading order in $1/L$

$$j_A = \begin{cases} \frac{\rho_A^+}{\frac{\rho_A^+}{D_A}+\frac{\rho_B^+}{D_B}}\frac{\rho^- - \rho^+}{L} & \text{for } \rho^- < \rho^+ \\ \frac{\rho_A^-}{\frac{\rho_A^-}{D_A}+\frac{\rho_B^-}{D_B}}\frac{\rho^- - \rho^+}{L} & \text{for } \rho^- > \rho^+ \end{cases} \tag{8}$$

Hence, as one expects, the A-current is always opposite the total reservoir gradient $\Delta\rho \equiv \rho^+ - \rho^-$, but it changes in a non-analytic fashion at $\rho^- = \rho^+$ where it vanishes to leading order in $1/L$. Interestingly, however, the current of B-particles may have the same sign as the exterior reservoir gradient of B-particles. This counterintuitive phenomenon is a pumping effect known from symporter ion channels. Thus we have obtained a quantitative theoretical description

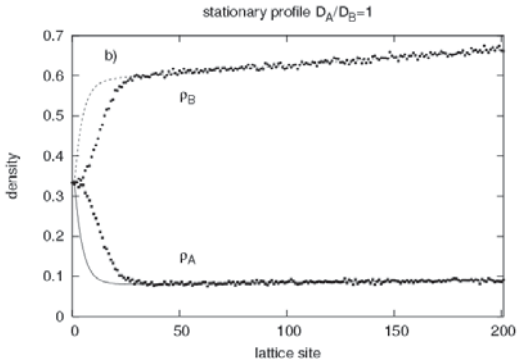

FIG. 2: Simulation of the stationary state with finite slope of the colour-blind density for lattice size $L = 100$. The boundary densities are $\rho_A^- = \rho_B^- = 1/3$, $\rho_A^+ = \frac{e}{1+e^{-1}+e}$ and $\rho_A^+ = \frac{e^{-1}}{1+e^{-1}+e}$.

of this pumping effect which was so far only known qualitatively by numerical simulation of the present model for a small lattice [5].

By changing the sign of the exterior gradient of the total, colourblind density we find a discontinuous boundary-induced phase transition in the steady state. The boundary layers switches from one boundary to the other and the order parameter, viz. the asymptotic space-averaged mean density, changes discontinuously. We find

$$\bar{\rho}_A = \lim_{L\to\infty}\frac{1}{L}\int_0^L dx\rho_A(x) \tag{9}$$

takes the value

$$\bar{\rho}_A = \frac{\rho_A^\pm}{\rho^\pm}\frac{\rho^+ + \rho^-}{2} \tag{10}$$

where the positive (negative) sign occurs for positive (negative) exterior gradient $\rho^+ - \rho^-$ of the total density $\rho^\pm = \rho_A^\pm + \rho_B^\pm$.

[1] A. Brzank and G.M. Schütz, *Boundary-induced bulk phase transition and violation of Fick's law in two-component single-file diffusion with open boundaries* Diffusion Fundamentals, **4** (2006), 7.1-7.12.

[2] J. Quastel, *Diffusion of Color in the simple exclusion process*, Comm. Pure Appl. Math. **45** (1992), 623-679.

[3] A. Brzank and G.M. Schütz, *Phase Transition in the two-component symmetric exclusion process with open boundaries*, J. Stat. Mech. (2007), P08028.

[4] K.F. Czaplewski, T.L. Reitz, Y.J. Kim and R.Q. Snurr *One-dimensional zeolites as hydrocarbon traps* Micropor. Mesopor. Mater. **56** (2002), 55

[5] T. Chou and D. Lohse, *Entropy-driven pumping in zeolites and biological channels* Phys. Rev. Lett. **82** (1999), 3552-3555.

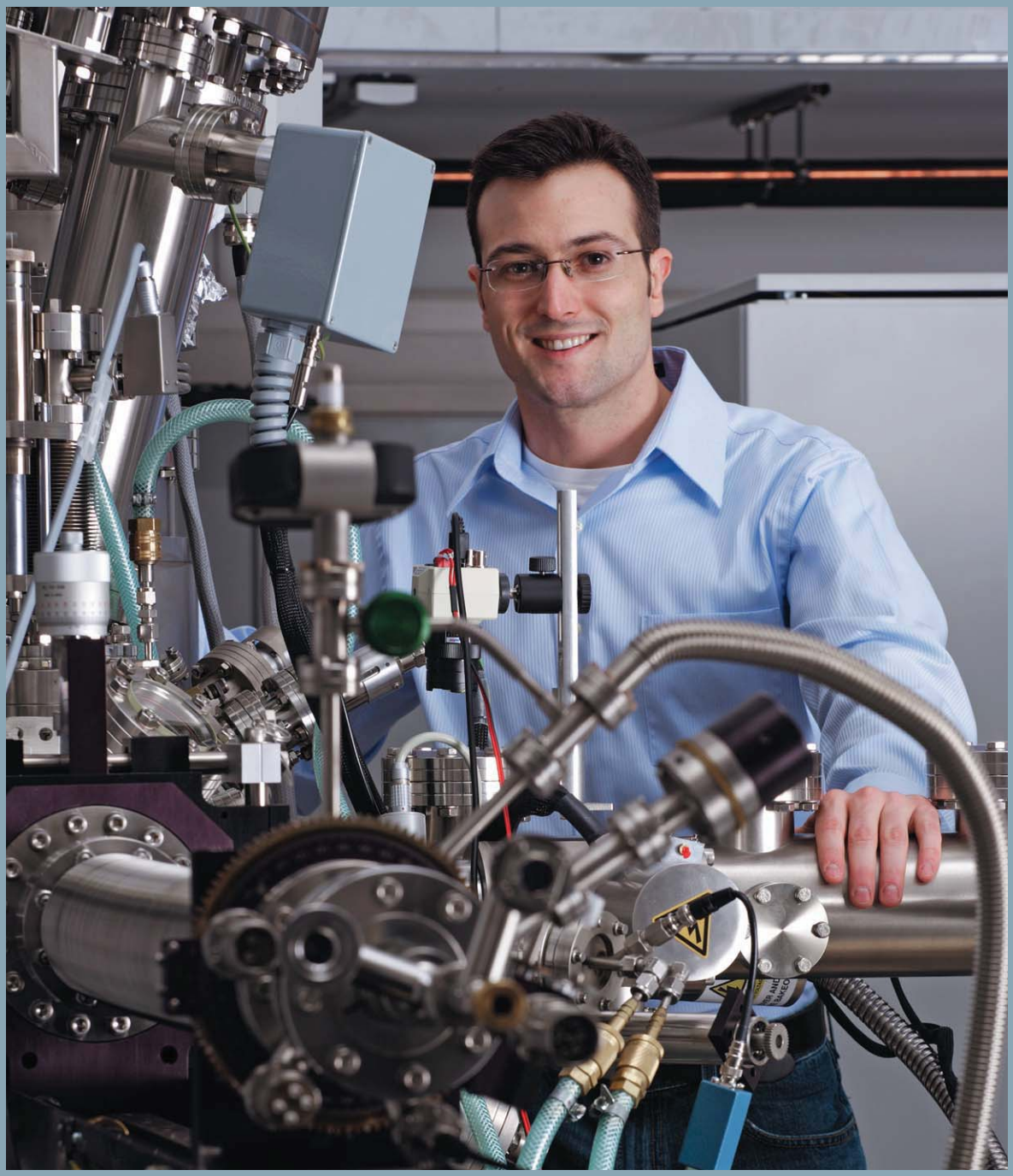

Physicists at the IFF are developing new materials for Spintronics. The Nano-Spintronics Cluster Tool combines several state of the art instruments in one facility and allows the study of magnetic systems on nanoscopic and mesoscopic lengthscales.

Information Technology with Nanoelectronic Systems

This research programme focuses on medium-term and long-term tasks in nanoelectronics, on emerging far-reaching concepts, and on issues of physics and technology well ahead of the mainstream development. On the eve of the transition from microelectronics to nanoelectronics, the traditional routes of down-scaling along the roadmap will no longer guarantee a long-term success. Exploratory research in the field of information technology is entering a new era and is unfolding into new degrees of freedom. This applies to all three major fields, information processing, information storage, and information transmission. The major routes of exploratory research in nanoelectronic systems to be followed are:

- scalability of device concepts,
- exploration of new material classes and phenomena,
- new concepts beyond conventional CMOS technology, and
- alternative architectures.

Our research towards these general goals utilizes three approaches, irrespective of the specific programme topics. One approach is dedicated to new electronic materials such as ferromagnetic and ferroelectric layer structures, group III nitrides, and electronically active organic molecules. These material classes are studied because of their potential for introducing improved or completely new functions onto Si chips and new emerging substrates. Another approach is devoted to process technologies for minimum feature sizes well below 100 nm. Apart from using conventional top-down approaches, which are limited to lithographically defined resolutions, we are investigating cost-effective bottom-up approaches, which aim at the generation and assembly of functions from self-organized inorganic nanostructures as well as tailored organic molecules at surfaces. Yet another approach explores novel electronic functions as the basis for new device concepts. These may aim at, for instance, bioelectronic applications, ultra-dense and non-volatile resistive memories, spin-controlled devices, Terahertz imaging systems, and self-organized semiconductor nanostructures.

Surface-, Edge- and Quantum-Well-States of Thin Bi Films for Spintronics

G. Bihlmayer[1], Yu. M. Koroteev[2], E. V. Chulkov[3], and S. Blügel[1]

[1] IFF-1: Quantum Theory of Materials
[2] Institute of Strength Physics and Materials Science, RAS, 634021, Tomsk, Russia
[3] Donostia International Physics Center (DIPC), 20018 San Sebastiàn/Donostia, Spain

Due to their electronic similarity with graphene sheets, surfaces and thin films of the semimetal bismuth have received quite some attention in the last years. In these materials the spin-Hall effect can lead to spin currents at the boundaries of thin films, which makes them potentially useful for spintronic applications. We studied the spin-polarization of surface- and quantum-well-states of thin Bi films in (111) and (110) orientation, as well as the electronic structure of semiconducting ultrathin Bi films which allows the prediction of quantum spin-Hall phases on a theoretical basis [1]. Comparison with experimental data shows that a Rashba-type spin-splitting of the surface states can also be observed in thin Bi(111) films deposited on Si substrates [2].

Bulk Bi is a semimetal with large nuclear number, leading to strong spin-orbit coupling effects. The surfaces of bismuth are metallic due to prominent surface states, which show a pronounced Rashba-type spin-splitting. Based on density functional theory calculations we studied thin $(1-6$ bilayers) films in (111) and (110) orientation. Due to the different coordination of the surface atoms in these two cases, a large variation of the conducting properties of the films is found, ranging from small-bandgap semiconducting to semimetallic and metallic [3]. Experimentally, ultrathin Bi films can be prepared on Si(111) substrates, which are electronically almost decoupled from the substrate [4]. On the surfaces of these films, surface states can be observed (Fig.1), which can be considered to form a two-dimensional electron gas (2DEG). Due to relativistic effects, an electric field $\mathbf{E}$ (e.g., the potential gradient normal to the surface) is seen by the moving electrons of the 2DEG as a magnetic field that couples to the spin of the electron. This leads to a spin-splitting of the surface states, caused by what is known as Rashba effect in the field of semiconductor spintronics. The Hamiltonian describing this coupling is

$$H_{\mathrm{R}} = \alpha_{\mathrm{R}}(|\mathbf{E}|)\,\boldsymbol{\sigma}\cdot(\mathbf{k}_{\parallel}\times\hat{\mathbf{e}}_z) \qquad (1)$$

where $\mathbf{k}_{\parallel} = (k_x, k_y, 0)$ characterizes the crystal momentum of a surface electron, $\boldsymbol{\sigma}$ are the Pauli matrices and $\hat{\mathbf{e}}_z = (0,0,1)$. α_{R} is called the Rashba parameter.

Surface states appear in the gaps of the projected bulk bandstructure. Since they cannot couple to the bulk states, they are localized in a few topmost layers of the crystal. In the case of a semimetal, where the bulk density of states at the Fermi level is (almost) zero, metallic surface states are the only available charge carriers at small bias voltages. Due to the strong Rashba-type spin splitting on the hexagonal Bi(111) surface, significant spin-accumulation effects can arise when a bias is applied. This intrinsic spin-Hall effect can be simulated for four-terminal nanostructure samples on the basis of the Landauer-Keldysh formalism, with a tight-binding Hamiltonian adapted to simulate the surface bandstructure obtained by density functional theory. Assuming that only nearest-neighbor hopping contributes to the transport properties, the Bi(111) surface can be substituted by a bilayer, where the atoms connect to form a buckled honeycomb-lattice. In contrast to semiconductor heterostructures, where the spin-precession lengths are in the order of several hundred nanometers, in Bi(111) the spin-precession length is about 4nm, which causes complicated spin- and charge accumulation patterns [5]. Additionally, these effects

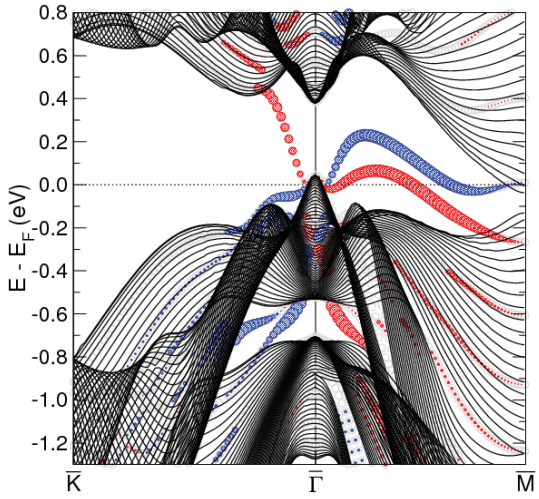

FIG. 1: Electronic structure of a 10 bilayer Bi(111) film: the bulk-projected bands are shown as black lines, in the gaps of the bulk bandstructure surface states evolve. Their spin-orientation on one side of the film is indicated by red and blue circles. The strength of the spin-polarization is reflected by the size of the circles. The gray symbols indicate the electronic states of the film.

depend on the direction of conductance as well as on the applied bias voltage.

The situation is different in the case of thin films: since a symmetric film has two equivalent surfaces with opposite $\mathbf{E}$, the bandstructure of these films will show Kramers degenerate bands. Nevertheless, on a particular side of the film a definite spin-orientation can be observed, as shown in Fig.1. Depending on the extent of the localization, in a thin film a coupling between the surface states on both sides of the film cannot be avoided, and the spin-polarization can be reduced. Such a $\mathbf{k}_{\|}$ dependent variation of the spin-polarization has indeed been observed experimentally [2]. This reduction of spin-polarization can also be seen from the size of the symbols in Fig.1, that decreases as the surface state approaches the bulk-projected bands at the edge of the Brillouin-zone (M-point). In the case of a quantum-well state, which extends through the whole film, no effective $\mathbf{E}$ arises and the spin-polarization is lost. Therefore quantum-well states, as can be observed in the vicinity of the borders of the Brillouin-zone (M-point in Fig.1), show no Rashba-type spin splitting. Experimentally, these quantum-well states have been observed in films up to 17 bilayer thickness [4], without any sign of a spin splitting. This indicates also that the interaction of the films with the Si(111) substrate is very weak, otherwise the broken inversion symmetry (finite $\mathbf{E}$) would be observable in the bandstructure.

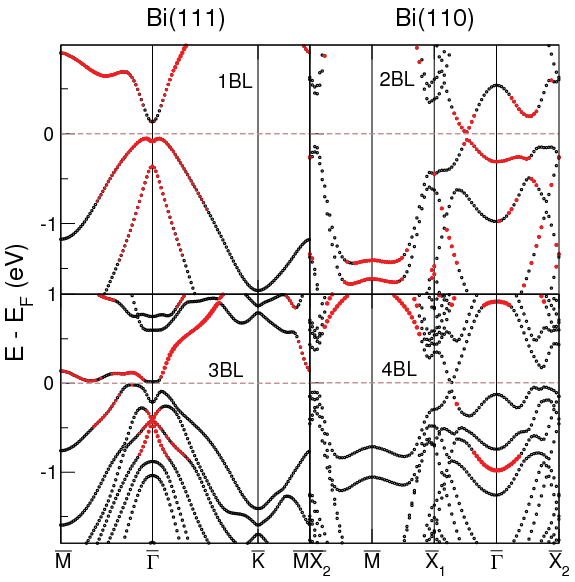

FIG. 2: Electronic structure for 1 and 3 bilayer Bi(111) films (left) and for 2 and 4 bilayer Bi(110) films (right). Red dots indicate states which have a significant weight in the vacuum region.

In ultrathin Bi films, the concept of surface state gradually looses its meaning as the film thickness is reduced. Below a thickness of four bilayers Bi(111) films get semiconducting (cf. left of Fig. 2). If the symmetry of the bands fulfills certain criteria, these ultrathin films can form a so-called spin-Hall phase [1]. In analogy to graphene-ribbons, stripes of these Bi films can support edge-states which can carry spin-currents. Edge-states of stripes can be considered to be one-dimensional analoga of the surface states that arise on both sides of a thin film.

Experimentally, very thin Bi films grow in black phosphorus (A17) structure, consisting of double-bilayers. A single bilayer of this structure is quite similar to the bilayers formed on the pseudocubic Bi(110) surface. Only beyond six bilayer thickness, the Bi films transform into the hexagonal Bi(111) films discussed above. Therefore, we studied also the electronic structure of ultrathin Bi(110) films, both in A7 (Bi) and A17 structure. From our calculations and scanning tunneling spectroscopy experiments it is evident that A17 films are semimetallic, while Bi(111) films show metallic surface states [6]. As can be seen from the bandstructures in Fig. 2 (right), two and four bilayer Bi(110) films are even semiconducting [3]. Another interesting aspect of the Bi(110) bandstructures is the avoided crossing of the bands at $\overline{\mathrm{X}}_1 - \overline{\Gamma}$, which again reminds of the graphene bandstructure with the well-investigated Dirac point.

As a consequence of this large variety of conducting properties of thin Bi films and the fact that the growth of Bi on semiconducting substrates is experimentally well studied, these films are promising candidates for applications in the field of spintronics. Furthermore, alloying Sb with Bi can be used to vary not only the lattice parameter but also the spin-orbit coupling strength and by doping with Sn it is possible to tune the band-filling for specific needs. Further calculations along these lines are in progress to stimulate and guide experimental efforts and to achieve a deeper understanding of the properties of the electronic states arising at the surfaces and edges of these materials.

[1] S. Murakami, Phys. Rev. Lett. **97**, 236805 (2006).

[2] T. Hirahara, K. Miyamoto, I. Matsuda, T. Kadono, A. Kimura, T. Nagao, G. Bihlmayer, E. V. Chulkov, S. Qiao, K. Shimada, H. Namatame, M. Taniguchi, and S. Hasegawa, Phys. Rev. B **76**, 153305 (2007).

[3] Yu. M. Koroteev, G. Bihlmayer, E. V. Chulkov, and S. Blügel, Phys. Rev. B (accepted, 2008).

[4] T. Hirahara, T. Nagao, I. Matsuda, G. Bihlmayer, E. V. Chulkov, Yu. M. Koroteev, P. M. Echenique, M. Saito, and S. Hasegawa, Phys. Rev. Lett. **97**, 146803 (2006).

[5] Ming-Hao Liu, G. Bihlmayer, S. Blügel, and Ching-Ray Chang, Phys. Rev. B **76** 121301(R) (2007).

[6] S. Yaginuma, K. Nagaoka, T. Nagao, G. Bihlmayer, Yu. M. Koroteev, E. V. Chulkov, and T. Nakayama, J. Phys. Soc. Jpn. **77**, 014701 (2008).

Prediction of High Curie Temperature in bcc-Co and FeCo Alloys

M. Ležaić, Ph. Mavropoulos, S. Blügel
IFF-1: Quantum Theory of Materials

In spintronics devices it is essential that the magnetic elements have a high Curie temperature, T_C, associated with the ferromagnetic phase transition. A T_C much higher than room temperature, RT, guarantees low magnetic fluctuations and better operational characteristics at RT. In particular for magnetic tunnel junctions a high T_C ensures temperature stability of the tunneling magnetoresistance. We determine from first principles the T_C of Co, FeCo alloys, and Fe. For bcc-Co, T_C=1420 K is predicted. This would be the highest T_C among the Co phases, suggesting that bcc-Co/MgO/bcc-Co tunnel junctions offer high magnetoresistance ratios even at RT.

In the past few years we are witnessing a compelling race of different research groups [1] hunting the maximum tunneling magneto-resistance ratio (TMR) of magnetic tunnel junctions [2] (MTJs). MTJs, made of two ferromagnetic electrodes separated by an insulating barrier, open vistas to a wide field of technological applications, in particular in non-volatile magnetic random access memory, or new type of recording heads for ultrahigh-density hard-disk drives. Recently, giant values of over 150% at RT have been experimentally achieved for fully epitaxial MgO-based MTJs [1, 3]. Theory predicts (at temperature $T = 0$) extremely high TMR of over 1000% for Fe/MgO/Fe and even higher for epitaxial bcc-Co/MgO/bcc-Co junctions [2]. Bcc-Co is a metastable phase, which has been successfully grown in contact with MgO, and epitaxial bcc-Co/MgO/bcc-Co(100) MTJs have shown a high TMR, unusually stable [3] with T.

In most MTJs there is a large difference of the TMR between cryogenic and room temperature. The TMR (relative change of resistance when the magnetic leads are coupled either ferromagnetically or antiferromagnetically) depends on the details of the electronic structure; at $T > 0$, magnetic excitations mix the two spin channels, decreasing the TMR. One can infer that a high T_C and spin stiffness entail a temperature stability of the magnetic structure and of the TMR. In this work [4] we investigate the Curie temperature of bcc-Co and $Fe_{1-x}Co_x$ alloys concluding that a high (calculated) [5] T_C of bcc-Co is responsible for the temperature stability [3] of TMR in Fe/bcc-Co/MgO/bcc-Co/Fe junctions.

For the calculation, *ab initio* total-energy results are mapped to the classical Heisenberg model from which T_C is found by a Monte Carlo method. The Hamiltonian reads

$$H = -\sum_{i,j\,;\,i\neq j} J_{ij}\,\vec{e}_i\cdot\vec{e}_j. \qquad (1)$$

The exchange constants J_{ij} between the magnetic moments at sites i and j are related to the Green function; $\vec{e}_i$ is a unit vector along the moment of atom i. For the *ab initio* calculations we employ the Korringa-Kohn-Rostoker Green function method [6], using the coherent potential approximation to treat the disorder in $Fe_{1-x}Co_x$. Our study includes Fe and Co in bcc and tetragonalized (bct) phases (considering growth on MgO(001)), and FeCo alloys.

Our results are summarized in Table 1. A striking effect is that the magnetization, exchange constants and T_C of Fe is very sensitive to structural changes, e.g., tetragonalization or moderate volume change (not shown here). This is in contrast to bcc Co and FeCo alloys. Also, the magnetization and T_C increase with Co concentration, peaking at $x = 0.5$ and $x = 0.75$, respectively. The change of the Fe properties upon increasing the Co concentration can be explained by observing that Fe progressively changes character from a weak ferromagnet (both majority- and minority-spin d-states, $d^\uparrow$ and $d^\downarrow$, are only partly occupied for pure Fe) to a strong ferromagnet ($d^\uparrow$ states become fully occupied); Co itself is a strong ferromagnet. As is long known [7], the average moment per unit cell, $\overline{M}$, first rises upon alloying with Co, due to the rapid increase of the Fe local moment, then peaks and drops for higher Co content (because of the comparatively lower Co moment).

In a weak ferromagnet the magnetic properties are sensitive to structural perturbations because an extended part of the Fermi surface has $d^\uparrow$ and $d^\downarrow$ character, allowing for $d^\uparrow$-$d^\downarrow$ charge transfer upon the structural perturbation. Such transfer can affect the local moment, but even more the spin susceptibility (and exchange constants J_{ij}) which is sensitive to $d^\uparrow$-$d^\downarrow$ Fermi-surface crossing because of virtual $d^\uparrow$-$d^\downarrow$ spin-flip excitations. In strong ferromagnets (Co or FeCo alloys), this mechanism becomes inert because the $d^\uparrow$ band is fully occupied, well under E_F. Thus the J_{ij} are more stable in Co and FeCo alloys.

We proceed to the discussion of T_C by introducing the coefficient $J_0 = \sum_{i\neq 0} J_{0i}$, corresponding to the

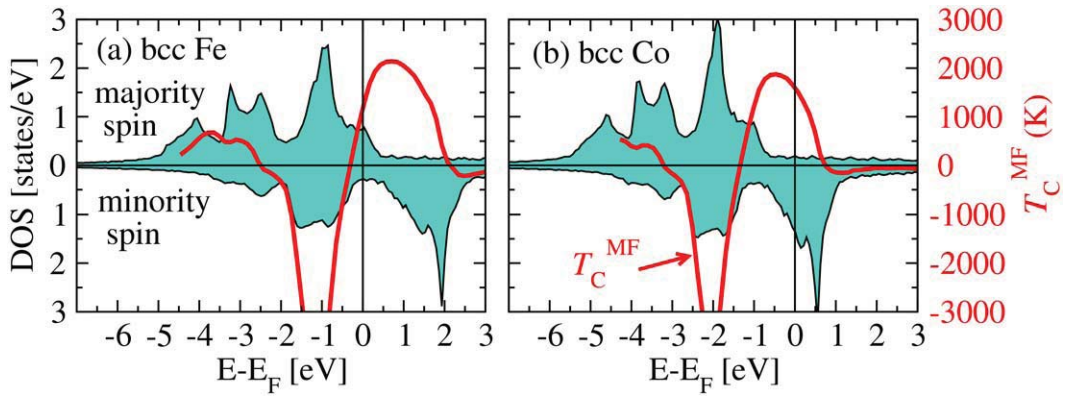

FIG. 1: Density of states (black line) and mean-field ordering temperature (red line) for bcc Fe (a) and bcc Co (b).

Alloy (c/a)	M_{Fe}	M_{Co}	$\overline{M}$	$\overline{M}_{\mathrm{exp}}$[7]	$J_1^{\mathrm{Fe-Fe}}$	$J_1^{\mathrm{Co-Co}}$	$J_1^{\mathrm{Fe-Co}}$	T_{C}
Fe bcc	2.107	–	2.107	2.22	17.45	–	–	970
Fe bct (0.909)	2.321	–	2.321	–	12.71	–	–	750
$Fe_{0.75}Co_{0.25}$ (dis.)	2.421	1.785	2.263	2.45	25.80	24.54	31.78	1390
$Fe_{0.50}Co_{0.50}$ (dis.)	2.523	1.778	2.151	2.35	28.55	22.05	30.76	1600
FeCo (ord.)	2.729	1.727	2.228	2.42	–	–	28.84	1660
$Fe_{0.25}Co_{0.75}$ (dis.)	2.560	1.759	1.959	–	26.64	20.01	28.33	1520
Co bcc	–	1.751	1.751	–	–	18.48	–	1420
Co bct (0.857)	–	1.740	1.740	–	–	16.76	–	1380
Co fcc	–	1.646	1.646	–	–	13.82	–	1280

TAB. 1: Calculated magnetic moments (μ_B), first-neighbor exchange constants J_1 (meV), and T_{C} (K) of bcc disordered (dis.) and ordered (ord.) FeCo alloys, bcc and bct Fe and Co, and fcc Co. For the bct structures, the in-plane lattice constant was adapted to MgO and c/a was relaxed. Experimental values are [5]: bcc Fe: $T_{\mathrm{C}} = 1043$ K; fcc Co: $T_{\mathrm{C}} = 1403$ K.

band-energy cost for flipping the magnetic moment of a single atom, reflecting a "single-site spin stiffness". It is related to the mean-field Curie temperature via $k_B T_{\mathrm{C}}^{\mathrm{MF}} = 2J_0/3$ (k_B is Boltzmann's constant). (Mean-field theory overestimates T_{C}, but it is a useful tool for trends analysis.) By treating E_F as a parameter, we calculate $T_{\mathrm{C}}^{\mathrm{MF}}(E)$ as a function of band filling; in this way we see the individual contribution of the states at each energy to the exchange interactions. In Fig. 1 we show $T_{\mathrm{C}}^{\mathrm{MF}}(E)$, together with the density of states, for bcc Fe and Co. The negative values of $T_{\mathrm{C}}^{\mathrm{MF}}(E)$ indicate an antiferromagnetic coupling, known from Cr. At higher energies the double-exchange mechanism sets in and $T_{\mathrm{C}}^{\mathrm{MF}}(E)$ obtains strong positive contributions as E crosses the final part of the $d^{\uparrow}$ states and the anti-bonding $d^{\downarrow}$ states. Finally it drops to zero once the $d^{\downarrow}$ states are filled.

In Fe, E_F is located at a steep, ascending point of $T_{\mathrm{C}}^{\mathrm{MF}}(E)$, before the maximum. Thus small structural perturbations result in band shifts with a strong influence on the T_{C} of Fe, as seen in Table 1. For Co, $T_{\mathrm{C}}^{\mathrm{MF}}(E)$ is descending at E_F, but is not as steep as for Fe. From this argument, Co is expected to have a higher and more robust T_{C} than Fe. In a FeCo alloy E_F is in-between, at the maximum of $T_{\mathrm{C}}^{\mathrm{MF}}(E)$; then one expects the highest and most robust T_{C}.

In conclusion, ferromagnetism is found to be more robust in bcc Co than in bcc Fe. The T_{C} of bcc Co is calculated to be the highest among all Co phases, and stable with respect to structural changes, even in tetragonalized structures. This is advantageous in the temperature dependent TMR of Co/MgO/Co MTJs compared to Fe/MgO/Fe, as observed in experiments [3]. We suggest FeCo/bcc-Co/MgO/bcc-Co/FeCo(100) as an ideal junction for high TMR at RT. The reasons for this are: (i) FeCo has the highest T_{C} and is thus an ideal back-lead. (ii) The T_{C} of bcc-Co is very high, promising lower magnetic fluctuations at the interface. (iii) Epitaxial bcc-Co/MgO(100) interfaces present excellent coherent transport properties [2] unlike a possibly disordered FeCo/MgO interface. We conclude that, at RT, the suggested junction has a higher TMR than Fe/MgO/Fe(100) or Fe/bcc-Co/MgO/bcc-Co/Fe(100).

[1] S.S.P. Parkin *et al.*, Nature Materials **3**, 862 (2004); S. Yuasa *et al.*, Nature Materials **3**, 868 (2004).

[2] E.Y. Tsymbal, O.N. Mryasov, and P.R. LeClair, J. Phys.: Condens. Matter **15**, R109 (2003); X.G. Zhang and W.H. Butler, Phys. Rev. B **70**, 172407 (2005).

[3] S. Yuasa *et al.*, Appl. Phys. Lett. **89**, 042505 (2006).

[4] M. Ležaić, P. Mavropoulos, and S. Blügel, Appl. Phys. Lett. **90**, 082504 (2007).

[5] T_{C} cannot be measured for bcc $Fe_{1-x}Co_x$ at high x, since these alloys transform to fcc at about 1200 K.

[6] SPR-TB-KKR package, H.Ebert and R.Zeller, http://olymp.cup.uni-muenchen.de/ak/ebert/SPR-TB-KKR

[7] R.M. Bozorth, *Ferromagnetism*, Van Nostrand, New York, 1951; D. I. Bardos, J. Appl. Phys. **40**, 1371 (1969).

Large Inverse TMR in $Co_2Cr_{0.6}Fe_{0.4}Al$ Based Magnetic Tunnel Junctions

A. D. Rata, H. Braak, D. E. Bürgler, C. M. Schneider

IFF-9: Electronic Properties
CNI: Center of Nanoelectronic Systems for Information Technology

Magnetic tunnel junctions based on the Heusler alloy $Co_2Cr_{0.6}Fe_{0.4}Al$ and MgO barriers fabricated by magnetron sputtering exhibit a large inverse tunneling magnetoresistance (TMR) effect of up to -66% at room temperature. The largest value of -84% at 20 K reflects a rather weak influence of temperature. The dependence on the voltage drop shows an unusual behavior with two almost symmetric peaks at ± 600 mV with large inverse TMR ratios and small positive values around zero bias. These results are of high relevance for applications, as they combine a large TMR ratio at a high output voltage with a moderate temperature dependence.

The tunnel magnetoresistance effect (TMR) is subject of intense research due to its potential for spintronic applications. The aim is to achieve a large TMR ratio at practical output voltages in combination with a weak temperature dependence. A promising strategy for obtaining large TMR effects is to use ferromagnetic (FM) electrodes with an *intrinsically* high spin polarization, such as half-metallic ferromagnets featuring 100% spin polarization of the carriers. Among the vast family of the half-metallic ferromagnets, the Heusler alloys are promising candidates due to their high Curie temperatures well above 300 K. In the last years, experimental efforts were concentrated on improving the structure of Heusler thin films and the properties of the interface between the Heusler electrode and the oxide barrier. Relatively high TMR ratios up to 90% at room temperature (RT) have been obtained using Co-based full-Heusler alloy thin films, in particular $Co_2Cr_{0.6}Fe_{0.4}Al$ (CCFA) [1]. Here we report on large *inverse* TMR values obtained from CCFA/MgO/$Co_{80}Fe_{20}$ magnetic tunnel junctions (MTJ) [2].

Details on the preparation and characterization of $Co_2Cr_{0.6}Fe_{0.4}Al$ (CCFA) Heusler thin films have been published elsewhere [2, 3]. In contrast to previous reports about the growth of CCFA films on MgO(001) substrates[1, 4], our CCFA films are grown at RT and adopt a different crystalline orientation with respect to the MgO(001) substrate [3]. The [011] direction of the CCFA films is parallel to [001] of the MgO(001) substrate. The CCFA films have the B2 structure, since the (111) reflection is absent in the X-ray diffraction patterns. Magnetization measurements of extended CCFA films reveal ferromagnetic ordering with Curie temperatures up to 630 K after annealing in vacuum at 773 K. The total magnetic moment found is about $2.5\mu_B$ per formula unit (f.u.). This value is small compared to the theoretical bulk value of $3.8\mu_B$/f.u., but still comparable to the moments reported in Ref. [4] for films grown at elevated temperature.

MTJs are prepared by magnetron sputtering at RT without breaking the vacuum with the layer sequence MgO(100) / MgO(40 nm) / CCFA(25 nm) / MgO(3 nm) / $Co_{80}Fe_{20}$(5 nm) / IrMn(15 nm). A 40 nm-thick MgO seed layer is deposited on the MgO substrate to improve the texture of the CCFA electrode. CCFA and MgO are deposited by DC and RF stimulated discharge, respectively, from stoichiometric targets. The completed stack is annealed *in-situ* for 1 hour at 523 K in order to improve the interface quality.

Junctions with an area from 3×3 up to 15×15 μm^2 with cross-bar electrodes are patterned for magnetotransport measurements in the current-perpendicular-plane (CPP) geometry by optical lithography. The transport measurements are performed with a DC setup in the standard 4-point geometry using a constant current source. $I - V$ characteristics measured at RT in zero field show nonlinear, *i.e.* non-Ohmic behavior.

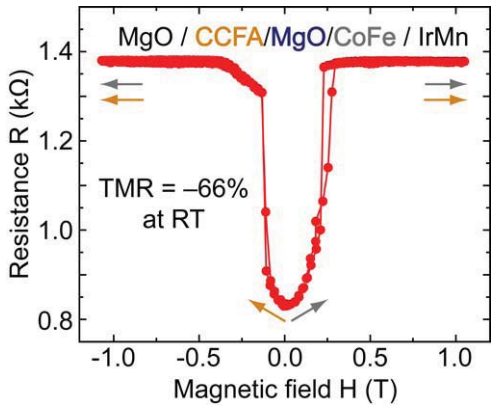

FIG. 1: TMR curve of a CCFA(25 nm)/MgO(3 nm)/$Co_{80}Fe_{20}$(5 nm) MTJ measured at RT.

In Fig. 1 we present a magnetoresistance curve measured at RT on a CCFA/MgO/$Co_{80}Fe_{20}$ MTJ deposited on MgO(100) substrates with a 40 nm-thick MgO seed layer. Obviously, we observe an *inverse* TMR effect. The TMR ratio defined as

TMR = $(R_{AP} - R_P)/R_{AP}$, where R_{AP} is the smallest resistance value in the antiparallel magnetization configuration and R_P denotes the highest resistance in the saturated state, reaches -66%. This TMR value at RT is relatively large for structures comprising a FM Heusler electrode. The bell-shaped MR curve depicted in Fig. 1 suggests a noncollinear orientation of the layers magnetizations for $H = 0$ due to magnetic coupling of the two FM layers (arrows in Fig. 1). This is also confirmed by SQUID measurements, where independent switching of the two electrodes is found to be hindered. Antiferromagnetic, Néel-type and biquadratic coupling due to interface roughness are the most likely coupling mechanisms.

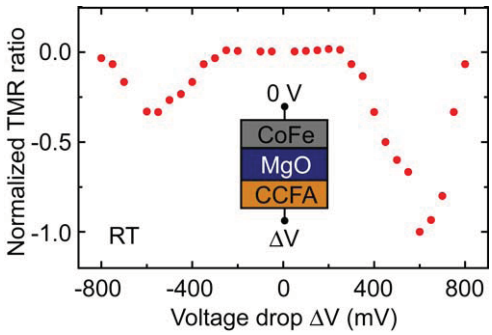

FIG. 2: Normalized TMR ratio of a CCFA(25 nm)/MgO(3 nm)/$Co_{80}Fe_{20}$(5 nm) MTJ as a function of the voltage drop ΔV across the junction measured at RT.

Figure 2 shows the typical dependence of the TMR ratio on the voltage drop ΔV across the MTJ measured in the parallel configuration at $H = \pm 1$ T. ΔV is experimentally controlled by varying the current bias supplied by the constant current source and is defined with respect to the $Co_{80}Fe_{20}$ electrode (see inset of Fig. 2).

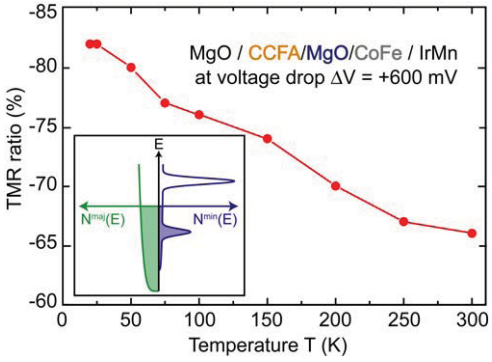

FIG. 3: Temperature dependence of the TMR ratio for a CCFA(25 nm)/MgO(3 nm)/$Co_{80}Fe_{20}$(5 nm) MTJ at $\Delta V = +600$ mV. Inset: Schematic spin-split DOS of CCFA.

In Fig. 3 we plot the temperature dependence of the TMR ratio measured at $\Delta V = +600$ mV. In contrast to MTJs with other Heusler electrodes, our MTJs show only a moderate temperature dependence. The TMR ratio increases from -66% at RT to -84% upon cooling down to 20 K. Similar behavior was reported in Ref. [5] for fully epitaxial CCFA/MgO/CoFe MTJs.

The most striking features of our results are (i) the dominant large *inverse* TMR, (ii) its strong dependence on the voltage drop ΔV, and (iii) the weak temperature dependence. The strong variation of the TMR ratio with the voltage drop, which clearly deviates from the usually found cusp-like behavior, and the weak temperature dependence suggest a strong influence of the DOS on the TMR. In the framework of Jullière's model, the TMR ratio can only be negative when the effective spin polarizations P_L and P_R on the left and right side of the barrier, respectively, are of opposite sign. Sharp features in the spin-split DOS of the electrodes give rise to a bias dependence of the effective polarizations and thus the TMR ratio. The nature of the bonding at the ferromagnet-insulator interface can influence the character of the tunnelling electrons and thus both size and sign of the effective polarization. Due to the preferential (110) orientation of our CCFA films, the bonding at the CCFA/MgO interface in our TMR structures is significantly different from the commonly found (100) orientation. The related differences in the band structures could be the reason for the inverse TMR ratios for certain ΔV in our experiment. Assuming that CCFA shows much sharper features in the spin-split DOS than $Co_{80}Fe_{20}$, *e.g.* due to a (pseudo-) gap and band edges, the data in Fig. 2 can be qualitatively explained by the schematic spin-split DOS of CCFA in the inset of Fig. 3. The large interval of 300-400 mV between the Fermi level and the onsets of the peaks in the model DOS of CCFA explains the much weaker temperature dependence than found for other systems.

In conclusion, we observed a large inverse TMR effect in magnetron sputtered CCFA/MgO/$Co_{80}Fe_{20}$ MTJs at RT. The TMR ratio shows an unusual dependence on the voltage drop ΔV across the structure with large negative values of up to -66% at $\Delta V = \pm 600$ mV and small positive values around zero bias. The temperature dependence is moderate with an increase from -66% to -84% ($\Delta V = +600$ mV) upon cooling from RT to 20 K. We proposed that these findings are related to density-of-states effects of the CCFA electrode or the CCFA/MgO interface. From the application point of view, our results are of high relevance, as they combine a large TMR ratio at a relatively high output voltage with a moderate temperature dependence.

[1] T. Marukame, T. Ishikawa, K.-I. Matsuda, T. Uemura, and M. Yamamoto, Appl. Phys. Lett. **88**, 262503 (2006).

[2] A. Rata, H. Braak, D. E. Bürgler, and C. M. Schneider, Appl. Phys. Lett. **90**, 162512 (2007).

[3] A. D. Rata, H. Braak, D. E. Bürgler, S. Cramm, and C. M. Schneider, Euro. Phys. J. B **52**, 445 (2006).

[4] R. Kelekar and B. M. Clemens, Appl. Phys. Lett. **86**, 232501 (2005).

[5] M. Yamamoto, T. Marukame, T. Ishikawa, K. Matsuda, T. Uemura, and M. Arita, J. Phys. D: Appl. Phys. **39**, 824 (2006).

Electric Switching of Magnetic Vortex Cores in Nanodisks

Y. Liu, S. Gliga, R. Hertel, C. M. Schneider
IFF-9: Electronic Properties

The planar vortex structure is a fundamental microscopic arrangement of the magnetization in sub-micron sized soft-magnetic ferromagnets. Its particular dynamic and static properties have triggered a large amount of interest in the last years. In particular, the vortex core – a thermally very stable, tiny region of only about 10 nm size in which the magnetization points perpendicular to the plane – exhibits a perfect bistable behavior, which makes them interesting candidates for binary data storage. Recently, a simple method to switch these vortex cores by means of in-plane magnetic fields has been demonstrated. Using micromagnetic simulations, we have investigated the influence of electrical current pulses on the magnetic vortex structure of a 200 nm Permalloy disk. Our simulations predict that a controlled switching of the vortex core can be obtained by applying suitably shaped electric current pulses, inducing a rapid switching of the vortex core. Compared with the previously known field-induced switching, the electrical route introduces the technologically appealing possibility to integrate vortices in electronic circuits and to address single nanomagnets within dense arrays.

In order to store information using a vortex core, mechanisms for a controlled switching of its orientation are required. Recently, it has been experimentally demonstrated that the vortex core could be switched by means of sinusoidal low field pulses applied in the plane of the sample [1]. In this case, the gyrotropic resonance was exploited: a low-frequency mode where the vortex rotates around its equilibrium position at sub-gigahertz frequency. In practice, the switching time can be defined as the time between the application of the field and the completion of the core switch. In this sense, the switching time of this resonant scheme is of the order of nanoseconds. Based on micromagnetic simulations, we have proposed a faster route to achieve the core reversal [2]. In this case, which does not use the gyrotropic resonance, the reversal is induced by a suitably shaped unipolar in-plane magnetic field pulse only a few picoseconds long. The switching of a vortex core by means of a magnetic field however presents a problem in terms of applicability: The lack of selectivity of individual elements. Reliably addressing a single nanodisk inside a dense array is very difficult using external fields. By means of advanced simulation techniques we found a new, fast and simple method to switch magnetic vortex cores by applying short *electric* current pulses, only one hundred picoseconds long [3]. The electric current pulse is applied in the plane of the element. We thus show that a fast toggle core switching mechanism can be triggered in a relatively simple way which is compatible with integrated circuits, thereby solving the issue of selectivity.

The study was performed using micromagnetic finite-element simulations based on the Landau-Lifshitz-Gilbert equation. We extended our micromagnetic code used in previous simulations [2] to consider the effect of the spin torque exerted by an electric current flowing through the sample. As a model system, we consider a disk-shaped Permalloy (Py) sample of $d = 200$ nm diameter and $t = 20$ nm thickness. The sample was discretized into ca. 216,000 irregular tetrahedral elements, corresponding to a cell size of about 3 nm. A homogeneous current density distribution was assumed.

The current-induced vortex core reversal was studied for short Gaussian-shaped current pulses ($\sigma = 100$ ps) of varying strengths. To obtain a core reversal, we found that for the considered sample the amplitude of these pulses must exceed a minimum value of j=6.7·10^{12}A/m^2. Although such a high current density might endanger the structural stability of the sample if it was applied continuously, the damaging effects of the current should be small in the present case where only ultrashort pulses are used.

A typical example of the vortex core reversal process is shown in Fig. 1, starting with a vortex whose core is pointing in the positive z-direction. Interestingly, the micromagnetic processes leading to the vortex core reversal with current pulses are identical to the ones we had previously found for magnetic field pulses [2]. To describe these processes in detail, we used an isosurface representation which precisely highlights the position of the vortex core. The core is located at the intersection of the $m_x = 0$ and $m_y = 0$ isosurfaces, *i.e* where the transverse component of the magnetization is maximal ($m_z = \pm 1$). As a result of the current flowing through the sample, the vortex structure is first heavily distorted and a pronounced out-of-plane “dip” in the magnetization is formed near

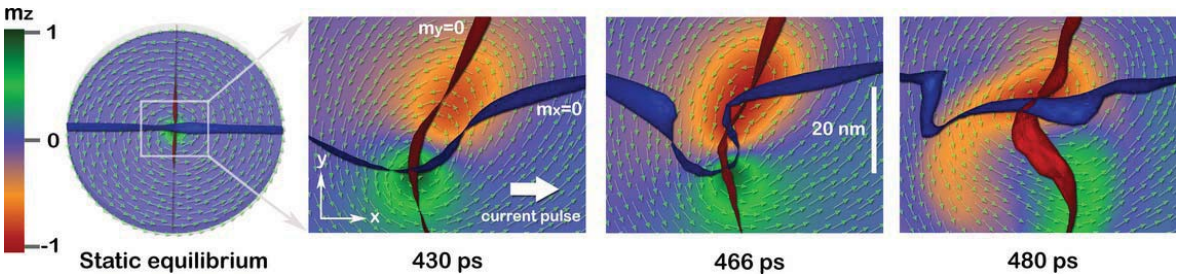

FIG. 1: Current-induced vortex core reversal in a Py nanodisk of 200 nm in diameter and 20 nm thickness. A Gaussian current pulse is applied in the sample plane with a strength of $7.4{\cdot}10^{12}$ A/m^2 and a width $\sigma = 100$ ps. The magnetic vortex structure at equilibrium is shown on the left. In the three frames on the right, the evolution of the magnetization is shown for a small region around the vortex core, where a vortex-antivortex pair nucleates. As the vortex is shifted in the direction of the electron flow prior to the pair creation, these frames are not taken in the same areas of the sample. The arrows represent the in-plane magnetization direction, while the color code displays the *z* component of the magnetization. The blue and red ribbons are the $m_x = 0$ and $m_y = 0$ isosurfaces, respectively. The time is measured from the moment the pulse is applied.

the vortex core. About 460 ps after the application of the pulse, the increasing distortion leads to the creation of a vortex-antivortex pair, which can unambiguously be recognized by the two additional crossings of the $m_x = 0$ and $m_y = 0$ isosurfaces. Both cores of the new pair are pointing in the opposite z-direction of the initial core [2]. The newly formed antivortex and the oppositely polarized initial vortex subsequently annihilate [4]. The latter subprocess unfolds over approximately 10 ps and leaves a single vortex core, which is oppositely polarized with respect to the initial one. The formation of vortex-antivortex pairs after application of short current pulses is consistent with recent experimental observations by Kläui *et al.* [5].

By increasing the pulse strength, it is possible to produce multiple switches. Multiple switches are a repeated series of vortex-antivortex pair creation and annihilation processes. The diagram in Fig. 2 shows the number of core switches as a function of the applied current's strength. Clear thresholds are observed. While the core reversal mechanism is mediated by the formation of a vortex-antivortex pair, it is the annihilation process which leaves the vortex with an oppositely-polarized core. As we demonstrated in Ref. [4], such an annihilation process is connected with a magnetic singularity (Bloch point). Since the energy of formation of a Bloch point is uniquely a function of the exchange constant, the annihilation (and thus the core reversal) process can only occur at specific energy values, resulting in the observed steps. A double core switching is obtained with current pulses of about $8.5{\cdot}10^{12}$ A/m^2, while triple and quadruple switches occur with pulses of $10{\cdot}10^{12}$ A/m^2 and $11{\cdot}10^{12}$ A/m^2, respectively. Ultimately, for very large currents (above $20{\cdot}10^{12}$ A/m^2), the vortex core is expelled from the sample.

In conclusion, we have presented the possibility of reversing the polarization of a magnetic vortex core using short current pulses. The magnetization reversal process, which consists of a complicated sequence of vortex-antivortex pair creation and annihilation events, unfolds on a time scale of ca. 40 ps, *i.e.* shorter than the duration of the pulses applied

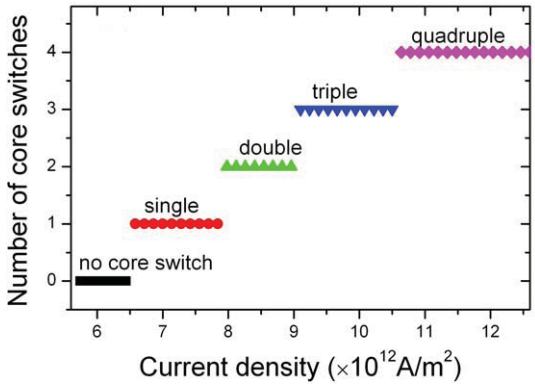

FIG. 2: Number of times the vortex core switches as a function of the applied current density.

in this study. Further investigations are required to explore the limits of the operational range for a controlled, single toggle switching in terms of pulse duration and pulse strength, and to determine how short a current pulse can be to trigger a vortex core reversal. The current-induced vortex core reversal opens the possibility of addressing individual magnetic elements in a vortex state within an array of nanoelements. This feature could make vortex cores interesting candidates for data storage purposes in future devices.

[1] B. Van Waeyenberge, A. Puzic, H. Stoll, K. W. Chou, K. W., T .Tyliszczak, R. Hertel, *et al.*, Nature 444, 461 (2006)

[2] R. Hertel, S. Gliga, M. Fähnle, and C. M. Schneider, Phys. Rev. Lett. 98, 117201 (2007)

[3] Y. Liu, S. Gliga, R. Hertel and C. M. Schneider, Appl. Phys. Lett. 91, 112501 (2007)

[4] R. Hertel and C. M. Schneider, Phys. Rev. Lett. 97, 177202 (2007)

[5] M. Kläui, M. Laufenberg, L. Heyne, D. Backes, *et al.*, Appl. Phys. Lett. 88, 232507 (2006)

Asymmetric Spin-Transfer Torque in Single-Crystalline Fe/Ag/Fe Nanopillars

R. Lehndorff, M. Buchmeier, D. E. Bürgler, A. Kákay, R. Hertel, C. M. Schneider

IFF-9: Electronic Properties
CNI: Center of Nanoelectronic Systems for Information Technology

We investigate current-perpendicular-plane giant magnetoresistance (CPP-GMR) and current-induced magnetization switching in single-crystalline Fe/Ag/Fe nanopillars of 70 nm diameter. The interplay between the in-plane, fourfold magnetocrystalline anisotropy of the Fe(001) layers and the spin-transfer torque (STT) gives rise to a two-step switching behavior, which allows an investigation of the angular dependences of CPP-GMR and STT. The results are compared to a theoretical model and contribute to a more fundamental understanding of spin-dependent transport in layered, magnetic nanostructures.

Spin-transfer torque (STT) and its effects of switching the magnetization or exciting steady-state magnetization precessional motions in nanometer-sized magnetic elements attracted a lot of interest since their prediction in 1996. These effects have been demonstrated experimentally and the understanding of STT-driven magnetization dynamics has grown quickly. However, there is still a lack of understanding of the microscopic origin of the STT. We use single-crystalline nanomagnets to gain further insight [1].

Giant magnetoresistance (GMR) and STT are two characteristic magnetotransport phenomena occurring in layered systems consisting of two ferromagnetic (FM) layers separated by a nonmagnetic (NM) interlayer. The common cause for these effects is the fact that the current passing through these layers is spin-polarized. There are two mechanisms giving rise to a spin polarization of the current: (i) The natural spin polarization of the charge carriers in a FM, caused by the imbalance of spin-up and spin-down density-of-states at the Fermi level and (ii) a gradient of the spin accumulation in the NM. For symmetric systems Slonczewski's unified theory [2] for GMR and STT yields for the angular dependences of the GMR $r(\vartheta)$ and the STT $\tau(\vartheta)$:

$$r(\vartheta) = \frac{R(\vartheta)-R(0^\circ)}{R(180^\circ)-R(0^\circ)} = \frac{1-\cos^2(\vartheta/2)}{1+\chi\cos^2(\vartheta/2)} \quad (1)$$

$$\tau(\vartheta) = \frac{\hbar IP\Lambda}{4Ae}\frac{\sin(\vartheta)}{\Lambda\cos^2(\vartheta/2)+\Lambda^{-1}\sin^2(\vartheta/2)} \quad (2)$$

$$\Lambda^2 = \chi+1 = AG\frac{R^+R^-}{2}. \quad (3)$$

$R(\vartheta)$ is the dependence of the resistance on ϑ, G the conductance of the interlayer, A the crossectional area of the nanopillar, $R^{+(-)}$ the total (interface and bulk) resistance for spin-up (spin-down) electrons for one side of the system, and $P = (R^- - R^+)/(R^- + R^+)$ is the spin polarization. The parameter Λ (or χ) is a measure for the deviation from the symmetric behavior, which is given by $\Lambda = 1$. In Fig. 1 we plot $r(\vartheta)$ and $\tau(\vartheta)$ for various values of Λ. The green dotted lines for $\Lambda = 1$ represent the symmetric case. In most cases an asymmetric behavior of both GMR and STT is theoretically expected, but has so far never been observed.

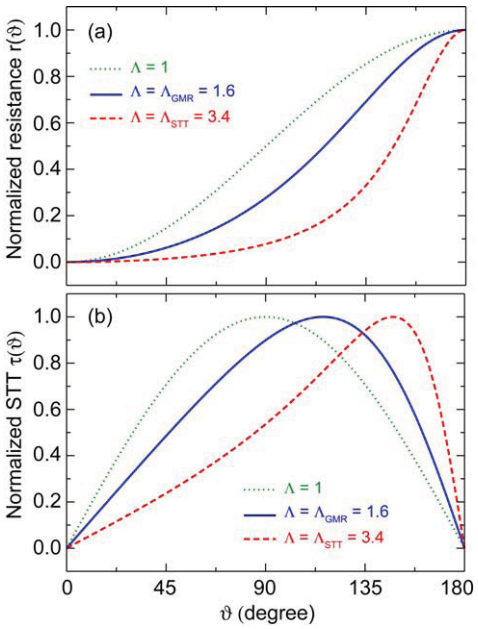

FIG. 1: (a) $r(\vartheta)$ and (b) $\tau(\vartheta)$ for three different Λ values according to Eqs. (1)-(3). The green line shows the symmetric behavior. The blue line results from our GMR data and the red line from our experimental ratio I_{c2}/I_{c1}.

A layer stack of 1 nm Fe, 150 nm Ag, 20 nm Fe (fixed FM), 6 nm Ag (NM), 2 nm Fe (free FM), and 50 nm Au is grown by molecular beam epitaxy onto an annealed GaAs(100) substrate. The free FM is structured into circular nanopillars with diameters of 70 nm by a combination of optical and e-beam lithography and ion beam etching. The 150 nm Ag buffer layer acts as bottom electrode and a bilayer of 5 nm Ti and 200 nm Au is finally evaporated onto the stack as a

top electrode (inset of Fig. 3). Preparation and fabrication procedures are described in Refs. [1, 3].

Figure 2 shows the CPP-GMR loop for the field applied along a hard axis of the Fe layers. The maximum GMR value amounts to 3.3%. The curves can be well reproduced by Stoner-Wohlfarth fits (red symbols), which reveal the details of the remagnetization process. An interesting situation occurs at 0 mT, where the two magnetizations rest in two different easy axes of the four-fold crystalline anisotropy of the Fe layers and, thus, include an angle of 90°.

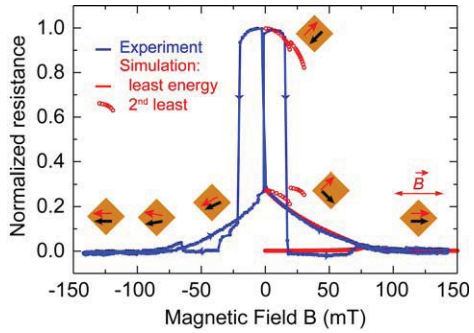

FIG. 2: CPP-GMR data (blue) measured at 5 K with the magnetic field applied along a hard axis of the single-crystalline Fe layers. Red symbols are solutions of Stoner-Wohlfarth fits. The edges of the squares indicate the magnetic easy axis of the Fe layers and the black (red) arrow the magnetization direction of the fixed (free) layer.

For the standard angular dependence of the GMR, $r(\vartheta) = \sin^2(\vartheta/2)$, $r(90°)$ would be 0.5. Instead in Fig. 2 we find a much lower value of 0.3. This deviation originates from spin accumulation at the FM/NM interfaces and yields according to Eqs. (1) and (3) an asymmetry parameter $\Lambda_{GMR} = 1.6 \pm 0.03$.

Figure 3 shows a dc current loop taken at an applied magnetic field of 5.6 mT parallel to a hard axis. Two switching processes can be distinguished upon increasing the current. The first one at +5.8 mA leads to an intermediate resistive state, the second at +7.3 mA to a high resistive state. When the current decreases the system falls back to the intermediate resistive level at +1.9 mA and to the low resistive level at -2.1 mA. The intermediate resistive level is assigned to a perpendicular alignment of the two magnetizations stabilized by the crystalline anisotropy. Obviously, the magnetization switches in two steps from the parallel to the antiparallel alignment *via* an intermediate 90° state. In the following I_{c1} (I_{c2}) denotes the critical current for switching from 0° to 90° (90° to 180°). The behavior in Fig. 3 is representative for magnetic fields of nearly any orientation, but with a magnitude well below the coercive field of the free layer. Under these conditions the anisotropy dominates the switching process. The first critical current value I_{c1} is reached, when the STT overcomes the damping, which is proportional to the effective field $H_{eff} = -dE/dM$. In our case, the anisotropy is the dominant contribution to H_{eff}. The second critical current I_{c2} is determined by the asymmetry of the STT with respect to $\vartheta = 90°$. As confirmed by simulations for this starting condition, a current excites a small-angle precession of the magnetization of the free layer around the easy axis at $\vartheta = 90°$. In this geometry, however, the precession is damped by the STT for one part of the precession trajectory with $\vartheta < 90°$, because then STT and damping are parallel and point towards the easy axis. For other parts of the trajectory with $\vartheta > 90°$ the two contributions are opposing each other and the STT acts as an excitation.

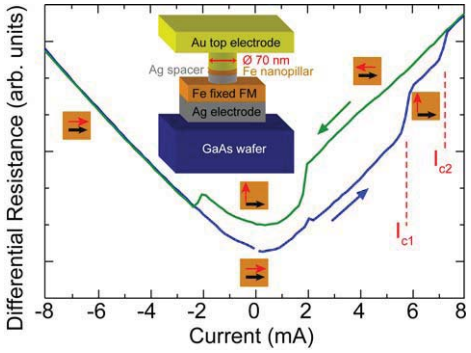

FIG. 3: Two-step current-induced switching of the free layer magnetization at 5 K. I_{c1} and I_{c2} denote the critical currents for the switching from parallel to perpendicular and from perpendicular to antiparallel alignment, respectively. Inset: Schematic sample structure.

The asymmetry of the STT favors excitation over damping. The stronger the asymmetry the lower I_{c2}. In the symmetric case, I_{c2} becomes very large, because the damping and exciting torques along the precession trajectory largely compensate each other. The experiment yields a ratio $I_{c1}/I_{c2} \approx 1.25$. We compare this ratio to results of macrospin simulations because it excludes uncertainties in nanopillar size, anisotropy constant, damping parameter α, or polarization P. We find that we have to increase Λ_{STT} in the simulations to $\Lambda_{STT} = 3.4$ in order to obtain good agreement between experiment and simulation. This value is also in accordance with the theoretical value $\Lambda = 4$ calculated by Eq. (3) using material specific parameters [4, 5].

In conclusion, the angular variation of both CPP-GMR and the critical current density for current induced magnetization switching in single-crystalline Fe/Ag/Fe nanopillars are asymmetric. This feature has been predicted by theory [2], but has not been observed so far. Our work confirms the importance of spin accumulation for GMR and STT.

[1] R. Lehndorff, D. E. Bürgler, A. Kákay, R. Hertel, and C. M. Schneider. Phys. Rev. B **76**, 214420 (2007).

[2] J. C. Slonczewski. J. Magn. Magn. Mater. **247**, 324 (2002).

[3] H. Dassow, R. Lehndorff, D. E. Bürgler, M. Buchmeier, P. A. Grünberg, C. M. Schneider, and A. van der Hart. Appl. Phys. Lett. **89**, 222511 (2006).

[4] J. J. Paggel, T. Miller, and T.-C. Chiang. Phys. Rev. Lett. **83** (1999).

[5] M. D. Stiles and D. R. Penn. Phys. Rev. B **61**, 3200 (2000).

Photon-Assisted Tunneling in a Carbon Nanotube Quantum Dot

C. Meyer, Ch. Spudat, C. M. Schneider

IFF-9: Electronic Properties

CNI: Center of Nanoelectronic Systems for Information Technology

Electronic devices become smaller and smaller. Silicon based technology as we know it today will reach its limit within the next decade. To go beyond this limit, we investigate new materials and methods for information processing. In this context, we are interested in the transport properties of carbon nanotubes, which are ideal one dimensional ballistic conductors. Electron spins in carbon nanotubes (CNTs) are expected to have long relaxation times due to the small spin-orbit coupling and the possible absence of nuclear spins. This could make CNT quantum dots very suitable candidates for a solid state quantum computing system [1]. We study photon-assisted tunneling (PAT) in a CNT quantum dot under microwave irradation (20 to 60 GHz) as a first step towards high-frequency control over such a spin qubit.

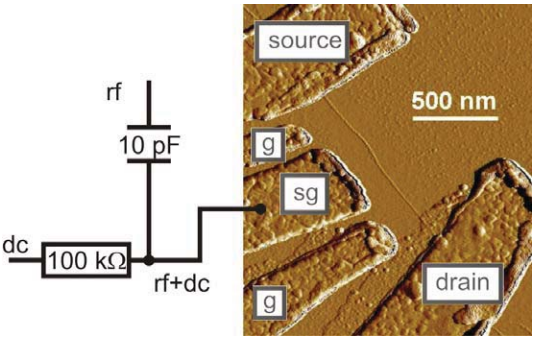

FIG. 1: Schematic layout of the device with low temperature bias-tee and AFM picture of a similar device as the one used for the experiments discussed here. The actual device has a total nanotube length of 940 nm between the Al contacts. The side gate (sg), which is flanked by two guard electrodes (g), has a width of 410 nm, and its distance to the CNT is about 200 nm.

Single-walled carbon nanotubes (SWCNTs) are grown using chemical vapor deposition (CVD) on a patterned Si/SiO_2 substrate. The quantum dot is formed between Aluminum source/drain contacts, and the potential can be tuned using an Aluminum side-gate (see Fig.1). The low work function of Aluminum ensures high tunnel barriers at low temperatures. We achieved tunneling rates $\Gamma << h\nu$, with ν the frequency of the rf signal, which allows us to clearly resolve the microwave-induced side peaks [2]. All measurements are performed at the base temperature of a dilution refrigerator. The high-frequency signal and dc gate voltage are added with a bias-tee at base temperature ($\sim$25 mK), and applied to the side gate. Two guard electrodes surrounding it are set to ground and suppress the capacitive coupling of the side gate to source and drain contacts. Fig.2 shows measurements of current versus gate voltage of the unperturbed Coulomb peak (dashed curve) and the peak splitting under high-frequency irradiation. As expected, the total splitting between the extra resonances in the current is $2h\nu$ and increases linearly with frequency. The insets of Fig.2 describe the PAT processes of a single-level system for the left and right side peak, respectively. Left of the main Coulomb resonance, when the quantum dot is in its N electron state and the electrochemical potential of the $N \leftrightarrow N+1$ resonance is above the bias window, an electron in the left lead can absorb a photon and tunnel onto the dot. This electron can then leave the dot to both sides with the same probability, but it contributes to the current only if it tunnels to the right lead. This process is frequency dependent, because as soon as an electron from the right lead can also absorb a photon and tunnel onto the dot, the net current from these two processes will be zero. To the right of the main resonance, the quantum dot is in its $N+1$ stable state and an electron on the dot can absorb a photon and tunnel out to the right lead. An electron can then enter from the Fermi sea of either of the leads and refill the level, but it contributes to the current only when entering from the left.

We then perform excited-state spectroscopy with PAT in order to study the frequency independent peaks at different microwave power and ν = 40.8 GHz. These peaks, at positions ϵ_{bc} = -83(7) μeV and ϵ_{ad}= 70(7) μeV relative to the Coulomb peak ϵ_{ac}, have their origin in tunneling through excited states initiated by a PAT process and are more apparent at high power while the main resonance decreases. Similar behavior has been observed in GaAs dots. We emphasize, however, that the PAT-induced excited state peak denoted here as bc has not been reported before, to the best of our knowledge. At the ϵ_{ad} peak tunneling occurs between the N electron ground state and an N+1 excited state, in case of the ϵ_{bc} peak, tunneling occurs between an N-electron excited state and the N+1 ground state.

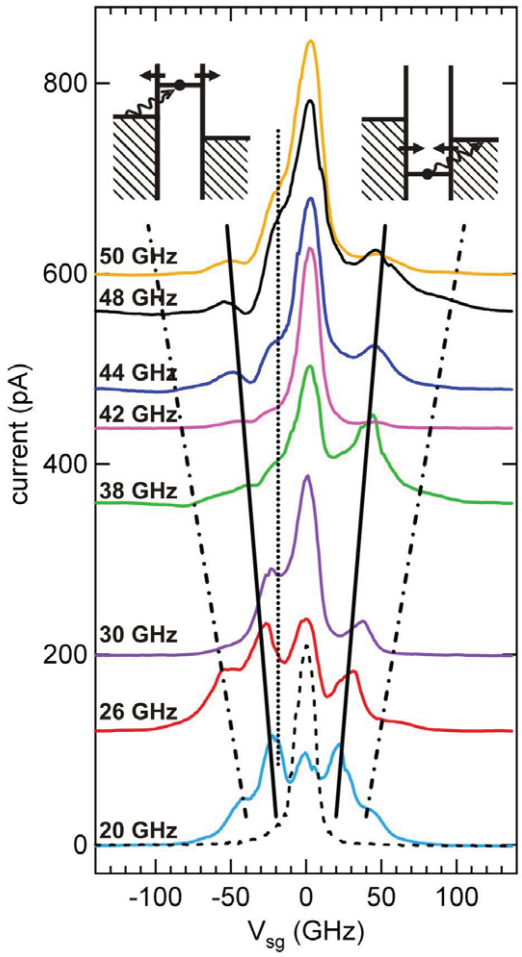

FIG. 2: Photon-assisted tunneling at different frequencies; ac source voltage amplitude V_{ac} = 71 mV (-10 dBm), bias voltage V_{SD} = 50 μeV. The dc side gate voltage V_{SG} is swept from 266.4 mV to 300 mV, and converted to an energy scale in GHz, using a conversion factor for the gate voltage to energy of $C_g/C_\Sigma \sim 0.03$. The Coulomb peak measured without rf irradiation (dashed curve) is compared to the traces with rf irradiation. The insets describe the basic PAT process below (left inset) and above (right inset) the main resonance. The black straight lines are guides to the eye for the one-photon satellites (solid) at positions $\pm h\nu$ away from the main Coulomb resonance, the two-photon side peaks (dash-dotted), and a frequency independent excited state that is visible at higher frequencies (dotted).

For better understanding of the power dependence of the excited states, we compare our data to the simulation of a model system described in [3]. In Fig.3, we compare the result of the simulation (solid lines) with the data (markers). We find good agreement for the main resonance (black), the ϵ_{bc} peak (blue), and the peak of $\epsilon_{ac} + h\nu$ (green) assuming a small asymmetry in the coupling of the microwaves $\alpha = \frac{eV}{h\nu}$ to the barriers ($\alpha_l = 0.95\alpha_r$). The functional dependence of the peak ϵ_{ad} (red) on the microwave power is the same in the simulation as in the data. However, the current is strongly enhanced compared to the simulation. A similar behavior has been observed for GaAs quantum dots as well and was explained by intra-dot excitations [4].

These observations are the first steps towards high-frequency control of carbon nanotube quantum dots, which is vital for using spin in nanotubes for quantum information processing.

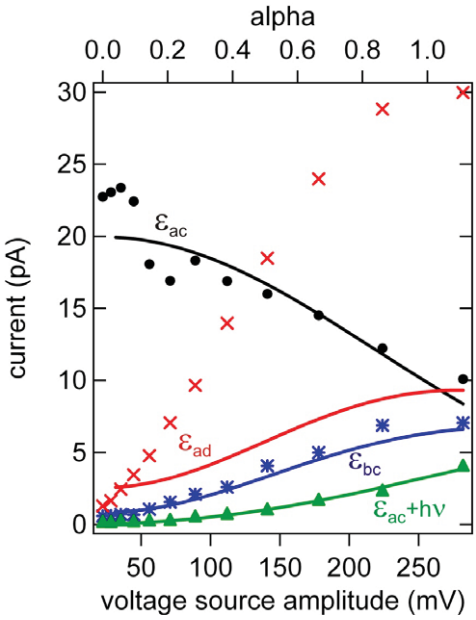

FIG. 3: Comparison between measured current (markers) and simulated current (solid line) for different peaks for differents microwave power at ν = 40.8 GHz.

[1] D. Loss, D. DiVincenzo, Phys. Rev. A **57**, 120 (1998)

[2] L. P. Kouwenhoven, S. Jauhar, K. McCormick, D. Dixon, P. L. McEuen, Yu. V. Nazarov, N. C. van der Vaart, C. T. Foxon, Phys. Rev. B **50**, 2019 (1994)

[3] C. Meyer, J. M. Elzermann, L. P. Kouwenhoven, Nano Letters **7**, 295 (2007)

[4] Ph. Brune, C. Bruder, H. Schoeller, Phys. Rev. B **56**, 4730 (1997)

Quantum Transport Through Single-Molecule Magnets: Berry-Phase Interference

M. R. Wegewijs[1,2], C. Romeike[2], W. Hofstetter[3], H. Schoeller[2]

[1] IFF-3: Theory of Structure Formation
[2] Institut für Theoretische Physik A, RWTH Aachen, 52056 Aachen, Germany
[3] Institut für Theoretische Physik, J. W. Goethe-Universität Frankfurt, 60438 Frankfurt am Main, Germany

We address the interplay of two quantum effects related to spin reversal in a single-molecule magnet (SMM): intrinsic coherent tunneling of the magnetization, involving a Berry phase, and Kondo spin-screening induced by exchange interaction with macroscopic electrodes. We show that these effects leave a clear fingerprint in the coherent electric transport through an *individual* molecular magnet when an external magnetic field is applied along different directions. This allows the microscopic orientation of a SMM in a transport junction to be identified from magneto-transport measurements alone. This is an issue central to the proposed application of SMMs in single-molecule spintronics and quantum-computation.

Single-molecule magnets (SMMs) exhibit interesting mesoscopic quantum interference effects in spin space [1]. In these molecules the substantial uniaxial magnetic anisotropy tends to align the large ground-state spin to a magnetic easy axis. Remarkably, for integer spin values S the magnetization direction remains completely uncertain due to quantum tunneling intrinsic to the SMM. This spin-tunneling is generated by non-commuting transverse anisotropy terms and reflects the microscopically reversible coherent magnetization dynamics. Associated with the spin tunneling is a geometric- or Berry-phase which is proportional to the magnetic flux enclosed by the two interfering semi-classical trajectories along which the spin can be reversed. This phase is revealed when an external magnetic field is applied along the magnetic hard axis of the molecule: the splitting of the lowest two eigenstates then oscillates as function of the field strength. At special so-called diabolical magnetic field values the spin-tunneling is even completely quenched and the splitting vanishes. For SMMs with a half-integer spin S these oscillations also occur, but they are phase-shifted by $\pi/2$ i.e. the magnetic states are Kramers-degenerate at zero field. The experimental demonstration of these oscillations for the Fe_8-SMM with spin $S = 10$ in [2] has been the most compelling proof of the coherent magnetization dynamics of SMM crystals and presents one of the major advances in the field of *molecular magnetism*.

Recent advances in the field of *nanoscopic transport* have made it possible to electrically contact an *individual* SMM in a nanogap [3] as sketched in Fig. 1.

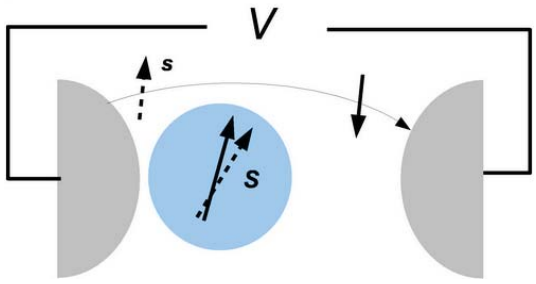

FIG. 1: (a) Transport setup: a SMM (blue) coupled to two voltage biased (V) electrodes. The antiferromagnetic exchange $J \sim \Gamma/(\Delta E\rho)$ is induced by coherent spin-dependent electron transfer between the electrodes, thereby only virtually charging the SMM ($\Gamma =$ tunnel coupling, $\Delta E =$ addition energy, $\rho = 1/(2W) =$ density of states, where $2W$ is the electronic band-width).

This raises an important question: How can one probe the unique magnetic properties of a SMM *embedded in an electronic circuit*? These are expected to differ from known free and bulk values and are at present unknown. Previously, we have theoretically demonstrated that these properties are reflected in the *coherent* electronic transport dominated by spin-fluctuations, see [4] for a review. Recently we have also addressed time-dependent magnetic phenomena in this regime [5]. For the interpretation of transport data as well as recently proposed applications of SMMs in spintronics and quantum-computing it is essential that the orientation of the magnetic easy axis and the anisotropy parameters are known. This question may be answered by measuring in particular the magnetic field dependence of the coherent transport.

Here we report how *the Berry-phase signature of a SMM allows for a full characterization of a SMM by magneto-transport measurements* [4]. The basic idea is that the spin-exchange scattering of conduction electrons from the electrodes attached to the SMM depends sensitively on the eigenstates of the SMM. The latter are non-trivial superpositions of spin-eigenstates whose coefficients are modulated by the external magnetic field, thereby revealing the Berry-phase in coherent oscillations of a zero-bias in

the conductance suppression. In contrast to all previous works on transport through SMMs, we have analyzed spin interference phenomena in the complete range of longitudinal and transverse magnetic fields, in both the regime of weak and strong exchange interaction with the electrodes.

At low bias voltage V and temperature T, where single-electron tunneling is suppressed by the strong quantum-confinement of electrons on the SMM and Coulomb interaction effects, the transport is governed by the antiferromagnetic exchange interaction between the molecular spin $\mathbf{S}$ (components S_x, S_y, S_z) and the local electron spin $\mathbf{s}$ of the electrodes. This magnetic interaction is thus induced by tunneling processes: spin-flips on the molecule correspond to charge transferred between the electrodes, as sketched in Fig. 1. The SMM has a complex magnetic excitation spectrum due to an easy-axis anisotropy D and a competing smaller transverse anisotropy B, in addition to the coupling to the easy- and hard-axis magnetic field components, H_z, H_x, respectively. The magnetic structure of the SMM, as described by the Hamiltonian

$$H_{\text{SMM}} = -DS_z^2 + B\left(S_x^2 - S_y^2\right) + \sum_{i=x,z} H_i S_i,$$

gives rise to a striking dependence of the electric transport on the strength and direction of the magnetic field. We have calculated the low temperature linear conductance $dI/dV|_{V=0} = (e^2/2)A(0)$ which essentially measures the zero-frequency local density of states $A(0)$ which we obtained using Wilson's NRG and Costi's T-matrix approach.

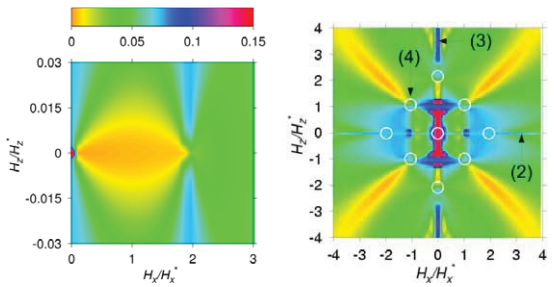

FIG. 2: (a) Weak exchange scattering: dependence of the zero-bias conductance (color bar unit: e^2/h) on transverse H_x and easy-axis magnetic field H_z for $S = 3/2$ and $J = 0.2W, D = W = 10B$. (b) Strong exchange scattering: magneto-conductance map ($V = 0$) for $S = 3/2$ and $J = 0.15W, D = 10^{-4}W = 10B$. The diabolical points are indicated by white circles.

In Figs 2 (a,b) we show maps of $dI/dV|_{V=0}$ as function of the easy-axis (H_z) and transverse (H_x) magnetic field for weak and strong spin-exchange scattering J, respectively. For $H_x = 0, H_z \geq 0$ the spin-exchange scattering between two sets of SMM-states with different magnetic symmetry results in a large zero-bias Kondo conductance of the SMM. In Fig. 2(a-b) the high conductance value due to the Kondo effect shows up in red for $H_x = 0$. Upon sweeping the field H_z along the SMMs easy-axis one encounters anti-crossings of states with the same magnetic symmetry. Around these special field values, the spin-tunneling strongly mixes the magnetic states of the SMM, thereby suppressing the transverse spin-exchange scattering. This results in a novel re-entrant behaviour of the Kondo effect.

In contrast, for finite transverse field H_x the magnetic symmetry is lowered and the Kondo effect is suppressed. The remaining conductance is however, still sensitive to interference in the exchange scattering as Fig. 2(a) shows. Surprisingly, we find a pronounced zero-bias *dip* in the conductance, which also shows up as a dip as function of an applied longitudinal magnetic field H_z (orange region in Fig. 2(a)). Basically, within the dip-region, the SMM ground state has zero expectation value of the spin due to quantum spin-tunneling which "averages out" the spin. Without a net spin, the spin-dependent scattering, responsible for transporting charge between the two electrodes (c.f. Fig. 1), is ineffective. Hence the conductance is suppressed. Upon sweeping the transverse field H_x the dip oscillates, the number of oscillations (here 1) depends on the value of the spin S, characteristic for the SMM. At the diabolical magnetic field values the dip closes and a finite conductance is recovered, but no Kondo peak. These diabolical points lie in the H_z, H_x plane on a regular grid when the magnetic fields are rescaled by factors $H_z^* = \sqrt{D^2 - B^2}$ and $H_x^* = \sqrt{2B(D+B)}$ which are fixed uniquely by the anisotropy parameters D and B characterising of the SMM. In Fig. 2(b), these points are marked by white circles. Clearly, in their vicinity, the magneto-conductance map has a locally complex structure. This happens only in the limit of strong exchange scattering where all magnetic excitations of the SMM participate in the transport. One can thus experimentally determine the microscopic magnetic properties of a single SMM from the positions of these points using only the macroscopic magneto-transport measurement data.

Acknowledgements: We acknowledge H. van der Zant, A. Cornia and P. Bruno for discussions and financial support of the NanoSci-ERA the EU-RTN Spintronics, and the IFMIT.

[1] D. Gatteschi and R. Sessoli, Angew. Chem. Int. Ed. **42**, 268 (2003).

[2] W. Wernsdorfer and R. Sessoli, Science **284**, 133 (1999).

[3] H. B. Heersche, Z. de Groot, J. A. Folk, H. S. J. van der Zant, C. Romeike, M. R. Wegewijs, L. Zobbi, D. Barreca, E. Tondello, and A. Cornia, Phys. Rev. Lett. **96**, 206801 (2006).

[4] M. R. Wegewijs, C. Romeike, H. Schoeller and W. Hofstetter, New J. Phys.,**9**, 344, (2007)

[5] D. Roosen, M. R. Wegewijs, and W. Hofstetter, Phys. Rev. Lett. (2008), in print.

Superconducting Spintronics: Josephson Junctions with Tailored Ferromagnetic Barrier

M. Weides and H. Kohlstedt

IFF-6: Electronic Materials

Superconductor / insulator / ferromagnet / superconductor Josephson junctions with a thickness step in the metallic ferromagnetic interlayer were fabricated. The step was defined by optical lithography and controlled etching. The step height is on the scale of a few angstroms. Experimentally determined junction parameters indicate a uniform F-layer thickness and the same interface transparencies for etched and non-etched F-layers. This technique could be used to tailor low-T_c Josephson junctions having locally controlled critical current densities, as needed for tunable resonators or magnetic-field driven electronics [M.Weides *et al.*, J. Appl. Phys. 101 (2007)]. It can be extended to other metallic multilayer systems such as magnetoresistance (GMR/TMR) devices where local variation of magnetic properties may enhance their functionality.

The work horse in superconducting electronics is the *Josephson junction* (JJ). A Josephson junction consists of two weakly coupled superconducting metal bars via a constriction, e.g. made up by a normal (N) metal or a tunnel barrier (I). Various types of JJs are routinely applied in ultra-high sensitive SQUID (Superconducting Quantum Interference Devices) magnetometers or voltage standards. At superconductive/magnetic metal (S/F) interfaces the superconducting order parameter Ψ is *spatially decaying and oscillating* inside the magnet (coherence length ξ_{F1}, oscillation length ξ_{F2}), whereas for a S/N system Ψ is simply *decaying* inside the metal. By combining the low-T_c $\mathrm{Nb/Al}$ technology with magnetic tunnel junctions new functionalities are predicted. In this framework so called 0–π Josephson junctions were recent focus of research activities [1].

The supercurrent through an SNS junction is given by $I = I_c \sin(\phi)$, where $\phi = \Psi_1 - \Psi_2$ is the phase difference of the superconducting electrode wave functions and $I_c > 0$ the maximum supercurrent through the junction. These junctions are so-called 0 JJs. In an SFS stack with ferromagnetic layer thickness $d_F \propto \xi_{F2}/2$, the amplitude of order parameter Ψ vanishes at the center of the F-layer and the order parameter has the opposite sign at the adjacent superconducting electrode. This state is described by a

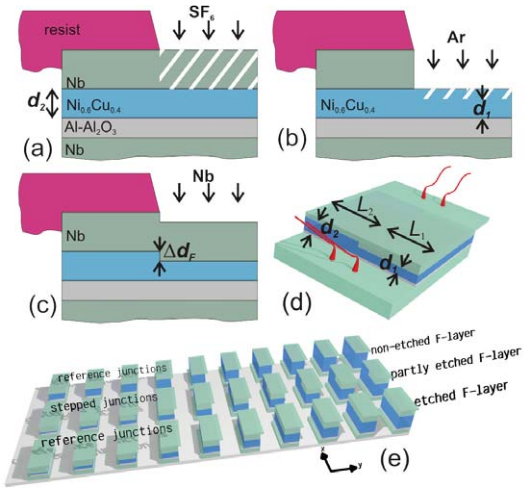

FIG. 1: (a) reactive etching of Nb with $\mathrm{SF_6}$ down to NiCu layer, (b) ion-etching of NiCu to set 0 coupling, (c) in situ deposition of cap Nb layer. Schematic layouts of stepped JJ based on SFS/SIFS technology (d) and of stepped JJs along with planar reference junctions (e). The F-layer (blue) thickness increases from left to right.

phase shift of π and these junctions are so-called π JJs. SFS or SIFS-type π JJs have a negative critical current, hence the Josephson relation can be rewritten: $I = -I_c \sin(\phi) = |I_c| \sin(\phi + \pi)$. For a variety of JJs a non-uniform critical current density j_c is desirable, e.g. for tunable superconducting resonators or magnetic-field driven electronic switches similar to SQUIDs. Our fabrication technology [2] permits the controlled change of only the ferromagnetic interlayer thicknesses d_1 and $d_2 = d_1 + \Delta d_F$, i.e. the local critical current density j_c. The case of non-uniform coupling phase within a *single* Josephson junction, i.e. one half is a 0 JJ ($d_F = d_1$) and the other half is a π JJ ($d_F = d_2$) is of particular interest. In such a 0–π junction a spontaneously formed vortex of supercurrent circulating around the 0–π phase boundary with flux $|\Phi| \leq \pm\Phi_0/2$ inside the JJs may appear [3]. The requirements for SIFS 0–π junctions are challenging. Here we present our technology background for stepped junctions with the focus on small parameter spreads. Our approach represents a considerable step forward to fulfil the extreme requirements on the implementation of conventional or quantum computing devices based on Josephson junctions.

The deposition and patterning of the stepped SIFS junctions was performed by sputtering and a four level photolithographic mask procedure. The F-layer was deposited with a gradient of thickness along y-axis on the S/I stack. The patterning of the desired step-like variation in d_F was done after the complete deposition of the SIFS stack. The parts of the JJ that were supposed to have a larger thickness d_2 were protected by photoresist, see Fig. 1. The step patterning process is depicted in Fig. 1 (a)–(c). The Nb cap layer was removed by reactive dry etching using $\mathrm{SF_6}$ with a high selectivity to the photoresist. A few tenth of nanometer Δd_F of NiCu were Ar ion etched at a very low power and rate to avoid any damaging of the NiCu film under the surface and to keep a good control over the step height. When the F-layer thickness was reduced down to the thickness d_1 the etching was stopped and $40\ \mathrm{nm}$ of Nb were deposited. The complete etching and subsequent Nb deposition was done in situ. The chip contained stacks with the new F-layer thicknesses d_1 (uniformly etched), d_2 (non-etched) and with step in the F-layer thickness from d_1 to d_2. The wedge shaped interlayer (Fig. 1 (e)) facilitates the quick fabrication of samples with various F-layer thickness and, at the same time, a low junction to junction deviation.

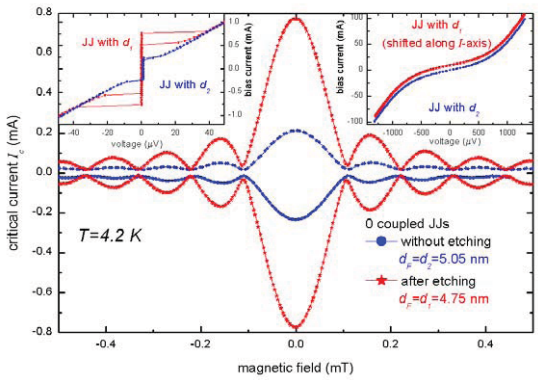

FIG. 2: $I_c(H)$ of etched (star) and non-etched (dots) JJs. The insets show IVCs for small and large bias current ranges in zero magnetic field. Both JJs are in the short JJ limit.

Fig. 2 shows IVC and $I_c(H)$ dependences for a non-etched junction (dot) with the F-layer thickness $d_2 = 5.05\ \mathrm{nm}$ and a uniformly etched junction (star) with thickness $d_1 = d_2 - \Delta d_F = 4.75\ \mathrm{nm}$. Both junctions were 0 coupled. The step height is $\Delta d_F = 0.3\ \mathrm{nm}$. The insets of Fig. 2 show the IVCs for small and large ranges of bias current. Besides the difference in I_c, the $I_c(H)$ dependence and the IVCs (right inset) showed no evidence for an inhomogeneous current transport for both samples. The larger I_c, but same resistance R and capacitance C led to a slightly hysteretic IVC of the etched sample. The resistance R is nearly independent from d_F as the voltage drop over the tunnel barrier is much larger than the serial resistance of a few nanometer thick metal [4]. A change of capacitance C would require a change of R, as both are determined by the dielectric tunnel barrier.

Fig. 3 depicts the measured magnetic diffraction pattern $I_c(H)$ of a stepped JJ along with calculated $I_c(h)$ curves. Both junctions halves are 0 coupled. The magnetic field axis h was scaled to fit the first measured minima of $I_c(H)$. Due to the rather steep slope of the $j_c(d_F)$ curve near the 0 to π crossover j_c is very sensitive to d_1 and d_2. We calculated $I_c(h)$ (dashes) using $d_1 = d_2 - \Delta d_F = 4.68\ \mathrm{nm}$ and $d_2 = 4.98\ \mathrm{nm}$ determined from reference junctions. Then d_2 was decreased by $0.04\ \mathrm{nm}$ (dots) and finally Δd_F increased by the same thickness, too (dashes-dots). The final calculation has the best agreement with data, although the total interface roughness (rms) of the multilayers should exceed $0.04\ \mathrm{nm}$ by far. The measurement and simulation in Fig. 3 show the good estimation and control of F-layer thicknesses.

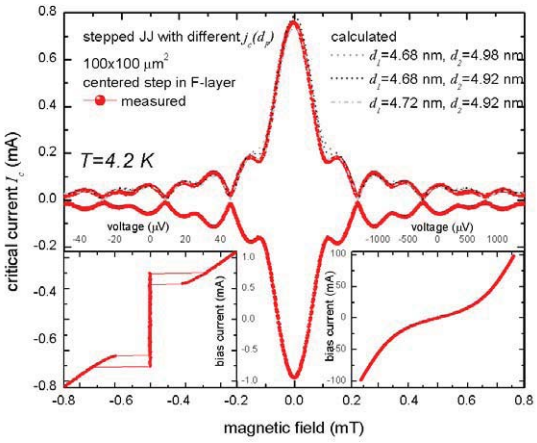

FIG. 3: $I_c(H)$ of a stepped 0–0 JJs (square shaped with $100\ \mu\mathrm{m}$ junction length) with $d_1 = 4.68\ \mathrm{nm}$ and $d_2 = 4.98\ \mathrm{nm}$ (determined from reference JJs) plus calculated $I_c(h)$.

Josephson junctions with a step in the ferromagnetic layer were fabricated. The etched and non etched SIFS junctions differ only by F-layer thickness. No inhomogeneities can be seen in the current transport characteristics of the etched junctions.

The patterning of stepped JJs allows free lateral placement of well-defined j_c's and/or local coupling regimes within a single junction. The patterning process could be adjusted to all thin film multilayer structure providing that the reactive etching rates of the layer materials differ. JJs with varying j_c and planar phase could be used for devices with special shaped $I_c(H)$ pattern or tunable superconducting resonators. The 0–π SIFS JJs with stepped F-layer allow to study the physics of fractional vortices with a good control of the ratio of symmetry between 0 and π parts.

M.W. is supported by DFG (project WE 4359/1-1).

[1] M. Weides *et al.*, Phys. Rev. Lett. **97**, 247001 (2006).

[2] M. Weides *et al.*, J. Appl. Phys. **101**, 063902 (2007).

[3] L. N. Bulaevskii *et al.*, Solid State Commun. **25**, 1053 (1978).

[4] M. Weides *et al.*, Appl. Phys. Lett. **89**, 122511 (2006).

Dephasing of a Qubit Via Interaction With a Gate Electrode

S. R. Woodford[1,2], A. Bringer[1,2], K. M. Indlekofer[3,2]

[1] IFF-1: Quantum Theory of Materials
[2] CNI: Center of Nanoelectronic Systems for Information Technology
[3] IBN-1: Semiconductor Nanoelectronics

Dephasing of quantum dots presents an intrinsic limitation on their usage for quantum computing. We investigated the dephasing of a spin qubit caused by the Coulomb interaction with the nearby gate electrode and show that this occurs on a much longer timescale than dephasing due to phonons. However, the effect grows rapidly stronger as the system size decreases and therefore it limits the potential miniaturization of these systems.

The development of a functional quantum computer is an important goal that has attracted much attention in recent years. The importance of quantum computing is due to the existence of "quantum algorithms" which solve certain problems, e.g. prime factorization, exponentially faster than they can be solved on a classical computer. This speedup is possible because the algorithms exploit the quantum mechanical properties (such as superposition and entanglement) of the quantum bits (qubits) [1].

However, since quantum mechanical systems can never be isolated completely from their environment, a prepared quantum state will decay with time. This passage from a quantum into a classical state involves two different types of decay — *dephasing* and *dissipation*. *Dephasing* refers to the loss of phase coherence of the superposition of states, i.e. the decay of the off-diagonal elements of the density matrix; *dissipation* describes the flow of energy out of the system, characterized by the decay of the diagonal elements of the density matrix. Both mechanisms destroy the quantum mechanical nature of the system. A system is a viable option for a quantum computer only if its dephasing and dissipation times are much longer than the average computation time [1].

Promising candidates for quantum computing are solid-state systems based on quantum dots, because of their scalability and the reliability with which they are fabricated. Two categories of quantum dot qubits exist — *spin* and *charge* qubits. Spin qubits encode information in the electron spin, using the "up" and "down" eigenstates. Charge qubits consist of a pair of quantum dots and use the position of the electron, "left" or "right", as the quantum variable. Charge qubits are easily addressed and manipulated, because of the strong interaction of a charge with external fields. However, this strong interaction causes the charge to dephase rapidly. Spin qubits, the subject of this report, dephase on a much longer timescale, but are usually much more difficult to address and manipulate.

Recently, however, a new technique for controlling the spin in a spin qubit has been demonstrated [2]. The quantum dot is subject to strong electric and magnetic fields. A circularly polarized laser pulse is passed through the qubit, creating an exciton with angular momentum $\pm\hbar$, depending on the polarization of the light. Because only heavy holes are optically active, the exciton is either e$\downarrow$h$\uparrow$ ($+\hbar$) or e$\uparrow$h$\downarrow$ ($-\hbar$); the magnetic field prevents these from mixing. Recombination of the exciton is prevented by the electric field, which causes the hole to tunnel out of the system (the electron is trapped due to its low mobility). Thus an "up" or a "down" electron can be selectively injected into the qubit by choosing the polarization of the light.

The electron remains in the qubit for up to 20 ms, after which the tunneling probability due to the electric field becomes very high [2]. The spin does not persist as long. In the magnetic field, the spin energies are separated. If the electron has been excited into the higher energy spin state, it is thermodynamically unstable and will lose energy to the environment. The spin lifetime due to scattering with phonons was calculated and accurately reproduced the measurements at high magnetic field B [3]. The lifetime scales as B^5 at very high fields ($B > 8$ T) and as B^4 for weaker fields ($B > 4$ T). However, the uncertainty in several of the parameters used, particularly the Dresselhaus velocity, indicates that spin-phonon scattering is not necessarily the only relevant mechanism for dissipation and dephasing. We have investigated an alternative dephasing mechanism that has been generally overlooked — the interaction of the electron with nearby gate electrodes.

Gate electrodes are metallic strips used to provide the electric field. They are a typical feature in quantum dot assemblies and are often used to define and control the qubits. Usually, gate electrodes are assumed to contribute only a classical electric field, despite having both quantum and thermal fluctuations. We have studied the effect of these fluctuations using the kinetic equation approach [4].

Fig. 1(a) shows a schematic diagram of the system under consideration. The quantum dot is strongly

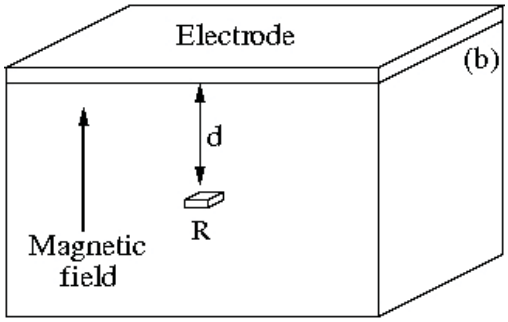

FIG. 1: (a) A schematic drawing of a spin qubit. As in Ref. [2], the magnetic field is parallel to the direction of strong confinement and orthogonal to the electrode.

confined in the direction parallel to the magnetic field. In the other two directions, a square potential well structure is assumed. The qubit is embedded in GaAs, which is asymmetric under inversion. This causes the Dresselhaus effect to produce a strong coupling between the spin and the charge distribution. This coupling allows both the phonon bath and the gate electrode, which usually only interact with charges, to interact with the spin. The Hamiltonian for the quantum dot is

$$H = H_0 + g\mu B\sigma_z - \beta(p_x\sigma_x - p_y\sigma_y), \qquad (1)$$

with the Dresselhaus velocity $\beta = 2 \pm 1 \times 10^5$ cm s^{-1}. The energy eigenfunctions of Eq. (1) were constructed numerically.

The evolution is determined via the density matrix. The qubit is coupled to the electrode using the statically screened Coulomb interaction. The initial state of the electrode is taken as thermal equilibrium, and we assume that there are no initial correlations between the qubit and the electrode. The kinetic equation method proceeds by integrating the density matrix over the electrode degrees of freedom, leading to an equation of motion for the reduced density matrix of the qubit. This equation contains memory effects — the qubit can cause a fluctuation in the gate and then interact with that fluctuation at a later time.

The kinetic equation is exact, but it cannot be solved exactly. We used the second-order Born approximation, in which qubit-induced fluctuations in the gate do not interact with each other (although they do interact with the thermal and quantum fluctuations of the gate itself). Certain correlation functions of the gate are required; these are determined by the Kubo formula and the generalized reflection coefficient, which is evaluated in the Drude approximation.

The kinetic equation is an integro-differential evolution equation. We solved it by evaluating the poles of the Laplace transform, confirming our results by simulations using a time-marching algorithm. Dephasing is exponentially fast, with the dephasing rate plotted in Fig. 2. The energy dissipation rate, not plotted, is marginally less than twice the dephasing rate. The dephasing rate depends on several parameters, e.g. the magnetic field and the distance between the gate and the dot d. We found that the dephasing rate scales as B^3, which is different to the scaling found experimentally at high fields.

We set the size of the dot in the weakly-confined directions to $R = 30$ nm and the temperature to $T = 100$ mK. The dependence on T and R have not yet been investigated. The thermal dependence may be very important at weak magnetic fields — in the phonon case it is responsbile for reducing the scaling of the dephasing rate from B^5 to B^4.

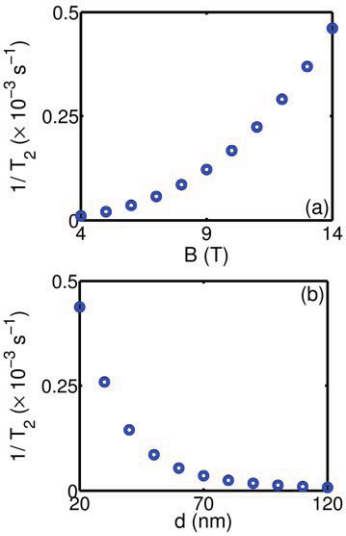

FIG. 2: The dephasing rate of the spin qubit due to the interaction with the gate electrode. (a): Dependence of the dephasing rate on magnetic field; here $d = 50$ nm. (b): Dependence on d, with the magnetic field set to $B = 8$ T. In all cases, the temperature is $T = 100$ mK and the dot size is $R = 30$ nm.

As seen in Fig. 2, the dephasing rates were found to be of the order of $10^{-3}\mathrm{s}^{-1}$. This is significantly slower than the typical phonon dephasing rate which is usually around $10^2\mathrm{s}^{-1}$ for the system parameters considered here [2]. Gate-induced dephasing yields a negligible contribution for the magnetic fields considered here. However, as $B \to 0$, the Coulomb dephasing rate decreases as B^3 (or possibly B^2 due to thermal effects), while the phonon rate decreases as B^4. These will meet at some critical magnetic field. Furthermore, the dephasing rate increases rapidly as the gate-dot separation is reduced, so that as the system is miniaturized, the Coulomb dephasing may become important.

The results shown here have not yet been published. However, the results of a parallel investigation of dephasing in *charge* qubits were published in Ref. [5].

[1] D. P. DiVincenzo, Fortschr. Phys. **48**, 771 (2000)

[2] M. Kroutvar, Y. Ducommun, D. Heiss, M. Bichler, D. Schuh, G. Abstreiter and J. J. Finley, Nature **432**, 81 (2004)

[3] A. V. Khaetskii and Y. V. Nazarov, Phys. Rev. B **64**, 125316 (2001)

[4] F. Haake, *Quantum statistics in optics and solid state physics* , Springer Tracts in Modern Physics 66, Springer, Berlin (1973)

[5] S. R. Woodford, A. Bringer and K. M. Indlekofer, Phys. Rev. B **76**, 064306 (2007)

THz Josephson Spectroscopy of Optical Phonons in [100]-Tilt $YBa_2Cu_3O_{7-x}$ Bicrystal Junctions

Y. Y. Divin

IFF-8: Microstructure Research
CNI: Center of Nanoelectronic Systems for Information Technology

Terahertz losses in the [100]-tilt $YBa_2Cu_3O_{7-x}$ bicrystal junctions at low temperatures were studied using Josephson spectroscopy. The absorption of Josephson radiation by optical phonons in $YBa_2Cu_3O_{7-x}$ was found to be reflected in the I-V curve of the junctions. The most prominent feature in the dI/dV vs. V curves is situated at the voltages V ≅ 9.5 mV, which gives the corresponding Josephson frequency of 152 cm^{-1} in a good agreement with the frequency of the strongest IR active optical phonons in $YBa_2Cu_3O_{7-x}$, polarized along the c-axis. Assignment of the observed localized features in the dI/dV vs. V curves is discussed according to available lattice dynamic calculations and experimental data for dynamic conduction σ(f) of $YBa_2Cu_3O_{7-x}$.

Due to much higher values of energy gaps 2Δ in high temperature superconductors, the ac Josephson effect in Josephson junctions made from these materials was expected to be observed in more extended frequency range, compared with that of in the junctions made from low-T_c superconductors. However, the conventional [001]-tilt high-T_c grain boundary Josephson junctions possess too low values of characteristic voltage I_cR_n [1], which governs the junction dynamics and should be of the values of the gap voltages 2Δ/e.

Significant improvement in junction quality was reached in the [100]-tilt high-T_c bicrystal junctions, where the I_cR_n-values up to 8 mV were observed [2], and, as follows from recent study of low-frequency noise in these junctions [3], the current transport is more spatially uniform. The highest frequency of 5.2 THz has been demonstrated for Josephson oscillations in the [100]-tilt junctions [4], but, being a record value for Josephson frequencies, it is still too low compared with the gap frequencies of bulk high-T_c materials.

We expect that some losses in the junction and its environment are responsible for weakening of the Josephson oscillations. At the temperature range, where the characteristic voltage $I_cR_n < kT/2e$, broadband losses, associated with oxygen deficit in the grain boundary, have been observed [5] by admittance Josephson spectroscopy [6]. Here, we report on our study of localized losses in the [100]-tilt $YBa_2Cu_3O_{7-x}$ grain-boundary junctions at low temperatures, where $I_cR_n \gg kT/2e$.

The [100]-tilt $YBa_2Cu_3O_{7-x}$ junctions were deposited on $NdGaO_3$ bicrystal substrates with a misorientation angle 2α of 2x11.3° and 2x14° by dc sputtering from a $YBa_2Cu_3O_{7-x}$ target and patterned by UV lithography and wet etching. A microphotograph (in transmitted light) of one of the fabricated junctions is shown in Fig.1. A 1μm-wide $YBa_2Cu_3O_{7-x}$ bridge is crossing the bicrystal substrate boundary, situated vertically in Fig.1. Electrical contacts and a broadband logperiodic antenna were made from Pt thin films, sputtered a top of the patterned $YBa_2Cu_3O_{7-x}$ thin film.

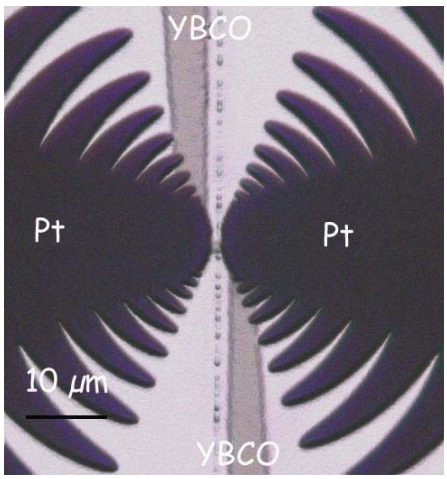

FIG. 1: Microphotograph of the fabricated [100]-tilt bicrystal junction in the form of a 1μm-wide $YBa_2Cu_3O_{7-x}$ thin-film bridge, crossing the bicrystal substrate boundary, with $YBa_2Cu_3O_{7-x}$ voltage leads and Pt logperiodic antenna, covering $YBa_2Cu_3O_{7-x}$ current leads.

The I-V curves of fabricated junctions demonstrated enhanced deviations from that of RSJ model, localized at some voltages at low temperatures, where $2eI_cR_n/kT \gg 1$. Reproducible fine structures were observed on the differential conductance dI/dV vs. voltage V for the [100]-tilt $YBa_2Cu_3O_{7-x}$ GB junctions at the voltages V ≅ 7.3 mV, 9.5 mV and 11.8 mV Fig. (2, below), which were independent on the junction resistances R_n, widths w or misorientation angles α. The visibility of these structures increases for low-resistance junctions, as shown in Fig. 2 (below). The most prominent feature is situated around volt-

ages V ≅ 9.5 mV. We might suspect that this feature is related to an interaction of tunneling carriers with some strong modes in the barrier or $YBa_2Cu_3O_{7-x}$ itself.

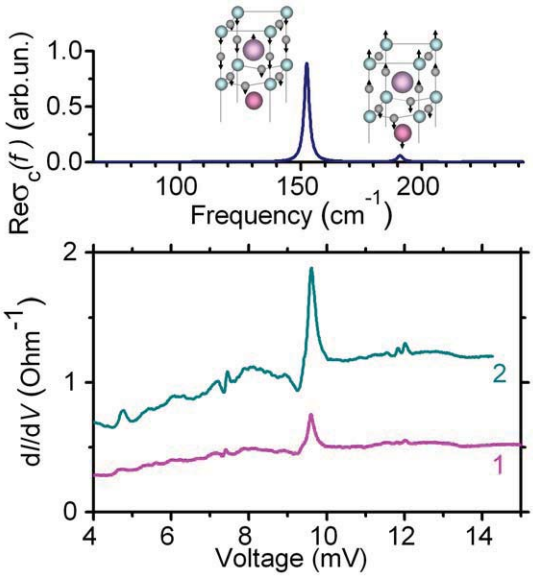

FIG. 2: Differential conductances dI/dV vs. voltage for two [100]-tilt $YBa_2Cu_3O_{7-x}$ GB junctions with widths w, equal to 1μm (1) and 2μm (2), and the I_cR_n-products of 6.5 mV at 5 K (below). Phonon contributions to the dynamic conductance Reσ_c (f) of $YBa_2Cu_3O_{7-x}$ [7] are shown above. Insets show atomic displacements in $YBa_2Cu_3O_{7-x}$ for phonon modes at 152 cm^{-1} (left) and 191 cm^{-1} (right) [8].

To clarify the mechanism of interaction, photon-assisted tunneling experiments have been carried out and the junction was illuminated by 96GHz radiation at various levels of intensities. The modification of the conductance curves are shown in Fig. 3. The conductance curve at large attenuation (60 dB) of 94GHz source has a peak at the voltage of 9.6 mV. With an increased level of 96 GHz intensity, the peak at 9.6 mV goes to the background level (10 dB) and then increases again (6 dB). Several satellite peaks appear at the voltage differences of integral numbers of $\pm$0.2 mV from the position of the main peak and also oscillate with increased power level. The difference in peak positions is corresponding to $hf/2e$ and this circumstance is a signature of photon-assisted *Josephson* tunneling, while this splitting for photon-assisted *quasiparticle* tunneling should be equal to hf/e.

Our experimental data (dI/dV vs. voltage V) have been compared with available dynamic conductance data $\sigma(f)$ for $YBa_2Cu_3O_{7-x}$, which are always the functions of frequency f. The frequency dependence of phonon contribution to the real part Re$\sigma_c(f)$ of the dynamic conductance of $YBa_2Cu_3O_{7-x}$ [7], polarized along the c-axis, is presented in Fig. 2 (above). As one can see from a comparison of Re$\sigma_c(f)$ and dI/dV vs. V, the main peak at 152 cm^{-1} corresponds to the pronounced odd-symmetric structure around V ≅ 9.5 mV, and the lower peak at 191 cm^{-1} corresponds to one of the features close to V ≅ 11.8 mV. The corresponding optical phonon modes of $YBa_2Cu_3O_7$, calculated from the lattice dynamics [8], are presented as insets in the upper part of Fig. 2. The feature at V ≅ 7.3 mV on the dI/dV vs. V might be attribute to the one of the in-plane polarized IR-active phonon mode at f ≅ 115 cm^{-1} [8].

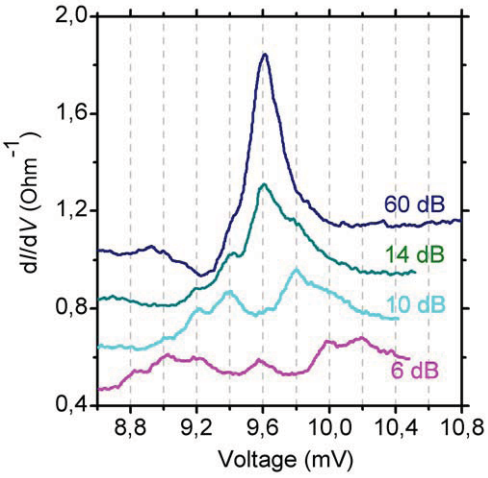

FIG. 3: Effect of electromagnetic radiation with the frequency f = 96 GHz and various levels of power on the conductance dI/dV vs. voltage V near a phonon peak at 9.6 mV. Each curve is shifted on 0.2 Ohm^{-1} down for attenuations 14, 10 and 6 dB.

We might interpret the peculiarities at V ≅ 7.3 mV, 9.5 mV and 11.8 mV as a result of shunting of Josephson oscillations by enhanced dynamic conductivity of $YBa_2Cu_3O_{7-x}$ electrodes at the frequencies close to the optical phonon frequencies. This effect is in accordance with Volkov's perturbation analysis [6], where the shunting of Josephson oscillations by external frequency-dependent admittance $Y_e(f)$ has resulted in a modification $\Delta I(V)$ of the I-V curve, proportional to a real part ReY_e (2eV/h) of the admittance.

Josephson spectroscopy might be applicable for study of electromagnetic environment of high-T_c junctions in the terahertz frequency range, including low-energy excitations in high-T_c materials.

[1] H. Hilgenkamp, J. Mannhart, Rev. Mod. Phys. **74** (2002) 485.

[2] Y. Y. Divin, U. Poppe, C.L. Jia, P.M. Shadrin, K. Urban, Physica C **372-376** (2002) 115.

[3] M.V. Liatti, U. Poppe, Y.Y. Divin, Appl. Phys. Lett. **88** (2006) 152504.

[4] Y.Y. Divin, M.V. Liatti, D.A. Tkachev, U. Poppe, Physica C **460-462** (2007) 1270.

[5] M.V. Liatti, U. Poppe, Y.Y. Divin, IEEE Trans. Appl. Supercond. **17** (2007) 314.

[6] A. F. Volkov, Radiotekhnika i Elektronika, **17** (1972) 2581(in Russian).

[7] L. Genzel , in: Millimeter and Submillimeter Wave Spectroscopy of Solids (ed.G. Grüner, Springer, Berlin, 1998) Ch.5.

[8] J. Humlicek, et al., Physica C **206** (1993) 345.

Thick Epitaxial $YBa_2Cu_3O_{7-x}$ Films for High-T_c Quantum Interferometers

M. I. Faley[1,2], S. B. Mi[1,2], C. L. Jia[1,2], U. Poppe[1,2], K. Urban[1,2], R. L. Fagaly[3]

[1] IFF-8: Microstructure Research
[2] CNI: Center of Nanoelectronic Systems for Information Technology
[3] Tristan Technologies, Inc., San Diego, CA 92121 USA

High total critical current and strong pinning of Abrikosov vortices in the superconducting electrodes are required for low-noise operation of superconducting quantum interference devices (SQUIDs) in magnetic fields. Crack-free epitaxial high-T_c dc-SQUID structures with a total thickness $\sim 5\mu$m and a surface roughness determined by 30 nm high growth spirals were prepared with $YBa_2Cu_3O_{7-x}$ (YBCO) films on MgO substrates buffered by a $SrTiO_3/BaZrO_3$-bilayer. HRTEM demonstrated a high quality epitaxial growth of the films. The YBCO films and SQUID structures deposited on the buffered MgO substrates had T_c > 91 K and critical current densities J_c > 3 MA/cm^2 at 77 K up to a thickness $\sim 5\mu$m. The application of thicker superconducting and insulator films helped us to increase the critical current and dynamic range of multilayer high-T_c flux transformers and improve the insulation between the superconducting layers [1].

Magnetometers based on superconducting quantum interference devices (SQUIDs) are the most sensitive sensors for measurements of magnetic field components (see, e.g., [2]). The use of high-T_c SQUIDs at 77 K and performing measurements without magnetic shielding significantly reduces the operational expenditure and broaden the field of SQUID applications. Present day high-T_c dc-SQUID magnetometers have demonstrated sensitivity better than 4 fT/$\sqrt{Hz}$ at 77 K in magnetic shielding [3]. In the case of unshielded operation, the SQUIDs are exposed to the Earth's magnetic field and electromagnetic fields. Such conditions impose strong requirements on the dynamic range, the slew rate and low frequency noise of the sensi-tive dc-SQUID systems. Pinning of Abrikosov vortices in the superconducting films of the SQUID body should be improved to reduce low-frequency noise in magnetic fields. This can be achieved by application of thicker superconducting films with highest and thickness-independent critical current density.

$BaZrO_3$ (BZO), $SrTiO_3$ (STO), $YBa_2Cu_3O_{7-x}$ (YBCO), and $PrBa_2Cu_3O_{7-x}$ (PBCO) films were deposited on symmetric 20° or 24° bicrystal or single crystal MgO substrates by the high-oxygen-pressure dc-sputtering technique. The STO/BZO-bilayer was used as an epitaxial buffer on the MgO substrates. The thermal expansion coefficients of MgO and YBCO are very similar and this has allowed us to produce up to $\sim 5\mu$m thick crack-free high-quality YBCO films and YBCO-PBCO structures. To reduce mechanical strain in the structures and for a better oxygenation of the thick YBCO films the samples were slowly heated (0.1°C/min) up to 700°C in a flow of pure (99.999 %) molecular oxygen followed by 0.1°C/min cooling to room temperature.

Significant progress was made in the preparation of high-quality crack-, hole-, and precipitate-free thick YBCO films. Observed by AFM the surface roughness of YBCO films was about 30 nm and was determined mainly by the YBCO growth spirals. The HRTEM images of the BZO/MgO and STO/BZO interfaces in the buffer layers of our structures were recently published [4, 5]. It was shown that the BZO buffer layer at the BZO/MgO interface provided the epitaxial growth of the top layer films with perovskite structures (STO, YBCO, and PBCO) on the rock-salt structure of MgO, while the matching of the lattice constants appeared by relaxation of the atomic structure at the STO/BZO interface. As a demonstration of the perfect epitaxial growth of YBCO films on the STO buffer layer we present here an HRTEM image of the interface between STO and YBCO films. It was determined (see Fig. 1) that the interface atomic layer has a $Ba_{1-x}Sr_xO$ composition so it belongs to both STO and YBCO layers.

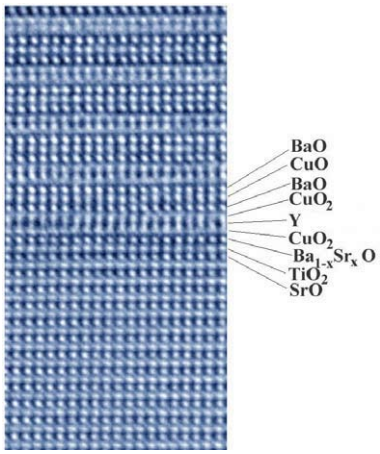

FIG. 1: HRTEM image of the YBCO/STO interface obtained in the [1$\bar{1}$0] direction.

The standard procedure for measuring the critical cur-rent density of the films by structuring narrow bridges is not convenient for thick films. The required currents are in the ampere range and can heat the sample at the contacts for the current inputs. A more practical and fast estimation of the critical current density can be done by a non-destructive permanent magnet method suggested in [6]. We measured the dependence of the repulsive force "F" between a 6 mm diameter permanent $SmCo_5$ magnet and an YBCO film of thickness "d". The magnet brought to a distance of $\sim$ 1 mm from the YBCO film, while the latter was immersed in liquid nitrogen at 77 K. A linear dependence F(d) was observed up to a film thickness of $\sim$ 5 μm (see Fig. 2).

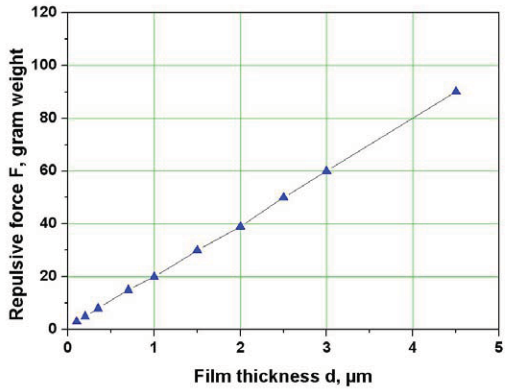

FIG. 2: Dependence of the maximum repulsive force "F" between the 6 mm $SmCo_5$ magnet and YBCO films vs. the film thickness "d".

The high and constant critical current density throughout the thickness of the thick YBCO films is a real challenge and important for all applications of high-T_c superconductors. The addition of non-superconducting nanoprecipitates of BZO or Y_2BaCuO_5 was suggested and successfully applied to increase the J_c of YBCO films [7, 8]. On the other hand, it is already well known [3] that the YBCO films deposited by high oxygen pressure sputtering technique naturally contain lattice-coherent non-superconducting Y_2O_3 nanoparticles of optimal size and separation. These nanoparticles are nearly spherical with a diameter of $\sim$ 20 nm and are homogeneously distributed with a separation of $\sim$ 30 nm [3]. A strong 3D pinning of the Abrikosov vortices is expected in the bulk of the thick films with a uniform local $J_c \sim 3.5$ MA/cm^2. Fortunately, we are able to produce much thicker YBCO films without cracks or thickness degradation of the current-carrying cross-section in the films, which is demonstrated, for example, by the good surface morphology of the thick films.

The linear dependence F(d) corresponds to a thickness-independent $J_c \sim 3.4$ MA/cm^2 according to the empirical relationship [6] $J_c \sim 0.17$ (F/d)[MA/cm^2], where F is the maximum repulsive force measured in gram weight and d is the film thickness in micrometers. For a small film thickness d $\sim$ 300 nm this J_c evaluation was additionally calibrated with a conventional direct 4-point measurement of the critical current. The currents induced in the thick YBCO films were able to shield the $\sim$ 1 kG strong magnetic field of the $SmCo_5$ magnet. At 77 K 1 cm wide strips of a 4.5 μm thick YBCO film have an estimated total critical current of $\sim$ 1.5 kA, which exceeds the critical current of the present day 2^{nd} generation high-T_c superconducting tapes of similar width about 15-fold.

High-quality thick and flat YBCO films are an important prerequisite for the preparation of present dc SQUID sensors. We used the thick (> 1 μm) YBCO films for the preparation SQUIDs with ramp-type or bicrystal Josephson junctions and multilayer flux transformers. In the case of ramp-type Josephson junctions, the thick top electrode shields the junction area thus improving the stability of operation in magnetic fields. It was observed that an increase of the low-frequency noise appeared first at magnetic fields above 300 μT while in the case of the SQUIDs with standard 100 nm thick electrodes this already takes place at a magnetic field of $\sim$ 100 μT.

The typical thickness of the YBCO film of the SQUID washer was $\sim$ 1.5 μm. The field sensitivity was improved by the multilayer flux transformers having total thickness of $\sim$ 3 μm. The critical current of the flux transformer $I_c \sim 0.3$ A at 77 K was limited by the cross-section area of the lines in the input coil of $\sim$ 10 μm^2. In the case of 8 mm flux transformers, this current provided a maximal dynamic range of about $\sim$ 190 μT while in the case of 16 mm flux transformers the maximal dynamic range was about $\sim$ 100 μT. These values are sufficient to follow changes of the magnetic field during movement of the sensors in the Earth's magnetic field.

[1] M. I. Faley, S. B. Mi, A. Petraru, C. L. Jia, U. Poppe, and K. Urban, *Physica C*, **460-462**, 1371 (2007).

[2] R. L. Fagaly, *Rev. Sci. Instr.* ***77***, 101101 (2006).

[3] M. I. Faley, C. L. Jia, U. Poppe, L. Houben, and K. Urban, *Supercond. Sci. Technol.*, **19**, S195 (2006).

[4] M. I. Faley, S. B. Mi, A.Petraru, C. L. Jia, U. Poppe, and K. Urban, *Appl. Phys. Lett.*, **89**, 082507 (2006).

[5] S. B. Mi, C. L. Jia, M. I. Faley, U. Poppe, and K. Urban, *J. Crystal Growth*, **300**, 478 (2007).

[6] A. Saito, K. Takeishi, Y. Takano, T. Nakamura, M. Yokoo, M. Mukaida, S. Hirano, S. Ohshima, *Physica C*, **426-431**, 1122 (2005).

[7] S. R. Foltyn, L. Civale, J. L. Macmanus-Driscoll, Q. X. Jia, B. Maiorov, H. Wang and M. Maley, *Nature Materials*, **6**, 631 (2007).

[8] J. Gutiérres, A. Llordés, Gázquez, Gibert, N. Romá, N. Ricart, A. Pomar, F. Sandiumenge, N. Mestres, T. Puig, and X. Obradors, *Nature Materials*, **6**, 367 (2007).

Nanoscale Phase Transitions in Phase Change Materials

R. O. Jones[1], J. Akola[1,2]

[1] IFF-1: Quantum Theory of Materials
[2] Nanoscience Center, University of Jyväskylä, Finland

Phase change (PC) materials are among the most promising candidates for the next generation of computer random access memory (RAM) and rewritable storage devices. Unlike conventional RAM, the content is not lost when power is disconnected. PC materials switch between amorphous and ordered states when an electric current or laser pulse is applied, and the state can be determined by monitoring the optical or electrical properties. It is remarkable that PC materials have become the basis of a whole industry while only sketchy information is available about the structures of the phases involved. We have used the IBM BlueGene/L computer to perform extensive simulations on the amorphous and ordered states of an alloy of germanium, antimony, and tellurium (Ge/Sb/Te) that is already used in DVD-RAM. These simulations provide insight into the structural units essential to the phase change process.

Computers and other electronic devices place ever-increasing demands on the density, speed, and stability of memory, and phase change (PC) materials are familiar to us as rewritable media (CD-RW, DVD-RW, DVD-RAM). Recently (January 2008), Warner Bros, the world's largest distributor of DVD films, announced that—from May this year—it would sell only the Blu-ray disc (BD) version of its products. Blu-ray discs, like commercially available DVD-RW storage devices and DVD-RAM, are based on films of alloys of Ge, Sb, and Te. The basis of their function is the rapid and reversible transition between the crystalline and amorphous forms of nanoscale bits ($\lesssim$ 100 nm), which arise from quenching after a localized and short ($\sim$ 1 ns) laser annealing to a temperature above the melting point. Longer laser heating ($\sim$ 50 ns) to a temperature above the glass transition temperature but below the melting point leads to a metastable crystalline form. The ideal storage materials of the future will be fast ($\sim$ 10 ns switching time), dense (bit diameter $\ll$ 50 nm), stable (several years per lost bit), long-lived ($> 10^{12}$ cycles per lost bit), and—naturally—with low manufacturing cost and power consumption. Such bit diameters would result in storage densities far in excess of those found in current commercial devices, such as those based on giant magnetoresistance (GMR).

PC optical memory devices have focused for over 20 years on films of semiconductors and semimetals with melting points that are low enough to allow laser-induced melting but high enough to prevent spontaneous crystallization. The materials of choice today are Ge/Sb/Te alloys [1], with particular focus on the pseudobinary compounds GeTe-Sb_2Te_3. One of them ($Ge_2Sb_2Te_5$, GST) is the basis of digital versatile disc-random access memories (DVD-RAM), and another ($Ge_8Sb_2Te_{11}$) is the basis of Blu-ray Disc (BD) technology.

To understand the properties of these materials it is essential to know the atomic arrangement ("structure") in the phases involved, but these are difficult to measure or to calculate in ternary alloys with a significant number (typically around 20%) of vacancies. In the case of GST, even the structure of the metastable crystalline form is a matter of debate, and the metastable nature of amorphous GST (bulk samples crystallize) has restricted experimental studies of this material. In any event, the analysis of experiments often requires wide-ranging assumptions about the atomic arrangements, an example being the widespread use of reverse Monte Carlo methods to find structural information from measured x-ray and neutron scattering experiments. A number of calculations have been performed in recent years, but the unit cells (with $\sim$ 60 atoms) are usually too small to describe structural details, and the simulation times (typically a few picoseconds) are too short to describe vibrational and other thermodynamic properties reliably. We have used the Blue Gene/L supercomputer in Jülich to extend greatly the range of density functional (DF) calculations on these and related materials. We have performed simulations on GST in a unit cell containing 460 atoms over several hundred picoseconds. We begin from a high temperature liquid in order to avoid bias towards particular structural types. In addition to the liquid and amorphous materials (at 900 K and 300 K, respectively), we have simulated rock-salt (ordered) structures of GST and states of the prototype PC material $Ge_{0.50}Te_{50}$. Full details are provided in Ref. [2].

Such simulations allow us to follow the motion of all atoms throughout, and we can determine pair-correlation functions for all atom types. The structures of the amorphous and crystalline phases show similarities, as the speed of the phase change be-

tween them would suggest, and the structure factors agree remarkably well with the results of scattering experiments (x-rays, neutrons) where available. Amorphous GST shows long-range ordering (at least to 10 Å) of Te atoms and a high degree of AB alternation (A: Ge, Sb; B: Te). This striking (and unexpected) result is illustrated in Fig. 1, where we highlight four-membered $ABAB$ rings. Since the crystalline (rocksalt) phase comprises perfectly ordered $ABAB$ squares, we can view the rapid amorphous-to-crystalline transition as a reorientation of such squares to form additional $ABAB$ bonds and cubic subunits in a locally "distorted octahedral" structure. A crucial component of these materials (and essential for an understanding of their properties) are the vacancies, and our simulations provide us with their shapes and distributions as well. In Fig. 2 we show a typical medium-sized vacancy (and the neighbouring bonds) in GST. Vacancies in the disordered phase provide the necessary space for the phase transition to take place.

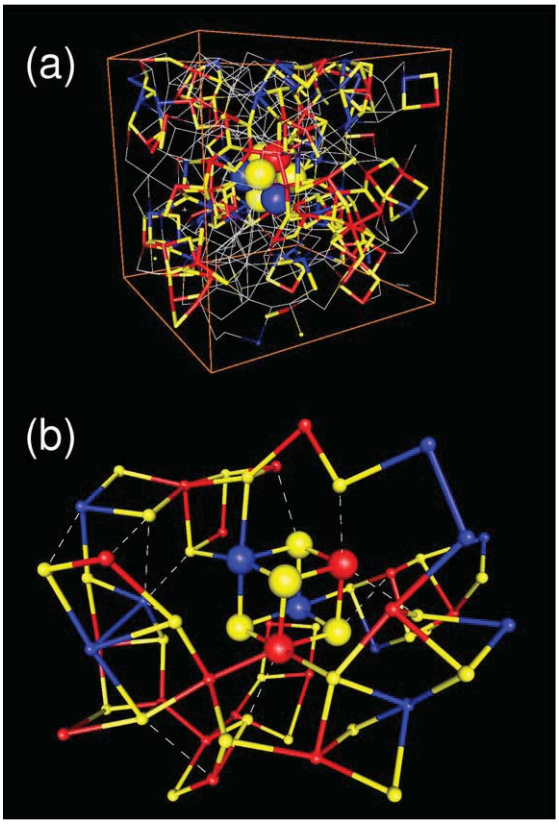

FIG. 1: $ABAB$ squares and cubes in amorphous $Ge_2Sb_2Te_5$. (a) Simulation box (24.6 Å, 460 atoms) with atoms and bonds of $ABAB$ squares and cube highlighted. Red: Ge, blue: Sb, yellow: Te. (b) Local environment of an $ABAB$ cube.

GST is just one of numerous Ge/Sb/Te alloys that are used in the world of phase change memories. In Ref. [2] we also provide a detailed discussion of GeTe and explain why it is much less attractive than GST for these purposes. More recently we have studied the eutectic alloy $Ge_{0.15}Te_{0.85}$, i.e. the binary Ge/Te alloy with the lowest melting point (650 K) [3]. We have found that there is no Te segregation at the eutectic composition, where the material resembles neither GeTe nor Te. By good fortune we have chosen the Blu-ray alloy $Ge_8Sb_2Te_{11}$ as our next system to study. It is natural to ask: Just what is it about the structure of this alloy that makes it the material of choice for the next generation of DVD? It will surprise many that the *de facto* future standard is a material whose structure is essentially unknown. We are confident that the results we present in next year's report will change this situation. In addition, our simulation trajectories and the well-equilibrated structures that result also allow us to calculate vibration frequencies. This provides us with another window into the properties of these materials, because there are good prospects that measured vibrational spectra of these materials will soon become available.

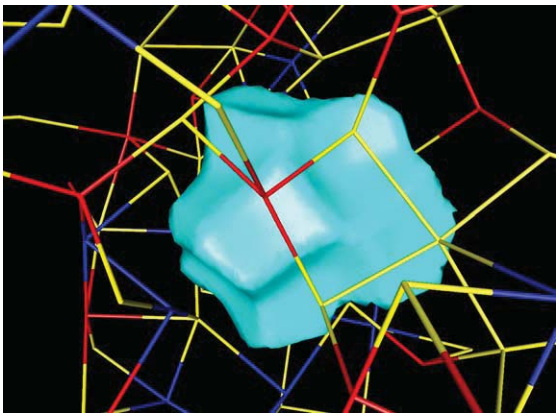

FIG. 2: A medium-sized cavity in $Ge_2Sb_2Te_5$.

This is a fascinating area in which to work. Do look at Ref. [2] for more details, and you must certainly return to these pages next year for the latest developments!

[1] M. Wuttig and N. Yamada, Nature Mater. **6**, 824 (2007) provide a review of the history of these materials.

[2] J. Akola and R. O. Jones, Phys. Rev. B **76**, 235201 (2007).

[3] J. Akola and R. O. Jones, submitted.

$Pb(Zr,Ti)O_3$ Thin Films on 3D-Capacitor Structures for FeRAM Applications Grown by a LI-ALD Method

S. Hoffmann-Eifert[1,2] T. Watanabe[1,2], C. S. Hwang[3], R. Waser[1,2]

[1] IFF-6: Electronic Materials
[2] CNI: Center of Nanoelectronic Systems for Information Technology (IEM)
[3] Department of Materials Science and Engineering and Inter-university Semiconductor Research Center, Seoul National University, Korea

Quaternary $Pb(Zr,Ti)O_x$ [PZT] films were deposited at 240°C by a combination of liquid injection atomic layer depositions (ALD) of binary PbO, TiO_x, and ZrO_x thin films. To find the optimum set of precursors different combinations of five precursors were tested: $Pb(C_{11}H_{19}O_2)_2$ [$Pb(DPM)_2$], $Ti(OC_3H_7)_2(C_{11}H_{19}O_2)_2$ [$Ti(Oi\text{-}Pr)_2(DPM)_2$] or $Ti(OC_3H_7)_4$ [$Ti(Oi\text{-}Pr)_4$], and $Zr(C_{11}H_{19}O_2)_4$ [$Zr(DPM)_4$] or $Zr(C_9H_{15}O_2)_4$ [$Zr(DIBM)_4$]. Each precursor was dissolved in ethylcyclohexane (ECH) and was separately injected into a vaporizer. Water vapor was used as oxidant. The deposition rates of the metal elements were investigated as a function of the input of the solutions. Using the set of 0.1M $Pb(DPM)_2$, $Ti(Oi\text{-}Pr)_4$, and $Zr(DIBM)_4$ solutions resulted in PZT films with good uniformity on 3D structured substrates. The Zr to Ti ratio in the as-deposited PZT films could be adjusted in the range up to Zr/Ti =1. This study suggests that the multi-layer stacking liquid delivery ALD process is an effective method for building up homogeneous layers of multi-component materials on desired 3D structures.

Perovskite-type oxide materials exhibit a broad spectrum of functional properties, like for example a high value of the electrical permittivity and ferroelectricity. In order to combine this functionality with state-of-the-art semiconductor memory devices, thin films of complex perovskites with a thickness of less than 20 nm have to be integrated into three dimensional trench structures with lateral diameter of about 100 nm and a depth in the micrometer regime. To achieve highest performance of the integrated capacitor structures the thin films have to be homogeneous in thickness and in composition. A fully conformal deposition into these deep trenches can only be achieved by means of an atomic layer deposition (ALD) process [1].

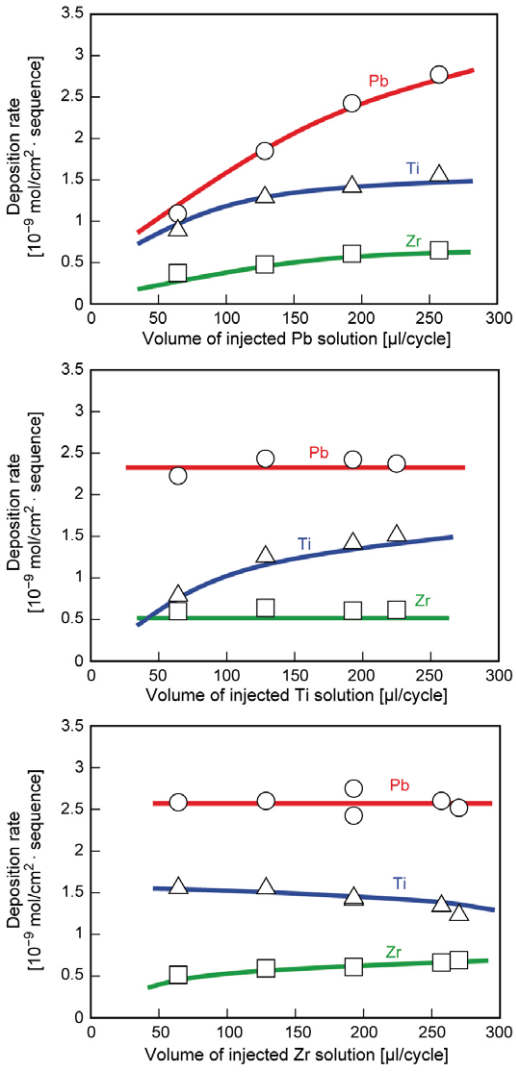

FIG. 1: Mole area density of each constituting element in the PZT film as a function of the input of $Pb(DPM)_2$, $Ti(Oi\text{-}Pr)_4$, $Zr(DIBM)_4$ solutions. The deposition temperature was 240°C and H_2O was used as oxidant.

In this work, we deposited quaternary $Pb(Zr_xTi_{1-x})O_3$ [PZT] films in a combination of binary ALD processes, aiming at a uniform coverage of 3D nano-structures both in the film thickness and the cation composition.

The PZT films were grown by a liquid injection ALD tool with a horizontal cold wall reactor. For the ALD-PZT process using $Ti(Oi\text{-}Pr)_2(DPM)_2$ we found a complex interdependence between increase of input of one precursor and the deposition rates of all

the three metal elements which resulted in inhomogeneous films. [3, 4] The films' quality was significantly improved by using the combination $Pb(DPM)_2$, $Ti(Oi\text{-}Pr)_4$, $Zr(DPM)_4$ dissolved in ECH with a concentration of 0.1 M. Two drawbacks were that the Pb/(Ti+Zr) ratio had to be adjusted by repetition of the PbO cycles for two times and that the Zr concentration in the PZT films could not be increased above 0.10. [4,5]

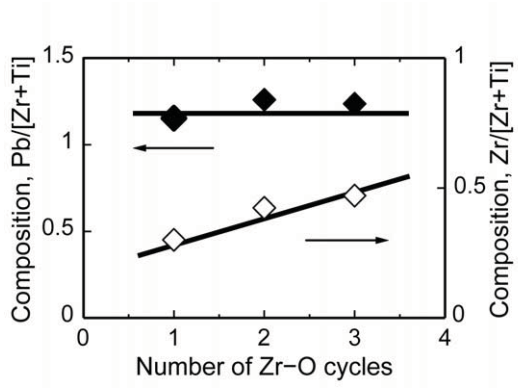

FIG. 2: Composition of the as deposited amorphous PZT film as a function of the number of Zr-cycles.

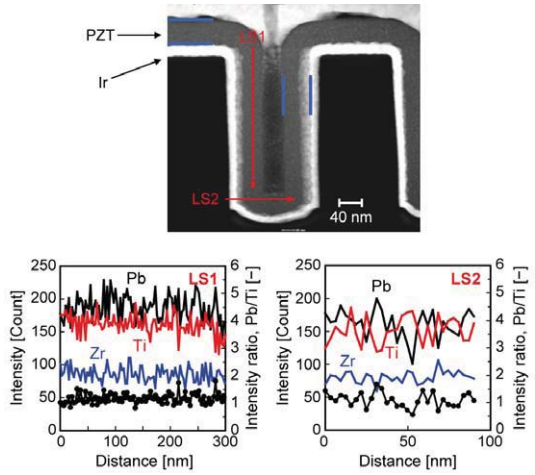

FIG. 3: Cross sectional TEM of a $Pb(Zr,Ti)O_3$ film deposited on a 3D silicon oxide structure pre-covered with an Ir bottom electrode layer. STEM-EDS analysis shows the uniformity of the cation composition in this film.

As and optimum choice of precursors we used $Pb(DPM)_2$, $Ti(Oi\text{-}Pr)_4$, $Zr(DIBM)_4$ and H_2O vapour as oxidant at a deposition temperature of 240°C. Figure 1 shows the deposition rate of each cation as a function of the volume of injected precursors. Self-regulated growth behavior was confirmed for Pb and Zr. The deposition rate of Ti did not completely saturate due to a catalytic decomposition of the precursor. [2] Amorphous PZT films exhibited a constant Pb/(Zr+Ti) ratio of about 1.2, while the Zr content can be adjusted by the number of Zr cycles as it is shown in Fig. 2. Analytical STEM studies were performed on films in amorphous state deposited on 3D structured substrates. Figure 3 shows that the film is homogeneous in thickness and in composition over the hole's profile. Planar films exhibit a polycrystalline perovskite structure after annealing at 700°C for 10 min in oxygen. A 70 nm thick ALD PZT film with a Zr-content of 0.46 showed reasonable hysteresis behaviour as depicted in Figure 5. The value of remanent polarization may be further increased by improving the crystal quality.

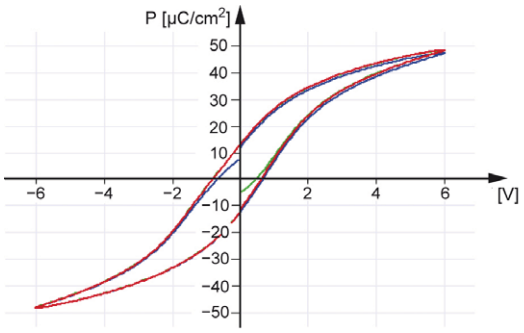

FIG. 4: Hysteresis measurements on a planar 70 nm thick PZT film with Zr content of 0.47. After deposition at 240°C the film was post-annealed at 700°C for 10 min in oxygen. Measurements: 100 Hz, room temperature.

We conclude that the liquid delivery ALD method is a promising tool for depositing multi-component metal oxide thin films conformally. The process will be further evaluated for $SrRuO_3$ layers used as an electrode layer with perovskite-type structure, and for other complex oxides studied in the field of higher-k materials.

The authors would like to thank Mr. W. Krumpen for XRF analysis, Dr. A. Schwedt for FIB fabrication, Mr. F. Dorn and Dr. T. Weirich for TEM analysis, Mr. M. Gebauer and Mr. M. Gerst for their technical support. SAES Getters S.p.A is gratefully acknowledged for supplying the precursors, and Toshima Inc. for their chemical support. The 3D- substrates were kindly provided by SAIT.

[1] A. Nagai, J. Minamidate, G. Asano, C. J. Choi, C-R. Cho, Y. Park, and H. Funakubo, *Electrochem. Solid-State Lett.*, **9**, C15-C18 (2006).

[2] T. Watanabe, S. Hoffmann-Eifert, C. S. Hwang, R. Waser, *J. Electrochem. Soc.* **153** (9), F199 (2006).

[3] T. Watanabe, S. Hoffmann-Eifert, S. Mi, C. Jia, R. Waser, C. S. Hwang, *J. Appl. Phys.* **101**, 014114 (2007).

[4] T. Watanabe, S. Hoffmann-Eifert, R. Waser, and C. S. Hwang, *15th Inter. Symp. Appl. Ferro. Proc.* (in press).

[5] T. Watanabe, S. Hoffmann-Eifert, F. Peter, S. Mi, C.L. Jia, C. S. Hwang, R. Waser, *J. Electrochem. Soc.* **154 (12)**, G262 (2007).

Conductive Oxygen Diffusion Barrier for High-κ Oxide Materials on Silicon Electrodes

B. Mesic, H. Schroeder

IFF-6: Electronic Materials
CNI: Center of Nanoelectronic Systems for Information Technology

In order to integrate high-κ oxide materials into CMOS capacitor dielectric or to use their superior dielectric property for capacitive stimulation of nerve cells directly on silicon chips it is necessary to prevent the formation of series-connected layers of low-κ materials such as SiO_2. We have developed a thin film layer stack with a conducting diffusion barrier, TaSiN, directly on a highly doped p^{++}Si chip used as bottom electrode in a metal/insulator/metal (MIM) thin film capacitor stack. Using (Ba,Sr)TiO_3 (BST) as dielectric in this stack the relative effective dielectric constant was up to 450 with leakage currents lower than 10^{-6} A/cm^2 at voltages lower than 2 V, reasonable values for the mentioned applications.

For the year 2011 at the latest, the semiconductor industry calls for the integration of high-κ materials (κ >100) in CMOS based chips, e.g. as capacitor dielectric in stacked DRAM cells, as documented in the International Technology Roadmap for Semiconductors [1] A prototype sample of a post-capacitor is shown in Fig. 1 [2]. The via of conducting poly-Si connecting to the CMOS region is separated from used Pt/(Ba,Sr)TiO_3(BST)/Pt thin film capacitor stack by a conducting diffusion barrier layer, TaSiN, to prevent mainly oxygen transfer from the BST through the Pt grain boundaries to the poly-Si surface and the possible formation of a series-connected low-κ SiO_2 layer, which would degrade the benefit of the high-κ BST dielectric. Unfortunately, an insulating TaSi(O,N) layer has formed at parts of the interface Pt/TaSiN. This layer would have a similar unwanted effect as SiO_2 if covering the whole interface area. Another possible application for high-κ materials on Si is the capacitive stimulation of nerve cells for investigations of the interaction at electric interfaces between chip based circuits and living cells as sketched in Fig. 2a [3]. Up to now TiO_2 (medium-$\kappa \approx$ 40) or similar HfO_2 are used for this purpose as can be seen in Fig. 2b [4]. It is also shown that a very thin insulating low-κ SiN_x layer is present reducing the effective dielectric constant to less than 40. Therefore, the use of a BST layer with κ of some hundred separated by conducting barrier layers from the Si would improve the capacitance considerably.

The main challenge for a good conducting bottom electrode with a barrier layer for the above applications is the thermal stability at the necessary high temperature for depositions or anneals of the dielectric layer in order to assure a high-κ material. Common obstacles are: a) Unwanted reactions within the layers or between them with formation of a non-conducting, low-κ dielectric layer; b) Changes of the microstructure such as recrystallization of amorphous parts or grain growth of crystalline parts sometimes resulting in unacceptable roughness for the thin films.

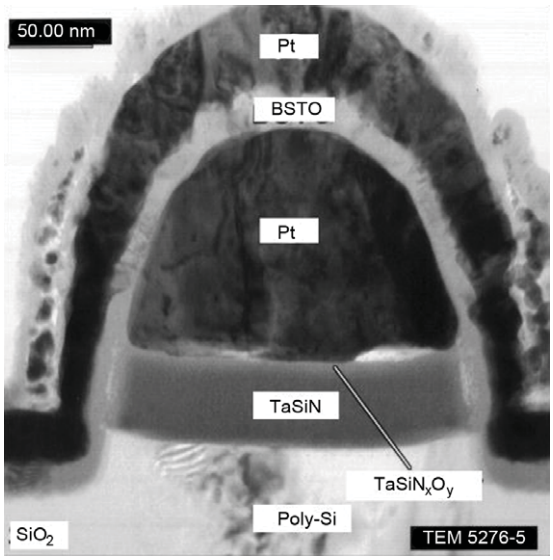

FIG. 1: TEM cross sectional micrograph of a prototype of Pt/BST/Pt post capacitor suitable for integration in 1GBit DRAM generation (feature size = 0.2μm) [2].

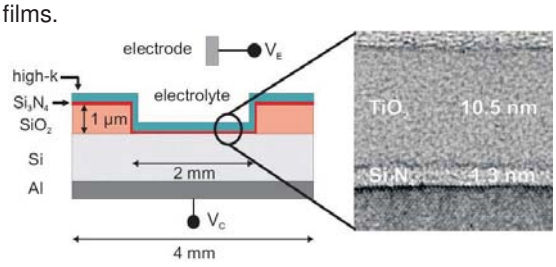

FIG. 2: Left: Principle setup for measurements of neuronal activity by capacitive stimulation [3]; Right: TEM cross sectional micrograph of a "state of the art" thin film stack with TiO_2 (k≈40) + SiN_x (k≈7) as dielectric layers on conductive Si [4].

An optimized stack structure as bottom electrode for

these applications has been developed [5] which is sketched in Fig. 3. The base is a wafer of very highly doped and therefore good conducting Si (p^{++}) on which three additional conducting thin films have been deposited by DC-sputtering (Pt, Ir) and RF-sputtering (TaSiN). The usual Si-oxide layer has been removed by etching before the deposition of the Pt film. This intermediate layer is necessary as it was found that a stack p^{++}Si/TaSiN develops an unacceptable high contact resistance when annealed at 500-700°C in oxygen ambient to simulate the recrystallization anneal for the high-κ oxide dielectric. This suggests the formation of an insulating layer at the p^{++}Si/TaSiN interface. In contrast, the stack p^{++}Si/Pt/TaSiN was found to keep very good conduction properties (that of the dominating thick p^{++}Si wafer) and excellent surface smoothness after anneals up to 700°C with an rms-value of $<$0.7 nm. It should be mentioned that during the anneals at T$\geq$500°C the intermediate Pt thin film (100nm) reacted nearly completely with the Si substrate by forming conductive platinum-silicides (PtSi,Pt_2Si, Pt_3Si) as detected by X-ray diffraction. Immediate deposition of a high-κ dielectric layer (BST) on the stack p^{++}Si/Pt/TaSiN and subsequent anneals at 500-700°C in oxygen ambient once more resulted in a non-conducting, low-κ layer at the interface, largely reducing the effective dielectric constant.

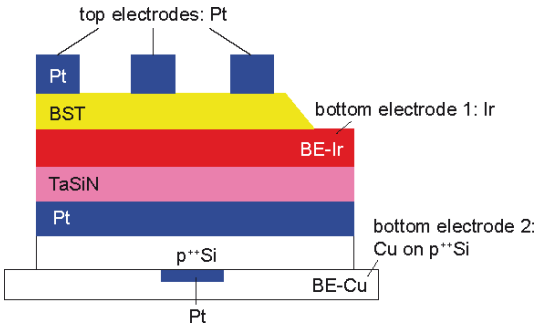

FIG. 3: Scheme of Cu/p^{++}Si/Pt/TaSiN/Ir/BST/Pt(top) stack used for a electrical characterization showing different bottom electrode configurations for the capacitor thin film stack [5].

Therefore, another metal protection layer was introduced (Pt or Ir) which terminates the bottom electrode stack, p^{++}Si/Pt/TaSiN/Ir(Pt). Unfortunately, the upper metal layer developed unacceptable roughness and reacted with the TaSiN underlayer, when annealed in oxygen at T$\geq$500°C. The Ir-layer was used because its properties were tolerable for T_{anneal} $<$600°C, 50-100°C higher than for Pt-layers. These facts limited the deposition and annealing temperatures for the high-κ oxide dielectric to about T$\leq$550°C. Therefore, in the optimized stack structure the $Ba_{0.7}Sr_{0.3}TiO_3$ was deposited at 550°C by pulsed laser deposition and subsequently annealed at that temperature in oxygen. In order to perform electrical measurements structured Pt top electrodes were deposited by a lift-off lithographic process.

Several different TaSiN compositions were investigated. They were produced by reactive RF-sputtering from two $TaSi_x$ targets (x=1, 2.7) with different mixtures of argon and nitrogen as sputter gas, different sputter power and at temperatures between RT and about 500°C. The optimized barrier was $Ta_{28}Si_{28}N_{44}$, produced at RT with 200 W sputter power and $Ar_{99}N_1$ sputter-gas, the composition was determined by Rutherford back-scattering experiments.

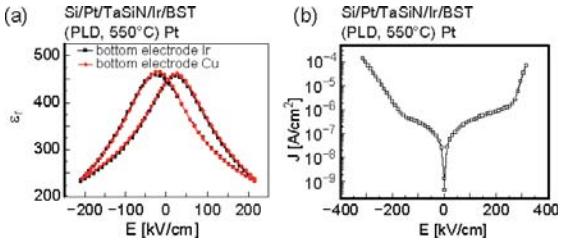

FIG. 4: a) Relative permittivity and b) Leakage current in a Cu/p^{++}Si/Pt/TaSiN/Ir/BST/Pt(top) capacitor stack after BST deposition at 550°C with PLD and RTA annealing at the same temperature in oxygen [5].

Electrical data of the stack p^{++}Si/Pt/TaSiN/Ir/BST/Pt(top) are presented in Figs. 4a and b for effective relative dielectric constant κ and leakage current, respectively. The effective κ was measured with two different bottom electrodes, as sketched in Fig. 3, the intermediate Ir giving a common MIM capacitor and the bottom of the p^{++}Si wafer metallized with Pt and Cu measuring the whole stack, respectively. The two curves in Fig. 4a are nearly perfectly identical showing no considerable influence of the multi-layer electrode stack as desired. The dielectric properties are very reasonable: The peak value of $\kappa \approx 450$ at nearly zero field demonstrates a large advantage for the biological application compared to the used dielectrics. The curve is largely tunable, the slight tendency to a butterfly curve may indicate some ferroelectricity in the thin BST film. The leakage current (Fig. 4b) is not completely symmetric expected for the different top and bottom electrode. The absolute current is below 10^{-6} A/cm^2 for fields lower than $\pm$ 200 kV/cm corresponding to $\pm$ 2 V, which reasonable for DRAM applications.

[1] http://www.itrs.net/Links/2006Update/2006UpdateFinal.htm.

[2] D.E. Kotecki *et al.*, IBM J. Res. Develop. **43**, 367 (1999).

[3] P. Fromherz, Neuroelectronic interfacing: semiconductor chips with ion channels, nerve cells, and brain, Ed. R. Waser, Wiley-VCH, Berlin, 781ff (2003).

[4] F. Wallrapp, P. Fromherz, J. Appl. Phys. **99**, 114103 (2006).

[5] B. Mesic, Thesis TH Clausthal 2008 and to be published

Evolution of the Resistive Switching Characteristics During Electroforming of Epitaxial Iron-Doped $SrTiO_3$ Thin Films

T. Menke[1,2], R. Dittmann[1,2], K. Szot[1,2], P. Meuffels[1,2], R. Waser[1,2,3]

[1] IFF-6: Electronic Materials
[2] CNI: Center of Nanoelectronic Systems for Information Technology
[3] Institut für Werkstoffe der Elektrotechnik II, RWTH Aachen

We investigated in detail the evolution of the I-V characteristics of epitaxially grown Pt/$SrTiO_3$(1at%Fe)/$SrRuO_3$ heterostructures during the electroforming process performed by repeated sweeping of a triangular shaped current signal. Within the first cycles, we observed hysteretic I-V curves which can be explained by the movement of oxygen ions and the resulting accumulation of charge at the $SrTiO_3$/electrode interface. After the electroformation the different voltage branches result from two different resistive states which are induced by a redox-induced local metal to insulator transition. Pulsed measurements on both types of curves showed the volatile character of the states in case of an unformed sample and affirmed the non-volatile behavior of a formed sample.

Resistive switching in ternary oxides, like $SrTiO_3$, is an interesting physical phenomenon from the fundamental point of view as well as in terms of its possible application in future resistive random access memories. There is strong experimental evidence that reversible resistive switching in $SrTiO_3$ single crystals and thin films [1] originates from a redox-process within extended defects resulting in a local metal-to-insulator transition. Nevertheless, there is still a lack of understanding the mechanisms occurring at the interface $SrTiO_3$/electrode interface during switching and during the electroforming process which usually has to be performed prior to the observation of stable resistive switching. The purpose of this work was to elucidate of the physical mechanisms at the interface $SrTiO_3$/electrode in different stages of the electroforming process.

The $SrTiO_3$(1at%Fe)/$SrRuO_3$ heterostructures were grown epitaxially on $SrTiO_3$ substrates by pulsed laser deposition, using the deposition conditions reported in reference [2]. Platinum dots with radii of 125μm, serving as top electrodes, were deposited by e-beam evaporation by a shadow mask technique.

We applied a triangular shaped current signal with an amplitude of 1mA and a frequency of 1Hz on an as-fabricated Pt/$SrTiO_3$(1at%Fe)/$SrRuO_3$ structure and measured the evolution of the corresponding voltage signal during 40 cycles. A selection of the resulting I-V curves are displayed in Fig.1. A typical I-V curve, which is recorded during the first cycles, is displayed in red. It shows a strongly non-linear shape with a hysteresis for both polarities. Since the voltage approaches the compliance at +10V in the positive branch, the hysteresis is not well pronounced in the positive branch. The type of I-V curve completely changes after several cycles, as depicted in Fig. 1. The voltage showed in the positive branch some discontinuous behavior (displayed in blue). The voltage drops abruptly below the compliance level and follows a noisy curve during the remaining positive sweep with a decreased resistance (see blue curve in Fig. 1). In contrary, the hysteresis on the negative branch remains nearly unchanged during this stage of forming. After several current sweeps, the voltage rises up to a branch with reduced resistance until it drops suddenly and approaches a different type of I-V curve. In this final shape of the I-V characteristic (displayed in black) a full current sweep exhibits two separated and stable voltage branches. This type of I-V curve can be explained by an electrically induced local metal to insulator transition which results in an abrupt non-volatile change of the electrical resistance of the sample with a Ron/Roff ratio up to five.

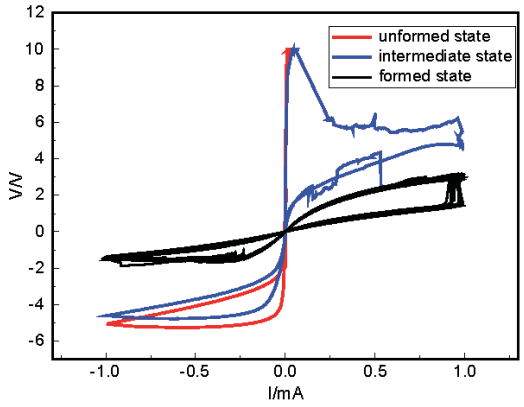

FIG. 1: Change of the I-V characteristic for a Pt/$SrTiO_3$(Fe)/$SrRuO_3$ sample by applying a triangular current signal leading to a change from a volatile to a non volatile hysteresis.

On both types of I-V characteristics, pulse measure-

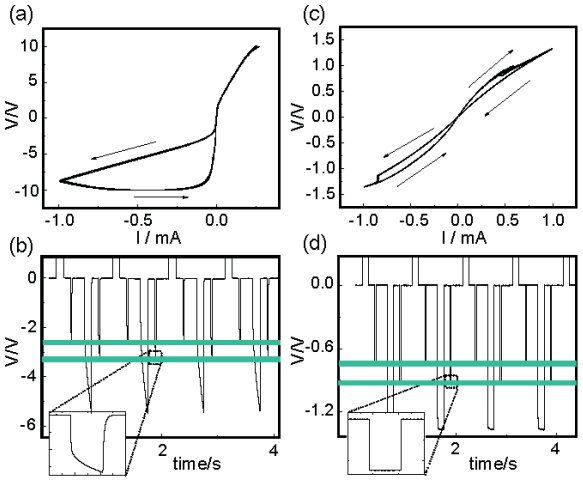

FIG. 2: I-V characteristics of a Pt/$SrTiO_3$(Fe)/$SrRuO_3$ sample with low current load (a) and a high current load (c). The diagrams (b) and (d) show the corresponding voltage response to an applied current driven pulse signal exhibiting of alternating write/erase pulses with amplitude of +/-1mA and duration of 125ms, each write/erase pulse is followed by a 20ms long readout pulse with amplitude of -500μA.

ments were performed. In figure 2 I-V curves of an unformed (a) and a formed sample (c) are displayed and the corresponding voltage response to the pulse signal are shown in (b) and (d). For both types of I-V curves, two different levels of the voltage response exhibit (marked with green bars) and therewith correspond to a difference in the resistance. For the unformed sample an increase of the measured voltage during the pulses is observable as can be seen in the inset of figure 2 (b) which indicates the volatility of the resistive states. This shape is similar for both types of resistance levels marked with green bars and points to the existence of an internal counterfield and therewith to a charging effect. This is not the case for the formed sample where the measured voltage stays constant during the applied pulses.

To clarify the origin of this charging behavior and the resulting volatility of the resistive states observed for the un-formed samples additional studies were performed. Figure 3 (a) depicts this type of I-V curve in more detail. The I-V curve exhibits an asymmetric shape with continuous hysteresis, without any jumps, on both polarities, but is much more significant in the negative branch. As can be seen in Fig. 3(a), the hysteresis becomes more pronounced and the satura-tion voltage is increased when the slope of dI/dt is decreased which hints to an accumulation of charge at the interface. By increasing the applied current the amount of accumulated charge at the interface increased and leads to an increasing internal counter field, see sketch in figure 3, which results in a saturation of the total voltage. The saturation voltage depends on the amount of moved charge and is therefore larger for a smaller dI/dt. The observed hysteretic effect results from the slow relaxation of the accumulated charge when the applied current is decreased. By keeping dI/dt constant at a value of

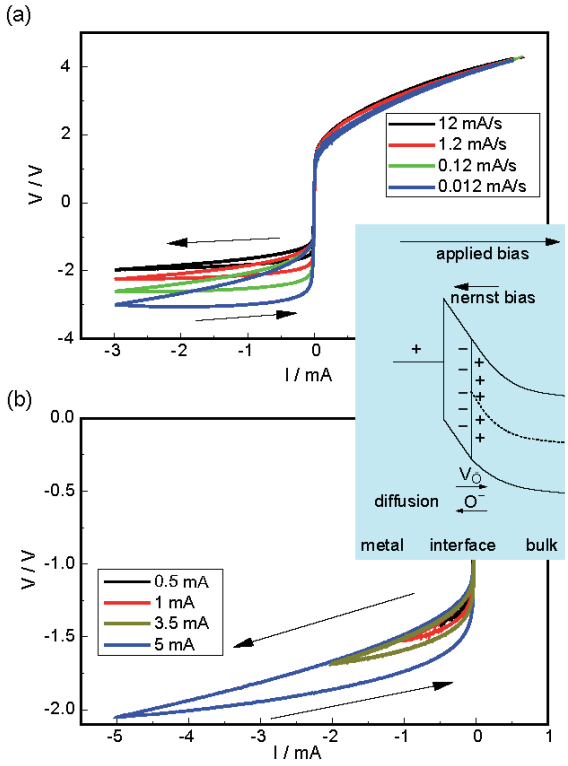

FIG. 3: I-V characteristics of a unformed Pt/$SrTiO_3$(Fe)/$SrRuO_3$ sample. Diagram (a) displays curves with different slopes of dI/dt and in diagram (b) for different cycles with a constant dI/dt of 2mA/s are shown. The inset presents a scheme for the movement of oxygen which explains the origin of the hysteresis.

2mA/s (see Fig. 3(b)) for different current amplitudes, the voltage always raised up on the same branch to their respective reversal point, which is quite reasonable because the amount of moved charge is equal for all curves during increasing the applied current. We suppose that the internal counter field originates from the accumulation of oxygen ions at the interface.

In summary, we showed that in the early stages of the formation a volatile hysteresis was observed originating from a movement of oxygen ions. In the later stage of electroforming the resistance decreases until finally the redox driven resistive switching state is obtained.

[1] K. Szot, W. Speier, G. Bihlmayer, and R. Waser, Switching the electrical resistance of individual dislocations in single-crystalline $SrTiO_3$, *Nat. Mater.* **5**, 312-20 (2006)

[2] K. Szot, R. Dittmann, W. Speier and R. Waser, Nanoscale resistive switching in $SrTiO_3$ thin films, *Phys. stat. sol.* **2**(1), R86-R88 (2007)

Resistive Switching in Ag-Ge-Se and Cu-SiO_2 With Extremely Low Write Currents

C. Schindler[1,2], M. Weides[1,2], M. Meier[1,2], R. Waser[1,2,3]

[1] IFF-6: Electronic Materials
[2] CNI: Center of Nanoelectronic Systems for Information Technology
[3] Institut für Werkstoffe der Elektrotechnik II, RWTH Aachen

Solid electrolytes such as $Ag_y(Ge_xSe_{1-x})_{1-y}$ allow rapid diffusion of metal ions and this makes them suitable for memory applications. We present our results on resistive switching in Ag/Ag-Ge-Se/Pt and Cu/Cu-SiO_2/Pt cells which show a resistance ratio of more than 5 orders of magnitude. The ON resistance depends on the write current which allows for multi-bit data storage. In case of the Ag-Ge-Se cells, the leakage current in the high resistance state can significantly be reduced by introducing an oxide layer within the chalcogenide film. Then, a current as low as 1nA is sufficient to switch these cells from a high to a low resistance state demonstrating the possibility of extremely low power consumption.

Non-volatile memory cells based on solid electrolytes such as Ge_xSe_{1-x} [1] or Ag_2S [2] are highly scalable and exhibit low switching voltages. They can be switched for more than 10^{10} cycles and they hold the resistance states even at elevated temperatures for more than 10 years. The switching mechanism is based on the formation and rupture of metallic filaments between an oxidizable top and an inert bottom electrode. Under positive bias application the top electrode is oxidized and due to the electric field, cations migrate through the solid electrolyte and are electrochemically reduced at the inert electrode. Consequently, a metallic path grows from the inert bottom electrode towards the top electrode until a conductive connection is established. By reversing the voltage polarity, this connection is ruptured and the cell transitions from the low (ON) to the high (OFF) resistance state. Recently, the same switching characteristics has been observed in memory devices based on Cu-SiO_2 [3]. So far, mainly write currents in the low μA region are reported. We now show the reduction of the write current by three orders of magnitude; a current as low as 1nA was sufficient for writing a Ag/Ag-Ge-Se/Pt [4] as well as a Cu-SiO_2 cell.

Our memory cells consisted of a continuous bottom electrode made of 100nm Pt followed by a 60nm thick Si_3N_4 layer with vias of a diameter of 2.5μm, 5μm, 10μm, 25μm, and 50μm. 50nm $Ge_{0.3}Se_{0.7}$ was deposited into the vias by radio frequency (rf) sputtering. The top electrodes had a diameter of 75μm and consisted of 50nm Ag. A schematic of the cell structure is shown in Figure 1. In case of the cells

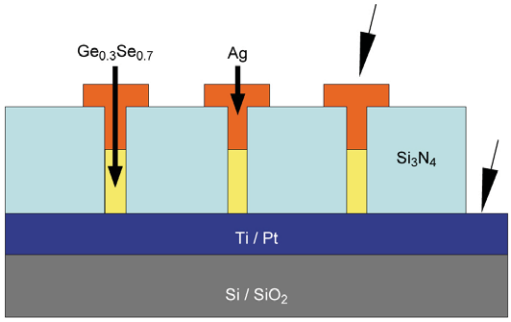

FIG. 1: Schematic of the cell structure. For electrical characterization, the Pt bottom electrode was grounded.

with Cu-SiO_2 as active layer, a continuous 25nm thick SiO2 film was deposited by rf-sputtering on the Pt bottom electrode and the Cu top electrodes had a diameter of 100 - 500μm.

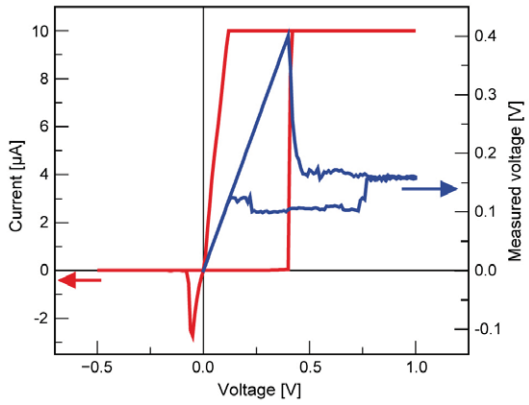

FIG. 2: Current-voltage characteristics of a Ag-Ge-Se cell with a diameter of 10μm. While the current was limited to 10μA, the voltage gradually decreased showing that the conductive path was further strengthened after the current compliance was reached.

Typical current-voltage (I-V) characteristics for a Ag-Ge-Se cell are shown in Figure 2. Initially, the film was in the OFF state. At ~400mV the cell switched on and reached the current compliance of 10μA. The memory cell switched back to the OFF state at ~ -70mV. Four point measurements revealed that as soon as the current compliance was reached, the voltage applied to the cell did not immediately drop to a constant value, but gradually decreased. This

corresponds to a decrease in resistance because of the formation of a stronger conductive connection with time. We found that the write currents can be reduced significantly by introducing a GeO_2 layer within the $Ge_{0.3}Se_{0.7}$ film. We assume that the GeO_2 layer is a barrier for the diffusion of excess Ag into the chalcogenide layer [5]. With the leakage current in the OFF state reduced to $\sim$0.15 pA/μm^2, resistive switching with a current compliance as low as 1nA was possible showing cell operation with an extremely low power consumption. The write current determines the resistance of the conducting path through the solid electrolyte because its formation is dependent on the degree of oxidation and reduction. With a write current range of over more than 5 orders of magnitude, the low resistance state was variable over the same range (kΩ to several hundred MΩ) as shown in Figure 3. This increases the opportunity

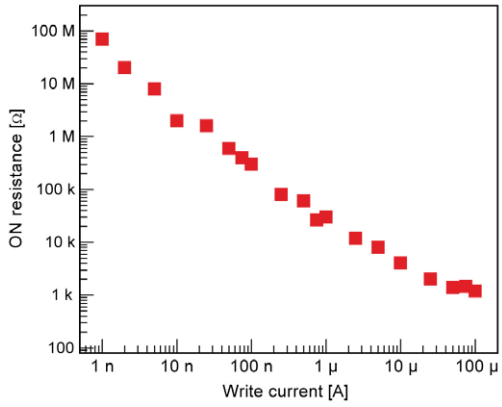

FIG. 3: The ON resistance is shown versus the write current. By varying the write current, the ON resistance can be varied over five orders of magnitude.

for multi-bit data storage in each memory cell. The low resistance state did not show a cell size dependence. Figure 4 shows the ratio of the ON resistance measured on a cell with a diameter of 2.5μm and the ON resistance of a cell with a diameter of 50μm as a function of the write current. The ratio does not exceed a value of 4 even though the cell cross sectional area changes by a factor of 400. This indicates that for all cell sizes only one conductive connection was established between the electrodes. The conductive path grows from the inert electrode towards the oxidizable electrode. As soon as the first ions are reduced, the electric field is highest on the tip of the growing metallic path. Therefore, this is the most probable site for further electrode-position and only one conductive connection grows through the solid electrolyte. This is a very promising result for future downscaling, as these memory cells do not depend on material-inherent defects which might not be addressable in case of very small cells.

Devices based on $Cu\text{-}SiO_2$ showed very similar switching characteristics as cells based on Ag-Ge-Se [4]. The write currents could be varied over the same range as for the Ag-Ge-Se cells and even at 1nA resistive switching could be observed. Figure 5 shows the I-V plot for a Ag-Ge-Se and a $Cu\text{-}SiO_2$

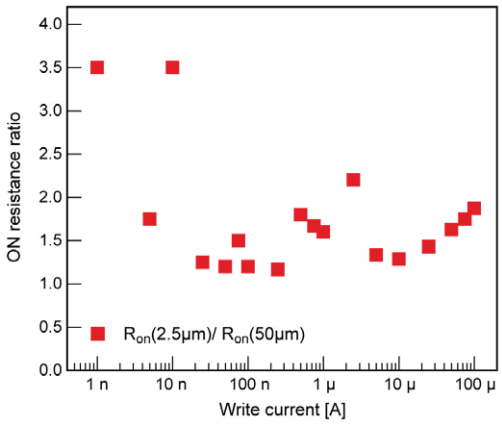

FIG. 4: The ON resistance ratio of cells with a via diameter of 2.5μm and 50μm is shown versus the write current. Although the cross sectional area of the cells varies by a factor of 400, the ON resistance does not vary by a factor of more than 4, suggesting that only one conductive path forms between the electrodes.

cell which were both written with a current of 1nA. The switching voltages and erase current level were

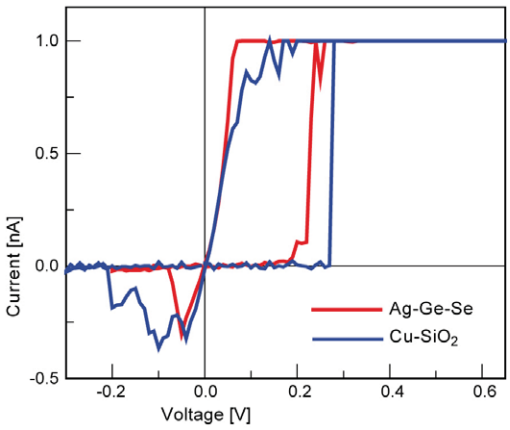

FIG. 5: Typical current-voltage characteristic of a resistively switching Ag/Ag-Ge-Se/Pt and Cu/Cu-SiO_2/Pt cell with a via diameter of 10μm (Ag-Ge-Se) and a top electrode diameter of 150μm (Cu-SiO2). The Pt electrode was grounded. The write current was limited to 1nA.

very similar, which suggests that the switching mechanism in the $Cu\text{-}SiO_2$ cells is based on the formation and rupture of a Cu connection between top and bottom electrode. These cells are promising candidates for future integration as they are based on materials already available in the current CMOS line.

[1] M.N. Kozicki, C. Ratnakumar, M. Mitkova, *Proceedings of the 7th Non-Volatile Memory Technology Symposium (NVMTS)*, 111-117 (2006).

[2] K. Terabe, T. Hasegawa, T. Nakayama, M. Aono, *NATURE* **433**, (2005).

[3] C. Schindler, S.P. Puthen Thermadam, R. Waser, M.N. Kozicki, *IEEE Transactions on Electron Devices* **54**, 2762-2768 (2007).

[4] C. Schindler, M. Meier, M.N. Kozicki, R. Waser, *Proceedings of the 8th Non Volatile Memory Technology Symposium*, (2007) in press.

[5] C. Schindler, X. Guo, A. Besmehn, R. Waser, *Z. Phys. Chem.* **221**, 1-10 (2007).

Realization of Self-Assembled Arrays of Nanoscale Resistive Switching Blocks in Thin Films of Nb-Doped $SrTiO_3$

R. Münstermann[1,2], R. Dittmann[1,2], K. Szot[1,2], S. Mi[3,4], C.-L. Jia[3,4], P. Meuffels[1,2], R. Waser[1,2]

[1] CNI: Center of Nanoelectronic Systems for Information Technology
[2] IFF-6: Electronic Materials
[3] IFF-8: Microstructure Research
[4] ERC: Ernst Ruska-Centre for Microscopy and Spectroscopy with Electrons

We report on the realization of self-assembled arrays of nanoscale resistive switching blocks in epitaxial Nb-doped $SrTiO_3$ thin films. These blocks have dimensions in the order of 30 nm and are embedded in an insulating matrix. They can be individually addressed by the tip of a conductive tip atomic force microscope and reversibly switched between a high and a low resistance state reaching an R_{off} to R_{on} ratio of up to 50. We suggest a connection between these nanoscale switching blocks and defect-rich nanoclusters which were detected with high resolution transmission electron microscopy.

Searching for new concepts of non-volatile resistive memory devices an upsurge of interest in thin perovskite films as resistive switching layers has arisen ever since the discovery of an electric field induced resistance change in manganites and titanates as well as zirconates. For undoped $SrTiO_3$ it was shown that the switching occurs along crystalline defects which extend through the sample and form a network of nanometer-sized filamentary conduction paths [1, 2]. This makes $SrTiO_3$ a very promising candidate for a non-volatile memory in the terabit regime. Doping $SrTiO_3$ with transition metals improves the stability of the resistive switching and may be a tool to influence the extension and the local distribution of switching units in $SrTiO_3$ thin films. In this work Nb-doped $SrTiO_3$ thin films are therefore investigated with a conductive tip atomic force microscope (LC-AFM). We explore the local current distribution and the arrangement of intrinsic nanoscale switching units of these films and relate it to the microstructure determined by high resolution transmission electron microscopy (HR-TEM).

Thin films were prepared by pulsed laser deposition (PLD) employing a KrF excimer laser (λ = 248 nm) with an energy density of 5 J/cm^2 at a frequency of 10 Hz. A $SrTiO_3$ target with a Nb-concentration of 1 wt% and commercially available $NdGaO_3$(110) substrates were used. The substrate temperature was set to 700 °C and the oxygen partial pressure during deposition was lower than 10^{-6} mbar. In order to investigate the local nature of the conductivity and the switching behaviour of the samples we performed LC-AFM measurements. All measurements were carried out with a Jeol JSPM 4210 microscope under vacuum conditions with a background pressure of 10^{-5} mbar employing a PtIr-coated AFM tip.

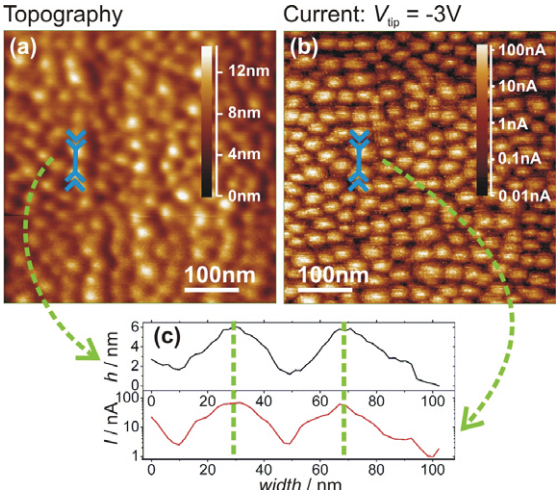

FIG. 1: Part a and b show LC-AFM images of a Nb-doped $SrTiO_3$ thin film. The surface of the film consists of protrusions with a conductive centre and practically non-conductive boundaries (part c) forming an array of conductive spots.

The LC-AFM topography image and the corresponding local current distribution of a 1 wt% Nb doped $SrTiO_3$ film is shown in figure 1. The images were recorded with a negatively biased tip (V_{tip} = -3 V). The surface exhibits a hilly morphology (figure 1a) and is covered with little protrusions. These protrusions correspond directly to roughly 30 nm wide circular spots in the current image (figure 1b): the centre of each protrusion is conductive, while the boundaries are almost non-conductive. This correlation becomes particularly clear by comparing two linescans drawn at the same place in the topography and the current image respectively (figure 1c). While similarly correlated systems described in the literature exhibit very irregular patterns, in our case the protrusions form an almost well ordered array of conducting spots.

By applying an external voltage between the tip and the sample it is possible to change the resistance of these conducting spots. The central part of figure 2 shows an *I-V* curve of a typical single conducting spot (indicated by the white dashed circle), which

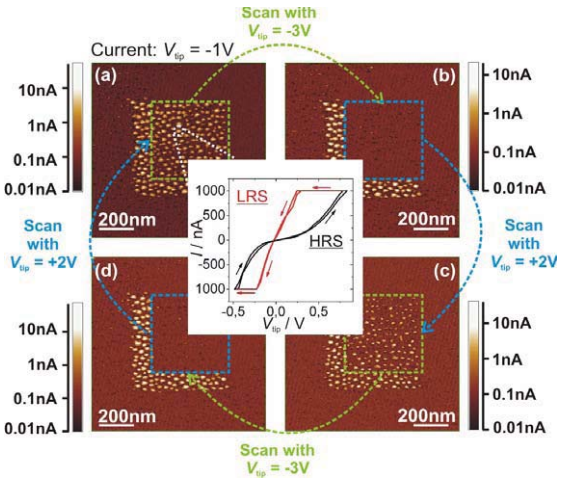

FIG. 2: Reversible resistive switching in Nb-doped Sr-TiO_3 deposited under low oxygen pressure. The current images show an array of conducting spots which can be switched between two fifferent resistance states.

was recorded by placing the AFM tip over the spot and varying the applied voltage. The *I-V* curve has a clear hysteresis and shows a bipolar switching behaviour with an R_{off} to R_{on} ratio of up to 50. The switching behaviour can be reproduced for a large amount of conducting spots by scanning the positively ($V_{tip} \geq$ 2 V) or negatively ($V_{tip} \geq$ -3 V) biased tip over a defined area of the sample: while in figure 2a all spots inside the inner square are conductive, a scan over the area of the green dashed square with a negative tip voltage of at least -3 V switches all spots inside the scan area "off" (figure 2b). A subsequent scan with a positive tip voltage of at least +2 V recovers the conductivity of the previously switched "off" spots (figure 2c), while yet another scan with -3 V switches them "off" again (figure 2d).
This switching behaviour is consistent with the current image in figure 1b which was recorded with a negative tip voltage of -3 V while switching the scanned area "off": The scan with the switching voltage of -3 V itself still shows the high conductivity of the low resistance state, while any following scan shows the almost non-conductive surface of the high resistance state.

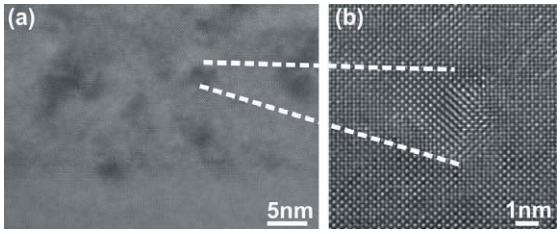

FIG. 3: HR-TEM investigations reveal defect-rich clusters embedded in the matrix of the film.

In order to understand the microstructure of the film and thus the structural nature of the protrusions or the conducting spots, HR-TEM measurements of a Nb-doped $SrTiO_3$ film grown under low oxygen pressure have been performed. They show that the film is grown coherently on the substrate without any misfit dislocations at the interface. It contains however a high density of defect-rich clusters with dimensions between 2 and 20 nm (figure 3). We suggest a connection between the nanoclusters and the conducting spots because of their similar size and distribution although the exact nature of this correlation is not yet completely clear.

Since the oxygen partial pressure has a major influence on the electrical measurements and since switching is only observable under vacuum conditions, we assume, that the switching process in Nb-doped $SrTiO_3$ can be explained by a local oxidation and reduction along a network of electrically connected, defect-rich nanoclusters. More experimental evidence is however necessary to either confirm or disprove this assumption.
In summary, we have succeeded in fabricating regular arrays of 30 nm wide resistive switching blocks in Nb-doped $SrTiO_3$ thin films, which can be switched between two different resistance states by applying an external voltage. We attribute these resistive switching blocks to the specific defect structure of our thin films.
This work was financially supported by Intel Inc., Santa Clara.

[1] K. Szot, W. Speier, G. Bihlmayer, R. Waser, Nat. Mater. 5, 2006, 312

[2] K. Szot, R. Dittmann, W. Speier, R. Waser, Phys. Status Solidi RRL 1, 2007, 86

Effect of Oxygen Ambient on the Bipolar Resistive Switching of Pt/TiO_2/Pt

D. S. Jeong[1,2], U. Breuer[3], T. Menke[1,2], H. Schroeder[1,2]

[1] IFF-6: Electronic Materials
[2] CNI: Center of Nanoelectronic Systems for Information Technology
[3] Central Division of Analytical Chemistry

In this report we investigate the effect of oxygen ambient on the bipolar resistive switching behavior of a Pt/TiO_2/Pt switching cell. By using time-of-flight secondary ion mass spectroscopy the oxygen incorporation into localized areas of the top and bottom electrodes after the electroforming process could be confirmed suggesting oxygen ions and/or oxygen vacancies are involved in the resistive switching. In order to confirm the effect of oxygen on the resistive switching behavior we carried out resistive switching measurements with variation of the oxygen pressure in the measurement chamber. The results showed changes in switching behavior implying that the Pt/TiO_2/Pt cell is open to the ambient atmosphere and able to exchange oxygen gas molecules with atmosphere.

Resistive switching behavior of TiO_2 is a very attractive subject due to its nonvolatile switching characteristics which is promising for application to resistive switching random access memory devices. A recent report has demonstrated that both unipolar resistive switching (URS) and bipolar resistive switching (BRS) behaviors can be observed in TiO_2 depending on the current compliance value during an electroforming process [1]. However, the mechanisms of electroforming, URS, and BRS have been hardly clarified yet leaving many open questions.

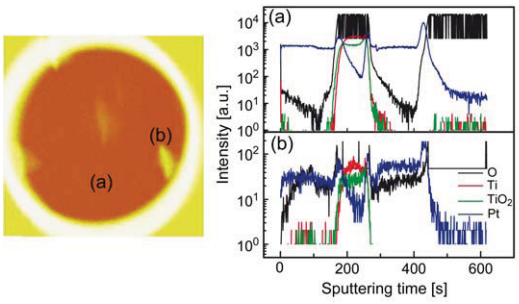

FIG. 1: 2-dimensional TOF-SIMS image of oxygen distribution over a Pt/TiO2/Pt cell. The depth profile of each element is shown on the right side. The profiles are from the dark region (a) and from the bright region (b).

Recently, Zhao et al. [2] have reported the influence of oxygen partial pressure on the resistive switching behavior of (Pr,Ca)MnO_3 suggesting oxygen vacancies are involved in the switching. In this report we demonstrate the involvement of oxygen ions and/or oxygen vacancies in the switching of a Pt/TiO_2/Pt switching cell by investigating oxygen ion distribution in the switching cell after switching using time-of-flight secondary ion mass spectroscopy (TOF-SIMS) and performing switching measurements with varying oxygen pressure.

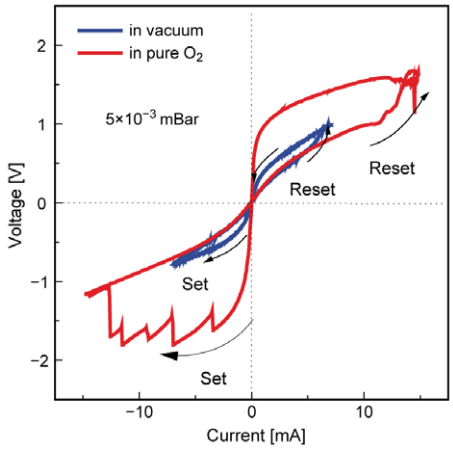

FIG. 2: The effect of the change in the ambient from vacuum to oxygen on a switching curve which shows reset and set switching under positive current and negative current, respectively.

For the fabrication of a Pt/TiO_2/Pt switching cell a blanket 27 nm thick TiO_2 film was deposited on a platinized Si wafer with sputter grown 100 nm thick Pt using reactive sputtering from a Ti-metal target. Circular-shaped top electrodes of 70 nm thick Pt were formed by a the lift-off process.
Electroforming was carried out by applying a positive voltage sweep on the top electrode (anode) with a sweep rate of 0.6 V/s and a current compliance of 50 μA. The electroforming took place at about 5 V. In order to identify the distribution of oxygen ions in the depth of the stack as well as over the cell area, two-dimensional scanning TOF-SIMS was used. Integrated oxygen ion contents along the depth over the whole switching cell can be seen in Fig. 1, where the brightness indicates the oxygen contents and the circle represents the top electrode. It can be noticed that the oxygen distribution in the circle is non-uniform showing several bright spots meaning more oxygen ions than in the rest of the area. The depth profiles of the areas (a) and (b) can

be seen on the right side of Fig. 1. The depth profile of the area (a) shows oxygen incorporation into the top electrode compared to that of the area (b). We also checked the oxygen ion distribution in a pristine switching cell, before electroforming, however, bright spots were barely detected. Therefore, we can consider the non-uniform distribution of oxygen ions to be attributed to the switching measurements including electroforming implying that oxygen ions and/or vacancies are involved in the switching.

Similar resistive switching measurements with applied current sweep were performed in a chamber where the ambient could be controlled. By changing the polarity of electroforming current (voltage) the circulation direction of the current-voltage (I-V) hysteresis can be changed, i.e. the polarities of set switching [high resistance state (HRS) → low resistance state (LRS)] voltage and reset switching [LRS → HRS] voltage are determined by the polarity of electroforming voltage. We activated two different switching modes on two different switching cells in vacuum. For one (mode A) the set and reset switchings occur under negative and positive voltages, respectively, and for the other (mode B) it is the opposite way. Fig. 2 shows that a sample formed into mode A stayed in that same mode when changing the ambient from vacuum to 5×10^{-3} mbar pure oxygen gas. However, the ratio of the HRS to the LRS became considerably larger. Fig. 3 shows the changes in switching curves with increasing oxygen pressure. First, the initial switching curve was measured in vacuum at a pressure lower than 5×10^{-7} mbar, see Fig. 3a. Second, the pressure was increased to 5×10^{-4} mbar by injecting pure oxygen gas, and then a switching measurement with 5 cycles was carried out, the results are shown in Fig. 3b. Third, after some waiting time at zero applied voltage another switching measurement with 5 cycles in the same atmosphere was performed, the results are shown in Fig. 3c. Finally, two additional measurements with 5 cycles each were carried out in an oxygen atmosphere at higher pressure (5×10^{-3} mbar), the results are plotted in Fig. 3d and e, respectively. Mode B underwent the transition to mode A as the pressure of oxygen increased. Therefore, we may conclude that mode A is the more stable switching mode in a pure oxygen ambient at pressures higher than 5×10^{-3} mbar.

Concerning the mechanism of the influence of oxygen on the switching behavior, we can take into account both cathodic and anodic reactions involving oxygen ions, for instance, $V_0^{\bullet\bullet} + 2e^- + 1/2O_2 \leftrightarrow O_0^x$, in which $V_0^{\bullet\bullet}$, and O_0^x mean an oxygen vacancy and an oxygen ion at a regular oxygen site, respectively [3]. The direction of the spontaneous reaction without applied voltage will be determined by the standard potentials at the interfaces. However, an applied voltage can change the rate and even the direction of the reaction, and the changes are opposite at cathode and anode. Therefore, it can be assumed that the two different switching curves measured in vacuum in Figs. 2 and 3 (the direction of the hysteresis is opposite) have different

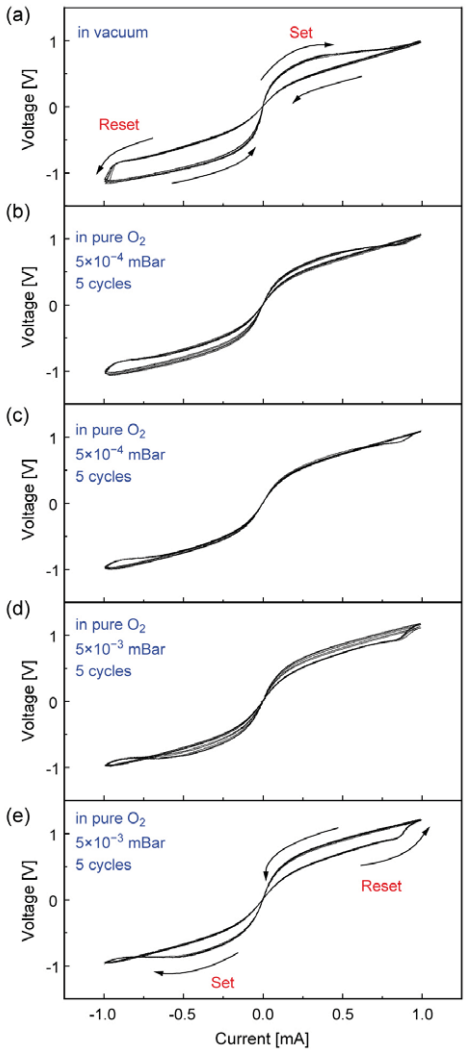

FIG. 3: Changes in resistive switching curves due to changing of oxygen pressure showing reset and set switching under negative and positive current, respectively.

active interfaces involved in the switching due to some asymmetry induced by the electroforming polarity. However, by increasing oxygen pressure the electrochemical reaction at one specific interface may become prominent so that the initially different switching modes become the same. The interface activated or changed by the external oxygen ambient is most probable the one at the TiO_2/top electrode because it is much easier to be influenced by the ambient atmosphere compared to the TiO_2/bottom electrode interface.

In summary, we observed the oxygen evolution in the switching cell after the electroforming and also the influence of oxygen ambient on the bipolar switching behavior. From the observations we can conclude that oxygen is directly involved in the switching even though the mechanism has to be elaborated in more detail.

[1] D. S. Jeong, H. Schroeder, and R. Waser, *Electrochem. Solid-State Lett.* **10**, G51 (2007).

[2] Y. B. Nian, J. Strozier, N. J. Wu, X. Chen, and A. Ignatiev, *Phys. Rev. Lett.* **98**, 146403 (2007).

[3] R. Waser and M. Aono, *Nat. Mat.* **6**, 833 (2007).

Low Current Resistance Switching in WO_3 Thin Films for Non-Volatile Memory Application

C. Kügeler[1], Y. Li[1], R. Waser[1,2]

[1] IFF-6: Electronic Materials
[2] Institut für Werkstoffe der Elektrotechnik 2, RWTH-Aachen, 52074 Aachen, Germany

The aim for faster computing and higher storage densities emphasis the need for novel concepts and materials. One scenario is that memories basing on the change of the electrical resistance will replace the currently charge driven concepts. We report on the deposition and characterization of solid electrolyte WO_3 thin films for non-volatile resistance switching memory applications (RRAM). The studies reveal multilevel switching which suggest storing more than one bit per cell and in addition the material switches with currents in the nanoampere range which is beneficial regarding power consumption aspects.

Triggered by the reinvention of the resistance switching phenomena in metal-insulator-metal (MIM) cells [1-3], recently those material systems attract the semiconductor industry, since they have the potential to overcome predicted road blockers and might find the way into memory as well as reconfigurable logic applications.

The resistance switching phenomena can be described in the way that e.g. the material is initially insulating which means exhibiting a high resistance. If an applied voltage exceeds a certain threshold voltage (V_{th}) the current rises abruptly, which means the resistance decreases dramatically. This low resistance state (LRS) is retained until the voltage polarity is reversed and exceeds a negative V_{th}. At this point the material switches back from the LRS to the high resistance state (HRS). LRS and HRS can be considered as "1" and "0" and can therefore be used for digital data storage. A wide variety of organic and inorganic materials show the resistance switching effect (e.g. TiO_2, NiO, GeSe, WO_3, (Pr,Ca)MnO_3, $SrTiO_3$:Cr, Cu:TCNQ) whereby the switching mechanism is classified due to thermal, ionic or electronic contributions. For details see [6] and the references therein.

WO_3 is known as solid-electrolyte, where diffused Cu ions form conducting filaments, which can be opened and closed by an electric field [7]. WO_3 thin films were deposited by high pressure sputtering from a WO_3 target using pure oxygen. The substrate temperature was in the range between room temperature and 700 °C and the deposition pressure was between 1 - 3 mbar resulting in deposition rates of a few nanometer per hour. XRD measurements prove that the films deposited at 700 °C are of crystalline nature and all other films are amorphous (Figure 1). SEM pictures prove this fact and show grains in the order of 100 nm diameter (WO_3 film @ 700 °C). In this paper we focus on electrical measurements on films deposited at 1 mbar and 200 °C. To create an active area of 5 × 5 μm^2, the films are deposited on an oxidized Si wafer with a structured Pt bottom electrode and a perpendicular Cu top electrode (Figure 2).

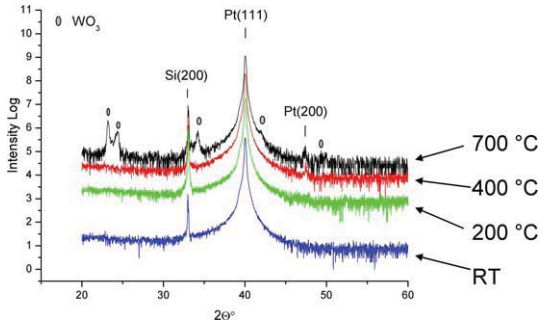

FIG. 1: XRD data of high-pressure sputtered WO_3 thin films at various temperatures.

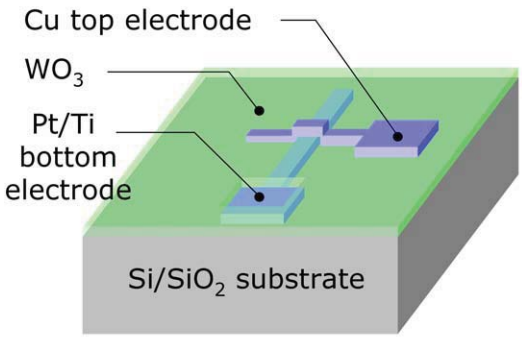

FIG. 2: Schematic view of a single cross junction.

Figure 3 shows a number of I(V) measurements with different current compliances measured sequentially on the cross junction. A current compliance on the positive side is needed to prevent the sample from thermal break down at the moment the resistance

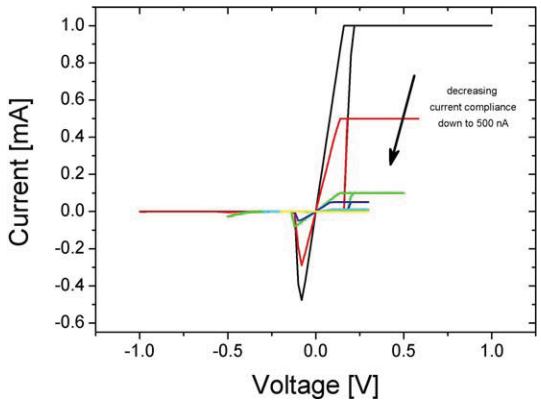

FIG. 3: I(V) measurement of WO_3 thin film using various current compliances.

changes from HRS to LRS by exceeding the positive threshold voltage. On the other hand currents during switch back operation (LRS to HRS) are smaller and therefore not limited by the compliance. The use of different compliance levels comes along with the potential to store more than one bit in one cell, since different resistances can be attributed to multiple bits by simply measuring the current during the read operation.

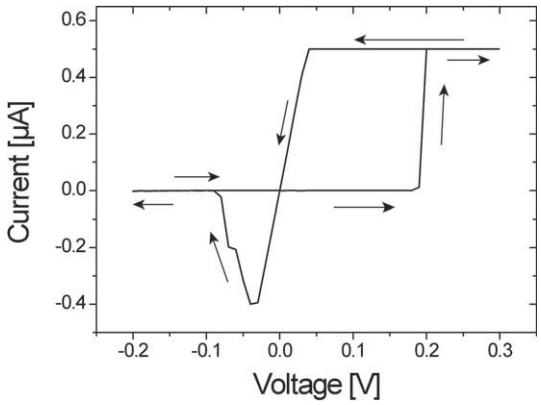

FIG. 4: Low current I(V) measurement. Current compliance is set to 500 nA.

Figure 4 gives a closer look to a low current measurement. The cell switches from HRS to LRS at 200 mV and is limited at only 500 nA. Low currents are desired in RRAM applications, because it is mandatory to reduce the power consumption with increas-ing integration density.

Figure 5 demonstrates write and non-destructive readout cycles. The inset shows the applied voltage pulses. First one set pulse (0.5 V, 1 s) was given followed by 1000 read pulses (100 mV, 20 ms). Then a negative reset pulse was made followed again by 1000 read cycles. The data show clearly the different current levels in "ON" and "OFF" state. Thereby, the current in "ON" state stays around 650 μA corresponding to 150 Ω whereas the resistance in "OFF" state is around 8 MΩ.

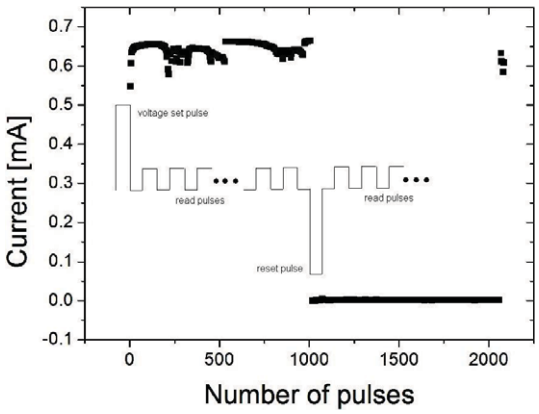

FIG. 5: Read and write cycles of a 5 $\times$ 5 μm^2 large WO_3 junction.

We have presented WO_3 thin films with Cu top electrodes exhibiting non-volatile resistance switching for memory applications. The films are of amorphous nature and show multilevel switching down to very low currents of only 500 nA, which obliges the demand for low power consumption devices. Further more the resistance states could be read for 1000 cycles. Thereby the read operation is non-destructive.

[1] A. Asamitsu, et al., *Nature*, vol. **388**, pp. 50-52 (1997).

[2] M. Kozicki, et al., *Electrochem. Soc.* Pp. 298-309 (1999).

[3] A. Beck, et al., *Appl. Phys. Lett.*, vol. **77**, pp. 139-141 (2000).

[4] G. Müller, et al. *IEDM Tech. Dig.*, pp. 567-570.(2004).

[5] T. Sakamoto, et al. *Appl. Phys. Lett.*, vol. **82**, pp. 3032-3034, (2003).

[6] R. Waser, et al. *Nature Materials*, vol. **6**, pp. 833-840 (2007).

[7] M. Kozicki, et al. *IEEE Trans On Nanotechnology*, vol. **5**, pp.535-544 (2006).

Resistance Switching of Atomic Layer Deposited (ALD) TiO_x Thin Films

L. Yang[1,3], T. Watanabe[1,3], S. Hoffmann-Eifert[1,3], C. Kügeler[1,3], A. Rüdiger[1,3], J. H. Xia[2,4], C. L. Jia[2,4], R. Waser[1,3]

[1] IFF-6: Electronic Materials
[2] IFF-8: Microstructure Research
[3] CNI: Center of Nanoelectronic Systems for Information Technology
[4] ERC: Ernst Ruska-Centre for Microscopy and Spectroscopy with Electrons

Titanium oxide was deposited at 240°C by liquid injection atomic layer deposition using titanium tetraisopropoxide (TTIP) dissolved in ethylcyclohexane (ECH) and water. The deposited 76 nm TiO_x film was analyzed by TEM and showed a nanocrystalline morphology. The ALD TiOx film sandwiched between Cu and Pt electrodes exhibited bipolar as well as unipolar resistance switching, which are applicable to non-volatile memory applications.

A huge variety of materials such as GeSe, TiO_2, $SrZrO_3$, SiO_2 and so on, which can be electrically switched between high resistance state (OFF) and low resistance state (ON) repeatedly, have been intensively studied for the next generation of non-volatile resistive random access memory (RRAM) and reconfigurable logic applications [1-5]. The deposition by ALD is considered since it is a surface reaction controlled process and thereby allows homogeneity and excellent film thickness controllability to be achieved on complex structures. So binary oxide films have the potential to be integrated into crossbar structures with the ease of the moderate integration effort as compared to the complementary metal-oxides semiconductors (CMOS).

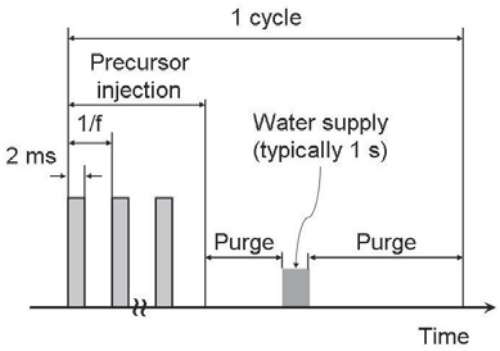

FIG. 1: Time table of the gas pulse injections in a cycle.

TiO_x thin films were deposited at 240°C using TTIP and reactant water on one square inch (111) Pt/Ti/SiO_2/(100)Si substrates. The sequential precursor, reactant gas supply and an appropriate inert gas purge is illustrated in Figure 1. The amount of the TTIP solution supplied to the reactor per cycle was changed by the number of the injections keeping the opening time constant (2 ms). The growth rate of the film shows saturation if injection frequencies more than 1 Hz are used, as shown in Figure 2 [6]. Cu top electrodes were deposited on the films by thermal evaporation at room temperature using photolithography in combination with lift-off process.

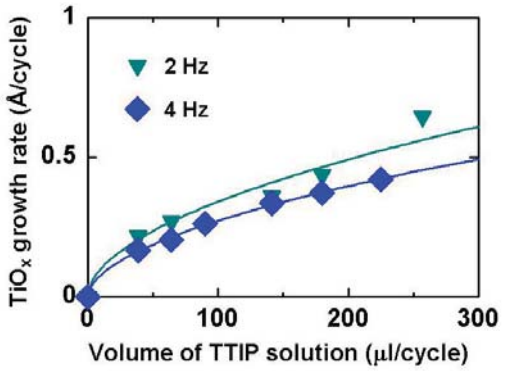

FIG. 2: Variety of the TiO_x film growth rates affected by the injection frequency of 0.05 M TTIP precursor as a function of the volume of injected TTIP solution.

As deposited films show amorphous structure in X-ray diffraction pattern [6]. Cross section TEM depicted in Figure 3 reveals a randomly orientated nanocrystalline structure, which was proved by selected area electron diffraction (SAED) analysis. The corresponding SAED pattern is shown in the inset of Figure 3 clearly indicating the polycrystalline structure of the TiO_x. The thickness of the very homogenous film was measured to 76 nm.

After electroforming such Cu/TiO_x/Pt sandwich structures exhibit bipolar switching in microampere range as well as unipolar switching in milliampere range. Figure 4 (a) shows the typical unipolar switching in such MIM pads structures, where the high resistance switches to low resistance state at positive V_{th+} (threshold voltage for switch ON) with 20 mA compliance current, and switch back to high resistance state at positive V_{th-} (threshold voltage for switch OFF), which is smaller than V_{th+}. Set ON and Set OFF are irrespective of the polarity of the bias. In the case of the bipolar switching (Figure 4 b) the Set ON or Set OFF are polarity dependent, it switches from OFF to ON state at positive V_{th+} and only switch OFF at negative V_{th-}. The TiO_x was also integrated into the micrometer crossbar structures.

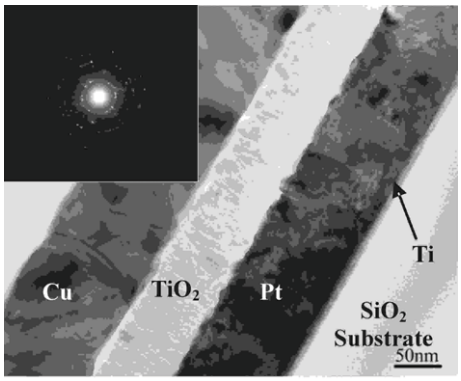

FIG. 3: TEM image of the Pt/TiO_x/Cu structure and the electron diffraction pattern in the inset, which shows the nanocrystalline structure of the deposited TiO_x film.

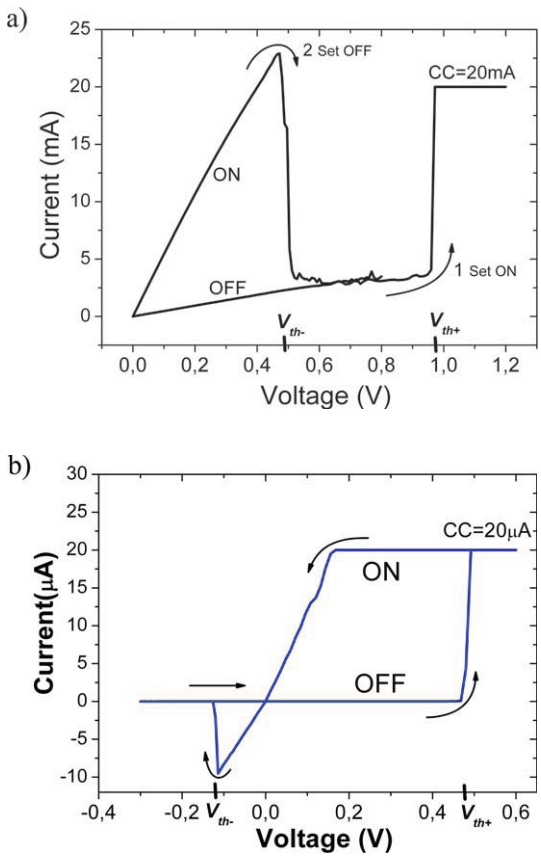

FIG. 4: a) Unipolar and b) bipolar resistive switching of a 76 nm-thick TiO_x film between Cu and Pt electrode in Pads structure (Ø =290 μm).

Figure 5 shows multilevel bipolar switching behaviour measured from a 4 μm^2 cross point, where every 5 continues cycles were performed with the same compliance current and the resistance of low resistance states are depended on the compliance current from 200 μA to 800 μA. The resistance of the ON state decreases with the increasing of compliance current, the ratio of OFF resistance to ON resistance read at 0.5 V ranges from 9 at 200 μA compliance current to 28 at 800 μA compliance current. On the base of the different resistance levels mutibit memory cell can be realized.

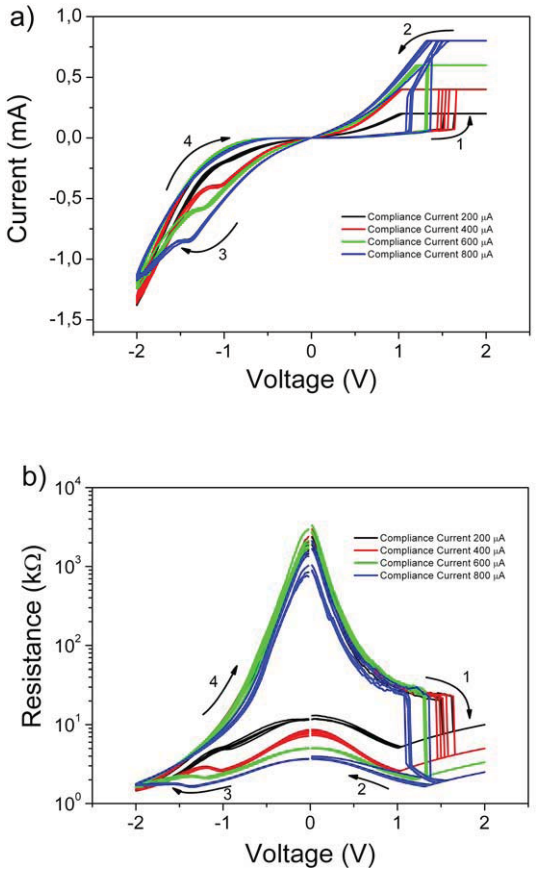

FIG. 5: Multilevel resistive switching behavior of a 2 μm × 2 μm cross point. a) I(V) curves with different compliance current, b) corresponding R(V) curves.

For the resistive switching devices based on TiO_2 the ALD process is advantageous because of two reasons: Firstly, homogenous films can be uniformly deposited on structure surfaces like e.g. crossbar structures; secondly films can be deposited in nearly amorphous nanocrystalline morphology due to the low deposition temperature. With Cu and Pt electrodes TiO_2 films show reproducible bipolar as well as unipolar resistive switching. Depending on the different compliance current the ON resistance states could be varied in different level.

[1] T.W. Hickmott, *Journal of Applied Physics* **33** pp 2669 (1962)

[2] A. Beck, *Applied Physics Letters* **77** pp 139 (2000)

[3] M.N. Kozicki, M. Mitkova, *Journal of Non-Crystalline Solids* **352** (6-7) pp 567-577 (2006)

[4] C. Schindler, S.C.P. Thermadam, R. Waser, *IEEE Transactions on Electron Devices* **54** (10) pp 2762-2768 (2007)

[5] R. Waser, M. Aono, *NATURE MATERIALS* **6** (11) pp 833-840 (2007)

[6] T. Watanabe, S. Hoffmann-Eifert, L. Yang, A. Rüdiger, C. Kügeler, C.S. Hwang, R. Waser, *Journal of the Electrochemical Society*, **154** (6) G134-G140, (2007).

Unit-Cell Scale Mapping of Ferroelectricity in Epitaxial Ferroelectric Films

C. L. Jia[1,3,4], V. Nagarajan[5], J. Q. He[1,3,4], L. Houben[1,3,4], T. Zhao[6], R. Ramesh[4], K. Urban[1,3,4], and R. Waser[2]

[1] IFF-8: Microstructure Research
[2] IFF-6: Electronic Materials
[3] CNI: Center of Nanoelectronic Systems for Information Technology
[4] ERC: Ernst Ruska-Centre for Microscopy and Spectroscopy with Electrons
[5] School of Materials Science and Engineering, University of New South Wales, Sydney NSW, Australia
[6] Dept of Materials Science and Dept of Physics, University of California, Berkeley, CA 94720, USA

By means of high-resolution transmission electron microscopy we map, on the unit-cell scale, the displacements of cations away from the centrosymmetry positions in an ultra-thin epitaxial $PbZr_{0.2}Ti_{0.8}O_3$ film on a $SrRuO_3$ electrode layer deposited on a $SrTiO_3$ substrate. Based on the off-centre displacements of the cations local polarization in the film is estimated. A systematic reduction of the atomic displacements is measured at the interfaces. This suggests that interface-induced suppression of the ferroelectric polarization plays a critical role in the size effect of nanoscale ferroelectrics.

Epitaxial ultra-thin films of ferroelectric oxides have attracted considerable attention with respect to potential applications in nanoelectronic high-density memory devices. The magnitude and stability of the switchable ferroelectric polarization are the central figures of merit for such devices. The switchable polarization, ΔP, is ideally twice the remnant polarization or spontaneous polarization, P_s, which arises as a result of the separation of the charge centre of cations from that of anions. Therefore, the local polarization of the film can in principle be investigated by measuring the atomic displacemens. In the present work, we map the atomic displacements of the cations by high-resolution transmission electron microscopy (HRTEM) and thus investigate *at the unit-cell scale* the polarization in an epitaxial ultra-thin, about 7 nm thick, film of $PbZr_{0.2}Ti_{0.8}O_3$ (PZT) on an $SrRuO_3$ (SRO) electrode deposited on a $SrTiO_3$ substrate using a 400 kV electron microscope.

Figure 1 shows schematically the tetragonal unit cell of ferroelectric PZT (a) and the unit cell of the underlying SRO electrode (b) in a projection along the crystallographic ***b***-axis. In PZT the position of the Zr/Ti atoms (red) as well as that of the O atoms (blue) is displaced along the ***c***-axis direction by a distance $\delta_{Zr/Ti}$ and δ_O with respect to the positions of centrosymmetry.

Figure 2 shows a [010] HRTEM image of the interface of the PZT/SRO heterostructure recorded employing a value of underfocus which is close to Scherzer conditions. The contrast minima correspond to the position of the cation columns projected along the crystallographic [010] direction. The interface is denoted by a thick horizontal arrow. The surface of the PZT layer

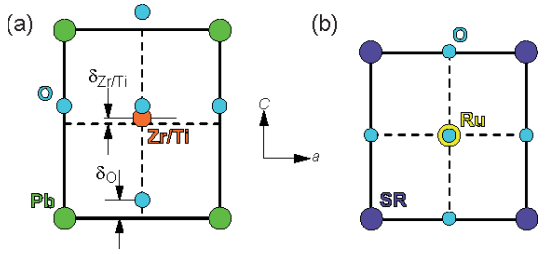

FIG. 1: (a) Tetragonal PZT ferroelectric phase in a projection along the crystallographic ***b***-axis. (b) Tetragonal centrosymmetric SRO.

(not visible in the image) is parallel to the SRO/PZT interface, and as measured in the image the thickness of the PZT layer is about 8 nm.

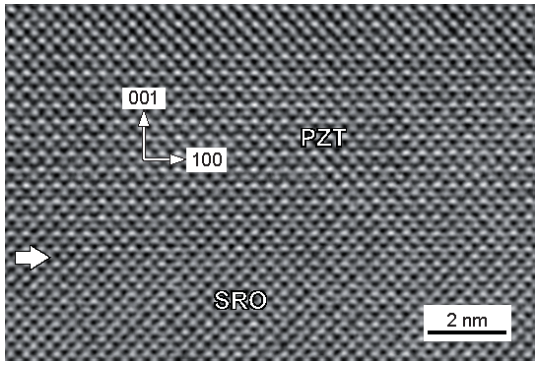

FIG. 2: [010] HRTEM image of the PZT/SRO heterostructure The thick arrow denotes the horizontal interface between the PZT and the SRO film layers.

In order to map local polarization in the film, which is the result of relative displacements of ions as shown in Fig.1, the image of Fig.2 is quantified. The positions of atoms are determined by performing an iterative procedure in which the imaging parameters and structure model are systematically varied until a stable best fit of the calculated contrast distribution to the experimental intensity data for the SRO and PZT layers is achieved [1]. We note that we shall only deal with shifts of atomic positions as a function of increasing distance from the SRO/PZT interface plane. Therefore, for a certain distance from the interface, we calculate a mean value by taking the average of the contrast minimum position data over

42 unit cells (16.4 nm) parallel to the interface. Figure 3a shows the experimental image obtained by this type of averaging. It can be compared with the image in Fig. 3b calculated on the basis of the final model of PZT/SRO and the optimum imaging parameters.

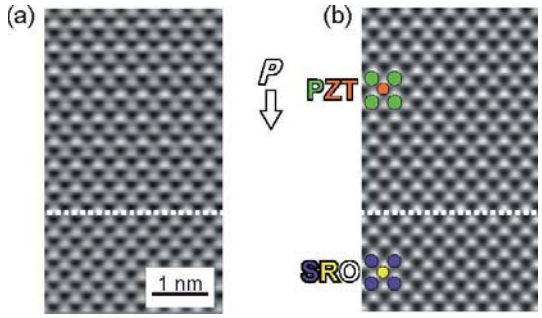

FIG. 3: (a) Image obtained from the experimental image of Fig.2 by averaging the intensity over 42 unit cells. (b) The image calculated on the basis of final structure model. The polarization direction of the PZT film is shown by an arrow *P*.

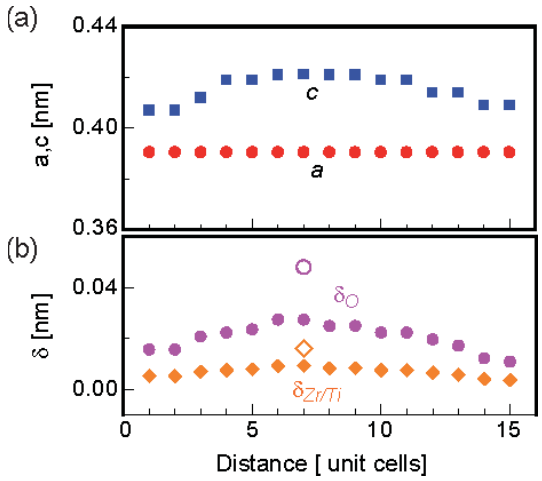

FIG. 4: The c- and a-axis parameters (a) and the displacement parameters $\delta_{Zr/Ti}$ and δ_O of the Zr/Ti and O atoms (b) as a function of the unit cell position from the interface.

In Fig. 4a we present the results of measurements for the ***c***-axis and ***a***-axis lattice parameter. The c-axis lattice parameter c of the PZT layer increases gradually with increasing distance from the interface reaching a maximum in the middle of the film. Figure 4b shows the displacements $\delta_{Zr/Ti}$ and δ_O of the Zr/Ti and O atoms, respectively, as a function of the unit cell position from the interface. Interestingly, the relative shifts of the atoms which result in the polarization of the ferroelectric phase are much smaller in the thin film system than in the bulk crystal open symbols).

In Fig. 5 we show the spontaneous polarization, P_s (full red circles) as a function of the distance from the interface calculated on the basis of the determined atomic displacements and the effective charge values of ions for PTO given in ref 2. The dotted line in

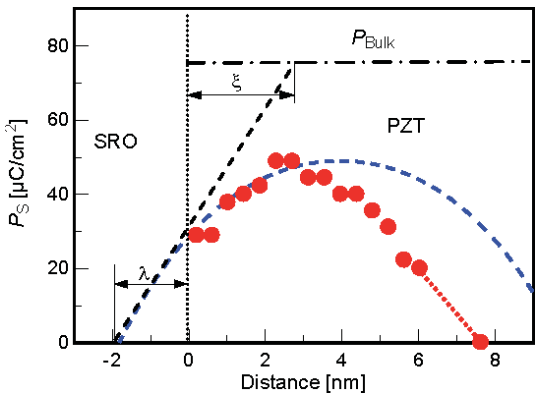

FIG. 5: Spontaneous polarization, P_s, calculated on the basis of the atomic shifts determined. The blue dashed-line curve is calculated for a system of an 8-nm ferroelectric layer sandwiched between metallic electrodes based on the Kretschmer-Binder model.

the left part indicates the SRO/PZT interface position. As one progresses from the centre of the PZT film towards the interface or the film surface the value of P_s decreases. This provides direct evidence for the fact that an interfacial layer with reduced polarization is formed in PZT. On the other hand, this behaviour supports the theoretical picture of surface-induced suppression of polarization based on a phenomenological theory [3]. From our data, an averaged value of the spontaneous polarization $\overline{P_s}$ over a film thickness is estimated as 40 $\mu C/cm^2$ for an 8-nm-thick film. This value for $\Delta\overline{P_s}(= 2\overline{P_s})$ fits quite well with the experimental data of about 70 $\pm$ 5 $\mu C/cm^2$ [4].

From our analysis, two key results are evident. Firstly, the displacements of the Zr/Ti and oxygen atoms decrease almost linearly from the film interior to the interface. It can imagine that as the film thickness is increased, the effect of the interface becomes weaker and weaker. This observation corresponds to the increase in switchable polarization with increasing film thickness. A second important result is the evidence for smaller displacements of the Zr/Ti atoms from the positions of centrosymmetry in the film interior where the ***c***-axis parameter is larger in comparison with the crystal data for the PTO ferroelectric phase. These smaller displacements are expected to lead to lower polarization. One possible role may be the kinetics of the growth process.

[1] C.L. Jia et al. *Nature Materials* **6**, 64 (2007).

[2] L. Bellaiche and D. Vanderbilt, *Phys. Rev. Lett.* **83**, 1347 (1999).

[3] R. Kretschmer and K. Binder, *Phys. Rev. B* **20**, 1065 (1979).

[4] V. Nagarajan et al., *J. Appl. Phys.* **100**,051609 (2006).

Elastic Stabilization of Single-Domain Ferroelectric State in Nanoscale Capacitors and Tunnel Junctions

N. A. Pertsev[1,2], H. Kohlstedt[1]

[1] IFF-6: Electronic Materials

[2] A. F. Ioffe Physico-Technical Institute, Russian Academy of Sciences, 194021 St. Petersburg, Russia

Taking into account the electrostrictive coupling between inhomogeneous polarization fluctuations and lattice strains in ferroelectrics films, we showed that in heterostructures involving strained epitaxial films and metal electrodes the single-domain state may remain stable against the transformation into polydomain state down to the nanometer scale. This result indicates that the ferroelectric states with opposite remanent polarizations can be stabilized even in nanoscale capacitors and tunnel junctions, which opens possibility of their memory applications.

Persistence of ferroelectricity in ultrathin films is an issue of high fundamental and practical interest. In particular, the stability of states with a nonzero net polarization represents a matter of primary importance. Indeed, the presence of such polarization is necessary for the memory applications of ferroelectric capacitors [1] and tunnel junctions [2].

Dependence of the polarization pattern **P(r)** on the film thickness may result from both long-range and short-range interactions. The most widely discussed cause of this size effect is the existence of a depolarizing field, which differs from zero even in thin films covered by metal electrodes [3, 4]. According to the theoretical predictions [3, 4], the depolarizing-field effect may lead to the complete disappearance of ferroelectric phase below some critical film thickness. In these studies, however, the film was assumed to remain in a single-domain state, although the depolarizing field $E_{\rm dep}$ tends to induce the formation of a 180° domain structure. Since this transformation strongly reduces the magnitude of $E_{\rm dep}$, it may prevent the ferroelectric to paraelectric phase transition in ultrathin films. In view of this possibility, the stability of a single-domain film against the appearance of 180° domains becomes an extremely important issue.

The stability problem can be solved by studying small inhomogeneous perturbations of the uniform polarization state [5]. The existing solutions of this problem [5, 6], however, ignore totally the fact that, owing to the electrostrictive coupling, the polarization fluctuations inevitably modify lattice strains [7]. In this work, we developed a rigorous solution of the stability problem for the single-domain state in ferroelectric films, which demonstrates that the electrostrictive coupling between polarization and strain may stabilize this state even in a few-nanometer-thick epitaxial layers.

We considered thin films of perovskite ferroelectrics grown on a thick cubic substrate inducing compressive in-plane strains in the film. At thicknesses t outside the nanoscale range, such films stabilize in the tetragonal c phase with the polarization **P** orthogonal to the substrate ($P_1 = P_2 = 0, P_3 \neq 0$). Neglecting for clarity the surface effects on **P(r)**, we assumed the film to be homogeneously polarized in the ground state and first determined the spontaneous polarization, which is necessary for the stability analysis. The film polarization can be calculated from the nonlinear equation of state derived by differentiating the film Helmholtz free energy. The total electric field E_3 inside the film may be found from the voltage drop V_a across the metal-ferroelectric-metal (MFM) heterostructure and the continuity condition of the electric displacement **D** = ε_0 **E** + **P** at the interfaces (ε_0 is the permittivity of the vacuum) [3]. The calculation shows that E_3 depends on the total capacitance c_i of the screening space charge in the electrodes [8]. The depolarizing field $E_{\rm dep}$ = -$P_3/(\varepsilon_0 + c_i t)$ formally renormalizes the coefficient $a_3{}^*$ of the lowest-order polarization term [7], transforming it into $a_3{}^{**}$ = $a_3{}^*$ + 1/[2/($\varepsilon_0 + c_i t$)]. Using this expression, one can calculate P_3 and $E_{\rm dep}$ as a function of the film thickness t at a constant misfit strain $S_m < 0$.

We performed these calculations for Pb($Zr_{0.5}Ti_{0.5}$)O_3 (PZT) and $BaTiO_3$ (BT) films grown on $SrTiO_3$, assuming S_m to be equal to a thickness-independent value attained in fully strained MFM trilayers. The spontaneous polarization P_s = P_3(V_a = 0) of PZT films was calculated in the P^6 approximation, while we used the P^8 approximation to find P_s of BT films. Since the capacitance c_i affects P_s only via the product c_i t, the dependences $P_s(t)$ corresponding to different electrode materials can be described by one universal curve $P_s(t_{\rm eff})$. The effective film thickness $t_{\rm eff}$ may be defined as $t_{\rm eff}$ = $(c_i/c_1)t$, where c_1 = 1 F/m^2.

The calculated curves $P_s(t_{eff})$ show that the out-of-plane polarization P_s vanishes at a critical film thickness t_0, which was regarded as a size-induced phase transition [4]. Just above t_0 the film polarization steeply increases with thickness and reaches values comparable to the bulk polarization. At c_i = 0.444 F/m^2 characteristic of $SrRuO_3$ electrodes, the calculation gives $t_0 \cong$ 2 nm for PZT films and $t_0 \cong$ 2.6 nm

for BT films [8]. Therefore, even nanoscale capacitors and tunnel junctions may have the out-of-plane polarization sufficient for the memory applications.

On the next stage of calculations, we analyzed a wave-like perturbation of the uniform polarization state along the x_1 axis. Since the polarization distribution becomes inhomogeneous, the equation of state should be replaced by the Euler equations involving the gradient terms. These second-order differential equations were derived in the 2D case for ferroelectrics with a cubic paraelectric phase. The polarization components involved in the Euler equations can be written as $P_3 = P_s + \delta P_3(x_3)\ \exp(ikx_1)$ and $P_1 = \delta P_1(x_3)\ \exp(ikx_1)$ with $\delta P_1, \delta P_3 \ll P_s$. Similar relations [e.g., $S_{11} = S_m + \delta S_{11}(x_3)\ \exp(ikx_1)$] can be introduced for the film strains S_{ij} and the electrostatic potential ϕ. Using these formulae and retaining only the lowest-order perturbation terms, we obtained two simultaneous differential equations for the functions $\delta P_i(x_3)$, $\delta S_{ij}(x_3)$, and $\delta\phi(x_3)$ [8].

In addition, four other equations must be satisfied. First, the electrostatic condition div **D** = 0 provides a relation between $\delta\phi$, δP_1 and δP_3. Second, the strains S_{ij} must obey the compatibility condition, which reduces to one nontrivial equation in our case. Third, the equations of mechanical equilibrium $\sigma_{ij,j}$ = 0 written for the film stresses σ_{ij} yield another two relations. In total, one obtains a system of six differential equations for six unknown functions: δP_1, δP_3, $\delta\phi$, δS_{11}, δS_{33} and δS_{13}. The analysis shows that the discussed system may be reduced to a pair of simultaneous equations, which involve only δP_3, δS_{11}, and their second and fourth derivatives [8]. These equations differ dramatically from the differential equation used to describe the stability problem formerly [5, 6] because the polarization wave creates an elastic wave in the film.

Since the obtained system is homogeneous, the solution should have the form $\delta P_1(x3) = A\ \exp(\lambda x_3)$, $\delta Si_{11}(x_3) = B\ \exp(\lambda x_3)$. This leads to a homogeneous system of two linear algebraic equations in the unknown coefficients A and B. Calculating the determinant Δ_λ of this system and setting it to zero, one obtains the characteristic equation $\Delta_\lambda(\lambda) = 0$ in the form of a quartic algebraic equation with respect to λ^2. When all roots $\lambda_n(k)$ of this equation are distinct, the general solution involves eight coefficients A_n satisfying a system of eight simultaneous equations, which follow from the boundary conditions [8].

Since this system is homogeneous, a nonzero solution for A_n exists only when its determinant Δ_A equals zero. By solving the equation $\Delta_A(k) = 0$ numerically, it is possible to check the existence of any root $k \neq 0$ at a given film thickness t, interfacial capacitance c_i, temperature T, and misfit strain S_m. If there are no such roots, the uniform polarization state remains stable against inhomogeneous polarization perturbations. The critical thickness t_c, at which the single-domain state becomes unstable, can be found as a maximum value of t at which a nonzero solution for k first appears.

We performed necessary numerical calculations for fully strained BT and PZT films grown on $SrTiO_3$. Since for our purposes it is sufficient to determine the upper bound $t_{c,max}$ of the critical thickness, we simplified the problem by setting the gradient coefficients g_{ln} to zero. The magnitude of $t_{c,max}$ may be computed for one particular interfacial capacitance c_i only, because the critical thickness is inversely proportional to c_i. We studied the case of two $SrRuO_3$ electrodes (c_i = 0.444 F/m^2). At room temperature, $t_{c,max}$ was found to be slightly below 2.98 nm for BT films and below 2.73 nm for PZT films.

The calculations also showed that $t_{c,max}$ strongly increases when compressive strain is reduced (Fig. 1). To clarify the role of the strain effect further, we computed the critical thickness in the absence of electrostrictive coupling ($q_{ln} = 0$), using the available estimates of gradient coefficients g_{ln}. It was found that t_c increased up to about 37 nm for BT films and 56 nm for PZT films at room temperature. Hence the strain effect reduces the critical thickness by more than a factor of ten.

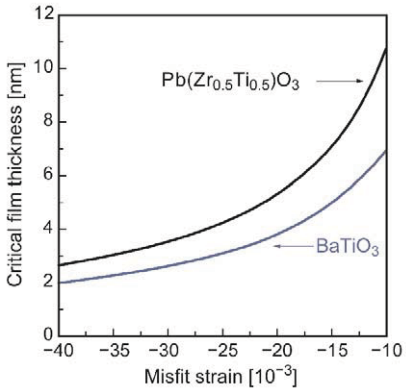

FIG. 1: Variation of the critical thickness $t_{c,max}$ with the misfit strain at room temperature calculated for epitaxial BT and PZT films sandwiched between $SrRuO_3$ electrodes (c_i = 0.444 F/m^2).

Thus, by combining highly strained epitaxial films with metallic electrodes having good screening properties it is possible to stabilize the single-domain ferroelectric state in nanoscale capacitors and tunnel junctions. Remarkably, this stabilization results from the electrostrictive coupling between polarization and strain, which was ignored previously [5, 6].

[1] J.F. Scott, *Ferroelectric Memories* (Springer, Berlin, 2000).

[2] H. Kohlstedt *et al.*, Phys. Rev. B **72**, 125341 (2005).

[3] R.R. Mehta, B.D. Silverman, and J.T. Jacobs, J. Appl. Phys. **44**, 3379 (1973).

[4] J. Junquera and Ph. Ghosez, Nature (London) **422**, 506 (2003).

[5] E.V. Chenskiĭ and V.V. Tarasenko, Sov. Phys. JETP **56**, 618 (1982).

[6] A.M. Bratkovsky and A.P. Levanyuk, cond-mat/0601484.

[7] N.A. Pertsev, A.G. Zembilgotov, and A.K. Tagantsev, Phys. Rev. Lett. **80**, 1988 (1998).

[8] N.A. Pertsev and H. Kohlstedt, Phys. Rev. Lett. **98**, 257603 (2007).

Direct Electrical Characterization of Embedded Ferroelectric Lead Titanate Nanoislands

S. Clemens[3], A.-C. Dippel[3], T. Schneller[3], R. Waser[1,2,3], S. Röhrig[1,2], A. Rüdiger[1,2]

[1] IFF-6: Electronic Materials
[2] CNI: Center of Nanoelectronic Systems for Information Technology
[3] Institut für Werkstoffe der Elektrotechnik II, RWTH Aachen

Lead titanate nanoislands embedded into a low-k dielectric matrix and dense lead titanate films are investigated in terms of their ferroelectric switching currents with special care devoted to capacitive and leakage contributions. Our findings with platinum and gold as collective top electrodes are compared to previous results and those of thin films and we discuss the remnant polarization and the coercive field within an equivalent circuit model. We demonstrate that a direct electrical characterization of sub 100 nm ferroelectric nanoislands becomes feasible if they are measured in parallel and provided that the thin film material parameters of both ferroelectric and the spin-on-glass are independently determined.

One approach to electrically study nanoscale ferroelectrics starts from an ensemble of dozens or hundreds of identical or similar ferroelectric nanoislands with collective top electrodes. For microscopic ensembles they may sometimes already be equipped with individual top electrodes [1] that can be contacted in parallel to obtain sufficient signal levels. However, as the structures under investigation become even smaller, the deposition as well as the etching of top-electrodes becomes increasingly demanding and has not been achieved to a satisfactory degree. We therefore tackle this situation from two sides: For one, we are growing template based ferroelectric nanoislands with a high degree of registration and a narrow size distribution [2, 3] well below 100 nm lateral extension and for the other we are embedding self-ordered ferroelectric nanoislands into a low-k dielectric [4]. With a chemical mechanical polishing (cmp) process, we are able to remove the upper layer of the dielectric to access the embedded grains. This procedure works for both embedded and free grains as illustrated by the piezoreponse of free unpolished and polished grains in Fig. 1 [5]. The idea is to eventually make contact to an ensemble of these nanoislands with collective top electrodes to measure them in parallel.

The spin-on glass we use as a low-k dielectric has excellent flow qualities and provides a correspondingly favorable planarization as illustrated in Fig. 2. The piezoelectrically active surface fraction thus becomes a function of the polishing time (cf. Fig. 3) and we are able to practically modify the aspect ratio of these

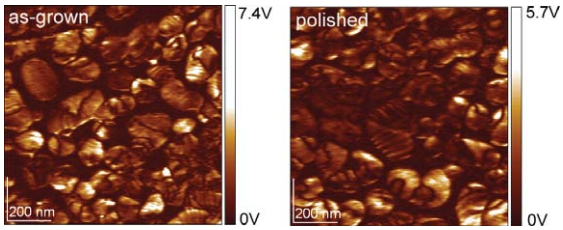

FIG. 1: Comparison of the piezoresponse signal for as grown (left) and polished grains of ferroelectric $PbTiO_3$.

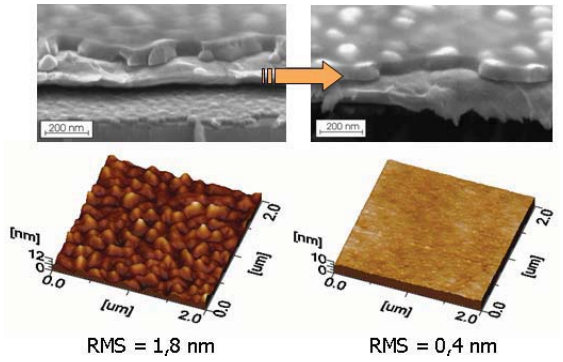

FIG. 2: SEM images of embedded grains in a low-k dielectric layer that is covering the whole area (left) even providing a thin layer on top of the highest grains and of a polished surface (right) where some of the grains are already exposed. The sur-face roughness considerably improves upon the polishing pro-cedure despite different rates for HSQ and $PbTiO_3$.

nanoislands from the thermo-dynamically driven initial size distribution all the way down to structures with an identical distribution of diameter but with an almost homogeneous height that we are able to tailor with nanometer precision [5]. Ferroelectric functionality of individual structures was controlled during intermediate process steps by the inversion of the piezoelectric tensor using the conductive tip of an AFM in a piezoresponse force microscopy configuration.

The general idea is thus to combine the two aforementioned approaches i.e. the fabrication of long-range ordered nanoislands by template growth together with the deposition of collective top electrodes

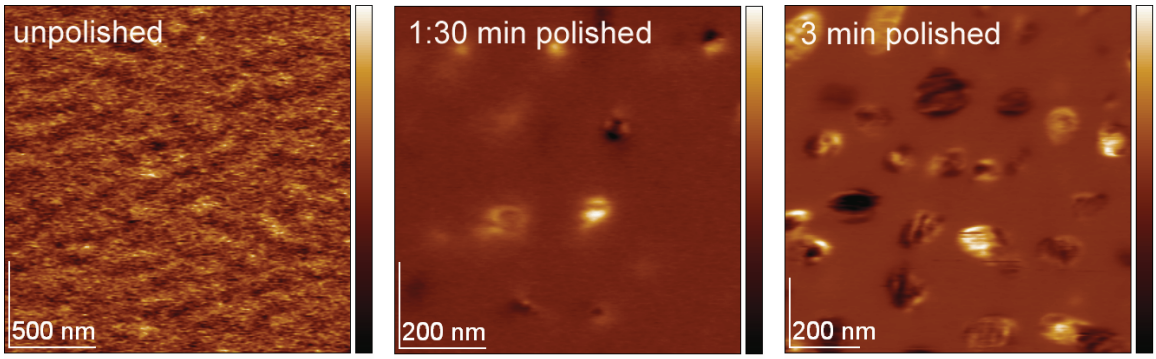

FIG. 3: Piezoresponse area fraction as a function of polishing time. While the upolished structure (left) is inactive, the structure reveals more and more features such as 90° stripe domains upon polishing.

after a chemical mechanical polishing steps to obtain an ensemble of almost identical ferroelectric nanoislands with a narrow size distribution. This allows identifying the averaged value over hundreds of these structures to any individual nanoisland. Recently, some progress was achieved with the description of the mass transport for template-controlled grains [6]. In contrast to the existing polycrystalline nanoislands on platinized silicon, ideal structures are single crystalline and single-domain epi-taxially grown. The use of template-controlled growth partially suppresses the nucleation at Pt-grain boundaries alreday and yields higher fractions of (111) orientation.

In order to quantify our data, we needed to determine whether the cmp process deteriorated the polarization properties as expressed by the displacement current. Screening of the bound surface charges in the free surface was changed as determined by deviations from Kittel's law i.e. domain widths for identical grain heights were smaller in polished grains indicating a more efficient screening which can be attributed to ionic components of the polishing slurry. However the displacement current itself should not be affected with an additional adsorbate layer. We used a dense film of polycrystalline lead titanate as a reference and got good agreement with the surface polarization in embedded ferroelectric nanoislands when the surface fraction is taken into consideration as illustrated in Fig. 4.

We subsequently simulated the experimentally determined switching curve with an equivalent circuit model as described in [4] which accounts quantitatively for the observed coercive field, the displacement currents, and the frequency dependence (not discussed here). However the leakage currents could not be handled within a model of constant leakage. Current research is devoted into a hysteretic behavior of this current which corresponds to a resistive switching behavior as observed in various materials of nanoscale thickness. However it is not yet obvious if the dominant resistive switching contribution stems from the ferroelectric itself or the HSQ film.

The way is now paved to integrate the template-grown ferroelectric nanoislands into a low-k dielectric

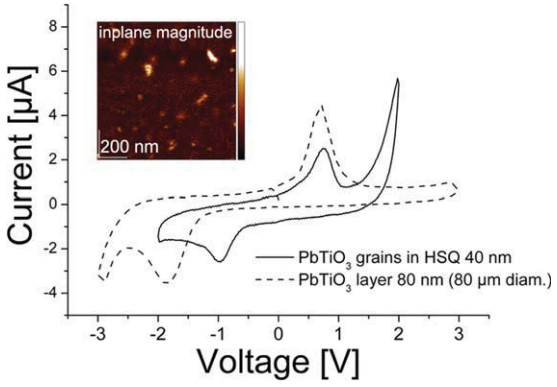

FIG. 4: Comparison of the ferroelectric switching curves for a dense $PbTiO_3$ film (dashed) and an ensemble of ferroelectric $PbTiO_3$ nanoislands (solid).

to demon-strate the characterization of these structures in parallel. Further work is devoted to extend this approach to epitaxial single-crystalline nanoislands.

[1] D.J. Jung, M. Dawber, A. Ruediger, J.F. Scott, H.H. Kim and Kinam Kim, *Appl. Phys. Lett.*, **81**, (2002) 2436

[2] S. Clemens, T. Schneller, A.van der Hart, F. Peter and R. Waser, *Adv. Mater.*, **17** (2005) 1357

[3] S. Bühlmann, B. Dwir, J. Baborowski and P. Muralt, *Appl. Phys. Lett.*, **80**, (2002) 3195

[4] S. Clemens, T. Schneller, R. Waser, A. Rüdiger, F. Peter, S. Kronholz, T. Schmitz and S. Tiedke, *Appl. Phys. Lett.*, **87** (2005) 142904

[5] S. Clemens, A. Rüdiger, S. Röhrig, T. Schneller and R. Waser, *Small*, **2** (2006) 500

[6] P. Muralt, *J. Appl. Phys.*, **100** (2007) 051605

Polarization and Lattice Strains in Epitaxial $BaTiO_3$ Films Grown by High-Pressure Sputtering

A. Petraru[1,3], N. A. Pertsev[1,3], H. Kohlstedt[1,3], U. Poppe[2,3], A. Solbach[4], U. Klemradt[4], R. Waser[1,3]

[1] IFF-6: Electronic Materials
[2] IFF-8: Microstructure Research
[3] CNI: Center of Nanoelectronic Systems for Information Technology
[4] II. Physikalisches Institut B, RWTH Aachen University, 52074 Aachen, Germany

High-quality $BaTiO_3$ films with thicknesses ranging from 2.9 to 175 nm were grown epitaxially on $SrRuO_3$-covered (001)-oriented $SrTiO_3$ substrates by high-pressure sputtering. The in-plane and out-of-plane lattice parameters were determined as a function of film thickness by x-ray reciprocal space mapping around the asymmetric ($\bar{1}00$) Bragg reflection. $BaTiO_3$ films were found to be fully strained by the $SrTiO_3$ substrate up to a thickness of about 30 nm. Polarization-voltage hysteresis loops were recorded at the frequen-cies 1-30 kHz. The observed thickness effect on the lattice parameters and polarization in $BaTiO_3$ films was analyzed in the light of strain and depolarizing-field effects using the nonlinear thermodynamic theory. The theoretical predictions are in reasonable agreement with the measured thickness dependences, although the maximum experimental values of the spontaneous polarization and the out-of-plane lattice parameter exceed the theoretical estimates (43 μC/cm^2 vs. 35 μC/cm^2 and 4.166 Å vs. 4.143 Å). Possible origins of the revealed discrepancy between theory and experiment are discussed.

The current trend towards the downscaling of microelectronic devices makes especially important the investigations of size effects on the physical properties of ferroelectric films. Barium titanate (BTO) is a classical ferroelectric material which was extensively investigated in bulk form in the past. It represents a good choice for experimental studies of the size effects in ferroelectric thin films because detailed comparison between observations and theoretical predictions is possible in this case. In particular, the nonlinear thermodynamic theory of epitaxial ferroelectric films can provide quantitative description of BTO films since the thermodynamic parameters of BTO crystals were recently determined with a good degree of precision [1]. This theory describes the influence of substrate-induced lattice strains on the polarization state of an epitaxial film and shows that these strains may induce the formation of new ferroelectric phases in BTO films and increase the spontaneous polarization largely. Moreover, several first-principles calculations were performed for ultrathin BTO films. The existence of a minimum film thickness for the stability of a single-domain ferroelectric state was predicted, below which it transforms into the paraelectric one owing to the depolarizing-field effect. Kim *et al.* showed that the film polarization strongly decreases in ultrathin films, but even the 5-nm-thick BTO film displays a well-defined polarization hysteresis loop [2].

For the better understanding of the nature of size effects in ferroelectric films, it is important to measure both the polarization and lattice parameters in a wide range of film thicknesses and to analyze their variations theoretically. We report here such measurements for BTO films grown by high-pressure sputtering on $SrRuO_3$-covered (001)-oriented $SrTiO_3$ substrates, with thickness ranging from 2.9 up to 175 nm. The surface of BTO films has a good degree of flatness, with an rms roughness of about 1.9 Å. In order to determine the lattice parameters of BTO films and to evaluate the substrate-induced strains, we performed the x-ray reciprocal space mapping (X-RSM) of our heterostructures around the asymmetric (103) Bragg reflection and the results for several different thicknesses are showed in the right Figure. The lattice parameters are shown in the upper left Figure. It can be seen that the films are fully strained by the STO substrate up to a thickness of 30 nm. For the investigation of the ferroelectric properties of BTO films, plate-capacitor structures were fabricated and polarization-voltage hysteresis loops of BTO capacitors were recorded at frequencies 1-30 KHz using an aixACCT TF Analyzer 2000. When the film thickness t is in the range of 25 to 100 nm, the P-V loop has practically ideal rectangular shape, which reflects high quality of fabricated BTO films and the absence of nonferroelectric ("dead") layers at the film/electrode interfaces. At the film thicknesses below 20 nm, the shape of P-V loops deteriorates progressively. The leakage current increases further in the thinnest fabricated film (t = 2.9 nm), but the capacitor is still not short-circuited. Although the hysteretic behavior disappears at t = 2.9 nm, the current-voltage dependence remains nonlinear.

To describe quantitatively the influence of substrate-induced lattice strains on the orientation and magnitude of the spontaneous polarization, we use the thermodynamic theory of epitaxial ferroelectric films. This theory is based on the polynomial expansion of the energy density in terms of the polarization components. Since the eight-order polarization terms in the free energy expansion were found recently to be

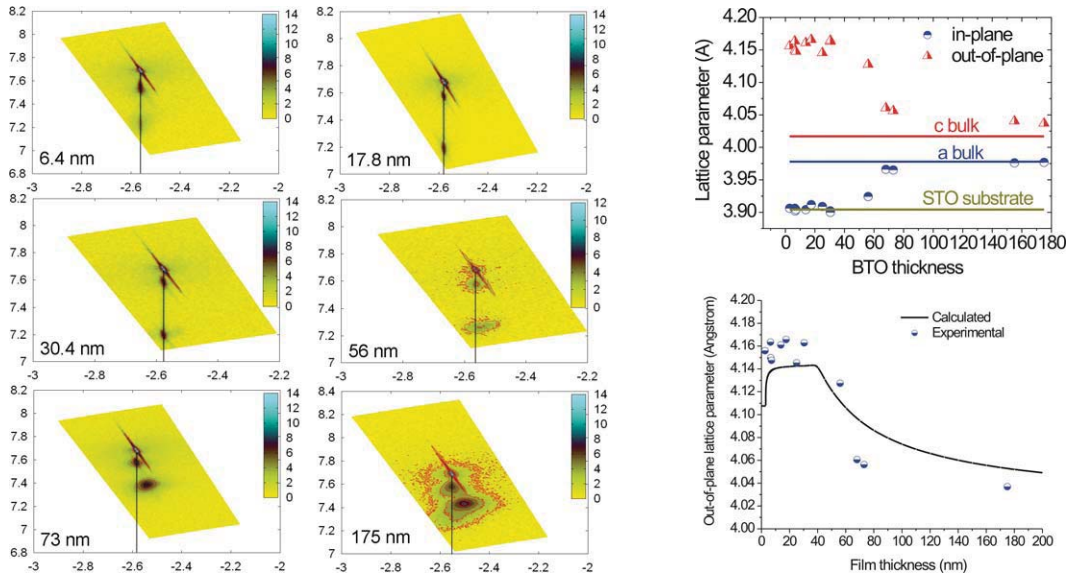

FIG. 1: Upper: X-ray reciprocal space mapping (X-RSM) around the asymmetric (103) Bragg reflection for Ba-TiO_3 films of several different thicknesses. Right (a) Variation of the lattice parameters as a function of film thickness; (b) Calculated and measured thickness dependence of the polarization in epitaxial BTO films.

important for the bulk BTO crystal, we employ the P^8 approximation to calculate the properties of BTO films [3]. It can be seen that, with decreasing thickness, the film polarization first gradually increases and then, below t = 25 nm, starts to drop down. The calculated and the experimental thickness dependence of spontaneous polarization are shown in lower left Figure. Gradual decrease of P_s with increasing thickness at t > 40 nm is caused by the strain relaxation, whereas the steep reduction of polarization in ultra-thin films is due to the depolarizing-field effect. The size-induced ferroelectric to paraelectric phase transition takes place at t = 2.6 nm in the single-domain approximation, which is close to the critical thickness of six unit cells predicted by the first-principles calculations for the same heterostructure [4]. However, at a slightly larger thickness of about 3 nm the single-domain state may already become unstable with respect to the formation of a 180° domain structure. The theoretical dependence $P_s(t)$ is qualitatively similar to the observed polarization variation with the film thickness, but there are two important distinctions between the theory and experiment. First, the maximum measured polarization (about 43 μC/cm^2) exceeds the theoretical value P_s = 35 μC/cm^2 considerably. Second, the strong decrease of polarization observed in ultrathin films starts at a larger thickness than the theoretically predicted one and proceeds more gradually.

The maximum polarization P_s 43 μC/cm^2 observed in our films is close to the values of 38.5 μC/cm^2 and 44 μC/cm^2 reported by Yanase *et al.* and Kim *et al.* for the same heterostructure. On the other hand, it is much smaller than the record polarization P_s 70 μC/cm^2 measured in the 200-nm-thick BTO films grown on $SrRuO_3$/$DyScO_3$ [5]. The thickness dependence of P_s in our films at $t \leq$ 30 nm is qualitatively similar to the dependence reported in Ref. [2]. The coercive field was found to be relatively weakly dependent on the film thickness, being about 150 kV/cm.

In conclusion, our experimental study confirmed that the polarization and lattice strains in epitaxial BTO films may vary with the film thickness considerably. The maximum measured value of the out-of-plane lattice parameter is very close to the value predicted by the nonlinear thermodynamic theory. In contrast, the maximum measured polarization exceeds the theoretical value significantly (by about 23%). The theoretical analysis demonstrates that the nonlinearity of the elastic properties alone cannot explain the discrepancy between the theory and experiment. Finally, we would like to note that reversible polarization may also increase in BTO films due to the presence of dipolar defects. Indeed, such defects were found to induce low-temperature ferroelectricity in (unstrained) thin films of STO, which is an incipient ferroelectric in the bulk form. However, the out-of-plane lattice parameter of these films at room temperature was significantly larger than the bulk lattice constant, probably because the dipolar defects involved oxygen vacancies. Hence it remains unclear whether the defect-induced additional increase of spontaneous polarization could be accompanied by a negligible lattice expansion. All in all, the origin of the polarization enhancement observed in epitaxial BTO thin films requires further experimental and theoretical investigations.

[1] Y. L. Li, L. E. Cross, and L. Q. Chen, *J. Appl. Phys.* **98**, 064101 (2005).

[2] D. J. Kim, et al., *Phys. Rev. Lett.* **95**, 237602 (2005).

[3] A. Petraru, N. A. Pertsev, H. Kohlstedt, U. Poppe, R. Waser, A. Solbach and U. Klemradt, *J. Appl. Phys.* **101** (11), 114106 (2007).

[4] J. Junquera and Ph. Ghosez, *Nature (London)* **422**, 506 (2003).

[5] K. J. Choi et al., *Science* **306**, 1005 (2004).

Microstructural Investigation of $SrTiO_3/BaZrO_3$ Bilayer Thin Films on MgO Substrates by Means of HRTEM

S. B. Mi, C. L. Jia, M. I. Faley, U. Poppe, K. Urban

IFF-8: Microstructure Research
CNI: Center of Nanoelectronic Systems for Information Technology
ERC: Ernst Ruska-Centre for Microscopy and Spectroscopy with Electrons

By means of aberration-corrected high-resolution transmission electron microscopy (HRTEM), the interfacial structure and the defect configuration in the $SrTiO_3/BaZrO_3$ heterofilms on MgO substrates are investigated. At the $BaZrO_3$/MgO interface, two types of interfacial structure, MgO/ZrO_2-type and MgO/BaO-type, are observed. Antiphase boundaries and dislocations are also found at the interface. The formation of these lattice defects is discussed in terms of film growth and structural imperfections of the substrate surface. At the $SrTiO_3/BaZrO_3$ interface, a high density of misfit dislocations is observed with different configurations. The formation of these dislocations contributes both to relaxation of the large misfit strain and to stopping the further propagation of lattice defects, which are formed in the $BaZrO_3$ layer, into the $SrTiO_3$ layer.

MgO is one of the preferable substrate candidates for microwave device applications owing to its low dielectric coefficient, low loss tangent and relatively low cost. However, direct epitaxial growth of the films for device applications on MgO may result in undersigned chemical reaction at the interface [1], or in-plane 45° rotation of grains due to the larger lattice mismatch [2]. In order to solve these problems, buffer layers on MgO are effectively used. Since the properties of thin-film devices strongly depend on the microstructure, the selection of these buffer layers plays an important role in optimizing the properties of the device films. The interfaces are the key issues in controlling the microstructure of the multilayer systems. Usually, due to the differences in crystal structures of these buffer layer materials, lattice defects are introduced at the interfaces which can then propagate into and thus affect the microstructure of the device film layers [3, 4].

In the present work [5], we investigate the microstructure of $SrTiO_3/BaZrO_3$ (STO/BZO) bilayer films on MgO substrates using the negative Cs imaging (NCSI) technique [6]. With the NCSI technique it is possible to image chemical elements with low nuclear charge such as oxygen together with the surrounding cations. With the first buffer layer of BZO the rock salt structure surface of MgO is covered and the perovskite structure surface is prepared for the next perovskite layer. Due to the small lattice mismatch (0.24 %) no in-plane rotation of grains is expected. The second layer of STO served as a lattice-matching layer in order to fit well to the lattice of device films such as $YBa_2Cu_3O_{7-\delta}$ and $(Ca,Ba)Nb_2O_6$. In these systems, the first interface MgO/BZO connects two different structural lattices and the second interface BZO/STO accommodates a large lattice mismatch.

Figure 1a shows the BZO/MgO interface viewed along the [100] zone axis of MgO. The interface in the <100> projection can be identified, as marked by the dotted line, by checking the stacking sequence of the atomic planes in the interface area. Interfacial steps with a height of one unit cell of MgO can be seen. Moreover, an interfacial dislocation with the projected Burgers vector of $a/2[0\bar{1}1]$ (a is the cubic lattice parameter) occurs, as indicated by an arrow. Based on the fact that a displacement component of half a unit cell parameter, a/2[001], along the out-of-plane direction in the BZO films, this displacement does not introduce additional lattice defects like stacking faults, it can be concluded that the starting atomic plane of BZO on MgO changes from BaO to ZrO_2 across the dislocation core. Figure 1b shows a similar interfacial dislocation at the interface viewed along the $[1\bar{1}0]$ zone axis. In the <110> projection, the BZO and MgO lattice, i.e. the projected (001) planes of BaO, ZrO_2 and MgO, can be easily distinguished due to the difference in image contrast for different types of atomic columns. Thus the interface can be located, as marked by the dotted line. An interfacial dislocation with the displacement vector $a/4[\bar{1}\bar{1}2]$ is indicated by an arrow. This vector can be considered as the projected component in the $(1\bar{1}0)$ plane of the Burgers vector a/2<101> or a/2<111>. Checking the stacking of the atomic planes of MgO and BZO, the image clearly shows that an additional BaO layer exists on the left side of the dislocation. The starting atomic plane of the BZO layer on the MgO surface changes from the BaO plane to the ZrO_2 plane across the dislocation core.

Figure 2a shows an interface area of BZO/MgO viewed along the $[1\bar{1}0]$ zone axis. Interface steps with a height of half a unit cell exist along the interface. Across these steps the BZO film grows smoothly by changing the starting atomic planes on the MgO substrate. Figures 2b and 2c show magnified interface parts with different starting planes. In (b) the inter-

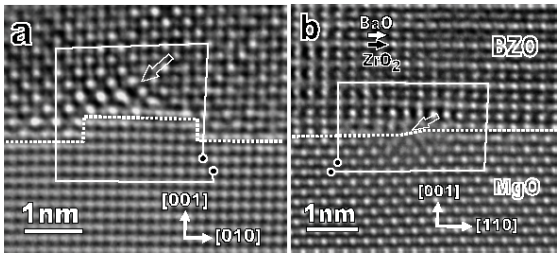

FIG. 1: Structure images of the interface areas between BZO and MgO viewed along (a) [100] and (b) [1$\bar{1}$0] zone axis. The interfaces of BZO/MgO are marked by dotted lines. Arrows denote the dislocations across which the interface changes structure from ZrO_2/MgO to BaO/MgO.

face has a structure with the BaO plane facing a MgO plane while at the interface in (c) the BZO layer connects with the ZrO_2 plane to MgO. The insets in (b) and (c) show simulated images based on structure models with the two types of interface configurations. The excellent match between the experimental and the simulated images supports the coexistence of the two types of interface structures. Besides the interface steps, an antiphase boundary (APB) is also observed in the image shown in fig. 2a, as denoted by a vertical arrow, starting from the interface between BZO/MgO and propagating into the BZO layer. At the starting point of the APB no interfacial step or other defect can be seen. This APB is recognized to relate to the change of the starting atomic plane of the BZO layer on MgO. To the right side of the APB a MgO plane faces the BaO atomic plane at the interface, while to the left side a MgO plane connects to the ZrO_2 plane.

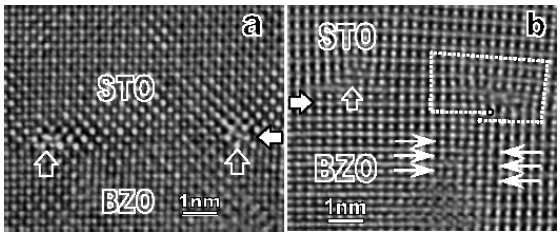

FIG. 2: (a) [1$\bar{1}$0] image of another interface area of BZO/MgO. The structure change of interface occurs across the interface steps with a height of half a unit cell. A vertical arrow shows an APB starting at the interface site where the interface structure changes. (b) Magnified image of the interface with a structure of BaO/MgO. (c) Magnified image of the interface with a structure of ZrO_2/MgO. The inserts in (c) and (d) show the corresponding calculated images for the specimen thickness of 4.0 nm and a defocus of +8.8 nm.

A typical area of the STO/BZO interface viewed along the [100] and [1$\bar{1}$0] zone axis is shown in fig. 3a and 3b, respectively. In fig. 3a, two misfit dislocations with Burgers vector of a[0$\bar{1}$0] can be seen at the interface as indicated by the vertical arrows. In fig. 3b, the a<100> misfit dislocation marked by the vertical arrow shows a projected Burgers vector of a/2[$\bar{1}\bar{1}$0]. An APB in the BZO layer terminates at a dislocation with a displacement vector of a/2[$\bar{1}\bar{1}\bar{1}$] at the interface of BZO/STO. The dislocation at the interface does not only accommodate the displacement of the APB, but also relieves the strain induced by the lattice mismatch. In the film system studied, it is found that the APBs induced at the BZO/MgO interface usually terminate in the dislocation at the STO/BZO interface. The high density of misfit dislocations at the STO/BZO interface plays a role in stopping the planar defects.

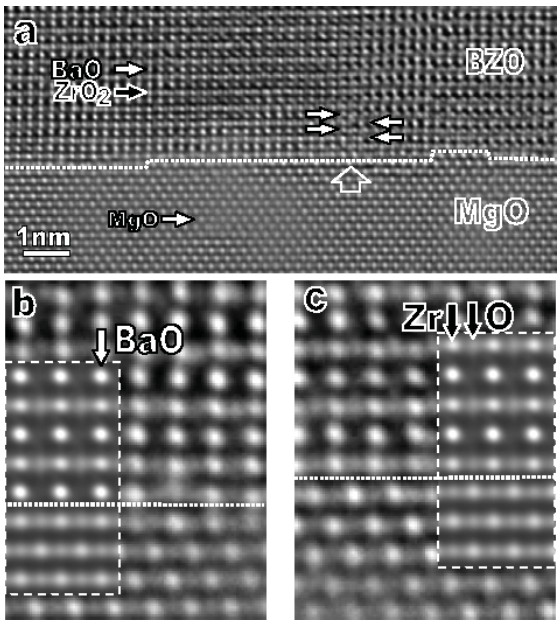

FIG. 3: Interface areas of STO/BZO viewed along (a) [100] and (b) [1$\bar{1}$0] zone axis. The horizontal arrows mark the interfaces. The a<100> type misfit dislocations at the interface of STO/BZO are indicated by vertical arrows. A Burgers circuit surrounds a partial dislocation which terminates an APB coming from the BZO layer.

In conclusion, with buffer of double layer, STO/BZO, we successfully prepare a relatively perfect surface for epitaxy of the next device film layer. Indeed, high-quality films of $YBa_2Cu_3O_{7-\delta}$ have been grown on such buffered MgO substrates [7].

[1] S.B. Mi, C.L. Jia, K. Urban, T. Heeg, J. Schubert, *J. Cryst. Growth* **291**, 243 (2006).

[2] B.H. Moeckly, S.E. Russek, D.K. Lathrop, R.A. Buhrman, J. Li, J.W. Mayer, *Appl. Phys. Lett.* **57**, 1687 (1990).

[3] C.L. Jia, X.H. Zeng, X.X. Xi, K. Urban, *Phys. Rev. B* **64**, 075416 (2001).

[4] S.B. Mi, C. L. Jia, T. Heeg, O. Trithaveesak, J. Schubert, K. Urban, *J. Cryst. Growth* **283**, 425 (2005).

[5] S.B. Mi, C.L. Jia, M.I. Faley, U. Poppe, K. Urban, *J. Cryst. Growth* **300**, 478 (2007).

[6] C.L. Jia, M. Lentzen, K. Urban, *Science* **299**, 870 (2003).

[7] M.I. Faley, S.B. Mi, A. Petraru, C.L. Jia, U. Poppe, K. Urban, *Appl. Phys. Lett.*, **89** 082507 (2006).

Self-Assembly of Mixed Monolayers of Mercaptoalkylferrocenes for Nanoscale Surface Patterning

S. Karthäuser[1,2], L. Müller-Meskamp[1,2], M. Homberger[3], U. Simon[3], R. Waser[1,2,4]

[1] IFF-6: Electronic Materials
[2] CNI: Center of Nanoelectronic Systems for Information Technology
[3] Institute of Inorganic Chemistry, RWTH Aachen
[4] Institut für Werkstoffe der Elektrotechnik II, RWTH Aachen

The self-assembly behaviour of a series of mercaptoalkylferrocenes embedded into ordered alkanethiol monolayers from solution is studied. Upon annealing, the inserted ferrocene derivatives form separated domains, which protrude as islands from the surrounding monolayer. The resulting thin films are characterized by UHV-STM and the density and the structure of the close-packed self-assembled monolayers is determined. Besides this the molecular structures of submonolayer phases of ferrocenes in mixed layers with alkanethiols are identified. The ferrocenes form a striped surface phase resulting in equispaced rows of ferrocene moieties. The obtained nanoscale lattice of functional groups offers interesting options for patterning of small, periodic surface structures with precise distance control via hydrocarbon spacers.

The fascinating power of molecular self-assembly is a promising tool for a possible integration of non-silicon technology into nanoelectronic devices [1]. A particularly well characterized system of self-assembled monolayers (SAM) is the system of alkanethiols on Au(111) substrates. These monolayers can be used to embed functional molecules into a mechanically stable and electrically insulating environment to study their electrical properties [2]. Especially interesting for future technological applications is the insertion of electroactive molecules like mercaptoalkylferrocenes. These molecules can be easily oxidized and reduced in solution and are well characterized by electrochemical methods [3], although the mercaptoalkylferrocenes tend to aggregate and form multilayers [4]. Therefore, to achieve stable layers with better defined properties, we inserted the mercaptoalkylferrocenes into SAMs of alkanethiols with an accordant molecular length and studied the structural properties of the mixed monolayers by UHV-STM [5-7].

Mixed monolayers of mercaptoalkylferrocenes and alkanethiols were assembled in a two step deposition process from ethanolic solutions onto crystalline, (111)-oriented Au thin-films on mica. This method starts from a preassembled close packed SAM consisting of insulating alkanethiols which is dipped in a second step into a solution of the electronically active molecules. During this step a moderate heating is performed to improve the quality of the monolayer. Structural investigations and scanning tunnelling spectroscopy were performed with a JEOL 4500 UHV-STM at a base pressure of 1×10^{-10} mbar.

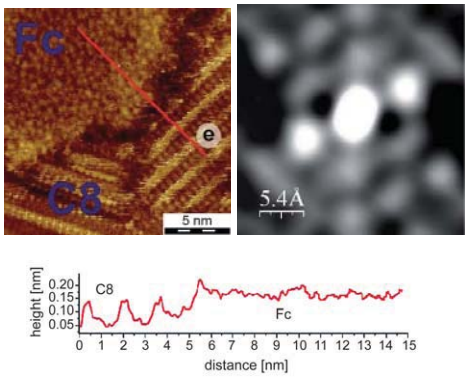

FIG. 1: 1,1"-dithiobis-ferrocene (Fc) inserted into an octanethiol (C_8) monolayer, showing the characteristically striped structure of lying-down alkanethiols and the disordered texture of the Fc-domain (left upper part). Upper right part: The self-correlation of the Fc-island structure indicates a loose hexagonal order. Lower part: profile of the octanethiol monolayer (C_8) and the Fc-monolayer (Fc).

The thus insertion processed, mixed monolayers of 1,1"-dithiobis-ferrocene (Fc) and octanethiol (C8) show two domain types differing in their surface structure (Figure 1). One displays the characteristic surface structure of an octanethiol SAM with a striped/lying-down phase while the second domain type, formed during insertion and annealing, consists of ferrocenes. From the homogenous height of the Fc-island a layer thickness of exactly one monolayer can be deduced. Autocorrelation of the Fc-island structure shows a weak hexagonal order and an average distance of 0.67 nm between the centres of two nearest neighbours. Assuming that the Fc's can be considered as small spheres in a hexagonal arrangement, an average surface area of 0.39 nm^2 per molecule is calculated. This phase separation, already taking place at moderate annealing conditions, indicates a high mobility of the embedded Fc's and a lower tendency for ferrocene-alkanethiol intermolecular interaction.

Analogous to the insertion of the Fc-molecules mercaptoalkylferrocenes with various alkane

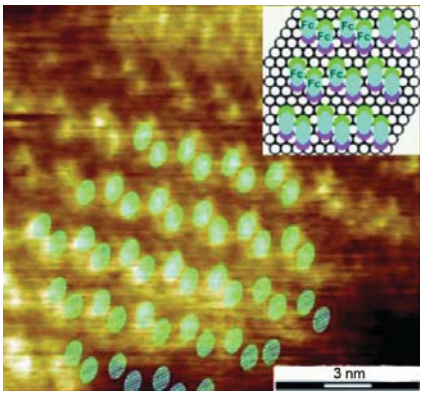

FIG. 2: Crystalline domain of bis-mercaptoundecanoyl-ferrocene ($Fc(OC_{11})_2$) embedded into an undecanethiol SAM (C_{11}) and the schematic of the suggested placement for the $Fc(OC_{11})_2$ molecules with respect to the gold lattice (inset). The green and pink dots represent the chemisorbed spacer groups, the bright blue ovals the associated ferrocene moiety.

spacer chains were inserted into an undecanethiol-monolayer (C_{11}). The mixed layers show the highly ordered SAM structure of alkanethiols and small islands of the ferrocene-derivatives with a crystalline order and a surface structure of elongated shapes, assumed as single ferrocene moieties (Figure 2). The resulting area of 0.7 nm^2 per molecule seems reasonable, compared to 0.39 nm^2 for Fc. An obvious feature of the ordered islands is the pairing of the ferrocene end-groups on the surface and since each ferrocene moiety of $Fc(OC_{11})_2$ is associated with two alkane spacer-chains, the four alkanethiol chains are identified to be in the same arrangement as in a c(4×2) unit cell. Besides the phase separated islands a number of spots is observed, indicating the existence of individual ferrocenes in the C_{11} monolayer. This hindered interdiffusion is attributed to the intermolecular interaction between the alkane chains of the ferrocene derivatives and the host matrix.

For layers deposited from mixed solutions with a long insertion step at elevated temperatures, partially desorbed structures are found. In difference to the layers compared so far, the alkanethiols as well as the ferrocene derivatives are flat-lying on the surface, forming striped domains with varying orientations and line spacings. Diverse striped structures can be distinguished which differ in texture between the prominent rows, pointing out different phases and defects, as shown in Figure 3. The double row structures appear frequently on the surface and show line spacings dependent on the ferrocene derivative incorporated. From comparison of the height profiles for alkanethiols and mercaptoalkylferrocenes a replacement of alkanethiols by mercaptoalkylferrocenes is deduced with the thiol headgroup and the alkane spacer of the ferrocene compounds being positioned in the same way as in a striped alkanethiol phase. The ferrocene endgroups point to the center, forming a double row, and the thiol headgroups build bright pairs with the next row.

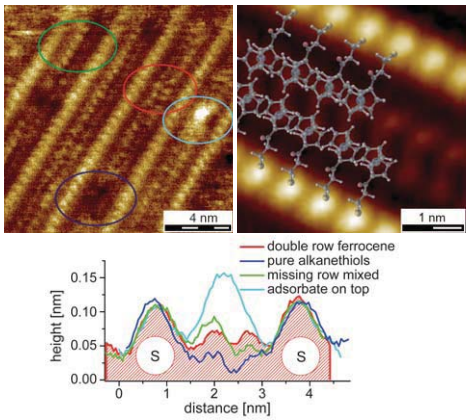

FIG. 3: Top left: A view of the different striped structures observed for mercaptopropanoyl-ferrocene ($FcOC_3$) is shown. The dark blue circle marks a missing central feature, the red one a double row, the green a single row, and the light blue additional adsorbates. Top right: A filtered STM scan of the lying-down, double row structure with the assumed molecular arrangement is given. Bottom: The profiles of the different structural variations of the lying-down phases marked in the left image are displayed.

In this report real space structural information of chemisorbed ferrocenes inserted into alkanethiol monolayers is given. For ferrocenes without spacer-chains, a strong tendency for phase separation and only slightly ordered structures are found, while crystalline domains are observed for ferrocenes with longer spacer chains. For lower coverage an interesting structure of lying-down ferrocenes and alkanethiols forming nanoscale pattern is obtained, whose period is shown to be defined by the length of the lying-down molecule. Thus the period of the structure can be controlled by the alkane spacer length, while the functionality of the ferrocene endgroup is still accessible. It can be concluded that in general it will be possible to generate striped surface structures with adjustable distances and desired chemical functionalities by systematic modification of an alkanethiol spacer and by using a customized endgroup.

[1] M. Homberger, S. Karthäuser, U. Simon, and B. Voigtländer, "Formation of Nanostructures by Self-Assembly" in "Information Technology" ed. by R. Waser, Wiley (2008).

[2] Z. Donhauser et al., Science **292**, 2303-2307 (2001).

[3] C. Chidsey, C. Bertozzi, T. Putvinski, and A. Mujsce, J. Am. Chem. Soc. **112**, 4301-4306 (1990).

[4] A. Viana, L. Abrantes, G. Jin, S. Floate, R. Nichols, and M. Kalaji, Phys. Chem. Chem. Phys. **3**, 3411-3419 (2001).

[5] L. Müller-Meskamp, B. Lüssem, S. Karthäuser, S. Prikhodovski, M. Homberger, U. Simon, and R. Waser, Phys. Stat. Sol. **203**, 1448-1452 (2006).

[6] L. Müller-Meskamp, B. Lüssem, S. Karthäuser, M. Homberger, U. Simon, and R. Waser, J. Phys. Conf. Ser. **61**, 852 (2007).

[7] L. Müller-Meskamp, S. Karthäuser, R. Waser, M. Homberger, and U. Simon, Langmuir accepted.

First-Principles Investigation of Terephthalic Acid on Cu(110)

N. Atodiresei[1], V. Caciuc[2], K. Schroeder[1], S. Blügel[1]

[1] IFF-1: Quantum Theory of Materials
[2] Physikalisches Institut, Westfälische Wilhelms Universität Münster

We performed first-principles calculations within the density functional theory aimed to investigate the two-dimensional geometry of one monolayer of terephthalic acid (TPA) adsorbed on Cu(110) surface. The key issue of our study is to elucidate if the molecule-molecule interactions include a hydrogen bond since such a bond would hinder the possibility to chemically functionalize this surface. Our simulated STM images help to experimentally discriminate between the TPA–Cu(110) geometries considered in our study.

The development of technologies based on molecular organic semiconductor materials have been proven to lead to reliable devices such as organic light-emitting diodes (OLEDs) commonly used in flat display industry. To circumvent the limits of a silicon-based microchip technology, special attention was focused on the development of electronic devices based on organic molecules. A very popular approach to construct such molecular electronic devices is to choose molecules that possess specific electronic properties and try to attach them between metallic or semiconductor leads. The practical success of this approach relies on hope that after adsorption the specific molecular properties will remain or that new properties with possible technological applications will be induced in the adsorbed molecules or at the molecule-substrate interface.

A much more systematic approach to construct reliable molecular electronic devices is to develop methods to *selectively* change the functionality of specific molecules adsorbed on surfaces. In this case one can use molecules that have several functional groups such that one of them can be utilized to anchor the molecules at the surface. The other functional groups are employed to modify *in situ* the molecular structure by reacting it with other specific molecules by means of well-known chemical reactions and so to induce the desired electronic properties in the molecular electronic device.

Recently, the practical possibility to chemically functionalize the Cu(110) surface upon adsorption of terephthalic acid (TPA) was experimentally investigated. It was shown that in the limit of low-coverage the TPA adopts a flat-lying adsorption geometry while in the case of high-coverage it undergoes a deprotonation process of one carboxylic group (COOH)

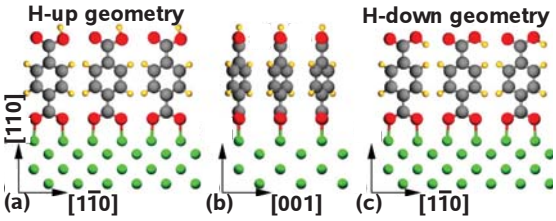

FIG. 1: Ball-and-stick model of the TPA adsorbed on Cu(110) surface. **(a)** At high coverage, the TPA molecule adsorbs with an upright orientation with the carboxylate groups (COO) aligned along $[1\bar{1}0]$ direction. In the adsorption configuration with lowest energy the H atom of the carboxylic group (COOH) is pointing towards the vacuum. **(b)** The lateral interactions between adjacent TPA molecules induces a rotation of the benzene ring (C_6H_4) with respect to the carboxylate plane by an angle of 24.7°. **(c)** Starting from a configuration with a hydrogen bond between two adjacent TPA molecules, the relaxed geometry is characterized by a H–O bond in the plane of the carboxylic group pointing towards the benzene ring.

which leads to an upright adsorption geometry. The latter case is of particular interest in the context of the surface functionalization process since only in this case the second carboxylic group of TPA is located at the vacuum interface (see Fig. 1(a)) and thus a substitution of the hydrogen or hydroxyl group (OH) by other organic molecules becomes possible.

Our *ab initio* study is performed within the framework of density functional theory (DFT) employing the generalized gradient approximation (GGA) for exchange-correlation energy functional. The Kohn-Sham equations have been solved self-consistently using the projector augmented-wave method (PAW). The Cu(110)-(2×1) surface was modeled by a periodic slab geometry. In each supercell, the slab consists of seven copper atomic layers and at each side of the slab one TPA molecule was adsorbed. The equilibrium geometry of the TPA-Cu(110) system was obtained by imposing an accuracy of the calculated Hellmann-Feynman forces better than 1 mRy/(atomic unit).

In the case of high-coverage, the TPA adsorbs with the oxygen atoms on top of copper ones in a densely packed p(2×1) phase and the bonding mechanism is similar to that evidenced for the adsorption of several

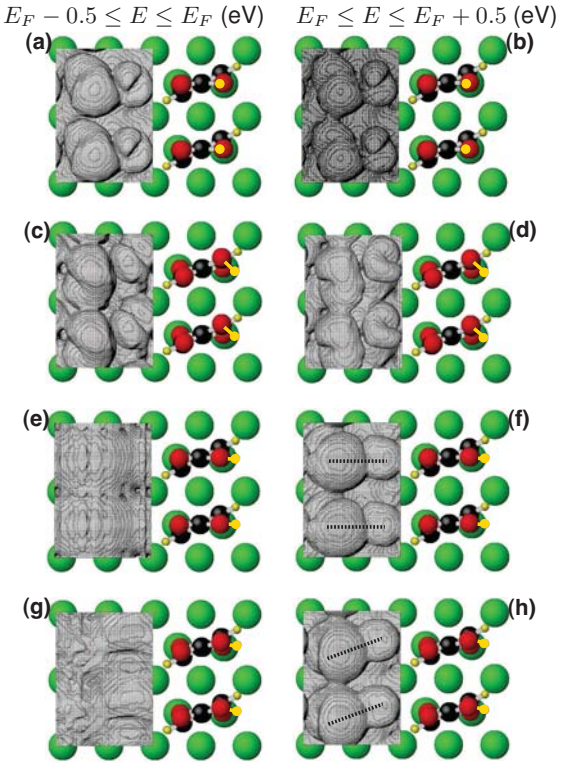

FIG. 2: The calculated constant-current STM images of one TPA monolayer chemisorbed on Cu(110) surface for an applied bias voltage of ± 0.5 eV. On the left the STM images correspond to the occupied states while those on the right describe the unoccupied ones. Four different adsorption geometries have been considered: H-up (a,b), H-up parallel (c,d), H-down (e,f) and H-down parallel (g,h).

monocarboxylic acids on Cu(110) surface. However, less information is known about the two-dimensional order induced by molecule-molecule interactions. In particular, it is not clear if a dimerization process involving the adsorbed TPA molecules takes place in this case. This is a critical aspect since a hydrogen bond between the TPA molecules adsorbed on Cu(110) surface would possibly hinder the functionalization of this surface. Therefore, the basic goal of our study is to elucidate the two-dimensional order of one TPA monolayer adsorbed on Cu(110) surface with a special emphasis on the geometrical structure of the carboxylic group. Our simulations show that the structure without a hydrogen bond (see Fig. 1(a)) is energetically more stable than that which would present such a bond. More precisely, a dimerized TPA-Cu(110) configuration with a hydrogen bond is structurally unstable and it relaxes to a geometry which exhibit an H–O bond in the carboxylic group plane oriented towards the benzene ring (see Fig. 1(c)). The total-energy of this adsorption configuration is slightly higher ($\approx$ 0.08 eV) than that with an H–O bond pointing towards the vacuum interface. This small energy difference opens the possibility that the hydrogen atom can fluctuate between these configurations. In consequence we verified if such a process can take place by evaluating the energy barriers separating these geometries. Even if such a transition has a small rate at room temperature, it can be accelerated by applying a voltage via an STM tip like in a controlled nanomanipulation process.

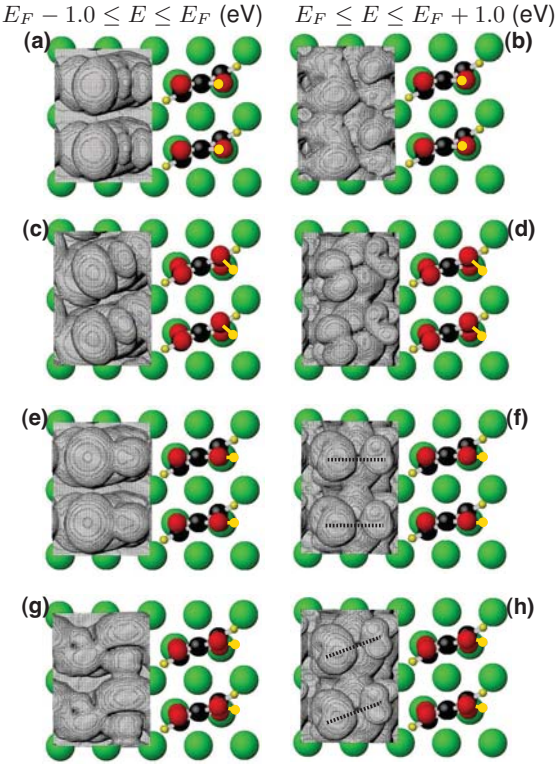

FIG. 3: The simulated constant-current STM images of one TPA monolayer chemisorbed on Cu(110) surface for an applied bias voltage of ± 1.0 eV. The order of the STM images is the same as in Fig.2.

By calculating the lateral variation of the energy integrated LDOS, we have simulated the STM images for all TPA adsorption configurations under consideration to provide a connection to experiments (see Figs. 2, 3). The simulated images exhibit larger differences for the considered adsorption geometries when imaging the occupied states compared to the unoccupied ones. By tuning the bias voltage the differentiation between the configurations could be appreciably enhanced and thus it is possible to unambiguously identify in experiments which specific TPA–Cu(110) geometry is investigated. It is also important to note that for an applied bias voltage of ± 0.5 eV our simulations predict that only H-up and H-up parallel adsorption geometries can be imaged by STM.

[1] D. S. Martin, R. J. Cole, and S. Haq, Phys. Rev. B **66**, 155427 (2002).

[2] N. Atodiresei, S. Blügel, and K. Schroeder, Phys. Rev. B **75**, 155407 (2007).

[3] N. Atodiresei, S. Blügel, and K. Schroeder, Phys. Rev. B **76**, 155433 (2007).

Post Processes for Bioelectronic CMOS Devices

S. Ingebrandt[1,2], M. Schindler[1,2], S. Meyburg[1,2], R. Stockmann[1,2], J. Moers[1,3], S. K. Kim[4], C. S. Hwang[4], C. Schindler[1,5], A. Offenhäusser[1,2]

[1] CNI: Center of Nanoelectronic Systems for Information Technology
[2] IBN-2: Bioelectronics
[3] IBN-1: Semiconductor Nanoelectronics
[4] Department of Materials Science and Engineering, Seoul National University, Seoul, Korea
[5] IFF-6: Electronic Materials

Sensors, which are designed and fabricated in complementary metal oxide semiconductor (CMOS) technology, have become increasingly important in the field of bioelectronics. The standardized industry processes enable a fast, cheap and reliable fabrication of biosensor devices with integrated addressing and processing units. However, the interfacing of such chips with a liquid environment has been a challenge in recent years. Especially for interfacing living cells with CMOS biosensors different elaborate post-processes have been proposed. Here we describe the different approaches for stable passivation of CMOS-like and CMOS biosensors, which we recently conducted in our institute.

Interfacing devices fabricated in modern CMOS processes with biological systems is in the focus of intense research [1-4]. An industry CMOS process enables the design of high-density biosensors combined with on-chip mixed signal circuitry for amplification, filtering and analog-to-digital conversion. For the stable passivation of the sensor chips for various bioelectronic applications in our institute, we conducted several different approaches in the past. Our standard field-effect transistor (FET) chips for interfacing with living cells have implanted feed lines, which can be easily passivated in a three layer stack of wet silicon oxide followed by low pressure vacuum deposition (LPCVD) of silicon nitride and silicon oxide [5]. This fabrication protocol, however, is not compatible with standard CMOS. Therefore, we recently focused on the development of post processes for CMOS biosensor chips based on floating-gate FET (FG-FET) structures as sensor input.

In a first step we fabricated CMOS-like sensor chips in our institute's cleanroom, in which we were able to adapt and modify certain steps [6]. The basis of this CMOS process was adopted from the Microfabrication Laboratory, University of California at Berkeley (4" Baseline CMOS Process, Version 5.0, Nov. 1997, 1.3 μm, twin-well, double poly-Si, double metal, http://microlab.berkeley.edu). In order to achieve a stable passivation of the devices against electrolyte solutions, we included additional fabrication steps and materials into our process. Main changes to the standard CMOS process were the substitution of aluminium by titanium silicide for all interconnects, the application of an additional passivation layer formed by LPCVD of silicon nitride and silicon oxide, and an oxidation step for the sensing areas. A schematics of the floating-gate structure and the layer stack of our CMOS-like chip is shown in Fig.1A. In Fig.1B a photograph of a FG-FET chip with an array of 32×32 sensors is shown.

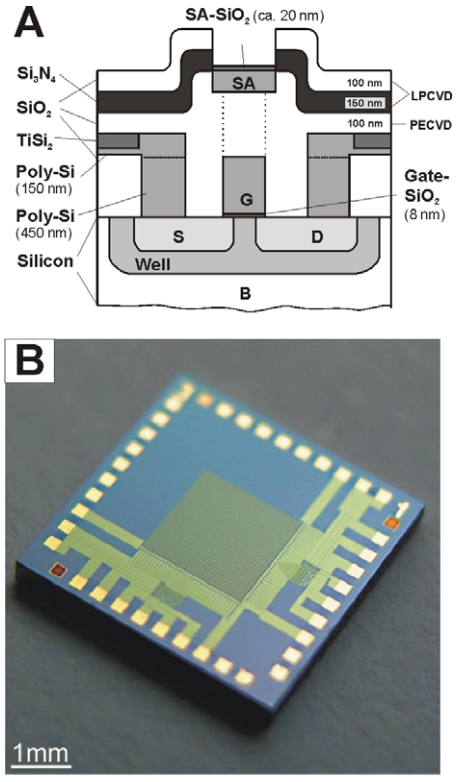

FIG. 1: (A) Cross section of a FG-FET sensor (not to scale). The lower part shows the silicon bulk (B), which was implanted by respective well, source (S) and drain (D) implantations. Lower gate oxide thickness was 8 nm (dry oxidation of silicon). The upper sensor area (SA) for interfacing with living cells was made from polysilicon, which was oxidized with 20 nm SiO_2 in a rapid thermal annealing process at 800°C. Contact lines were made from polysilicon, which was silicided outside of the FG-FET structures with titanium. A stable passivation of these contact lines was achieved by the use of plasma enhanced chemical vapor deposition (PECVD) of oxide, LPCVD of nitride, and LPCVD of oxide. B: Photograph of a chip with an array of 32×32 FG-FETs. Rows and columns can be addressed with two 5 bit decoders.

In a second step we developed in cooperation with

the Department of Materials Science and Engineering, Seoul National University, Korea, a novel and single step passivation of a CMOS biosensor using a bio-compatible high-permittivity thin film [7]. The passivation layer can be directly applied to the top aluminium layer of a CMOS process.

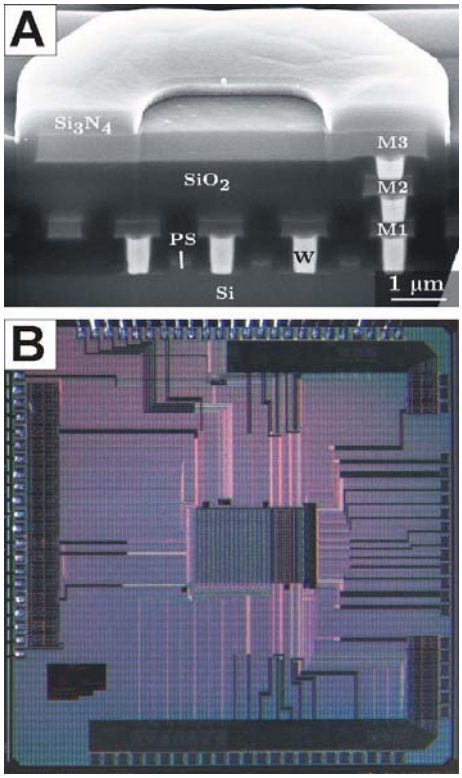

FIG. 2: A: Cross section through a pixel in the CALIBUR sensor array etched by using a FIB. In this scanning electron micrograph the aluminium interconnect layers (M1, M2, and M3) and the polysilicon gates (PS) on top of the silicon dye (Si) and the tungsten plugs (W) are visible. B: Image of the CALIBUR chip. The sensor array with 64×64 pixels can be seen in the center. To the right side the amplifier units are attached to the array.

The post process was developed to be applied to our recently fabricated CMOS sensors array with 64Œ64 sensor pixels capable of cell stimulation and recording at an interpixel pitch of only 12.5 μm (CALIBUR). In Fig 2A a cross section of a single pixel out of the FG FET array and in Fig 2B the microscopy image of the chip layout can be seen. Since it was fabricated in a complete CMOS process, the use of aluminium as interconnect layer was unavoidable. Therefore we developed a simple and single step passivation process for this chip [7]. The demands for the passivation layer were high capacitance, low leakage current in electrolyte, best biocompatibility and moderate process temperatures. We chose a layer sandwich of aluminium oxide and hafnium oxide prepared using atomic layer deposition at only 250°C. Electrical IV and capacitance measurements as well as electrochemical leakage current measurements were performed on films grown on aluminium bottom electrodes as test chips. At a thickness of only 50 nm the films showed a very low leakage current and were stable up to 6 V (Fig 3B). They had high capacitance (about 0.2 μF/cm^2) and a good biocompatibility (Fig.3A).

In future we will optimize and expand this process to the wafer level to obtain enough chips for upcoming cell measurements.

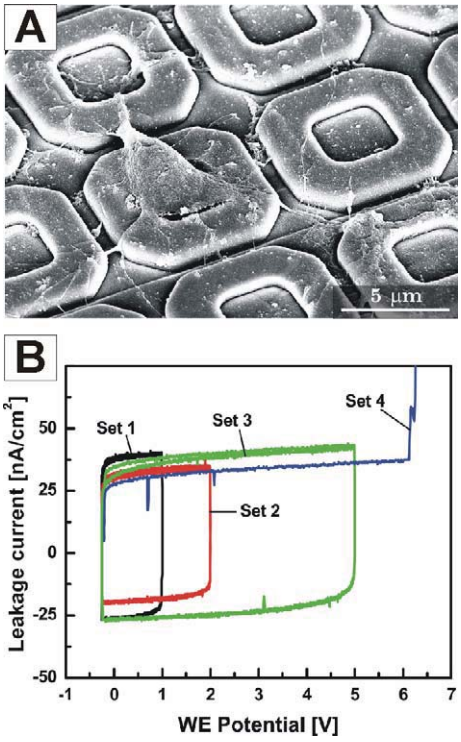

FIG. 3: A: Scanning electron micrograph of a rat cortical neuron on the sensor input structure of the CALIBUR chip, which was passivated by an AO/HO multilayer. B: Electrochemical IV characteristics of a 50 nm AO/HO multilayer.

Acknowledgements: We thank R. Helpenstein and B. Hofmann for cell culture and SEM fixation, D. ESSer for the FIB preparation, and M. Banzet for the silicon test chips. Financial support came from the DFG-Graduiertenkolleg 1035 "Biointerface" and from the Volkswagen Stiftung.

[1] J. Bausells, J. Carrabina, A. Errachid, and A. Merlos, Sens. Actuator B-Chem. **57**, 56 (1999).

[2] B. D. DeBusschere, and G. T. A. Kovacs, Biosens. Bioelectron. **16**, 543 (2001).

[3] F. Hofmann, B. Eversmann, M. Jenkner, A. Frey, M. Merz, T. Birkenmaier, P. Fromherz, M. Schreiter, R. Gabl, K. Plehnert, M. Steinhauser, G. Eckstein, and R. Thewes, ESSDERC 2003, Proc. 33rd European Solid-State Device Research Conference, New York 2003, p. 167.

[4] F. Heer, W. Franks, A. Blau, S. Taschini, C. Ziegler, A. Hierlemann, and H. Baltes, Biosens. Bioelectron. **20**, 358 (2004).

[5] A. Offenhäusser, C. Sprössler, M. Matsuzawa, and W. Knoll, Biosens. Bioelectron. **8**, 819 (1997).

[6] S. Meyburg, R. Stockmann, J. Moers, A. Offenhäusser, and S. Ingebrandt, Sens. Actuator B-Chem., **128**, 208 (2007).

[7] M. Schindler, S.K. Kim, C.S. Hwang, C. Schindler, A. Offenhäusser, and S. Ingebrandt, phys.stat.sol. (RRL), **2**, 4 (2008).

UV-Nanoimprint Lithography with Polymer Molds

S. Gilles[1,2], D. Mayer[1,2], M. Prömpers[1,2], M. Meier[1,3], C. Kügeler[1,3], A. Offenhäusser[1,2]

[1] CNI: Center of Nanoelectronic Systems for Information Technology
[2] IBN-2: Bioelectronics
[3] IFF-6: Electronic Materials

UV-Nanoimprint Lithography (UV-NIL) is considered as emerging lithography technology for future nanofabrication. To make the method affordable polymers are demanded as alternative low-cost mold materials. In this report, a UV-NIL process with molds made of polymer materials novel for this application is demonstrated. These polymers were found to show high performance in the patterning with UV-NIL. Imprinted structures with feature sizes of sub-50-nm are shown.

Patterning of surfaces in the nanometer range is a key issue in both nanoscience and nanotechnology. Nanoimprint Lithography (NIL) has been an emerging technology for future nanofabrication since it was introduced by Chou et al. in 1995 [1]. NIL is considered to be an alternative to Optical Lithography (OL) and Electron Beam Lithography (EBL) by combining the advantages of high resolution, low costs and high throughput. Particularly, UV-based NIL (UV-NIL) [2] appears to be promising for the production of patterns in the sub-50-nm range for having the advantage of processing at room temperature in contrast to thermal NIL. Thereby problems arising in connection with thermal stress are circum-vented.

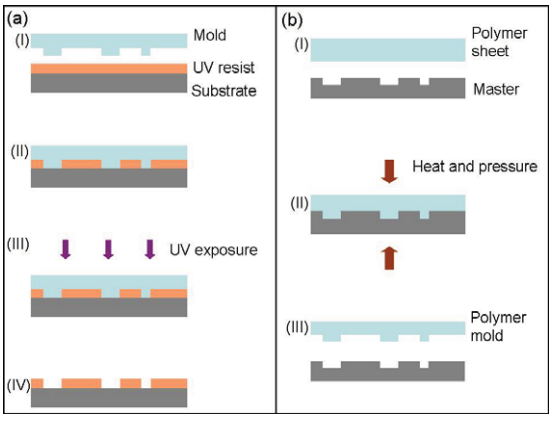

FIG. 1: Schematic process of UV-NIL (a) and Hot Embossing (b).

NIL is based on an embossing principle. The main process steps of UV-NIL are shown in Figure 1a. First, a liquid precursor is applied as resist to a substrate by spin coating. A structured mold is pressed into the resist layer forcing the fluid to flow into the cavities. In the next step, the monomeric molecules in the precursor cross-link by exposure to UV light to form a cured polymeric film. The mold is separated from the cured resist, leaving a negative copy of the mold surface. The structures can be transferred into the underlying layers or be used as functional pattern themselves.

A UV transparent mold is required due to the fact that the resist is cross-linked by the exposure to UV light. Commonly, quartz or silica molds with nanoscale surface-relief features are fabricated by EBL. During the EBL process charging of the mold surface can occur due to the nonconductive nature of the dielectric materials. This charging effect can severely distort the electron beam and affect the pattern resolution and fidelity [3]. Hence effort has to be spent on avoiding this effect. Altogether, the fabrication of these molds remains difficult and expensive. Since the mold fabrication is considered to be the bottleneck in pushing UV-NIL towards a profitable industrial method [4], alternative approaches are highly demanded. Potential substituents for quartz or silica are UV transparent polymer materials. Elastomers [5] as well as plastomers [6] have been successfully tested for UV-NIL with sub-100-nm resolution. Especially stiffer plastomeric materials are promising due to their similarity to silicon in means of mechanical properties. The applicability of a polymer as mold material depends furthermore on its surface properties. The surface energy should be low, so that the mold can be easily released from the substrate after the imprint without rupture of sticky resist fractions. The feasibility to fabricate numerous polymer molds with the aid of a single master makes the expensive master production affordable. The whole mold process becomes cost-effective.

To create a polymer mold, first a master with negative form of the desired mold is fabricated by conventional lithography. A silicon master (Figure 2a) containing structures of lines and spaces with widths ranging from 1000 to 75 nm was used for the formation of the polymer molds. To ensure the separation between mold and master, the master was coated with a layer of 1H,1H,2H,2H-perfluorooctyltrichlorosilane as release agent by chemical vapor deposition.

The plastic mold can then be replicated from the master by Hot Embossing as shown in Figure 1b.

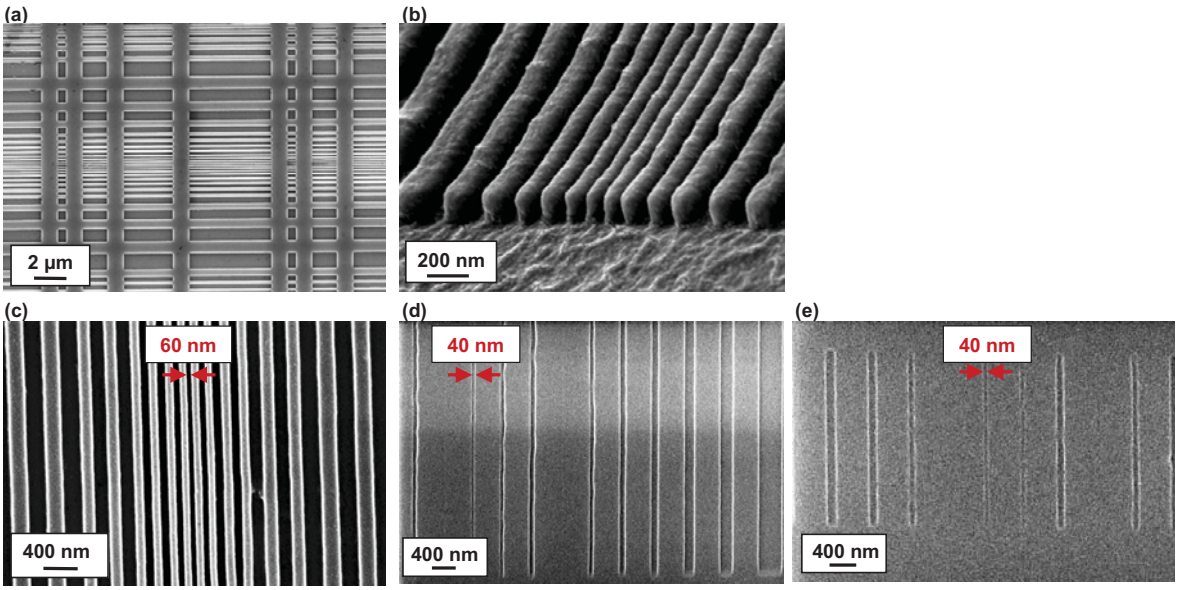

FIG. 2: SEM images illustrating a Nanoimprint procedure: Silicon master with test structure cavities (a), Surlyn mold covered with a sputtered gold layer under an observation angle of 60° (b), structures imprinted with Surlyn (c,d) or Fluon (e) molds in UV resist.

Polymer sheet and master are pressed together at a temperature above the glass transition temperature of the polymer. After cooling down to room temperature, the embossed polymer mold is peeled off the master. The plastomers Surlyn 1702 (DuPont) and Fluon ETFE (Asahi Glass Company) were used as mold materials. Surlyn is an ethylene/methacrylic acid copolymer and was recently found to be appropriate for creation of nanoscale features by Soft Lithography [7]. Due to its stiffness (Young's modulus approx. 190 MPa), even small relief structures are not deformed during the imprint process. Fluon ETFE is an ethylene tetrafluoroethylene material that is also used as protective film for solar cells due to its good UV transparency. For each mold, the material was pressed against the silicon master with a pressure of 2 bar (Surlyn) or 7 bar (Fluon) and a temperature of 120°C (Surlyn) or 240°C (Fluon) for 5 minutes. A nanoimprint tool NX2000 from Nanonex Corp. was used for the Hot Embossing procedure. An image of a Surlyn mold (coated with a sputtered gold layer for SEM measurement) is shown in Figure 2b. It can be seen from the image that even smallest protrusions of the mold were exactly replicated, upright standing and separated. The high surface roughness visible in this image is assumed to be caused by the gold deposition. This is confirmed by measurements of the following imprint step, where the replicated structures did not show such roughness (Figure 2c,d).

Prior the nanoimprint, the silicon substrates were first coated with a PMMA based under layer resist Nanonex NXR-3010 and subsequently with Nanonex UV resist NXR-2010. The use of an under layer resist is mandatory in order to promote adhesion between substrate and UV resist. Inside the NX2000 the mold was pressed into the resist with a pressure of 38 bar. During this process the test pattern with structures down to 60 nm separated by gaps of 90 nm was transferred into the resist (Figure 2c). In advancing experiments with even smaller patterns it was possible to replicate single line structures down to 40 nm (Figure 2d,e). Good agreement between original and transferred patterns was obtained. The patterning resolution is rather limited by the mold fabrication than by the nanoimprint process itself. No ripping off of resist was observed for all experiments.

In summary, we demonstrated UV-Nanoimprint Lithography with molds made of polymer materials novel for this application. Stiffness, UV transparency and surface energy of the polymers Surlyn and Fluon were found to be appropriate for the purpose of UV-NIL. Patterning in the sub-50-nm range was achieved by the demonstrated process. Finally, we conclude that the chosen plastomers are well suited as mold materials for fabrication of nanopatterns by UV-NIL.

Acknowledgement: D.Schwaab

[1] S.Y. Chou, P.R. Krauss, P.J. Renstrom, *J. Vac. Sci. Technol. B* **14**, 3114 (1996)

[2] M. Colburn, S. Johnson, M. Stewart, S. Damle, T. Bailey, B. Choi, M. Wedlake, T. Michaelson, S.V. Sreenivasan, J. Ekerdt, C.G. Willson, *Proc. SPIE* **3676**, 379 (1999)

[3] L.J. Guo, *Adv. Mater.* **19**, 495 (2007)

[4] M.Watts, *Impattern Solutions Inc.*, NaPa Day 2007

[5] N.Koo, M.Bender, U.Plachetka, A.Fuchs, T.Wahlbrink, J.Bolten, H.Kurz, *Microelectron. Eng.* **84**, 904 (2007)

[6] D.Y. Khang, H.H. Lee, *Langmuir* **20**, 2445 (2004)

[7] D. Schwaab, *Dissertation*, RWTH Aachen University (2006)

Crossbar Array Architectures With Embedded Bottom Electrodes Fabricated With UV Nanoimprint Lithography

M. Meier[1,3], S. Gilles[2,3], C. Nauenheim[1,3], D. Mayer[2,3], A. Rüdiger[1,3], C. Kügeler[1,3], R. Waser[1,3]

[1] IFF-6: Electronic Materials
[2] IBN-2: Bioelectronics
[3] CNI: Center of Nanoelectronic Systems for Information Technology

UV nanoimprint lithography (UV NIL) is used to realize crossbar structures which are suitable for next generation memory and logic devices. These devices are built by a resistance switching material sandwiched between two perpendicularly arranged metal nanoelectrodes. The advantage of such architecture in addition to its simplicity is the high integration density. Crossbar arrays with 200 nm electrodes and single cross junctions with 30 nm electrodes width were achieved. The bottom electrodes were embedded and planarized by spin on glass, such that an even surface for the realization of the top electrodes by UV NIL could be obtained. Electrical measurements were used to prove the concept of crossbar array devices fabricated with nanoimprint.

Nanoimprint lithography (NIL) is a suitable tool for next generation lithography applications [1]. It convinces with its high throughput potential due to a parallel process as well as the possibility of nanometer resolution. UV NIL was used to fabricate nanosized devices, respectively nanocrossbar arrays [2].

The device includes two layers of metal lines arranged perpendicular to each other. Future applications of crossbar arrays are memory and logic devices, where functional materials (e.g., WO_3, TiO_2, NiO, $Ge_{0.3}Se_{0.7}$) are integrated in between the two metal electrodes. Hence, one single cross can act as a memory cell since the material in between the electrodes can be switched to a high or low resistive state by applying an electrical potential to the electrodes of the crosspoint. Two resistive states represent a logical "1" or "0" in a binary memory or logic system.

By scaling the individual crosses down to the nanometer range the integration density of crossbar arrays is increased. With nanoimprint lithography a reduction of the critical dimension of crossbar arrays can be achieved [3], [4]. UV imprint is used for patterning the electrode metal by employing a Nanonex-2000 imprint system which is using an air-cushion press to apply a homogenous distributed pressure to wafer and mold [5].

The molds for UV NIL were fabricated by e-beam lithography followed by a CF_4 reactive ion beam etching process on transparent four inch SiO_2 wafers. An Ionfab300^{plus} system from Oxford Instruments was used for all etching processes. The surface of the mold was coated with an anti adhesion layer (a 1H,1H,2H,2H-perfluorodecyltrichlorosilane) in order to support his release from the substrate after the imprint process.

A four inch Si/SiO_2 wafer with a top layer of 30 nm Pt was used as starting system for the fabrication of crossbar arrays. A double layer resist stack from Nanonex consisting of a 200 nm thick PMMA based under layer and a 100 nm thick UV sensitive top layer resist was spin-coated on the wafer. During imprint the liquid top layer resist crosslinks by applying UV light and converts into a solid polymer which replicates the structures of the mold. After structuring the bilayer resist in a two step dry etching process with CF_4 and O_2 the patterns were transferred into the underlying 30 nm thick Pt layer by Ar sputtering. The fabrication of the bottom electrodes was accomplished by ashing residuals of resist in oxygen plasma.

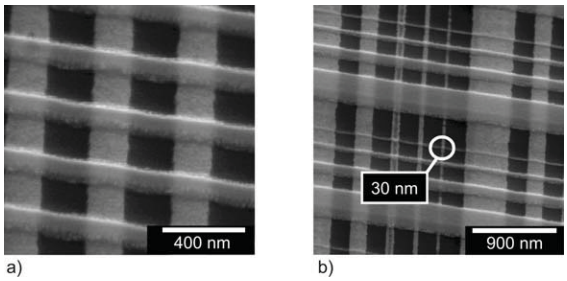

a) b)

FIG. 1: a) Crossbar array with embedded bottom electrodes fabricated with UV NIL, 200 nm line width, 30 nm metal thickness, b) Test cross junctions with embedded bottom electrodes, line width from 500 nm down to 30 nm, 30 nm electrode thickness.

A challenge during the fabrication of crossbars occurs due the uneven surface of the bottom electrode containing wafer. The top electrodes could include steps at the crosspoints of the electrodes due to the overlap of bottom and top structures. This promotes the risk of short circuit formations or enhanced electrical fields at these steps during the operation of the crossbar array. One solution is the embedding of the bottom electrodes. The bottom electrodes were pla-

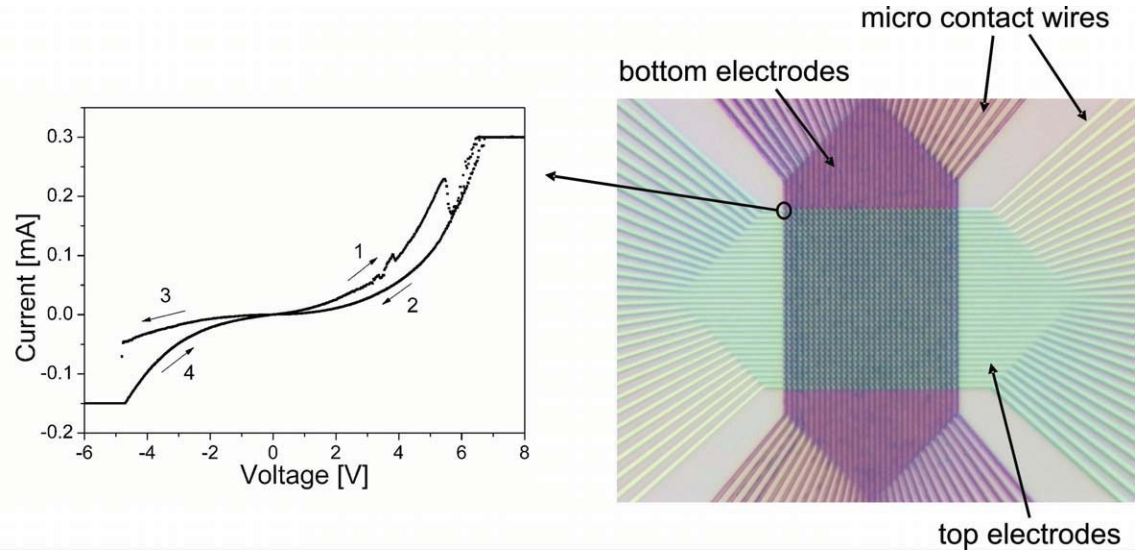

FIG. 2: I/V-curve (left side) of a corner cell measured at a 1024 bit array (optical microscope image, right side). The dimension of the cross junction is 500 x 500 nm^2.

narized with spin on glass (ACCUGLASS T-111; Honeywell). The spin on glass was hardened by baking and then etched in an Ar dry etching process until the bottom electrodes surface was exposed. Hence, the following processes could be performed on a planar surface.

For the realization of crossbar devices a functional material layer, 30 nm thick TiO_2, was deposited on the bottom electrodes. After that the top electrodes were processed in the same way as the bottom electrodes (without embedding). The alignment of top to bottom structures was done with a standard Mask Aligner MA-6 from SÜSS MicroTec AG.

Fabricated crossbar arrays with embedded bottom electrodes are shown in Figure 1a). The electrodes are approximately 200 nm wide and 30 nm high. The difference in height between electrode area and electrode free area was reduced to few nanometers by the spin on glass and so the crossing points are very shallow. Figure 1b) shows a test pattern of crossed electrodes with different widths. It can be seen that also smaller crossbar junctions were realized with the illustrated embedding method. The line width reaches from 500 nm down to 30 nm.

We were able to demonstrate by electrical measurements on a corner of a 500 nm x 500 nm, 1024 bit crossbar array with a sandwiched 30 nm thick TiO_2 layer, that it is possible to switch the functional material between a low and high resistive state in crossbar devices fabricated with UV NIL (Figure 2). The direction of the switching cycle is indicated by arrows. The switching voltage was around +/- 5 V and the ratio between the high resistive and the low resistive state was approximately 5.

In conclusion the concept of crossbar arrays working as memory or logic devices and the fabrication process for the realization of array structures have been pointed out. Crossbar arrays with embedded bottom electrodes with 200 nm line widths were realized. Single cross junctions down to 30 nm were achieved. The realization of devices fabricated with UV nanoimprint lithography was demonstrated by electrical measurements on crossbar arrays with sandwiched TiO_2 as resistance switching material.

Acknowledgment: The authors would like to thank S. Trellenkamp and A. v. d. Hart for the support with e-beam lithography.

[1] S. Y. Chou, P. R. Krauss, P. J. Renstrom, *J. Vac. Sci Technol.* **B 14(6)**, 4129 - 4133 (1996)

[2] M. Meier, C. Nauenheim, S. Gilles, D. Mayer, C. Kügeler, R. Waser, *33rd International Conference on Micro- and Na-no-Engineering 2007 - Proceedings*, 71 - 72 (2007), paper submitted

[3] G.-Y. Jung, E. Johnston-Halperin, W. Wu, Z. Yu, S.-Y. Wang, W. M. Tong, Z. Li, J. E. Green, B. A. Sheriff, A. Boukai, Y. Bunimovich, J. R. Heath, R. S. Williams, *Nano Letters* **6**, 351 - 354 (2006)

[4] J. E. Green, J. W. Choi, A. Boukai, Y. Bunimovich, E. Johnston-Halperin, E. Delonno, Y. Luo, B. A. Sheriff, K. Xu, Y. S. Shin, H.-R. Tseng, J. F. Stoddart, J. R. Heath, *Nature* **445**, 414 - 417 (2007)

[5] H. Gao, H. Tan, W. Zhang, K. Morton, S. Y. Chou, *Nano Letters* **6**, 2438 - 2441 (2006)

Integration of TiO_2 into Nano-Crossbar Arrays with 100 nm Half Pitch for Resisitve RAM Applications

C. Nauenheim[1,2], R. Rosezin[1,2], C. Kügeler[1,2], A. Rüdiger[1,2], S. Trellenkamp[2,3], R. Waser[1,2,4]

[1] IFF-6: Electronic Materials
[2] CNI: Center of Nanoelectronic Systems for Information Technology
[3] IBN-PT: Process Technology
[4] Institut für Werkstoffe der Elektrotechnik II, RWTH Aachen

Non-volatile resistively switching TiO_2 is integrated into nano-crossbar arrays and nano-cross-points scaled down to a feature size of 100 nm by electron beam lithography. This represents a fast fabrication route for high density prototype test structures of passive memory cores with two terminal devices. The structures and the integrated material is electrically characterized to gain an insight into the general properties of nano-crossbar arrays with resistively switching TiO_2 and to define the demands for an external CMOS control system.

The persistent increase of memory integration density expressed by Moore's law illustrates the demand for ever smaller structures: Nano-crossbar arrays are therefore widely investigated [1]. Nonvolatile and resistively switching materials with two stable states such as TiO_2 are integrated as two terminal memory devices to efficiently create a RRAM bit pattern [2, 3]. Fig. 1 illustrates how these cells are integrated into crossbar arrays where the simple design reduces the cell size per bit to 4 F^2. The switching material covers the whole chip area and every junction at a cross point is an addressable cell of a RRAM. Since the array consists of passive elements, additional active external circuitry is required for the operation to address the cells, set and reset their state and read the stored information [4, 5].

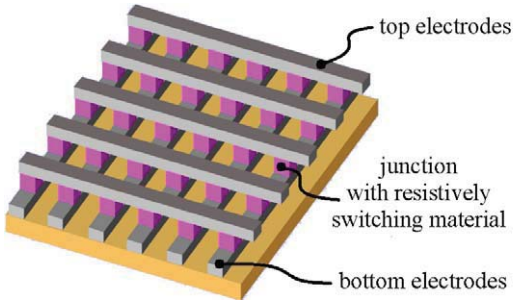

FIG. 1: Pattern of a crossbar array. The metallic top and bottom electrode (grey) sandwich the functional layer (pink) of a resistively switching material which is only illustrated at the junctions.

We report on a novel fabrication route to create crossbar arrays in the nanometer range. Structures of Pt electrodes with resistively switching TiO_2 / Ti layers offer a model system to study the properties of passive crossbar arrays and the specific requirement of these systems concerning external control structures for a CMOS hybrid.

ALD deposited TiO_2 showed promising, non-volatile switching characteristics in micro structures and is convenient to integrate at low temperature [6]. Additionally, the material is temperature stable and compatible with CMOS devices. As a proof of concept a 50 nm thick TiO_2 layer was deposited via rf-sputtering of Ti in an oxygenated atmosphere [7]. The layer was integrated into photo lithographically structured micro-crosspoints with 50 nm thick Pt electrodes fabricated via a lift-off process. Fig. 2 shows the current response of a pulse pattern for a 1 $\times$ 1 μm^2 cross-point structure. Extended investigations confirm the promising resistive switching properties of the material for 6000 cycles.

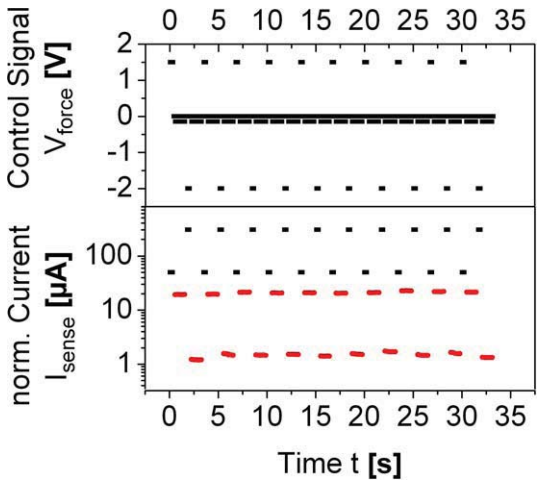

FIG. 2: Pulse pattern measurement. The set/reset voltages were 1.5 V and -2 V (upper graph), respectively, and both signals were limited at 50 μA and -300 μA. Pulse duration was 300 ms. The read voltage amounted to -0.15 V without any current limit, and the corresponding response was around 20 μA for '1' state and 2 μA for '0' state, respectively (lower graph). Here, pulse duration was 150 ms.

Electron Beam Lithography in combination with a lift-off process is used to fabricate prototype test crossbar structures with a feature size of 100 nm (Fig. 3).

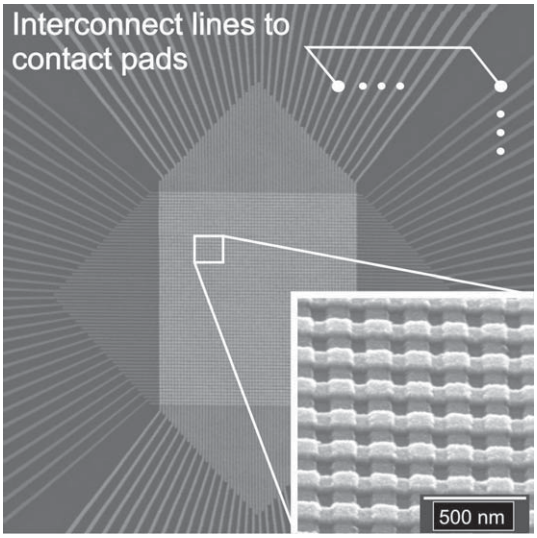

FIG. 3: SEM picture of 64 x 64 bit nano-crossbar array with 100 nm half-pitch. The SEM inspection shows no structural defect within the array.

The lift-off process forms the metal electrodes using a two layer resist on a 1" x 1" SiO_2 substrate. The bottom resist is a copolymer PMMA/MA with a thickness of 60 nm and the top resist is a PMMA polymer with a thickness of 25 nm. An electron beam dose of 200 μC cm^{-2} is necessary to write the 100 nm lines in the resist in order to expose the substrate along the specified structure during the development. As the copolymer is more sensitive to the electron beam than the polymer, this results in a larger expansion of the resist gap of the bottom layer, respectively a staged overhanging resist edge. This is mandatory for well defined metal structures after lift-off and in consequence no additional etching process is required to remove the residual resist in the gap. A combination of 5 nm Ti as adhesion layer with a 20 nm Pt film, which is deposited by electron beam evaporation serves as electrode material. Subsequently a non structured 30 nm thick TiO_2 layer is sputtered as abovementioned. Finally, the electron beam lithography and the lift-off process are repeated to create the orthogonally arranged top electrode structures. The fabricated structures comprise single cells (1 x 1 bit), words (1 x n bit) and arrays (n x n bit) with half pitches down to 100 nm and sizes of n = 8, 16, 32 and 64 (Fig. 3).

To get a general understanding of the resistive switching in the integrated TiO_2 layer we characterized a single 100 x 100 nm^2 cell. The initial state of the cell is high resistive with a resistance of several GΩ and a diode like behavior. A current driven electroforming process with an increasing current (10 nA s^{-1}) initializes the cell into the low resistive 'ON' state. Under this condition the cell exhibits nonlinear I(V) and R(V) characteristics shown in Fig. 4. A negative voltage switches the cell to the high resistive, respectively 'OFF'-state by exceeding a certain threshold value V^-_{th}. This 'OFF' state differs for several orders of magnitude from the initial state and is

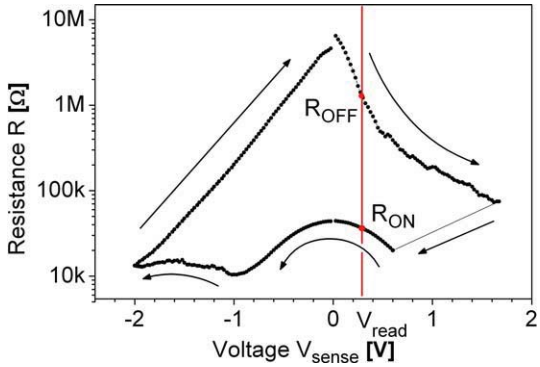

FIG. 4: I(V) characteristic of a single 100 x 100 nm$_2$ cell measured via Kelvin probing and the corresponding R(V) curve.

also non-linear. To switch back into the 'ON'-state, the polarization is changed and a positive threshold V^+_{th} has to be exceeded. A current limiter prevents the cell from a destructive electrical breakdown at 30 μA which leads to an abrupt jump in the I(V) curve. A nondestructive readout of the cell is performed by voltages within the range from V^-_{th} to V^+_{th}, and the resistance condition is nonvolatile even if no supply voltage is applied. In Fig. 4 a read out voltage of 0.3 V exemplifies a resistance of 1.275 MΩ for the 'OFF'-state and 36.274 kΩ for the 'ON'-state corresponding to a ratio of 35. The high resistance ratio in combination with a high R_{ON} value and the feature of current determined readout instead of charge determination accommodates the demands for a CMOS hybrid.

We fabricated nano-crossbar arrays by electron beam direct writing and integrated resistively switching TiO_2. By downscaling to feature sizes of 100 nm we create addressable patterns with sizes up to 4096 bit and a potential density of 2.5 Gbit cm^{-2}. Single memory cells were electrically characterized and showed non-volatile bipolar resistance switching. The electrical characterization was done in sweep as well as in pulse mode. The electrical properties fulfill the demands for an integration and characterization of resistively switching materials.

[1] J. E. Green et al. *Nature*, vol. **445**, pp. 414-417, 2007.

[2] A. Beck et al. *Appl. Phys. Lett.*, vol. **7**, pp. 139-141, 2001.

[3] R. Waser, and M. Aono, *Nature Materials*, vol. **6**, pp. 833-840, 2007.

[4] J. Mustafa, and R. Waser, *IEEE Trans. Nanotechn.*, vol. **5**, pp. 687-691, 2006.

[5] A. Flocke, and T. G. Noll, *in 33rd European Solid-State Circuits Conference*, Munich 2007, pp. 328-331.

[6] C. Nauenheim et al., *2nd Workshop on Integrated Electroceramic Functional Structures, Berchtesgaden*, 2007.

[7] D. S. Jeong et al., *Appl. Phys. Lett.*, vol. **89**, pp. 2909-1-3, 2006.

A part of the IFF activity is devoted to the development of novel scattering techniques and the construction and continuous improvement of instruments at large facilities. The KWS-2 small-angle neutron diffractometer, to show one example, has been moved from the Jülich reactor FRJ-2 to the Munich reactor FRM II. With the high flux supplied by FRM II's cold neutron source and a newly designed neutron guide and with a new collimator system allowing a larger experimental flexibility KWS-2 belongs to the best instruments of such a kind worldwide.

Photo: W. Schürmann

Large-Scale Facilities for Research with Photons, Neutrons and Ions

This research programme coordinates the activities taking place at the large scale facilities involved in the HGF research field Structure of Matter. These facilities offer unique research opportunities with photons, neutrons and ions for a multitude of science disciplines, ranging from physics, chemistry, biology and geology to material science, engineering science, and environmental research. A particular feature of this programme is the support of external user groups, which utilize the major part of the available access time. These user groups come mainly from universities, but also from non-university research institutions and industry.

With its excellence in neutron research – manifested in the Jülich Centre for Neutron Science (JCNS) – the IFF supplies a key contribution to this research programme. The strong reputation of the IFF in the German and international neutron landscape is closely related to:

- a powerful in-house research in the area of condensed matter focusing particularly on soft matter and magnetism,
- a large user operation in these research areas being extensively supported by IFF experts and facilities,
- a science-driven programme for the development of new methods and instruments, and
- exploitation of the novel neutron research opportunities provided by pulsed MW spallation sources.

The IFF neutron research is carried out to a large extent at the new state-of-the-art research reactor FRM II in Munich and at the ILL in Grenoble (France), with new opportunities being created at the SNS spallation source in Oak Ridge (USA). These activities are a cornerstone of the HGF programme "Condensed Matter Physics" and provide important contributions also to other HGF programmes, such as "Information Technology with Nanoelectronic Systems".

SPHERES: First Productive Experiments

J. Wuttke[1], G. J. Schneider[1], L. C. Pardo Soto[1,2], M. Prager[3], Q. Shi[4], A. Budwig[5], G. Hansen[5], A. Ioffe[1], H. Kämmerling[5], F.-J. Kayser[6], H. Kolb[7], A. Nebel[1], V. Ossovyi[1], H. Schneider[1], P. P. Stronciwilk[1], D. Richter[3]

[1] JCNS: Jülich Centre for Neutron Science
[2] Departament de Física i Enginyeria Nuclear, Universitat Politècnica de Catalunya, Barcelona
[3] IFF-5: Neutron Scattering
[4] Afdelingen for Materialeforskning, Forskningscenter Risø, Danmarks Tekniske Universitet, Roskilde
[5] Zentralabteilung Technologie
[6] Zentralinstitut für Elektronik
[7] Forschungsneutronenquelle Heinz Maier-Leibnitz, Technische Universität München, Garching

Commissioning of the new backscattering spectrometer SPHERES made decisive progress in 2007. The signal-to-noise ratio was increased from 1:165 to 1:330. First productive experiments have been performed. The user program is started.

Commissioning of SPHERES is approaching the final stage. By the end of 2006, we had demonstrated *in principle* that the instrument will produce competitive spectra. By the end of 2007, stability and performance have improved to the point where productive experiments are becoming routine. We aspire to obtain the permanent operation permit in the first half of 2008. The instrument is now open for regular user proposals.

Technical upgrades: Initially, test experiments were hampered by instabilities of vital components, namely the neutron velocity selector and the phase-space transform chopper. These problems being understood and solved, all subsystems of SPHERES are now running stable for entire reactor cycles.

A cryostat, lent by FRM II, was adapted to the detector geometry of SPHERES. Accessible temperature ranges are now 4…330 K and 10…550 K, depending on configuration.

Software development continued throughout the year. Computer control has been extended to the Doppler drive. Basic spectrometer operation is now possible through a graphic user interface. Measurements can be scripted. The beam shutter and other safety-critical components are controlled by a SPS.

Neutronic improvements: Extensive tests were performed, aiming at a better understanding of the remaining neutronic noise. We temporarily divided primary and secondary spectrometer by a huge boron rubber barrier, and we moved neutron detectors around to localise leakages. In the event, we improved the shielding around the primary beam path, especially around the monochromator, and around the exit channel of the chopper.

In measurements on a standard scatterer (without sample environment), we achieved a signal-to-noise ratio of 330:1 in the large-angle detectors (Fig. 1). At least a third of the remaining noise is caused by fast neutrons that are created in the ^{6}Li absorbers in the chopper. As anticipated in the last report, replacing these absorbers by boron ceramics is a major effort We are currently installing a purpose-built lifting gear that will give us access to the chopper wheel. As there is no way to balance the activated wheel, it is necessary to build a new one. It is foreseen to transfer the PG crystals from the old to the new wheel in summer 2008. By this measure alone, we will reach a signal-to-noise ratio of 500:1.

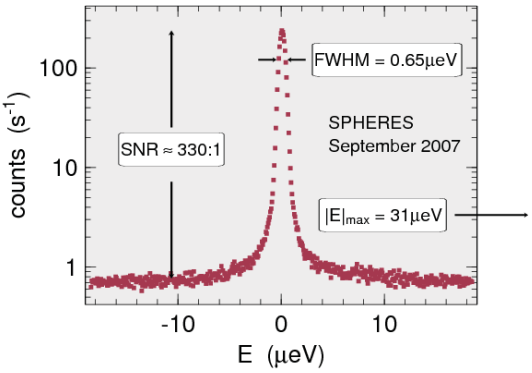

FIG. 1: Resolution function of the large-angle detectors.

Commissioning of the five small-angle detectors just started. After firsts improvements of the neutronic shielding, we obtained signal-to-noise ratios between 50:1 and 100:1; the energy resolution (fwhm) lies between a good 0.93 μeV and an unacceptable 2.3 μeV It might be necessary to rethink the analyser and detector geometry before substantial progress can be made.

Productive experiments: In the last three reactor cycles of 2007, we performed an increasing number of test experiments. These experiments provided us invaluable guidance in preparing for routine operation At the same time, they produced full-fledged results First experimental reports from satisfied test users have arrived.

Rotational dynamics and quantum tunneling were studied in several compounds. Measurements on methylxanthines, a biologically important class of molecules, were used to conclude a study that was begun on the old Jülich backscattering spectrometer BSS [1]. In theophylline, a doublet tunneling band is

observed at 15.1μeV and 17.5μeV (Fig. 2). This is in agreement with the room temperature crystal structure, implying that no phase transition occurs with cooling. In caffeine, orientational disorder leads to a 2.7μeV broad distribution of tunneling bands around the elastic line.

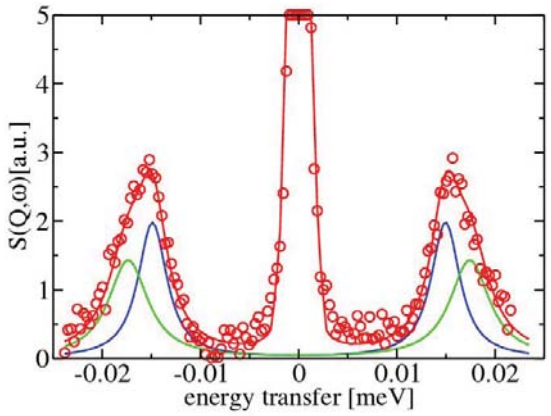

FIG. 2: Spectrum of anhydrous theophylline at 3K. Based on the crystal structure, the broad tunneling peak could be interpreted as an unresolved doublet of equal intensities [1].

To characterize the temperature dependence of quasielastic scattering, we went beyond the elastic ("fixed-window") scans customarily measured in neutron backscattering. Given the high flux at SPHERES, it would be a waste of measuring time to restrict temperature scans to the elastic channel. Instead, during temperature ramps we measure a rapid succession of inelastic spectra. After the event, we integrate over appropriate energy windows to obtain elastic and inelastic scattering as function of temperature.

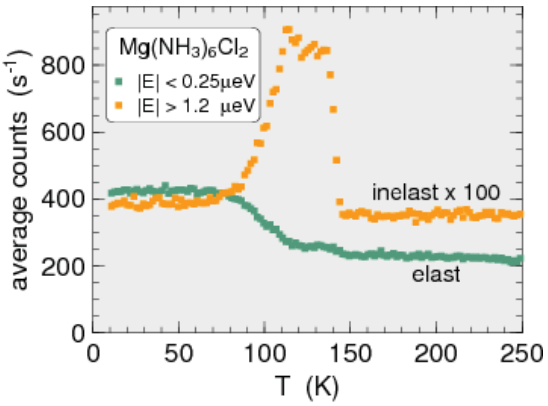

FIG. 3: Inelastic and elastic scattering from $Mg(NH_3)_6Cl_2$ as function of temperature. Note the phase transition at 140 K which shows up much more clearly in the inelastic than in the elastic signal. From a "friendly-user" experiment of Shi, Jacobsen, Vegge, Lefmann from Risø.

Such inelastic temperature scans are particularly useful in localising dynamic phase transitions. Fig. 3 shows a striking example: the rotation of ammonia in $Mg(NH_3)_6Cl_2$ undergoes a transition at 140 K. This transition shows up much more clearly in the inelastic than in the elastic scattering intensity.

Some Freon compounds form a plastic phase in which the molecules sit in a regular lattice, but rotate more or less freely. This phase has an exceptionally high fragility. Above the glass transition, there is another dynamic phase transition at about 130K. Above this transition, we see a rapid increase of quasielastic broadening, which we attribute to jumps between trans and gauche conformations (Fig. 4).

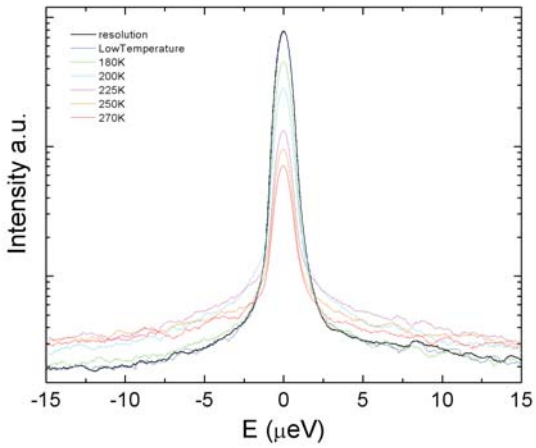

FIG. 4: In the plastic phase of freon, conformational jumps lead to quasielastic broadening.

[1] M. Prager, A. Pawlukojc, A. Wischnewski, and J. Wuttke, J. Chem. Phys. 127, 214509 (2007).

KWS-2 Small-Angle Neutron Diffractometer of JCNS at FRM II

A. Radulescu[1], H. Frielinghaus[1], V. Pipich[1], P. Busch[1], V. Ossovyi[1], T. Kohnke[1], A. Ioffe[1], D. Schwahn[2], M. Heiderich[2], U. Bünten[2], R. Hanslik[3], K. Dahlhoff[3], G. Hansen[3], G. Kemmerling[4], R. Engels[4], H. Kleines[4], D. Richter[1,2]

[1] JCNS: Jülich Centre for Neutron Science
[2] IFF-5: Neutron Scattering
[3] Zentralabteilung Technologie
[4] Zentralinstitut für Elektronik

The KWS-2 small-angle neutron diffractometer was reconstructed at the Research Neutron Source Heinz Maier-Leibnitz (FRM II) in Garching-München. With a high flux supplied by the cold neutron source of FRM II and the newly designed optimized neutron guide and with a new collimation system allowing a larger experimental flexibility KWS-2 belongs to the best instruments of such a kind world-wide. KWS-2 became operational in September 2007 resuming the contribution to the in-house research activity in the traditional field of soft-matter and the user program.

The KWS-2 small-angle neutron diffractometer was moved from the Jülich reactor FRJ-2 to the Munich reactor FRM II in 2006. The instrument is now positioned at the end of the vertically "S-shaped" neutron guide NL3a-o [1]. During the reconstruction phase the instrument was upgraded aiming its optimization either for high intensity or for high resolution modes. Due to these upgrades, the positioning of

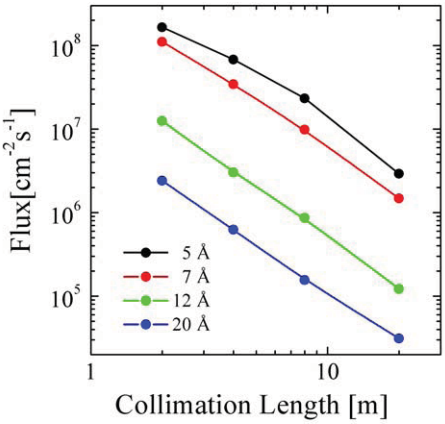

FIG. 1: The neutron flux at KWS-2 measured at the sample position for the reactor power of 20MW and cold neutron source filling of 10.5 l (with 30x30 mm^2 entrance aperture).

the instrument in the FRM II neutron guide hall and the particular beam characteristics, some constituent parts of KWS-2 were subject of major changes.

The first change is concerned with the increase of the beam size from 30x30 mm^2 to 50x50 mm^2. The instrument was equipped with a new system of neutron guides (18 pieces x 1 m length, with a m=1.3 NiMo-Ti nonmagnetic coating). New collimation apertures have been installed: 5 variable apertures made of ceramic ^{10}B, which allow either symmetric or slit-like opening with sizes between 1x1 and 50x50 mm^2 (placed at 2, 4, 8, 14 and 20 m before the sample position) and 14 fixed ^{10}B coated apertures having a size of 50x50mm^2. The combination of the

FIG. 2: View of the KWS-2 SANS instrument at FRM II (summer 2007); on the right side the open collimation housing of KWS-1 SANS instrument can be seen.

larger beam size with the old collimation housing required a new design of the working principle and automatic control of the new guide-aperture system: distinct carriers for the neutron guides and apertures allowing them to move independent from each other in or out of the beam have been installed.

Another major change is caused by the high neutron flux delivered by the FRM II reactor: a massive combined lead and boron shielding was installed around the velocity selector and the collimation housing in

order to keep the level of γ and neutron background within the limits required by the radioprotection safety. Optimization, adjustment and test of the new

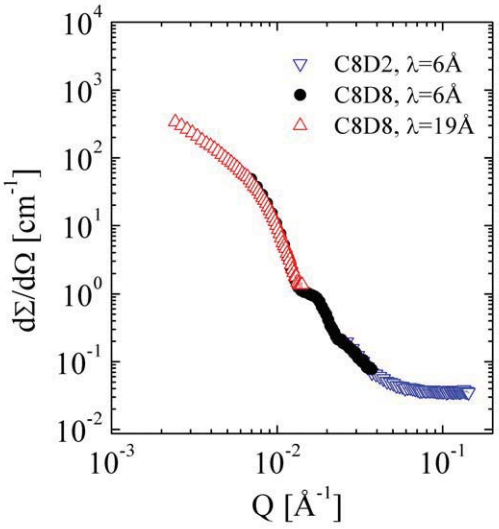

FIG. 3: The scattering pattern of silica particles in a mixed ethanol/water solvent measured over the nominal Q-range of KWS-2 by using 2 sample-to-detector distances (2 m and 8 m) and 2 wavelengths, 6 and 19 Å ; the collimation length was in all cases 8 m.

collimation system and shileding was carried out in the first half of 2007. The velocity selector was calibrated using standard samples (opal and silver behenate [2, 3]); the neutron flux at the sample position was measured for different wavelengths and collimation lengths using monitors and was calibrated by gold foils activation measurements (Fig. 1). For the nominal filling of the FRM II cold source (13 l) KWS-2 has a flux very close (30% lower) to that of the world leading SANS instrument - the D22 at the ILL, Grenoble.

Concerning the detection system, because of the limited space available the 20 m long detector tube of KWS-2 will go out of the present neutron guide hall and located partially into the extension building next to the old FRM I reactor. Because the presently available space in the FRM II guide hall permits only the installation of a 14 m long detector tube (Fig. 2), KWS-2 was setup in a temporary, shorter configuration. The installation of the complete detector housing will be possible only after joining the FRM II guide hall with the FRM I ring laboratory.

The shorter version of the detection system (allowing for a maximal sample-to-detector distance of 8 m) implied that, in order to cover the nominal Q-range (0.002 - 0.2 Å $^{-1}$), two wavelenghts must be used, namely 6 Å and 19 Å . As an example, the results obtained on the system of silica particles in mixed protonated/deuterated ethanol/water solvent [4] are

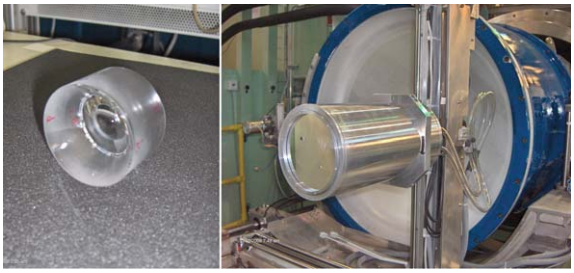

FIG. 4: The upgrades permitting the high-resolution operation mode of KWS-2: parabolic lenses (left) and high-resolution detector (right).

presented in Fig. 3: the experimental data obtained with these two wavelengths were corrected for the scattering from empty cell and detector sensitivity, callibrated in absolute units using a standard sample and radially averaged in order to deliver the scattering cross section of this system.

The KWS-2 instrument became operational in the short version at the beginning of September 2007 when it was opened for internal and external users.

Further upgrading of KWS-2 was continued in the second half of 2007 in parallel with the user program: the optical focusing elements (MgF_2 parabolic lenses, Fig. 4, left) were implemented within the end segment of the collimation system towards the sample position and a "small" high-resolution detector (spatial resolution of about 1x1 mm^2) was installed in front of the conventional detector (Fig. 4, right). The high-resolution detector can be moved to any position covered by the large detector and used in the combination with the lenses allowing us to cover the Q-range down to 2x10^{-4}Å . The test and optimization of the focusing operational mode and the high-resolution detector are currently in progress.

[1] A.Radulescu and A.Ioffe. *Nucl.Instr.and Meth. A*, in press.

[2] H.Graetsch and K.Ibel. *Phys.Chem.Minerals*, 24:102, 1997.

[3] U.Keiderling, R.Gilles, and A.Wiedenmann. *J.Appl.Cryst.*, 32:456, 1999.

[4] J.Kohlbrecher, J.Buitenhuis, G.Meier, and M.P.Lettinga. *J.Chem.Phys*, 125:44715, 2006.

Superconducting Solenoids for the NSE Spectrometer at the SNS

M. Ohl[1], M. Monkenbusch[1], T. Kozielewski[1], Ch. Tiemann[2], A. Paul[3], W. Walter[4], M. Borlein[4], B. Schrauth[4]

[1] IFF-5: Neutron Scattering
[2] ZAT: Central Department of Technology
[3] IFF-4: Scattering Methods
[4] Babcock Noell Nuclear

A Neutron spin-echo spectrometer (NSE) of the next generation is under construction for the Spallation Neutron Source (SNS) in Oak Ridge, USA. A NSE spectrometer measures tiny velocity changes of the neutrons encoded by the neutrons spin clock at a sample while the Neutron spin precesses in large magnetic fields following Bloch's equation. This instrument will be the best of its class both with respect to resolution and dynamic range. In order to reach this ambitious goal, a large magnetic precision field integral before and after the sample is required which directly scales linearly with the resolution of the instrument. Therefore two superconducting solenoids will be used to allow for a higher magnetic field integral. Here, we present the basic design of the solenoids which have been developed in a joint project study by Juelich Research Center (FZJ) and Babcock Noell GmbH (BNG).

At the high power target station of the SNS, the most advanced NSE will be operational in 2009. The goal for the instrument is to reach a new world record of "energy" - resolution - about 5 times higher than all other neutron scattering techniques - and a dynamic range of about six decades in energy resolution. Exploiting superconducting technology and developing novel field correction elements, the maximum achievable Fourier time - this qualifies the resolution - will be extended to at least 1 μs [1, 2]. For generic NSE type instruments superconducting technology is so far not well known. However it will be the first time that superconducting technology is applied to achieve a world record in the "energy" resolution. The solenoids will generate an integrated magnetic flux density of 1.8 Tm. To reduce the fringe field, active shielding is foreseen resulting at the same in a reduced "cross talk" of both solenoids with each other. To minimize vibrations modern pulse-tube cryocoolers cool the NbTi windings below Tc [3]. A special feature of the magnet system is the position measurement with an accuracy in the order of micrometers for the windings in the cryostat during operation. This information is required for the adjustment of so called Fresnel coils outside the cryostat. Together with the setup of these correction elements, a field integral homogeneity better than 10^{-6} for different Neutron paths through one of the solenoids will be achieved.

We wish to hint to the fact that both solenoids generate a huge magnetic field. Here a cross talk between the primary and the secondary solenoid is expected. To avoid major influence at certain scattering angles up to 83° angle between the first and second arm of the spectrometer an outer solenoid has been implemented for compensation of the stray fields. At maximum field a stray field of about 1G 1.5 m perpendicular to the symmetry axis is expected which is low enough to avoid this cross talk.

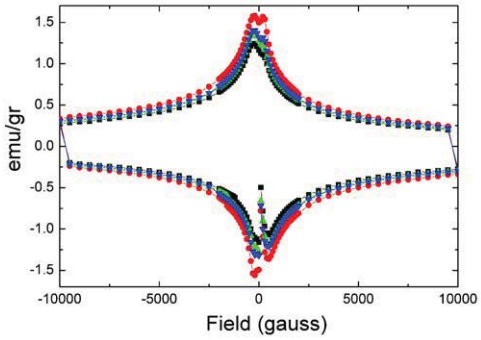

FIG. 1: Magnetization as measured with a SQUID magnetometer and normalised to the mass of the sample.

For the NSE main solenoids, an insulated single strand NbTi superconducting wire with the following characteristics was chosen due to the field quality demands: filament diameter 6 μm, bare strand diameter 0.825 mm. To ensure minimal hysteresis effects [4, 5] SQUID measurements have been performed of more than 25 strands. Most of them showed a maximum magnetization per mass of more than 2.5emu/g. However finally it turned out that the strand made by Furukawa had minimal magnetization effects below 1.6emu/g for all four windings for the pair of solenoids. Figure 1 shows the magnetization curves of the four strands selected finally for the final system.

As already mentioned, field integrals for different Neutron paths through the main solenoids must be

below 10^{-6} Tm. To realize the field homogeneity, very precise mechanical winding of the solenoid coils from insulated single strands is necessary and the information of the cold mass position will be delivered to the correction coils which will interplay and finally yield a homogeneity of 10^{-6}Tm. So called hexapods will adjust these correction coils as a function of the position of the cold mass with an accuracy of several μm.

Each main solenoid system consists of the following: A winding pack with two concentric superconducting solenoids, a cryostat with two pulse tube cryocoolers, additional resistive phase and sample solenoids, position measurement system with an accuracy to measure the cold mass of about 1μm. A sketch view is shown in the Figure 2. In December the installation of the optical position measurement system took place beside further construction work at the solenoids. The solenoid which finally had been adjusted optically and assembled is shown in Figure 3 with an open front plate.

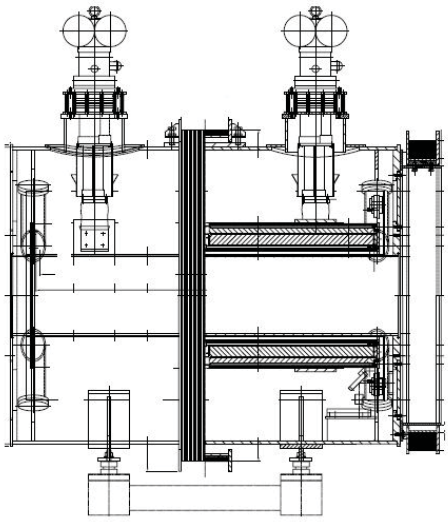

FIG. 2: Solenoid system with windings for a field integral up to 1.8Tm and actively shielded, with two pulse tube cooler and additional resistive sample and phase coils around the cryostructure of the solenoid.

To summarize, the design of a superconducting solenoid system for a NSE spectrometer is presented. The application of superconducting technology makes it possible to reach an unprecedented resolution and dynamic range for the experiment. To achieve the necessary field quality also at low field values, high manufacturing precision is necessary but not sufficient. Also the superconductor must be chosen such that hysteresis magnetization is minimized. The cryogenic system is a so called dry system with cryocoolers providing the operation temperature for the superconducting coils. Cryocoolers expand and compress a cryogene medium in

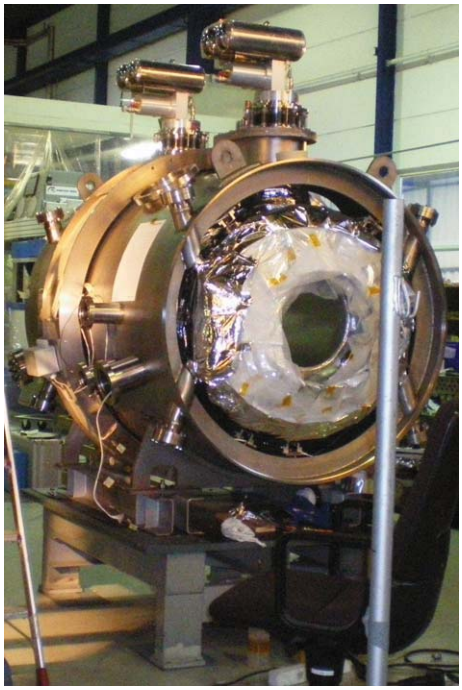

FIG. 3: Implemented superconducting windings wound on the thermally shielded core in its cryostat enclosure as of December 2007.

the coldfinger and are therefore a vibrating system. Special emphasis was placed on preventing possible vibration from the coil system. Therefore PT coolers were preferred to more conventional GM coolers. Possible movements of the superconducting coils inside the cryostat on a micrometer scale between measurements will deteriorate the resolution of the NSE spectrometer. Therefore such movements are optically measured and then the magnetic field will be corrected by additional Fresnel coils. The pair of solenoids is at the moment under construction at BNG. In early 2008 the NSE spectrometers solenoids will be installed at the SNS by the Juelich research center.

[1] D. Richter et.al., "High Resolution Time-of-Flight Neutron Spin-Echo Spectrometer for the SNS," Science Case Document for the EFAC Meeting in 03/2003 to apply for abeamline at the SNS, Oak Ridge, TN„USA.

[2] Neutron Spin Echo Proceedings, *Lecture Notes in Physics V* 128, ed. F. Mezei,Springer, Berlin (1979)

[3] G. Thummes, "Pulsrohrkühler für Temperaturen des flüssigen Heliums: Entwicklungsstand, Anwendungen, Tendenzen," *DKV-Tagung, Bonn, 2003*.

[4] Ch. P. Bean, "Magnetization of Hard Superconductors," Phys. Rev. Letters, Vol. 8, p 250-253, 1962.

[5] Ch. P. Bean, "Magnetization of High Field Superconductors," Rev. of Modern Physics, Vol. 36, p 31-39, 1964.

TOPAS Getting on Stage

J. Voigt[1,2], M. Prager[3], G. Vehres[3], H. Kämmerling[4], A. Heynen[4], K. Bussmann[2], Th. Brückel[2]

[1] JCNS: Jülich Centre for Neutron Science
[2] IFF-4: Scattering Methods
[3] IFF-5: Neutron Scattering
[4] Zentralabteilung für Technologie

The realization of the new neutron time-of-flight spectrometer TOPAS has started. The concept comprises a long focusing neutron guide for high intensity with an energy selection by two fast rotating Fermi choppers and spatial resolution by a large position sensitive detector. Dynamics and structure of novel materials can be studied simultaneously on the ps time scale and the atomic length scale. All components of the instrument are at the forefront of the technical development and can be realized only by bringing technical and scientific expertise together.

Inelastic neutron scattering has proved to be one of the most powerful techniques for the study of dynamics in novel materials. Our understanding of phonons, magnetic excitations, hydrogen bonding in materials, and soft-modes at phase transitions has come primarily from the results of inelastic neutron scattering studies. In recent years, this technique has been used to examine an ever-widening range of subjects and phenomena such as the dynamics of polymers, the nature of disordered and amorphous materials, phase transitions in geological materials and subtle electron-lattice interactions. By the use of thermal neutrons, a large range in energy and momentum transfer can be probed. In the direct time-of-flight geometry, the measurement of the momentum transfer is decoupled from the measurement of the energy transfer. Time-of-flight spectroscopy from single crystals explores simultaneously the $(\vec{Q}, \omega)$ space and maps a variety of excitations by covering a large solid angle with detectors. Accordingly, TOPAS can be used for a wide range of applications, particularly for novel materials. Since TOPAS is designed for full polarization analysis, it will be particularly useful for the study of highly correlated electron systems (e.g. high T_c superconductors). Further applications include molecular systems, nanoparticles, catalytic processes ....

In a time-of-flight spectrometer the time is measured, in which the neutrons travel from a chopper via the sample to the detector. If the velocity of the neutron at the chopper is known, the velocity after the interaction with the sample can be determined from the time, in which the neutron arrives at the detector. The resolution of such an instrument is given by the length of the neutron pulse, geometric differences in the flight path (i.e. the sample size) and the accuracy of the neutron detection. These timing uncertainties have to be compared to the total time of flight. By increasing the flight path from the sample to the detector the resolution can be improved. However, one has to make sure, that fast neutrons from the next pulse do not arrive prior to slow neutrons of the actual pulse (frame overlap). Since the neutrons are delivered continously from the reactor, we have the freedom to vary the time frame, which defines the energy range, and the neutron velocity (see Fig. 2 a)). Hence energy resolution and intensity can be adopted to the specific experimental problem by simply adjusting the chopper timing. The energy resolution for various initial neutron energies is shown in Fig. 2 b) as a function of the energy transfer between sample and neutron. The scientific requirements pose strong technical challenges for all components of the instrument. A central component is the neutron guide with supermirrors m$= 3$. It has an elliptical shape to focus a high intensity onto the sample with only a few reflections. Details of the neutron guide design have been reported in [1].

Starting from the reactor wall, the next component is the coarse chopper system. These are two very massive chopper discs that block the background radiation from entering the neutron guide. Whenever one chopper opens the neutron beam, the other is in a closed position. To provide a maximum transmission for variable neutron velocities, the frequency can be adopted. The rotation speed of the discs with a mass of approximately 200 kg reaches up 9000 rpm and puts strong demands on the material properties and the acceleration units.

The Fermi chopper system selects a narrow range of velocities out of the neutron spectrum and introduces the time structure on the beam, which is needed for the energy analysis. Each of them provides neutron pulses with a typical length of 10 μs. The neutron velocity can be varied by the variation of the phase angle between both choppers. Since the neutron guide converges towards the sample position, the size of the choppers is different. The first chopper has a window of size 110×70 mm^2, the second chopper close to the sample 60×30 mm^2. Their rotation speed ranges up to 28000 rpm for the first chopper and 36000 rpm for the second chopper. The high rotation speed of the second chopper allows a high energy resolution mode for neutron energies below 60 meV,

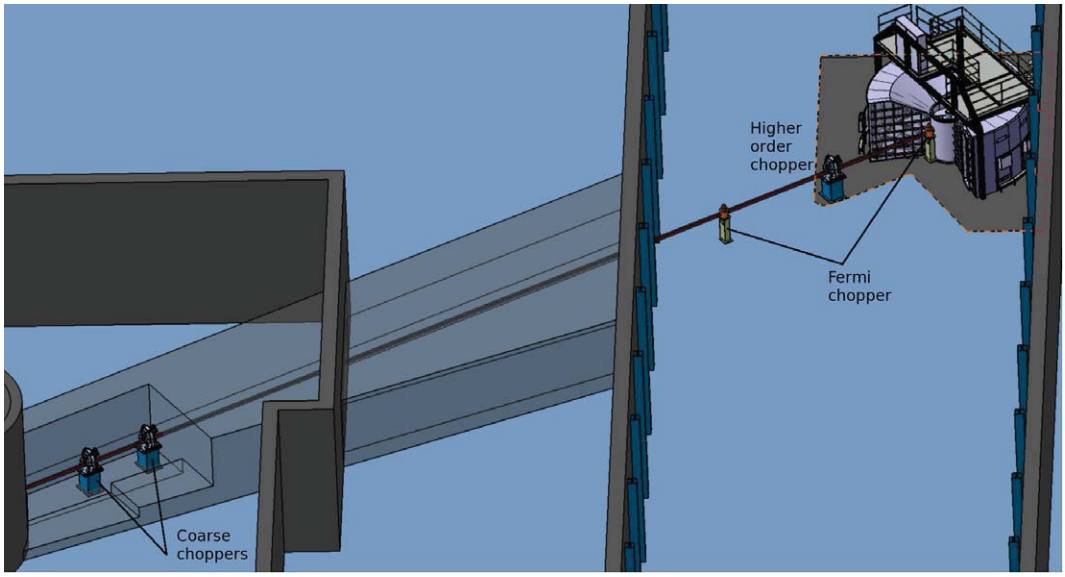

FIG. 1: Overview of TOPAS. The distance between reactor wall and sample position is 48 m. The coarse chopper system is shown on the left. The phase between the choppers is fixed to block the direct sight onto the reactor core at any time. The two Fermichoppers in front of the secondary spectrometer monochromatise the neutron beam. The secondary spectrometer around the sample (2.5 m sample to detector distance) is evacuated to reduce the background due to air scattering.

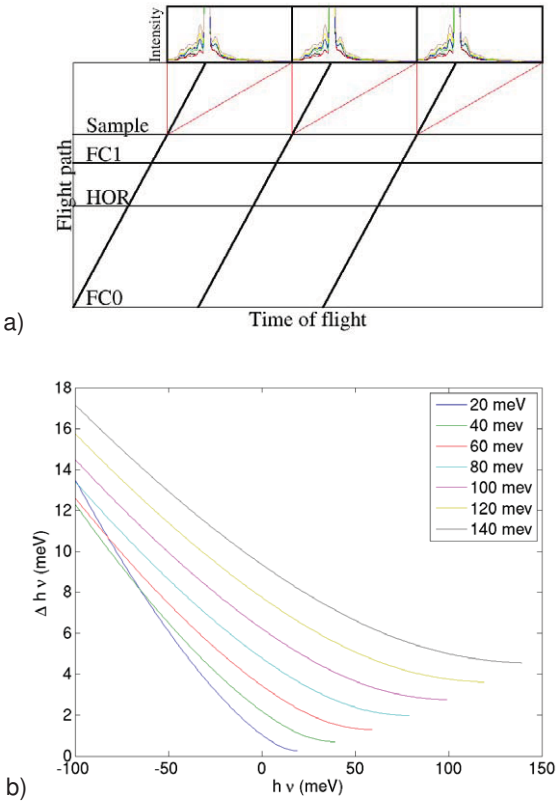

FIG. 2: a) Flight-path diagram: The velocity of the neutrons is defined by the phase between the Fermi choppers FC0 and FC1. The HOR choppers removes higher orders. Neutrons are scattered at $t_1 = 0$ at the sample. The slowest neutrons of interest arrive at the detector at t_2. t_2 determines the time frame. b) Energy resolution for different initial neutron energies E_i.

in which the second chopper runs at twice the speed of the first chopper.

The monochromatic neutrons travel through the evacuated sample chamber. Various sample environments can be placed on a sample table, which allows the tilting of the sample. These degrees of freedom are necessary particularly for studies of single crystals, where the crystal coordinate system has to be aligned with the laboratory coordinate system.

The sample chamber is directly connected to the detector chamber. The whole flight path of the neutrons is evacuated. The diameter of the evacuated volume is 7 m, the height 2.5 m. Because the detector vessel will deform, when it is evacuated, the detectors and the sample table are mechanically decoupled to keep the relation between the two coordinate systems fixed.

The position sensitive detector is at the heart of the instrument. It consists of approximately 400 linear tubes with a diameter of 2.5 cm mounted in vacuum at a distance of 2.5 m from the sample, mechanically decoupled from the surrounding vessel. This results in a solid angle coverage of π steradian. The spatial resolution along the tube is better than 2.5 cm. The time resolution of the detector electronics is 50 ns. The electrical connections have to be outside the vacuum to avoid discharge effects. The tubes are displaced radially to have a gapless coverage of the solid angle despite the gap necessary for sealing 400 tubes.

The developements of TOPAS to a highly versatile instrument for all areas of condensed matter research is ongoing with increasing momentum. The next steps include the design for the polarization analysis, which will be a unique feature of the spectrometer.

[1] J. Voigt, M. Prager, T. Kulessa, Th. Brückel, Jahresbericht des Forschungszentrums 2006

POWTEX: BMBF-Funding Granted for the High Intensity TOF Diffractometer

H. Conrad[1], A. Houben[2], J. Voigt[1], W. Schweika[1], Th. Brückel[1]

[1] IFF-4: Scattering Methods
[2] RWTH Aachen University, Institute for Inorganic Chemistry

In 2007 the BMBF decided to grant the funding of the new high intensity neutron time-of-flight diffractometer called POWTEX. The instrument to be installed at the new Munich reactor (FRM II) will provide the large chemistry and materials science communities with a powerful tool for rapid data acquisition. The conceptual design is based on time-of-flight technique, which is expected to be superior to a standard monochromator instrument by at least an order of magnitude in intensity, particularly for small samples of less than a cubic centimeter. The construction of this innovative type of diffractometer utilizes modern neutron components such as focusing super mirror neutron guides, a 4-unit high speed disk chopper system and the linear position sensitive detectors covering a large solid angle. The diffractometer design is equally well suited for the texture analysis of large geological and archeological samples.

Fundamental objectives of solid state chemistry and materials science are the development of new materials, their analytical characterizations and studies of their structures and properties. For that purpose preparative methods have to be directly related to structure determination, since this is a prerequisite for designing materials of specific properties.

Demands of solid state chemists for a neutron diffractometer are a suitable d-spacing resolution (δd/d $\cong$ 0.5 %), a d-spacing range of about 0.5 Å to 15 Å and high intensity on small samples ($\leq$ 0.5 cm^3).

A central aspect of geological research is focused on plate tectonics, i.e. relative movements in the lithosphere. These movements are connected to faults and shear zones where rocks have been deformed temperature dependently. Mineral grains are affected by these deformation processes in forming preferred crystallographic orientations, the so-called texture.

Among others neutron diffraction is the strongest experimental method due to the high penetration capability of neutrons and the large neutron beam cross sections which allow the investigation of volume textures of high grain statistics. An instrument is needed capable of collecting many pole figures of many samples in a reasonable time. A large position sensitive detector installed at a time-of-flight diffractometer compensates for pole figure scanning reducing measuring time by at least two orders of magnitude.

The proposed time-of-flight diffractometer is designed for high intensity even with samples of as little as 0.5 cm^3 at a reasonably good resolution of d-spacings, i.e.

$$\delta d/d \leq 5\times10^{-3} \quad (1)$$

Equation (1) can be appropriately expressed in terms of parameters needed for establishing a technical solution of a time-of-flight instrument, viz.

$$(\delta d/d)^2 = \left[(\delta t/t)^2 + (\delta L/L)^2 + (\delta\theta \cot\theta)^2\right] \quad (2)$$

where t is the neutron flight time across a flight path L and θ is half the scattering angle. In order to fulfil the requirement of equation (1) each of the terms in equation (2) contributing to the relative uncertainty δd/d must not exceed 2.8×10^{-3}. Applying modern technologies like super mirror guides, high speed disk choppers with magnetic bearings and linear position sensitive ^{3}He detectors an instrument can be designed so as to reach these goals. A schematic representation of the instrument is shown in Fig. 1.

Neutrons from the 5$\times$10 cm^2 beam channel SR5 of the FRM II are focused onto a pulse defining double-disk chopper by a 27 m long "ballistic" beam compressor made of m = 3 supermirror guides, i.e. guides with three times the critical glancing angle of nickel coated guides. The beam of 1$\times$1 cm^2 at the puls chopper is then again transported by a neutron guide passing the wavelength band chopper and the frame overlap suppressing chopper with a total flight path of 11.5 m to the sample. The 1 cm^2 of this focus of the second double ballistic guide is placed at an average pulse chopper at a detector distance of 13.5 m. The other two choppers of Fig. 1 are needed to define both the position of the wavelength band, which will be accessible and to prevent cross talk of consecutive pulses.The most important features of the instrument are high intensity by exploiting a large fraction of the Debye-Scherrer rings, variable d-spacing and resolution ranges, no limitations in determining peak positions (using position sensitive detectors on a cylindrical surface) and unrestricted utilization as both a POWder and a TEXture diffractometer. Additionally, the large detector cylinder will provide enough space for challenging experiments e.g.

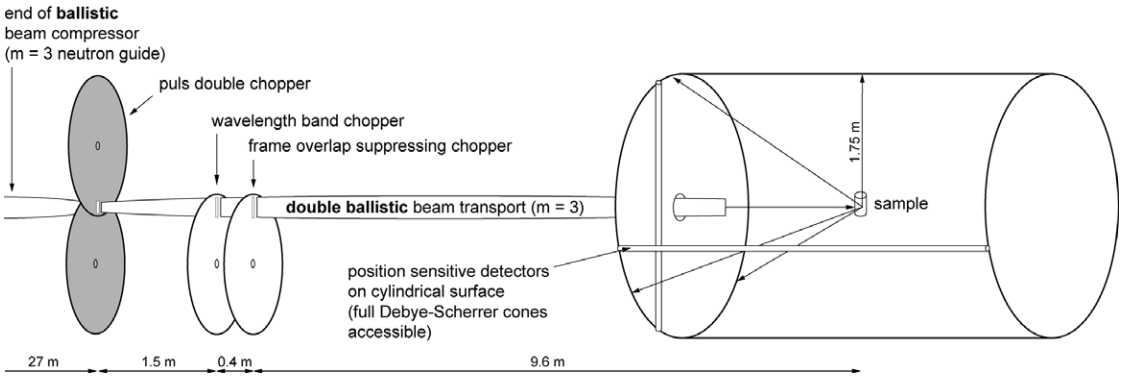

FIG. 1: Schematic layout of the time-of-flight diffractometer POWTEX (not to scale).

in-situ investigations of chemical reactions or phase transitions as function of temperature, pressure and magnetic field.

Analytical performance estimates have shown that the neutron current at the sample position will be approximately equal for both a monochromator and a time-of-flight diffractometer. However, the absence of the resolution asymmetry of the time-of-flight method will result in an intensity gain for detected neutrons of more than an order of magnitude. The optimization of the numerous components of the instrument can be better followed up quantitatively with modern Monte Carlo techniques such as the VITESS code developed at the HMI. In fact, these simulations show that the proposed time-of-flight diffractometer outperforms the best conventional monochromator instrument D20 (ILL) by about a factor of 30. Examples of these numerical calculations are given in figures 2 through 4.

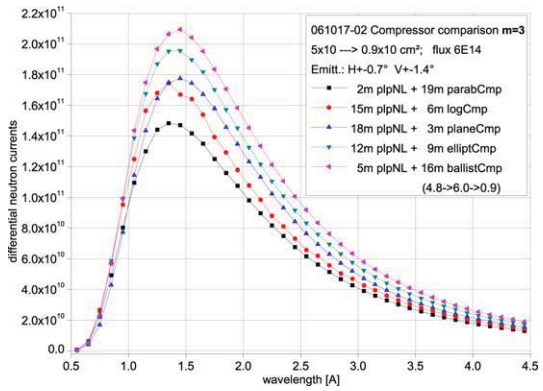

FIG. 2: Intensity as a function of wavelength at the pulse chopper slit for five different compressor geometries.

Intensities at the end of different beam compressors are shown in Fig. 2. Five geometrical shapes have been modeled and independently optimized. Only the optimum performance for each geometry is displayed in Fig. 2.

Our Monte-Carlo simulations confirm a desired focal spot size of 1 cm^2 at the sample position as shown in Fig. 3. Another important performance feature is the angular divergence at the sample position (cf. equation 2). The numerical calculations yield a

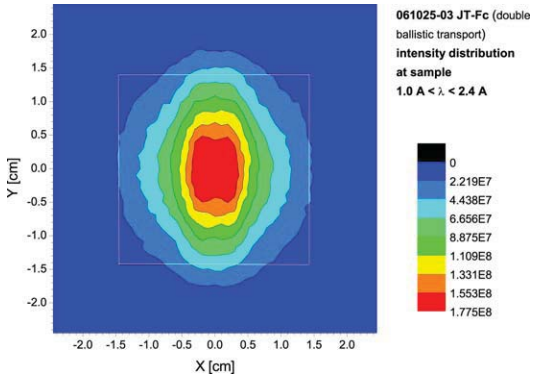

FIG. 3: 2-D intensity distribution at the sample (white square depicts guide exit cross section, 0.75 m upstream). The neutron current density in the flat top is 3.5×10^7 $cm^{-2}s^{-1}$.

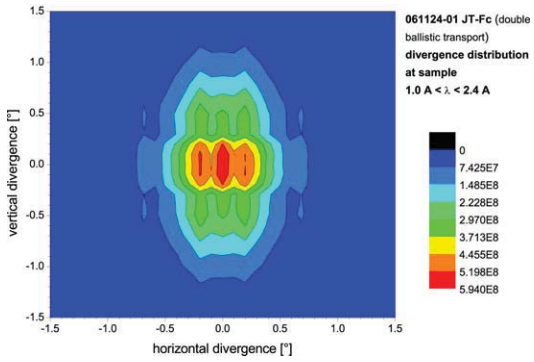

FIG. 4: 2-D beam divergence distribution at the sample.

divergence better than one degree as can be seen in the 2-dimensional divergence distribution presented in Fig. 4.

POWTEX is engineered and will be built by FZ Jülich to be part of the JCNS instrumentation at the FRM II in Munich. It will be located at the new eastern experimental hall ("Osthalle"). Professor Dronskowski from the Institute for Inorganic Chemistry at the RWTH Aachen University, representing the large German community of solid state chemists was granted a first funding of about €1.7 million for the first three years. Additional BMBF funding supports the "Geowissenschaftliches Zentrum Göttingen" to include instrumental aspects for geo science applications.

Progress on SEOP Development and First Ideas for Onbeam-SEOP

K. Nünighoff[1], P. Hiller[1], R. Mueller[1], A. Ioffe[2], P. Busch[2]

[1] IFF-4: Scattering Methods
[2] JCNS: Jülich Centre for Neutron Science

The SEOP (Spin Exchange Optical Pumping) method [1] enables the polarisation of ^{3}He gas in compact assemblies. Thus this method is well suited to install the polariser directly on the instrument. The first instrument of JCNS which will use a ^{3}He analysator cell with onbeam SEOP is the small angle scattering instrument KWS-1. In this report we will describe our progress in cell preparation and we will discuss a first design of an analysator cell for KWS-1.

During the last year we have improved our filling station for preparation of ^{3}He neutron spin filter cells. The cells were constructed and reblown from GE180 glass. After the cells were mounted on a manifold, cells and manifold were rinsed with acetone and water. In the next step the cells were evacuated and baked at 400°C for ≈2 weeks. When the vacuum inside the cells is lower than 10^{-7} mbar, the filling procedure can start. In the first step the Rb is condensed into the cell. Then a few mbar (≈30 mbar) of N_2 as a quencher is filled into the cells and the ^{3}He gas is filled to the desired pressure of the cell. To be able to seal off the cells from the manifold, the cells have to be cooled down with liquid N_2 to reduce the pressure inside the cell below the atmospheric pressure. After improving our filling station (replacing of polymer seals with aluminium seals, avoiding pressure reducers, replacing defective valves) cells with lifetimes up to 340 h have been produced. Tab. 1 shows all cells produced at FZJ and their lifetimes. It can be seen, that we are now able to produce cells with excellent life times.

cell	diam. x len.	T1	remarks
Juel	5 cm x 5 cm	463 h	filles at ISIS
Juel-1	6 cm x 6 cm	-	not working
Juel-2	5 cm x 5 cm	84 h	partly oxidized
Juel-3	6 cm x 6 cm	180 h	partly oxidized
Juel-4	5 cm x 5 cm	1.42 h	flourescence light
Juel-5	6 cm x 6 cm	6 h	vacuum loss
Juel-6	5 cm x 5 cm	89 h	vacuum loss
Juel-7	5 cm x 5 cm	342 h	o.k.
Juel-8	6 cm x 6 cm	320 h	o.k.

TAB. 1: SEOP cells produced at FZJ with dimensions (diameter x length), measure lifetimes T1 and some remarks.

The cells were polarised with a 795 nm laser with a power of 30 W. The relative ^{3}He polarisation was measured with NMR during pump-up. After switching off the laser the lifetime T1 could be determined by fitting an exponential decay function through the data points. In Fig. 1 the experimental data for cell Juel-7 are shown. This cell has a diameter of 5 cm and a length of 5 cm and is filled with 1.2 bar ^{3}He gas. It can be seen that after more than 20 h of pumping the maximum polarisation was not reached. The observed lifetime is 342 h. Rotating the cell by 180° results in a slightly longer lifetime of 367 h. This indicates low paramagnetic impurities inside the cell, which cause an additional relaxation term.

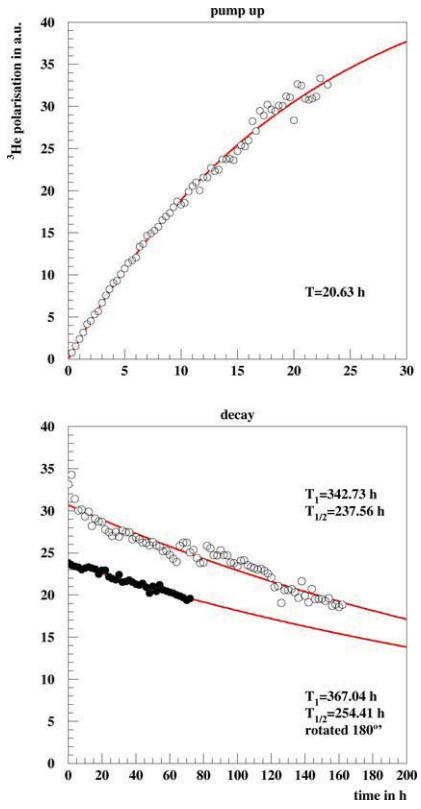

FIG. 1: Relative ^{3}He polarisation during pump-up (upper panel) and relaxation after switching off the laser (lower panel).

Two of the cells listet in Tab. 1, namely Juel and Juel-7, were additionally measured with neutrons on the MIRA instrument at FRM II to obtain the absolute

FIG. 2: Protoype of a double cell for onbeam SEOP. The upper cell will be used for polarising the ^{3}He gas and the lower cell will serve as the neutron spin filter cell.

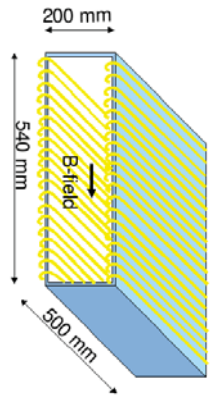

FIG. 3: Design of the new magnetostatic cavity.

value of ^{3}He polarization. Cell Juel achieved an excellent maximum polarization of 79 % and Juel-7 was polarized up to 72 %. The lifetime T1 of the cells inside a magnetostatic cavity mounted on the instrument was measured to be 367 h for Juel and 300 h for Juel-7.

One highlight of the cell production task was the preparation of a double cell. Fig. 2 shows the finished cell. The laser passes through the upper cell –which contains the Rb– to polarise the ^{3}He gas and the neutron beam passes through the lower cell, which will serve as a spin filter cell. If this prototype will work, more complicated geometries of spin filter cells could be realised, while the gas itself can be polarised in a simple cylindrical or spherical cell.

To explore the possibility to polarise the cell inside a magnetostatic cavity –mandatory for an onbeam option– the design of our first cavity [2] was changed according to a design from ILL [3]. Now the winding of the coil is along the long side (see Fig. 3) instead along the short side of the cavitiy. This alternative way of winding turn the magnetic field by 90°, thus giving more space for coupling the laser light into the cavitiy and the cell. The laser beam will be guided by mirrors into the cavitiy and will illuminate the cell from the side walls, whereas the neutron beam will pass through the face side. By this solution no mirrors are needed in the neutron beam which might scatter neutrons. As can be seen in Fig. 4 the region where the relative field gradient is lower than $1{\cdot}10^{-4}$ 1/cm is larger than in the old design. This opens the possibility to operate cells with a diameter up to 16 cm inside such a cavity.

KWS-1 shall be operated with three wavelengths: 4.5 Å, 7 Å, and 12 Å. Because it is not possible to design a single SEOP cell optimised for all three wavelengths, for each single wavelength a seperate cell will be used. To achive a maximum quality factor

$$Q = T_n \cdot A^2 \qquad (1)$$

a pressure length product of 26 bar·l·cm is needed [4]. Here T_n is the transmission of the incident neutron beam and A is the analysing/polarising power of the filter. To cover the whole solid angle of $\pm 7.5°$ and assuming a distance between sample position and filter cell of 35 cm a diameter of 10 cm is needed. With a length of 4 cm the cell needs a pressure of 0.54 bar, 0.93 bar, and 1.44 bar for 12 Å, 7 Å, and 4.5 Å respectively. Assuming an achivable ^{3}He polarisation of 70 %, a transmission T_n of 30 % and a polarisation of 87 % can be expected.

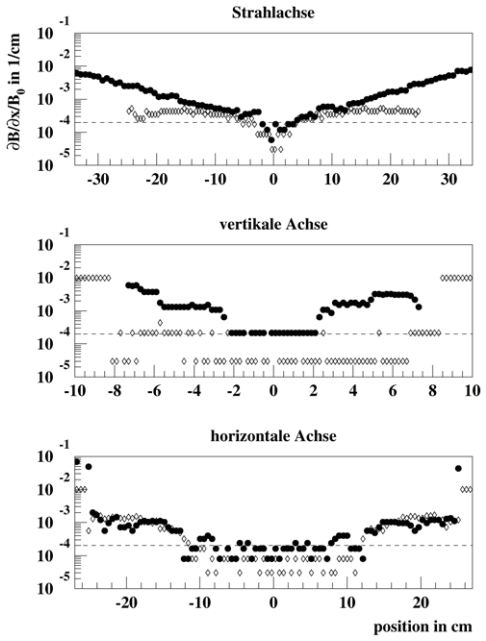

FIG. 4: Comparison of the field gradients of the old design (filled symbols) and the new design (open circles) for a magnetostatic cavity to host the SEOP cells calculated with ANSYS.

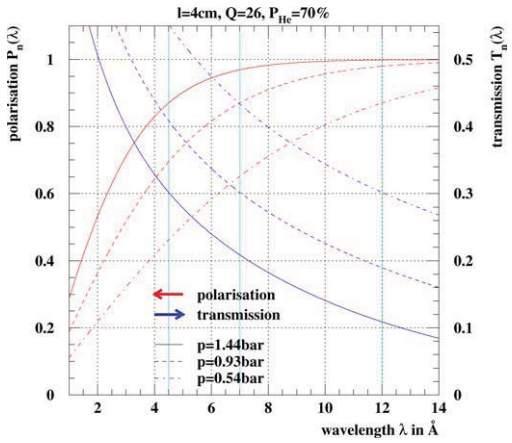

FIG. 5: Transmission and polarisation of three SEOP cells optimised for the three wavelengths foreseen at KWS-1 assuming an incoming unpolarised beam and a ^{3}He polarisation of 70 %.

[1] M.A. Bouchat, T.R. Carver, and C.M. Varnum, Phys.Rev.Let. **5** (1960) 373

[2] K. Nünighoff, P. Hiller, R. Mueller and A. Ioffe, IFF Scientific Report 2006, p. 174

[3] A.K. Petoukhov et al., NIM A 560 (2006)

[4] F. Tasset and E. Ressouche, NIM A **359** (1995) 537

DNS - An Instrument for Unraveling Complex Magnetic Correlations Via Polarization Analysis

Y. Su[1,2], W. Schweika[1,2], R. Mittal[1,2], E. Küssel[1,2], F. Gossen[1,2], B. Schmitz[1,2], K. Bussmann[1,2], M. Skrobucha[3], A. Ioffe[1,2], Th. Brückel[1,2]

[1] JCNS: Jülich Centre for Neutron Science
[2] IFF-4: Scattering Methods
[3] Zentralabteilung Technologie

The construction of the new polarized time-of-flight spectrometer DNS at FRM II has reached the first milestone with the delivery of the first neutrons and intense polarized neutron beams in September of 2007. Shortly after the starting of the instrument commissioning with polarized neutrons in the diffraction mode in the last reactor cycle, DNS has been steadily producing sound experimental results to unravel complex magnetic correlations in a wide range of emergent materials via polarization analysis.

FIG. 1: The new DNS at FRM II

DNS is a new cold neutron multi-detector time-of-flight spectrometer with both longitudinal and vector polarization analysis at FRM II. This allows the unambiguous separation of nuclear coherent, spin incoherent and magnetic scattering contributions simultaneously over a large range of scattering vector **Q** and energy transfer E. With its compact size DNS is optimized as a high intensity instrument with medium **Q**- and E- resolution. DNS is therefore ideal for the investigations of magnetic, lattice and polaronic correlations in many frustrated magnets and highly correlated electrons. With its unique combination of single-crystal time-of-flight spectroscopy and polarization analysis, DNS is also complimentary to many modern polarized cold neutron triple-axis spectrometers.

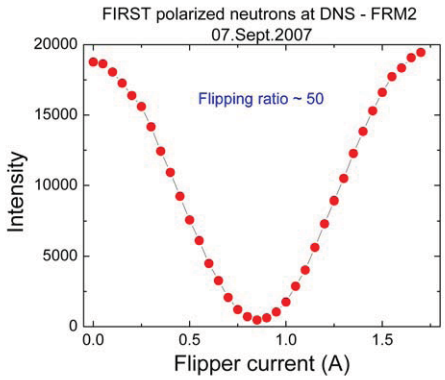

FIG. 2: First polarized neutrons at the new DNS demonstrating the high flipping ratio of 50 achieved

The relocation of major components from Juelich and the construction of the new DNS at FRM II have started in 2006. The first phase of this project is to implement the diffraction mode with polarized neutrons. Soon after the installation of the double-focusing pyrolytic graphite monochromator and secondary spectrometer in the summer (as shown in Fig.1), the first neutrons and intense polarized neutron beam were delivered to DNS in September. Newly constructed polarizer and polarization analyzers, both using m = 3 Schärpf bender-type focusing supermirrors, perform extremely well. A polarized neutron flux as high as 5 x 10^6 n/s/cm^2 has been achieved at the neutron wavelength with 4.74 Å. The polarization rate of the incident neutron beams is nearly 96%, as shown in Fig.2. The expanded analyser bank over a 2θ range of 120 degrees has largely improved the measurement efficiency. The radiation shielding at both monochromator housing and secondary spectrometer has also been improved. The radiation background at the DNS measurement area has met the strict requirement imposed by the radiation protection regulations. This paves the way for the first commissioning experiments.

In the last reactor cycle of 2007, a number of polarized neutron experiments on both powder and single-crystal samples have been successfully undertaken at DNS. One typical application of polarization analysis on powder samples at DNS is to separate magnetic scattering from nuclear coherent and spin incoherent scattering on antiferromagnets and paramagnets via XYZ-method. High polarized flux and the improved efficiency on polarization analysis allow us to obtain high quality data on the investigation of the magnetic structure of manganese carbodiimide (MnNCN) powder, as shown in Fig.3. In comparison to the old data taken with non-polarized neutron powder diffraction at the dedicated powder diffractomter SV-7 at FRJ-2, the DNS data is much superior. It provides the comprehensive information on magnetic reflections and their temperature dependence.

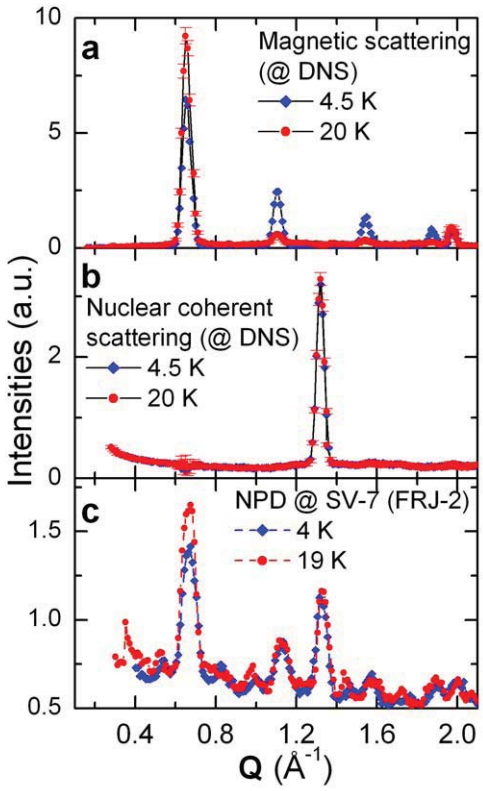

FIG. 3: Investigations of the magnetic structure of MnNCN via powder neutron diffraction. (a) and (b): pure magnetic and nuclear coherent scattering, respectively determined at DNS with polarization analysis. (c): former data from SV-7 without polarization analysis

Another typical application is to map out the reciprocal space together with polarization analysis on single crystal samples. Intensive testing experiments on various Kagome spin systems, pyrochlore spin ice and perovskite CMR manganites have been carried out. The routines for the data treatment have also been implemented. Some types of very peculiar magnetic correlations due to high geometrical frustrations and strong electronic correlations have been revealed from these new experiments with polarization analysis. One such example is the observation of the rod-like paramagnetic diffuse scattering in the so-called cooperative Jahn-Teller distorted regime on highly correlated CMR manganites, as shown in Fig.4. This rod-like diffuse feature is a clear indication of the presence of strongly anisotropic magnetic exchange interactions due to orbital ordering.

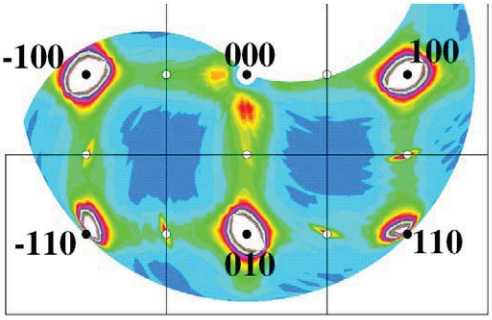

FIG. 4: Paramagnetic diffuse scattering at 220 K measured on a large single crystal of $La_{0.875}Sr_{0.125}MnO_3$ via polarization analysis

The successful commissioning of DNS with intense polarized neutrons in the diffraction mode and subsequent successful applications have proven capabilities of DNS as an unique instrument with polarization analysis. However, the full potential of DNS can only be realized after the completion of the second phase of the DNS project - installations of a massive position sensitive detector bank and high-performance double chopper system. These two new components are expected to be in operation before the end of 2008.

In collaboration with the Institute of Inorganic Chemistry of RWTH Aachen, we would like to thank Manuel Krott and Andreas Houben for permitting us to use the MnMCN data taken both from DNS and SV-7.

Commissioning of the Very Small Angle Neutron Scattering Instrument KWS-3

E. Kentzinger[1,2], G. Goerigk[2], A. Ioffe[2], D. Richter[3,2], Th. Brückel[1,2]

[1] IFF-4: Scattering Methods
[2] JCNS: Jülich Centre for Neutron Science
[3] IFF-5: Neutron Scattering

KWS-3 is a very small angle neutron scattering instrument running on the focusing mirror principle. In Jülich it allowed performing scattering experiments with a wave vector transfer resolution between 10^{-4} and 10^{-3} Å^{-1}, bridging a gap between Bonse-Hart and pinhole cameras. This instrument is now transferred into the guide hall of the FRM II neutron source in Garching. It is now placed at the end of a dedicated neutron guide, allowing the use of larger wavelengths than in Jülich and leading to an improvement of resolution in wave vector transfer. The intensity gain with respect to Jülich is at the moment by a factor of 7.

Ultra-small angle (U-SANS) and small angle neutron scattering (SANS) experiments are performed by two different types of instruments to cover a combined Q-range from 10^{-5} Å^{-1} up to 1 Å^{-1}. Bonse-Hart cameras (Double Crystal diffractometers) are used for U-SANS experiments, whereas the "standard" SANS experiment is performed using a pinhole camera. In principle, the Q-range of both instrument classes overlaps. Typical U-SANS instruments like S18 (ILL) or PCD (NIST) may reach maximum Q-vectors of 5×10^{-3} Å^{-1}. The disadvantage of these instruments is that they do not allow taking a full area image on a 2D position sensitive detector. On the other hand, the well-known pinhole instrument D11 at Institut Laue-Langevin (France) reaches a minimum Q-vector of 5×10^{-4} Å^{-1} by use of large wavelengths and sample-to-detector distances (≈40m). But the required instrumental settings push both types of instruments to their limits, mainly due to signal-to-noise level and the reduced flux at sample position.

The use of neutron lenses as additional elements of a pinhole SANS instrument has been tested to overcome this intensity problem [1]. An alternative design is realized by the KWS-3 instrument [2]. The principle of this instrument is a one-to-one image of an entrance aperture onto a 2D position-sensitive detector by neutron reflection from a double-focusing elliptical mirror. It permits to perform SANS studies with a scattering wave vector resolution between 10^{-4} and 10^{-3} Å^{-1} with considerable intensity advantages over conventional pinhole-SANS instruments. Therefore it perfectly bridges the "Q-gap" between U-SANS and SANS: Very Small Angle Scattering (V-SANS). The increasing need for these intermediate Q-vectors arises from the growing interest in biological and colloidal samples, which typically have characteristic length scales in the μm range. An investigation of the multilevel structures in partially crystalline polymer solutions performed using a combination of those three above depicted types of SANS instruments can be found in Ref. [3].

The main innovation and challenge of KWS-3 was to build a large mirror having a shape as close as possible to an ellipsoid and with a surface roughness less than 5 Å (rms). The mirror is a 1.2 m long, 0.1 m wide and 0.05 m thick toroidal double focusing Zeodur mirror of 11 m focal length, and coated with 1000 Å ^{65}Cu and 100 Å Al as a protection layer. At such a short mirror length with respect to the focal length, the toroidal shape is a good enough approximation to an elliptical shape. The reflection plane has been chosen to be horizontal, reducing the deterioration of the image due to gravity. A photo of the mirror is given in FIG. 1.

FIG. 1: Photo of the toroidal mirror installed inside its vacuum chamber.

A detailed description of this instrument has already been given in Ref. [2]. Its realisation in Jülich is depicted in FIG. 2. KWS-3 in Jülich was using the single wavelength of 12.5 Å, thanks to the use of a multilayer double monochromator deflecting neutrons from the neutron guide NG-II-A of KWS-1.

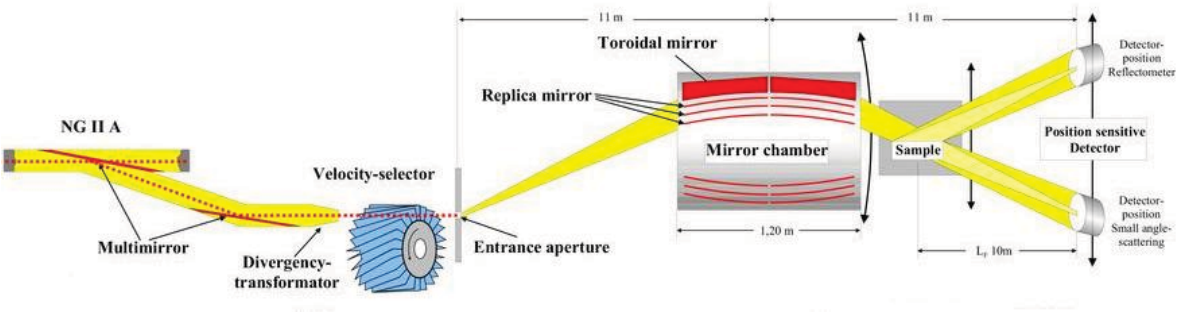

FIG. 2: Realisation of KWS-3 in Jülich.

KWS-3 is now installed inside the neutron guide hall of FRM II between the instruments KWS-2 and REFSANS. It is situated at the end of a dedicated neutron guide, allowing the use of wavelengths larger than 12.5 Å and therefore increasing its resolution in wave vector transfer. Resolutions close to 10^{-5} Å^{-1} should be accessible in this way.

A first image of the entrance aperture on the detector has been obtained. In FIG. 3 the image of a 2×2 mm^2 aperture is depicted. As seen on that picture, the full width at half maximum (FWHM) of the image is 2.4×2.4 mm^2 exactly the same as in Jülich! Today, the contrast of the image is not yet as good as it was at its original location in Jülich. A possible explanation might be in a yet non-proper setting of the detector electronics. The flux on the detector is 4000 neutrons/s, 7 times larger than in Jülich.

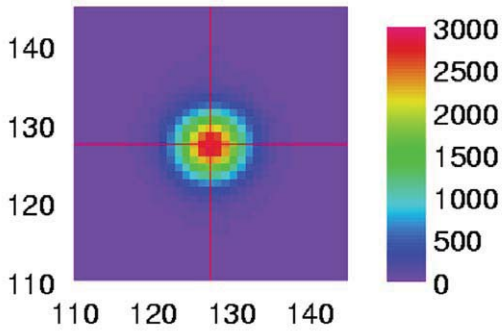

FIG. 3: Image of a 2x2 mm^2 entrance aperture on the position sensitive detector of KWS-3. The horizontal and vertical coordinates are in units of pixels. The distance between two pixels is 0.4 mm.

The beam profile short after the entrance aperture has also been investigated. It consists of three vertical stripes, the stripes being themselves intensity modulated (FIG. 4). The distribution of the beam in three stripes is explained by the different widths of the neutron guide and the divergency transformator (cf. FIG. 2). The source of intensity modulation within the stripes is not yet entirely clarified. Simulations indicate that it originates from images of the cold source due to the multiple reflections in the neutron guide, which are visible due to the strong directional resolution when we apply a small entrance aperture.

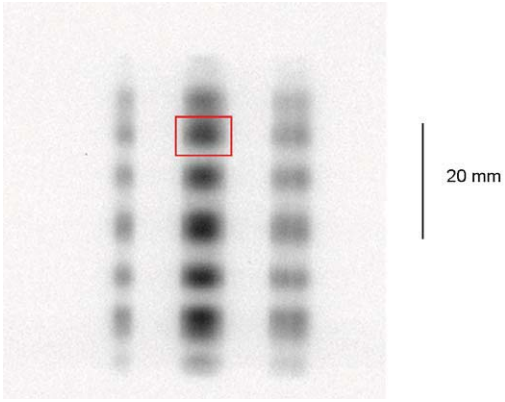

FIG. 4: Beam profile 60 cm behind the 2×2 mm^2 entrance aperture of the instrument recorded on an image plate detector and at a neutron wavelength of 12.5 Å.

After the commissioning of the instrument, further upgrades will follow. In particular, we will equip the instrument with polarized neutrons and a polarization analyzis for the purpose of magnetic studies.

[1] M.R. Eskilden et al., Nature 391, 563 (2000); S.-M. Choi et al., J. Appl. Cryst. 33, 793 (2000)

[2] B. Alefeld et al., Physica B 283, 330 (2000); E. Kentzinger et al., Physica B 350, e779 (2004)

[3] A. Radulescu et al., Macromolecules 39, 6142 (2006)

The Polarizing Guide System for the J-NSE Spectrometer at the FRM II

O. Holderer[1], M. Monkenbusch[2], G. Borchert[3], C. Breunig[3], K. Zeitelhack[3]

[1] JCNS: Jülich Centre for Neutron Science
[2] IFF-5: Neutron Scattering
[3] ZWE FRM II, TU München, D-85747 Garching, Germany

The neutron spin-echo instrument, J-NSE has been moved from the the FRJ-2 in Jülich to the guide hall of the new FRM II reactor. In order to supply an intense beam of polarized neutrons at the assigned new position of the instrument a neutron guide system had to be designed and build to transport neutrons from the available partial beam window of the neutron guide NLII at the wall of the guide hall to the proper spectrometer. Polarization of the short wavelengths is achieved in a bent section with a m=3 FeSi multilayer coating. Due to the total reflection of FeSi, longer wavelengths pass unpolarized and need an additional short polarizer at the entrance of the instrument. For a neutron wavelength band of 10% FWHM centered at 7Å the flux of $1 \times 10^7/\mathrm{cm}^2\mathrm{s}$ at the sample has been achieved.

Neutron spin echo (NSE) spectroscopy provides the highest resolution (corresponding down to a few nano eV) in inelastic neutron scattering[1, 2], with applications in the study of slow dynamics of soft matter systems as e.g. polymer melts or micro-emulsions or in paramagnetic scattering (spin glasses). The normalized intermediate scattering function is measured in terms of polarization loss of the scattered neutrons. As input the instrument accepts a polarized beam with a wide velocity distribution and thereby yields the necessary scattering intensity.

The Jülich NSE spectrometer (J-NSE) had been installed in the neutron guide hall of the Jülich research reactor FRJ-2 [3]. Due to the end-of-operation of the FRJ-2 reactor the instrument (see fig. 1) has been technically updated and transferred to the FRMII in Garching supplying a considerably higher neutron flux. The neutrons from the FRMII cold source have to be polarized and transported efficiently to the J-NSE instrument. The dedicated neutron guide system which is described here is designed to serve this purpose. At the new position at the FRM II, the J-NSE is connected to a dedicated fraction of the neutron guide NL2, i.e. NL2a-o. Using the mechanical velocity selector included into the guide section it is possible to use wavelengths λ between 4.5 and 19Å. This gives an enormous increase in the dynamic range of the spin echo spectrometer, since the fouriertime on which the intermediate scattering function depends $t \propto \int |B| dl\ \lambda^3$, where the first factor, the field integral $\int |B| dl$ alone allows for a 1:10^3 variation.

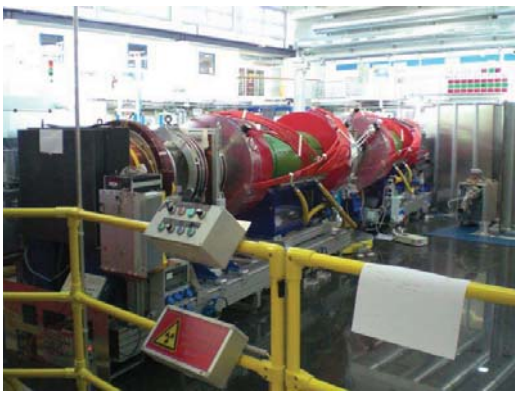

FIG. 1: View on the J-NSE instrument at the FRMII.

The neutron guide NL2a-o separates by a bent part of 8m length inside the radiation shielding casemate from the neighboring NL2 section that leads to the time-of-flight spectrometer TOF-TOF. The radius of curvature is 160m which on the one side yields sufficient distance from the TOF-TOF feeding guide at the position of the instrument and on the other hand polarizes the beam in the range from λ=2.5$\cdots$8Å by reflection from a m=3 (spin-up) and m=0.65 (spin-down) FeSi multilayer produced by T. Krist, NOB. The m-value denotes the ratio of the total reflection angle compared with that from a plain Ni coating as reference. Due to the high primary flux at the curved section a cobalt containing coating was discarded because the long term buildup of considerable ^{60}Co activation. Because of the unpolarized total reflection of FeSi below m=0.65 the longer wavelengths λ =8$\cdots$16Å need an additional short polarizer at the entrance of the proper NSE instrument. After the bent section a mechanical selector (which currently limits $\lambda \geq$4.5Å) is inserted followed by 10m of tapered ^{58}Ni covered guide which ends with a cross section of 60$\times$60mm^2. The NSE-spectrometer uses only a limited divergence of the neutron beam, since the sample position is approximately 3.5m behind the end of the neutron guide. A supermirror (NiTi) coating instead of ^{58}Ni would mainly increase the flux with high divergence and is therefore not necessary in our case, which also simplifies the shielding of the neutron guide. The additional long wavelength polarizer consist of a 60cm long piece of neutron guide with

2 separating walls, the reflecting guide surface and both sides of the walls are covered with an m=3 FeSi multilayer (Swiss Neutronics). For the short wavelength configuration, this polarizer acts as a simple piece of neutron guide. It follows directly the last part of the ^{58}Ni-Guide. For polarizing the long wavelengths, the whole NSE spectrometer is turned by $\Theta = 4^0$ and the long wavelength polarizer is moved to an angle of $\Theta/2 = 2^0$. This leads to a reflection at the polarizing walls and to a deviation of the beam of 4^0. The initial bent section after the NL2a-o separation is embedded into a vertical guide and magnetization field $>$ 30mT which is generated by NbFeB magnet columns between soft iron plates on top and below the guide. After the bent section with FeSi multilayer coating the field is reduced to 6mT. On a 1m section before the selector a smooth turn of the vertical field direction into the longitudinal field from a solenoid around the neutron guide is performed such that the neutron spins follow adiabatically the field direction. The selector is surrounded by a solenoid to preserve the polarization during the neutron passage. The subsequent 10m of neutron guide are surrounded by a coil with about 2 turns/cm which yields B=2.5mT at a current of 10A. Finally the additional polarizer for long wavelengths is surrounded by a solenoid able to sustain 5mT and to create a (once in a while needed) magnetizing field of 30mT during a few seconds.

The flux at the end of the neutron guide, i.e. at the entrance of the NSE spectrometer has been measured by gold-foil activation. The wavelength band has been set by the mechanical velocity selector (10%FWHM). Short wavelengths are sufficiently polarized whereas the longer wavelengths need an additional polarizer. Thus beyond 12Å the gold foil activation detects the sum of both spin directions. The flux at the end of the guide ranges from polarized 4.5 $\times 10^7$/cm^{2}s for wavelength shorter than λ = 7Å down to 1$\times 10^7$/cm^{2}s at λ =16Å. The wavelengths beyond 9-10Å are insufficiently polarized and need the additional polarizer. On the non-guided path of $\simeq$3.5m between neutron guide exit and sample position the larger divergence of the long wavelength neutrons leads to a considerable dilution effect on the flux at the sample position. A reduction of the flipping ratio with increasing wavelength results from the total reflection of both spin components. The additional polarizer is used at a fixed deviation angle of 4^0. For λ= 8Å the flipping ratio is significantly enhanced by the polarizer (from below 7 to above 25), however, the angluar acceptance there is not fully developed to the desired value due to limitation of m. On the other hand at 19Å the total reflection edge (m=0.6) of the polarizer starts to contribute. The flux at the sample position was measured with a calibrated beam monitor. All correction elements and flippers in the beam path were installed. Considering the polarization the flux obtained in the straight configuration may be used up to 8 to 9Å beyond that the 4^0 configuration with active polarizer is to be employed. The wavelength dependence of the flux at the sample position is illustrated in figure 2 for the situation without extra polarizer (usable for $\lambda \leq 9$) and

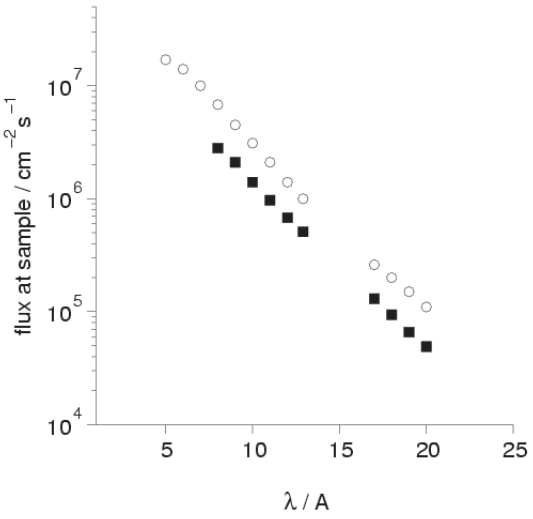

FIG. 2: Flux at the sample position as function of wavelength setting of the selector. Open symbols correspond to straight configuration of the spectrometer with inactive secondary polarizer, solid symbols show result from the 4^0 setting with active polarizer.

with polarizer (usable for $\lambda \geq 8$). A Maxwell spectrum emitted from a small source is expected to deliver a flux $\Phi_0 \lambda^{-5} \exp(-h^2/(2m_n\lambda^2 k_B T))$, since the wavelength band is prepared by a selector with constant relative width, i.e. $\Delta\lambda \propto \lambda$ the λ^{-5} dependence is mitigated to $\Phi \propto \lambda^{-4}$. The flux at the sample for 7Åmatches that of the ILL instrument IN15, however, the decrease at longer wavelength is steeper for the J-NSE. The latter effect has still to be understood.

In summary the flux a the new position of the J-NSE at the FRMII yields 15 times the flux at 8Å that was obtained at the old position in the FRJ-2 guide hall, in addition the flexibility to choose 4.5$\leq \lambda \leq$19Å has been gained by the combined effect of the new reactor source and the tailored neutron guide system. Further details may be found in ref. [4].

[1] F. Mezei, ed., *Neutron Spin Echo*, no. 128 in Lecture Notes in Physics Vol. 128 (Springer, Berlin, Heidelberg, New York, 1980).

[2] F. Mezei, C. Pappas, and T. Gutberlet, eds., *Neutron Spin Echo Spectroscopy*, no. 601 in Lecture Notes in Physics (Springer, Berlin, Heidelberg, New York, 2003).

[3] M. Monkenbusch, R. Schatzler, and D. Richter, Nucl. Inst. & Methods In Physics Research A 399, 301 (1997).

[4] O. Holderer, M. Monkenbusch, G. Borchert, C. Breunig, and K. Zeitelhack, Nucl. Inst. & Methods In Physics Research A, in press.

Status of the New Reflectometer of JCNS at the FRM II: MARIA

S. Mattauch[1], U. Rücker[2], K. Bussmann[2], V. Fracassi[3], R. Schmitz[3], A. Budwig[3], F. Suxdorf[4], P. Kämmerling[4], H. Kleines[4], A. Ioffe[1], Th. Brückel[2]

[1] JCNS: Jülich Centre for Neutron Science
[2] IFF-4: Scattering Methods
[3] Zentralabteilung Technologie
[4] Zentralinstitut für Elektronik

At the outstation of the Jülich Center for Neutron Science JCNS at FRM II, a new reflectometer MARIA will be build. This instrument will be optimized for the study of magnetic nanostructures, serving the rapidly growing field of Spintronics or Magnetoelectronics, i.e. information storage, transport and processing using the spin of the electrons. The instrument will have unique features, such as polarization analysis for large angular range, extreme focusing to small sample sizes, high flux, largely variable wavelength band selection, GISANS option, provision for kinematic studies down to the μs range, in-situ sample preparation etc.. Its neutronic performance was optimized by Monte Carlo simulations and specially developed codes for various neutron optical devices.

The overall layout of this instrument is as follows:

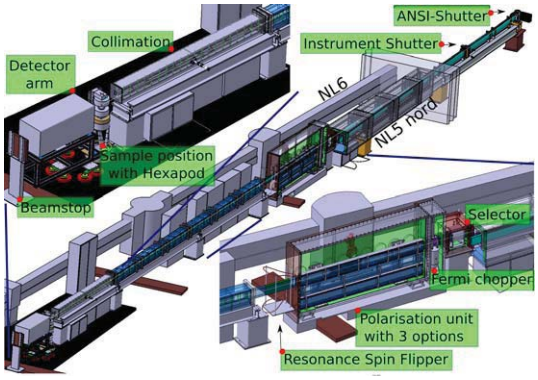

FIG. 1: Illustration of the magnetism reflectometer MARIA at the FRM II.

In Fig. 1 a schematic drawing of the instrument is shown. On the upper left hand corner the instrument starts with the main shutter and a cross section of 170x29mm^2 of the neutron guide. Up to the selector the guide is horizontally curved with a radius of 400m to cut off neutrons with wavelengths below 3.5Å. At the same time the height of the guide is slightly reduced to fit the window of the velocity selector. To optimise the intensity of the neutron beam at the sample position and the measurement strategy we have decided to use a 10% velocity selector to monochromatise the neutrons. Behind the selector a Fermi-chopper allows to reduce the wavelength spread to values between 1% and 3% if desired. In the polarisation unit a double reflection polarising or a non-polarising guide for maximum intensity can be selected by the user. With the resonance spin flipper it is possible to change the polarisation of the incoming neutron beam. Already in the polarisation unit the vertical elliptical focussing starts and ends at the last slit of the collimation, 50cm in front of the sample position. The collimation allows one to set the angular resolution of the incident neutron beam. For reflectometer mode the vertically focussing ellipse is continued along the collimation. In GISANS mode, absorbers prevent the vertical focussing and two sets of slits result in two dimensional collimation of the beam. The combination of the two modes without compromising the intensity of any of them is a unique feature and has never before been realised. The combination of these optical devices have been optimised by simulations with the VITESS suite as well as with specialised programs for the detailed understanding of selector, Fermi-chopper and elliptical focussing properties.

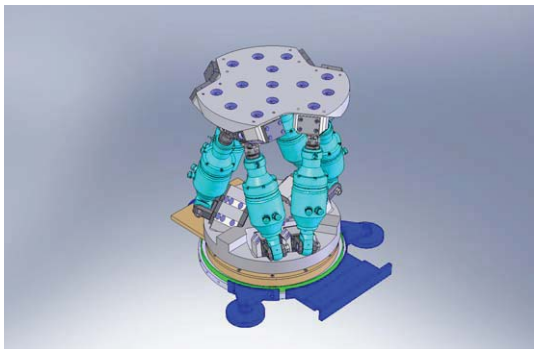

FIG. 2: Illustration of the sample table (hexapod).

Sample and heavy sample environment (up to 700kg) can be adjusted flexibly in every direction using a Hexapod (see Fig. 2)). The detector arm carries the detector shielding, housing spin flipper, polarisation analyser and the 2D-detector. The detector arm will be moved with air cushions on a polished granite floor.

The main activities in the last year brought the instrument from a vision to a living object under construction.

a) Selector: The support of the selector is under construction at the ZAT workshop. The combined boron and lead shielding to prevent the surroundings from radiation is already designed and ordered. Keeping the dense situation of the selector, Fermi chopper and polarisation housing with the neighbouring neutron guide in mind, this is a challenging task and requires a strong cooperation with the FRM II team.

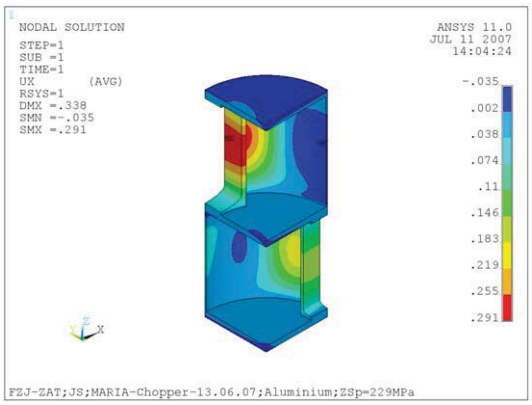

FIG. 3: FE-simulation of the Fermi chopper (radial shift in mm at operating speed).

b) Fermi chopper: Although the Fermi chopper is not planned to be build in the first stage of the instrument a proof of concept is needed here. Therefore FE-simulations of a Fermi chopper rotor (Fig. 3) has been made and showed the principle possibility of such a solution. In Fig. 3 the radial shift in mm is shown at operating speed and the maximum shift of 0.3 mm and is hence in the limit.

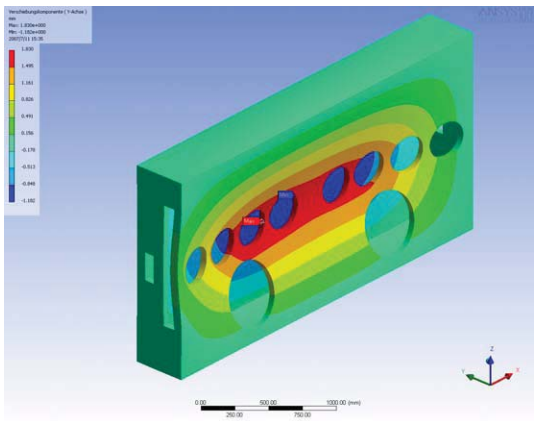

FIG. 4: FE calculations of the deformation of the polarisation housing under vacuum.

c) Polarisation housing: FE-simulations (Fig. 4) have shown that even a steel housing with 100mm thick walls will deform severely (more then 1mm) under vacuum. Therefore the changer of the neutron guides (the alignment has to be in the range of 0.1mm) has to be decoupled completely from the walls of the housing. The housing is now designed and will be under construction shortly.

d) Collimation: The collimation (see Fig. 5) is the end of the guide and the most important part for the focusing of the vertically elliptic neutron guide. The construction of the absorber plates looks simple, but has to work quite accurately not to damage the expensive super mirrors. The design is done and construction will start shortly.

e) Slits: The slits in front and behind the collimation, are designed and one test specimen is already running. The slit in front of the collimation has to work inside vacuum, hence the whole guide from behind the selector down to the end of the collimation is one vacuum housing. This is done to minimise the loss of neutrons and with that of intensity due to vacuum windows.

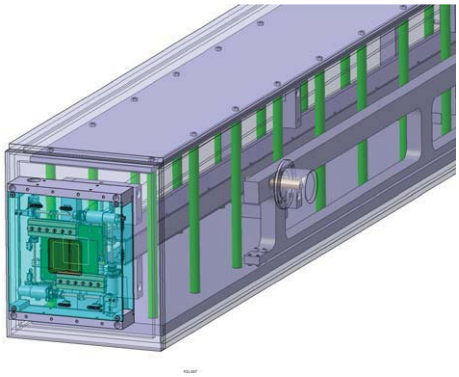

FIG. 5: Drawing of the collimation, the absorbers (grey plates) of the GISANS mode and the four segment slit.

f) Sample table: In Fig. 2 the Hexapod is shown. The design made together with the company is pushed to the limits in accuracy, speed, workspace and weight load. The hexapod will be delivered in February 2008.

g) Electronics: All the motors, switches, encoders, power supplies, vacuum pumps, cooling systems and electronic racks have been designed and now ZEL is working on the wiring diagram. Construction will take place shortly.

A lot of work has been done in the last year and the major components of MARIA should be available during 2008, so that the instrument should see the first neutrons at the end of 2008.

On 12 March 2007, the 38th international Spring School run by the IFF opened its doors. Over a period of two weeks, leading scientists gave 243 students and young researchers from 23 countries a comprehensive overview of the most modern physics research methods that are available for nanoresearch today.

Appendix

Publications

Adam, R.; Khivintsev, Y.; Hertel, R.; Schneider, C. M.
Dynamic properties of arrays of ferromagnetic rectangular bars
Journal of Applied Physics, 101 (2007), 09F516

Ahmad, M. M.; Yamada, K.; Meuffels, P.; Waser, R.
Aging-induced dielectric relaxation in barium titanate ceramics
Applied Physics Letters, 90 (2007), 112902

Akola, J.; Jones, R. O.
Structural phase transitions on the nanoscale: The crucial pattern in the phase-change materials $Ge_2Sb_2Te_5$ and GeTe
Physical Review B, 76 (2007), 235201-1 – 235201-10

Allgaier, J.; Willbold, S.; Chang, T.
Synthesis of Hydrophobic Poly(alkylene oxide)s and Amphiphilic Poly(alkylene oxide) Block Copolymers
Macromolecules, 40 (2007) 3, 518 – 525

Angst, M.; Hermann, R.; Schweika, W.; Kim, J.-W.; Khalifah, P.; Xiang, H.; Whangbo, M.-H.; Kim, D.-H.; Sales, B.; Mandrus, D.
Incommensurate charge order phase in Fe_2OBO_3 due to geometrical frustration
Physical Review Letters, 99 (2007), 256402-1 – 256402-4

Angst, M.; Khalifah, P.; Hermann, R.; Xiang, H. J.; Whangbo, M.-H.; Varadarajan, V.; Brill, J. W.; Sales, B. C.; Mandrus, D.
Charge order superstructure with integer iron valence in FE_2OBO_3
Physical Review Letters, 99 (2007), 086403-1 – 086403-4

Arrott, A. S.; Hertel, R.
Mode anticipation fields for symmetry breaking
IEEE Transactions on Magnetics, 43 (2007) 6, 2911

Atodiresei, N.; Caciuc, V.; Schroeder, K.; Blügel, S.
First-principles investigation of terephthalic acid on Cu(110)
Physical Review B, 76 (2007), 115433

Atodiresei, N.; Schroeder, K.; Blügel, S.
Density-functional theory study on the arrangement of adsorbed formate molecules on Cu(110)
Physical Review B, 75 (2007), 115407

Barashenkov, I. V.; Woodford, S. R.
Interactions of parametrically driven dark solitons. II. Néel-Bloch interactions
Physical Review E, 75 (2007), 026605

Barashenkov, I. V.; Woodford, S. R.; Zemlyanaya, E. V.
Interactions of parametrically driven dark solitons. I. Néel-Néel and Bloch-Bloch interactions
Physical Review E, 75 (2007), 26604

Bauer, E.; Kaldarar, H.; Lackner, R.; Michor, H.; Steiner, W.; Scheidt, E. W.; Galatanu, A.; Marabelli, F.; Wazumi, T.; Kumagai, K.; Feuerbacher, M.
Superconductivity in the complex metallic alloy phase ß-Al_3Mg_2
Physical Review B, 76 (2007), 014528

Bauer, M.; Wiemann, C.; Lange, J.; Bayer, D.; Rohmer, M.; Aeschlimann, M.
Phase propagation of localized surface plasmons probed by time-resolved photoemission electron microscopy
Applied Physics A, 88 (2007) 3, 473 – 480

Bedanta, S.; Kentzinger, E.; Petracic, O.; Kleemann, W.; Rücker, U.; Paul, A.; Brückel, T.; Cardoso, S.; Freitas, P. P.
Polarized neutron reflectivity studies on granular $Co_{80}Fe_{20}/Al_2O_3$ multilayers
Physica B: Condensed Matter, 397 (2007), 65 – 67

Belhadji, B.; Bergqvist, L.; Zeller, R.; Dederichs, P. H.; Sato, K.; Katayama-Yoshida, H.
Trends of exchange interactions in dilute magnetic semiconductors
Journal of Physics: Condensed Matter, 19 (2007), 436227

Belitsky, V.; Maric, N.; Schütz, G. M.
Phase transition in a cellular automaton model of a highway on-ramp
Journal of Physics A – Mathematical and General, 40 (2007), 11221 – 11243

Bergqvist, L.; Dederichs, P. H.
A theoretical study of half-metallic antiferromagnetic diluted magnetic semiconductors
Journal of Physics: Condensed Matter, 19 (2007), 216220

Bihlmayer, G.
Density-functional Theory of Magnetism
Fundamentals and Theory / ed.: H. Kronmüller, St. Parkin. – Chichester, Wiley, 2007. – (Handbook of Magnetism and Advanced Magnetic Materials; 1). – 978-0-470-02217-7. – S. 3

Bihlmayer, G.
Electronic Structure of Matter: Basics and Density Functional Theory
Probing the Nanoworld: Microscopies, Scattering and Spectroscopies of the Solid State; lecture manuscripts of the 38th Spring School 2007 / ed.: K. Urban ... – Jülich, Forschungszentrum, Verlag, 2007. – (Schriften des Forschungszentrum Jülich. Reihe Materie und Material / Matter and Materials; 34). – 978-3-89336-462-6. – S. A3.1 – A3.24

Bihlmayer, G.; Blügel, S.; Chulkov, E. V.
Enhanced Rashba spin-orbit splitting in Bi/Ag(111) and Pb/Ag(111) surface alloys from first principles
Physical Review B, 75 (2007), 195414

Blochowicz, T; Gögelein, C.; Spehr, T.; Müller, M.; Stühn, B.
Polymer-induced transient networks in water-in-oil microemusions studied by small-angle x-ray and dynamic light scattering
Physical Review E, 76 (2007) 4, 041505

Blügel, S.
Electronic Structure of Matter: Reduced Dimensions
Probing the Nanoworld : Microscopies, Scattering and Spectroscopies of the Solid State; lecture manuscripts of the 38th Spring School 2007 / ed.: K. Urban ... – Jülich, Forschungszentrum, Verlag, 2007. – (Schriften des Forschungszentrum Jülich . Reihe Materie und Material / Matter and Materials; 34). – 978-3-89336-462-6. – S. A5.1 – A5.30

Blügel, S.; Bihlmayer, G.
Magnetism of Low-Dimensional Systems: Theory
Fundamentals and Theory / ed.: H. Kronmüller, St. Parkin. – Chichester, Wiley, 2007. – (Handbook of Magnetism and Advanced Magnetic Materials; 1). – 978-0-470-02217-7. – S. 598

Bode, M.; Heide, M.; von Bergmann, K.; Ferriani, P.; Heinze, S.; Bihlmayer, G.; Kubetzka, A.; Pietzsch, O.; Blügel, S.; Wiesendanger, R.
Chiral magnetic order at surfaces driven by inversion asymmetry
Nature, 447 (2007), 190

Bóta, A.; Varga, Z.; Goerigk, G.
Biological systems as nanoreactors: Anomalouls small-angle scattering study of the CdS nanoparticle formation in multilamellar vesicles
Journal of Physical Chemistry B, 111 (2007) 8, 1911 – 1915

Bóta, A.; Varga, Z.; Goerigk, G.
Vesicles as reactors of nanoparticles: an anomalous small-angle X-ray scattering study of the domains rich in copper ions
Journal of Applied Crystallography, 40 (2007), s259 – s263

Botar, B.; Kögerler, P.; Hill, C. L.
Tetrairon and Haxairon Hydroxo/Acetato clusters stabilized by multiple polyoxometalate scaffolds, structures, magnetic properties, and chemistry of a dimer and a trimer
Inorganic Chemistry, 46 (2007), 5398 – 5404

Botti, S.; Schindlmayr, A.; Del Sole, R.; Reining, L.
Time-dependent density-functional theory for extended systems
Reports on Progress in Physics, 70 (2007), 357

Bowen, M.; Maurice, J.-L.; Barthélémy, A.; Bibes, M.; Imhoff, D.; Bellini, V.; Bertacco, R.; Wortmann, D.; Seneor, P.; Jacquet, E.; Vaurès, A.; Humbert, J.; Contour, J.-P.; Colliex, C.; Blügel, S.; Dederichs, P. H.
Using half-metallic manganite interfaces to reveal insights into spintronics
Journal of Physics: Condensed Matter, 19 (2007), 315208

Bräuhaus, D.; Schindler, C.; Böttger, U.; Waser, R.
Radiofrequency sputter deposition of germanium-selenide thin films for resistive switching
Thin Solid Films, 516 (2007), 1223

Bräuhaus, D.; Schorn, P.; Böttger, U.; Waser, R.
Signal form influences on the fatigue behavior of PZT thin film capacitor
16th IEEE International Symposium on Ferroelectrics. – 2007. – S. 69 – 71

Brener, E. A.; Hüter, C.; Pilipenko, D.; Temkin, D. E.
Velocity Selection Problem in the Presence of the Triple Junction
Physical Review Letters, 99 (2007), 105701

Brener, E. A.; Marchenko, V. I.; Spatschek, R.
Influence of strain on the kinetics of phase transitions in solids
Physical Review E, 75 (2007), 041604

Brener, E. A.; Temkin, D. E.
Melting of alloys along the inter-phase boundaries in eutectic and peritectic systems
Acta Materialia, 55 (2007), 2785 – 2789

Brückel, T.
A neutron primer: Elastic scattering and the properties of the neutron
Neutron scattering : Laboratory Course held at Forschungszentrum Jülich and the research reactor FRM II of TU Munich / ed.: Th. Brückel, G. Heger, D. Richter, R. Zorn. – Jülich, Forschungszentrum, Zentralbibliothek, 2007. – (Schriften des Forschungszentrum Jülich. Reihe Materie und Material/ Matter and Materials; 38).
– 978-3-89336-489-3. – S. 2-1 – 2-31

Brückel, T.
Atomic and magnetic structures in crystalline materials: Neutron and x-ray scattering
Probing the Nanoworld : Microscopies, Scattering and Spectroscopies of the Solid State; lecture manuscripts of the 38th Spring School 2007 / ed.: K. Urban ... – Jülich, Forschungszentrum, Verlag, 2007. – (Schriften des Forschungszentrum Jülich . Reihe Materie und Material/Matter and Materials; 34). – 978-3-89336-462-6. – S. D1.1 – D1.47

Brückel, T.
Magnetism
Neutron scattering : Laboratory Course held at Forschungszentrum Jülich and the research reactor FRM II of TU Munich / ed.: Th. Brückel, G. Heger, D. Richter, R. Zorn. – Jülich, Forschungszentrum, Zentralbibliothek, 2007. – (Schriften des Forschungszentrum Jülich . Reihe Materie und Material / Matter and Materials; 38).
– 978-3-89336-489-3. – S. 15-1 – 15-19

Brückel, T. (Hrsg.); Heger, G. (Hrsg.); Richter, D. (Hrsg.); Zorn, R. (Hrsg.)
Neutron Scattering: Laboratory Course held at Forschungszentrum Jülich and the research reactor FRM II of TU Munich
Jülich, Forschungszentrum, Zentralbibliothek, 2007
Schriften des Forschungszentrums Jülich. Reihe Materie und Material / Matter and Material; 38
9783893364893

Bürgler, D. E.; Gareev, R. R.; Pohlmann, L. L.; Braak, H.; Buchmeier, M.; Luysberg, M.; Schreiber, R.; Grünberg, P. A.
Antiferromagnetic interlayer exchange coupling across epitaxial Si spacers
Magnetic Nanostructures / ed.: B. Aktas, L. Tagirov, F. Mikailov. – Berlin, Springer, 2007. – (Springer Series in Material Science; 94). – 978-3-540-49334-1. – S. 133 – 146

Brzank, A.; Schütz, G. M.
Phase transition in the two-component symmetric exclusion process with open boundaries
Journal of Statistical Mechanics: Theory and Experiment, 8 (2007), P08028

Buchenau, U.; Wischnewski, A.; Ohl, M.; Fabiani, E.
Neutron scattering evidence on the nature of the boson peak
Journal of Physics: Condensed Matter, 19 (2007), 205106

Buchenau, U.; Zorn, R.; Ohl, M.; Wischnewski, A.
Dielectric and thermal relaxation in the energy landscape
Philosophical Magazine, 87 (2007) 3/5, 389 – 400

Buchmeier, M.; Dassow, H.; Bürgler, D. E.; Schneider, C. M.
Intensity of Brillouin light scattering from magnetic multilayers with noncollinear spin configurations: Theory and experiment
Physical Review B, 75 (2007), 184436

Buchmeier, M.; Schneider, C. M.; Werner, J.; Elefant, D.; Teresiak, A.; Behr, G.; Schumann, J.; Arushanov, E.
Magnetic properties of polycrystalline $Co_2Cr_{1-x}Fe_xAl$ alloys
Journal of Magnetism and Magnetic Materials, 313 (2007), 157 – 163

Cano-Cortéz, L.; Dolfen, A.; Merino, J.; Behler, J.; Delley, B.; Reuter, K.; Koch, E.
Spectral broadening due to long-range Coulomb interactions in the molecular metal TTF-TCNQ
European Physical Journal B, 56 (2007) 3, 173 – 176

Cao, R.; Anderson, T.M.; Piccoli, P.M.B.; Schultz, A.J.; Koetzle, T.F.; Geletii, Y.V.; Slonkina, E.; Hedman, B.; Hodgson, K.O.; Hardcastle, K.I.; Fang, X.; Kirk, M.L.; Knottenbelt, S.; Kögerler, P.; Musaev, D.G.; Morokuma, K.; Takahashi, M.; Hill, C.L.
Terminal gold-oxo complexes
Journal of the American Chemical Society, 129 (2007), 11118

Chang, J.; Pailhés, S.; Shi, M.; Månsson, M.; Claesson, T.; Tjernberg, O.; Voigt, J.; Perez, V.; Patthey, L.; Momono, N.; Oda, M.; Ido, M.; Schnyder, A.; Mudry, C.; Mesot, J.
When low- and high-energy electronic responses meet in in cuprate superconductors
Physical Review B, 75 (2007), 224508-1 – 224508-6

Chang, L. J.; Terashita, H.; Schweika, W.; Chen, Y. Y.; Gardner, J. S.
$HoTbTi_2O_7$, the mixtures of spin ice and spin liquid
Journal of Magnetism and Magnetic Materials, 310 (2007), 1293 – 1294

Cherifi, S.; Hertel, R.; Locatelli, A.; Watanabe, Y.; Potdevin, G.; Ballestrazzi, A.; Balboni, M.; Heun, S.
Tuning the domain wall orientation in thin magnetic strips using induced anisotropy
Applied Physics Letters, 91 (2007), 092502

Cherstvy, A. G.
Effect of a Low-Dielectric Interior on DNA Electrostatic Response to Twisting and Bending
Journal of Physical Chemistry B, 111 (2007), 12933 – 12937

Cooper, G. J. T.; Newton, G.N.; Kögerler, P.; Long, D.-L.; Engelhardt, L.; Luban, M.; Cronin, L.
Structural and compositional control in {M12} Cobalt and Nickel coordination clusters detected magnetochemically and with Cryospray mass spectrometry
Angewandte Chemie-International Edition, 46 (2007), 1340

Costi, T. A.; Liebsch, A.
Quantum Phase Transition in the Two-Band Hubbard Model
Physical Review Letters, 99 (2007), 236404

De Luca, E.; Waigh, T. A.; Monkenbusch, M.; Kim, J. S.; Jeon, H. S.
Neutron spin echo study of the dynamics of micellar solutions of randomly sulphonated polystyrene
Polymer, 48 (2007), 3930 – 3934

De Raychaudhury, M.; Pavarini, E.; Andersen, O. K.
Orbital fluctuations in the different phases of $LaVO_3$ and YVO_3
Physical Review Letters, 99 (2007), 126402

De Santis, M.; Gauthier, Y.; Tolentino, H. C. N.; Bihlmayer, G.; Blügel, S.; Langlais, V.
Structure and magnetic properties of Mn/Pt(110)-(1x2): A joint x-ray diffraction and theoretical study
Physical Review B, 75 (2007), 205432

Devi, A.; Bhakta, R.; Milanov, A.; Hellwig, M.; Barreca, D.; Tondello, E.; Thomas, R.; Ehrhart, P.; Winter, M.; Fischer, R.
Synthesis and characterisation of zirconium–amido guanidinato complex: a potential precursor for ZrO_2 thin films
Dalton Transactions, 17 (2007), 1671 – 1676

Dhont, J. K. G.; Wiegand, S.; Duhr, S.; Braun, D.
Thermodiffusion of Charged Colloids: Single-Particle Diffusion
Langmuir, 23 (2007), 1674 – 1683

Di Napoli, S.; Llois, A. M.; Bihlmayer, G.; Blügel, S.
Magnetic order in RMn_2Ge_2 (R=Y,Ca) compounds and their solid solutions with $LaMn_2Ge_2$
Physical Review B, 75 (2007), 104406

Dippel, A.C.; Schneller, T.; Gerber, P.; Waser, R.
Morphology control of highly-transparent indium tin oxide thin films prepared by a chlorine-reduced metallo-organic decomposition technique
Thin Solid Films, 515 (2007) 7/8, 3797 – 3801

Döbrich, K. M.; Bihlmayer, G.; Starke, K.; Prieto, J. E.; Rossnagel, K.; Koh, H.; Rotenberg, E.; Blügel, S.; Kaindl, G.
Electronic band structure and Fermi surface of ferromagnetic Tb: Experiment and theory
Physical Review B, 76 (2007), 035123

Dolfen, A.; Luo, Y. L.; Koch, E.
Simulating materials with strong correlations on Blue Gene/L
Parallel Computing: Architectures, Algorithms and Applications: Proceedings of the International Conference ParCo 2007 / ed.: C. Bischof, M. Bücker, P. Gibbon, G. Joubert, Th. Lippert, B. Mohr, F. Peters. – Jülich, Forschungszentrum, 2007. – 978-3-9810843-4-4. – S. 601 – 608

Dolinsek, J.; Apih, T.; Jeglic, P.; Smiljanic, A.; Bilusic, A.; Bihar, Z.; Smontara, A.; Jaglicic, Z.; Heggen, M.; Feuerbacher, M.
Magnetic and transport properties of the giant-unit-cell $Al_{3.26}Mg_2$ complex metallic alloy
Intermetallics, 15 (2007), 1367 – 1376

Eisenriegler, E.; Bringer, A.
Polymer depletion profiles around nonspherical colloidal particles
Journal of Chemical Physics, 127 (2007), 034904

Emtsev, V. V.; Ehrhart, P.; Poloskin, D. S.; Emtsev, K. V.
Comparative studies of defect production in heavily doped silicon under fast electron irradiation at different temperatures
Journal of Materials Science – Materials in Electronics, 18 (2007), 711 – 714

Enkovaara, J.; Wortmann, D.; Blügel, S.
Spin-polarized tunneling between an antiferromagnet and a ferromagnet: First-principles calculations and transport theory
Physical Review B, 76 (2007), 054437

Faley, M.; Mi, S. B.; Petraru, A.; Jia, C. L.; Poppe, U.; Urban, K.
Reduction of strain in high temperature superconductor thin film devises
Physica C, 460-462 (2007), 1371 – 1372

Fan, T.-H.; Dhont, J. K. G.; Tuinier, R.
Motion of a sphere through a polymer solution
Physical Review E, 75 (2007), 011803

Fan, T.-H.; Xie, B.; Tuinier, R.
Asymptotic analysis of tracer diffusivity in nonadsorbing polmyer solutions
Physical Review E, 76 (2007), 051405

Faulhaber, E.; Stockert, O.; Schmalzl, K.; Jeevan, H. S.; Deppe, M.; Geibel, C.; Steglich, F.; Loewenhaupt, M.
Spatial separation of antiferromagnetism and superconductivity in $CeCu_2Si_2$
Journal of Magnetism and Magnetic Materials, 310 (2007), 295 – 297

Ferriani, P.; Turek, I.; Heinze, S.; Bihlmayer, G.; Blügel, S.
Magnetic Phase Control in Monolayer Films by Substrate Tuning
Physical Review Letters, 99 (2007), 187203

Feuerbacher, M.; Thomas, C.; Makongo, J. P. A.; Hoffmann, S.; Carrillo-Cabrera, W.; Cardoso, R.; Grin, Y.; Kreiner, G.; Joubert, J.-M.; Schenk, T.; Gastaldi, J.; Nguyen-Thi, H.; Mangelinck-Noel, N.; Billial, B.; Donnadieu, P.; Czyrska-Filemonowicz, A.; Zielinska-Lipiec, A.; Dubiel, B.; Weber, T.; Schaub, P.; Krauss, G.; Gramlich, V.; Christensen, J.; Lidin, S.; Fredrickson, D.; Mihalkovic, M.; Sikora, W.; Malinowski, J.; Brühne, S.; Proffen, T.; Assmus, W.; de Boissieu, M.; Bley, F.; Chemin, J.-L.; Schreuer, J.; Steurer, W.
The Samson phase, ß-Mg_2Al_2, revisited
Zeitschrift für Kristallographie, 222 (2007), 259 – 288

Feygenson, M.; Kentzinger, E.; Ziegenhagen, N.; Rükker, U.; Goerigk, G.; Wang, Y.; Brückel, T.
Contrast variation by anomalous X-ray scattering applied to investigation of the interface morphology in a giant magnetoresistancwe Fe/Cr/Fe trilayer
Journal of Applied Crystallography, 40 (2007) 3, 532 – 538

Fielden, J.; Long, D.-L.; Slawin, A. M. Z; Kögerler, P.; Cronin, L.
Ligand and counterion control of Ag(I) architectures: Assembly of a {Ag8} ring cluster mediated by hydrophobic and Ag...Ag interactions
Inorganic Chemistry, 46 (2007), 9090

Fleer, G. J.; Skvortsov, A. M.; Tuinier, R.
A Simple Relation for the Concentration Dependence of Osmotic Pressure and Depletion Thickness in Polymer Solutions
Macromolecular Theory and Simulations, 16 (2007), 531 – 540

Fleer, G. J.; Tuinier, R.
Analytical phase diagram for colloid-polymer mixtures
Physical Review E, 76 (2007), 041802

Fleer, G. J.; Tuinier, R.
The critical endpoint in phase diagrams of attractive hard spheres
Physica A, 379 (2007), 52 – 58

Frank, C.; Frielinghaus, H.; Allgaier, J.; Prast, H.
Nonionic Surfactants with Linear and Branched Hydrocarbon Tails: Compositional Analysis, Phase Behavior, and Film Properties in Bicontinuous Microemulsions
Langmuir, 23 (2007) 12, 6526 – 6535

Freysoldt, C.; Eggert, P.; Rinke, P.; Schindlmayr, A.; Godby, R. W.; Scheffler, M.
Dielectric anisotropy in the GW space-time method
Computer Physics Communications, 176 (2007), 1 – 13

Friák, M.; Schindlmayr, A.; Scheffler, M.
Ab initio study of the half-metal to metal transition in strained magnetite
New Journal of Physics, 9 (2007), 5

Frielinghaus, H.
Small-angle scattering model for multilamellar vesicles
Physical Review E, 76 (2007), 051603-1 051603-8

Frielinghaus, H.
Structure of soft matter: Small angle scattering
Probing the Nanoworld: Microscopies, Scattering and Spectroscopies of the Solid State; lecture manuscripts of the 38th Spring School 2007 / ed.: K. Urban ... – Jülich, Forschungszentrum, Verlag, 2007. – (Schriften des Forschungszentrum Jülich. Reihe Materie und Material/Matter and Materials; 34). – 978-3-89336-462-6. – S. D5.1 – D5.27

Furukawa, Y.; Nishisaka, Y.; Kumagai, K.; Kögerler, P.
Spin structure of the nanoscale molecular magnet V15 cluster revealed by 51V-NMR
Journal of Magnetism and Magnetic Materials, 310 (2007), 1429 – 1431

Furukawa, Y.; Nishisaka, Y.; Kumagai, K.; Kögerler, P.; Borsa, F.
Local spin moment configuration in the frustrated s = 1/2 Heisenberg triangular antiferromagnet V15 determined by NMR
Physical Review B, 75 (2007), 220402

Galanakis, I.; Mavropoulos, P.
Spin-polarization and electronic properties of half-metallic Heusler alloys calculated from first principles
Journal of Physics: Condensed Matter, 19 (2007) 31, 315213

Galanakis, I.; Özdogan, K.; Sasioglu, E.; Aktas, B.
Ab initio design of half-metallic fully compensated ferrimagnets: The case of Cr_2MnZ (Z=P, As, Sb, and Bi)
Physical Review B, 75 (2007), 172405

Galanakis, I.; Özdogan, K.; Sasioglu, E.; Aktas, B.
Doping of Mn_2VAl and Mn_2VSi Heusler alloys as a route to half-metallic antiferromagnetism
Physical Review B, 75 (2007), 092407

Gao, G. Y.; Yao, K. L.; Sasioglu, E.; Sandratskii, L. M.; Liu, Z. L.; Jiang, J. L.
Half-metallic ferromagnetism in zinc-blende CaC, SrC, and BaC from first principles
Physical Review B, 75 (2007), 174442

Gapinski, J.; Patkowski, A.; Banchio, A. J.; Holmqvist, P.; Meier, G.; Lettinga, M. P.; Nägele, G.
Collective diffusion in charge-stabilized suspensions: Concentration and salt effects
Journal of Chemical Physics, 126 (2007), 104905

Goerigk, G.; Huber, K.; Schweins, R.
Probing the extent of the Sr^{2+} ion condensation to anionic polyacrylate coils: A quantitative anomalous small-angle x-ray scattering study
Journal of Chemical Physics, 127 (2007), 154908-1 – 154908-8

Goerigk, G.; Williamson, D. L.
Correlation between the photoconductivity and the nanostructure of hot-wire deposited silicon-germanium alloys analyzed by anomalous small-angle x-ray scattering
Photovoltaic Cell and Module Technologies. – International Society of Optical Engineering, 2007. – (Proceedings of the SPIE; 6651). – S. 66510D/1 – 66510D/13

Göritz, D.; Maurer, C.; Schneider, G. J.; Bissem, H. H.
Temperature dependence of dynamic mechanical properties of filled elastomeres
Proceedings of the 11th International Seminar on Elastomers, 23.09.2007-27.09.2007, Freiburg. – 2007. – S. 69

Goll, G.; Stockert, O.; Prager, M.; Yoshino, T.; Takabatake, T.
Low energy excitations in CeBiPt
Journal of Magnetism and Magnetic Materials, 310 (2007), 1773

Götze, I.; Noguchi, H.; Gompper, G.
Relevance of angular momentum conservation in mesoscale hydrodynamics simulations
Physical Review E, 76 (2007), 046705

Gompper, G. (Hrsg.); Schick, M. (Hrsg.)
Colloidal Order: Entropic and Surface Forces
Weinheim, Germany, Wiley-VCH, 2007
Soft Matter; 3 – 9783527313709

Grandjean, F.; Hermann, R. P.; Popiel, E.; Long, G. J.
A Mössbauer spectral study of the $GdCo_{4x}Fe_xB$ compounds
Journal of Applied Physics, 101 (2007), 023917-1 – 023917-6

Grosskinsky, S.; Schütz, G. M.; Willmann, R. D.
Rigorous results on spontaneous symmetry breaking in a one-dimensional driven particle system
Journal of Statistical Physics, 128 (2007), 587 – 606

Grünberg, P.; Bürgler, D. E.; Dassow, H.; Rata, A. D.; Schneider, C. M.
Spin-transfer phenomena in layered magnetic structures: Physical phenomena and material aspects
Acta Materialia, 55 (2007), 1171

Grushko, B.; Velikanova, T.
Formation of quasiperiodic and related periodic intermetallics in alloy systems of aluminum with transition metals
Calphad – Computer Coupling of Phase Diagrams and Thermochemistry, 31 (2007) 2, 217 – 232

Guo, X.; Schindler, C.; Menzel, S.; Waser, R.
Understanding the switching-off mechanism in Ag^+ migration based resistively switching model systems
Applied Physics Letters, 91 (2007), 133513

Gutiérrez, J.; Barandiarán, J. M.; Bermejo, F. J.; Mondelli, C.; Romano, P.; Fouquet, P.; Monkenbusch, M.
Evidence for two disparate spin dynamic regimes within Fe-substituted $La_{0,7}$ $Pb_{0,3}(Mn_{1-x}Fex)O_3$ ($0 \leqslant x \leqslant 0,2$) colossal magentoresistive manganites: Neutron spin-echo measurements
Physical Review B, 76 (2007) 18, 184401

Gwan, J. F.; Baumgaertner, A.
Cooperative Transport in a Potassium Ion Channel
Journal of Chemical Physics, 127 (2007), 045103

Gwan, J. F.; Baumgaertner, A.
Ion Transport in a Nanochannel
Journal of computational and theoretical nanoscience: for all theoretical and computational aspects in science, engineering, and biology, 4 (2007), 50 – 56

Halder, S.; Schneller, T.; Waser, R.
Enhanced stability of platinized silicon substrates using an unconventional adhesion layer deposited by CSD for high temperature dielectric thin film deposition
Applied Physics A, 87 (2007), 705 – 708

Halder, S.; Schneller, T.; Waser, R.
Microstructure and electrical properties of $BaTiO_3$ and $(Ba,Sr)TiO_3$ ferroelectric thin films on nickel electrodes
Journal of Sol-Gel Science and Technology, 42 (2007), 203

Hanuschkin, A.; Wortmann, D.; Blügel, S.
Image Potential and Field States at Ag(100) and Fe(110) Surfaces
Physical Review B, 76 (2007), 165417

Harris, R. J.; Schütz, G. M.
Fluctuation theorems for stochastic dynamics
Journal of Statistical Mechanics: Theory and Experiment, (2007), P07020

Harris, R. J.; Stinchcombe, R. B.
Scaling approach to related disordered stochastic and free-fermion models
Physical Review E, 75 (2007), 031104

Heeg, T.; Roeckerath, M.; Schubert, J.; Zander, W.; Buchal, Ch.; Chen, H. Y.; Jia, C. L.; Jia, Y.; Adamo, C.; Schlom, D. G.
Epitaxially stabilized growth of orthorhombic $LuScO_3$ thin films
Applied Physics Letters, 90 (2007), 192901-1 – 192901-3

Heggen, M.; Deng, D.; Feuerbacher, M.
Plastic deformation properties of the orthorhombic complex metallic alloy phase $Al_{13}Co_4$
Intermetallics, 15 (2007), 1425 – 1431

Heinisch, H. L.; Trinkaus, H.; Singh, B. N.
Kinetic Monte Carlo studies of the reaction kinetics of crystal defects that diffuse one-dimensionally with occasional transverse migration
Journal of Nuclear Materials, 367-370 (2007) 1, 332 – 337

Heiss, A.; Schwahn, D.
Formation and Structure of Calciprotein Particles: The Calcium Phosphate – Ahsg/Fetuin-A Interphase
The Biology of Biominerals Structure Formation / ed.: E. Bäuerlein, P. Behrens, M. Epple. – Weinheim, Wiley-VCH, 2007. – (Handbook of Biomineralization; 1).
– Chapter 24, S. 415 – 433

Hennings, A.; Semouchkina, E.; Baker, A.; Semouchkin, G.; Waser, R.; Lanagan, M.
Development of Miniature LTCC Filter for TV Broadcasting Bank by Using Substrates of Mixed Dielectrics
Proceedings of the 37th European Microwave Conference, October 2007, Munich. – 2007. – S. 866 – 869

Henry, J.; Vincent, L.; Averty, X.; Marini, B.; Jung, P.
Effect of a high helium content on the flow and fracture properties of a 9Cr martensitic steel
Journal of Nuclear Materials, 367-370 (2007) 1, 411 – 416

Hermann, R. P.; Grandjean, F.; Kafle, D.; Brown, D. E.; Johnson, C. E.; Kauzlarich, S. M.; Long, G. J.
Antimony-121 Mössbauer Spectral Study of the $Eu_{14}MnSb_{11}$ and $Yb_{14}MnSb_{11}$ Zintl Compounds
Inorganic Chemistry, 46 (2007), 10736 – 10740

Hertel, R.
Guided Spin Waves
Handbook of Magnetism and Advanced Magnetic Materials / ed.: H. Kronmüller, S. Parkin. – Chichester, UK, Wiley, 2007. – 978-0-470-02217-7. – S. 1003 – 1020

Hertel, R.; Gliga, S.; Fähnle, M.; Schneider, C. M.
Ultrafast nanomagnetic toggle switching of vortex cores
Physical Review Letters, 98 (2007), 117201

Hirahara, T.; Miyamoto, K; Matsuda, I.; Kadono, T.; Kimura, A; Nagao, T.; Bihlmayer, G.; Chulkov, E. V.; Qiao, S.; Shimada, K; Namatame, H.; Taniguchi, M.; Hasegawa, S.
Direct observation of spin splitting in bismuth surface states
Physical Review B, 76 (2007), 153305

Hirahara, T.; Nagao, T.; Matsuda, I.; Bihlmayer, G.; Chulkov, E. V.; Koroteev, Yu. M.; Hasegawa, S.
Quantum well states in ultrathin Bi films: Angle-resolved photoemission spectroscopy and first-principles calculations study
Physical Review B, 75 (2007), 035422

Holderer, O.; Frielinghaus, H.; Monkenbusch, M.; Allgaier, J.; Richter, D.; Farago, B.
Hydrodynamic effects in bicontinuous microemulsions measured by inelastic neutron scattering
European Physical Journal E, 22 (2007), 157 – 161

Holmqvist, P.; Kleshchanok, D.; Lang, P. R.
Unexpected slow near wall dynamics of spherical colloids in a suspension of rods
Langmuir, 23, 12010-12015

Holmqvist, P.; Dhont, J. K. G.; Lang, P. R.
Colloidal dynamics near a wall studied by evanescent wave light scattering: Experimental and theoretical improvements and methodological limitations
Journal of Chemical Physics, 126 (2007), 044707

Iatrou, H.; Frielinghaus, H.; Hanski, S.; Ferderigos, N.; Ruokolainen, J.; Ikkala, O.; Richter, D.; Mays, J.; Hadjichristidis, N.
Architecturally induced multiresponsive vesicles from well-defined polypeptides. Formation of gene vehicles
Biomacromolecules, 8 (2007) 7, 2173 – 2181

Ibberson, R. M.; Prager, M.
Temperature-dependent crystal structure analysis of methyl iodide by high-resolution neutron powder spectroscopy
Zeitschrift für Kristallographie, 222 (2007), 416

Ioffe, A.
Neutron Sources
Neutron scattering: Laboratory Course held at Forschungszentrum Jülich and the research reactor FRM II of TU Munich ed.: Th. Brückel, G. Heger, D. Richter, R. Zorn. – Jülich, Forschungszentrum, Zentralbibliothek, 2007. – (Schriften des Forschungszentrum Jülich . Reihe Materie und Material/Matter and
Materials; 38). – 978-3-89336-489-3. – S. 1-1 – 1-11

Ioffe, A.; Bodnarchuk, V.; Bussmann, K.; Mueller, R.
Larmor labeling by time-gradient magnetic fields
Physica B: Condensed Matter, 397 (2007), 108 – 111

Jeglic, P.; Komelj, M.; Klanjsek, M.; Tkalec, U.; Vrtnik, S.; Feuerbacher, M.; Dolinsek, J.
Orientation-dependent NMR study of the giant-unit-cell intermetallics β-Al_3Mg_2, Bergman-phase $Mg_{32}(Al,Zn)_{49}$, and ξ′-$Al_{74}Pd_{22}Mn_4$
Physical Review B, 75 (2007), 014202

Jeong, D. S.; Schroeder, H.; Waser, R.
Coexistence of bipolar and unipolar resistive switching behavior in a Pt/TiO_2/Pt stack
Electrochemical and Solid State Letters, 10 (2007), G51 – G53

Jia, C. L.; Nagarajan, V.; He, J. Q.; Houben, L.; Zhao, T.; Ramesh, R.; Urban, K.; Waser, R.
Unit-cell scale mapping of ferroelectricity and tetragonality in epitaxial ultrathin ferroelectric films
Nature Materials, 6 (2007), 64

Jungblut, S.; Tuinier, R.; Binder, K.; Schilling, T.
Depletion induced isotropic-isotropic phase separation in suspensions of rod-like colloids
Journal of Chemical Physics, 127 (2007), 244909

Kajiyoshi, K.; Kambe, T.; Mino, M.; Nojiri, H.; Kögerler, P.; Luban, M.
Direct estimation of zero-field energy gap in the nano-scale single molecular magnet V_{15}
Journal of Magnetism and Magnetic Materials, 310 (2007), 1203 – 1205

Kallmayer, M.; Schneider, H.; Jakob, G.; Elmers, H. J.; Balke, B.; Cramm, S.
Interface magnetization of ultrathin epitaxial $Co_2FeSi(110)/Al_2O_3$ films
Journal of Physics D – Applied Physics, 40 (2007), 1552 – 1557

Kang, K.; Wilk, A.; Patkowski, A.; Dhont, J. K. G.
Diffusion of spheres in isotropic and nematic networks of rods: Electrostatic interactions and hydrodynamic screening
Journal of Chemical Physics, 126 (2007), 214501

Katayama-Yoshida, H.; Sato, K.; Fukushima, T.; Toyoda, H.; Kizaki, H.; Dinh, V. A.; Dederichs, P. H.
Theory of ferromagnetic semiconductors
Physica Status Solidi A, 204 (2007) 1, 3

Kentzinger, E.
Diffusion des neutrons polarisés en incidence rasante
14èmes Journées de la Diffusion Neutronique: Ecole Thématique; Surfaces, Interfaces, Milieux confinés par Diffusion de Neutrons = JDN 14 / ed.: A. Brulet. – Murol, France, EDP Sciences, 2006. – (Collection de la Societe Francaise de la Neutronique; 8). – S. 23 – 42

Kentzinger, E.; Frielinghaus, H.; Rücker, U.; Ioffe, A.; Richter, D.; Brückel, T.
Probing lateral magnetic nanostructures by polarized GISANS
Physica B: Condensed Matter, 397 (2007), 43 – 46

Kever, T.; Böttger, U.; Schindler, C.; Waser, R.
On the origin of bistable resistive switching in metal organic charge transfer complex memory cells
Applied Physics Letters, 91 (2007), 083506

Kiebach, R.; Näther, C.; Kögerler, P.; Bensch, W.
$[V^{IV}_{15}Sb^{III}_{6}O_{42}]^{6-}$: an antimony analogue of the molecular magnet $[V_{15}As_6O_{42}(H_2O)]^{6-}$
Dalton Transactions, (2007) 30, 3221 – 3223

Kirstein, O.; Prager, M.; Grimm, H.; Buchsteiner, A.; Wischnewski, A.
Quasielastic neutron scattering experiments including activation energies and mathematical modeling of methyl halide dynamics
Journal of Chemical Physics, 127 (2007), 094504

Kita, R.; Polyakov, P.; Wiegand, S.
Ludwig-Soret Effect of Poly(N-isopropylacrylamide): Temperature Dependence Study in Monohydric Alcohols
Macromolecules, 40 (2007) 5, 1638 – 1642

Kleshchanok, D.; Lang, P. R.
Steric Repulsion by Adsorbed Polymer Layers Studied with Total Internal Reflection Microscopy
Langmuir, 23 (2007), 4332 -4339

Koch, E.
Electronic Structure of Matter: Electron Correlations
Probing the Nanoworld: Microscopies, Scattering and Spectroscopies of the Solid State; lecture manuscripts of the 38th Spring School 2007 / ed.: K. Urban ... – Jülich, Forschungszentrum, Verlag, 2007. – (Schriften des Forschungszentrum Jülich . Reihe Materie und Material / Matter and Materials; 34). – 978-3-89336-462-6. – S. A4.1 – A4.20

Köbler, U.; Hoser, A.
Critical magnetic behaviour in one and two dimensions
Journal of Magnetism and Magnetic Materials, 311 (2007), 523 – 529

Köbler, U.; Hoser, A.
First order spin flop transition in yttrium iron garnet (YIG)
Solid State Communications, 142 (2007), 350 – 354

Köbler, U.; Hoser, A.
The crossover from atomistic to continuous dynamic symmetry at the magnetic phase transition
Solid State Communications, 142 (2007), 600 – 604

Köbler, U.; Hoser, A.
The impact of renormalization group theory on magnetism
European Physical Journal B, 60 (2007), 151 – 159

Köbler, U.; Hoser, A.; Mueller, R. M.; Fischer, K.
Complex critical magnetic behaviour in three dimensions
Journal of Magnetism and Magnetic Materials, 315 (2007), 12 – 25

Köbler, U.; Thomas, C.
Universality in the heat capacity of magnetic and superconducting solids for $T \geq 0$
Physica B: Condensed Matter, 395 (2007), 39 – 47

Kohlbrecher, J.; Bollhalder, A.; Vavrin, R.; Meier, G.
A high pressure cell for small angle neutron scattering up to 500 MPa in combination with light scattering to investigate liquid samples
Review of Scientific Instruments, 78 (2007), 125101

Kohyama, T.; Gompper, G.
Defect Scars on Flexible Surfaces with Crystalline Order
Physical Review Letters, 98 (2007), 198101-1 – 198101-4

Kozhevnikov, S.; Ott, F.; Kentzinger, E.; Paul, A.
Enhanced off-specular scattering in magnetic neutron waveguides
Physica B: Condensed Matter, 397 (2007), 68 – 70

Lago, J.; Micotti, E.; Corti, M.; Lascialfari, A.; Bianchi, A.; Carretta, S.; Santini, P.; Procissi, D.; Baek, S. H.; Kögerler, P.; Baines, C.; Amato, A.
Low-energy spin dynamics in the giant keplerate molecule $\{Mo_{72}Fe_{30}\}$: A muon spin relaxation and ^1H NMR investigation
Physical Review B, 76 (2007), 064432

Lang, P. R.
Depletion interaction mediated by polydisperse rods
Journal of Chemical Physics, 127 (2007), 124906

Lebedev, D. V.; Monkenbusch, M.; Shalguev, V. I.; Lantsov, V. A.; Isaev-Ivanov, V. V.
Dynamic properties of RecA protein filaments from E-coli and P-aeruginosa investigated by neutron spin echo
Biofizika, 52 (2007) 5, 799 – 803

Lehndorff R.; Buchmeier M.; Bürgler D.; Kakay A.; Hertel R.; Schneider C. M.
Asymmetric spin-transfer torque in single-crystalline Fe/Ag/Fe nanopillars
Phys. Rev. B 76 (21) 214420 (2007)

Lettinga, M. P.; Grelet, E.
Self-diffusion of rodlike viruses through smectic layers
Physical Review Letters, 99 (2007), 197802

Lezaic, M.; Mavropoulos, Ph.; Blügel, S.
First-principles prediction of high Curie temperature for ferromagnetic bcc-Co and bcc-FeCo alloys and its relevance to tunneling magnetoresistance
Applied Physics Letters, 90 (2007), 082504

Li, H. F.; Su, Y.; Perßon, J.; Meuffels, P.; Walter, J. M.; Skowronek, R.; Brückel, T.
Neutron-diffraction study of structural transition and magnetic order in orthorhombic and rhombohedral $La_{7/8}Sr_{1/8}Mn_{1-\gamma}O_{3+\delta}$
Journal of Physics: Condensed Matter, 19 (2007), 176226-1 - 176226-12

Li, H.; Su, Y.; Perßon, J.; Meuffels, P.; Walter, J.; Skowronek, R.; Brückel, T.
Correlation between structural and magnetic properties of $La_{7/8}Sr_{1/8}Mn_{1-\gamma}O_{3+\delta}$ with controlled nonstoichiometry
Journal of Physics: Condensed Matter, 19 (2007), 016003-1 – 016003-12

Liebsch, A.; Ishida, H.
Subband Filling and Mott Transition in $Ca_{2-x}Sr_xRuO_4$
Physical Review Letters, 98 (2007), 216403

Liu, M.-H.; Bihlmayer, G.; Blügel, S.; Chang, Ch.-R.
Intrinsic spin-Hall accumulation in honeycomb lattices: Band structure effects
Physical Review B, 76 (2007), 121301(R)

Liu, Y.; Gliga, S.; Hertel, R.; Schneider, C. M.
Current-induced magnetic vortex core switching in a Permalloy nanodisk
Applied Physics Letters, 91 (2007), 112501

Loukakos, P. A.; Lisowski, M.; Bihlmayer, G.; Blügel, S.; Wolf, M.; Bovensiepen, U.
Dynamics of the Self-Energy of the Gd(0001) Surface State Probed by Femtosecond Photoemission Spectroscopy
Physical Review Letters, 98 (2007), 097401

Lounis, S.; Mavropoulos, Ph.; Zeller, R.; Dederichs, P. H.; Blügel, S.
Noncollinear magnetism of Cr and Mn nanoclusters on Ni(111): Changing the magnetic configuration atom by atom
Physical Review B, 75 (2007), 174436

Lund, R.; Willner, L.; Richter, D.; Iatrou, H.; Hadjichristidis, N.; Lindener, P.
Unraveling the equilibrium chain exchange kinetics of polymeric micelles using small-angle neutron scattering – architectural and topological effects
Journal of Applied Crystallography, 40 (2007), s327 – s331

Lüssem, B.; Müller-Meskamp, L.; Karthäuser, S.; Homberger, M.; Simon, U.; Waser, R.
Electrical Characterization of Biphenylalkanethiol SAMs
Journal of Physical Chemistry C, 111 (2007), 6392

Lyatti, M.; Divin, Y.; Volkov, O.; Pavlovskii, V.; Gubankov, V.; Urban, K.
Signal and Noise Characteristics of Terahertz Frequency-Selective and Broadband High-Tc Josephson Detectors
IEEE Transactions on Applied Superconductivity, 17 (2007), 332 – 335

Lyatti, M. V.; Poppe, U.; Divin, Y. Y.
Electrical transport and noise properties of [100]-tilt $YBa_2Cu_3O_7$-x grain-boundary junctions with high IcRn product
IEEE Transactions on Applied Superconductivity, 17 (2007) 2, 314 – 317

Maccarrone, S.; Frielinghaus, H.; Allgaier, J.; Richter, D.; Lindner, P.
SANS Study of Polymer-Linked Droplets
Langmuir, 23 (2007) 19, 9559 – 9562

Mangiapia, G.; Ricciardi, R.; Auriemma, F.; de Rosa, C.; Lo Celso, F.; Triolo, R.; Heenan, R. K.; Radulescu, A.; Tedeschi, A. M.; D'Errico, G.; Paduano, L.
Mesoscopic and Microscopic Investigation on Poly(vinyl alcohol) Hydrogels in the Presence of Sodium Decylsulfate
Journal of Physical Chemistry B, 111 (2007) 9, 2166 – 2173

Martyanov, O. N.; Yudanov, V. F.; Lee, R. N.; Nepijko, S. A.; Elmers, H. J.; Hertel, R.; Schneider, C. M.; Schönhense, G.
Ferromagnetic resonance study of thin film antidot arrays: Experiment and micromagnetic simulations
Physical Review B, 75 (2007), 174429

Mattern, N.; Gemming, T.; Goerigk, G.; Eckert, J.
Phase separation in amorphous Ni-Nb-Y alloys
Scripta Materialia, 57 (2007), 29 – 32

Mavropoulos, P.; Galanakis, I.
A review of the electronic and magnetic properties of tetrahedrally bonded half-metallic ferromagnets
Journal of Physics: Condensed Matter, 19 (2007) 31, 315221

McPhie, M. G.; Nägele, G.
Long-time self-diffusion of charged colloidal particles: Electrokinetic and hydrodynamic interaction effects
Journal of Chemical Physics, 127 (2007), 034906

Meszaros, G.; Kronholz, S.; Karthäuser, S.; Mayer, D.; Wandlowski, Th.
Electrochemical Fabrication and Characterization of Nanocontacts and nm-sized Gaps
Applied Physics A, 87 (2007), 569 – 575

Meuffels, P.
Decoherence and the quantum measurement problem (Letter to the Editor)
American Journal of Physics, 75 (2007), 1063

Meuffels, P.
Propane gas sensing with high-density $SrTi_{0.6}Fe_{0.4}O_{(3-\gamma)}$ ceramics evaluated by thermogravimetric analysis
Journal of the European Ceramic Society, 27 (2007), 285

Meyer, C.; Elzerman, J. M.; Kouwenhoven, L. P.
Photon-assisted tunneling in a Carbon nanotube quantum dot
Nano Letters, 7 (2007), 295 – 299

Mi, S. B.; Jia, C. L.; Faley, M.; Poppe, U.; Urban, K.
High resolution electron microscopy of microstructure of $SrTiO_3/BaZrO_3$ bilayer thin films on MgO substrates
Journal of Crystal Growth, 300 (2007), 478 – 482

Micklitz, T.; Costi, T. A.; Rosch, A.
Magnetic field dependence of dephasing rate due to diluted Kondo impurities
Physical Review B, 75 (2007), 054406

Mlynarczyk, M.; Szot, K.; Petraru, A.; Poppe, U.; Breuer, U.; Waser, R.; Tomala, K.
Surface layer of $SrRuO_3$ epitaxial thin films under oxidizing and reducing conditions
Journal of Applied Physics, 101 (2007) 2, 023701 – 0237011

Mokrousov, Y.; Atodiresei, N.; Bihlmayer, G.; Heinze, S.; Blügel, S.
The interplay of structure and spin-orbit strength in the magnetism of metal-benzene sandwiches: from single molecules to infinite wires
Nanotechnology, 18 (2007), 495402

Mokrousov, Y.; Bihlmayer, G.; Blügel, S.; Heinze, S.
Magnetic order and exchange interactions in monoatomic 3d transition-metal chains
Physical Review B, 75 (2007), 104413

Monkenbusch, M.
Soft Matter Dynamics: Neutron spin echo spectroscopy and X-ray correlation spectroscopy
Probing the Nanoworld: Microscopies, Scattering and Spectroscopies of the Solid State; lecture manuscripts of the 38th Spring School 2007 / ed.: K. Urban ... – Jülich, Forschungszentrum, Verlag, 2007. – (Schriften des Forschungszentrum Jülich. Reihe Materie und Material / Matter and Materials; 34). – 978-3-89336-462-6. – S. D6.1 – D6.27

Müller, M.; Matthes, F.; Schneider, C. M.
Photoemission study of the Fe(001)/MgO interface for varying oxidation conditions of magnesium oxide
Journal of Applied Physics, 101 (2007), 09G519

Müller-Meskamp, L.; Lüssem, B.; Karthäuser, S.; Homberger, M.; Simon, U.; Waser, R.
Self-Assembly of Mixed Monolayers of Mercaptoundecylferrocene and Undecanethiol studied by STM
Journal of Physics : Conference Series, 61 (2007), 852

Niedzwiedz, K.; Wischnewski, A.; Monkenbusch, M.; Richter, D.; Genix, A.-C.; Arbe, A.; Colmenero, J.; Strauch, M.; Straube, E.
Polymer Chain Dynamics in a Random Environment: Heterogeneous Mobilities
Physical Review Letters, 98 (2007), 168301

Noguchi, H.; Gompper, G.
Swinging and Tumbling of Fluid Vesicles in Shear Flow
Physical Review Letters, 98 (2007), 128103

Noguchi, H.; Gompper, G.
Transport coefficients of dissipative particle dynamics with finite time step
Europhysics Letters, 79 (2007), 36002

Noguchi, H.; Kikuchi, N.; Gompper, G.
Particle-based mesoscale hydrodynamic techniques
Europhysics Letters, 78 (2007), 10005

Notbohm, S.; Tennant, D. A.; Lake, B.; Canfield, P. C.; Fielden, J.; Kögerler, P.; Mikeska, H.-J.; Luckmann, C.; Telling, M. T. F.
Temperature effects on multi-particle scattering in a gapped quantum magnet
Journal of Magnetism and Magnetic Materials, 310 (2007), 1236

Oberdisse, J.; Hine, P.; Pyckhout-Hintzen, W.
Structure of interacting aggregates of silicia nanoparticles in a polymer matrix: Small-angle scattering and reverse Monte-Carlo simulations
Soft Matter, 3 (2007) 2, 476 – 485

Osorio, E. A.; O'Neill, K.; Wegewijs, M.; Stuhr-Hansen, N.; Paaske, J.; Bjornholm, T.; van der Zant, H. S. J.
Electronic excitations of a single molecule contacted in a three-terminal configuration
Nano-Letters 7, (2007), 3336

Özdogan, K.; Aktas, B.; Galanakis, I.; Sasioglu, E.
Influence of mixing the low-valent transition metal atoms (Y, Y=Cr, Mn, Fe) on the properties of the quaternary $CO_2[Y_{1-x}Y^*_x]Z$ (Z=Al, Ga, Si, Ge, or Sn) Heusler compounds*
Journal of Applied Physics, 101 (2007), 073910

Özdogan, K.; Galanakis, I.; Sasioglu, E.; Aktas, B.
Defects-driven appearance of half-metallic ferrimagnetism in Co–Mn-based Heusler alloys
Solid State Communications, 142 (2007) 9, 492 – 497

Parshin, D. A.; Schober, H. R.; Gurevich, V. L.
Vibrational instability, two-level systems, and the boson peak in glasses
Physical Review B, 76 (2007), 064206

Patkowski, A.; Gapinski, J.; Meier, G.; Kriegs, H.
Isotropic Brillouin spectra of liquids having an internal degree of freedom
Journal of Chemical Physics, 126 (2007), 014508

Paul, A.; Braak, H.; Bürgler, D. E.; Schreiber, R.; Rata, D.; Grünberg, P.; Schneider, C. M.; Brückel, T.
Polarized neutron reflectivity of dilute magnetic semiconductors
Physica B: Condensed Matter, 397 (2007), 59 – 61

Paul, A.; Brückel, T.; Kentzinger, E.; Rücker, U.
Magnetization reversal in trained exchange biased multilayers
Journal of Physics: Condensed Matter, 19 (2007), 086229-1 – 086229 -9

Paul, A.; Buchmeier, M.; Schneider, C. M.; Brückel, T.
Magnetization reversal via symmetric rotation of layers in exchange biased multilayers
Journal of Applied Physics, 101 (2007), 123913-1 – 123913-10

Paul, A.; Schneider, C. M.; Stahn, J.
Reversal mechanism and suppression of training in an exchange-coupled system
Physical Review B, 76 (2007), 184424-1 – 184424-7

Perroni, C. A.; Bercioux, D.; Marigliano Ramaglia, V.; Cataudella, V.
Rashba quantum wire: exact solution and ballistic transport
Journal of Physics: Condensed Matter, 19 (2007), 186227

Perroni, C. A.; Ishida, H.; Liebsch, A.
Exact diagonalization dynamical mean-field theory for multi-band materials: Effect of Coulomb correlations on the Fermi surface of $Na_{0.3}CoO_2$
Physical Review B, 75 (2007), 045125

Persson, B. N. J.
Wet adhesion with application to tree frog adhesive toe pads and tires
Journal of Physics: Condensed Matter, 19 (2007) 37, 376110

Persson, B. N. J.; Kato, T.; Ueba, H.; Volokitin, A. I.
Vibrational heating of molecules adsorbed on insulating surfaces using localized photon tunneling
Physical Review B, 75 (2007), 193404

Pertsev, N. A.; Dittmann, R.; Plonka, R.; Waser, R.
Thickness dependence of intrinsic dielectric response and apparent interfacial capacitance in ferroelectric thin films
Journal of Applied Physics, 101 (2007), 074102

Pertsev, N. A.; Kohlstedt, H.
Elastic stabilization of a single-domain ferroelectric state in nanoscale capacitors and tunnel junctions
Physical Review Letters, 98 (2007), 257603

Peter, L.; Weihnacht, V.; Toth, J.; Padar, J.; Pogany, L.; Schneider, C. M.; Bakonyi, I.
Influence of superparamagnetic regions on the giant magnetoresistance of electrodeposited Co–Cu/Cu multilayers
Journal of Magnetism and Magnetic Materials, 312 (2007) 2, 258 – 265

Petraru, A.; Pertsev, N. A.; Kohlstedt, H. H.; Poppe, U.; Waser, R.; Solbach, A.; Klemradt, U.
Polarization and lattice strains in epitaxial $BaTiO_3$ films grown by high-pressure sputtering
Journal of Applied Physics, 101 (2007), 114106

Pilipenko, D.; Spatschek, R.; Brener, E. A.
Crack propagation as a free boundary problem
Physical Review Letters, 98 (2007), 015503

Pipich, V.; Balz, M.; Tremel, W.; Schwahn, D.
Mineralization of Calcium Carbonate in the Presence of Ovalbumin – an Exploration with Small Angle Neutron Scattering
Biomineralization: From Paleontology to Materials Science; Proceedings of the Ninth International Symposium in Pucón 2005 / ed.: J. L. Arias, M. S. Fernández. – 2007. – S. 477 – 485

Polyakov, P.; Zhang, M.; Müller-Plathe, F.; Wiegand, S.
Thermal diffusion measurements and simulations of binary mixtures of spherical molecules
Journal of Chemical Physics, 127 (2007), 014502

Pradeep, C. P.; Long, D.-L.; Kögerler, P.; Cronin, L.
Controlled assembly and solution observation of a 2.6 nm polyoxometalate 'super' tetrahedron cluster: $[KFe_{12}(OH)_{18}(\alpha\text{-}1,2,3\text{-}P_2W_{15}O_{56})_4]^{29-}$
Chemical Communications, (2007), 4254 – 4256

Prager, M.; Desmedt, A.; Allgaier, J.; Russina, M.; Jansen, E.; Natkaniec, I.; Pawlukojc, A.; Press, W.
Methyl group rotation and whole molecule dynamics in methyl bromide hydrate
Phase Transitions, 80 (2007) 6/7, 473

Prager, M.; Pawlukojc, A.; Wischnewski, A.; Wuttke, J.
Inelastic neutron scattering study of methyl groups rotation in some methylxanthines
Journal of Chemical Physics, 127 (2007) 214509

Prager, M.; Sawka-Dobrowolska, W.; Sobczyk, L.; Pawlukojc, A.; Grech, E.; Wischnewski, A.; Zamponi, M.
X-ray diffraction and inelastic neutron scattering study of 2,6-dimethylpyrazine chloranilic acid complex
Chemical Physics, 332 (2007), 1 – 9

Prager, M.; Wischnewski, A.; Bator, G.; Grech, E.; Pawlukojc, A.; Sobczyk, L.
INS spectroscopic study of the 1:1 tetramethylpyrazine (TMP) squaric acid (H_2SQ) complex
Chemical Physics, 334 (2007), 148 – 153

Pranzas, P. K.; Dornheim, M.; Bösenberg, U.; Fernandez, J. R. A.; Goerigk, G .; Roth, S. V.; Gehrke, R.; Schreyer, A.
Small-angle scattering investigations of magnesium hydride used as a hydrogen storage material
Journal of Applied Crystallography, 40 (2007) Suppl. 1, s383 – s387

Przepiorzynski, P.; Mi, S.; Grushko, B.; Surowiec, M.
An investigation of the Al-Ni-Rh phase diagram between 50 and 100 at% Al
Intermetallics, 15 (2007), 7, 918 – 928

Psiuk, B.; Szade, J.; Schroeder, H.; Haselier, H.; Mlynarczyk, M.; Waser, R.; Szot, K.
Photoemission study of $SrTiO_3$ surface layers instability upon metal deposition
Applied Physics A, 89 (2007) 2, 451 – 455

Radulescu, A.; Schwahn, D.; Stellbrink, J.
Hierarchical structures formed by partially crystalline polymers in solution: from fundamentals to applications – a combined conventional, focusing and ultra-small-angle neutron scattering study
Journal of Applied Crystallography, 40 (2007), s97 – s100

Rata, A. D.; Braak, H.; Bürgler, D. E.; Schneider, C. M.
Large inverse tunneling magnetoresistance in $Co_2Cr_{0.6}Fe_{0.4}Al/MgO/CoFe$ magnetic tunnel junctions
Applied Physics Letters, 90 (2007), 162512

Rata, A. D.; Braak, H.; Bürgler, D. E.; Schneider, C. M.
Large tunneling magnetoresistance effect at high voltage drop for Co-based Heusler alloy/MgO/CoFe junctions
Journal of Applied Physics, 101 (2007), 09J503

Rebbouh, L.; Hermann, R. P.; Grandjean, F.; Hyeon, T.; An, K.; Amato, A.; Long, G. J.
^{57}Fe Mössbauer spectral and muon spin relaxation study of the magnetodynamics of monodispersed γ-Fe_2O_3 nanoparticles
Physical Review B, 76 (2007), 174422-1 – 174422-12

Rediguieri, C. F.; de Freitas, O.; Lettinga, M. P.; Tuinier, R.
Thermodynamic Incompatibility and Complex Formation in Pectin/Caseinate Mixtures
Biomacromolecules, 8 (2007), 3345 – 3354

Richter, D.
Polymer dynamics: from synthetic polymers to proteins
Journal of Applied Crystallography, 40 (2007), s28 – s33

Ripoll, M.; Winkler, R. G.; Gompper, G.
Hydrodynamic screening of star polymers in shear flow
European Physical Journal E, 23 (2007), 349 – 354

Ritchie, C.; Burkholder, E. M.; Long, D.-L.; Adam, D.; Kögerler, P.; Cronin, L.
Exploiting the multifunctionality of organocations in the assembly of hybrid polyoxometalate clusters and networks
Chemical Communications, (2007) 5, 468

Rodriguez-Fernández, J.; Perez-Juste, J.; Liz-Marzán, L. M.; Lang, P. R.
Dynamic Light Scattering of Short Au Rods with Low Aspect Ratios
Journal of Physical Chemistry C, 111 (2007), 5020 – 5025

Roitsch, S.; Heggen, M.; Lipinska-Chwalek, M.; Feuerbacher, M.
Single-crystal plasticity of the complex metallic alloy phase ß-Al-Mg
Intermetallics, 15 (2007), 833 – 837

Romeike, C.; Wegewijs, M. R.; Ruben, M.; Wenzel, W.; Schoeller, H.
Spin blockade in a charge-switchable molecular magnet
Phys. Rev. B 75, (2007), 064404

Rother, G.; Melnichenko, Y. B.; Cole, D. R.; Frielinghaus, H.; Wignall, G. D.
Microstructural characterization of adsorption and depletion regimes of supercritical fluids in nanopores
Journal of Physical Chemistry B, 111 (2007) 43, 15736 – 15742

Rubio-Retama, J.; Tamimi, F. M.; Heinrich, M.; Lopez-Cabarcos, E.
Synthesis and Characterization of Poly(magnesium acrylate) Microgels
Langmuir, 23 (2007) 16, 8538 – 8543

Rücker, U.; Kentzinger, E.
Thin film systems: Scattering under grazing incidence
Probing the Nanoworld: Microscopies, Scattering and Spectroscopies of the Solid State; lecture manuscripts of the 38th Spring School 2007 / ed.: K. Urban ... – Jülich, Forschungszentrum, Verlag, 2007. – (Schriften des Forschungszentrum Jülich. Reihe Materie und Material / Matter and Materials; 34). – 978-3-89336-462-6. – S. D4.1 – D4.46

Rüdiger, A.; Waser, R.
Size effects in ferroelectric nanostructures
Journal of Alloys and Compounds, (2007) 15231, 2005.12.133

Rzhevsky, A. A.; Krichevtsov, B. B.; Bürgler, D. E.; Schneider, C. M.
Interfacial magnetization in exchange-coupled Fe/Cr/Fe structures investigated by second harmonic generation
Physical Review B, 75 (2007), 144416

Rzhevsky, A. A.; Krichevtsov, B. B.; Bürgler, D. E.; Schneider, C. M.
Magnetization dynamics induced by ultrashort optical pulses in Fe/Cr thin films
Physical Review B, 75 (2007), 224434

Rzhevsky, A. A.; Krichevtsov, B. B.; Su, Y.; Schneider, C. M.
Probing the (001) surface of magnetite crystals by second harmonic generation
Journal of Physics: Condensed Matter, 19 (2007), 396006-1 – 396006-10

Sager, W. F. C.
Microemulsion Templating
Nanostructured Soft Matter: Experiment, Theory, Simulation and Perspectives / ed.: A. V. Zvelindovsky. – Berlin, Springer, 2007. – (NanoScience and Technology). – 978-1-402-06329-9. – S. 3 – 44

Sandratskii, L. M.; Singer, R.; Sasioglu, E.
Heisenberg Hamiltonian description of multiple-sublattice itinerant-electron systems: General considerations and applications to NiMnSb and MnAs
Physical Review B, 76 (2007), 184406

Sarau, G.; Gliga, S.; Hertel, R.; Schneider, C. M.
Magnetization reversal of micron-scale Cobalt structures with a nanoconstriction
IEEE Transactions on Magnetics, 43 (2007) 6, 2854

Sato, K.; Dederichs, P. H.; Katayama-Yoshida, H.
First-Principles Study on the Ferromagnetism and Curie Temperature of Mn-Doped AlX and InX (X = N, P, As and Sb)
Journal of the Physical Society of Japan, 76 (2007), 024717

Schindler, C.; Guo, X.; Besmehn, A.; Waser, R.
Resistive switching in $Ge_{0.3}Se_{0.7}$ films by means of copper ion migration
Zeitschrift für physikalische Chemie, 221 (2007) 11/12, 1469 – 1478

Schindler, C.; Thermada, S. C. P.; Waser, R.; Kozicki, M. N.
Bipolar and unipolar resistive switching in Cu-doped SiO_2
IEEE Transactions on Electron Devices, 54 (2007), 2762

Schindlmayr, A.
Interaction of Radiation with Matter: Part II: Light and Electrons
Probing the Nanoworld : Microscopies, Scattering and Spectroscopies of the Solid State; lecture manuscripts of the 38th Spring School 2007/ed.: K. Urban ... – Jülich, Forschungszentrum, Verlag, 2007. – (Schriften des Forschungszentrum Jülich. Reihe Materie und Material / Matter and Materials; 34). – 978-3-89336-462-6. – S. A1.21 – A1.36

Schindlmayr, A.; Scheffler, M.
Quasiparticle Calculations for Point Defects at Semiconductor Surfaces
Theory of Defects in Semiconductors / ed.: D. A. Drabold, S. K. Estreicher. – Berlin, Springer, 2007. – (Topics in Applied Physics; 104). – 978-3-540-33400-2. – S. 165 – 192

Schmalzl, K.
Volume and pressure dependence of ground-state and lattice dynamical properties of BaF_2 from density-functional methods
Physical Review B, 75 (2007), 014306-1 – 014306-11

Schmalzl, K.; Strauch, D.
Static Pockels constants p_{ij} and p_{ijk} of CaF_2 and BaF_2 under strain from ab initio calculations
Physical Review B, 76 (2007), 205106-1 – 205106-8

Schneider, G. J.; Göritz, D.
Dependence of the mechanical properties on the morphology of fillers
Proceedings of the 11th International Seminar on Elastomers, 23.09.2007-27.09.2007, Freiburg. – 2007. – S. 95

Schneller, T.; Waser, R.
Chemical modifications of $Pb(Zr_{0.3},Ti_{0.7})O_3$ precursor solutions and their influence on the morphological and electrical properties of the resulting thin films
Journal of Sol-Gel Science and Technology, 42 (2007), 337 – 352

Schober, H. R.; Parshin, D. A.; Gurevich, V. L.
Quasi-localized vibrations, boson peak and tunneling in glasses
Journal of Physics : Conference Series, 92 (2007), 012131

Schönhals, A.; Schick, C.; Frick, B.; Mayorova, M.; Zorn, R.
Molecular Dynamics in Glass-forming Poly(phenyl methyl siloxane) as investigated by Broadband Thermal, Dielectric and Neutron Spectroscopy
Journal of Non-Crystalline Solids, 353 (2007), 3853 – 3861

Schönhals, A.; Schick, Ch.; Huith, H.; Frick, B.; Mayorova, M.; Zorn, R.
Molecular Mobility of Poly (phenyl methyl siloxane) Investigated by Thermal, Dielectric and Neutron Spectroscopy
Polymeric Materials Science and Engineering, 97 (2007), 948 – 949

Schroeder, H.
A model for a resistive switch memory cell with rechargeable space charge
Integrated Ferroelectrics, 90 (2007), 113 – 120

Schroeder, H.; Jeong, D. S.
Resistive switching in a $Pt/TiO_2/Pt$ thin film stack – a candidate for a non-volatile ReRAM
Microelectronic Engineering, 84 (2007), 1982 – 1985

Schütz, G. M.; Harris, R. J.
Hydrodynamics of the Zero-range Process in the Condensation Regime
Journal of Statistical Physics, 127 (2007) 2, 419 – 430

Schwahn, D.; Ma, Y.; Cölfen, H.
Mesocrystal to Single Crystal Transformation of D,L-Alanine Evidenced by Small Angle Neutron Scattering
Journal of Physical Chemistry C, 111 (2007) 8, 3224 – 3227

Schweika, W.
Magnetic fluctuations: Polarized neutron scattering
Probing the Nanoworld: Microscopies, Scattering and Spectroscopies of the Solid State; lecture manuscripts of the 38th Spring School 2007 / ed.: K. Urban ... – Jülich, Forschungszentrum, Verlag, 2007. – (Schriften des Forschungszentrum Jülich. Reihe Materie und Material / Matter and Materials; 34). – 978-3-89336-462-6. – S. D2.1 – D2.20

Schweika, W.
Polarized neutron scattering
Neutron scattering: Laboratory Course held at Forschungszentrum Jülich and the research reactor FRM II of TU Munich / ed.: Th. Brückel, G. Heger, D. Richter, R. Zorn. – Jülich, Forschungszentrum, Zentralbibliothek, 2007. – (Schriften des Forschungszentrum Jülich. Reihe Materie und Material / Matter and Materials; 38). – 978-3-89336-489-3. – S. 3-1 – 3-23

Schweika, W.; Hermann, R.; Prager, M.; Perßon, J.; Keppens, V.
Dumbbell rattling in thermoelectric zinc antimony
Physical Review Letters, 99 (2007), 125501-1 – 125501-4

Schweika, W.; Valldor, M.; Lemmens, P.
Approaching the ground state of the kagomé antiferromagnet
Physical Review Letters, 98 (2007), 067201-1 – 067201-4

Seeck, O.; Kentzinger, E.
Continuum description: Grazing incidence neutron scattering
Neutron scattering: Laboratory Course held at Forschungszentrum Jülich and the research reactor FRM II of TU Munich / ed.: Th. Brückel, G. Heger, D. Richter, R. Zorn. – Jülich, Forschungszentrum, Zentralbibliothek, 2007. – (Schriften des Forschungszentrum Jülich . Reihe Materie und Material/ Matter and Materials; 38). – 978-3-89336-489-3. – S. 5-1 – 5-26

Shiratori, Y.; Magrez, A.; Kasezawa, K.; Kato, M.; Röhrig, S.; Peter, F.; Pithan, C.; Waser, R.
Noncentrosymmetric phase of submicron $NaNbO_3$ crystallites
Journal of Electroceramics, 19 (2007) 4, 273 – 280

Shiratori, Y.; Pithan, C.; Dornseiffer, J.; Waser, R.
Raman scattering studies on nanocrystalline $BaTiO_3$, Part I – isolated particles and aggregates
Journal of Raman Spectroscopy, 38 (2007) 10, 1288 – 1299

Shiratori, Y.; Pithan, C.; Dornseiffer, J.; Waser, R.
Raman scattering studies on nanocrystalline $BaTiO_3$, Part II – consolidated polycrystalline ceramics
Journal of Raman Spectroscopy, 38 (2007) 10, 1300 – 1306

Sinibaldi, R.; Ortore, M. G.; Spinozzi, F.; Carsughi, F.; Frielinghaus, H.; Cinelli, S.; Onori, G.; Mariani, P.
Preferential hydration of lysozyme in water/glycerol mixtures: A small-angle neutron scattering study
Journal of Chemical Physics, 126 (2007) 23, 235101-1 – 235101-9

Smontara, A.; Smiljanic, I.; Bilusic, A.; Jaglicic, Z.; Klanjsek, M.; Roitsch, S.; Dolinsek, J.; Feuerbacher, M.
Electrical, magnetic, thermal and thermoelectric properties of the "Bergman phase" $Mg_{32}(Al,Zn)_{49}$ complex metallic alloy
Journal of Alloys and Compounds, 430 (2007), 29 – 38

Spatschek, R.; Brener, E. A.
Cracking a material problem: a study in fracture
Physics World, 20 (2007) 6, 32 – 37

Spatschek, R.; Brener, E.; Pilipenko, D.
Crack Propagation as a Free Boundary Problem
Key Engineering Materials, 345-346 (2007), 429

Spatschek, R.; Fleck, M.
Influence of stress on interface kinetics
Philosophical Magazine Letters, 87 (2007), 909 – 914

Spatschek, R.; Müller-Gugenberger, C.; Brener, E.; Nestler, B.
Phase Field Modeling of Fracture and Stress Induced Phase Transitions
Physical Review E, 75 (2007), 066111

Spinozzi, F.; Mariani, P.; Saturni, L.; Carsughi, F.; Bernstorff, S.; Cinelli, S.; Onori, G.
Met-myoglobin Association in Dilute Solution during Pressure-Induced Denaturation: an Analysis at pH 4.5 by High-Pressure Small-Angle X-ray Scattering
Journal of Physical Chemistry B, 111 (2007), 3822 – 3830

Steffens, P.; Sidis, Y.; Link, P.; Schmalzl, K.; Nakatsuji, S.; Maeno, Y.; Braden, M.
Field-Induced Paramagnons at the Metamagnetic Transition of $Ca_{1.8}Sr_{0.2}RuO_4$
Physical Review Letters, 99 (2007), 217402-1 217402-4

Stellbrink, J.; Niu, A.; Allgaier, J.; Richter, D.; Koenig, B. W.; Hartmann, R.; Coates, G. W.; Fetters, L. J.
Analysis of Polymeric Methylaluminoxane (MAO) via Small Angle Neutron Scattering
Macromolecules, 40 (2007), 4972 – 4981

Streb, C.; Ritchie, C.; Long, D.-L.; Kögerler, P.; Cronin, L.
Modular assembly of a functional polyoxometalate-based open framework constructed from unsupported Ag1...Ag1 interactions
Angewandte Chemie-International Edition, 46 (2007), 7579

Su, Y.
Charge and orbital ordering: Resonant x-ray scattering
Probing the Nanoworld: Microscopies, Scattering and Spectroscopies of the Solid State; lecture manuscripts of the 38th Spring School 2007 / ed.: K. Urban ... – Jülich, Forschungszentrum, Verlag, 2007. – (Schriften des Forschungszentrum Jülich. Reihe Materie und Material / Matter and Materials; 34). – 978-3-89336-462-6. – S. D7.1 – D7.25

Svete, M.; Houben, L.; Tillmann, K.; Mader, W.
Imaging Light Atoms at Sub-Angström Resolution in an Image Side Cs-Corrected Electron Microscope FEI Titan 80-300
Microscopy and Microanalysis, 13 (2007) Suppl. s3, 30 – 31

Szekely, N. K.; Almasy, L.; Radulescu, A.; Rosta, L.
Small-angle neutron scattering study of aqueous solutions of pentanediol and hexanediol
Journal of Applied Crystallography, 40 (2007) Suppl. 1, s307 – s311

Szot, K.; Bihlmayer, G.; Speier, W.; Waser, R.
Klein und schnell – Die Speichertechnologie der Zukunft
100 Produkte der Zukunft: Wegweisende Ideen, die unser Leben verändern werden / ed.: Th. W. Hänsch. – Berlin, Econ, 2007. – 978-3-430-20035-6. – S. 132

Tehei, M.; Franzetti, B.; Wood, K.; Gabel, F.; Fabiani, E.; Jasnin, M.; Zamponi, M.; Oesterhelt, D.; Zaccai, G.; Ginzburg, M.; Ginzburg, B. Z.
Neutron scattering reveals extremely slow cell water in a Dead Sea organism
Proceedings of the National Academy of Sciences of the United States of America, 104 (2007), 766 – 771

Temleitner, L.; Pusztai, L.; Schweika, W.
The structure of liquid water by polarized neutron diffraction and everse Monte Carlo modelling
Journal of Physics: Condensed Matter, 19 (2007), 335207-1 – 335207-12

Theis-Bröhl, K.; Toperverg, B. P.; Westphalen, A.; Zabel, H.; McCord, J.; Höink, V.; Schmalhorst, J.; Reiss, G.; Weis, T.; Engel, D.; Ehresmann, A.; Rücker, U.
Polarized neutron reflectometry study on a magnetic film with an ion beam imprinted stripe pattern
Superlattices and Microstructures, 41 (2007), 104 – 108

Thomas, R.; Bhakta, R.; Milanov, A.; Devi, A.; Ehrhart, P.
Thin Films of ZrO_2 for High-k Applications Employing Engineered Alkoxide- and Amide-Based MOCVD Precursors
Chemical Vapor Deposition, 13 (2007) 2/3, 98 – 104

Thomas, R.; Ehrhart, P.; Roeckerath, M.; van Elshocht, S.; Rije, E.; Luysberg, M.; Boese, M.; Schubert, J.; Caymax, M.; Waser, R.
Liquid Injection MOCVD of Dysprosium Scandate Films: Deposition Characteristics and High-k Applications
Journal of the Electrochemical Society, 154 (2007), G147 – G154

Thomas, R.; Rije, E.; Ehrhart, P.; Milanov, A.; Bhakta, R.; Baunemann, A.; Devi, A.; Fischer, R.; Waser, R.
Thin Films of HfO_2 for High-k Gate Oxide Applications from Engineered Alkoxide- and Amide-Based MOCVD Precursors
Journal of the Electrochemical Society, 154 (2007) 3, G77 – G84

Tuinier, R.; Taniguchi, T.; Wensink, H. H.
Phase behavior of a suspension of hard sperocylinders plus ideal polymer chains
European Physical Journal E, 23 (2007), 355 – 365

Ueba, H.; Persson, B. N. J.
Action spectroscopy for single-molecule motion induced by vibrational excitation with a scanning tunneling microscope
Physical Review B, 75 (2007), 041403

Vaccaro, M.; Accardo, A.; D'Errico, G.; Schillén, K.; Radulescu, A.; Tesauro, D.; Morelli, G.; Paduano, L.
Peptides and Gd Complexes Containing Colloidal Assemblies as Tumor-Specific Contrast Agents in MRI: Physicochemical Characterization
Biophysical Journal, 93 (2007), 1736 – 1746

Vainio, U.; Pirkkalainen, K.; Kisko, K.; Goerigk, G.; Kotelnikova, N. E.; Serimaa, R.
Copper and copper oxide nanoparticles in a cellulose support studied using anomalous small-angle x-ray scattering
European Physical Journal D, 42 (2007), 93 – 101

Varga, Z.; Bóta, A.; Goerigk, G.
Localization of dihalogenated phenols in vesicle systems determined by contrast variation X-ray scattering
Journal of Applied Crystallography, 40 (2007) , s205 – s208

Voigt, J.
Magnetic and lattice excitations: Neutron and x-ray spectroscopies
Probing the Nanoworld: Microscopies, Scattering and Spectroscopies of the Solid State; lecture manuscripts of the 38th Spring School 2007/ed.: K. Urban ... – Jülich, Forschungszentrum, Verlag, 2007. – (Schriften des Forschungszentrum Jülich. Reihe Materie und Material / Matter and Materials; 34). – 978-3-89336-462-6. – S. D3.1 – D3.19

Voigt, J.; Persson, J.; Kim, J. W.; Bihlmayer, G.; Brükkel, Th.
Strong coupling between the spin polarization of Mn and Tb in multiferroic $TbMnO_3$ determined by x-ray resonance exchange scattering
Physical Review B, 76 (2007), 104431-1 – 104431-5

Volokitin, A. I.; Persson, B. N. J.; Ueba, H.
Giant enhancement of noncontact friction between closely spaced bodies by dielectric films and two-dimensional systems
Journal of Experimental and Theoretical Physics, 104 (2007) 1, 96 – 110

von Bergmann, K.; Heinze, S.; Bode, M.; Bihlmayer, G.; Blügel, S.; Wiesendanger, R.
Complex magnetism of the Fe monolayer on Ir(111)
New Journal of Physics, 9 (2007), 396

Voss, J.; Jacobson, H.S.; Zamponi, M.; Lefmann, K.; Vegge, T.; Shi, Q.
Hydrogen dynamics in Na_3AlH_6: A combined density functional theory and quasielastic neutron scattering study
Journal of Physical Chemistry B, 111 (2007), 3886

Walter, W.; Borlein, M.; Eyßelein, F.; Gehring, M.; Kozielewski, T.; Kramer, A.; Monkenbusch, M.; Ohl, M.; Paul, A.; Schrauth, B.; Tiemann, Ch.
Design of a pair of superconducting solenoids for a neutron spin-echo spectrometer at the SNS
IEEE Transactions on Applied Superconductivity, 17 (2007) 2, 1209 – 1212

Waser, R.; Aono, M.
Nanoionics-based resistive switching memories
Nature Materials, 6 (2007), 833

Watanabe, T.; Hoffmann-Eifert, S.; Mi, S.; Jia, C.; Waser, R.
Growth of ternary $PbTiO_x$ films in a combination of binary oxide atomic layer depositions
Journal of Applied Physics, 101 (2007), 014114

Watanabe, T.; Hoffmann-Eifert, S.; Peter, F.; Mi, S.; Jia, C.; Hwang, C. S.; Waser, R.
Liquid injection ALD of Pb(Zr,Ti)O_x thin films by a combination of self-regulating component oxide processes
Journal of the Electrochemical Society, 154 (2007), G262 – G269

Watanabe, T.; Hoffmann-Eifert, S.; Yang, L.; Rüdiger, A.; Kügeler, C.; Hwang, C. S.; Waser, R.
Liquid Injection Atomic Layer Deposition of TiO_x Films Using $Ti[OCH(CH_3)_2]_4$
Journal of the Electrochemical Society, 154 (2007), G134 – G140

Wegelin, F.; Valdaitsev, D.; Krasyuk, A.; Nepijko, S. A.; Schönhense, G.; Elmers, H. J.; Krug, I.; Schneider, C. M.
Magnetization dynamics in microscopic spin-valve elements: Shortcomings of the macrospin picture
Physical Review B, 76 (2007) 13, 134410

Wegewijs, M. R.; Romeike, C.; Schoeller, H.; Hofstetter, W.
Magneto-transport through single molecule magnets: Kondo-peaks, zero-bias dips, molecular symmetry, and Berry's phase
New J. of Phys. 9, (2007), 344

Weides, M.; Kohlstedt, H.; Waser, R.; Kemmler, M.; Pfeiffer, J.; Koelle, D.; Kleiner, R.; Goldobin, E.
Ferromagnetic o-pi Josephson junctions
Applied Physics A, 89 (2007), 613

Weides, M.; Schindler, C.; Kohlstedt, H.
Low T_c Josephson junctions with tailored barrier
Journal of Applied Physics, 101 (2007), 063902

Wentao, Yu.; Houben, L.; Tillmann, K.; Mader, W.
Phase Contrast and HAADF Imaging of Structures in In_2O_3-ZnO Compounds in Cs-Corrected Electron Microscopes
Microscopy and Microanalysis, 13 (2007) Suppl. s3, 28 – 29

Wiegand, S.; Ning, H.; Kita, R.
Universal concentration dependence of the soret coefficient in aqueous systems
Journal of Non-Equilibrium Thermodynamics, 32 (2007) 3, 193

Wiegand, S.; Ning, H.; Kriegs, H.
Thermal diffusion forced rayleigh scattering setup optimized for aqueous mixtures
Journal of Physical Chemistry B, 111 (2007), 14169

Wille, H.-C.; Hermann, R. P.; Sergueev, I.; Leupold, O.; van der Linden, P.; Sales, B. C.; Grandjean, F.; Long, F. J.; Rüffer, R.; Shvyd'ko, Yu. V.
Antimony vibrations in skutterudites probed by ^{121}Sb nuclear inelastic scattering
Physical Review B, 76 (2007), 140301(R)

Winkler, R. G.
Diffusion and segmental dynamics of rodlike molecules by fluorescence correlation spectroscopy
Journal of Chemical Physics, 127 (2007), 054904

Winkler, R. G.; Cherstvy, A. G.
Adsorption of Weakly Charged Polyelectrolytes onto Oppositely Charged Spherical Colloids
Journal of Physical Chemistry B, 111 (2007), 8486 – 8493

Woodford, S. R.; Bringer, A.; Blügel, S.
Interpreting magnetization from Faraday rotation in birefringent, magnetic media
Journal of Applied Physics, 101 (2007), 053912

Woodford, S. R.; Bringer, A.; Indlekofer, K. M.
Dephasing of a quantum dot due to the Coulomb interaction with a gate electrode
Physical Review B, 76 (2007), 064306 – 064313

Wuttke, J.
Inelastic Crystal Spectrometers
Neutron Scattering: Lectures of the JCNS Laboratory Course held at Forschungszentrum Jülich and the research reactor FRM II of TU Munich / ed.: T. Brückel, G. Heger, D. Richter, R. Zorn. – Jülich, Forschungszentrum, Zentralbibliothek, 2007. – (Schriften des Forschungszentrums Jülich. Reihe Materie und Material / Matter and Materials; 38).
– 978-3-89336-489-3. – S. 9-1 – 9-17

Yan, M.; Hertel, R.; Schneider, C. M.
Calculations of three-dimensional magnetic normal modes in mesoscopic permalloy prisms with vortex structure
Physical Review B, 76 (2007), 094407

Yang, Y.; Burkhardt, T. W.; Gompper, G.
Free energy and extension of a semiflexible polymer in cylindrical confining geometries
Physical Review E, 76 (2007), 011804

Yang, Z.; Lichtenwalner, D.; Morris, A.; Menzel, S.; Nauenheim, C.; Gruverman, A.; Krim, J.; Kingon, A.
A new test facility for efficient evaluation of MEMS contact materials
Journal of Micromechanics and Microengineering, 17 (2007), 1788

Zembilgotov, A. G.; Böttger, U.; Waser, R.
Comment on "Dielectric tunability of (110) oriented barium strontium titanate epitaxial films on (100) orthorhombic substrates" [Appl. Phys. Lett. 89, 042903 (2006)]
Applied Physics Letters, 90 (2007), 036101

Zhang, F.; Skoda, M. W. A.; Jacobs, R. M. J.; Zorn, S.; Martin, R. A.; Martin, C. M.; Clark, G. F.; Goerigk, G.; Schreiber, F.
Gold Nanoparticles Decorated with Oligo(ethylene glycol) Thiols: Protein Resistance and Colloidal Stability
Journal of Physical Chemistry B, 111 (2007) 49, 12229 – 12237

Zhang, Z.; Berns, A. E.; Willbold, S.; Buitenhuis, J.
Synthesis of poly(ethylene glycol) (PEG)-grafted colloidal silica particles with improved stability in aqueous solvents
Journal of Colloid and Interface Science, 310 (2007), 446 – 455

Zhang, Z.; Buitenhuis, J.
Synthesis of Uniform Silica Rods, Curved Silica Wires, and Silica Bundles Using Filamentous fd Virus as a Template
Small, 3 (2007), 3, 424 – 428

Zorn, R.
Multiple scattering correction of neutron scattering elastic scans
Nuclear Instruments and Methods in Physics Research Section A, 572 (2007), 874 – 881

Ph.D. Theses

Elgeti, J.
Sperm and Cilia Dynamics
Jülich, Forschungszentrum Jülich, Institut für Festkörperforschung, 2007
Köln, Univ., Diss., 2007

Feygenson, M.
Magnetic and structural properties of thin films and nanoparticles studied by scattering methods
Jülich, Forschungszentrum, Zentralbibliothek, 2007
Schriften des Forschungszentrums Jülich. Reihe Materie und Material/Matter and Material; 39 – 9783893364909
Aachen, RWTH, Diss., 2007

Gwan, J.-F.
The molecular mechanism of multi-ion conduction in K^+ channels
Jülich, Forschungszentrum, Zentralbibliothek,2007
Berichte des Forschungszentrums Jülich; JUEL-4245
Duisburg-Essen, Univ., Diss., 2007

Kleshchanok, D.
Polymer-induced interactions: measured by direct and indirect measurements
Jülich, Forschungszentrum Jülich, Institut für Festkörperforschung, 2007
Aachen, RWTH, Diss., 2007

Kronholz, St.
Integration von Nanostrukturen durch alternative Methoden: Mizellen-Deposition, Template-Wachstum und Nanogaps
Jülich, Forschungszentrum, Zentralbibliothek, 2007
Schriften des Forschungszentrums Jülich. Reihe Informationstechnologie/Information Technology; 15
9783893364787
Aachen, RWTH, Diss., 2007

Lounis, S.
Theory of Magnetic Transition Metal Nanoclusters on Surfaces
Jülich, Forschungszentrum, Zentralbibliothek, 2007
Schriften des Forschungszentrums Jülich. Reihe Materie und Material/Matter and Materials; 41
9783893365012
Aachen, RWTH, Diss., 2007

Maccarrone, S.
Microemulsions with polymer additives
Jülich, Forschungszentrum Jülich, Institut für Festkörperforschung, 2007
Münster, Univ., Diss., 2007

Müller, M.
Electronic Structure of Ferromagnet-Insulator Interfaces: Fe/MgO and Co/MgO
Jülich, Forschungszentrum, Zentralbibliothek, 2007
Schriften des Forschungszentrums Jülich. Reihe Materie und Material/Matter and Materials ; 40
9783893364930
Duisburg-Essen, Univ., Campus Duisburg, Diss., 2007

Nandy, B.
Theoretical studies of the chemotaxis of biological cells
Jülich, Forschungszentrum Jülich, Institut für Festkörperforschung, 2007
Duisburg-Essen, Univ., Diss., 2007

Niedzwiedz, K.
Polymer dynamics in miscible polymeric blends
Jülich, Forschungszentrum Jülich, Institut für Festkörperforschung, 2007
Münster, Univ., Diss., 2007

Ning, H.
Thermal diffusion behavior of complex fluid mixtures
Jülich, Forschungszentrum Jülich, Institut für Festkörperforschung, 2007 – 9789036524643
Twente, Univ., Diss., 2007

Puchalla, J.
Metallorganische Chemische Gasphasenabscheidung (MOCVD) ferroelektrischer Dünnschichten: Herstellung und Charakterisierung
Jülich, Forschungszentrum, Zentralbibliothek, 2007
Schriften des Forschungszentrums Jülich. Reihe Informationstechnik/Information Technology ; 17
9783893364923
Aachen, RWTH, Diss., 2007

Weides, M.
Josephson Tunnel Junctions with Ferromagnetic Interlayer
Jülich, Forschungszentrum, Zentralbibliothek, 2007
Schriften des Forschungszentrums Jülich. Reihe Informationstechnik/Information Technology ; 13 – 9783893364725
Köln, Univ., Diss., 2006

Zhang, Z.
Surface Modification of Colloidal Silica Particles and Fd Viruses
Jülich, Forschungszentrum Jülich, Institut für Festkörperforschung, 2007
9789036525138
Twente, Univ., Diss., 2007

Diploma Theses

Bannykh, A.
Josephson tunnel junction with ferromagnetic interlayer in clean limit
Jülich, Forschungszentrum Jülich,
Institut für Festkörperforschung, 2007
Moscow State University, Russia

Betzinger, M.
Efficient implementation of the non-local exchange potential within the FLAPW method
Jülich, Forschungszentrum Jülich,
Institut für Festkörperforschung, 2007
RWTH Aachen, Germany

Haan, M.
Simulations of a biological ion channel
Jülich, Forschungszentrum Jülich,
Institut für Festkörperforschung, 2007
Universität Duisburg-Essen, Germany

Hanuschkin, A.
Ab Initio Calculations of Confined Electronic States at Surfaces by Green Function Embedding
Jülich, Forschungszentrum Jülich,
Institut für Festkörperforschung, 2007
RWTH Aachen, Germany

Heers, S.
Influence of exchange and correlation on the conductance in semi-infinite scattering setups
Jülich, Forschungszentrum Jülich,
Institut für Festkörperforschung, 2007
Universität Hamburg, Germany

Gierlich, A.
Treatment of Electronic Correlation in Magnetic Materials within the Fluctuation-Exchange Method
Jülich, Forschungszentrum Jülich,
Institut für Festkörperforschung, 2007
RWTH Aachen, Germany

Lennartz, C.
Selbstorganisation von Carboxylsäure Derivaten auf Cu(110) Oberflächen,
Jülich, Forschungszentrum Jülich,
Institut für Festkörperforschung, 2007
RWTH Aachen, Germany

Peralagu, U.
Herstellung und Charakterisierung von $NbAl_2O_3Nb$ Proben mit gestufter Tunnelbarriere,
Jülich, Forschungszentrum Jülich,
Institut für Festkörperforschung, 2007
University of Glasgow, UK

Schicho, S.
Characterization of strontium titanate thin films depending on the microstructure of the platinum bottom electrode
Jülich, Forschungszentrum Jülich,
Institut für Festkörperforschung, 2007
TU Bergakademie Freiberg, Germany

Zacherle, T.
Struktur und Dynamik von Polymer-clay-composites: Untersuchungen mittels Neutronenstreuung
Jülich, Forschungszentrum Jülich,
Institut für Festkörperforschung, 2007
RWTH Aachen, Germany

Conferences and Schools

March 12 – 23	38. IFF Spring School – Probing the Nanoworld Forschungszentrum Jülich, Germany
September 3 – 14	Neutron Scattering Labcourse Forschungszentrum Jülich, Germany
October 1 – 5	International Soft Matter Conference Eurogress Aachen, Germany

Kolloquia

January 12	Gregory B. McKenna Texas Tech University, USA *Equilibrium Behavior of Complex Liquids: Thermodynamic and Dynamic Fragilities and the Kauzmann Paradox Unresolved*
January 26	Ulrich K. Rößler Leibniz Institute for Solid State & Materials Research, Dresden, Germany *Localized and Modulated States in Chiral Magnets*
February 2	David Tomanek Michigan State University, USA *Self-Assembling Nano-LEGO: From Clusters to Wires*
March 2	Eckhard Spohr Forschungszentrum Jülich, Germany *A Microscopic View of the Polymer Electrolyte Membrane Fuel Cell – Atomistic Simulations of Proton Generation and Transport*
April 20	Walter Federle University of Cambridge, Great Britain *Walking with Sticky Feet: Biomechanics of Surface Attachment in Insects*
May 5	Tomasz Dietl Polish Academy of Sciences, Poland *Ferromagnetism and Semiconductors*
June 1	Thomas Thurn-Albrecht Universität Halle-Wittenberg, Germany *Controlling Polymer Crystallization by External Constraints*
June 15	Frans Spaepen MIT, Cambridge, USA *Mechanical Properties of Metallic Glasses*
June 22	Han Meijer Eindhoven University, Netherlands *Predicting Polymer Properties Directly from Processing Conditions*
June 29	Juerg Hutter University of Zurich, Switzerland *Large Scale Electronic Structure Calculations*
November 23	Doros Theodorou National Technical University Athens, Greece *Hierarchical Simulations of Polymeric Materials*
November 30	Maarten Rolf Wegewijs Forschungszentrum Jülich, Germany *Single-Molecule Quantum Transport*

Institute of Solid State Research (IFF)

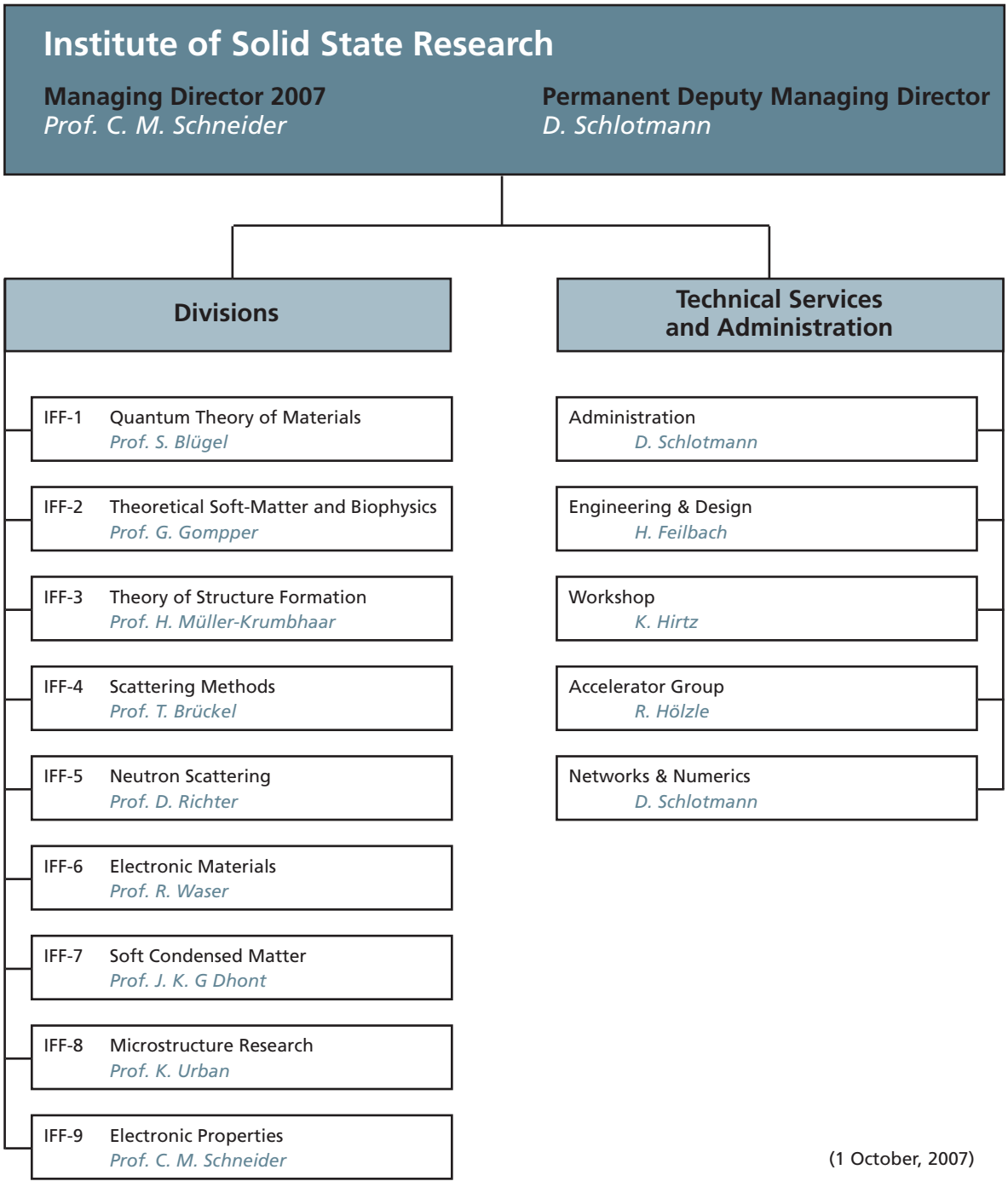

(1 October, 2007)

Personnel

Staff members (centrally financial)	
• Scientific Staff	168
Including those funded externally	*33*
• Technical Staff	54
Including those funded externally	*4*
Staff members of service-groups	33
Administrations incl. Secretaries	17
Graduate students	59
Including those funded externally	*8*
Diploma students	24
Trainees	28
Guests Scientists staying for two weeks or longer	185
Invited lectures	137

Scientific Advisory Board

Joint Scientific Council
The joint Scientific Council of the IFF and IBN advises the Institute and the committees of Research Centre Jülich and functions as a supervisory board. The members of the council are leading scientists from research and industry. They are appointed for five years.

Prof. Dr. Georg Bednorz
IBM Research GmbH, Rüschlikon (CH)

Prof. Dr. Wim J. Briels
University Twente, AE Enschede (NL)

Dr. Kurt Clausen
Paul Scherrer Institut, Villingen (CH)

Dr. Manfred Horstmann
AMD Saxony LLC & Co. KG, Dresden (D)

Prof. Dr. Klaus Kern
Max-Planck-Institut, Stuttgart (D)

Prof. Dr. Jürgen Kirschner
Max-Planck-Institut, Halle (D)

Prof. Dr. Beate Klösgen
University of Southern Denmark, Odense (DK)

Prof. Dr. Hilbert von Löhneysen
Forschungszentrum Karlsruhe (D)

Prof. Dr. Werner Press (Chairman)
Christian Alberts-Universität Kiel (D)

Prof. Dr. Friederike Schmid
Universität Bielefeld (D)

Prof. Dr. Herbert Schöller
RWTH Aachen (D)

Prof. Dr. Clivia M. Sotomayor-Torres
University College Cork (IRE)

Prof. Dr. Hans-Rainer Trebin
Universität Stuttgart (D)

Prof. Dr. Gero Vogl
Universität Wien (A)

Scientists

Adam, Roman
Electronic properties

Albrecht, Wolfgang
Electronic materials

Allgaier, Jürgen
Neutron scattering

Appavou, Marie-Sousai Deveramban
Jülich Centre for Neutron Science

Arend, Nikolas
Jülich Centre for Neutron Science

Atodiresei, Nicolae
Quantum Theory of Materials

Auth, Thorsten
Theoretical Soft-Matter and Biophysics

Balanetskyy, Sirgiy
Microstructure research

Barthel, Juri
Microstructure research

Baumgarten, Lutz
Electronic properties

Baumgärtner, Artur
Theoretical Soft-Matter and Biophysics

Bechthold, Paul-Siegfried
Electronic properties

Belushkin, Maxim
Theoretical Soft-Matter and Biophysics

Biehl, Ralf
Neutron scattering

Bihlmayer, Gustav
Quantum Theory of Materials

Blügel, Stefan
Quantum Theory of Materials

Botar, Bogdan
Electronic properties

Braak, Heiko
Electronic properties

Brener, Efim
Theory of structure formation

Brückel, Thomas
Scattering methods

Buchmeier, Matthias
Electronic properties

Buitenhuis, Johan
Soft condensed matter

Bürgler, Daniel-Emil
Electronic properties

Busch, Peter
Jülich Centre for Neutron Science

Cannavacciuolo, Luigi
Theoretical Soft-Matter and Biophysics

Carsughi, Flavio
Neutron scattering

Chaput, Laurent
Quantum Theory of Materials

Chatterjee, Sakuntala
Theoretical Soft-Matter and Biophysics

Chatterji, Apratim
Theoretical Soft-Matter and Biophysics

Chelakkot Govindalayam, Raghunat
Theoretical Soft-Matter and Biophysics

Chelaru, Liviu Ionut
Electronic properties

Cherstvy, Andrey
Theoretical Soft-Matter and Biophysics

Claver-Cabrero, Ana
Neutron scattering

Conrad, Harald
Scattering methods

Costi, Theodoulos
Theory of structure formation

Cramm, Stefan
Electronic properties

Dahbi, Louisa
Neutron scattering

Deac-Renner, Alina Maria
Electronic properties

Dhont, Jan-Karel
Soft condensed matter

Dittmann, Regina
Electronic materials

Divin, Yuri
Microstructure research

Ebert, Philipp-Georg
Microstructure research

Faley, Mikhail
Microstructure research

Feuerbacher, Michael
Microstructure research

Foster Leslie, John Ray
Neutron scattering

Friedrich, Christoph
Quantum Theory of Materials

Frielinghaus, Henrich
Jülich Centre for Neutron Science

Goerigk, Günter
Jülich Centre for Neutron Science

Gompper, Gerhard
Theoretical Soft-Matter and Biophysics

Götze, Ingo Oliver
Theoretical Soft-Matter and Biophysics

Grimm, Hans
Neutron scattering

Grimminger, Jens
Electronic materials

Grushko, Benjamin
Microstructure research

Guo, Xin
Electronic materials

Gutberlet, Thomas
Jülich Centre for Neutron Science

Harish, Ramanna
Theoretical Soft-Matter and Biophysics

Harris, John
Quantum Theory of Materials

Heggen, Marc
Microstructure research

Heide, Marcus
Quantum Theory of Materials

Heilmann, David Bernhard
Theory of structure formation

Heiß, Alexander
Neutron scattering

Hermann, Raphael
Scattering methods

Hertel, Riccardo
Electronic properties

Hoffmann-Eifert, Susanne
Electronic materials

Holderer, Olaf
Jülich Centre for Neutron Science

Holmqvist, Peter
Soft condensed matter

Houben, Lothar
Microstructure research

Huang, Chien-Cheng
Theoretical Soft-Matter and Biophysics

Ioffe, Alexander
Jülich Centre for Neutron Science

Jia, Chunlin
Microstructure research

Jiang, Run
Theoretical Soft-Matter and Biophysics

Jiang, Xiuli
Neutron scattering

Kakay, Attila
Electronic properties

Kang, Kyongok Ok
Soft condensed matter

Karthäuser, Silvia
Electronic materials

Kavich, Jerald
Quantum Theory of Materials

Kentzinger, Emmanuel
Scattering methods

Koch, Erik Eduard
Quantum Theory of Materials

Köbler, Ulrich
Scattering methods

Kögerler, Paul
Electronic properties

Kohlstedt, Herbert Hermann
Electronic materials

Kriegs, Hartmut Oskar Kurz
Soft condensed matter

Krug, Ingo Peter
Electronic properties

Kügeler, Carsten
Electronic materials

Landrock, Sebastian
Microstructure research

Lang, Peter Robert
Soft condensed matter

Lazic, Predrag
Quantum Theory of Materials

Lentzen, Markus
Microstructure research

Lettinga, Minne Paul
Soft condensed matter

Lezaic, Marjana
Quantum Theory of Materials

Liebsch, Ansgar
Quantum Theory of Materials

Lonetti, Barbara
Neutron scattering

Lounis, Samir
Quantum Theory of Materials

Lustfeld, Hans
Quantum Theory of Materials

Luysberg, Martina
Microstructure research

Mattauch, Stefan Hans Josef
Jülich Centre for Neutron Science

Matthes, Frank
Electronic properties

Mavropoulos, Phivos
Quantum Theory of Materials

McPhie, Mathieu Gordon
Soft condensed matter

Meier, Gerhard
Soft condensed matter

Meuffels, Paul
Electronic materials

Meyer, Carola
Electronic properties

Mi, Shaobo
Microstructure research

Miao, Jun
Electronic materials

Mittal, Ranjan
Jülich Centre for Neutron Science

Monkenbusch, Michael
Neutron scattering

Müller-Krumbhaar, Heiner
Theory of structure formation

Nägele, Gerhard
Soft condensed matter

Niu-Ebert, Aizhen
Neutron scattering

Noguchi, Hiroshi
Theoretical Soft-Matter and Biophysics

Nünighoff, Kay Uwe
Scattering methods

Ohl, Michael
Neutron scattering

Paul, Amitesh
Scattering methods

Persson, Bo
Quantum Theory of Materials

Perßon, Jörg
Scattering methods

Pertsev, Nikolay
Electronic materials

Petraru, Adrian Ion
Electronic materials

Pilipenko, Denis
Theory of structure formation

Pipich, Vitaliy
Jülich Centre for Neutron Science

Pithan, Christian
Electronic materials

Plucinski, Lukasz
Electronic properties

Pollmeier, Klaus
Scattering methods

Poppe, Ulrich
Microstructure research

Prager, Michael
Neutron scattering

Pyckhout-Hintzen, Wim
Neutron scattering

Radulescu, Aurel
Jülich Centre for Neutron Science

Rata, Aurora Diana
Electronic properties

Richter, Dieter
Neutron scattering

Ripoll Hernando, Maria Soledad
Theoretical Soft-Matter and Biophysics

Rücker, Ulrich
Scattering methods

Rüdiger, Andreas
Electronic materials

Sager, Wiebke
Soft condensed matter

Saptsov, Roman
Theory of structure formation

Sarau, George
Electronic properties

Schindlmayr, Arno
Quantum Theory of Materials

Schmalzl, Karin Elisabeth
Jülich Centre for Neutron Science

Schmidt, Wolfgang
Jülich Centre for Neutron Science

Schneider, Claus Michael
Electronic properties

Schneider, Gerald-Johannes
Jülich Centre for Neutron Science

Schroeder, Herbert
Electronic materials

Schütz, Gunter-Markus
Theoretical Soft-Matter and Biophysics

Schwahn, Dietmar
Neutron scattering

Schweika, Werner
Scattering methods

Spatschek, Robert Philipp Maximilian
Theory of structure formation

Stellbrink, Jörg
Neutron scattering

Su, Yixi
Jülich Centre for Neutron Science

Szot, Krzysztof
Electronic materials

Tao, Yu-Guo
Theoretical Soft-Matter and Biophysics

Terashita, Hirotoshi
Scattering methods

Thust, Andreas
Microstructure research

Tillmann, Karsten
Microstructure research

Tuinier, Remko
Soft condensed matter

Upadhyay, Chandan
Soft condensed matter

Urban, Knut
Microstructure research

Vliegenthart, Gerard Adriaan
Theoretical Soft-Matter and Biophysics

Voigt, Jörg Jakob
Jülich Centre for Neutron Science

Waser, Rainer
Electronic materials

Watanabe, Takayuki
Electronic materials

Wegewijs, Maarten Rolf
Theory of structure formation

Weides, Martin Peter
Electronic materials

Wiegand, Simone
Soft condensed matter

Wiemann, Carsten
Electronic properties

Willner, Lutz
Neutron scattering

Winkler, Roland
Theoretical Soft-Matter and Biophysics

Wischnewski, Andreas
Neutron scattering

Wortmann, Daniel
Quantum Theory of Materials

Wuttke, Joachim
Jülich Centre for Neutron Science

Xiao, Yinguo
Scattering methods

Yan, Ming
Electronic properties

Yoon, Songhak
Electronic materials

Zamponi, Michaela
Jülich Centre for Neutron Science

Zeller, Rudolf
Theory of structure formation

Zorn, Reiner
Neutron scattering

Graduate Students

Al-Zubi, Ali
Quantum Theory of Materials

Betzinger, Markus
Quantum Theory of Materials

Brodeck, Martin
Neutron scattering

Chen, Han Yuan
Microstructure research

Disch, Sabrina
Scattering methods

Dolfen, Andreas
Quantum Theory of Materials

Feygenson, Mikhail
Scattering methods

Fleck, Michael
Theory of structure formation

Frank, Sandra
Theoretical Soft-Matter and Biophysics

Freimuth, Frank
Quantum Theory of Materials

Fu, Zhendong
Scattering methods

Gierlich, Andreas Gottfried
Quantum Theory of Materials

Gliga, Sebastian
Electronic properties

Gögelein, Christoph
Soft condensed matter

Gugenberger, Clemens
Theory of structure formation

Heers, Swantje
Quantum Theory of Materials

Heidelmann, Markus
Microstructure research

Hüter, Claas
Theory of structure formation

Kleshchanok, Dzina
Soft condensed matter

Kowalzik, Peter
Electronic materials

Korolkov, Denis
Scattering methods

Lehndorff, Ronald
Electronic properties

Lennartz, Maria Christina
Electronic materials

Li, Haifeng
Scattering methods

Lipinska-Chwalek, Marta Agata
Microstructure research

Maccarrone, Simona
Neutron scattering

Manheller, Marcel
Electronic materials

Mayorova, Maria
Neutron scattering

Meier, Matthias
Electronic materials

Menke, Tobias
Electronic materials

Mennig, Martin Julius
Electronic properties

Meßlinger, Reginhard Sebastian
Theoretical Soft-Matter and Biophysics

Müller, Martina
Electronic properties

Müller-Meskamp, Lars
Electronic materials

Münstermann, Ruth Christine
Electronic materials

Nandy, Bidisha
Theory of structure formation

Nauenheim, Christian
Electronic materials

Niedzwiedz, Katarzyna
Neutron scattering

Ning, Hui
Soft condensed matter

Nusser, Klaus
Neutron scattering

Pavlyuchkov, Dmytro
Microstructure research

Polyakov, Pavel
Soft condensed matter

Rahmanizadeh, Kourosh
Theory of structure formation

Reckermann, Felix David
Theory of structure formation

Röhrig, Serge
Electronic materials

Roitsch, Stefan
Microstructure research

Schindler, Christina
Electronic materials

Schützendorf, Patrick Rene
Electronic materials

Shanmugavadivelu, Gopinath
Soft condensed matter

Shen, Wan
Electronic materials

Soni, Rohit
Electronic materials

Spudat, Chrisian
Electronic properties

Tranca, Ionut Claudiu
Theory of structure formation

Woodford, Simon
Quantum Theory of Materials

Wysocki, Adam Miroslaw
Theoretical Soft-Matter and Biophysics

Yang, Chunyan
Quantum Theory of Materials

Yang, Lin
Electronic materials

Yang, Yingzi
Theoretical Soft-Matter and Biophysics

Zhang, Zhenkun
Soft condensed matter

Technical Staff

Bergs, Wolfgang
Scattering methods

Bickmann, Konrad
Electronic properties

Bierfeld, Hermann-Josef
Electronic materials

Bläsen, Franz
Networks and Numerical Methods

Bongartz, Dieter
Networks and Numerical Methods

Bremen, Arnd
Design/Workshop

Bünten, Ulrich
Neutron scattering

Bünten, Wilhelm Detlef
Neutron scattering

Bussmann, Klaus Max
Scattering methods

de Waal, Sylvia-Maria
Soft condensed matter

Emmerich, Hans-Matthias
Design/Workshop

Erven, Andreas
Jülich Centre for Neutron Science

Esser, Heinz-Peter
Design/Workshop

Feilbach, Herbert
Design/Workshop

Frech, Stephan
Neutron scattering

Friedrich, Jochen
Electronic materials

Funk-Kath, Ursula
Networks and Numerical Methods

Gebauer, Manfred
Electronic materials

Gehlhaar, Reimund Werner
Design/Workshop

Gerst, Marcel
Electronic materials

Gossen, Frank
Jülich Centre for Neutron Science

Graf, Karl-Heinz
Microstructure research

Hahn, Christoph
Networks and Numerical Methods

Haselier, Haselier
Electronic materials

Heckmann, Reinhardt
Networks and Numerical Methods

Heiderich, Manfred
Neutron scattering

Heinen, Josef
Networks and Numerical Methods

Henkel, Dorothea
Networks and Numerical Methods

Hermanns, Bernd
Electronic materials

Heydmann, Philipp
Networks and Numerical Methods

Hiller, Peter
Scattering methods

Hintzen, Maria-Elisabeth
Neutron scattering

Hirtz, Kurt
Design/Workshop

Hoffmann, Hans-Jürgen
Soft condensed matter

Hölzle, Micha Marc Gerhard
Jülich Centre for Neutron Science

Horriar-Esser, Christel
Scattering methods

Jansen, Thomas
Design/Workshop

John, Holger
Electronic materials

Johnen, Karl-Heinz
Design/Workshop

Jungbluth, Heinrich
Scattering methods

Kinzel, Gernot
Networks and Numerical Methods

Klein, Horst
Scattering methods

Kluck, Günther
Neutron scattering

Köhne, Franz-Josef
Electronic properties

Kohnke, Thomas
Jülich Centre for Neutron Science

Kozielewski, Tedeusz
Neutron scattering

Küpper, Bernhard
Electronic properties

Küssel, Eckhard
Scattering methods

Lauer, Jürgen
Electronic properties

Leuchtenberg, Anton
Design/Workshop

Lingenbach, Peter Josef
Design/Workshop

Macht, Kay
Jülich Centre for Neutron Science

Makovicka, Cerstin
Electronic materials

Matulewski, Anton
Design/Workshop

Meertens, Doris
Microstructure research

Nebel, Andreas Fabian
Jülich Centre for Neutron Science

Nguyen, Vu-Thanh
Neutron scattering

Olefs, Bodo-August
Networks and Numerical Methods

Ossovyi, Vladimir
Jülich Centre for Neutron Science

Pfeifer, Heinz
Electronic properties

Pieper, Werner
Microstructure research

Pohl, Maria
Design/Workshop

Radermacher, Bert Hubert
Design/Workshop

Rehfisch, Jessica
Design/Workshop

Reisen, Christian
Neutron scattering

Sachsenhausen, Hans-Rudolf
Design/Workshop

Sausen-Malka, Ulrike
Neutron scattering

Schätzler, Reinhardt
Neutron scattering

Schätzler, Liane
Networks and Numerical Methods

Schmidt, Marita
Microstructure research

Schmitz, Berthold-Klaus
Scattering methods

Schneider, Harald Michael
Jülich Centre for Neutron Science

Schnitzler, Helmut-Hubert
Design/Workshop

Schnitzler, Jens-Willi
Design/Workshop

Schramm, Franz-Josef
Design/Workshop

Schreiber, Reinert
Electronic properties

Schumacher, Miriam Helga
Networks and Numerical Methods

Sellinghoff, Karin
Soft condensed matter

Speen, Hans-Rolf
Microstructure research

Starc, Thomas
Neutron scattering

Stefelmanns, Hans-Peter
Design/Workshop

Stollenwerk, Robert
Neutron scattering

Stronciwilk, Peter
Jülich Centre for Neutron Science

Sybertz, Wilma
Microstructure research

Terberger, Hernz
Accelerator Group

Thomas, Carsten
Microstructure research

Thomas, Rita
Networks and Numerical Methods

Triefenbach, Dieter
Soft condensed matter

Vehres, Guido
Neutron scattering

Wassenhoven, Gabriele-Marie
Microstructure research

Werges, Fred
Scattering methods

Westphal, Elmar
Networks and Numerical Methods

Wingerath, Kurt
Networks and Numerical Methods

Würtz, Eva Maria
Microstructure research

Administrative Staff and Secretaries

Böhr, Heinz-Peter
Administration

Borges, Martina
Neutron scattering

Deckwitz, Susanne
Administration

Garcia y Gonzales, Maria
Electronic materials

Geisler, Helmut
Administration

Göcking, Marie-Luise
Soft condensed matter

Gollnick, Jutta
Electronic properties

Griesen, Johann Engelbert
Administration

Hölzle, Rainer
Accelerator Group

Köppchen, Barbara-Dorothea
Scattering methods

Mintmans, Stephanie
Jülich Centre for Neutron Science

Mirea, Elena
Administration

Ockenfels, Silke
Administration

Opitz, Daniela
Neutron scattering

Oubenkhir, Saida
Neutron scattering

Paffen, Helga
Theoretical Soft-Matter and Biophysics

Rische-Radloff, Ingrid
Microstructure research

Schlotmann, Dirk
Administration

Schnitzler, Anna Christine
Neutron scattering

Sittardt, Hanne
Administration

Snyders, Friederike-Luise
Theory of structure formation

Wassenhoven, Gertrud
Administration

Wenzik, Angela
Technical Services and Administration

Winkler, Ute
Quantum Theory of Materials

Scientists on Leave

Appavou, Marie-Sousai Deveram
Jülich Centre for Neutron Science, München, Germany

Arend, Nikolas
Jülich Centre for Neutron Science, München, Germany

Auth, Thorsten
Weizmann-Institut, Israel

Bo, Persson
Spallation Neutron Source, Oak Ridge, USA

Busch, Peter
Jülich Centre for Neutron Science, München, Germany

Brodeck, Martin
Donostia International Physical Center, San Sebastian, Spanien

Deac-Renner, Alina Maria
Spallation Neutron Source, Oak Ridge, USA

Frielinghaus, Henrich
Jülich Centre for Neutron Science, München, Germany

Goerigk, Günter
Jülich Centre for Neutron Science, München, Germany

Gutberlet, Thomas
Jülich Centre for Neutron Science, München, Germany

Holderer, Olaf
Jülich Centre for Neutron Science, München, Germany

Ioffe, Alexander
Jülich Centre for Neutron Science, München, Germany

Jiang, Ying
Chinese Academy of Science, Beijing, China

Jiang, Xiuli
Jülich Centre for Neutron Science, München, Germany

Mattauch, Stefan Hans Josef
Jülich Centre for Neutron Science, München, Germany

Mittal, Ranjan
Jülich Centre for Neutron Science, München, Germany

Müller, Martina
Francis Bitter Magnet Laboratory, Massachusetts, USA

Nünighoff, Kay Uwe
Hahn-Meitner-Institut, Berlin, Germany

Pipich, Vitaliy
Jülich Centre for Neutron Science, München, Germany

Radulescu, Aurel
Jülich Centre for Neutron Science, München, Germany

Schindlmayr, Arno
University of Paderborn, Germany

Schmalzl, Karin Elisabeth
Institut Laue Langevin, Grenoble, France

Schmidt, Wolfgang
Institut Laue Langevin, Grenoble, France

Schneider, Gerald-Johannes
Jülich Centre for Neutron Science, München, Germany

Spatschek, Robert Phillip
University of California, Davis, USA

Su, Yixi
Jülich Centre for Neutron Science, München, Germany

Wuttke, Joachim
Jülich Centre for Neutron Science, München, Germany

Yang, Chunyan
Chinese Academy of Science, Beijing, China

Zamponi, Michaela
Spallation Neutron Source , Oak Ridge, USA

Guest Scientists

Australia

Foster, Dr., Leslie John Ray
Neutron scattering
University of New South Wales, Sydney

Belgium

Reddy, Naveen Krishna
Soft condensed matter
Katholieke Universiteit Leuven

Verberck, Bart
Theoretical Soft-Matter and Biophysics
University of Antwerp

Brasil

Lazo, Matheus
Theoretical Soft-Matter and Biophysics
Universidade Federel de Santa Maria, Alegrete

Rediguieri, Camila
Soft condensed matter
Universidade Sáo Paulo, Ribeirao Preto

Canada

Arrott, Prof. Dr., Anthony S.
Electronic properties
Simon Fraser University, Vancouver

Schmidt, Benjamin
Theoretical Soft-Matter and Biophysics
University of Toronto

China

Fu, Zhendong
Scattering methods
Peking University, Beijing

Han, Xiujun
Theory of structure formation
Northwestern Polytechnical University, Xian

Jiang, Ying
Microstructure research
Chinese Academy of Sciences Peking

Li, Ying
Electronic materials
Xian University

Liu, Yaowen
Electronic properties
Tongli Universität, Shanghai

Na, Lei
Electronic properties
Fudan University Shanghai

Tian, Gengfang
Scattering methods
China Institute of Atomic Energy, Beijing

Xia, Junhai
Microstructure research
Dalian University of Technology, Liaoning Province

Yang, Hao
Electronic materials
Chinese Academy of Sciences Peking

Zhou, Zhiyay
Electronic materials
Chinese Academy of Sciences Shanghai

Denmark

Sivebak, Ion
Quantum Theory of Materials
Technical University of Denmark

Finland

Akola, Dr., Jaakko Eemeli
Quantum Theory of Materials
University of Jyväskylä

France

Baud, Stephanie
Quantum Theory of Materials
Laboratoire de Physique Moleculaire, Besancon Cedex

Bécu, Dr., Lydiane
Soft condensed matter
Polymeres, Colloides, Interfaces (CNRS), Le Mans

Cherifi, Salia
Electronic properties
CNRS Laboratoire Neal, Grenoble

Heinrich, Dr., Martine
Neutron scattering
Louis Pasteur University, Strasbourg

Zaccai, Joseph
Neutron scattering
Institut de Biologie Structurale, Grenoble

Zhang, Zhenkun
Soft condensed matter
C.R.P.P Avenue Albert Schweitzer, Pessac

Germany

Alami, Dr., Jones
Microstructure research
RWTH Aachen

Al-Hada, Dr., Mohamed
Electronic properties
Technische Universität Berlin

Arunthavarajah, Abiramy
Soft condensed matter
Fachhochschule Jülich

Belushkin, Maxime
Neutron scattering
Universität Bonn

Betzinger, Markus
Quantum Theory of Materials
RWTH Aachen

Böttger, Dr., Ulrich
Electronic materials
RWTH Aachen

Boussinot, Dr., Guillaume
Theory of Structure Formation
RWTH Aachen

Bräuhaus, Dennis
Electronic materials
RWTH Aachen

Caciuc, Dr., Vasile
Quantum Theory of Materials
Westfälische Wilhelms-Univerisität, Münster

Clemens, Sven
Electronic materials
RWTH Aachen

Darlinski, Grzegorz
Electronic materials
RWTH Aachen

Dehoff, Carsten
Electronic materials
RWTH Aachen

Dimyati, Dr., Arbi
Microstructure research
RWTH Aachen

Dippel, Ann-Christin
Electronic materials
RWTH Aachen

Dronskowski, Dr., Richard
Scattering methods
RWTH Aachen

Egelhaaf, Prof. Dr., Stefan Ulrich
Neutron scattering
Heinrich-Heine Universität, Düsseldorf

Evertz, Udo
Electronic materials
RWTH Aachen

Farahzadi, Azadeh
Quantum Theory of Materials
RWTH Aachen

Fechler, Nina
Soft condensed matter
Universität Kassel

Gabel, Sebastian
Soft condensed matter
RWTH Aachen

Ghadimi, Dr. rer. nat., Reza
Microstructure research
RWTH Aachen

Glatzel, Stefan
Soft condensed matter
Universität Kassel

Grychtol, Patrik
Electronic properties
Universtität Kaiserslautern

Haan, Matthias
Theoretical Soft-Matter and Biophysics
Universität Duisburg-Essen

Harneit, Wolfgang
Electronic properties
Freie Universität Berlin

Heilmann, David Bernhard
Quantum Theory of Materials
Rheinische Friedrich-Wilhelms-Universität Bonn

Heins, Martina
Electronic materials
RWTH Aachen

Heiß, Dr. rer. nat., Wolf-Alexander
Neutron scattering
Universitätsklinikum Aachen

Hennings, Dr. rer. nat., Detlef
Electronic materials
Philips Forschungslabor Aachen

Hönig, Andreas
Quantum Theory of Materials
Stiftung Caesar Bonn

Hoser, Dr., Andrzej
Scattering methods
Universität Hannover

Houben, Andreas
Scattering methods
RWTH Aachen

Jansen, Ekkehard
Scattering methods
Universität Bonn

Jungblut, Swetlana
Soft condensed matter
Johannes-Gutenberg-Universität Mainz

Kaiser, Alexander
Electronic properties
Universität Duisburg-Essen

Kever, Thorsten
Electronic materials
RWTH Aachen

Keymer, Jürgen
Quantum Theory of Materials
Max-Planck-Institut Stuttgart

Kikuchi, Norio
Theoretical Soft-Matter and Biophysics
Martin-Luther-Univerisität Halle Wittenberg

Klemradt, Dr. rer. nat., Uwe
Electronic materials
RWTH Aachen

Klopstra, Bart
Electronic materials
RWTH Aachen

Kögerler, Paul
Electronic properties
RWTH Aachen

Konstantinidis, Nikolaos
Theory of structure formation
RWTH Aachen

Linn, Eike
Electronic materials
RWTH Aachen

Madenci, Dilek
Neutron scattering
Heinrich-Heine Universität, Düsseldorf

Mayer, Prof. Dr., Joachim
Microstructure research
RWTH Aachen

Menzel, Stephan
Electronic materials
RWTH Aachen

Mesic, Biljana
Electronic materials
Technische Universität Clausthal-Zellerfeld

Mokrousov, Dr., Yuriy
Quantum Theory of Materials
Universität Hamburg

Müller, Paul
Scattering methods
RWTH Aachen

Plonka, Rafael
Electronic materials
RWTH Aachen

Reichenberg, Bernd
Electronic materials
RWTH Aachen

Sacharow, Lilli
Quantum Theory of Materials
Universität Hamburg

Sangiovanni, Giorgio
Quantum Theory of Materials
Max-Planck-Institut Stuttgart

Sarau, George
Electronic properties
Universität Duisburg-Essen

Sasioglu, Ersoy
Quantum Theory of Materials
Max-Planck-Institut Halle

Schmelzer, Sebastian
Electronic materials
RWTH Aachen

Schmitz, Thorsten
Electronic materials
aisACCT Systems GmbH, Aachen

Schneller, Theodor
Electronic materials
RWTH Aachen

Shanmugavadivelu, Gopinath
Soft condensed matter
Fachhochschule Aachen

Solbach, Axel
Electronic materials
RWTH Aachen

Sologubenko, Alla
Microstructure research
RWTH Aachen

Sottmann, Dr. rer. nat., Thomas
Neutron scattering
Universität zu Köln

Straube, Prof., Ekkehard
Neutron scattering
Martin-Luther-Univerisität Halle Wittenberg

Tiedke, Stephan
Electronic materials
RWTH Aachen

Uslu, Fahri
Microstructure research
RWTH Aachen

Weirich, Thomas
Microstructure research
RWTH Aachen

Weng, Robert
Electronic materials
RWTH Aachen

Greece

Iatrou, Dr., Ermolaos
Neutron scattering
University of Athens

Michailidou, Vassiliki
Soft condensed matter
FORTH Institute of Electronic Structure

Tsigkri, Angeliki
Soft condensed matter
Foundation for Research and Technology-Hellas

Voudouris, Panayiotis
Soft condensed matter
FORTH Institute of Electronic Structure Heraklion

Hungary

Bene, Dr., Julius
Quantum Theory of Materials
Roland Eötvös University Budapest

Kaufmann, Dr., Zotan
Quantum Theory of Materials
Roland Eötvös University Budapest

Szábo, Dr., Gabor
Quantum Theory of Materials
Roland Eötvös University Budapest

Vass, Szabolcs
Soft condensed matter
KFKI Atomic Energy Res. Institute, Budapest

India

Arya, Dr., Ashok
Microstructure research
Bhaba Atomic Research Centre, Trombay, Mumbal

Banerjee, Debjani
Electronic properties
Indian Institute of Technology, Mumbai

Chakraborty, Monodeep
Quantum Theory of Materials
Institute of Physics, Orissa

Chogondahalli Muniraju, Naveen Kumar
Scattering methods
Indian Institute of Science, Bangalore

Chowdhury, Debashish
Theoretical Soft-Matter and Biophysics
Indian Institute of Technology, Kanpur

Dattagupta, Sushanta Kumar
Theory of structure formation
IISER Kolkata

Mani Krishna, Karri Venkata
Microstructure research
Bhaba Atomic Research Centre, Trombay, Mumbal

Nandy, Bidisha
Theoretical Soft-Matter and Biophysics
Indian Institute of Technology, Kharagpur

Qureshi, Mohammad
Electronic properties
Indian Institute of Technology, Kanpur

Reddy, P. Kathik
Neutron scattering
Indian Institute of Technology, Assam

Soumya, Jyoti Ray
Electronic properties
Indian Institute of Science, Bangalore

Iran

Bamdad, Kourosh
Theoretical Soft-Matter and Biophysics
Tarbiat Modarres University, Tehran

Khoshnood, Atefeh
Theoretical Soft-Matter and Biophysics
Sharif University Tehran

Israel

Baran, Mor
Microstructure research
Technion Israel Institute of Technology, Haifa

Drozdow, Maria
Microstructure research
Technion Israel Institute of Technology, Haifa

Kaplan, Wayne
Microstructure research
Technion Israel Institute of Technology, Haifa

Kauffmann, Yaron
Microstructure research
Technion Israel Institute of Technology, Haifa

Sadan, Hila
Microstructure research
Technion Israel Institute of Technology, Haifa

Italy

Botti, Dr., Alberto
Neutron scattering
Universita di Roma Tre, Roma

Carbone, Dr., Guiseppe
Quantum Theory of Materials
Politecnico di Bari

Ferriani, Dr., Paolo
Quantum Theory of Materials
Physics Department Modena

Lamura, Antonio
Theoretical Soft-Matter and Biophysics
Instituto Applicazioni Calcolo, CNR, Bari

Mangiapia, Gaertano
Neutron scattering
Universita degli studi di Napoli

Perroni, Dr., Antonio Carmine
Quantum Theory of Materials
Physics Department Napoli

Picozzi, Dr., Silvia
Quantum Theory of Materials
Universita di L'Aquila

Popkov, Vladislav
Theoretical Soft-Matter and Biophysics
Università degli Studi di Salerno

Tartaglino, Ugo
Quantum Theory of Materials
INFM Democtritos National Simulation Center, Trieste

Triolo, Alessandro
Neutron scattering
IPCF-CNR, Messina

Japan

Egami, Yoshiyuki
Quantum Theory of Materials
Osaka University, Osaka

Ishida, Hiroshi
Quantum Theory of Materials
Nihon University, Tokyo

Katayama-Yoshida, Hiroshi
Theory of structure formation
Osaka University, Osaka

Kita, Rio
Soft condensed matter
Tokai University Hiratsuka

Kojo, Masashi
Quantum Theory of Materials
Osaka University, Osaka

Kotani, Prof., Takao
Quantum Theory of Materials
Osaka University, Osaka

Ogura, Dr., Masako
Theory of Structure Formation
Osaka University, Osaka

Ohta, Tadashi
Quantum Theory of Materials
Osaka University, Osaka

Ono, Dr., Tomoya
Quantum Theory of Materials
Osaka University, Osaka

Sato, Kazunori
Theory of structure formation
Department of condensed matter physics, Osaka

Shibuya, Kesiuke
Electronic materials
University of Tokyo, Kashiwa

Shishidou, Tatsuya
Quantum Theory of Materials
Hiroshima Science University

Taniguchi, Takashi
Soft condensed matter
Yamagata University

Watanabe, Dr., Taka
Electronic materials
Department of Innovative and Engineered Materials, Midori-ku

Yamauchi, Kunihiko
Quantum Theory of Materials
Osaka University

Yanagisawa, Susumu
Quantum Theory of Materials
Osaka University

Korea

Jeong, Doo Seok
Electronic materials
Seoul National Univeristy Shillim-dong, Gwanak-gu

Kim, Seong Keun
Electronic materials
Seoul National Univeristy Shillim-dong, Gwanak-gu

Yoon, Songhak
Electronic materials
Department of Materials Sci. & Eng., Pohang

Netherlands

Bouhassoune, Mohammed
Quantum Theory of Materials
Eindhoven University of Technology, Einhoven

Poland

Banachowicz, Dr., Ewa
Soft condensed matter
A. Mieckiewicz University, Poznan

Cichocki, Prof. Dr., Bogdan
Soft condensed matter
University of Warsaw

Gapinski, Dr., Jacek
Soft condensed matter
A Mickiewicz University, Poznan

Grzelakowski, Krzysztof Piotr
Electronic properties
Wroclaw University

Kowalski, Wojciech
Microstructure research
University of Silesia, Kattowice

Patkowski, Prof., Adam
Soft condensed matter
A. Mieckiewicz University, Poznan

Pilch, Michal
Electronic materials
University of Silesia, Kattowice

Ratajczyk, Dr., Monika
Soft condensed matter
A. Mieckiewicz University, Poznan

Romania

Chelaru, Dr., Liviu Ionut
Electronic properties
University Lasi

Russia

Bodnarchuk, Victor
Jülich Centre for Neutron Science
Joint Institute for Nuclear Research, FLNP, Dubna

Marchenko, Vladimir
Theory of structure formation
Russian Academy of Science, Chernogolovka

Rzhevsky, Alexey
Electronic properties
Ioffe Institute, St. Petersburg

Samoilov, Prof. Dr., Vladimir
Quantum Theory of Materials
Moscow State University

Volokitin, Alexander
Quantum Theory of Materials
Department of Physics, Samara

Spain

Arbe, Dr., Maria Aranzazu
Neutron scattering
Università degli Studi di Salerno

Avila, Dr., David
Microstructure research
Universidad Complutense de Madrid

Banchio, Prof. Dr., Adolfo
Soft condensed matter
Universidad Nacional de Cordoba

Colmenero, Prof. Dr., Juan
Neutron scattering
Universidad del País Vasco, San Sebastian

Hijon de Miguel, Carmen
Theoretical Soft-Matter and Biophysics
University of Madrid

Lund, Dr., Reidar
Neutron scattering
Università degli Studi di Salerno

Pardo Soto, Luis Carlos
Jülich Centre for Neutron Science
Ministerio de Educacion y Ciencia CMECI, Madrid

Sweden

Bergqvist, Lars, Tore
Theory of structure formation
Uppsala University

Swiss

Vavrin, Ronny
Soft condensed matter
ETHZ & PSI, Villigen

Taiwan

Kuan, Jean-Feng
Theoretical Soft-Matter and Biophysics
National Center for High Performance

Lin, Jung-Hsing
Quantum Theory of Materials
Research Center for Applied Science, Taipei

Liu, Ming-Hao
Quantum Theory of Materials
National Taiwan University

Ukraine

Velikanova, Tamara
Microstructure research
National Academy of Sciences of Ukraine, Kiev

Zaikina, Oleksandra
Microstructure research
I. N. Frantsevich Institut Materials Science, Kiev

USA

Burkhardt, Theodore
Theoretical Soft-Matter and Biophysics
Temple University, Philadelphia

Fadley, Prof. Dr., Charles
Electronic properties
ALS Berkeley

Fetters, Dr., Lewis J.
Neutron scattering
Cornell University

Kavich, Jerald
Quantum Theory of Materials
Argonne National Laboratory

Luettmer-Strathmann, Jutta
Soft condensed matter
University of Akron

Luo, Yuan Lung
Quantum Theory of Materials
University of Washington, Seattle

Slonczewski, John
Electronic properties
IBM Yorktown, New York

Velev, Julian
Quantum Theory of Materials
University of Nebraska-Lincoln

Wignall, Dr., George D.
Neutron scattering
Oak Ridge National Laboratory, Tennessee

IFF Scientists Teaching at Universities

PD Dr. Artur Baumgärtner
Duisburg

Prof. Paul-Siegfried Bechthold
Köln

Prof. Stefan Blügel
Aachen

Prof. Thomas Brückel
Aachen

PD Dr. Daniel-Emil Bürgler
Köln

Prof. Jan-Karel Dhont
Düsseldorf

PD Dr. Philipp-Georg Ebert
Aachen

Prof. Gerhard Gompper
Köln

PD Dr. Riccardo Hertel
Halle-Wittenberg

PD Dr. Erik E. Koch
Aachen

PD Dr. Herbert H. Kohlstedt
Köln

PD Dr. Peter R. Lang
Düsseldorf

PD Dr. Hans Lustfeld
Duisburg

Prof. Heiner Müller-Krumbhaar
Aachen

Prof. Gerhard Nägele
Düsseldorf

Prof. Eva Pavarini
Aachen

Prof. Dieter Richter
Münster

Prof. Claus M. Schneider
Duisburg-Essen

Prof. Herbert Schroeder
Aachen

Prof. Gunter-Markus Schütz
Bonn

PD Dr. Werner Schweika
Aachen

Prof. Krzysztof Szot
Katowice

Dr. Remco Tunier
Aachen

Prof. Knut Urban
Aachen

Prof. Rainer Waser
Aachen

PD Dr. Simone Wiegand
Köln

Prof. Roland Winkler
Ulm

PD Dr. Reiner Zorn
Münster

Imprint

Published by:
Forschungszentrum Jülich GmbH
Institut für Festkörperforschung (IFF)
52425 Jülich, Germany

Phone: +49 2461 61-4465
Fax: +49 2461 61-2410

E-mail: wwwiff@fz-juelich.de
Internet: www.fz-juelich.de/iff/e_iff

Conception and Editorial:
Angela Wenzik
Claus M. Schneider
(IFF)

Design and Graphics:
Clarissa Reisen
Dieter Laufenberg
(Graphic Department)

Layout Research Reports:
Ursula Funk-Kath
Dorothea Henkel
Liane Schätzler
Kurt Wingerath
(IFF)

Pictures:
Forschungszentrum Jülich
except otherwise noted

Print:
Medienhaus Plump GmbH
Rheinbreitbach

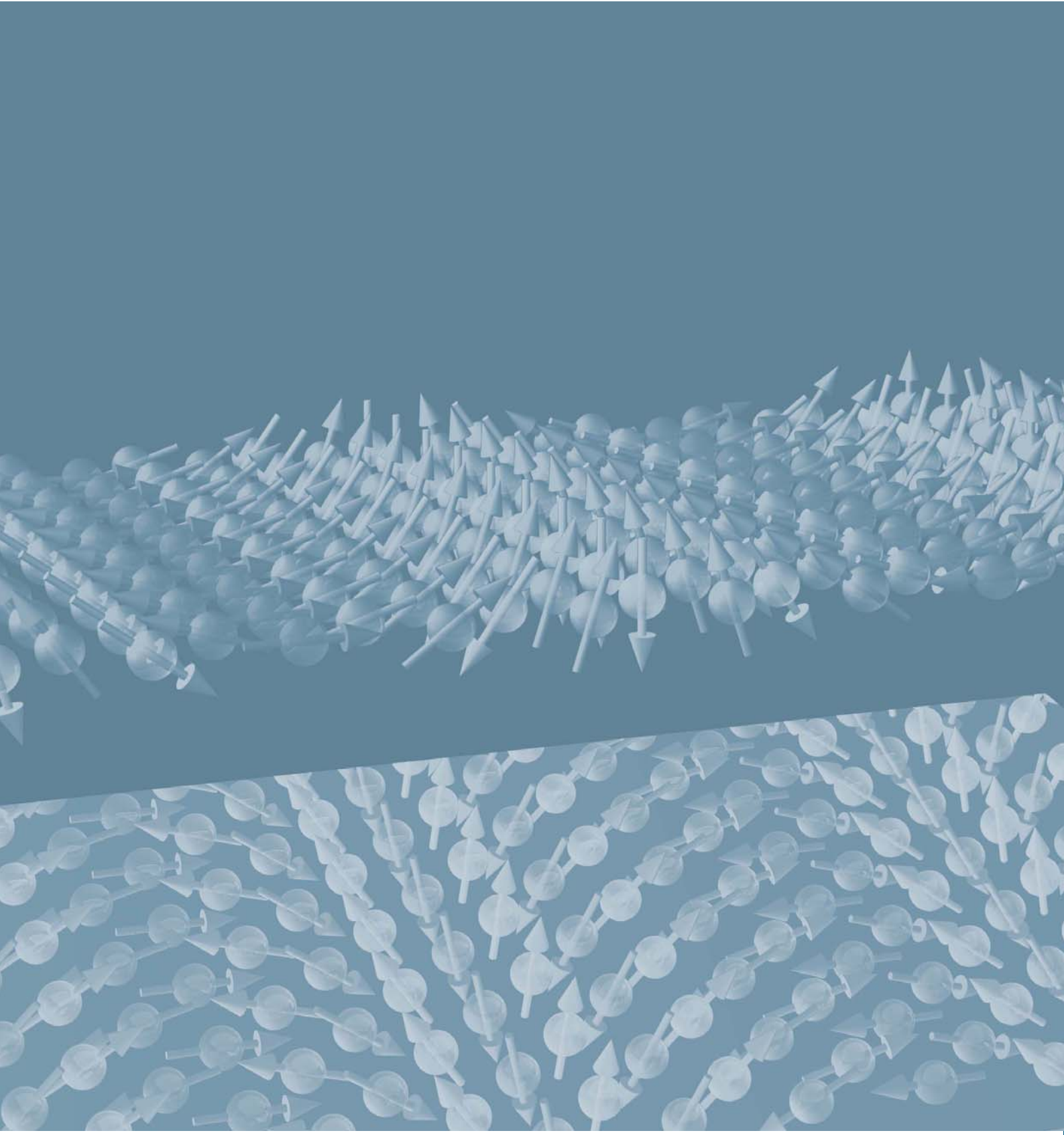

JÜLICH
FORSCHUNGSZENTRUM